Quantitative Characterization of Impacts of Coupled Geomechanics and Flow on Safe and Permanent Geological Storage of CO_2 in Fractured Aquifers

Award Number: DE-FE0023305

Final Scientific Report
Project period: 1 October 2014 – 30 September 2018

Prepared for:
U.S. Department of Energy
National Energy Technology Laboratory

31 December 2018

PI: Professor Yu-Shu Wu, Colorado School of Mines

(ywu@mines.edu, 303-384-2093)

Submitted by: Dr. Philip Winterfeld, Co-PI, Colorado School of Mines

(pwinterf@mines.edu, 303-384-2366)

Submitting Organizations: Colorado School of Mines
1500 Illinois St., Golden, CO 80401

Lawrence Berkeley National Lab
1 Cyclotron Road, Berkeley, CA 94720

Philip H. Winterfeld

Digitally signed by Philip H. Winterfeld
DN: cn=Philip H. Winterfeld, o=Colorado School of Mines, ou=Petroleum Engineering Department, email=pwinterf@mines.edu, c=US
Date: 2018.12.19 11:31:51 -07'00'

Disclaimer

Abstract

This is the final scientific report for the award DE-FE0023305, entitled "Quantitative Characterization of Impacts of Coupled Geomechanics and Flow on Safe and Permanent Geological Storage of CO_2 in Fractured Aquifers." The work has been divided into six tasks.

In Task 2, we characterized rock properties, which are important when developing a quantitative approach for understanding and predicting geomechanical effects on large-scale CO_2 injection and long-term storage in the subsurface. Rock properties of interest for this characterization include porosity, permeability, elastic constants, strength, and heat capacity. We measured rock properties for three different rock types: concrete, sandstone and shale. These properties were obtained from the acoustic measurement, permeability and porosity measurement, Brazilian test, the uniaxial compressive test, and heat capacity measurement. Then, using the Brazilian technique to fracture samples, we measured their permeability under brine injection for varying effective stresses, followed by similar measurements of permeability under sc-CO_2 injection. Permeability to brine and sc-CO_2 decreased as the effective stress increased. The apparent permeability to sc-CO_2 was an order of magnitude less than that for brine, a consequence of CO_2 being the non-wetting fluid.

In Task 3, we developed understandings and correlations for CO_2 injection pressure induced fracturing. We initially fractured four eight inch cubes of concrete with brine to establish a standard test procedure. Then, additional concrete samples were fractured using brine. Confining stresses were exerted on the samples and brine was injected at a constant rate into a borehole that was previously drilled into the concrete cube. The borehole pressure was measured and fracture initiation was identified as a peak in the pressure profile. That was followed by fracture propagation, which was identified as a plateau in the pressure profile, and finally the fracture reached the sample surface. The sample surfaces were photographed before and after fracturing, which enabled determination of where the fracture reached the sample surface. Afterwards, aqueous food dye solution was injected into the fractured concrete samples to color the fracture planes. The borehole was filled with food dye solution in advance, a gas pulse was transmitted to the borehole, and the borehole was then shut in to allow the food dye to be driven into existing fractures. Then, the concrete samples were broken down by high-pressure gas injection to reveal the geometry and morphology of the hydraulic fractures. In addition, acoustic measurements were conducted on multiple locations on each face of the concrete samples before and after injection for comparison. This comparison was used to confirm changes in the internal structure of the concrete sample, namely the formation of fractures. There were six concrete samples fractured with brine. Afterwards, concrete samples were fracture using sc-CO_2. The main change in experimental procedure was the inclusion of temperature control, since in the field, we mostly encounter temperature and pressure conditions above the supercritical point of CO_2. The concrete samples were pre-heated in an oven to elevate their temperature, and thermal tape was used to heat the CO_2 to a temperature above its supercritical temperature. Two concrete samples were fractured using liquid CO_2, four concrete samples were fractured using gaseous CO_2, and twenty two concrete samples were fractured using sc-CO_2. For the concrete samples fractured using sc-CO_2, three had pre-existing hydraulic fractures on the surface near the wellbore, and two were water saturated (as opposed to containing only air). Two concrete samples were composite samples, with a high

permeability ball in the center, in order to represent CO_2 injection into a high permeability zone surrounded by a low permeability sealing formation. Later, we fractured five shale samples, obtained from the Niobrara shale outcrop, with sc-CO_2. The injection rate was constant, confining stresses were applied, the shale samples were pre-heated in an oven to the desired temperature, and the sample was then fractured. An analysis of the failure type was done for many of the concrete samples, based on the predicted break down pressure for tensile and shear failure, and it was found that most samples fractured due to shear failure. Also, the presence of induced fractures has little to no effect on the fracture initiation pressure, but significantly changes the fracture morphology. The CO_2 fracturing in water saturated samples behaved much similar to brine induced fracturing. There was a significant difference of breakdown pressure for injection of CO_2 and brine, where the breakdown pressure for CO_2 induced fracturing is generally around the minimum horizontal stress and that for brine is much higher. Finally, the fracture orientation for most samples with large confining stress differential was perpendicular to the minimum horizontal stress. When the stress differential, especially the difference between the two directions with the smallest stresses was small, the fracture orientation was determined not only by the minimum stress direction, but also the magnitude of the confining stress, the tensile strength of the rock, and the breakdown pressure.

In Task 4, we modified our coupled flow-geomechanical models to model fracture growth and propagation in storage formations and caprocks. These flow-geomechanical models are TOUGH2-CSM and TOUGH2-FLAC. The TOUGH2-CSM fluid and heat flow formulation is based on the TOUGH2 formulation of mass and energy conservation equations that govern fluid and heat flow in general multiphase, multicomponent, multi-porosity systems. The TOUGH2-CSM simplified geomechanical formulation is based on the linear theory of elasticity applied to multi-porosity non-isothermal (thermo-multi-poroelastic) media. We previously derived, from the fundamental relations of the linear theory of elasticity, an equation relating mean stress, pore pressures, temperatures, and body force (the Mean Stress equation) that we added to the TOUGH2-CSM fluid and heat flow equations. We extended the TOUGH2-CSM simplified geomechanical formulation to calculate the entire stress tensor by deriving equations for stress tensor components from derivatives of the Cartesian thermo-multi-poroelastic Navier equation components. In addition, we derived equations for stress tensor components in rz-coordinates. We solved these geomechanical equations using the integral finite difference method. This method utilizes momentum fluxes obtained by "factoring" a divergence operator out of each geomechanical equation.

In Task 5, we did a literature survey to determine suitable correlations for fracture initiation, growth, and propagation. After surveying numerous papers, we modified TOUGH2-CSM to model stress dependent fracture initiation and growth using the Mohr-Coulomb criterion for shear failure in faults and caprock and the condition of negative minimum effective stress for tensile failure. Tensile failure results in a fracture whose width depends on the difference between fracture pressure and minimum stress and whose propagation is based on the difference between the stress intensity factor at the fracture tip and the rock toughness. The TOUGH-FLAC model is based on the FLAC3D ubiquitous joint model, extended for the modeling of permeability changes induced by changes in effective normal stress across fractures as well permeability changes caused by shearing along fractures.

In Task 6, we validated our coupled flow-geomechanical models using analytical solutions and problems from the literature. We validated the TOUGH2-CSM modifications using analytical solutions to the displacement from a uniform load on a semi-infinite elastic medium and the two-dimensional Mandel-Cryer effect. Those were followed by a sample problem to test our stress tensor calculations, which was for injection into a single-phase reservoir with constant properties. Comparisons of our simulator to published results were done on for the depletion of a single-phase reservoir with stress dependent porosity, two examples from the In Salah gas project, an axisymmetric baserock–reservoir–caprock system with a normal faulting stress regime that had thermally induced shear stresses, simulations of CO_2 leakage through caprock in a two-dimensional reservoir in Cartesian coordinates, and predictions of caprock failure from CO_2 injection into an axisymmetric reservoir. Finally, we simulated CO_2 injection pressure-induced fracturing from one of our laboratory studies, Sample 39, and obtained a fracture profile.

We also validated the TOUGH2-FLAC model for fluid driven fracture growth against solutions based on the KGD model and a case with an inclined fracture that was loaded from the boundaries to achieve wing-crack propagation. The strain softening tensile behavior and softening of modulus considering a simple damage approach was verified by a simulation representing hydraulic fracturing stress measurement around a vertical well. Finally, the model was validated against deep fracture zone opening and surface uplift at In Salah with inverses analysis used to improve the match of simulation with field data.

In Task 7, we developed a scheme based on inverse modeling that can be used to identify caprock leakage. Injection of fluid into a reservoir results in a time varying pressure profile that depends on the properties of the rock and the fluid. The presence of significant caprock leakage would effect this pressure profile and we used inverse modeling, namely the Levenberg-Marquardt method, to determine the leakage location from the pressure profile. A two-dimensional and a three-dimensional example based on published data were presented. The published simulation was run and its results were considered as "field" data. In the two-dimensional example, a simulation of CO_2 injection into a two-dimensional aquifer-caprock system, the caprock had a vertical fault through which leakage could occur. The location of this leakage was obtained from our inverse modeling scheme. In the three-dimensional example, the simulation domain had four geological layers, one of which was the injection zone that contained a horizontal injection well. We simulated fractures as high permeability gridblocks, introduced a fracture that spanned the caprock depth, and ran a simulation to obtain "field" data. Then, using our inverse modeling scheme, we obtained the location of that fracture.

Table of Contents

Executive Summary

The primary objective of this project is to develop a quantitative approach for understanding and predicting geomechanical effects on large-scale CO_2 injection, flow and long-term storage in the subsurface with evaluation tools and techniques for assessing and validating CO_2 flow, storage potential and risk of leakage in fractured and/or porous reservoirs. The project will study injection pressure induced rock deformation and fracturing processes by combining laboratory studies and coupled flow-geomechanics modeling. The understandings and correlations obtained will be incorporated into the high-performance TOUGH2-CSM simulator developed at CSM and other specialized coupled geomechanics modeling tools developed at LBNL to develop modeling tools for modeling CO_2-injection induced rock mechanical processes associated with CO_2 storage in reservoirs to quantify flow, storage, and potential leakage pathways as well as remediation measures.

The project's tasks are listed below (Task 1 is project management).

Task 2. Development of correlations of CO_2 injection enhanced fracture permeability by laboratory studies.

Task 3. Development of fundamental understandings and correlations of occurrence of CO_2 injection pressure induced fracturing by laboratory studies.

Task 4**.** Development of CO_2 flow and geomechanics-coupled mathematical models and numerical schemes for modeling fracturing growth and propagation in storage formations and caprocks.

Task 5. Incorporation of CO_2 injection enhanced fracture properties and fracturing correlations/models into reservoir simulators.

Task 6. Concept and flow-mechanics coupled model validation using field data of stress measurement and/or land surface uprise.

Task 7. Development, implementation and application of advanced modeling and optimization schemes to maximize storage capacity and to identify leaking locations.

Tasks 4-6 are concerned with development and validation of simulation models and form a continuum. In what follows, elements of one of those tasks might appear in another.

In Task 2, we characterized rock properties, which are important when developing a quantitative approach for understanding and predicting geomechanical effects on large-scale CO_2 injection and long-term storage in the subsurface. Rock properties of interest for this characterization included porosity, permeability, elastic constants, strength, and heat capacity. We measured rock properties for three different rock types: concrete, sandstone and shale. These properties were obtained from the acoustic measurement, permeability and porosity

measurement, Brazilian test, the uniaxial compressive test, and the heat capacity measurement. Then, using the Brazilian technique to fracture samples, we measured their permeability under brine injection for varying effective stresses, followed by similar measurements of permeability under sc-CO_2 (super critical CO_2) injection. Permeability to brine and sc-CO_2 decreased as the effective stress increased. The apparent permeability to sc-CO_2 was an order of magnitude less than that for brine, a consequence of CO_2 being the non-wetting fluid.

In Task 3, we developed understandings and correlations for CO_2 injection pressure induced fracturing. We initially fractured four eight inch cubes of concrete with brine to establish a standard test procedure. Then, additional concrete samples were fracture using brine. Confining stresses were exerted on the samples and brine was injected at a constant rate into the borehole that was previously drilled into the concrete cubes. The borehole pressure was measured and fracture initiation was identified as a peak in the pressure profile, followed by fracture propagation, which was identified as a plateau in the pressure profile, and finally the fracture reached the sample surface. The sample surfaces were photographed before and after fracturing, which enabled identification of where the fracture reached the sample surface. Afterwards, aqueous food dye solution was injected into the fractured concrete samples to color the fracture planes. The borehole was filled with food dye solution in advance, a gas pulse was transmitted to the borehole, and the borehole was then shut in to allow the food dye to be driven into the existing fractures. Then, the concrete samples were broken down by high-pressure gas injection to reveal the geometry and morphology of the hydraulic fractures. In addition, acoustic measurements were conducted on multiple locations on each face of the concrete samples before and after brine for comparison. This comparison is used to confirm changes in the internal structure of the concrete sample, namely the formation of fractures. There were six concrete samples fractured with brine. Afterwards, concrete samples were fracture using sc-CO_2. The main change in experimental procedure was the inclusion of temperature control, since in the field, we mostly encounter temperature and pressure conditions above the supercritical point of CO_2. The concrete samples were pre-heated in an oven to elevate their temperature, and thermal tape was used to heat the CO_2 to a temperature above its supercritical temperature. Two concrete samples were fractured using liquid CO_2, four concrete samples were fractured using gaseous CO_2, and twenty two concrete samples were fractured using sc-CO_2. For the concrete samples fractured using sc-CO_2, three had pre-existing hydraulic fractures on the surface near the wellbore, and two were water saturated. Two concrete samples were composite samples, with a high permeability ball in the center, in order to represent CO_2 injection into a high permeability zone surrounded by a low permeability sealing formation. Later, we fractured five shale samples, obtained from the Niobrara shale outcrop, with sc-CO_2. The injection rate was constant, confining stresses were applied, the shale samples were pre-heated in an oven to the desired temperature, and the sample was then fractured. An analysis of the failure type was done for many of the concrete samples, based on the predicted break down pressure for tensile and shear failure, and it was found that most samples fractured due to shear failure. Also, the presence of induced fractures has little to no effect on the fracture initiation pressure, but significantly changed the fracture morphology. The CO_2 fracturing in water saturated samples behaved much similar to brine induced fracturing. There was a significant difference of breakdown pressure for injection of CO_2 and brine, where the breakdown pressure for CO_2 induced fracturing is generally around

the minimum horizontal stress and that for brine is much higher. Finally, the fracture orientation for most samples with large confining stress differential was perpendicular to the minimum horizontal stress. When the stress differential, especially the difference between two directions with smallest stresses, was small, the fracture orientation was dominated not only by the stress direction, but also the magnitude of the confining stress, tensile strength of the rock, and break down pressure.

In Task 4, we modified our coupled flow-geomechanical models to model fracture growth and propagation in storage formations and caprocks. These flow-geomechanical models are TOUGH2-CSM and TOUGH2-FLAC. The TOUGH2-CSM fluid and heat flow formulation is based on the TOUGH2 formulation of mass and energy conservation equations that govern fluid and heat flow in general multiphase, multicomponent, multi-porosity systems. The TOUGH2-CSM simplified geomechanical formulation is based on the linear theory of elasticity applied to multi-porosity non-isothermal (thermo-multi-poroelastic) media. We previously derived from the fundamental relations of the linear theory of elasticity an equation relating mean stress, pore pressures, temperatures, and body force (the Mean Stress equation) that we added to the TOUGH2-CSM fluid and heat flow equations. We extended the TOUGH2-CSM simplified geomechanical formulation to calculate the entire stress tensor by deriving equations for stress tensor components from derivatives of the Cartesian thermo-multi-poroelastic Navier equation components. In addition, we derived equations for stress tensor components in rz-coordinates. We solved these geomechanical equations using the integral finite difference method. That method utilized momentum fluxes obtained by "factoring" a divergence operator out of each geomechanical equation.

In Task 5, we did a literature survey to determine suitable correlations for fracture initiation, growth, and propagation. After surveying numerous papers, we modified TOUGH2-CSM to model stress dependent fracture initiation and growth using the Mohr-Coulomb criterion for shear failure in faults and caprock and the condition of negative minimum effective stress for tensile failure. Tensile failure results in a fracture whose width depends on the difference between fracture pressure and minimum stress and propagates based on the difference between the stress intensity factor at the fracture tip and the rock toughness. The TOUGH-FLAC model is based on the FLAC3D ubiquitous joint model, extended for the modeling of permeability changes induced by changes in effective normal stress across fractures as well permeability changes caused by shearing along fractures.

In Task 6, we validated our models using analytical solutions and problems from the literature. We validated the TOUGH2-CSM modifications using the analytical solutions to the displacement from a uniform load on a semi-infinite elastic medium and the two-dimensional Mandel-Cryer effect. Those were followed by a sample problem to test our stress tensor calculations, which was for injection into a single-phase reservoir with constant properties. Comparisons of our simulator to published results were done on for the depletion of a single-phase reservoir with stress dependent porosity, two examples for the In Salah gas project, an axisymmetric baserock–reservoir–caprock system with a normal faulting stress regime that had thermally induced shear stresses, simulations of CO_2 leakage through caprock in a two-dimensional reservoir in Cartesian coordinates, and predictions of caprock failure from CO_2

injection into an axisymmetric reservoir. Finally, we simulated CO_2 injection pressure-induced fracturing from one of our laboratory studies, Sample 39, and obtained a fracture profile.

We also validated the TOUGH2-FLAC model for fluid driven fracture growth against solutions based on the KGD model and a case with an inclined fracture that was loaded from the boundaries to achieve wing-crack propagation. The strain softening tensile behavior and softening of modulus considering a simple damage approach was verified by a simulation representing hydraulic fracturing stress measurement around a vertical well. Finally, the model was validated against deep fracture zone opening and surface uplift at In Salah with inverses analysis used to improve the match of simulation with field data.

In Task 7, we developed a scheme based on inverse modeling that can be used to identify caprock leakage. Injection of fluid into a reservoir results in a time varying pressure profile that depends on the properties of the rock and the fluid. The presence of significant caprock leakage would effect this pressure profile and we used inverse modeling, namely the Levenberg-Marquardt method, to determine the leakage location from the pressure profile. A two-dimensional and a three-dimensional example based on published data were presented. The published simulation was run and its results were considered as "field" data. In the two-dimensional example, a simulation of CO_2 injection into a two-dimensional aquifer-caprock system, the caprock had a vertical fault through which leakage could occur. The location of this leakage was obtained from our inverse modeling scheme. In the three-dimensional example, the simulation domain had four geological layers, one of which was the injection zone that contained a horizontal injection well. We simulated fractures as high permeability gridblocks, introduced a fracture that spanned the caprock depth, and ran a simulation to obtain "field" data. Then, using our inverse modeling scheme, we obtained the location of that fracture.

Report Details

The primary objective of this project is to develop a quantitative approach for understanding and predicting geomechanical effects on large-scale CO_2 injection, flow and long-term storage in the subsurface with evaluation tools and techniques for assessing and validating CO_2 flow, storage potential and risk of leakage in fractured and/or porous reservoirs. The project will study injection pressure induced rock deformation and fracturing processes by combining laboratory studies and coupled flow-geomechanics modeling. The understandings and correlations obtained will be incorporated into the high-performance TOUGH2-CSM simulator developed at CSM and other specialized coupled geomechanics modeling tools developed at LBNL to develop modeling tools for modeling CO_2-injection induced rock mechanical processes associated with CO_2 storage in reservoirs to quantify flow, storage, and potential leakage pathways as well as remediation measures.

The project's tasks are listed below (Task 1 is project management).

Task 2. Development of correlations of CO_2 injection enhanced fracture permeability by laboratory studies.

Task 3. Development of fundamental understandings and correlations of occurrence of CO_2 injection pressure induced fracturing by laboratory studies.

Task 4**.** Development of CO_2 flow and geomechanics-coupled mathematical models and numerical schemes for modeling fracturing growth and propagation in storage formations and caprocks.

Task 5. Incorporation of CO_2 injection enhanced fracture properties and fracturing correlations/models into reservoir simulators.

Task 6. Concept and flow-mechanics coupled model validation using field data of stress measurement and/or land surface uprise.

Task 7. Development, implementation and application of advanced modeling and optimization schemes to maximize storage capacity and to identify leaking locations.

Tasks 4-6 are concerned with development and validation of simulation models and form a continuum. In what follows, elements of one of those tasks might appear in another.

Task 2: Development of correlations of CO_2 injection enhanced fracture permeability by laboratory studies.

Rock Property Measurements

Characterizing rock properties are important when developing a quantitative approach for understanding and predicting geomechanical effects on large-scale CO_2 injection and long-term storage in the subsurface. Rock properties of interest for this characterization include porosity, permeability, elastic constants, strength, and heat capacity. We measured rock properties for three different rock types: concrete, sandstone and shale. The standards for tests obtaining these properties have dimensional requirements for the rock cores used in the tests, and Table 2.1 presents those standards. The measurements done are the acoustic one, permeability and porosity measurement, Brazilian test, and the uniaxial compressive test. The test for heat capacity is described later.

Table 2.1. Core dimension requirement for different measurements

Test	Concrete		Sandstone		Shale	
	Diameter (inch)	Length (inch)	Diameter (inch)	Length (inch)	Diameter (inch)	Length (inch)
Acoustic	2	4	1.5	3	1.5	3
Permeability & Porosity	1	1	1	1	1	1
Brazilian Test	2	1	1.5	0.75	1.5	0.75
Uniaxial Compression Test	2	4	1.5	3	1	2
					0.75	1.5

Acoustic measurement

The acoustic measurement provides the velocity of compressional and shear waves in the material. From these two velocities and the density, the dynamic mechanical modulus and Poison's ratio are obtained. These measurements are done using P-wave and S-wave pulsers/receivers and an oscilloscope. Figure 2.1 shows the experimental setup for the acoustic measurement and Table 2.2 shows the equations used to obtain the mechanical moduli from the P-wave and S-wave velocities.

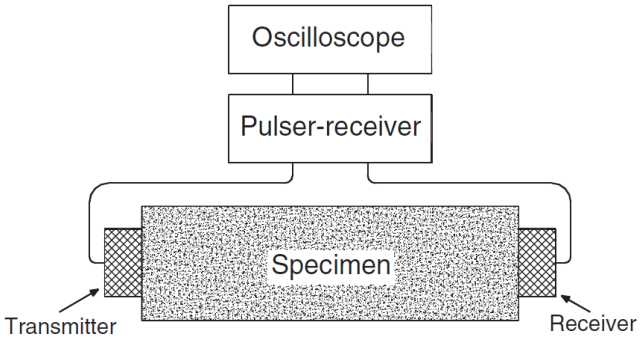

Figure 2.1. Experiment setup for acoustic measurement.

Table 2.2. Wave equations and mechanical modulus equations

Property Name	Equation Used
Constraint Modulus, M	$M = \rho V_p^2$
Shear Modulus, G	$G = \rho V_s^2$
Bulk Modulus, K	$K = M - \frac{4}{3}G$
Young's Modulus, E	$E = \frac{G(3M - 4G)}{M - G}$
Poisson's Ratio, υ	$\upsilon = \frac{M - 2G}{2M - 2G}$

Note ρ is density, V_p and V_s are compressional and shear wave velocity respectively.

Permeability and porosity measurements

Permeability and porosity are measured using the CMS-300 apparatus, shown in Figure 2.2 and detailed in Figure 2.3, which is manufactured by CoreLab. Helium flows through the core samples under a confining stress of 500 psi at ambient conditions (65 ºF and 11.87 psia).

Figure 2.2. Core Measurement System, Model 300 (CMS-300) by CoreLab.

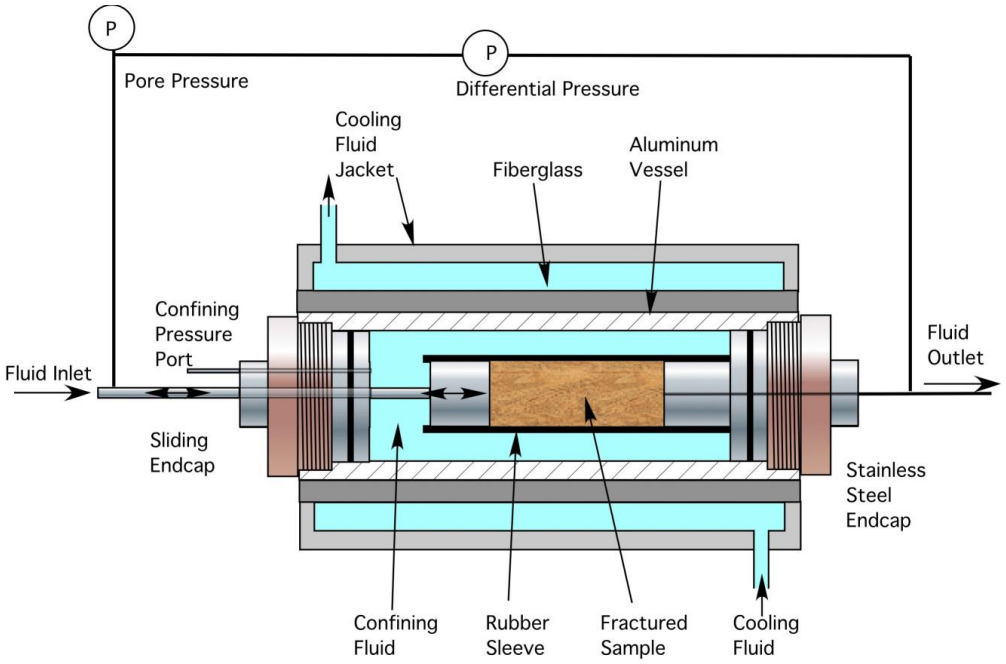

Figure 2.3. Permeability test apparatus.

Brazilian test

Brazilian test, also known as the splitting tensile strength test, is used to determine the tensile strength of cylindrical specimens, such as molded cylinders and drilled cores. The test methodology in the laboratory follows the American Society of Testing and Materials (ASTM) standards. A loading frame, manufactured by MTS Systems Corporation, is used for the test and it can measure both load (force) and displacement at the same time. It is shown in Figure 2.4.

During the Brazilian test, a specimen is placed in the middle of the two machine platens, shown in Figure 2.5. The loading frame is under strain-control during testing (0.5 mm per minute). As the load on the specimen increases, the specimen will split in the middle along the loading direction due to tensile stress. The tensile strength of the rock sample is then calculated using the following:

$$\sigma_t = \frac{2P}{\pi LD} \tag{2.1}$$

where σ_t is splitting tensile strength, P is the maximum applied load indicated by the testing machine, L is thickness of the specimen and D is diameter of the specimen.

Figure 2.4. Load frame by MTS.

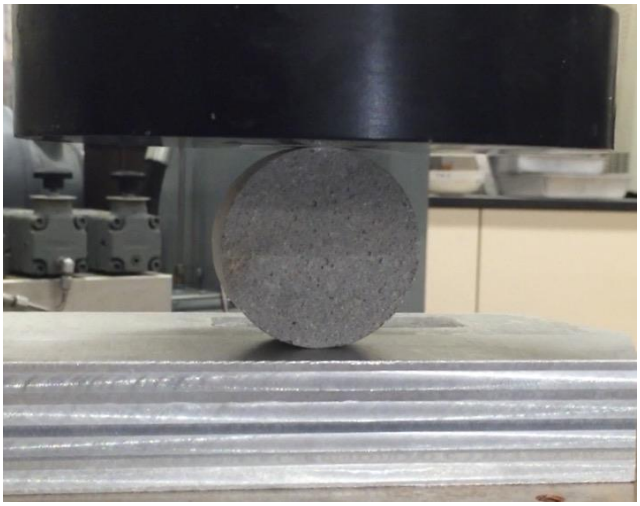

Figure 2.5. Testing setup for Brazilian test.

Uniaxial compression test

The uniaxial compression test measures the compressional strength of cylindrical specimens under no confining pressure or stress. Specimens are loaded axially up to failure or any other prescribed level. The apparatus used for the uniaxial compression test is a loading frame. The uniaxial compressive strength of specimens is determined by the maximum loading during testing:

$$\sigma_c = \frac{F}{A} \tag{2.2}$$

where σ_c is uniaxial compressive strength of the specimen, F is the maximum loading force during testing and A is the cross section area of the specimen.

The uniaxial compression test for shale samples uses the MTS loading frame described earlier. The uniaxial compression test for concrete samples and sandstone samples uses the loading frame shown in Figure 2.6. It has a hydraulic piston powered by a pneumatic pump. The uniaxial compressive strength of concrete and sandstone exceeds the maximum allowable load for the MTS loading frame. However, the loading frame in Figure 2.6 can only measure the load (force) during tests and is not as accurate as the MTS loading frame.

Figure 2.6. Loading frame.

Measurements on Concrete

The concrete samples are common surrogates for rocks in laboratory rock testing because they are easily made and sample properties are do not vary much. In addition, the results from concrete samples can also establish a base for sandstone and shale samples, which are more difficult to obtain. The concrete samples are made from Type II Portland cement with a constant ratio of water to dry sand.
Table 2.3 shows the composition of the concrete samples.

Table 2.3. Composition of concrete samples

Composition	Weight (kg)	Ratio to Cement
Sand	4	2.5
Cement	1.6	1
Water	0.88	0.55

The concrete cores are made using cylindrical molds. We have two different types of molds, plastic molds with a 2 inch diameter and 4 inch length, and steel molds with a 3 inch diameter and 6 inch length. The concrete samples are put into water after one day of curing. The underwater phase will last for one month in order to allow the concrete samples to reach their maximum strength. After water curing, the samples are dried under ambient conditions prior to use.

Acoustic measurement

The results from acoustic measurements are shown in Table 2.4.

Table 2.4. Acoustic measurement results for concrete samples

Property Name	Values
Compressional Velocity, V_p	4190 to 4240 m/s
Shear Velocity, V_s	2393 to 2517 m/s
Constraint Modulus, M	36.3 GPa (5.26×10^6 psi)
Shear Modulus, G	12.5 GPa (1.81×10^6 psi)
Bulk Modulus, K	20.1 GPa (2.90×10^6 psi)
Young's Modulus, E	30.0 GPa (4.35×10^6 psi)
Poisson's Ratio, υ	0.243

Permeability and porosity measurement

Figure 2.7 shows the concrete core samples used for permeability and porosity measurement. The detailed results of permeability and porosity measurement for concrete cores are shown in Table 2.5. The average porosity of the concrete samples is 9.56% and the average permeability is around 9 micro-Darcy (0.009 mD).

Figure 2.7. Concrete core samples used for permeability and porosity measurement in CMS300.

Table 2.5. Permeability and porosity results from CMS-300 for concrete samples

	Sample Number		
	C-1	C-2	C-3
Diameter	1.003 inch	1.003 inch	1.003 inch
Length	0.975 inch	1.121 inch	1.002 inch
Weight	25.65 g	29.69 g	26.53 g
Bulk Volume	12.624 cc	14.514 cc	12.974 cc
Bulk Density	2.032 g/cc	2.046 g/cc	2.045 g/cc
Pore Volume	1.145 cc	1.334 cc	1.351 cc
Porosity	9.07%	9.19%	10.41%
Permeability	8.15×10^{-3} mD	7.31×10^{-3} mD	1.07×10^{-3} mD

Brazilian test

Figure 2.8 shows concrete samples for the Brazilian test. Figure 2.9 shows typical load and deformation curves for concrete samples during the Brazilian test. The detailed results of tensile strength measurements for concrete cores are shown in Table 2.6. The average tensile strength of the concrete samples is 2.878 MPa (418 psi).

Figure 2.8. Concrete samples for Brazilian test.

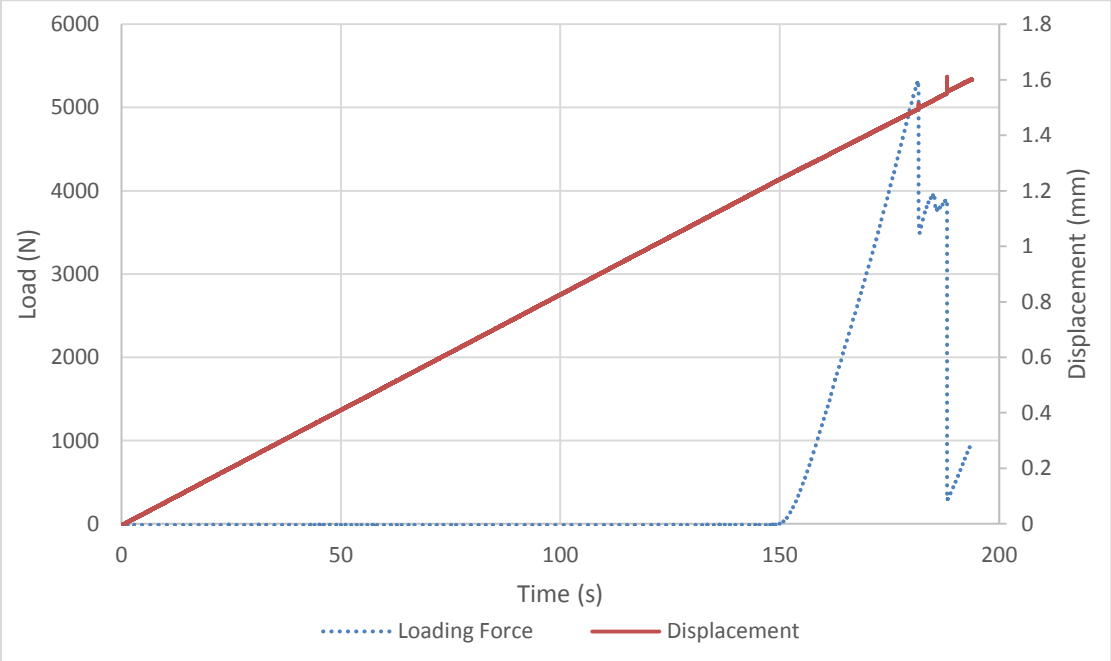

Figure 2.9. Typical load and displacement curves for concrete samples.

Table 2.6. Tensile strength results for concrete cores

	Sample Number		
	C-1 Br	C-2 Br	C-3 Br

Diameter	2.032 inch	2.030 inch	2.037 inch
Thickness	1.011 inch	1.016 inch	1.027 inch
Maximum Loading Force	7118.281 N	5324.916 N	5676.197 N
Tensile Strength	3.419 MPa (496 psi)	2.547 MPa (370 psi)	2.677 MPa (388 psi)

Uniaxial compression test

Figure 2.10 shows concrete samples for the uniaxial compression test. The typical loading force curve for concrete samples is shown in Figure 2.11. The fluctuations in the loading curve are due to the vibration of the hydraulic pump during pressurization. The detailed results of uniaxial compressional strength measurements for concrete samples are shown in Table 2.7. The average uniaxial compressional strength of concrete samples is 37.343 MPa (5416 psi).

Figure 2.10. Concrete samples for uniaxial compression test.

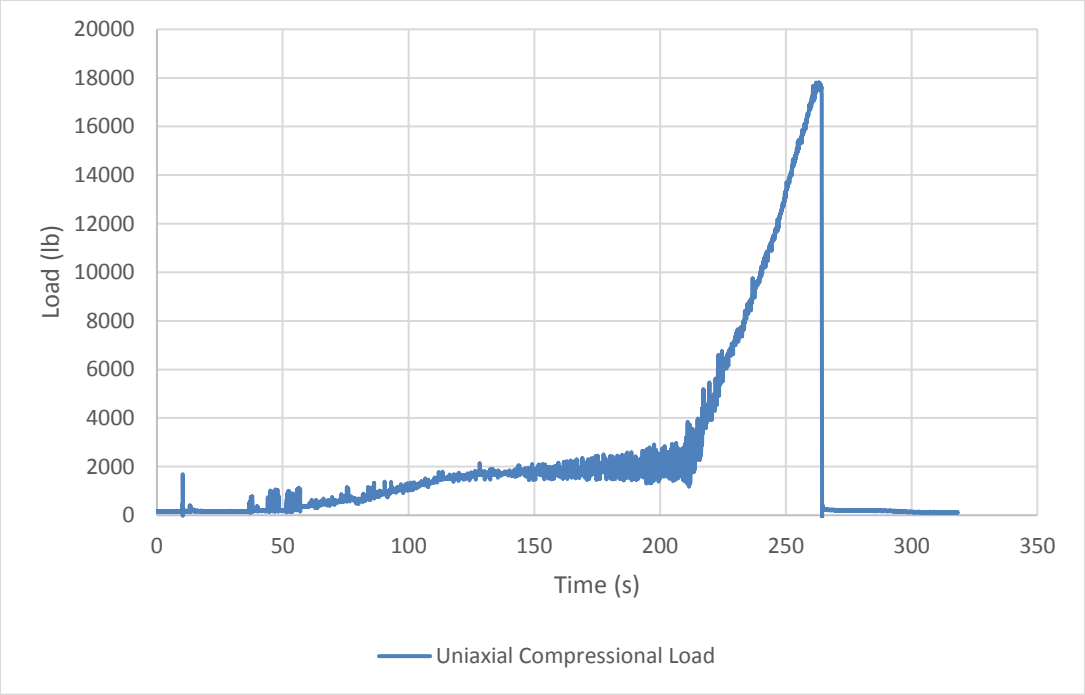

Figure 2.11. Typical uniaxial compressional loading curve for concrete samples.

Table 2.7. Uniaxial compressional strength results for concrete cores

	Sample Number		
	C1-5 UC	C1-7 UC	C1-8 UC
Diameter	2.047 inch	2.041 inch	2.050 inch
Thickness	3.99 inch	4.047 inch	4.036 inch
Maximum Loading Force	17,267 lb	17,813 lb	18,356 lb
Uniaxial Compressional Strength	36.169 MPa (5246 psi)	37.528 MPa (5443 psi)	38.333 Mpa (5560)

Measurements on Sandstone

The sandstone samples were gathered from an outcrop in the Williams Fork Formation in Western Colorado. The cores were wet drilled from the rock chunks, from which several 8 inch cube blocks were cut for tri-axial tests. All cores were dried at ambient conditions for several days before any measurements.

Acoustic measurement

The results from the acoustic measurement on the sandstone samples are shown in Table 2.4.

Table 2.8. Acoustic measurement results for sandstone samples

Property Name	Values
Compressional Velocity, V_p	7320 to 7695 m/s

Shear Velocity, V_s	4760 to 4940 m/s
Constraint Modulus, M	124 GPa (17.98×10^6 psi)
Shear Modulus, G	52 GPa (7.54×10^6 psi)
Bulk Modulus, K	55 GPa (7.98×10^6 psi)
Young's Modulus, E	118 GPa (17.11×10^6 psi)
Poisson's Ratio, υ	0.142

Permeability and porosity measurement

Figure 12 shows the sandstone core samples used for permeability and porosity measurement. The detailed results of permeability and porosity measurement for sandstone cores are shown in Table 2.5. The average porosity of the sandstone samples is 11.47% and the average permeability is around 0.349 mD. The porosity and permeability of the sandstone samples are larger than that of the concrete samples.

Figure 12. Sandstone core samples used for permeability and porosity measurement in CMS300.

Table 2.9. Permeability and porosity results from CMS-300 for sandstone samples

	Sample Number		
	SS-1	SS-2	SS-3
Diameter	1.000 inch	1.001 inch	1.001 inch
Length	1.127 inch	1.094 inch	1.048 inch
Weight	31.83 g	30.74 g	29.62 g
Bulk Volume	14.505 cc	14.108 cc	13.515 cc
Bulk Density	2.194 g/cc	2.179 g/cc	2.192 g/cc

Pore Volume	1.671 cc	1.610 cc	1.565 cc
Porosity	11.52%	11.41%	11.58%
Permeability	0.609 mD	0.252 mD	0.187 mD

Brazilian test

Figure 2.13 shows the sandstone samples for the Brazilian test. Figure 2.14 shows the typical load and deformation curves for sandstone samples during the Brazilian test. The detailed results of tensile strength measurements for sandstone cores are shown in Table 2.10. The average tensile strength of sandstone samples is 5.505 MPa (653 psi).

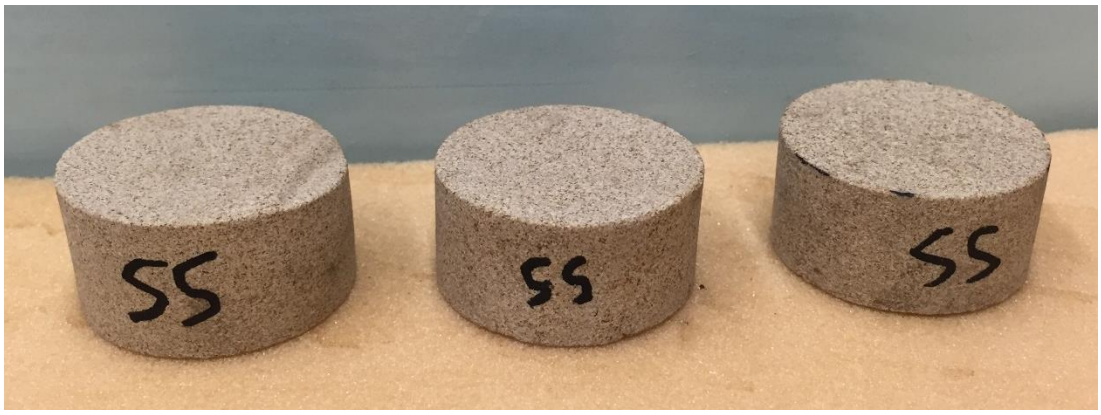

Figure 2.13. Sandstone samples for Brazilian test.

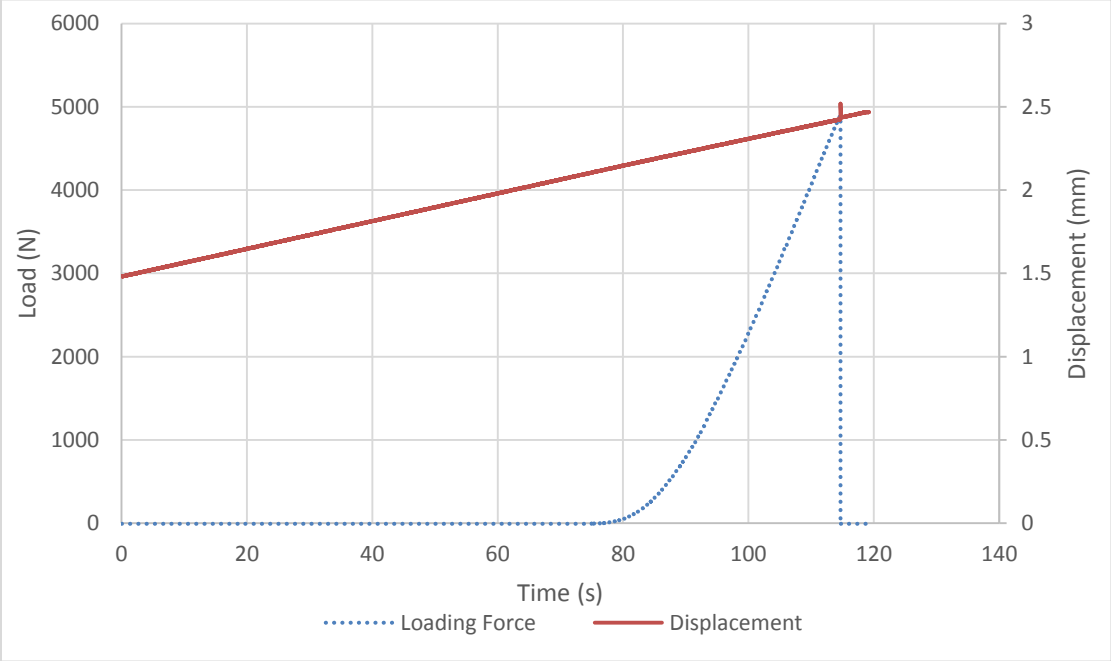

Figure 2.14. Typical load and displacement curve for sandstone samples.

Table 2.10. Tensile strength results for sandstone cores

	Sample Number

	SS-1 Br	SS-2 Br	SS-3 Br
Diameter	1.499 inch	1.497 inch	1.497 inch
Thickness	0.742 inch	0.751 inch	0.771 inch
Maximum Loading Force	5372 N	5196 N	4896 N
Tensile Strength	4.769 MPa (691 psi)	4.561 MPa (661 psi)	4.186 MPa (607 psi)

Uniaxial compression test

Figure 2.15 shows the sandstone samples for the uniaxial compression test. The typical loading force curve for the sandstone samples is shown in Figure 2.16. The detailed results of uniaxial compressional strength measurements for the sandstone samples are shown in Table 2.11. The average uniaxial compressional strength of sandstone samples is 41.457 MPa (6013 psi).

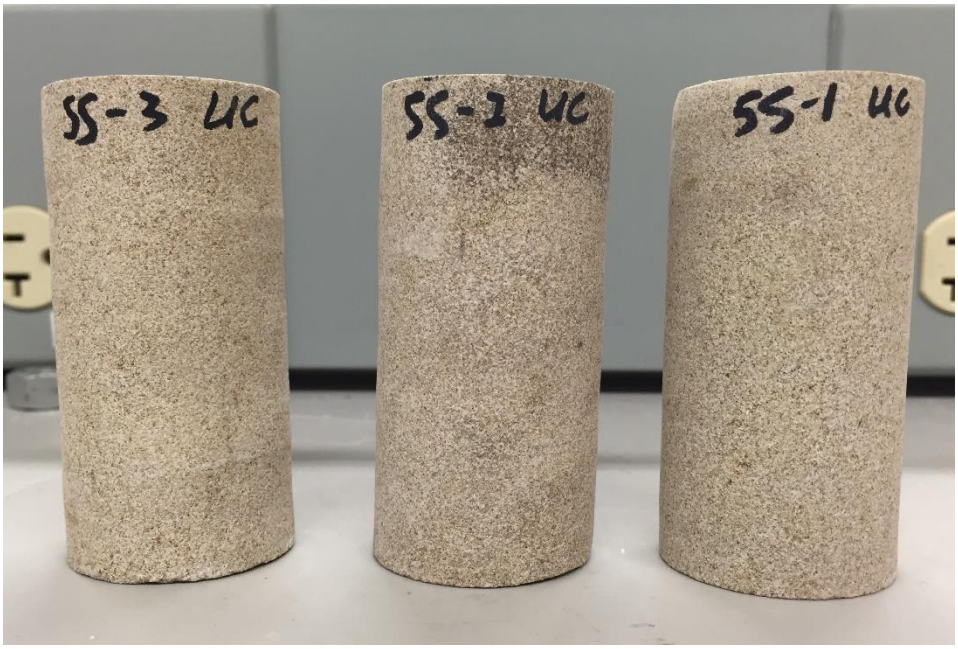

Figure 2.15. Sandstone samples for uniaxial compression test.

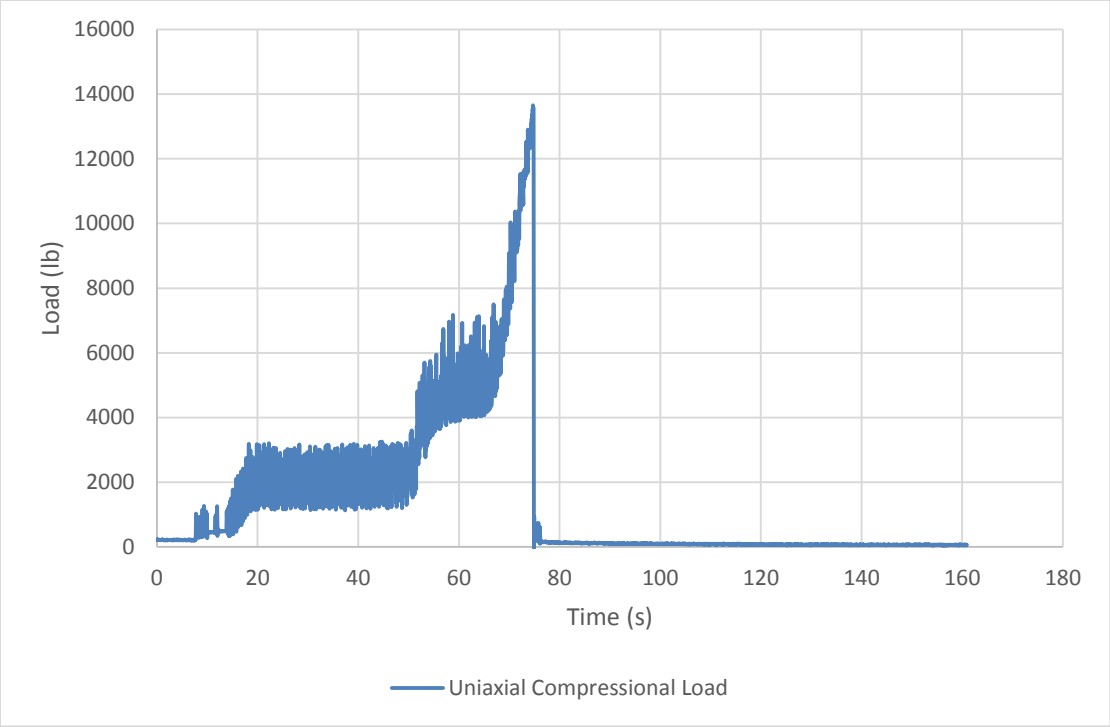

Figure 2.16. Typical uniaxial compressional loading curve for sandstone samples.

Table 2.11. Uniaxial compressional strength results for sandstone cores

	Sample Number		
	SS-1 UC	SS-2 UC	SS-3 UC
Diameter	1.499 inch	1.496 inch	1.496 inch
Thickness	3.012 inch	2.990 inch	3.030 inch
Maximum Loading Force	10,592 lb	13,657 lb	7,493 lb
Uniaxial Compressional Strength	41.410 MPa (6006 psi)	53.569 MPa (7770 psi)	29.391 MPa (4263 psi)

Measurements on Shale

The shale samples were gathered from a shallow buried layer of Niobrara formation, which is about 10 feet to 30 feet under the surface, located north of Boulder, CO. The cores were dry drilled from the big chunks from which several 8 inch cube blocks were cut for the tri-axial tests. After coring, all shale cores were dry cut into the desired length with their cross sections grinded very carefully.

Acoustic measurement

The results from the acoustic measurements for the shale samples are shown in Table 2.12. The shale samples tend to have the highest moduli values for the three rock types.

Table 2.12. Acoustic measurement results for shale samples

Property Name	Values
Compressional Velocity, V_p	4920 to 5001 m/s
Shear Velocity, V_s	2767 to 2816 m/s
Constraint Modulus, M	61.2 MPa (8.88×10^6 psi)
Shear Modulus, G	19.5 GPa (2.83×10^6 psi)
Bulk Modulus, K	35.5 GPa (5.15×10^6 psi)
Young's Modulus, E	49.3 GPa (7.15×10^6 psi)
Poisson's Ratio, υ	0.268

Permeability and porosity measurement

Figure 2.17 shows the shale core samples used for permeability and porosity measurements. The detailed results for permeability and porosity measurements on the shale cores are shown in Table 2.13. The average porosity of the shale samples is 6.65% and the average permeability is around 1 micro-Darcy (1.06e-3 mD). The porosity and permeability of the shale samples are the lowest of all the samples. The permeability of the shale samples is about 100 times smaller than that of the sandstone samples.

Figure 2.17. Shale core samples used for permeability and porosity measurement in CMS300.

Table 2.13. Permeability and porosity results from CMS-300 for shale samples

	Sample Number		
	SH-1	SH-2	SH-3
Diameter	1.004 inch	1.004 inch	1.003 inch
Length	0.984 inch	1.031 inch	0.930 inch
Weight	30.20 g	32.05 g	28.96 g
Bulk Volume	12.766 cc	13.376 cc	12.041 cc

Bulk Density	2.366 g/cc	2.396 g/cc	2.405 g/cc
Pore Volume	0.873 cc	0.890 cc	0.776 cc
Porosity	6.84%	6.65%	6.44%
Permeability	1.05×10^{-3} mD	1.05×10^{-3} mD	1.07×10^{-3} mD

Brazilian test

Figure 2.18 shows the shale samples for the Brazilian test. Figure 2.19 shows the typical load and deformation curves for the shale samples during the Brazilian test. Shale samples, as shown in Figure 2.20, tend to be very ductile during tests, which causes several peaks to appear in the loading curves. The detailed results of tensile strength measurements for shale cores are shown in Table 2.14. The average tensile strength of the shale samples is 8.455 MPa (1226 psi). The large difference between the two shale samples may result from the coring direction difference with respect to the sedimentary bedding plan or from some pre-existing fractures within the samples.

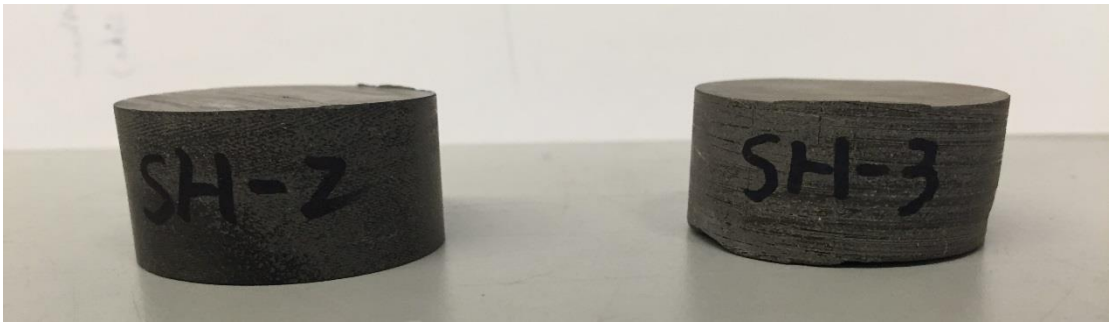

Figure 2.18. Shale samples for Brazilian test.

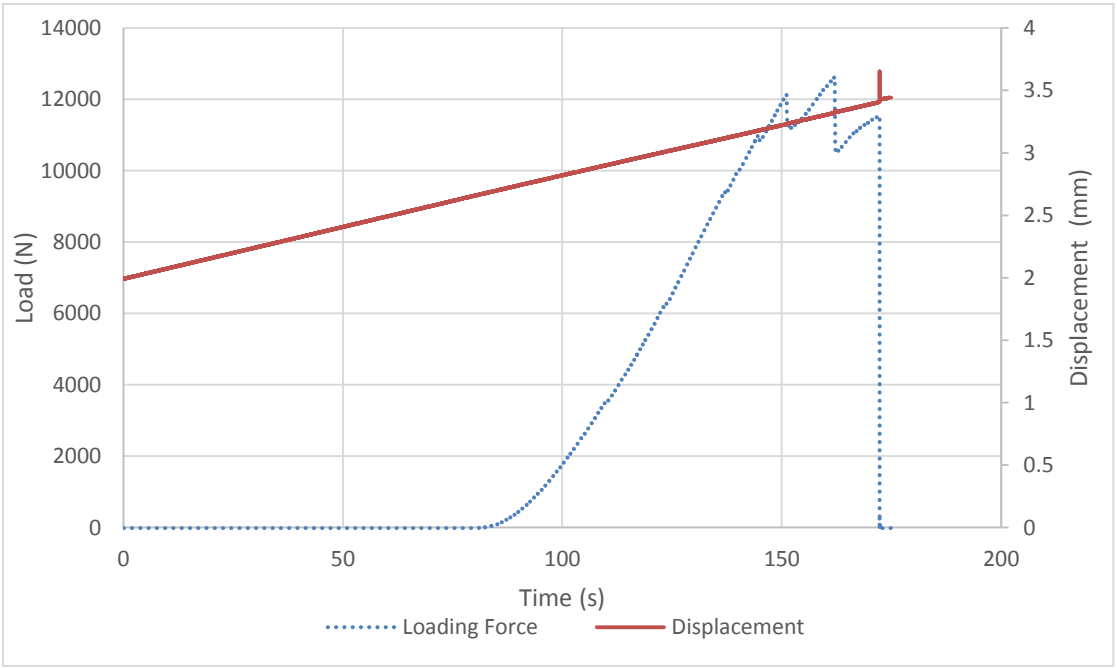

Figure 2.19. Typical load and displacement curve for shale samples.

Table 2.14. Tensile strength results for shale cores

	Sample Number	
	SH-2 Br	SH-3 Br
Diameter	1.501 inch	1.494 inch
Thickness	0.743 inch	0.699 inch
Maximum Loading Force	12,624 N	6074 N
Tensile Strength	11.170 MPa (1620 psi)	5.740 MPa (832 psi)

Figure 2.20. Shale sample SH-2 Br after Brazilian test.

Uniaxial compression test

Figure 2.21 shows the shale samples used for the uniaxial compression test. The typical loading curve for the shale samples is shown in Figure 2.22. The shale samples also show ductility in these tests as well as in Brazilian ones. The detailed results of uniaxial compressional strength measurements for the shale samples are shown in Table 2.15. The average uniaxial compressional strength of the shale samples is 54.585 MPa (7917 psi). The big difference among samples may also result from bedding plane or pre-existing fractures.

Figure 2.21. Shale samples for uniaxial compressional test.

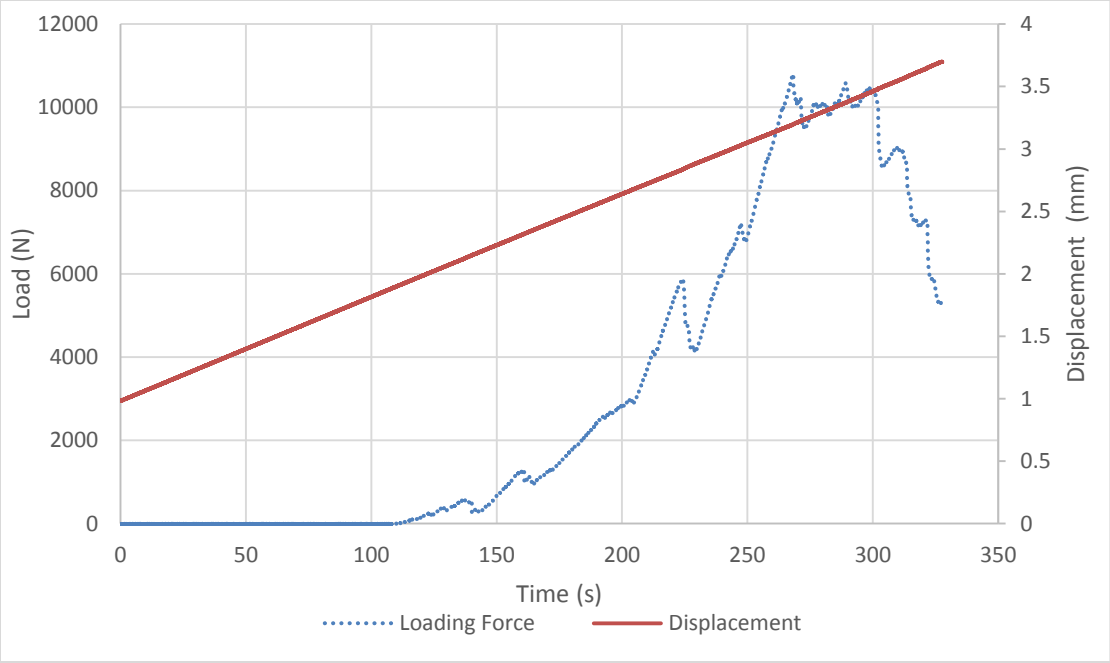

Figure 2.22. Typical Uniaxial Compressional Loading Curve for Shale Samples.

Table 2.15. Uniaxial compressional strength results for shale cores

	Sample Number		
	SH-1 UC	SH-2 UC	SH-3 UC
Diameter	1.004 inch	0.755 inch	0.757 inch
Thickness	2.057 inch	1.483 inch	1.486 inch
Maximum Loading Force	31,553 N	10,804 N	18,750 N
Uniaxial Compressional Strength	61.775 MPa (8960 psi)	37.404 MPa (5425 psi)	64.576 MPa (9366 psi)

Thermal Property Measurements: Specific Heat

In this section, the specific heat measurements for different samples are conducted. A calorimeter, thermocouple, weight scale, and a data acquisition system are used for this measurement. The calorimeter is a passive one and has no heat sources, as shown in Figure 2.. It isolates the sample and heat transfer fluid, creating an adiabatic environment. The weight scale, as shown in Figure 2.234, is used to determine the mass of the samples and the amount of heat transfer fluid used during measurements. The thermocouple can provide a temperature reading with a small fluctuation of about ±0.2 ºC.

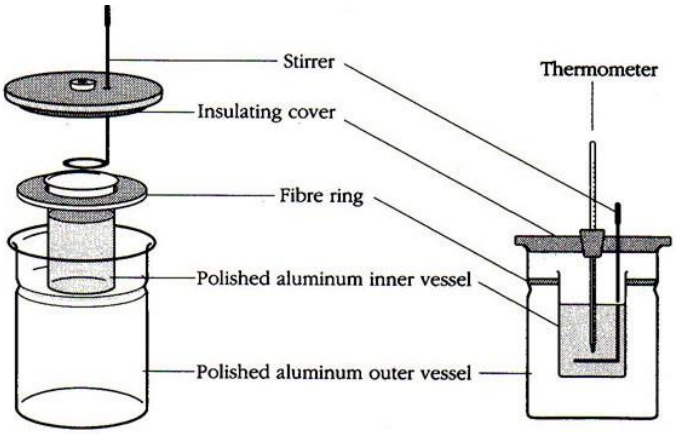

Figure 2.23. The components of a calorimeter (MiniScience.com).

Figure 2.234. Weight scale.

The measurements are conducted for samples initially at ambient temperature (24.8ºC or 76.6ºF) and for heat transfer fluid (water) at temperatures from 50ºC to 70ºC (122ºF to 158ºF). Before the measurement, the calorimeter is calibrated to obtain the heat capacity of its aluminum inner vessel. In addition, a calibration for heat loss of the calorimeter is conducted from 65ºC to 35 ºC (149ºF to 95ºF). The heat loss rate as a function of temperature is obtained to mitigate the calorimeter's non-perfect isolation. The heat loss calibration curve is as shown in Figure 2.

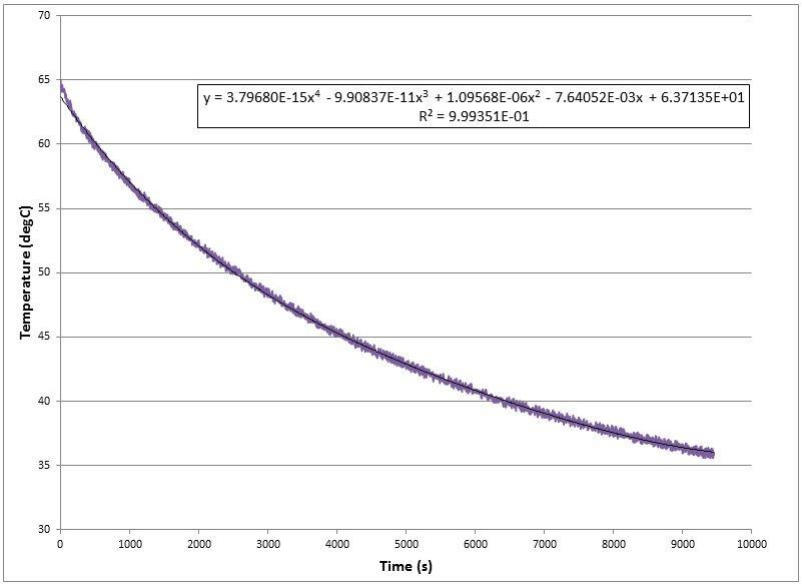

Figure 2.25. Heat loss calibration curve.

During a specific heat measurement, heat transfer fluid is first poured into a calorimeter. After the temperature becomes stable, a rock sample at 24.8ºC will be gently dropped into the heat transfer fluid. The temperature change will be recorded during the measurement. Once the temperature reaches equilibrium, the specific heat will then be calculated.

The calculation of the specific heat of a sample is based on an energy balance. During the measurements, the heat or energy released by the high temperature objects is transferred to the low temperature objects or to the environment, which is considered as a heat loss. Thus, the following relation can be then obtained:

$$\left(c_{p-water}m_{water} + C_{al}\right)\Delta T_w = \dot{Q}_{avg}\Delta t + c_{p-sample}m_{sample}\Delta T_{sample} \tag{2.3}$$

where $c_{p-water}$ is specific heat of water, m_{water} is mass of water used in this measurement, C_{al} is heat capacity of the aluminum inner vessel of the calorimeter from calibration, ΔT_w is the temperature change of water, $\dot{Q}_{avg}$ is the average heat loss rate during measurement, Δt is time used to reach equilibrium after the sample is dropped into the heat transfer fluid, $c_{p-sample}$ is the sample specific heat, m_{sample} is the sample mass, and ΔT_{sample} is the sample temperature change.

A typical temperature profile for the measurement is shown in Figure 2.25. The time for a dropped sample to reach equilibrium is shaded with brown. The specific heat of the sample is the only unknown in Equation 2.3 and can be solved for.

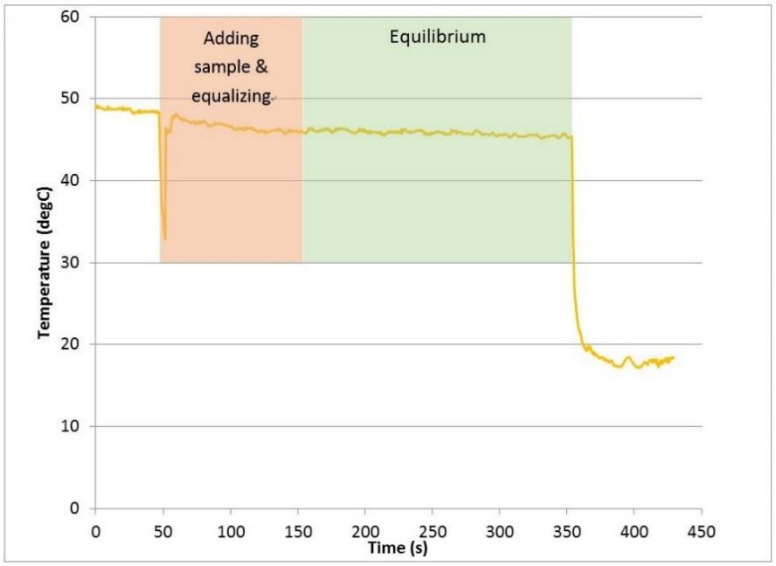

Figure 2.25. Temperature profile for specific heat measurement for Sample SH-2.

Specific heat for concrete, sandstone and shale

The specific heat of concrete, sandstone and shale were measured following the procedure outlined in the previous section. The same core samples used for porosity and permeability measurements were used for measurement of specific heat.

The specific heat for the concrete samples ranged from 859 J/(kg·K) to 912 J/(kg·K), with an average of 891 J/(kg·K). The specific heat for the sandstone samples ranged from 782 J/(kg·K) to 922 J/(kg·K), with an average of 857 J/(kg·K). The specific heat for the shale samples ranged from 916 J/(kg·K) to 1067 J/(kg·K), with an average of 990 J/(kg·K). The detailed results are shown in Table 2.1, Table 2.17, and Table 2.1.

Table 2.16. Specific heat of concrete samples

	Sample Number		
	C-1	**C-2**	**C-3**
Specific Heat	901 J/(kg·K)	859 J/(kg·K)	912 J/(kg·K)
Average Specific Heat	891 J/(kg·K)		

Table 2.17. Specific heat of sandstone samples

	Sample Number		
	SS-1	**SS-2**	**SS-3**

Specific Heat	782 J/(kg·K)	922 J/(kg·K)	868 J/(kg·K)
Average Specific Heat	857 J/(kg·K)		

Table 2.18. Specific heat of shale samples

	Sample Number		
	SH-1	**SH -2**	**SH -3**
Specific Heat	988 J/(kg·K)	1067 J/(kg·K)	916 J/(kg·K)
Average Specific Heat	990 J/(kg·K)		

The results of the specific heat measurements fluctuate significantly. Several possible sources of error have been addressed during data analysis. First, the calorimeter is made of aluminum, which may result in significant heat loss over a period of time. Second, the sample used is a core, which has a relatively small contact surface compared to chips or crushed samples. This will lead to longer equilibration time and higher heat loss during measurement. Third is the fluctuating reading from the thermocouple. This might be caused by the interior electric noise of the data acquisition system or a disturbance from air and fluid. Fourth, the picking of the end points of heat transfer process can also lead to errors.

There are several ways to improve the accuracy of the measurements. The heat transfer fluid temperature can be set at room temperature while samples are heated in an oven. This can mitigate the heat loss during measurements since the calorimeter and fluid as a whole will be at a lower temperature. The samples can be crushed into chips or powder to maximize the contact area for heat transfer, thus shortening the time to reach equilibrium and less heat loss. The temperature sensing device can be substituted by one with higher resolution for a more stable reading.

Permeability versus effective stress for brine injection

In this section, we measure the permeability of fractured samples under varying effective stress. The Brazilian technique was used to fracture a sample of Gray Berea. Spacers 0.02 mm thick were placed at the open corners, shown in Figure 2.26.

Figure 2.26. Split Gray Berea core with spacers.

The core was reassembled to match the surfaces with the spacers in place and a Teflon sleeve was shrunk onto the core. The Teflon was wrapped in aluminum foil, then wrapped again in virgin Teflon, and placed in a Viton sleeve in an X-ray transparent aluminum core holder shown in Figure 2.27.

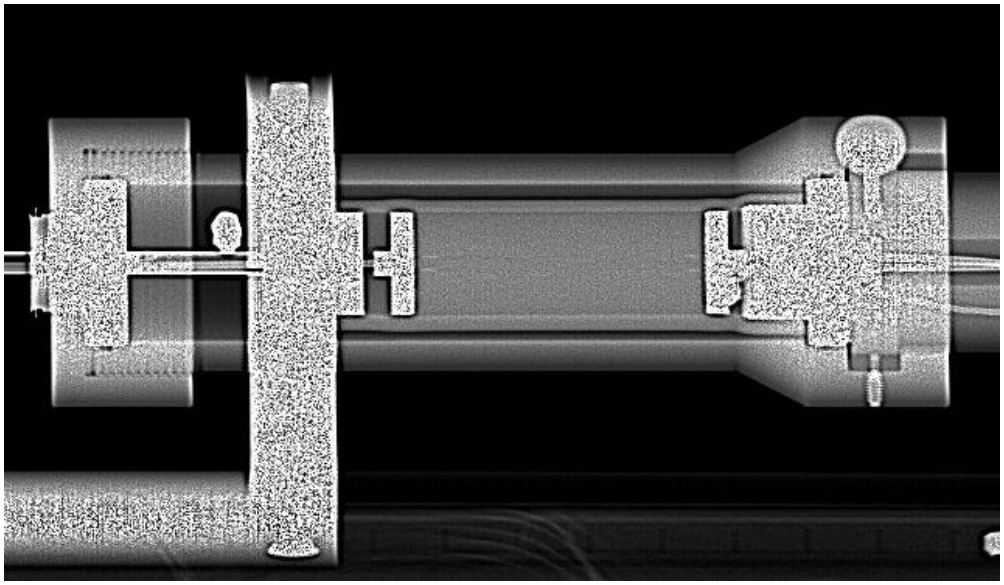

Figure 2.27. X-ray scan of core in coreholder. Spacers are visible at the left and right sides of the core.

Confining pressure was applied using nitrogen gas. Air was flowed at specific flowrates using an ISCO 1000D syringe pump, and differential pressure was measured using a Rosemount 3051 differential pressure transmitter and verified using an Omega 0-30 psi pressure calibrator. Permeabilities were computed for each effective stress using four flowrates, shown in Figure 2.28.

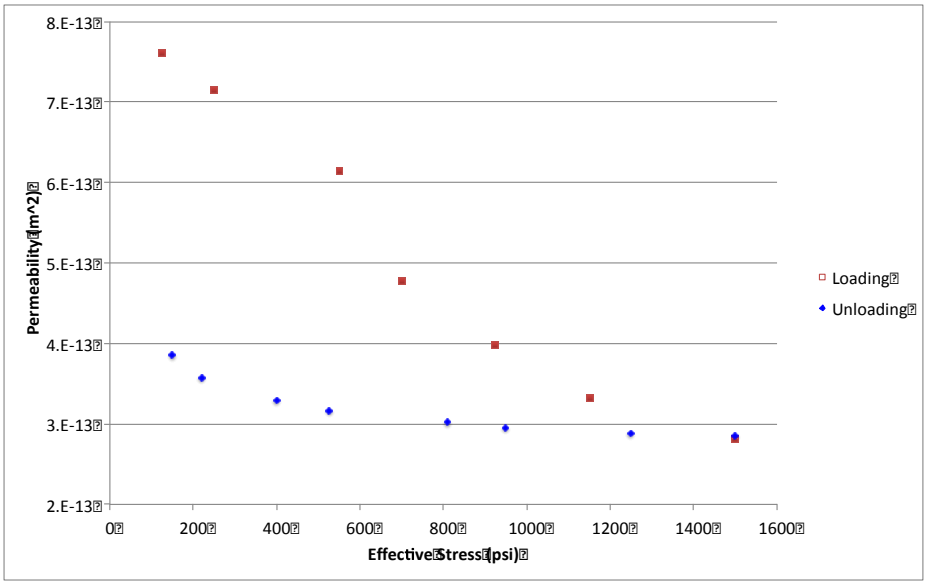

Figure 2.28. Calculated permeabilities for varying effective stresses for the first loading and unloading cycle using Gray Berea. The permeability for flow between flat plates with an aperture of 0.02 mm is 3.3 x 10^{-11} m^2.

The core was X-ray CT scanned at each condition to observe changes in the fracture aperture. Figure 2.29 shows rough computations of the fracture aperture for each case. The indicated aperture requires further correction but is presented to show the procedural development. The horizontal purple stripe across each image approximately 40% from the top is an internal standard and does not represent an actual aperture. Correct aperture maps like these can be used to compute permeability, phase saturations for different capillary pressures, and relative permeabilities.

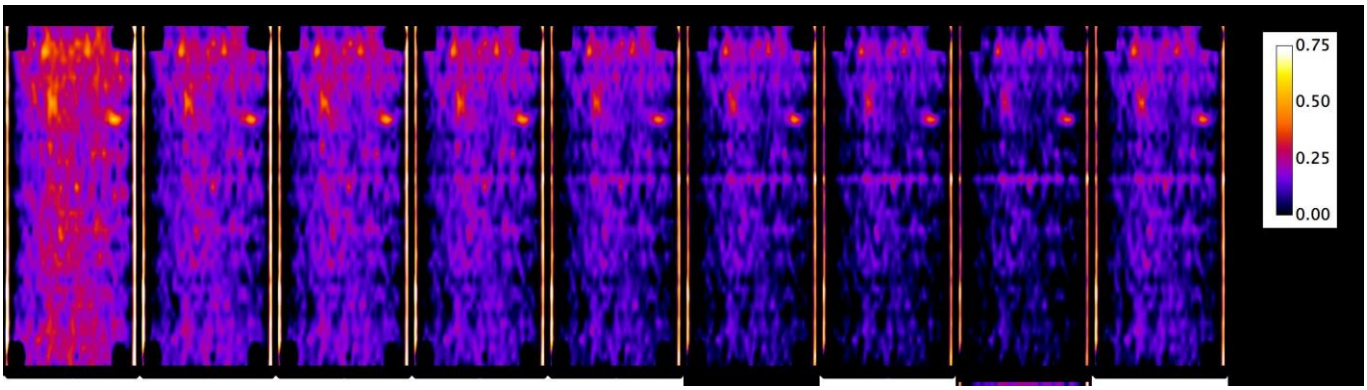

Figure 2.29. Computed fracture apertures for 0, 125, 250, 550, 700, 925, 1150, 1500, and 0 psi effective stress. Scale is mm.

We then measured the permeability versus effective stress for another Gray Berea sample using brine. Confining pressure was applied using nitrogen gas controlled using an ISCO 500 D syringe pump. A mild brine (0.01 M) was flowed at specific flowrates using another ISCO 500D syringe pump, and differential pressure was measured using an Azbil differential pressure transmitter calibrated with an Omega 0-30 psi pressure calibrator. Permeabilities were computed for each effective stress using four to five flowrates at each confining pressure, shown in Figure 2.30.

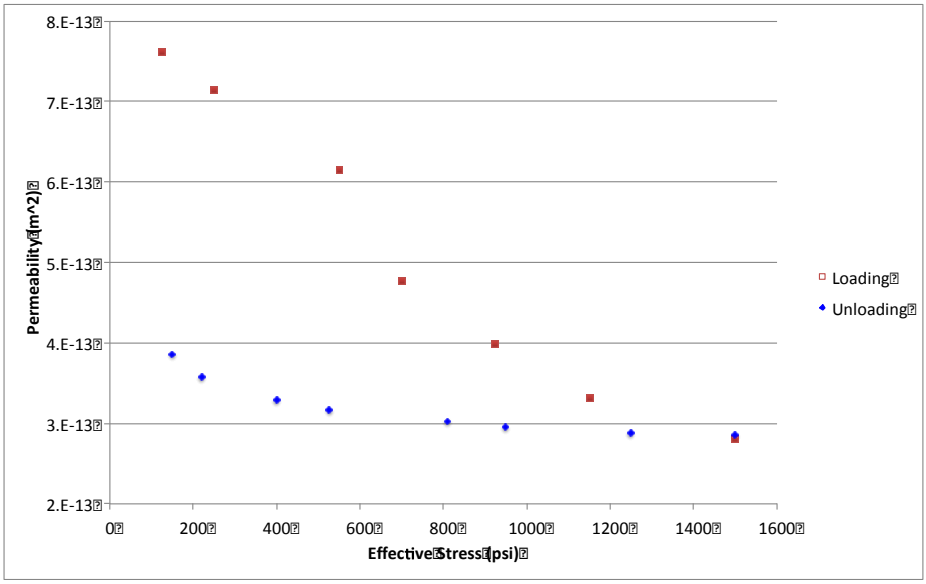

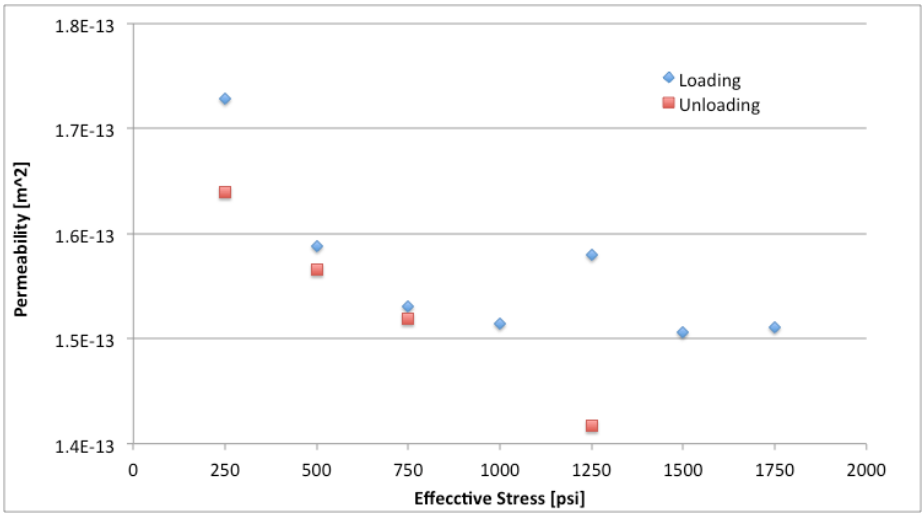

Figure 2.30. Top, calculated gas permeabilities for varying effective stresses for the first loading and unloading cycle using Gray Berea. Bottom, those from brine. The permeability for flow between flat plates with an aperture of 0.02 mm is 3.3 x 10^{-11} m^2 indicating the aperture is small and variable.

The core behaved differently for gas injection versus brine injection. The permeability with brine is about a factor of two lower than the gas permeability. We attributed that to mobilization of cuttings from the coring when injecting brine, whereas a significant gas flow would be required to mobilize them while injecting gas.

Again, we used X-ray CT scanning at each effective stress to observe changes in the fracture aperture. Figure 2.31 shows aperture distribution for each effective stress case. Little change is observed in the statistical aperture distribution beyond an effective stress of 500 psi. The aperture distribution flattens from 250 psi effective stress to 500 psi, and minor changes are seen at higher effective stresses.

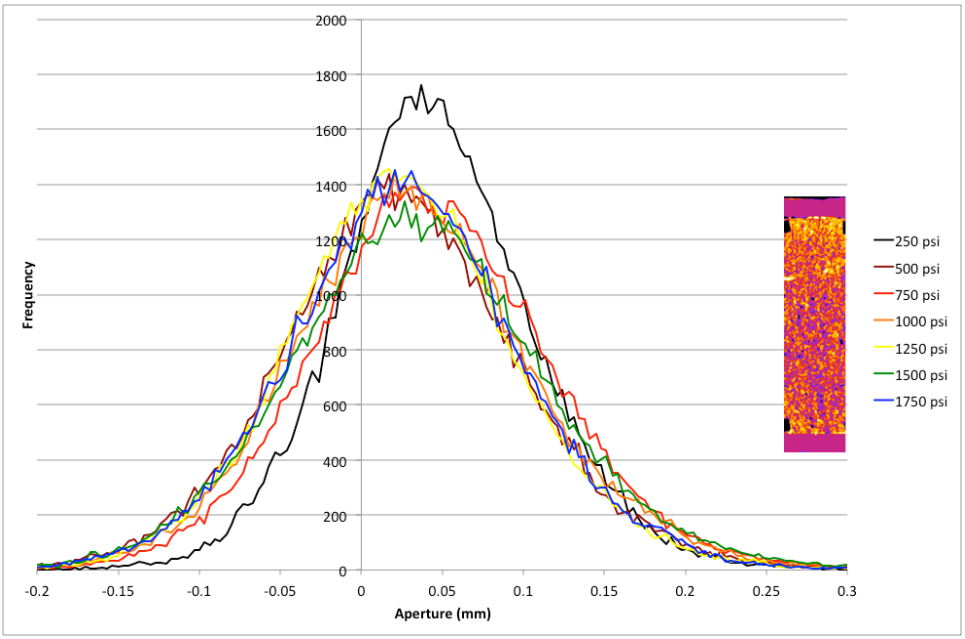

Figure 2.31. Computed fracture apertures distributions for 250, 500, 750, 1000, 1250, 1500, and 1750 psi effective stresses. The inset is an image of the aperture map at 250 psi effective stress. Note that the aperture is higher at the ends and in the vicinity of the spacers (black).

The core used in the following was used previously in a gas permeability test. The gas permeability setup was modified to allow flow of multiple phases at controlled temperatures, shown in Figure 2.32. The brine, 3 M potassium iodide, was used to provide X-ray contrast. A CT scan of the brine-saturated core under 900 psi effective stress is shown in Figure 2.33. Permeability was measured numerous times at varying flow rates at each effective stress, shown in Figure 2.34. Variability in computed permeability was highest for lower flow rates, and decreased for higher flow rates where the differential pressure was easier to measure and the system controls were in better balance. The initial permeability is consistent with the final permeabilities measured (during unloading) in Figure 2.30. As expected, the permeability declined with increased effective stress, which caused the fracture to close. The lowest measured permeability was in the range of measured saturated permeability of unfractured specimens.

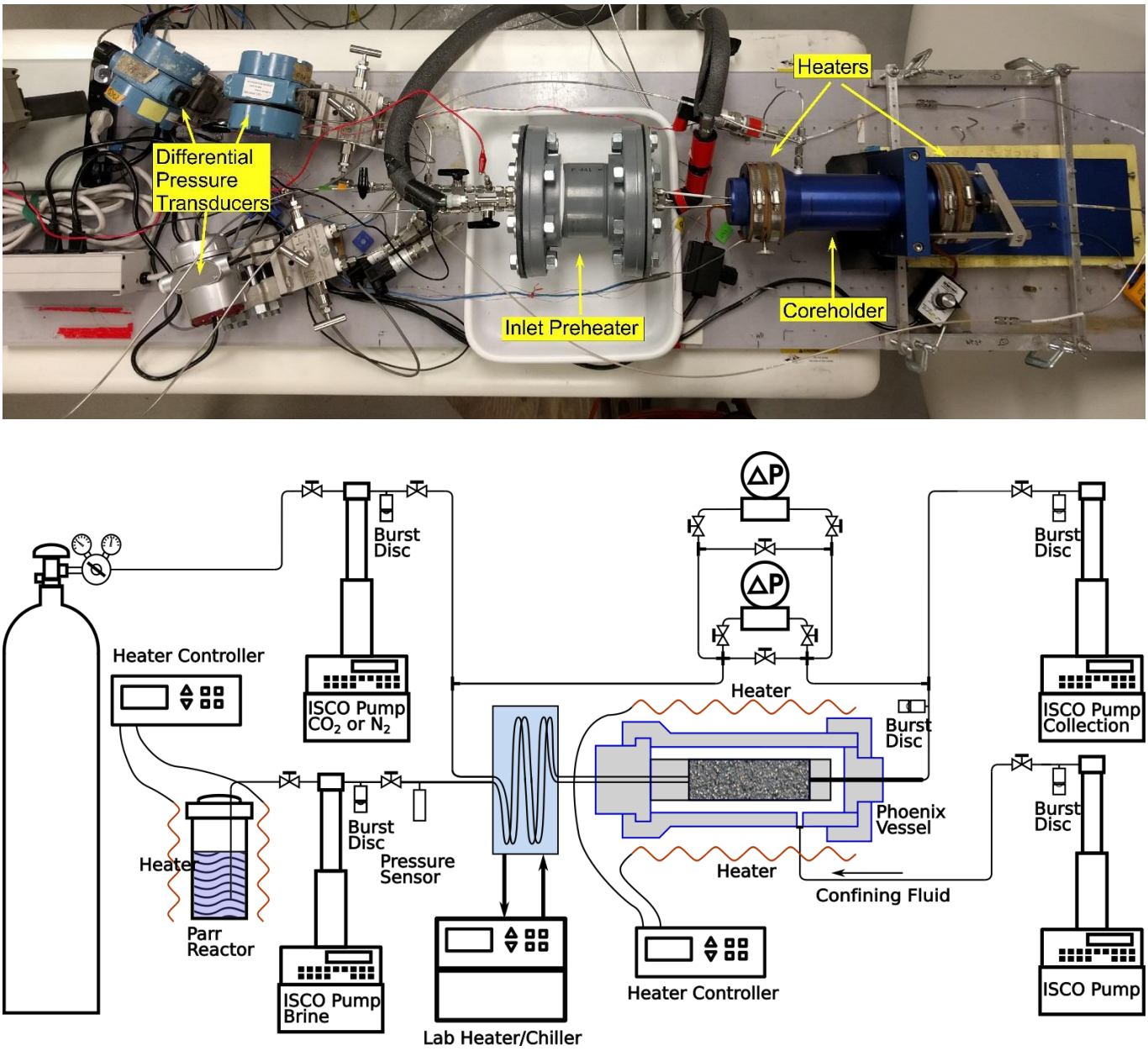

Figure 2.32. Top – Photo of differential pressure instrumentation, preheater, and coreholder on X-ray CT table prior to insulation. Bottom – schematic of setup. One differential pressure transducer is used for measurement, a second for control (if flowing in that mode), and the third (not shown on schematic) for fine control of low effective stresses.

Two other features were observed in the plot. Under constant conditions for the loading branch of the curve (0-20,000 s), the permeability decreased slightly over time. There were a number of reasons for that, including continued aperture closure as rock grains break, and transport of fines. This constant decrease did not occur on the unloading branch of the curve (after 20,000 s).

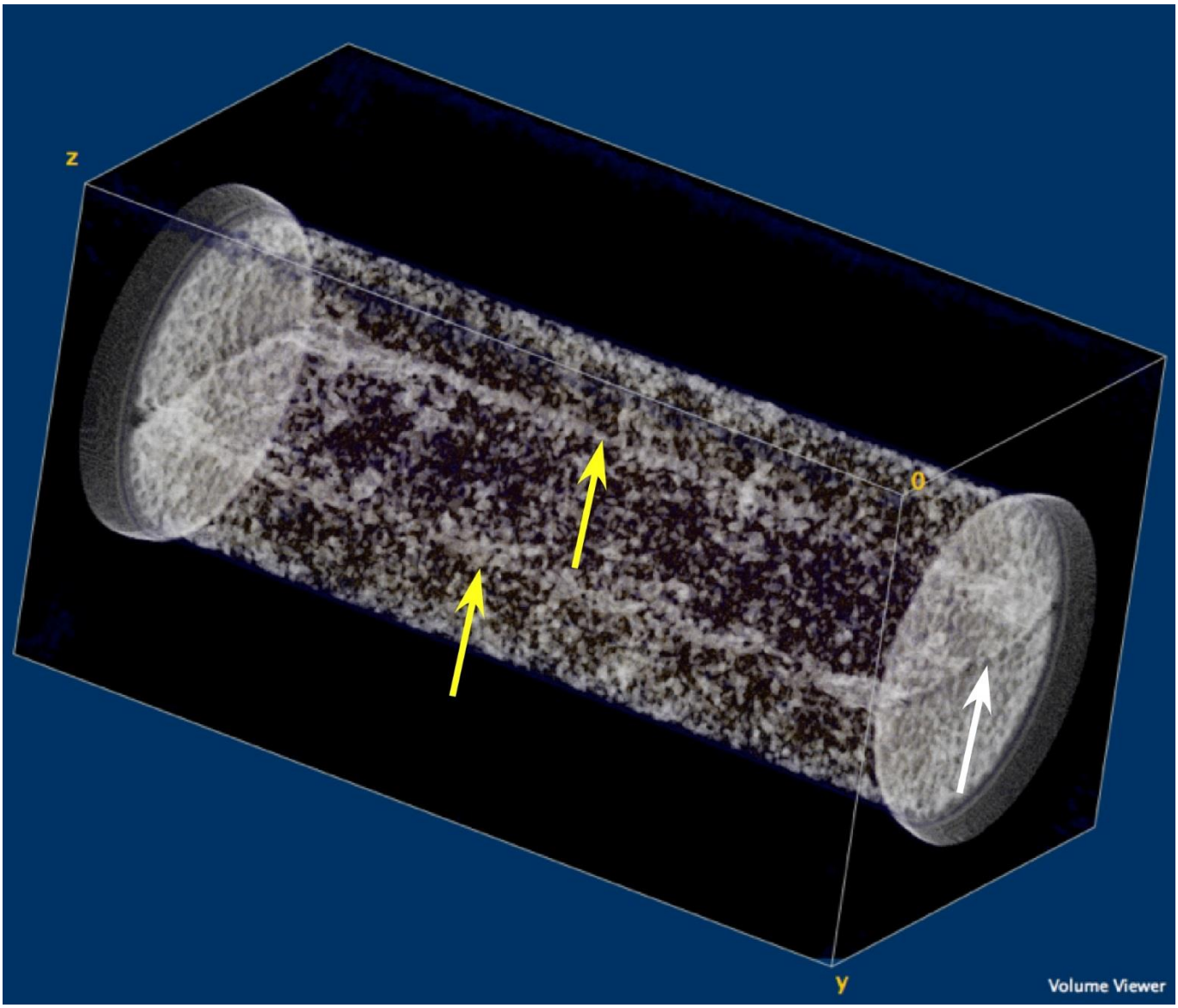

Figure 2.33. X-ray CT scan of 1.5 inch diameter Berea Gray split core saturated with 3 M KCl brine. The fracture is identified by the white arrow. A wider aperture is seen along the outside regions of the fracture (yellow arrows).

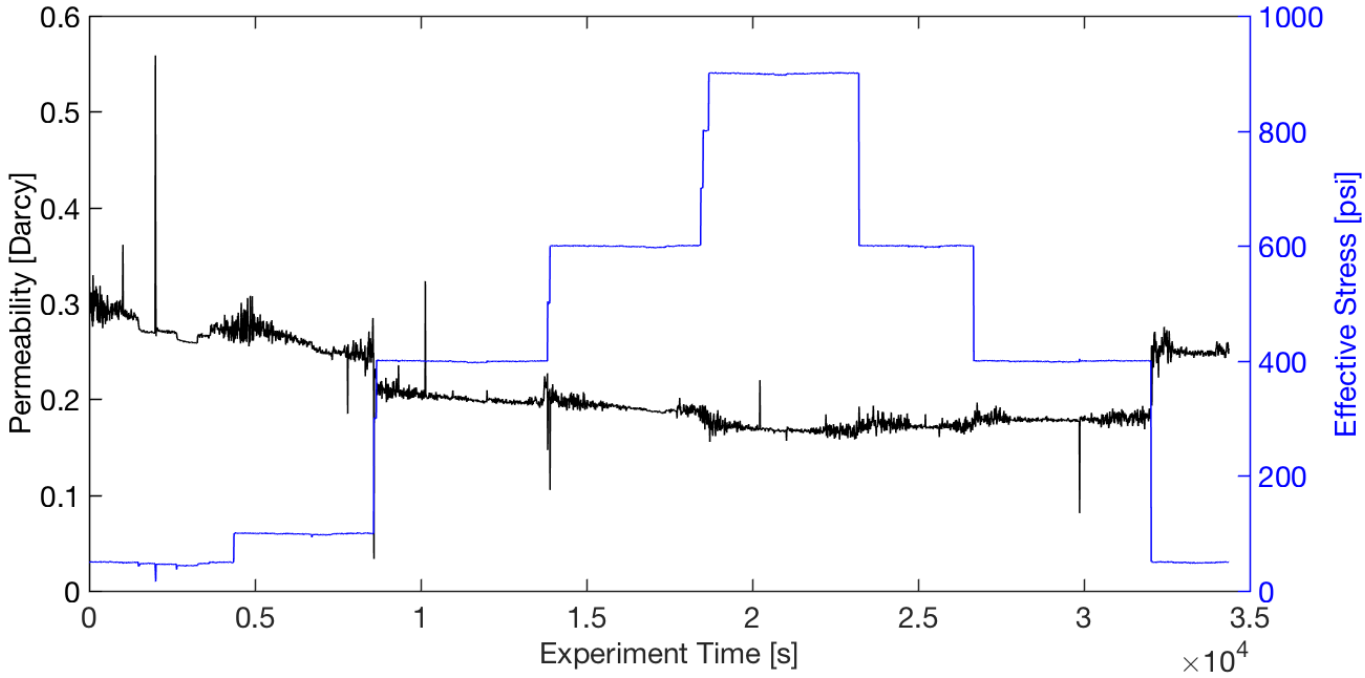

Figure 2.34. Brine permeability (black curve) vs effective stress (blue curve). The x-axis is experiment time, in seconds.

Permeability versus effective stress for sc-CO_2 injection

We measured effective permeability for sc-CO_2 flow through a brine-saturated sample. Images of CO_2 invading the rock are shown in Figure 2.35 for the whole core and Figure 2.36 for the aperture. Both of these images come from early time (~4 minutes flow at 2 ml/min). In Figure 2.35, brighter regions qualitatively indicate remaining brine. Flow is from right to left, and it is clear that under these conditions, CO_2 is being forced both through the aperture and through the rock. The brighter region at the left shows that at the early time, the CO_2 has not completely swept the brine, but that CO_2 has nearly swept the brine out of the upstream (right) side of the core. Figure 2.36 shows the CO_2 invasion in the aperture, with brighter regions indicating higher sc-CO_2 saturations. This invasion is consistent with that shown in Figure 2.35, with partial displacement of the brine early in the test. Figure 2.37 shows preliminary sc-CO_2 effective permeability measurements versus effective stress. As with the permeability measurements for the brine-saturated core, a number of flow rates were used at each effective stress. The high variability in permeability occurs primarily for the lowest flow rates. The measurements show system noise, not electrical noise. This noise could originate from a number of sources, including snap-off events in the sample or tubing, or control issues on the back-pressure pump.

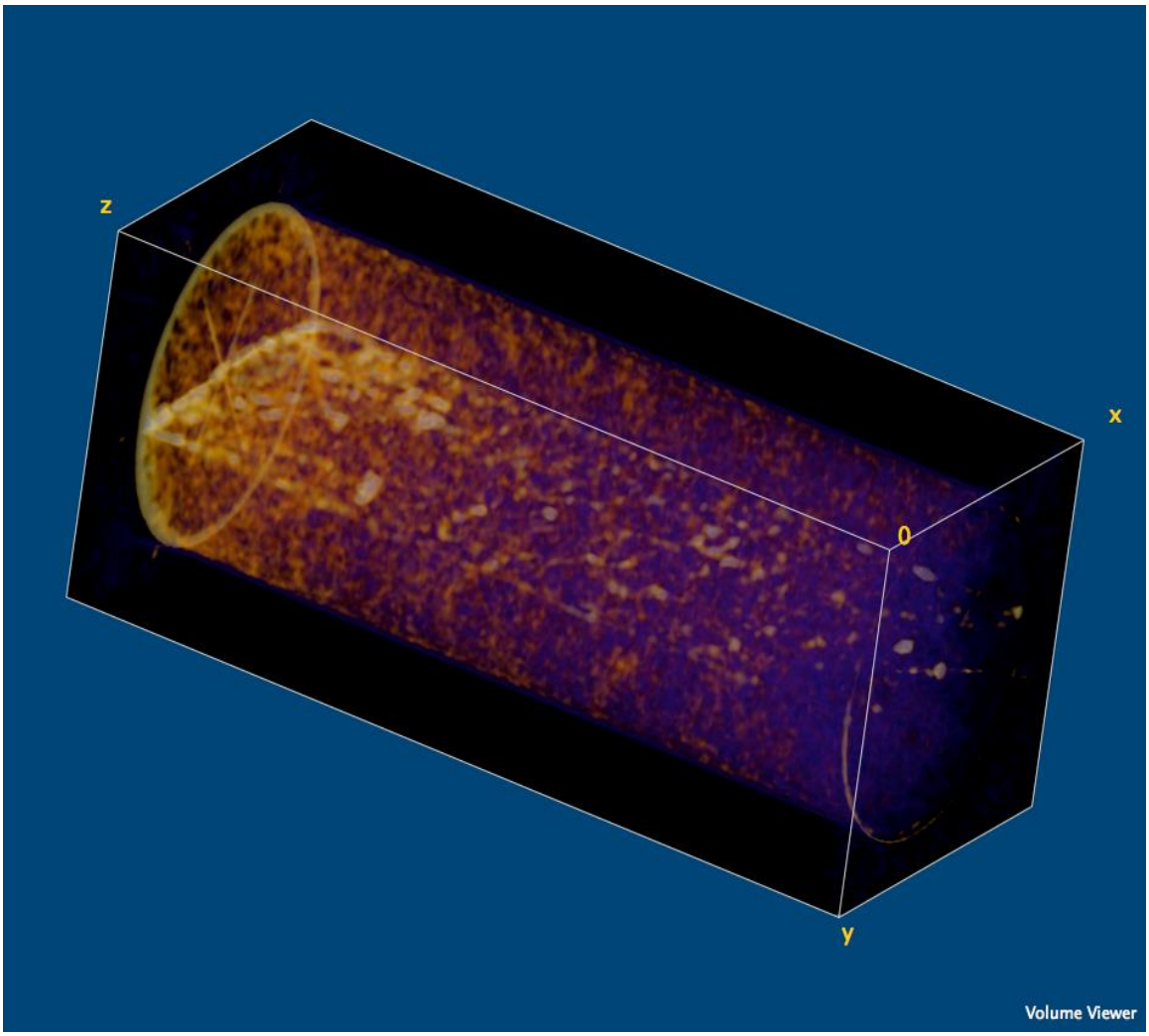

Figure 2.35. Differential CT scan of the saturations at 4 minutes subtracting the initial brine saturated state. The brighter colors represent the brine. Flow is from the right.

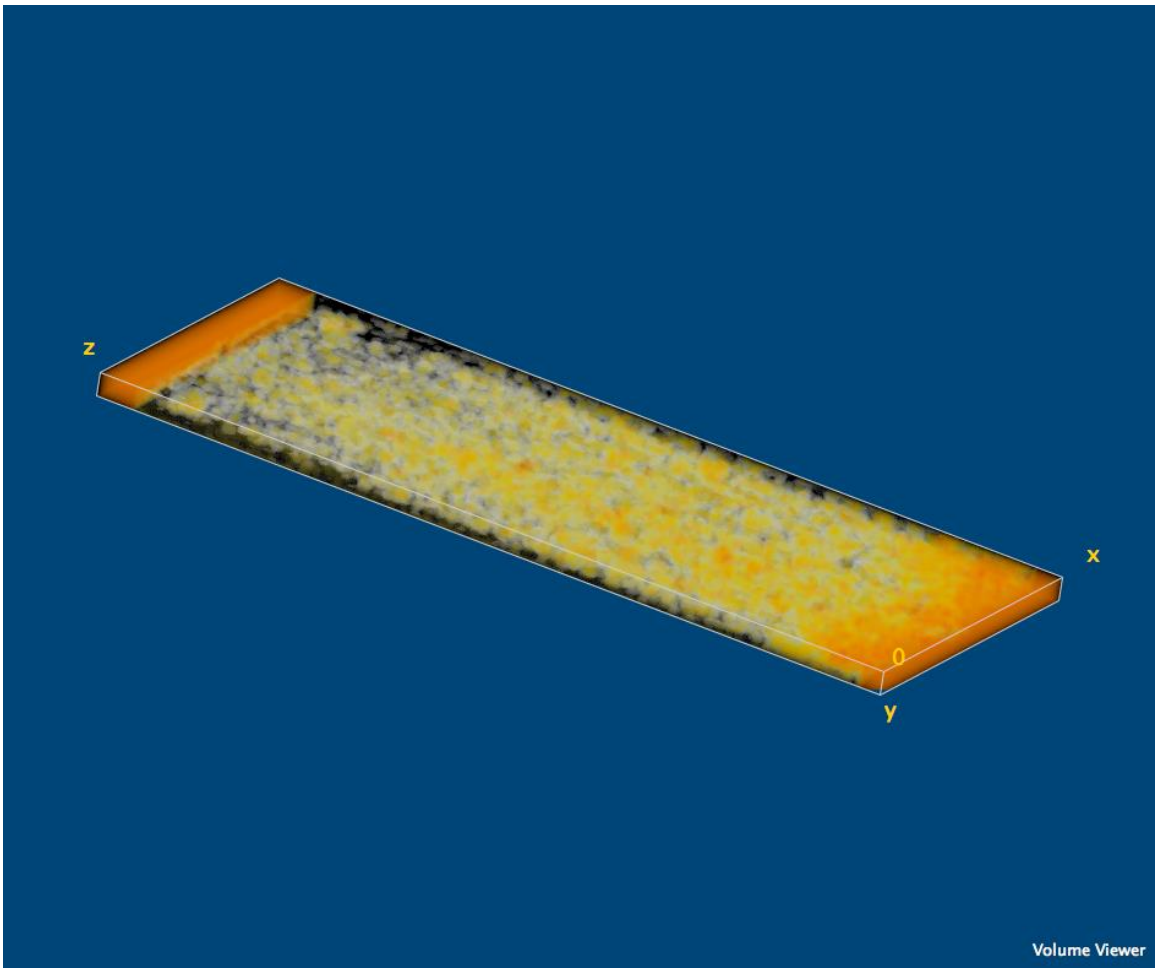

Figure 2.36. Differential CT scan of the saturations in the aperture at 4 minutes subtracting the initial brine saturated state. The brighter colors here represent the sc-CO_2. Flow is from the right.

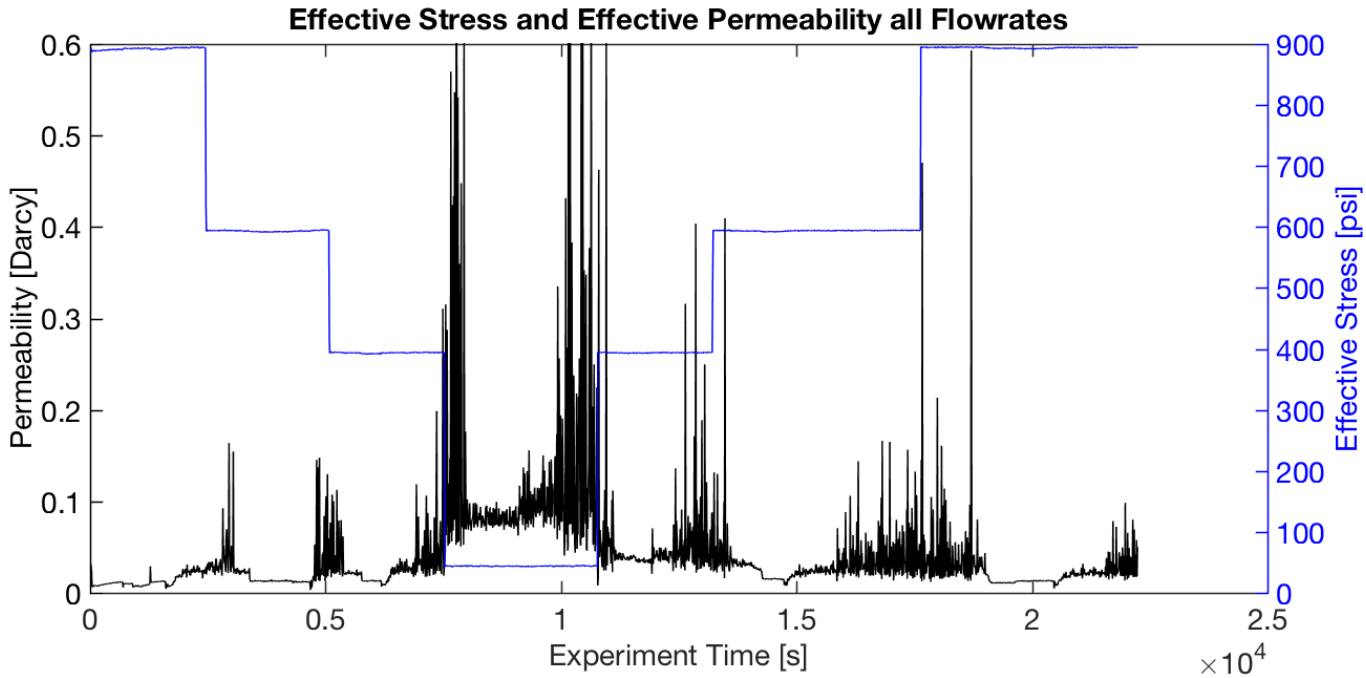

Figure 2.37. Effective (relative) sc-CO_2 permeability (black curve) vs effective stress (blue curve). The x-axis is experiment time, in seconds.

During the sc-CO_2 experiments, we identified a CO_2 bypass mechanism in our system. We were using the widely accepted Teflon/metal/Viton sleeve combination used by many, and careful image analysis shows that some CO_2 is being transported in or near the sleeve, shown in Figure 2.38.

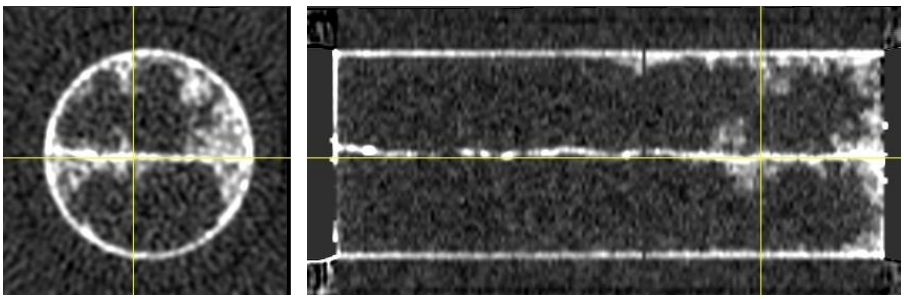

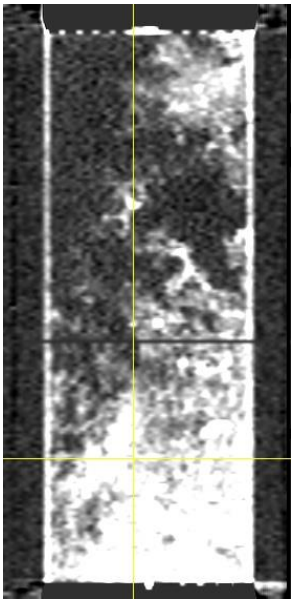

Figure 2-38. Three cross sections showing CO_2 (bright) in the fractured sandstone sample and sleeve. CO_2 flows through the fracture, is present in the matrix, and also along the outer perimeter (sleeve).

Consequently, we designed a different sleeve structure for our samples, using a Kapton (polyimide) film in place of the Teflon for a sleeve liner, and a high-saturated nitrile elastomer sleeve, shown in Figure 2.39.

Figure 2.39. Nugget sandstone core wrapped in polyimide film.

We then tested this using a ~1 md Nugget sandstone. This layered sandstone is composed of rounded grains with local cement inclusions. This sandstone was fractured using the Brazilian technique and Figure 2.40 shows the result with the layering clearly apparent.

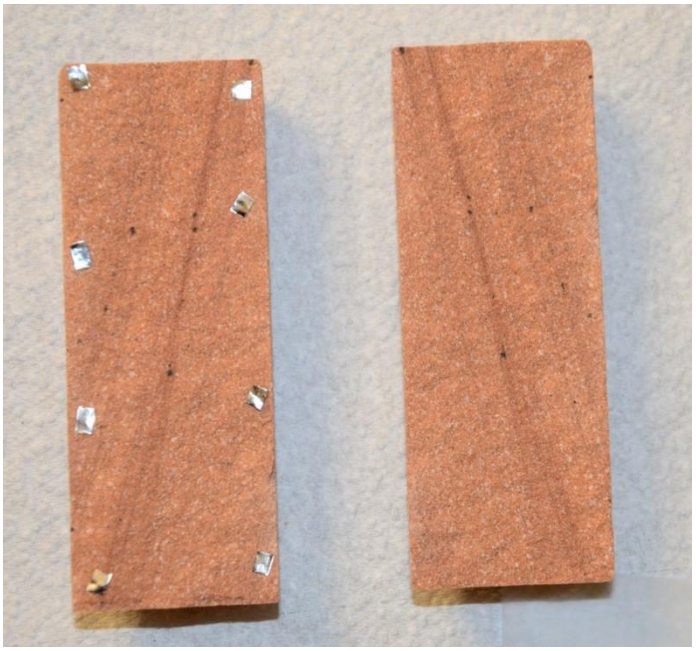

Figure 2.40. 1.5 inch diameter Nugget sandstone core halves with 50 micron NiCdFe shims.

Upon fracturing, there was some material loss along the fracture plane. In addition, we used eight small NiCdFe shims (~50 micron thick) to separate the halves, shown in Figure 2.40. X-ray CT scanning shows the resulting aperture under a 100 psi effective stress, shown in Figure 2.41.

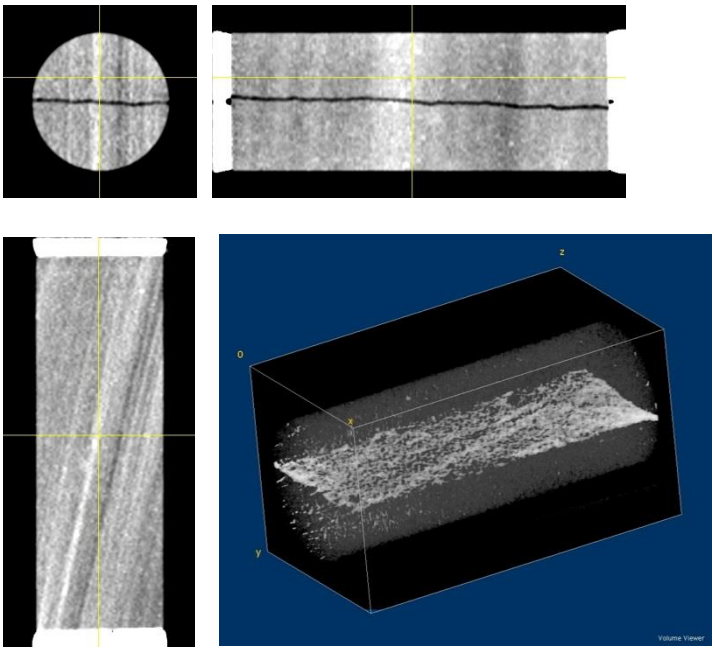

Figure 2.41. Three perpendicular cross sections from an X-ray CT scan showing the fracture aperture (dark) and layered structure of the sandstone. The yellow cross hairs on each image correspond to the same location in the sample. The lower right image shows the aperture in the core.

Preliminarily porosity structure was computed from saturated and unsaturated CT scans, shown in Figure 2.42. The resulting porosities are computed on a voxel basis, and the voxel size is 193x193x625 microns.

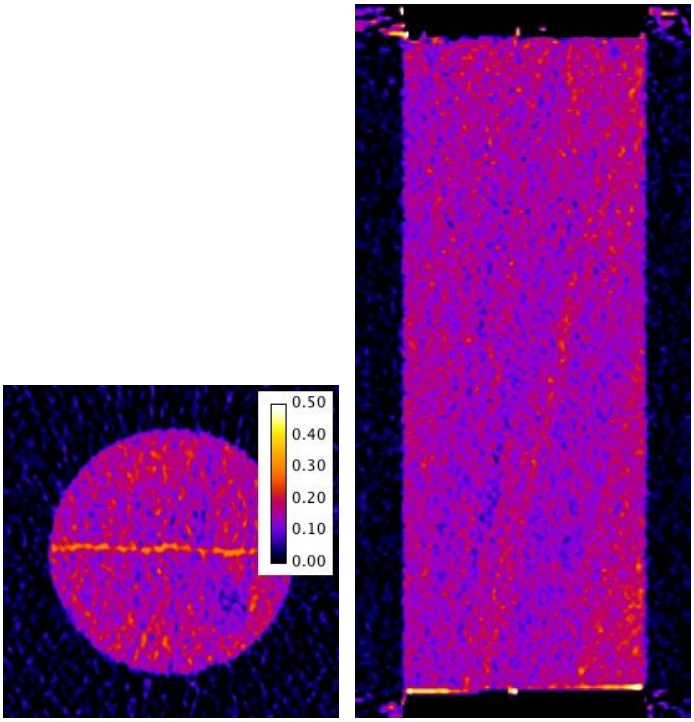

Figure 2.42. Porosity structure, computed from saturated and unsaturated CT scans

We continued our investigation of the changing effective stress on flow through fractured sandstone by conducting a set of experiments on Nugget Sandstone cores, which were briefly described above. The cores were purchased from Kocurek Industries (South Caldwell, TX) as a batch of 1.5 inch diameter by 4 inch long cores. Nominal properties for this Utah sandstone are 1-5 mD- brine permeability, 9.4-10.6% porosity, and an unconfined compressive strength of 16,000 psi. The cores were fractured parallel to the core axis using the Brazilian technique. Eight nickel-iron-cadmium shims, selected for corrosion resistance, 0.04 mm thick and about 2 mm x 2 mm in extent were distributed on one face of the fracture, and the two halves matched as closely as possible. The core was wrapped in polyimide film which has a low permeability to CO_2, and the assembly was placed in a highly saturated nitrile elastomer sleeve, selected because of its resistance to CO_2 degradation. The sleeve was installed in an aluminum core holder that is transparent to X-rays, such that the core butted against the stainless steel end pieces. On the inlet end there were two influent tubes allowing co-injection of different fluids. On the outlet end, there was a single tube. The space between the elastomer sleeve and the pressure vessel was filled with nitrogen, and this pressure was controlled using an Isco 500D high-pressure syringe pump.

Both CO_2 and brine were fed to the core using Isco 500D syringe pumps, and backpressure was controlled and fluid taken up by a fourth high-pressure syringe pump, shown in Figure 2.43. Pressures were measured using Wika pressure transducers in addition to those on the Isco

pumps, calibrated in-house to an Omega pressure calibrator. Pressure differential was measured using an Azbil differential pressure transmitter. Data was collected using a Keithley 2700 data logger controlled using a computer with a custom code written in Labview®.

The core holder was mounted to the travelling table of a General Electric Lightspeed 16 slice medical CT scanner. Voxel size was set to 0.193 x 0.193 x 0.625 mm and scans were performed at 120 kV and 160 mA. CT scans were taken as warranted by the work, with dry and saturated scans taken for saturation calculations. Core deformation, not only in the fracture region, was also observed as the effective stress changed. Approximately 49 sets of scans were collected over the duration of the test. An example showing the average porosity of 18 slices (0.193 mm thick) perpendicular to the bedding is presented in Figure 2.44. The porosity computed from the CT scans using the difference between the brine-saturated and dry scans ranges from about 11% to about 20%; both values are higher than the bounds Kocurek estimates.

The core was initially vacuum saturated with brine (5 g/L NaCl) under a low effective stress. The effective stress was determined by independently controlling both the pore pressure and the confining pressure. Flow through the core was induced by maintaining the influent side at a constant pressure, and withdrawing fluid on the downstream side. This tended to work well with a relatively incompressible fluid being displaced by a more compressible fluid. Pumps were maintained at room temperature, and volumetric flowrates were measured at room temperature. Pore pressures for the brine tests ranged from 100 - 2100 psi, and 950-2100 psi for the CO_2 tests. All brine permeability measurements were made for at least 3 flow rates, with data plotted such that the slope of the line represents permeability. Plotting the data in this fashion allows direct observation of nonlinearity indicating other effects. None were observed. For CO_2 apparent permeability measurements, flow was constantly delivered at 0.09 ml/min CO_2, 0.01 ml/min brine.

The set of tests included measuring the apparent permeability of the fractured sandstone over a range of effective stresses with brine as the permeant. Following this, the permeant was changed to 90% sc-CO2, 10% water. The reason for the mixture was to allow the test to occur on a system without using a CO_2 humidifier, while eliminating evaporation effects. Again, a range of effective stresses was investigated.

Measured apparent permeabilities are shown in Figure 2.45. Initial brine measurements were made increasing the effective stress by initially increasing confining pressure while maintaining the pore pressure. Repeated measurements were made at the effective stress of 1600 psi, to determine the possibility of an inward leak of confining gas resulting in the decrease of apparent permeability seen at that condition. The confining and pore pressures were elevated, and the permeability values returned to the expected curve due to the compression of gas that may have leaked into the core. The confining and pore pressures were sequentially changed to 2400 and 300 psi, respectively to obtain an effective stress of 2100 psi. Several valves in the system have maximum allowable working pressures of 2500 psi, thus the confining pressure was not increased further. To decrease effective stress, the pore pressure was increased stepwise to 2100 psi while leaving the confining pressure at 2400 psi. The permeability values at low initial effective stresses are not plotted in Figure 2.45 as they were an order of magnitude higher than at the effective stress of 500 psi. As expected, as the effective

stress increased, the permeability decreased. Figure 2.46 shows a single representative X-ray CT slice of the changes in the system between the 500 psi effective stress and 2100 psi effective stress conditions. No change in density is indicated by the yellow color. Locations where density increases between conditions are dark (purple or black) and regions where density decreases are light. The outer purple circle is the confining nitrogen (increases in density as the nitrogen pressure increases), the next circle inside that is the nitrile sleeve. The bright narrow circle inside the nitrile sleeve is the result of the rock densities in the 500 psi case being replaced by nitrile in the 2100 psi case (smaller sample). The dark central fracture changes indicate rock replacing brine, also indicating a decreasing size.

Upon decreasing effective stress, the permeability increased indicating the opening of the aperture, but did not reach that of the initial condition. This indicates that the shims were deformed and some of the asperities in the aperture were smashed at the higher effective stresses. This is not surprising as some material was removed upon the initial fracturing. No produced solids were identified.

Measurements using CO_2 started with the confining and pore pressures being 2400 and 2100 psi, respectively (300 psi effective stress), and the pore pressure was gradually lowered to about 900 psi resulting in about 1500 psi effective stress. The pressure was not lowered beyond 900 psi as the CO_2 in the ambient temperature pumps would separate into 2-phase liquid/gas systems and difficulties in process control could occur.

The apparent permeability when the CO_2 reached the rock decreased one order of magnitude from the brine permeability, and to the extent visible, CT images show the CO_2 flowing in the fracture only at low effective stress. This change in permeability was not unexpected, as CO_2 would be expected to be the non-wetting fluid. This expectation has been called into question recently, as changed in wettability have been observed by others (Wang and Tokunaga, 2015; Tokunaga et al., 2013; Wan et al., 2014; Kim et al., 2012). As effective stress increased, the permeability decreased as expected by as much as about 30%. This closing of the fracture forced CO_2 into the matrix into higher porosity regions likely also having larger pore throat sizes (Figure 2.47). These two conditions do not always occur together.

The changing effective stress affected the rock permeability and also the sample size. These were indicated by pressure differential for the permeability measurements and CT measurements for rock size. The fracture was expected to close upon increasing effective stress. This would affect the permeability, as one could model the flow in two parallel flow paths (rock and fracture), with one of the flow paths being restricted as the effective stress increased. If the rock were infinitely strong, the increasing effective stress would only shift core halves together. Figure 2.46 and the entire data set it was extracted from suggest fracture closes, resulting in the more obvious (bright) changes on the outer rim of the rock on the top and bottom. But there appeared to be some compaction on the sides as well. The CT noise was too high to be conclusive here, but this is suggested.

The system permeability continued to change with increasing effective stress, but this change was beginning to level out at the higher effective stresses. It was somewhat surprising that the permeability recovered as much as it did upon the reduction of effective stress, as the fracture

closing was assumed to be due to brittle asperities breaking. The permeability increased by about 50% as the effective stress was reduced.

Introduction of the CO_2 into the brine-saturated core was begun at low effective stress to allow flow through the aperture if possible. Increasing the effective stress forced the CO_2 into the matrix in higher porosity bands subparallel to the axis of the core. This began at an effective stress of about 1000 psi, indicating the fracture flow pathway was sufficiently closed at this stress. We did not measure the capillary entry pressure of either the rock or the fracture.

Measurements of the apparent permeability of the system to sc-CO_2 as the effective stress declined were not made. It was felt that the system had changed sufficiently due to the drainage and residual presence of CO_2 in the pore space.

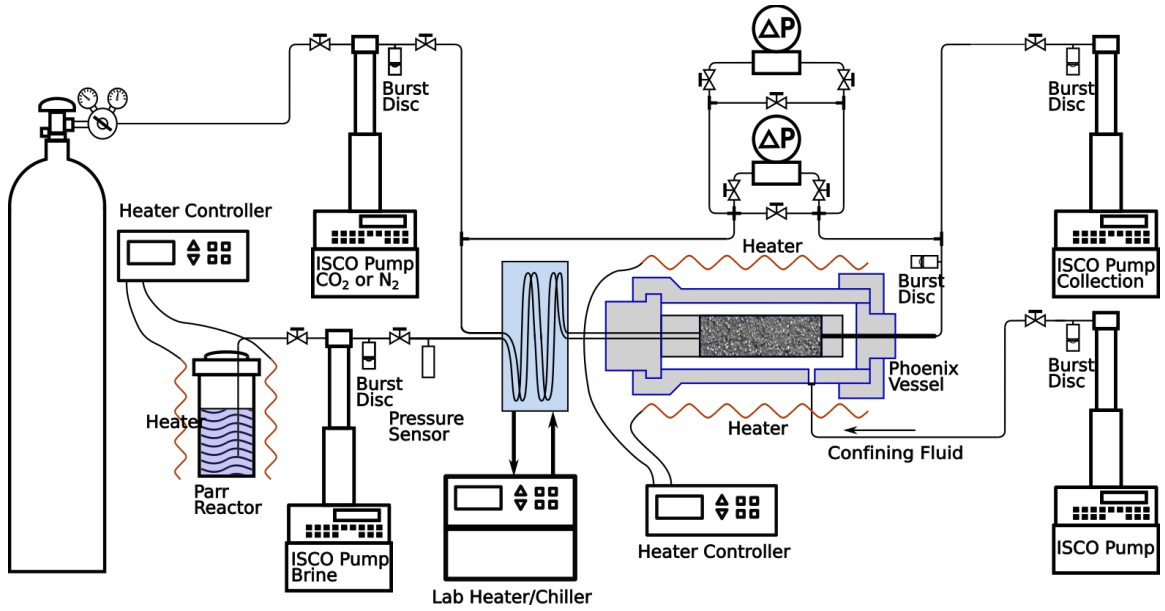

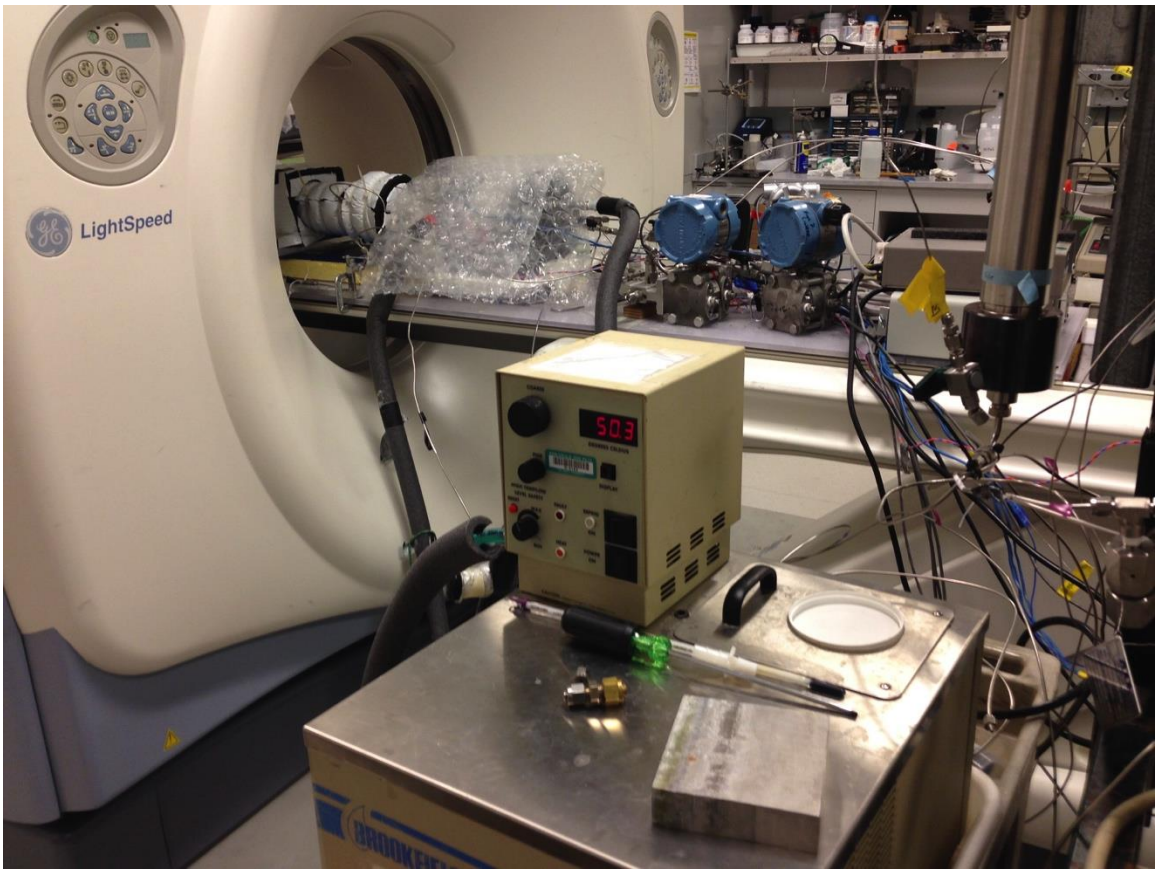

Figure 2.43. Top - experiment setup. Bottom – setup on scanner table

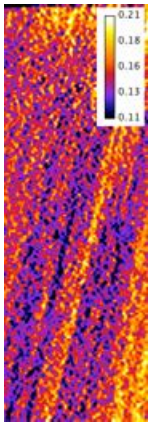

Figure 2.44. Average porosity of 18 slices each 0.193 mm thick showing bedding.

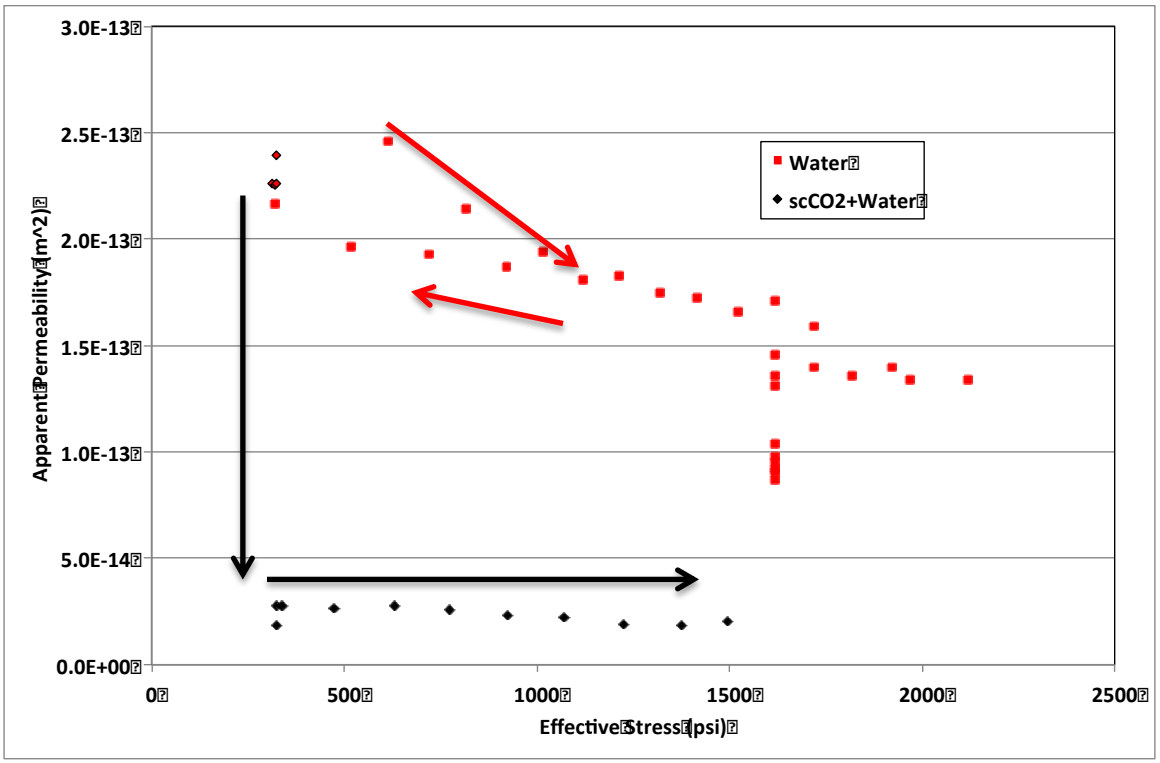

Figure 2.45. Measured apparent permeabilities for brine (red squares) and sc-CO_2 (black diamonds)

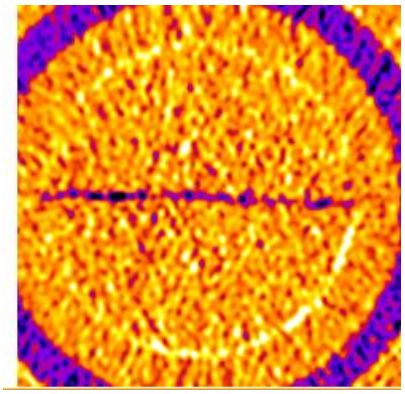

Figure 2.46. Difference between 500 psi and 2100 psi effective stress. No change in density is yellow. Locations where density increases between conditions are dark (purple or black) and where they decrease light, neutral changes are yellow. Outer purple circle is the confining nitrogen (increases in density as the pressure increases), the next circle inside that is the nitrile sleeve. The bright narrow circle is the result of the subtraction rock densities in the 500 psi case being replaced by nitrile in the 2100 psi case (smaller sample). The central fracture changes indicate rock replacing brine.

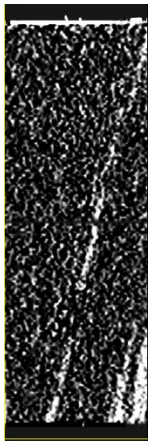

Figure 2.47. CT image showing CO_2 (bright) flow through the matrix near the fracture. Flow is from bottom to top. Note – this image is not from the exact same slices as Figure 2.4.

For the brine, the effective stress was raised from 300 psi to 2100 psi by increasing the confining stress, and then lowered to 300 psi by increasing pore pressure. The effective stress with the sc-CO_2 was increased from 300 to 1475 psi by lowering the pore pressure while maintaining the confining pressure, shown in Figure 2.48. CT scanning was performed at numerous junctures to aid in understanding the system

.

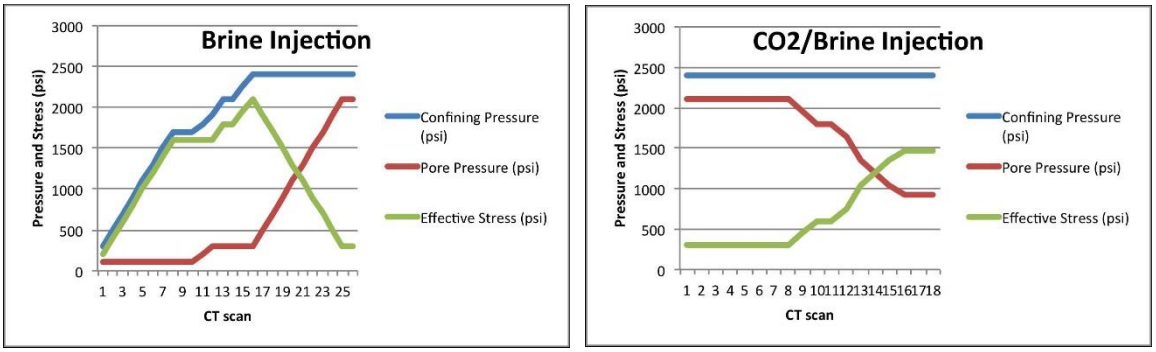

Figure 2.48. Pressure/stress pathways for brine permeability (left) and CO_2/Brine permeability (right).

Our analysis included three regions of interest (ROI). CT data were analyzed using imageJ (Schneider et al., 2012a) and FIJI (Schindelin et al., 2012b). The first ROI is the entire sample cylinder with a little of the elastomer sleeve, shown in Figure 2.49a. The data we showed were differences between sets of CT scans, thus the density of the elastomer should not change resulting in no net density change. The size of the ROI provides a slight volume increase over the sample by itself. The second region of interest, shown in Figure 2.49b, is the sample core volume excluding the sleeve. The third region is near the aperture, shown in Figure 2.49c, attempted to ignore the matrix. The differences (177 slices per scan, 19 sets of data) were performed by subtracting the set of images at time *x* from the initial case (low effective stress). This resulted in elevated values where a lighter material replaced a heaver one and darker colors where a heavier material replaced a lighter one. Thus, where sc-CO_2 replaces brine, the

signal is bright. In the images in Figure 2.49, dark circles with corresponding light circles (see top right corner of Figure 2.49a) resulted from a translation of a portion of the apparatus with respect to the rest of it. The image stacks were aligned based on the sample itself, minimizing this effect for the sample.

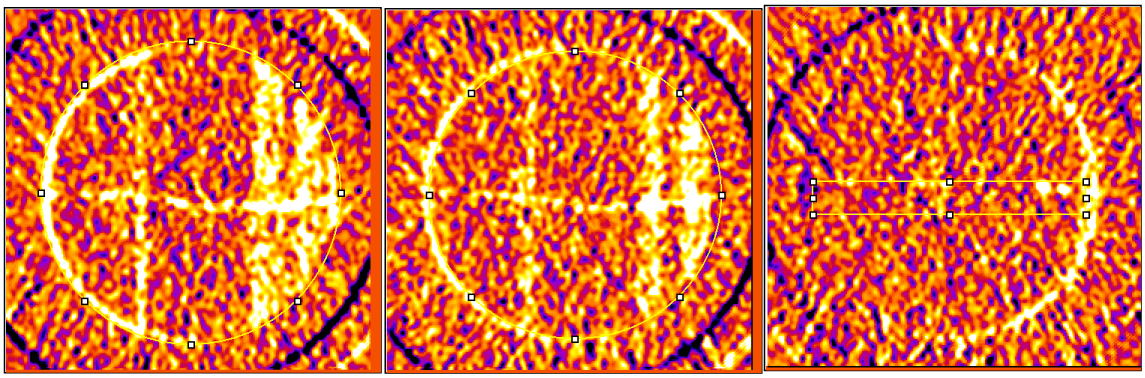

a. b. c.

Figure 2.49. Difference of X-ray CT scan slices showing the regions of interest. In these images, no change from the reference initial state is orange. Density decreases are shown in yellow to white, and dark colors indicate a decrease in density (Here these are primarily from parts of the system translating relative to each other between scans). a. circle including edge, b. circle not including edge, and c, near-aperture rectangle.

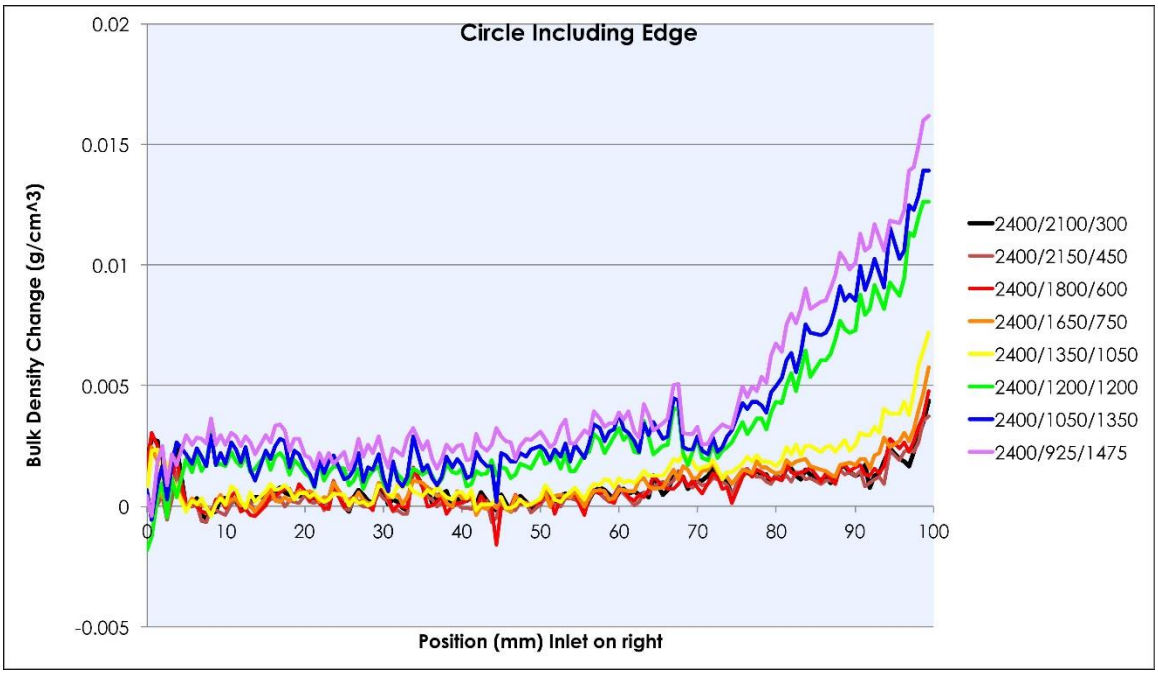

a.

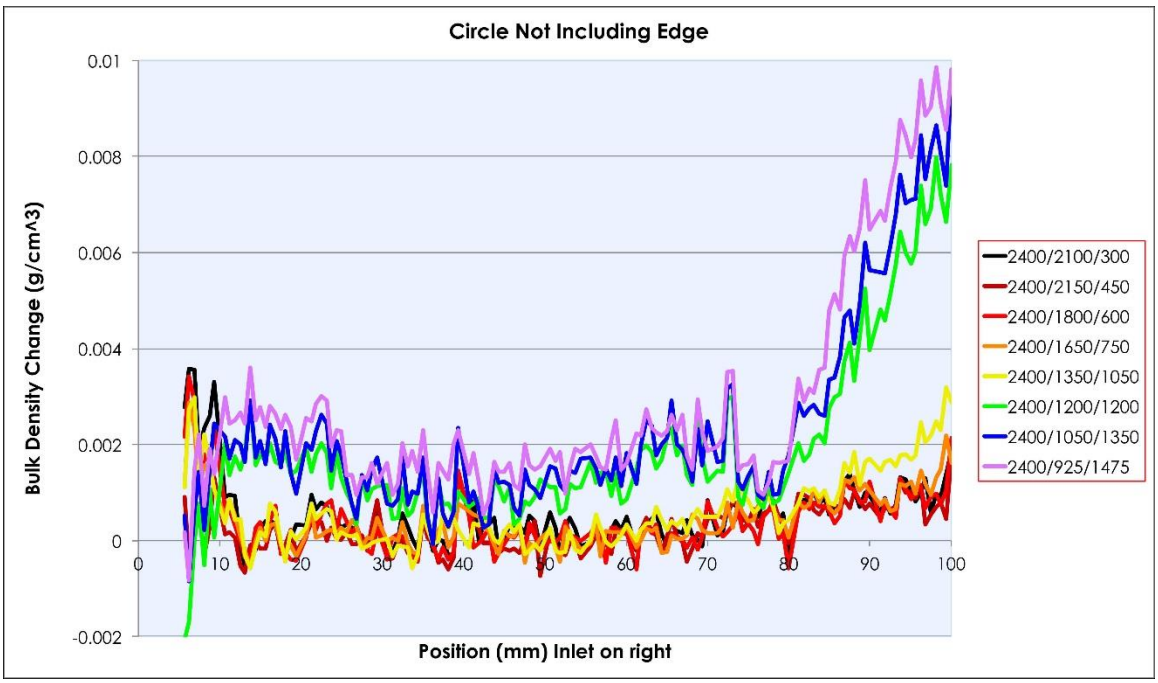

b.

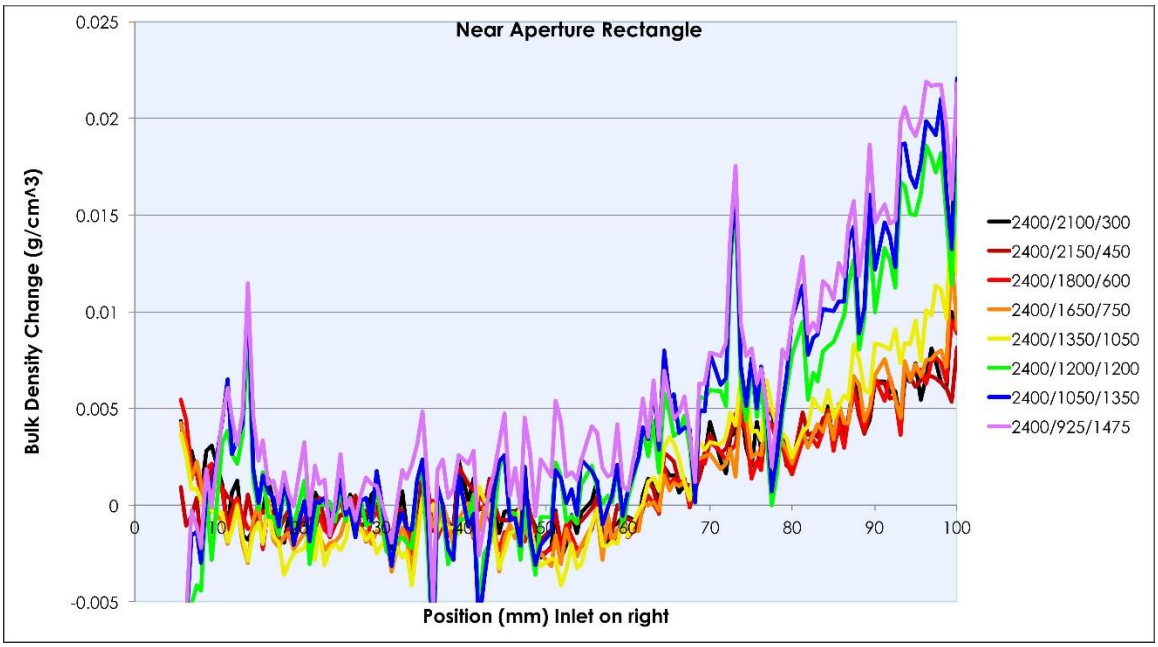

c.

Figure 2.50. Bulk density changes for each CT slice. Note that the inlet is on the right, and the actual bulk density changes are negative. a. entire sample with some of the sleeve, b. sample immediately inside the sleeve, and c. a rectangular prism near the aperture.

Over the test, the sc-CO_2 invaded into both the medium and the aperture. Recall that for the brine permeability test, the permeability changed over the entire range of effective stresses, but did not return to the initial value at the end of the test. This indicated that the aperture was compressed at elevated stress, and some of that deformation remained. As is often the case, the sc-CO_2 saturation was higher at the injection end of the sample throughout the test, shown in

Figure 2.50. The actual saturations have not been computed because of the changing density of CO_2 over the range of effective stresses caused by pore pressure changes. In viewing Figure 2.50a, as the series of tests progressed, the entire curves moved vertically upwards. This was due to increasing sc-CO_2 saturation and decreasing CO_2 density.

Figures 2.50a and 2.50b were directly comparable, as the sample sizes were approximately the same. Figure 2.450b showed slightly lower changes in bulk density overall due to the processes occurring at the sleeve, and the interim peaks were at slightly different locations. The magnitude of the bulk density changes in Figure 2.50c were typically higher because of the smaller selected volume concentrating the volume with changes. In addition, the curve shape also was slightly different as the aperture heterogeneity was different from the matrix heterogeneity.

A question that arose from the analysis was whether CO_2 was transported along the sleeve wall. There is clearly a bright region over part of the slice shown at the rock/sleeve interface, shown in Figure 2.51a and Figure 2.51b. Again there may be multiple causes. The most probable reason was CO_2 could be displacing water.

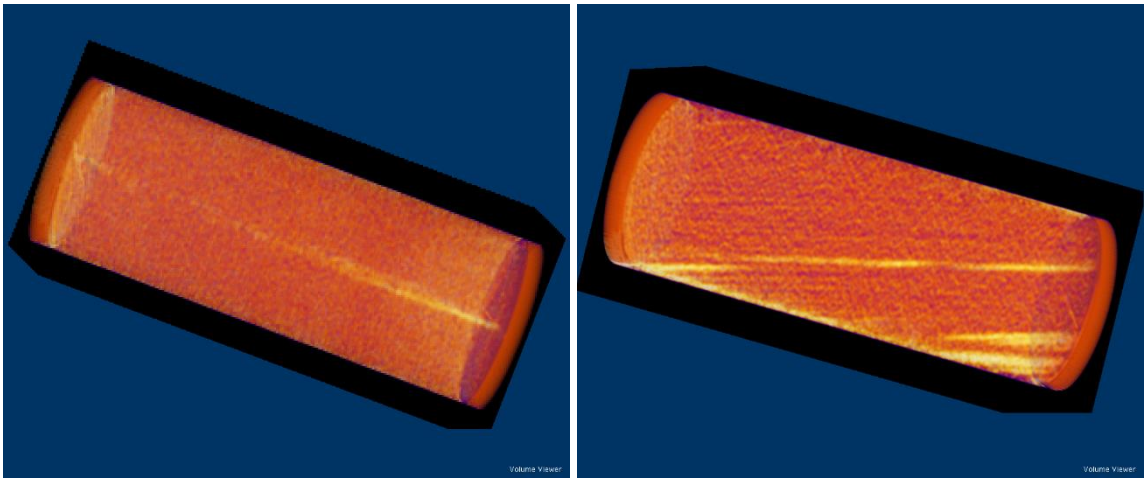

a. b.

Figure 2.51. Projection views of the differenced CT data showing the location of the sc-CO_2. In a. we view along the aperture and see the CO_2 there. In b. we are viewing perpendicularly to the aperture, focusing on the CO_2 in the matrix.

Task 3. Development of fundamental understandings and correlations of occurrence of CO_2 injection pressure induced fracturing by laboratory studies.

Fracturing using brine

Laboratory equipment

The equipment used for conducting hydraulic fracturing experiments include a tri-axial loading system, an injection pump, and data acquisition devices.

The tri-axial loading system is a pneumatic powered hydraulic press frame. It consists of three hydraulic pistons. Two of the pistons are in horizontal directions and perpendicular to each other. Both of these two pistons are located in a carbon steel containment ring with counter blocks to provide counter stress, as shown in Figure 3.1. Another one is in the vertical direction and fixed on the loading frame, as shown in Figure 3.2. The hydraulic pistons are powered by three manually controlled pneumatic pumps. The tri-axial loading system can provide up to 4500 psi stress in horizontal direction and 6000 psi stress in vertical direction on an 8 inch cubic block.

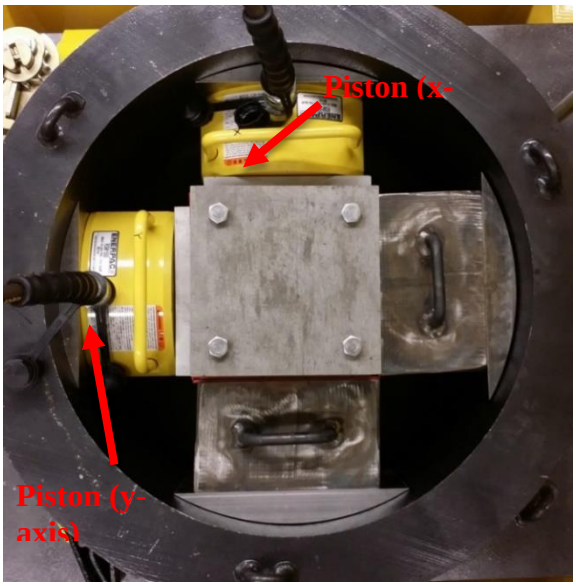

Figure 3.1: Pistons in Horizontal Direction within Containment Ring.

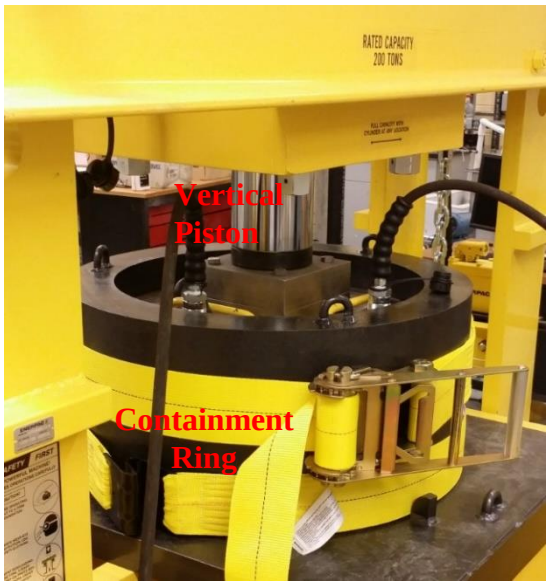

Figure 3.2: Vertical Piston on Rolling Frame and Containment Ring.

The injection pump used for hydraulic fracturing experiment is ISCO 500HPx, manufactured by Teledyne Isco, which is shown in Figure 3.3. The ISCO 500HPx is a large capacity high pressure syringe pump. It can provide precise, predictable flow and pressure control at flow rates from sub-microliter to 408 mL/min. The maximum output volume of one stroke is 507.38 ml before refilling. This pump can work within the pressure range of 10 to 5000 psi, which is ideal for both hydraulic and super-critical CO_2 fracturing.


Figure 3.3: ISCO 500HPx.

The data acquisition devices used in the hydraulic fracturing experiments include temperature sensors and pressure transducers. Temperature sensors used in the experiments are Type T thermocouples, which are made of copper and constantan and suited for temperature measurements in the -200 to 350 ºC range. Up to seven thermocouples can be used in an experiment. Pressure transducers are used to monitor pressure inside the wellbore of a sample, and injection gas pressure in the gas accumulator. The pressure transducers are rated up to 3000 psi and are connected to the data acquisition system, which can provide real time reading or monitoring while testing.

Initial experiments

All of the concrete samples used for testing had a six inch borehole, with the upper two inches impervious to flow. We began these experiments by hydraulically fracturing four concrete samples with brine. The objective of these experiments was to get a better understanding of the fracturing process for concrete samples and thus establish a standard test procedure. The confining stresses were 500 psi in x-direction, 750 psi in y-direction, and 1000 psi in z-direction. Two of these concrete samples were fractured at low pressure and the other two at high pressure.

Two concrete samples, Sample 32 and Sample 33, were fractured at relatively low pressure, about 450 psi. The borehole pressure profile of Sample 32 is shown in Figure 3.4. The flow rate for Sample 32 was increased from 5 ml/min to 50 ml/min at break down. The multiple flow rates resulted in the spiking pressure profile. The fracture initiation is the highest peak, around 1600 seconds and at around 450 psi. This indicated that a relative large and conductive hydraulic fracture opened inside Sample 32 at that pressure. After fracture initiation, the fracture began to propagate, causing the borehole pressure to decrease. Eventually, the fracture reached the surface of the sample. The injection rate could not maintain the borehole pressure, so it dropped to almost ambient pressure. The second peak was caused by setting flow rate to 200 ml/min, which opened a major fracture. Figure 3.5 shows the surfaces of Sample 32 after the test. The water trace on the bottom and right surface was a clear indication of fracture location. The hydraulic fracture extended from the borehole to the bottom of Sample 32, which is contained in the plane perpendicular to the minimum horizontal stress direction.

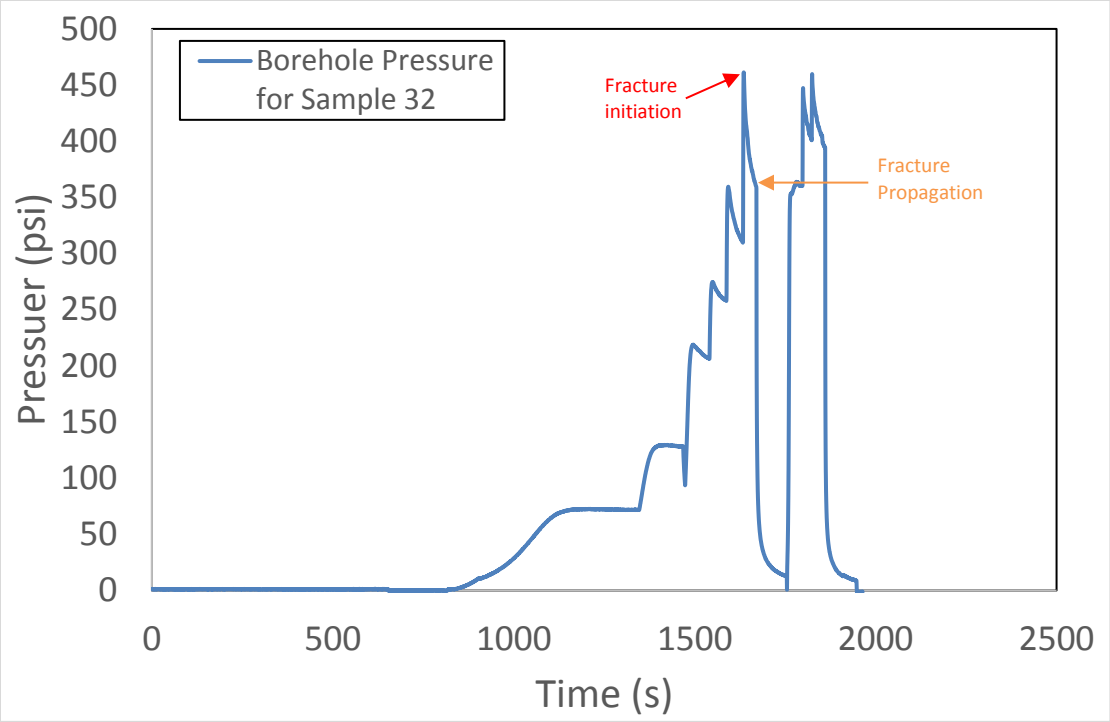

Figure 3.4: Borehole Pressure Profile of Sample 32.

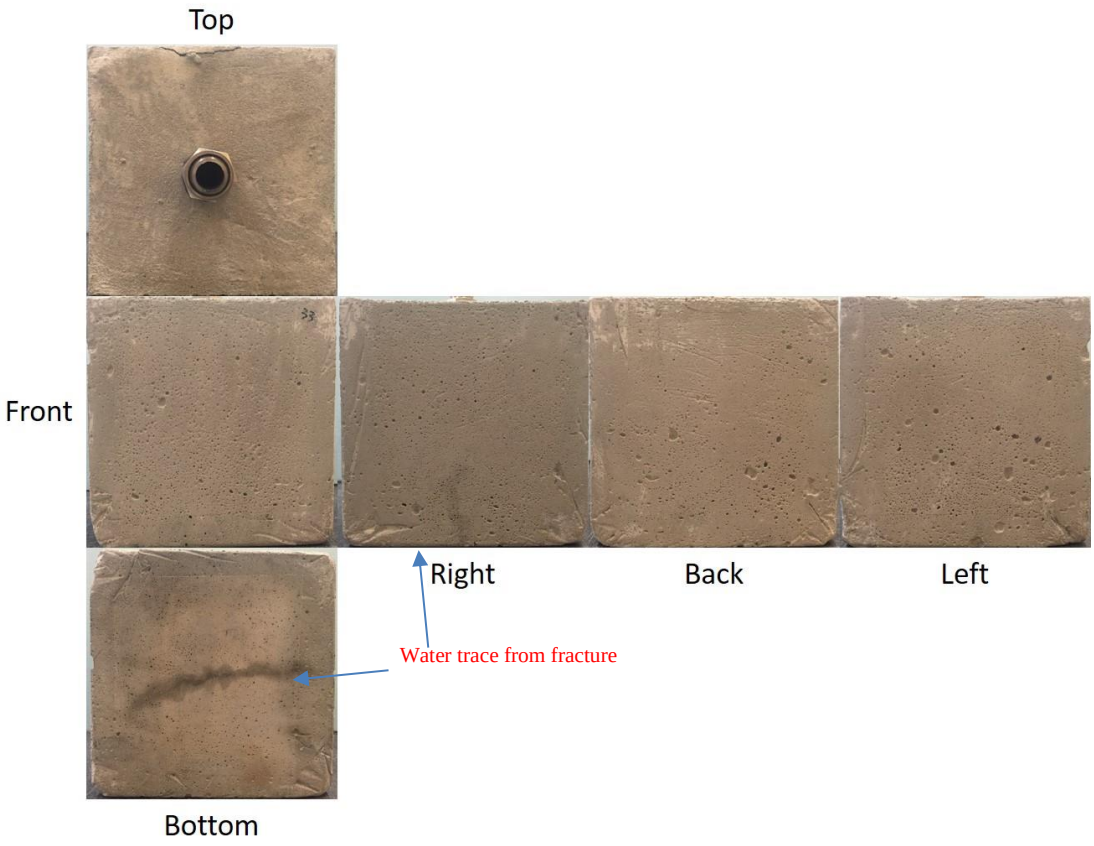

Figure 3.5: Surfaces of Sample 32 after Brine Fractured.

The pressure profile for Sample 33 is shown in Figure 3.6. The break down pressure for this sample is slightly over 450 psi. The pressure profiles are much simpler than those for Sample 32 because the injection rate was constant (200 ml/min). Also, there is no visible fracture or water trace observed for Sample 33.

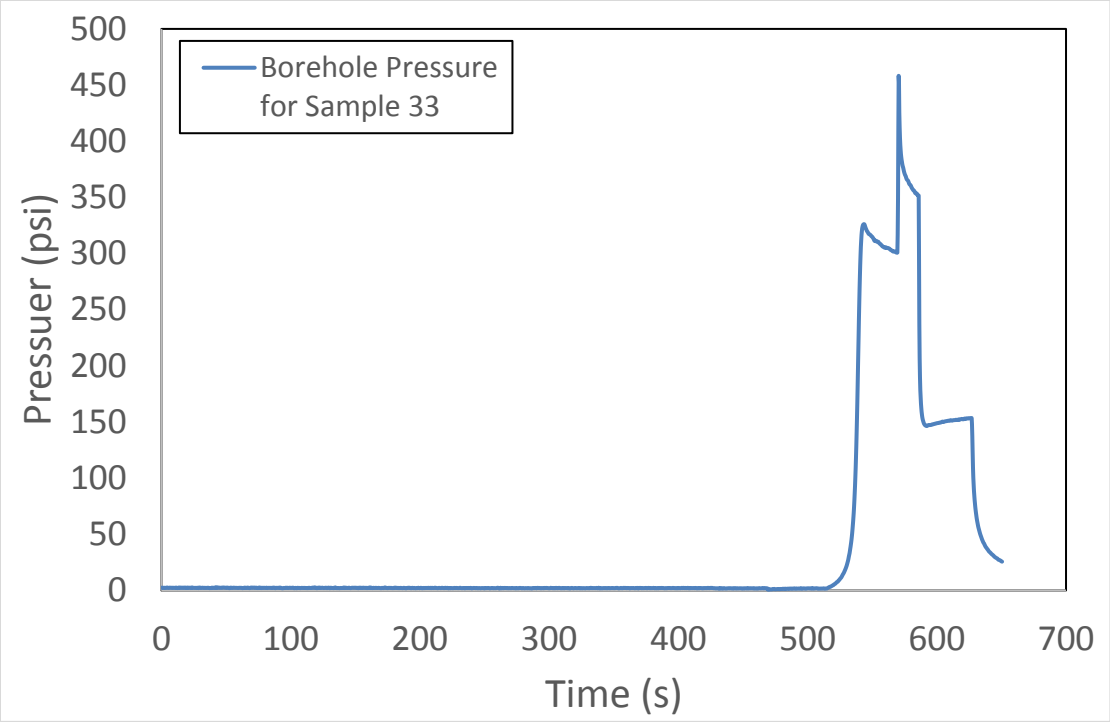

Figure 3.6: Borehole Pressure Profile of Sample 33.

Samples 37 and 38 were fractured at higher pressure, around 1000 psi. The pressure profile for Sample 37, shown in Figure 3.7, is relatively simple. After the wellbore filled with brine, at about 500 seconds, the wellbore pressure built up very quickly to about 1100 psi. Then, the fracture was initiated and propagated very fast, causing a much faster pressure decrease than the low pressure fractured samples. After fracturing, the flow rate was increased to verify the existence of hydraulic fractures.

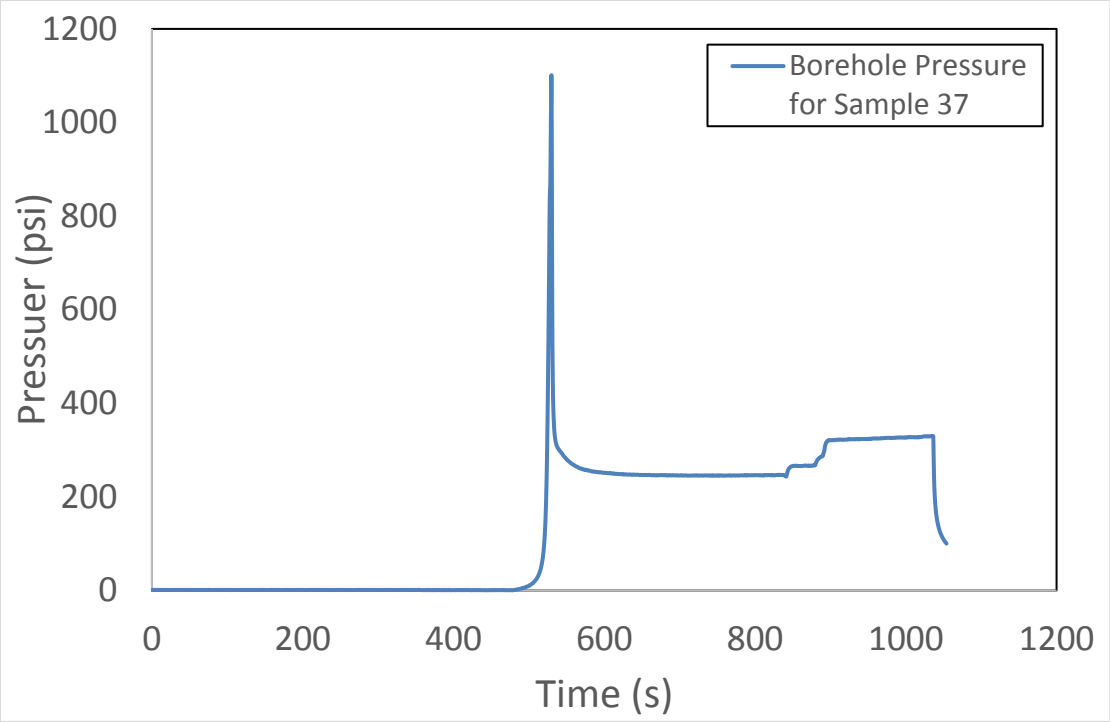

Figure 3.7: Borehole Pressure Profile of Sample 37.

The results from Sample 38 were more complex, since multiple attempts for higher flow rates were made after the initial break down, as shown in Figure 3.8. Sample 38 fractured at about 900 psi, following the same pressure pattern as for Sample 37. The objective for higher injection rates is to try to extend the fracture and increase the fracture width so that it could be observed after the experiment. However, Sample 37 and Sample 38 did not have visible fractures on their surfaces.

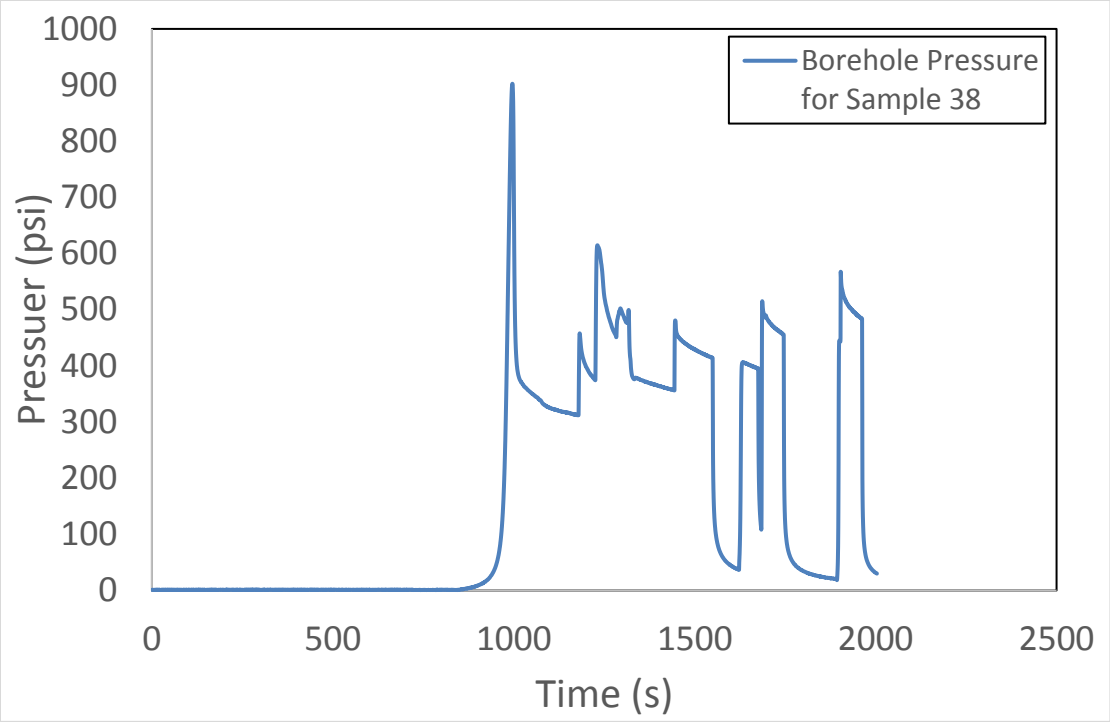

Figure 3.8: Borehole Pressure Profile of Sample 38.

The results from these four experiments show two types of fracture initiation and propagation. Both samples for each type show very similar pressure profiles during fracturing. These observations may indicate pre-existing fractures in the low pressure fractured samples, which cause pressure concentration at the tips of these pre-existing fractures that can lower the break down pressure to almost the fracture propagation pressure. Because pre-existing fractures might be induced during the drilling of the borehole, we will use more caution when drilling them.

Additional laboratory equipment and procedures

After the initial four initial experiments, new experimental equipment to measure acoustic velocity was introduced as well as procedures used to evaluate fracturing treatment efficacy.

The acoustic measurement provides the internal P-wave (compressional) and S-wave (shear) velocities at certain points on the surfaces of the samples. The wave velocity will be higher in a solid material than a material with fractures between the measuring locations. Thus, by comparison of the compressional and shear wave velocities before and after hydraulic fracturing treatment, the existence of fractures within the rock sample medium can be qualitatively proven.

The equipment used for acoustic measurement includes an Olympus pulser, two Olympus transducers and an Agilent DSO-X 2004A digital oscilloscope, as shown in Figure 3.9.

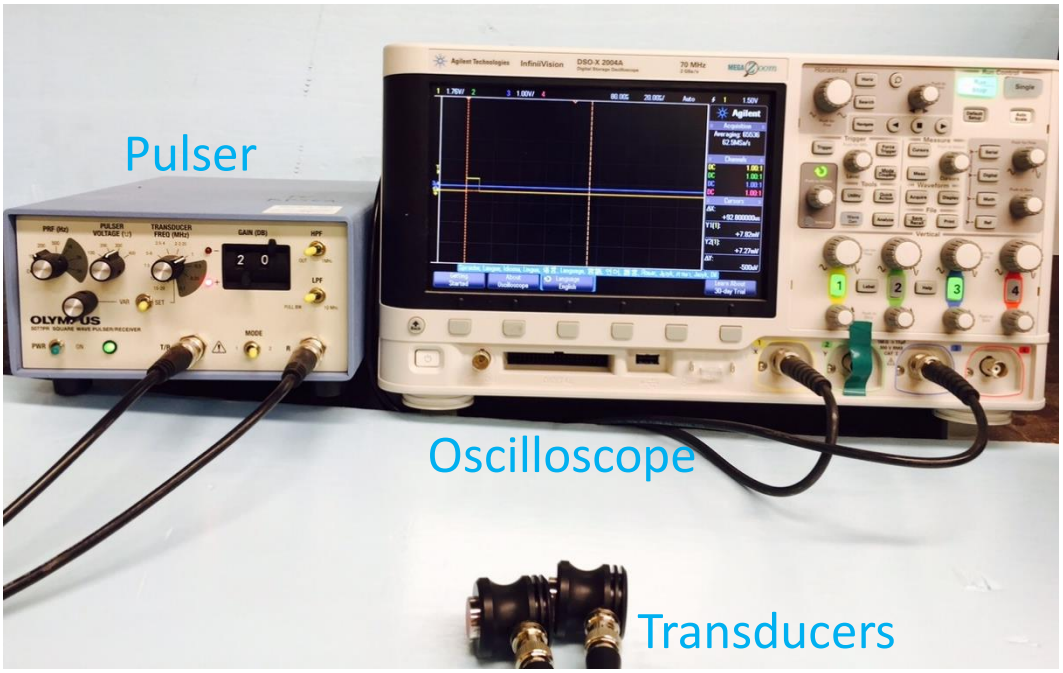

Figure 3.9. Olympus pulser, transducers and Agilent DSO-X 2004A digital oscilloscope.

A pressure decay test was performed to evaluate the permeability of samples. The wellbore of a sample was first pressurized by nitrogen gas to 175 psi (1.2 MPa) with the venting needle valve closed. Then, the inlet of the wellbore was shut by closing the needle valve on the inflow tubing. The gas inside wellbore and in the connected tubing space was forced by pressure to flow through the sample to the ambient environment, causing the pressure to decay with time. The pressure decay curve was used to characterize the average permeability of the rock sample. By comparing the pressure decay curve before and after each cryogenic fluid treatment, the effectiveness of the treatment was revealed.

To identify the hydraulic fractures created inside the rock samples, we first injected food dye aqueous solution into the borehole at low pressure and then fractured the block with high pressure nitrogen gas under the original tri-axial stress conditions. By applying this food dye coloring and gas fracturing technique, the fracture planes inside concrete samples were successfully revealed.

Additional experiments: Samples 39 and 40

The two new samples were fractured using the same procedures as before. The confining stresses were doubled (1000 psi in the x-direction, 1500 psi in the y-direction, and 2000 psi in the z-direction) and the injection rate was constant at 40 mL/min. Sample 39 fractured at 1656 psi, as indicated by the injection pressure peak in Figure 3.10. The fracture propagated after initiation and took around 190 seconds to reach the surface. The propagation pressure was about 600 psi. By comparing photos of the surfaces of Sample 39 before and after the experiment, shown in Figure 3.11 and Figure 3.12, a much smaller fracture than in the previous samples was found on Surface 2 (surface number appears in the surface's upper right corner in

these figures; Surface 1 is not numbered), which is perpendicular to the minimum horizontal stress direction. The larger fracture locating at the right side of Surface 2 was due to the cornering effect of the tri-axial loading frame, because the hydraulic pistons and counter blocks were not perfectly perpendicular to each other. The black dots showing in Figure 3.12 were the residual from the couplant used for acoustic measurement.

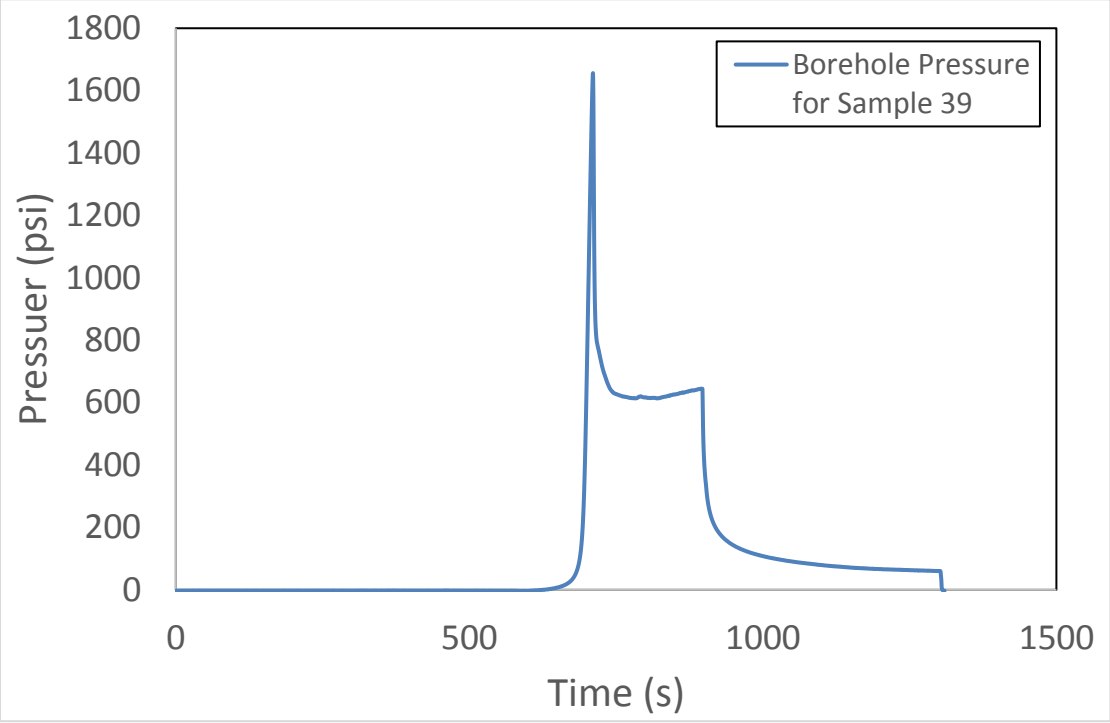

Figure 3.10: Borehole pressure profile of Sample 39.

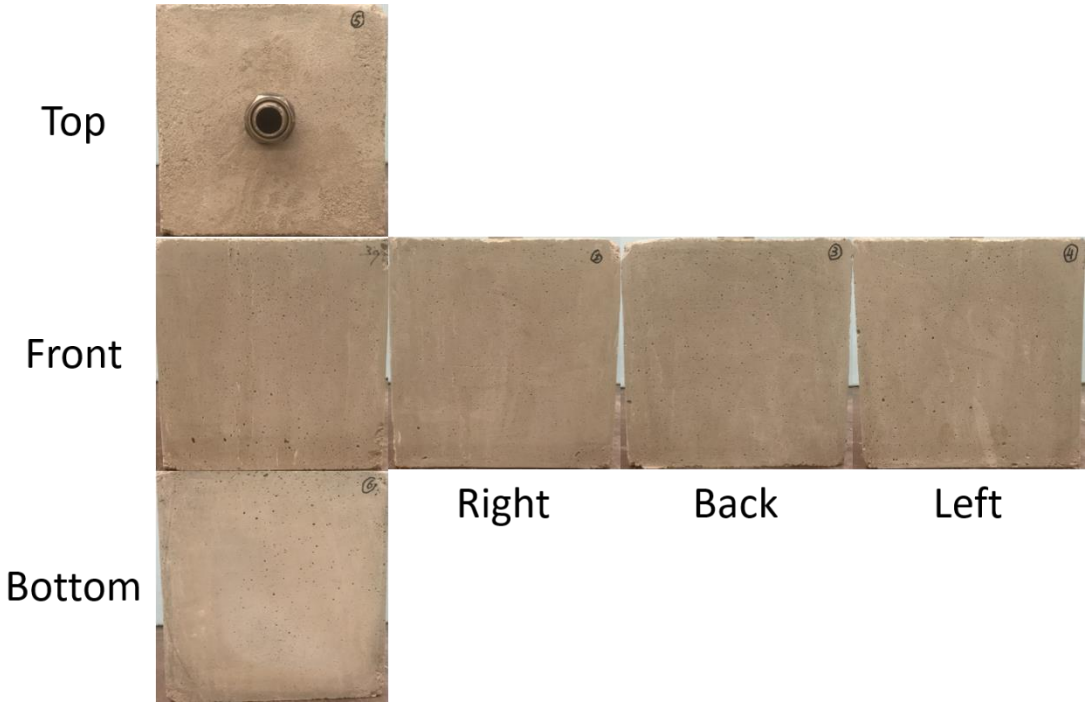

Figure 3.11: Surfaces of Sample 39 before brine fracturing.

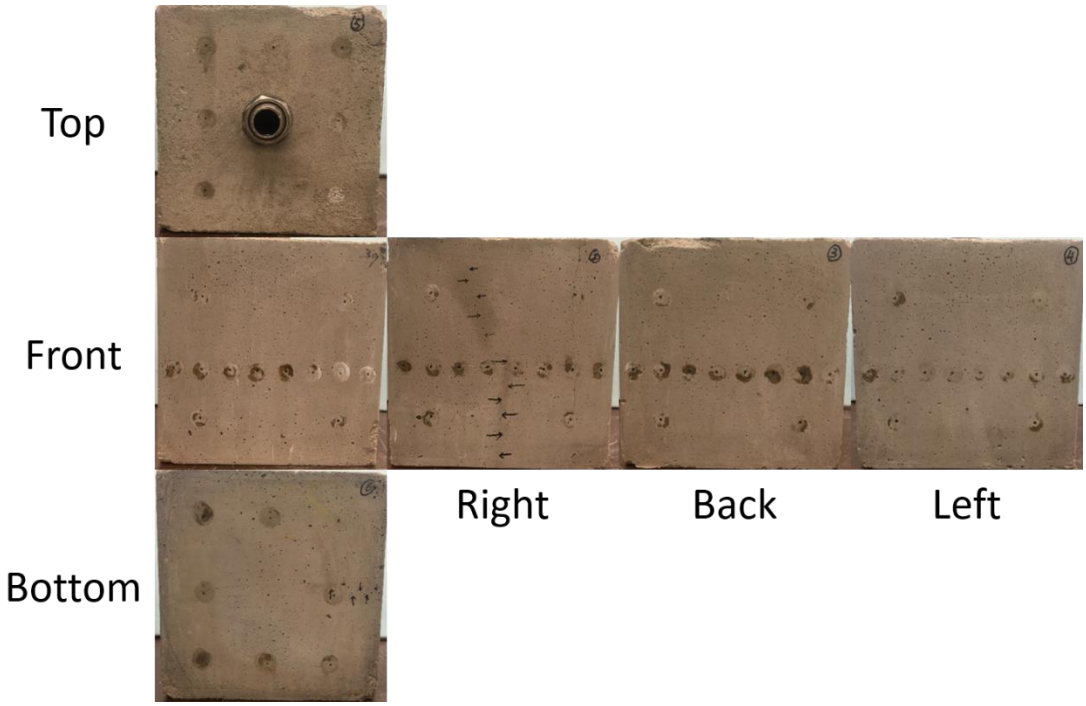

Figure 3.12: Surfaces of Sample 39 after brine fracturing.

Sample 40 fractured at 2424 psi, as indicated by the pressure peak in Figure 3.13. The propagation pressure was around 1600 psi. However, there was no significant pressure drop during injection. The pressure drop at the end of the experiment was due to the shut-down of the pump. By comparing the surfaces of Sample 40 before and after treatment, shown in Figure 3.14 and Figure 3., the only hydraulic fracture was found at the top surface of the sample, Surface 5 in Figure 3..

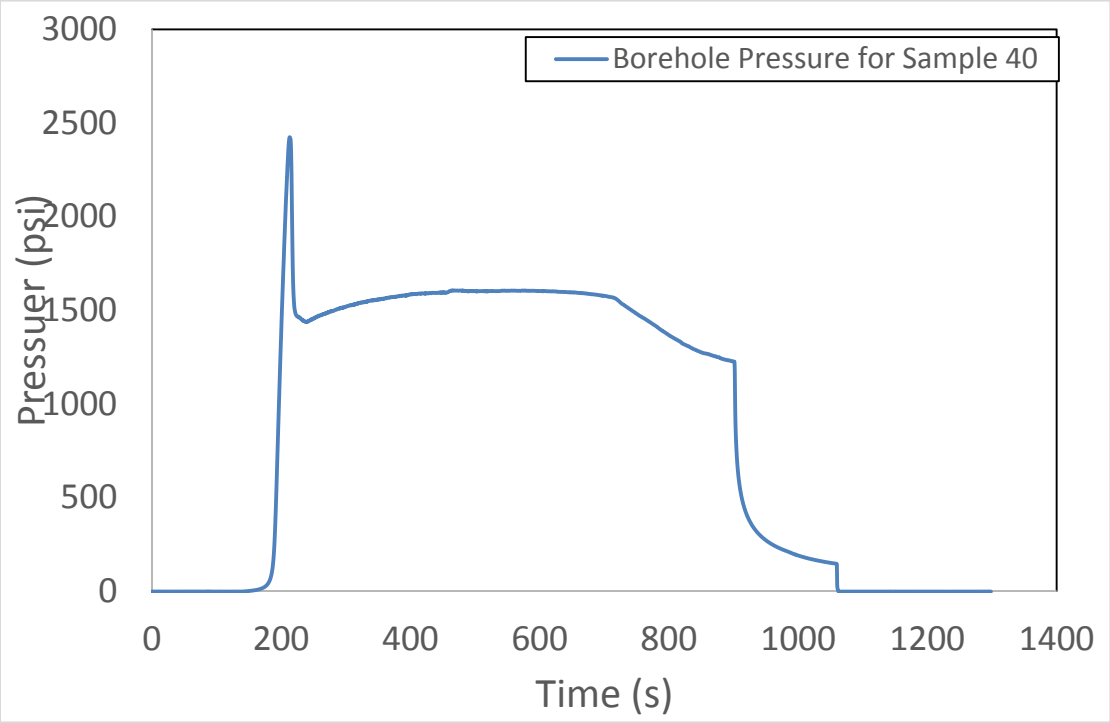

Figure 3.13: Borehole pressure profile of Sample 40.

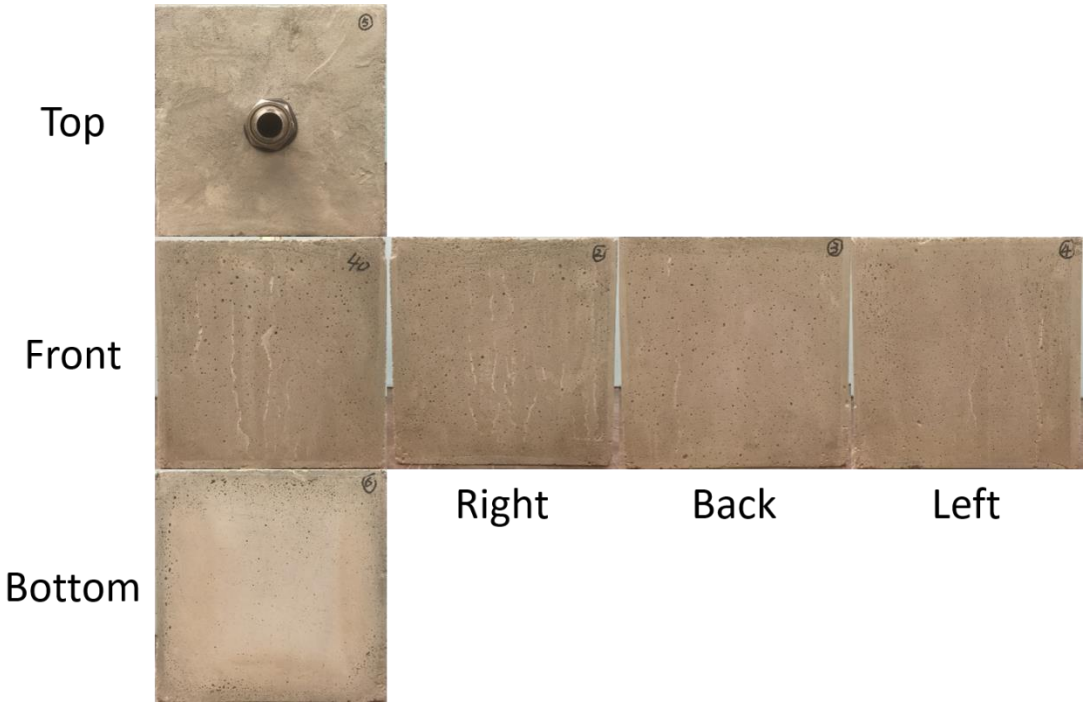

Figure 3.14: Surfaces of Sample 40 before brine fractured.

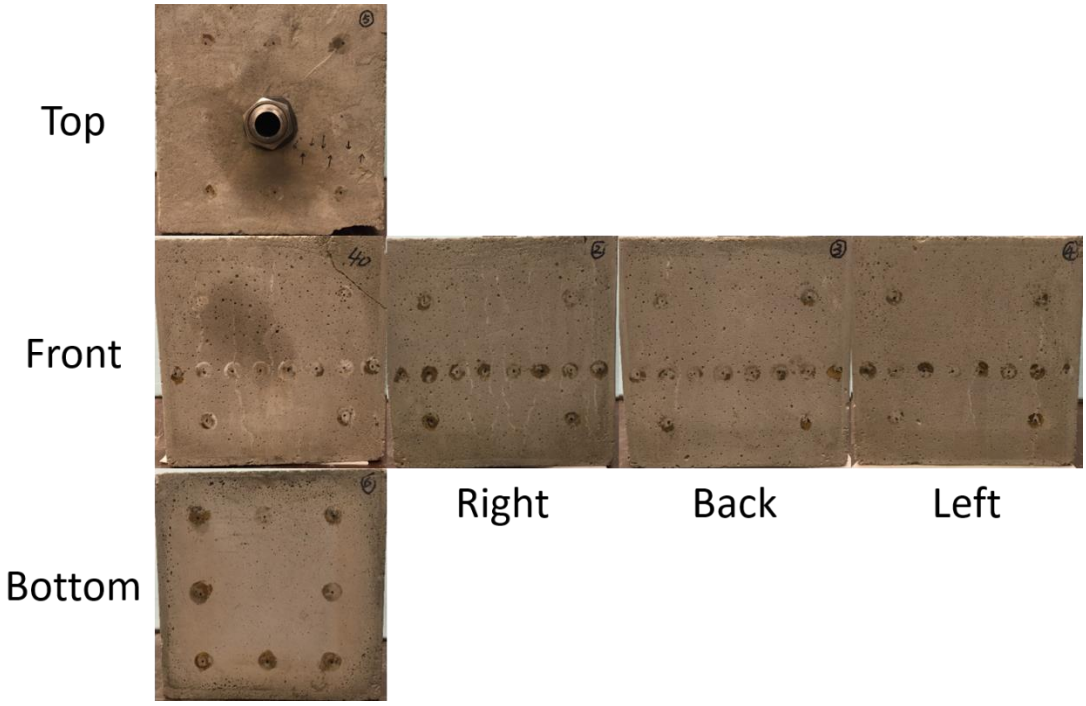

Figure 3.15: Surfaces of Sample 40 after brine fractured.

Fracture identification

Aqueous food dye solution was injected into five previously brine-fractured concrete samples (samples 32, 33, 38, 39, and 40) to color the fracture planes. The borehole was filled with food dye solution in advance, a gas pulse of ~200 psi was transmitted to the borehole, and the borehole was then shut in to allow the food dye to be driven into existing fractures. Then the concrete samples were broken down by high-pressure gas injection to reveal the geometry and morphology of the hydraulic fractures. In addition, acoustic measurements were conducted on multiple locations on each face of Sample 39 and 40 before and after brine fracturing for comparison.

Sample 32 was fractured by injecting brine under tri-axial stresses of 500 psi in the x-direction, 750 psi in the y-direction, and 1000 psi in the z-direction. As the first case, we increased the injection rate from 5 ml/min to as high as 100 ml/min once the pressure leveled out or passed a peak. The peak pressures at injection rates of 50 ml/min and 100 ml/min are 356.45 psi and 458.29 psi, respectively. During the late stage of the injection, brine flowed out from the top surface of the concrete sample. The fracture planes of Sample 32 had rugged surfaces and opened perpendicular to the minimum horizontal stress (x-axis), as shown in Figure 3.6 and Figure 3.17. The dye solution migrated in the hydraulic fractures around the lower four inches of the borehole and finally seeped out through the crack on the top surface, the same way as the injected brine did.

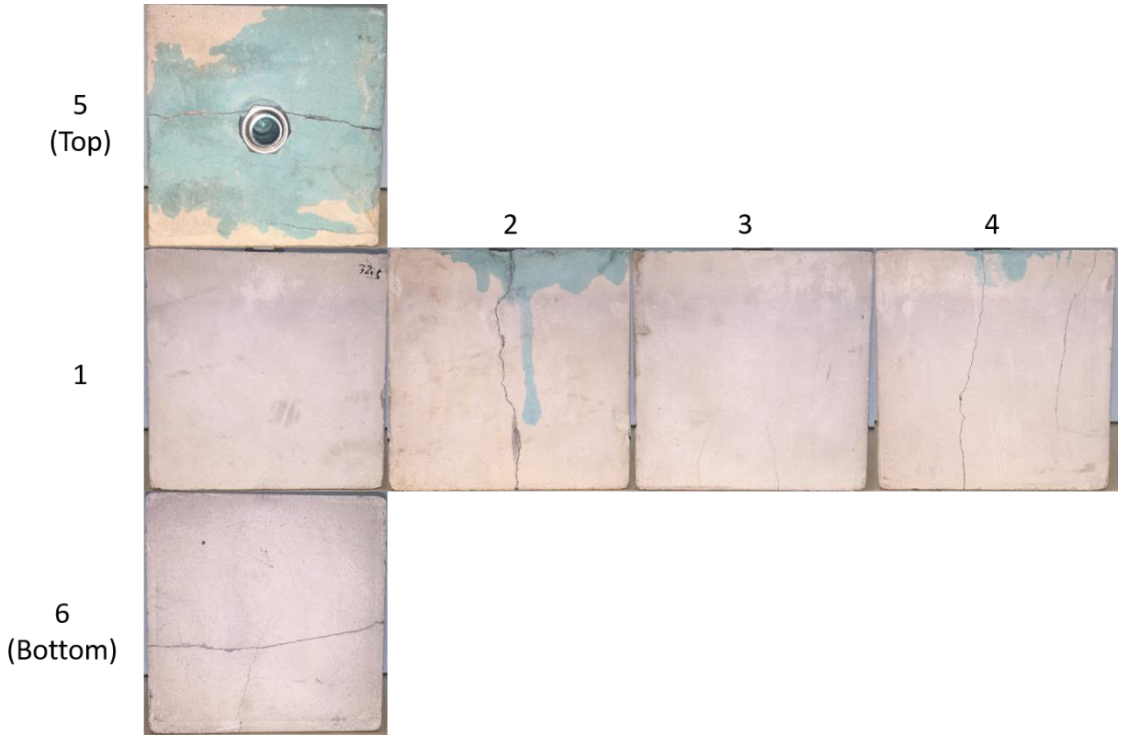

Figure 3.16. Surfaces of Sample 32 after dyeing and gas breakdown.

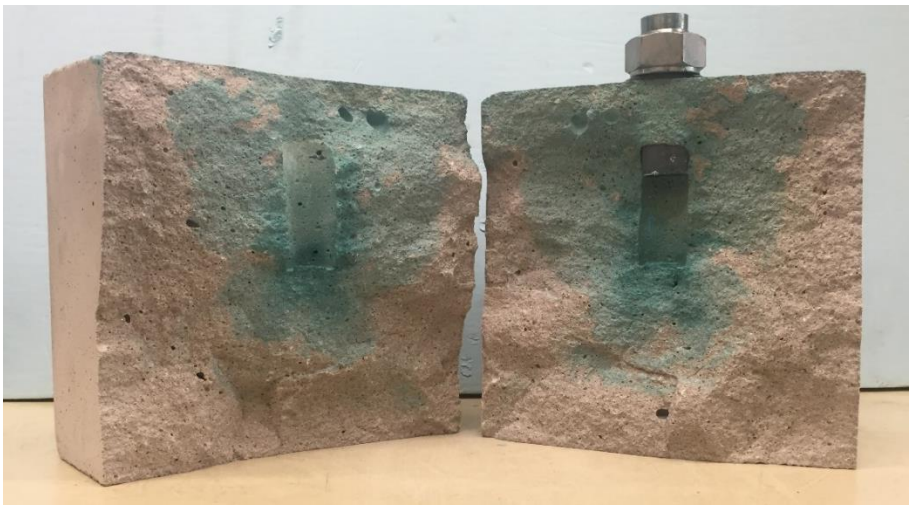

Figure 3.17: Internal fracture morphology of Sample 32 after dyeing and gas breakdown.

Under tri-axial stresses of 500 psi in the x-direction, 750 psi in the y-direction, and 1000 psi in the z-direction, Sample 33 was fractured by injecting brine first at 100 ml/min and then 200 ml/min, achieving two peak pressures at 321.08 psi and 453.24 psi, respectively. After the peak pressure, brine seeped out from a crack in the bottom surface of the concrete block. The fracture planes of Sample 33 after dyeing and gas breakdown are shown in Figure 3.18 and Figure 3.19. Similar to Sample 32, the fracture planes opened perpendicular to the minimum horizontal stress direction with only a slight deviation. The wellbore drilled in Sample 33 is six inches long, thus the bottom hole is only two inches away from the bottom surface of the sample, creating a weak region along the borehole. Therefore, brine preferentially broke through from the bottom hole, as validated by our observation of the water seepage during the brine injection and the dye coloring on the fracture planes.

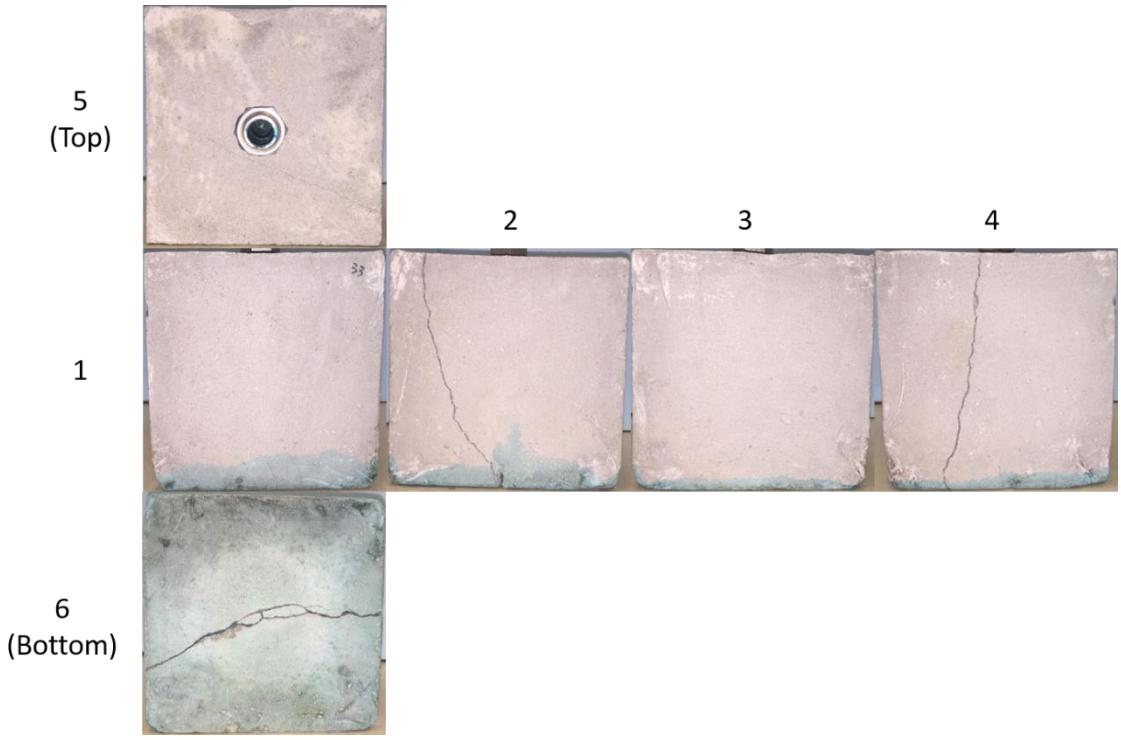

Figure 3.18: Surfaces of Sample 33 after dyeing and gas breakdown.

Figure 3.19: Internal fracture morphology of Sample 33 after dyeing and gas breakdown.

Sample 38 was fractured at 898.30 psi by injecting brine at a constant rate of 20 ml/min under tri-axial stresses of 500 psi in the x-direction, 750 psi in the y-direction, and 1000 psi in the z-direction. Brine seepage was seen near the wellhead on the top surface, on Surface 1 and Surface 2, as indicated by the dark regions on these faces in Figure 3.20. The fracture planes of Sample 38 after dyeing and gas breakdown are shown in Figure 3.21. Unlike Sample 32 and Sample 33, the fracture planes were irregular and drastically deviated from the direction that is perpendicular to the minimum horizontal stress. After relaxing the tri-axial stresses for brine injection, one of the block corners was found to be broken, as seen in Figure 3.20, due to

uneven block surface. This uneven surface could cause unbalanced stress loading on the concrete sample, resulting in arbitrary fracture initiation and propagation as revealed by the dye coloring.

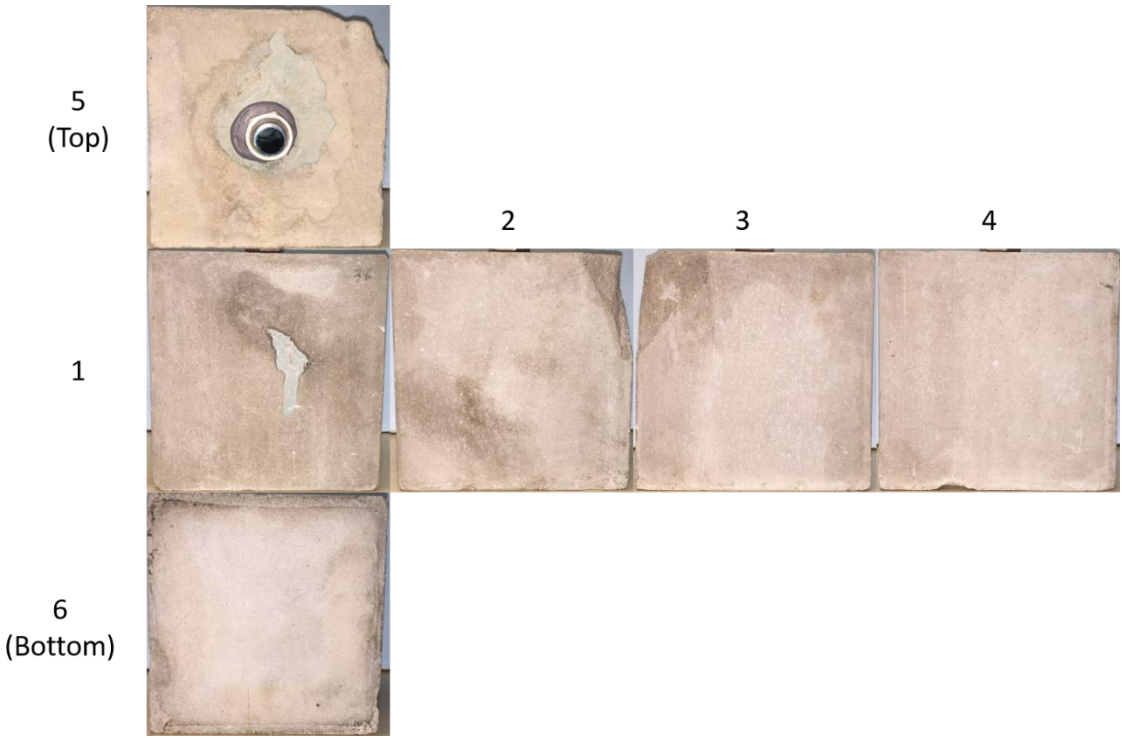

Figure 3.20: Surfaces of Sample 38 after dyeing. Uneven loading broke the corner of surface 2, 3, and 5.

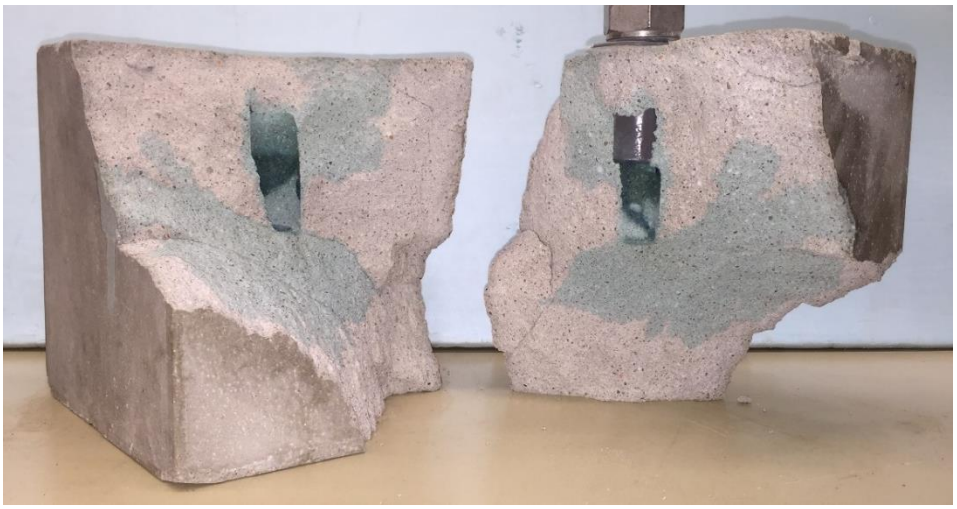

Figure 3.21: Internal fracture morphology of Sample 38 after dyeing and gas breakdown.

Sample 39 was fractured at a peak pressure of 1656.26 psi by injecting brine at a constant rate of 40 ml/min under tri-axial stresses of 1000 psi in the x-direction, 1500 psi in the y-direction, and 2000 psi in the z-direction. The surfaces of Sample 39 before brine injection, after brine injection, and after dyeing and gas breakdown are shown in Figure 3.22, Figure 3.23, and Figure 3.24, respectively. The major hydraulic fracture planes were generated perpendicular to the minimum horizontal stress direction, as observed on Surface 2 and Surface 6 in Figure 3.23. After gas fracturing, dye solution only colored a small region surrounding the wellbore, as shown in Figure 3.24. However, in this case, we consider that the fracture planes should be much larger, as suggested by the blue curve in Figure 3.24. The reasons were: 1) we observed water seepage out of cracks on Surface 2 and Surface 6; 2) the dye solution injection for this sample is insufficient, since no remaining dye solution was observed in the borehole after dye injection.

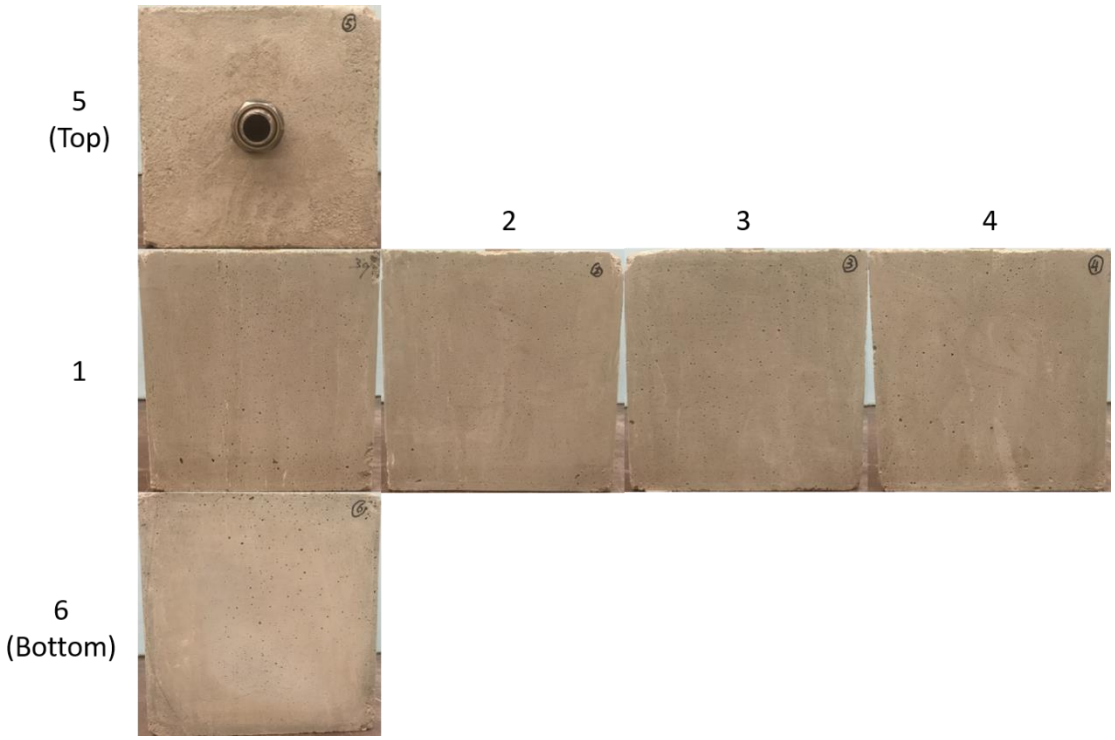

Figure 3.22: Surfaces of Sample 39 before brine injection.

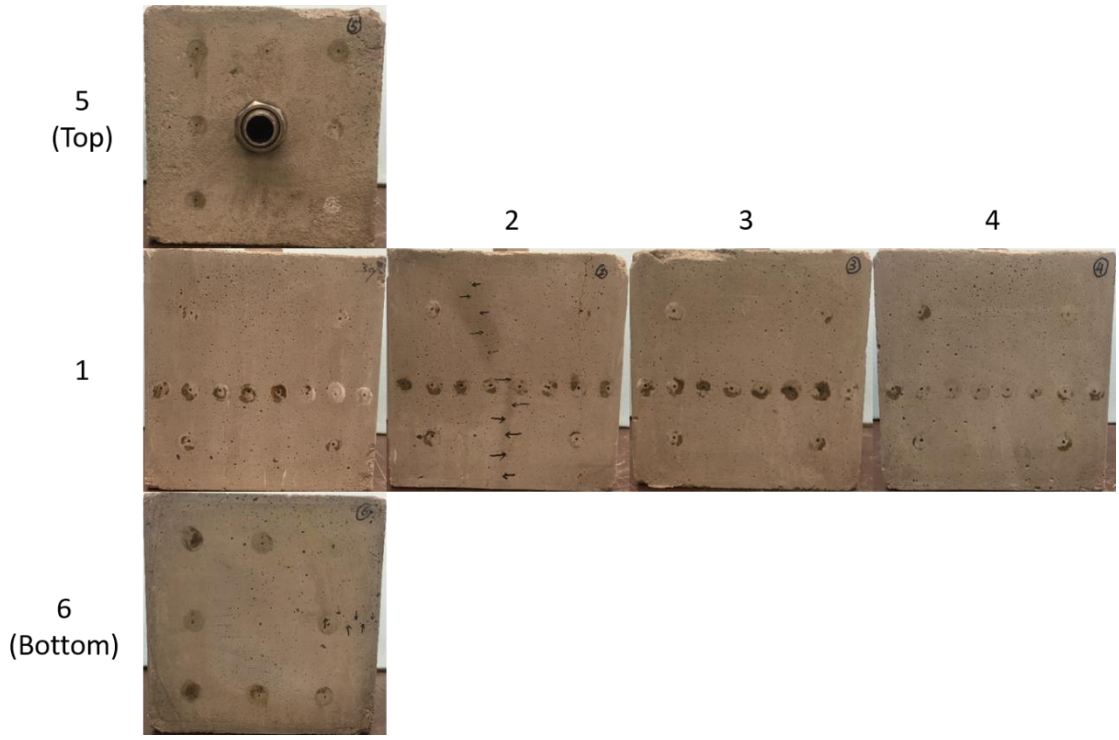

Figure 3.23: Surfaces of Sample 39 after brine injection.

Figure 3.24: Internal fracture morphology of Sample 39 after dyeing and gas breakdown.

Acoustic measurements were conducted on each pair of opposite faces of Sample 39. The signatures of P-waves and S-waves before and after brine injection are shown in Figure 3.25 through Figure 3.30. The results show that for all measurement locations on Surface 1 and Surface 3 (the minimum horizontal stress direction) both P- and S-waves experienced significant delay in travel time, which agrees with the fact that the major fracture planes were generated perpendicular to the minimum horizontal stress. Similar features can also be seen

from P- and S-wave comparisons for Surface 2 and Surface 4, and Surface 5 and Surface 6, suggesting that after brine injection, the internal structure of the concrete sample has been changed.

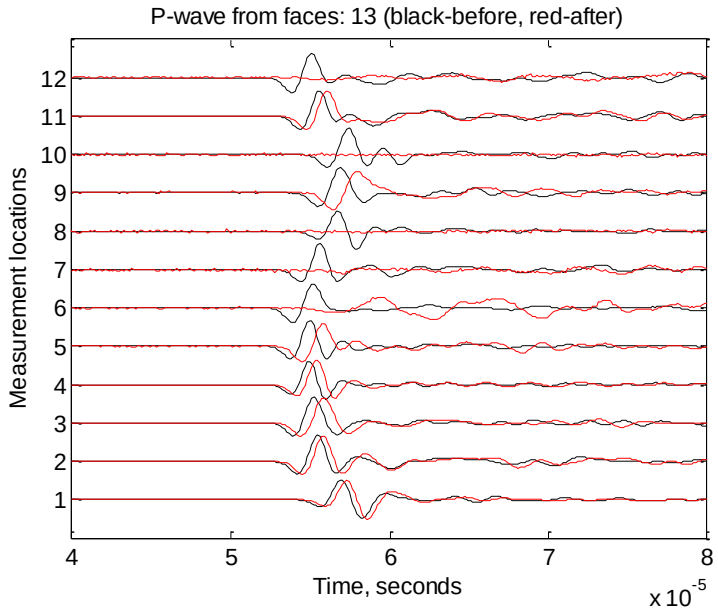

Figure 3.25: P-wave acoustic signatures measured from 12 locations on Surface 1 and Surface 3 before and after brine fracturing of concrete Sample 39.

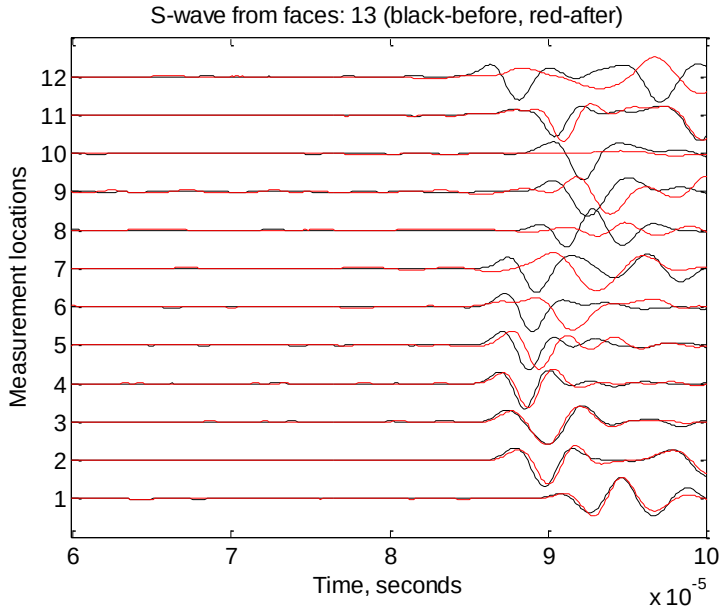

Figure 3.26: S-wave acoustic signatures measured from 12 locations on Surface 1 and Surface 3 before and after brine fracturing of concrete Sample 39.

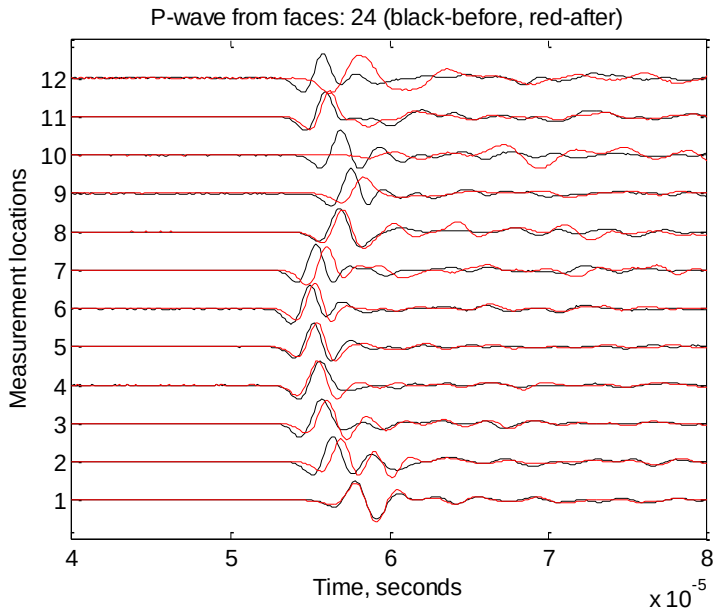

Figure 3.27: P-wave acoustic signatures measured from 12 locations on Surface 2 and Surface 4 before and after brine fracturing of concrete Sample 39.

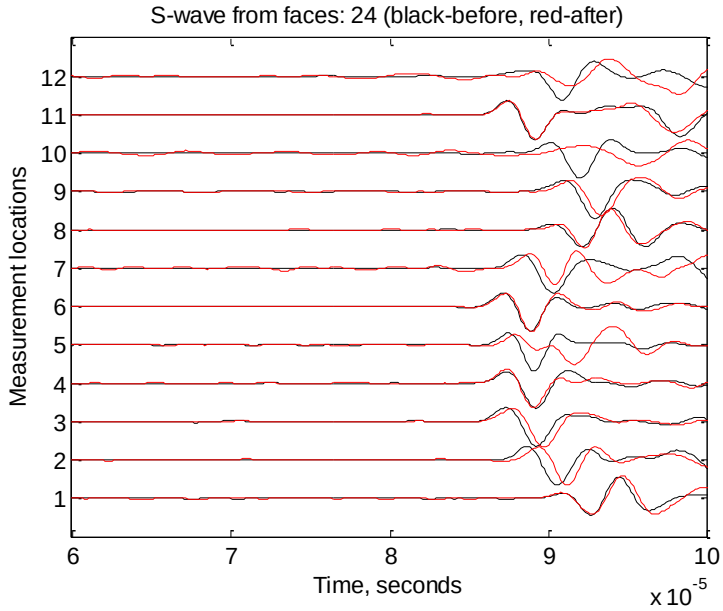

Figure 3.28: S-wave acoustic signatures measured from 12 locations on Surface 2 and Surface 4 before and after brine fracturing of concrete Sample 39.

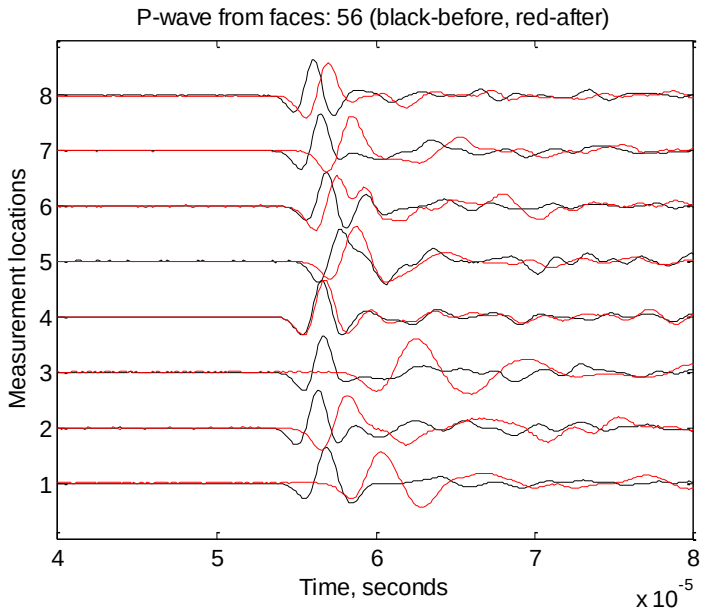

Figure 3.29: P-wave acoustic signatures measured from 12 locations on Surface 5 and Surface 6 before and after brine fracturing of concrete sample 39.

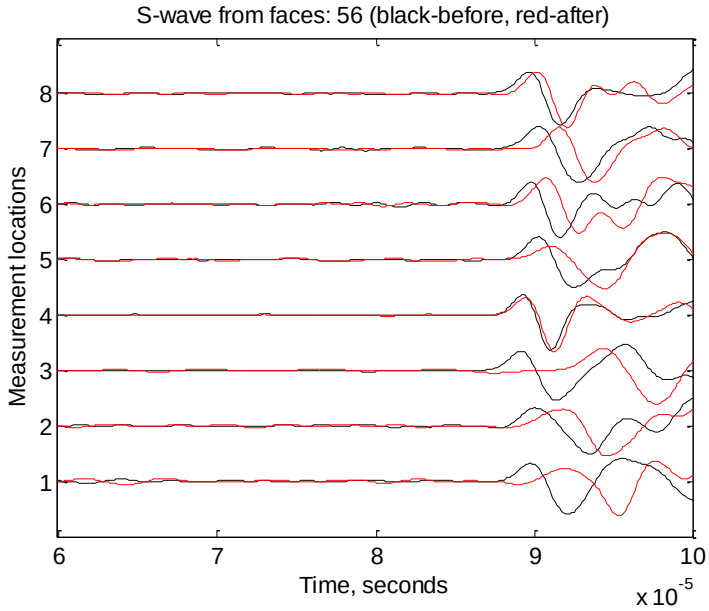

Figure 3.30: S-wave acoustic signatures measured from 12 locations on Surface 5 and Surface 6 before and after brine fracturing of concrete sample 39.

Sample 40 was fractured at the same conditions with Sample 39. Brine was injected at a constant rate of 40 ml/min under tri-axial stresses of 1000 psi in the x-direction, 1500 psi in the y-direction, and 2000 psi in the z-direction, and the peak pressure achieved was 2424.14 psi. The surfaces of Sample 40 before and after brine fracturing are shown in Figure 3.31 and

Figure 3.32. Similar to Sample 38, an uneven loading effect was observed at the top right corner on Surface 1, causing a diagonal fracture plane from borehole to Surface 2, as shown in Figure 3.33 and Figure 3.34. The major fracture planes across the borehole, although with large deviation, are generally perpendicular to the minimum horizontal stress direction.

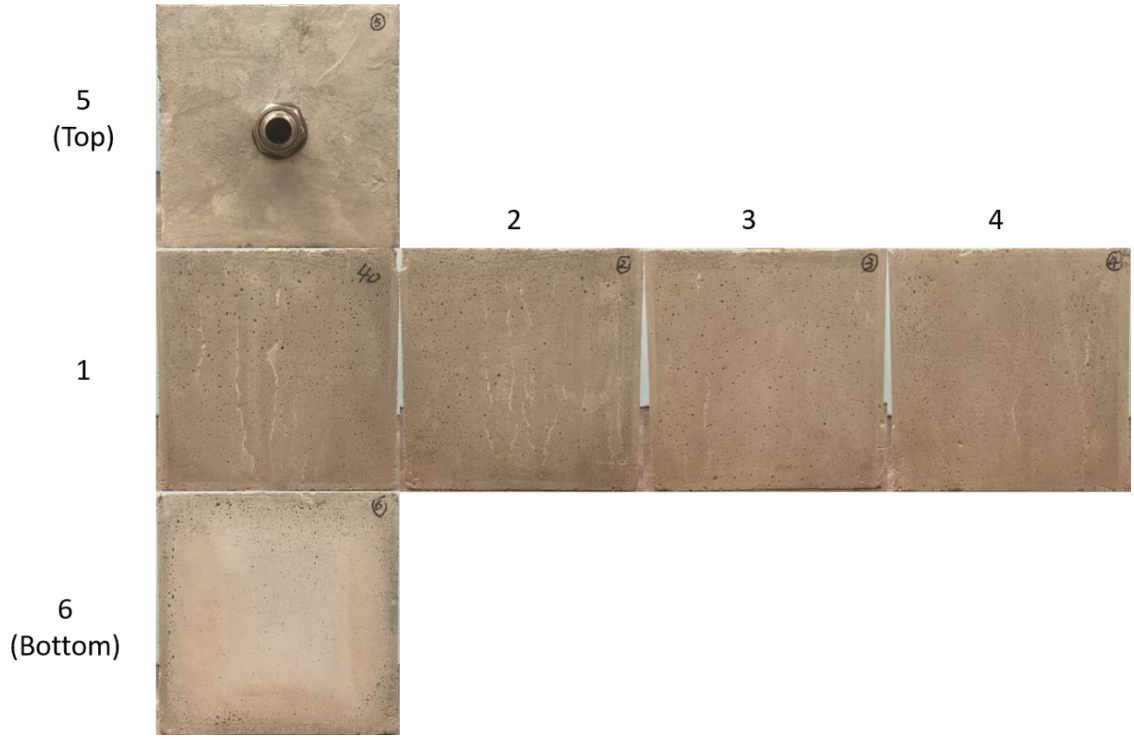

Figure 3.39: Surfaces of Sample 40 before brine injection.

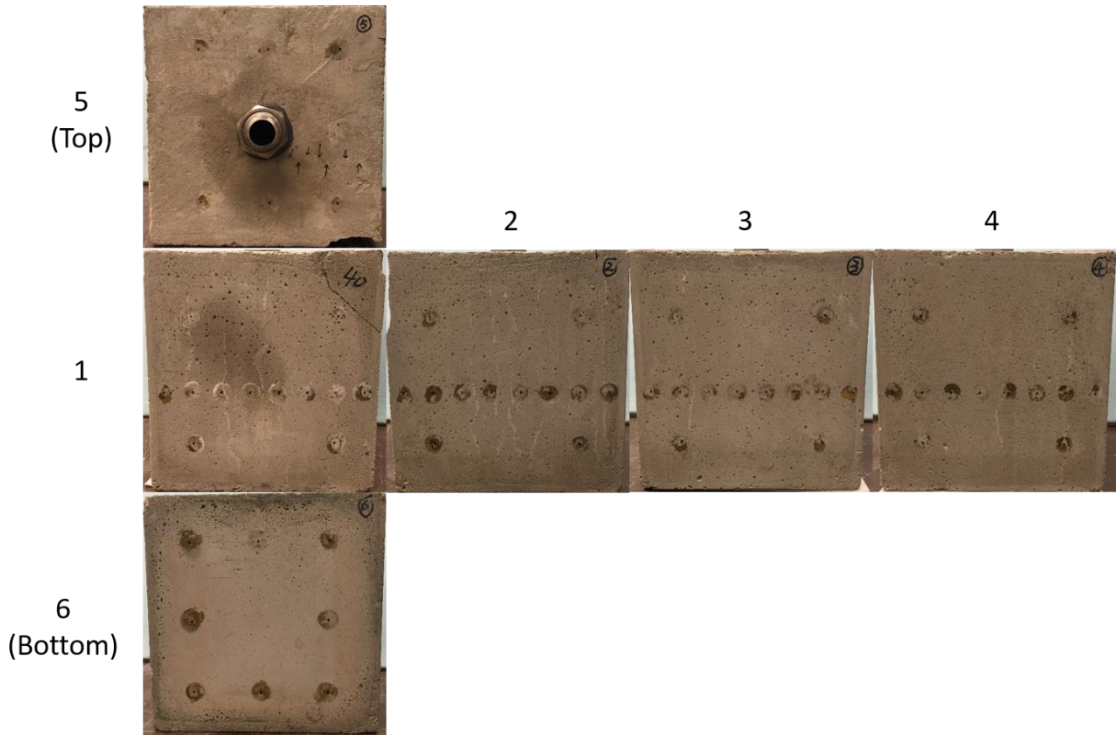

Figure 3.32: Surfaces of Sample 40 after brine injection.

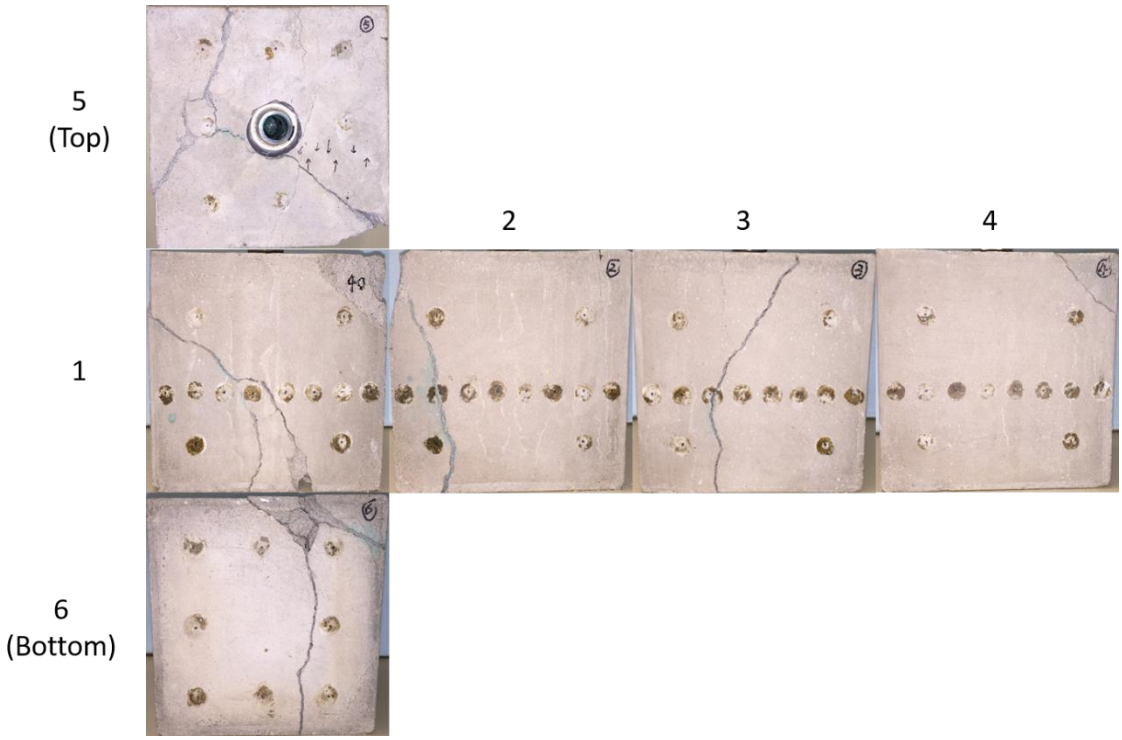

Figure 3.33: Surfaces of Sample 40 after dye and gas break-down.

Figure 3.34: Internal fracture morphology of Sample 40 after dyeing and gas breakdown.

The results of acoustic measurements on each pair of opposite faces of Sample 40 for P-waves and S-waves before and after brine injection are shown in Figure 3.35 through Figure 3.40. By comparing the fracture planes with the measurement locations, arrival delays for all P- and S-waves were expected. However, as is obvious from the acoustic signatures, signals measured from some locations after brine fracturing were delayed, while others arrived earlier. These unexpected signatures could have possibly been a result of residual brine saturation in the concrete sample, and/or tri-axial stress compression, etc.

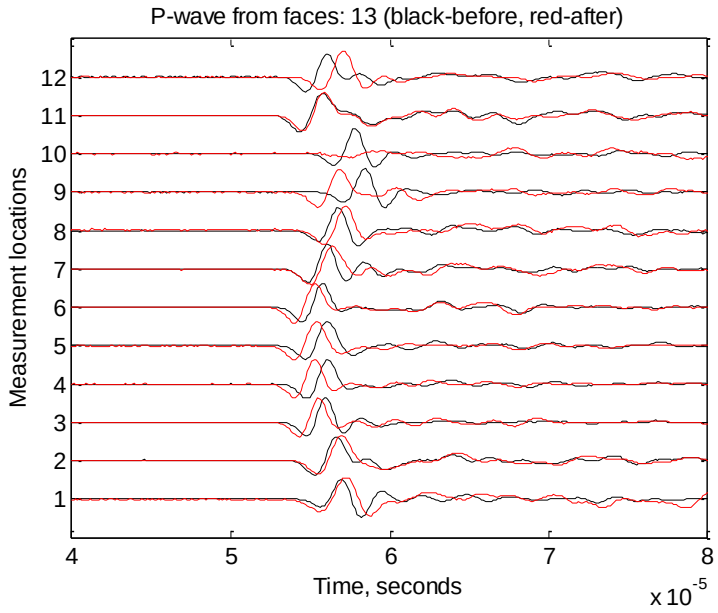

Figure 3.35: P-wave acoustic signatures measured from 12 locations on Surface 1 and Surface 3 before and after brine fracturing of concrete Sample 40.

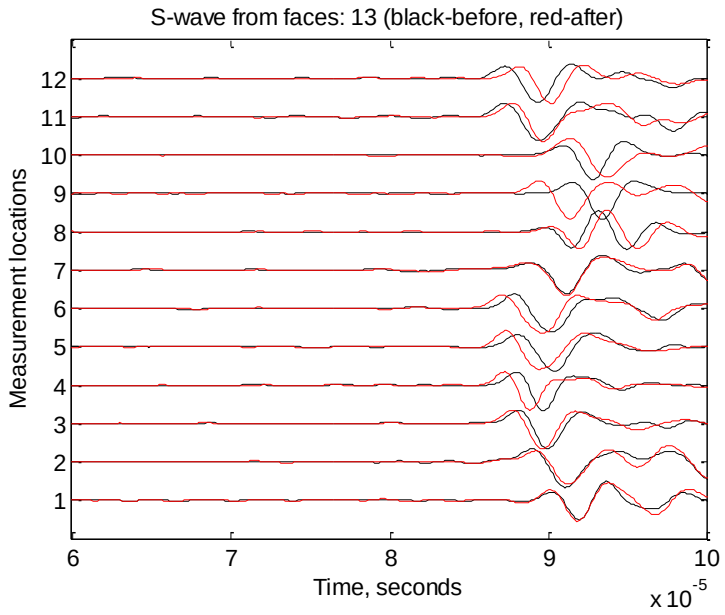

Figure 3.36: S-wave acoustic signatures measured from 12 locations on Surface 1 and Surface 3 before and after brine fracturing of concrete Sample 40.

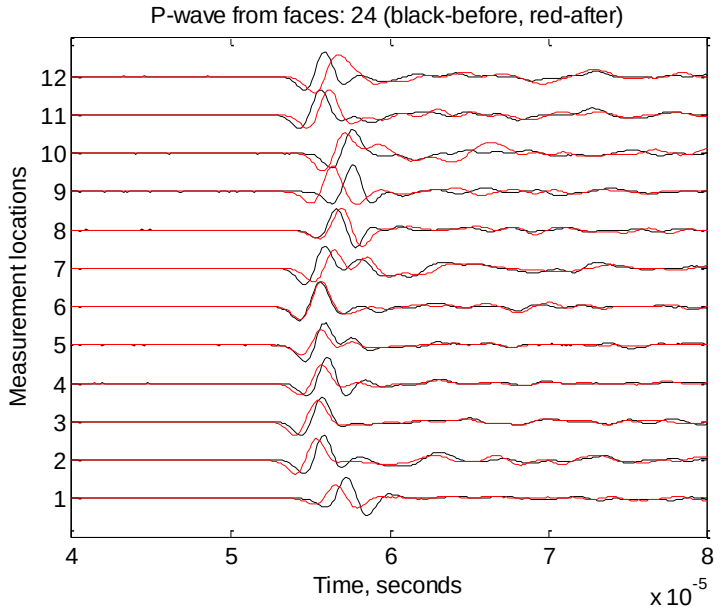

Figure 3.37: P-wave acoustic signatures measured from 12 locations on Surface 2 and Surface 4 before and after brine fracturing of concrete Sample 40.

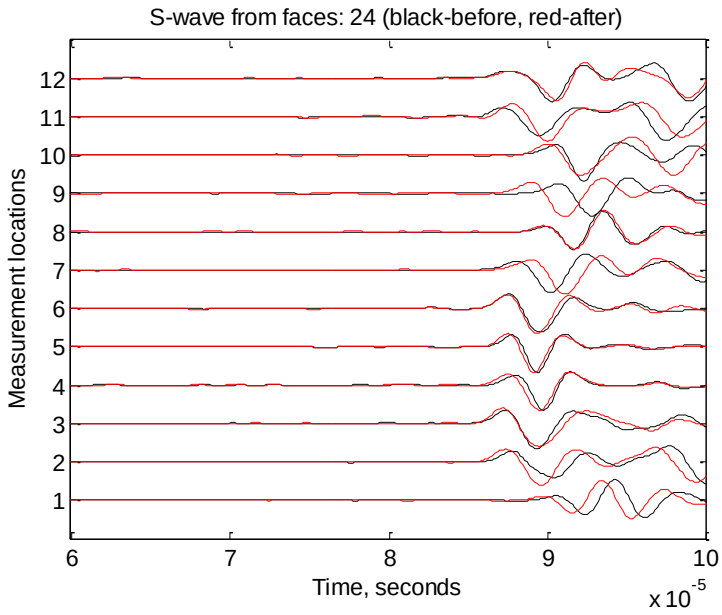

Figure 3.38: S-wave acoustic signatures measured from 12 locations on Surface 2 and Surface 4 before and after brine fracturing of concrete Sample 40.

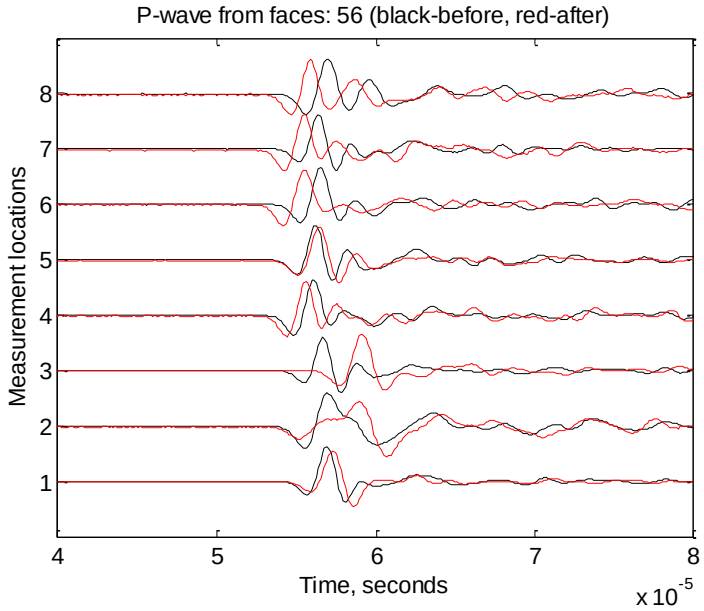

Figure 3.39: P-wave acoustic signatures measured from 12 locations on Surface 5 and Surface 6 before and after brine fracturing of concrete Sample 40.

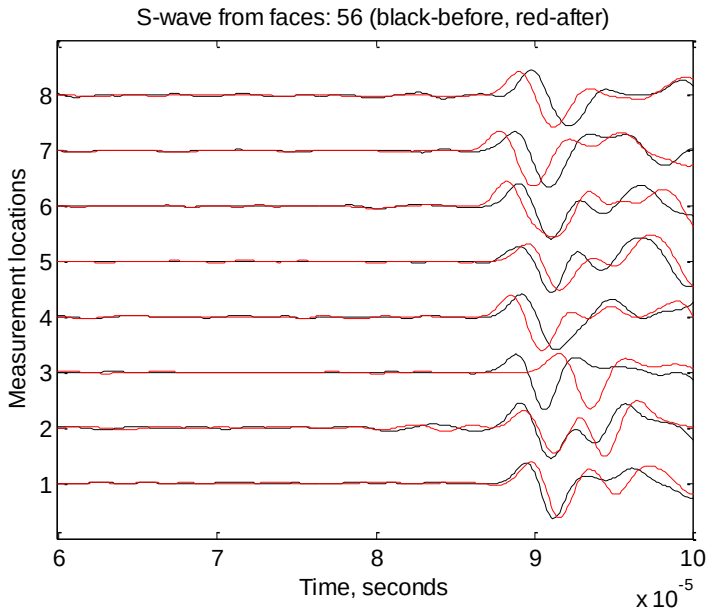

Figure 3.40: S-wave acoustic signatures measured from 12 locations on Surface 5 and Surface 6 before and after brine fracturing of concrete Sample 40.

Fracturing using CO_2

Laboratory equipment and procedures

The equipment used for CO_2 injection is analogous to the brine injection setup. An ISCO pump is used to withdraw liquid CO_2 from the source tank and to inject it into the borehole of samples, as shown in Figure 3.41. Since in the field we mostly encounter temperature and pressure conditions above the supercritical point of CO_2, i.e. 31 °C and 7.38 MPa, temperature control has been added to the system to maintain a high enough temperature. Specifically, the concrete samples can be pre-heated in an oven to elevate its temperature to a certain level, and then installed in the tri-axial loading frame. Before injection, liquid CO_2 is first drawn from the CO_2 tank into the pump. Thermal tape is used to heat the pump cylinder filled with CO_2 to the temperature above its supercritical temperature. Once the target temperature is achieved, liquid CO_2 will be injected into the borehole until the sample is fractured by CO_2. Later, we further modified our experimental procedure to ensure that CO_2 can be injected into the concrete samples at temperatures and pressures above the supercritical point. We pre-heated the concrete samples in an oven to elevate its temperature to a desired level, and then the sample is set up in the tri-axial loading frame and the pipelines connected.

The CO_2 injection experiments conducted generally followed the procedure below. Some concrete samples were treated in simpler ways before this procedure was formalized.

1. Surface cleaning and well bore installation.
2. Pre-injection tri-axial stress loading for ~40 mins to mitigate the compaction effect on acoustic emissions.

3. Take pictures of the sample surfaces.
4. Acoustic emission measurements.
5. Pressure decay under no stress loading using 180 psi nitrogen gas.
6. CO_2 injection until sample fractures.
7. Take pictures if obvious fractures were generated on sample surfaces.
8. Acoustic emission measurements.
9. Pressure decay under no stress loading using 180 psi nitrogen gas.
10. Fracture coloring by pressurizing dye solution into generated fractures.
11. Heat the sample to dry dye solution if necessary.
12. Gas fracturing under tri-axial stresses loading
13. Gas fracturing under no stress loading.
14. Take pictures of the internal fracture planes and sample surfaces.

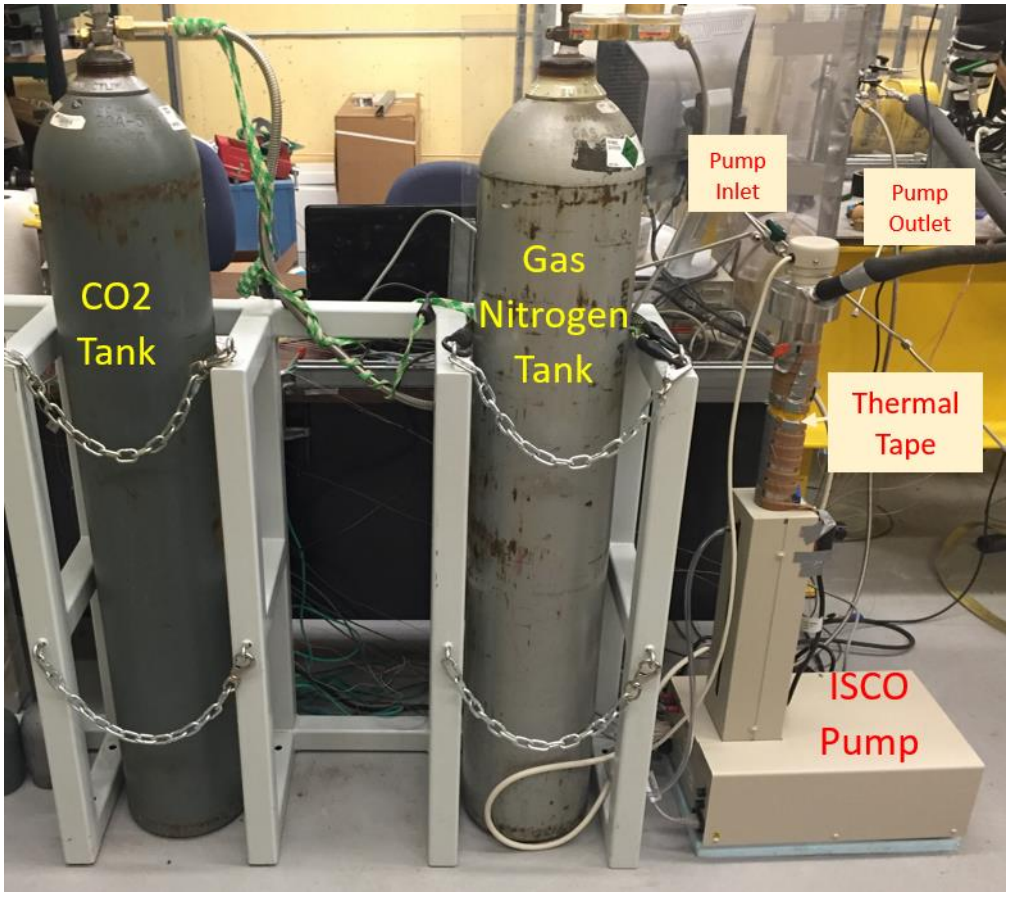

Figure 3.41: Delivery system for supercritical CO_2 injection.

Experiment results

Concrete Sample 27

Concrete Sample 27 was pre-heated to 40 °C then installed in the tri-axial loading frame. The confining stresses applied on Sample 27 were 1000 psi in the x-direction, 1500 psi in the y-direction, and 2000 psi in the z-direction, shown in Figure 3.42. The liquid CO_2 was heated in the pump to the supercritical temperature of about 45 °C and then was injected into the sample at a constant rate of 40 ml/min. As shown in Figure 3.43, after about 24 mins, the first 508 ml CO_2 ran out, corresponding to the first pressure peak. Then the pump was refilled and CO_2 injection was continued from about 35 mins. Sample 27 was fractured at about 43 mins with a pressure peak of 1145.40 psi, generating corresponding stress responses in x-, y-, and z-directions in Figure 3.42. The increase of stress in the x-direction indicates that the major fracture planes were initiated perpendicular to the minimum horizontal stress direction. The plateau in the pressure profile was due to the pump refilling and reheating. During injection, the borehole temperature was maintained around 30 °C as shown in Figure 3.44, so CO_2 in borehole was in the liquid state but close to the supercritical point. A leaking sound happened right after the pressure reached the peak pressure. Then about 20 seconds later, the sample was broken down and the CO_2 in borehole evaporated quickly. Due to the rapid heat loss from CO_2 evaporation, the borehole temperature instantaneously dropped to around -15 °C.

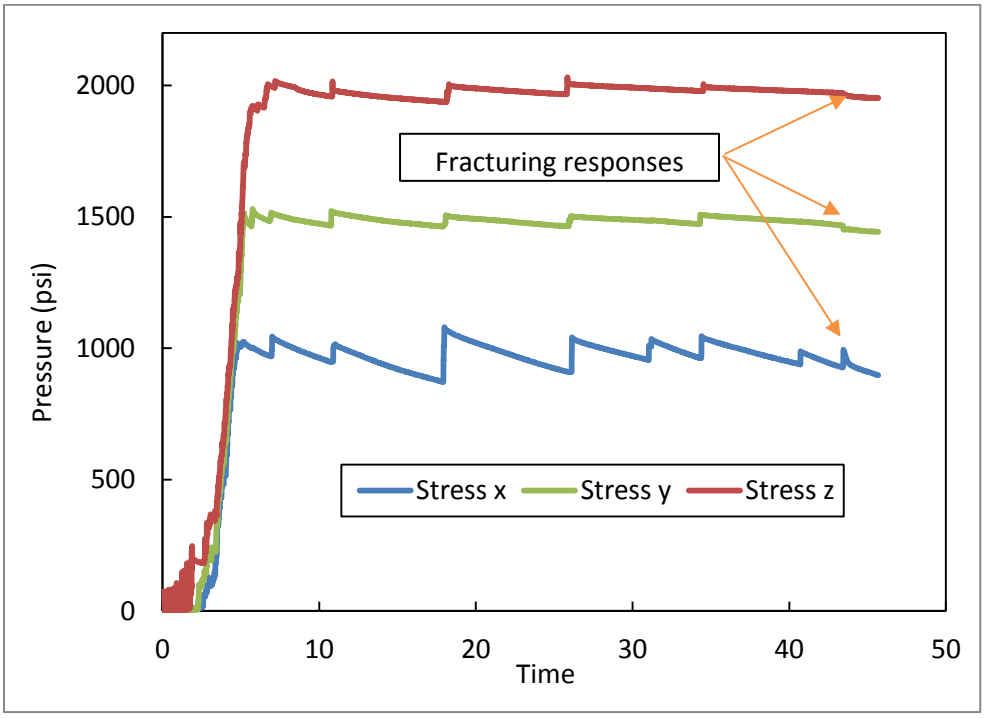

Figure 3.42: Tri-axial stresses applied on concrete Sample 27.

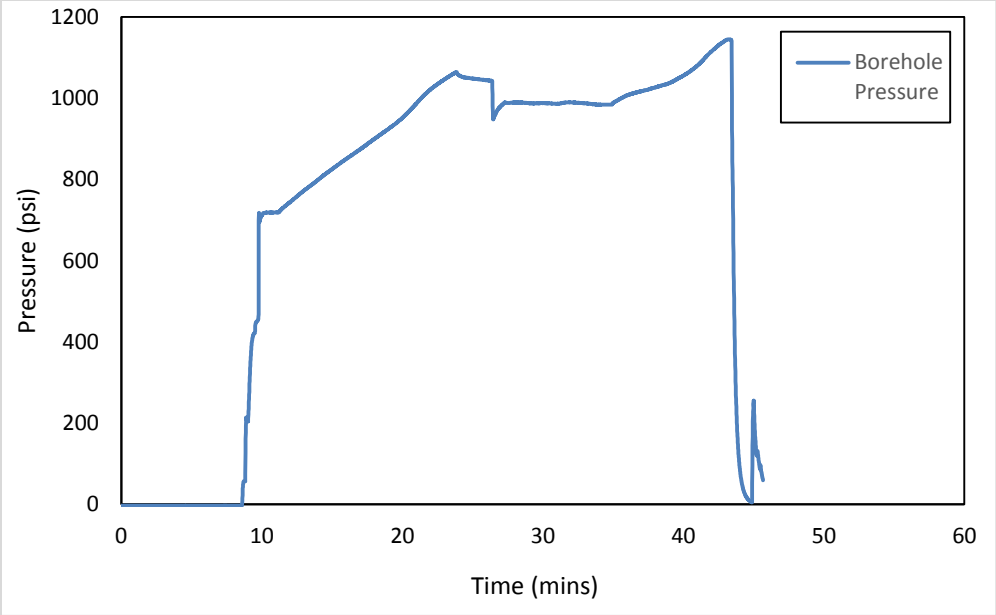

Figure 3.43: Borehole pressure during CO_2 injection.

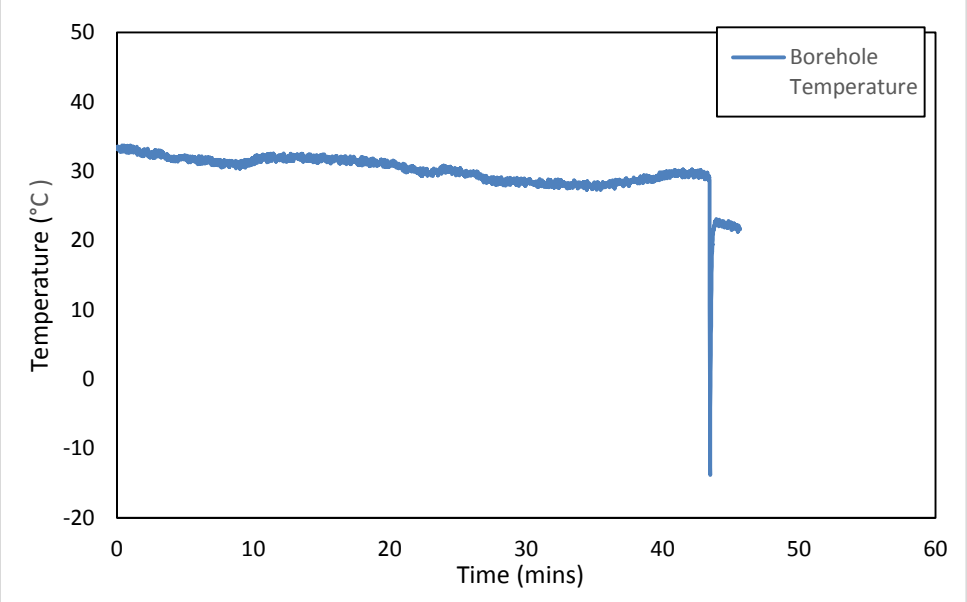

Figure 3.44: Borehole temperature during CO_2 injection.

Pressure decay tests were conducted on Sample 27 before and after CO_2 injection. The results are shown in Figure 3.. After CO_2 fracturing, the conductivity of the artificial fracture was so large that the gas pressure could not be built up to originally desired 175 psi. The maximum pressure it could reach was about 70 psi. And it only took several seconds for all the gas inside borehole of Sample 27 to leak off.

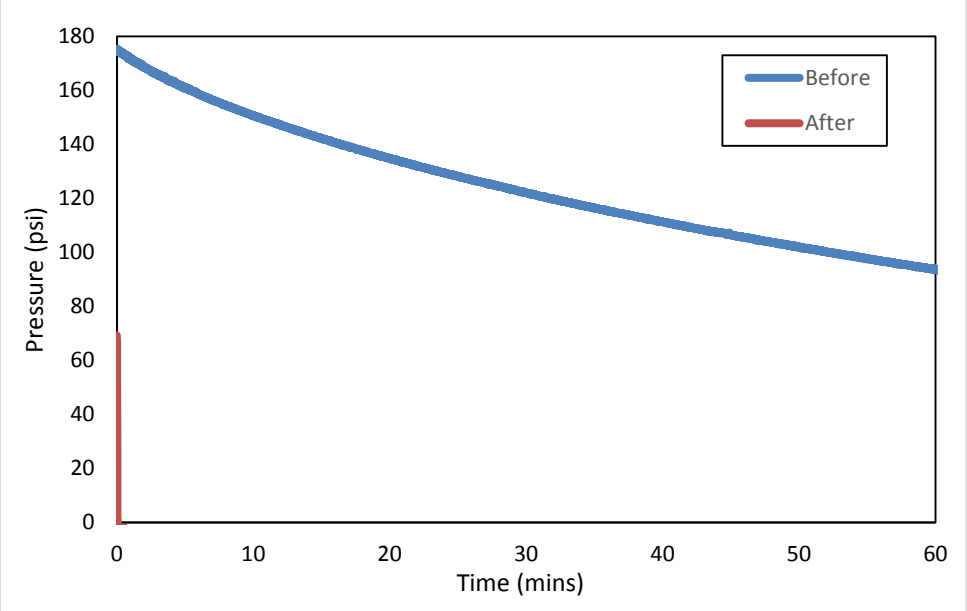

Figure 3.45: Pressure decay profiles for before and after CO_2 injection.

Photos were taken for each face of Sample 27 before and after CO_2 injection for comparison, as shown in Figure 3.46 and Figure 3.47. A visible single fracture, which opened right across the borehole center in a plane perpendicular to the minimum horizontal stress, was observed. Then Sample 27 was colored by injecting food dye solution and broken down with gas nitrogen. Figure 3.48 shows that the fracture generated is vertically straight with very smooth surfaces. A small area around wellbore exhibited lighter color as compared to the rest area, which needed further investigation on whether it was related to liquid (potentially super critical) CO_2 treatment.

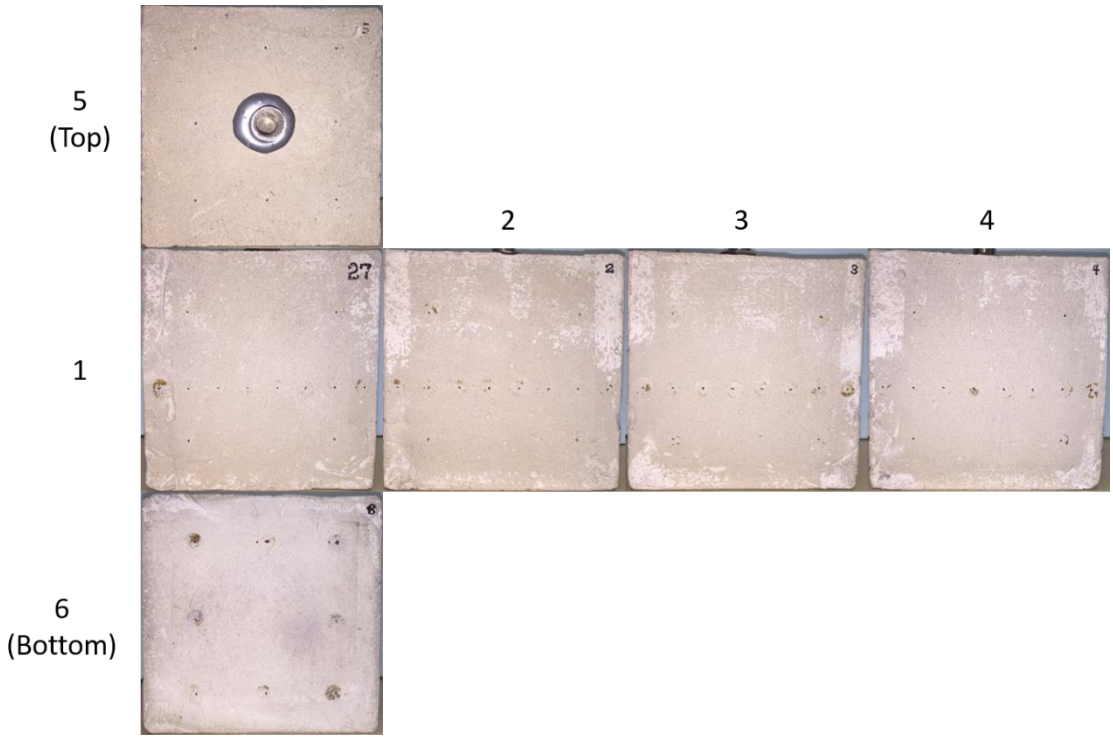

Figure 3.46: Surfaces of Sample 27 before CO_2 injection.

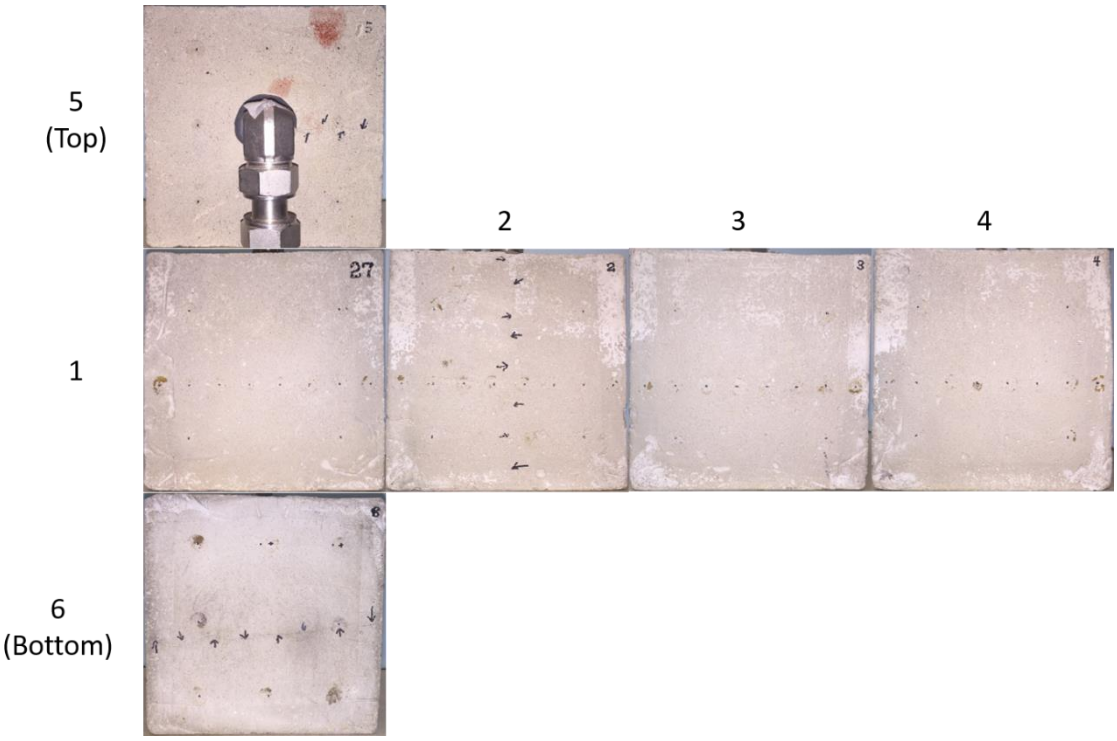

Figure 3.47: Surfaces of Sample 27 after CO_2 injection.

Figure 3.48: Fracture planes of Sample 27 after dyeing and gas breakdown.

The results of P-wave measurements conducted on Sample 27 are shown in Figure 3.49, Figure 3.50, and Figure 3.51. The P-wave measurements on Surface 1 and Surface 3 on Sample 27 show significantly change in the wave velocities and amplitudes, which is consistent with the fracture profile in Figure 3.48. For other measurements on Surface 2 and Surface 4, and Surface 5 and Surface 6, the results showed very small difference before and after CO_2 injection. For the shear wave measurements, which are not shown in this report, the wave velocities after CO_2 injection were faster than those before the CO_2 injection.

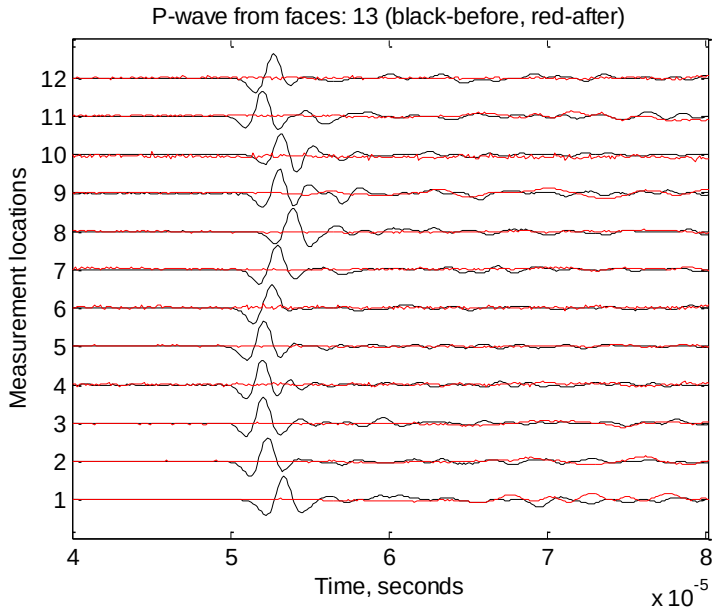

Figure 3.49: P-wave acoustic signatures measured from 12 locations on Surface 1 and Surface 3 before and after brine fracturing of concrete Sample 27.

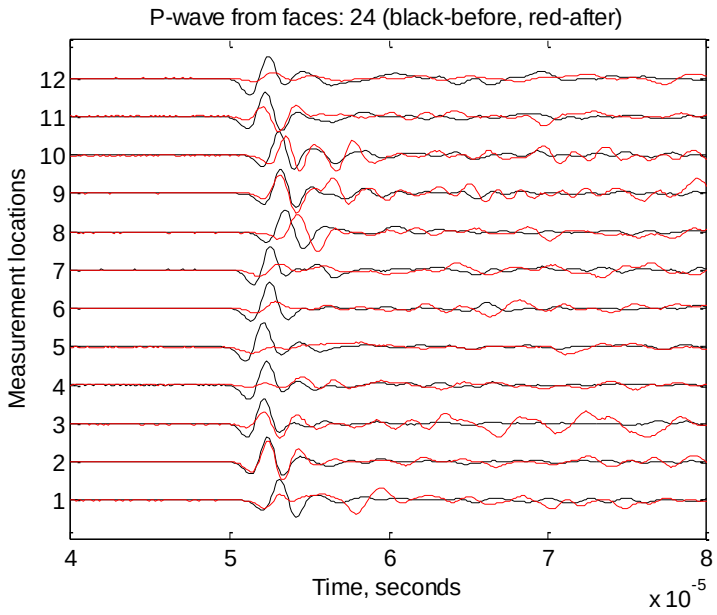

Figure 3.100: P-wave acoustic signatures measured from 12 locations on Surface 2 and Surface 4 before and after brine fracturing of concrete Sample 27.

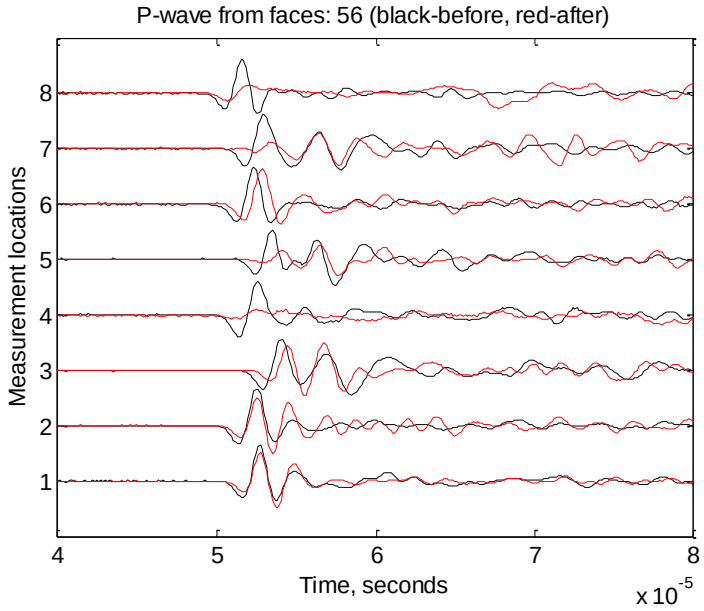

Figure 3.51: P-wave acoustic signatures measured from 8 locations on Surfaces 5 and Surface 6 before and after brine fracturing of concrete Sample 27.

We then conducted CO_2 injection induced fracturing experiments on six more concrete samples (28, 29, 46, 47, 48, and 49). Sample 47 was treated by sc-CO_2, Sample 29 was treated by liquid CO_2 injection, and Samples 28, 46, 48, and 49 were treated by gaseous CO_2. In addition, one more concrete sample (Sample 11) was used to investigate the effect of high tri-

axial stress loading on acoustic signatures by purely applying multiple cycles of stress loading without any CO_2 treatment.

Concrete Sample 11

Multiple cycles of tri-axial stress loading of 1000 psi in the x-direction, 1500 psi in the y-direction, and 2000 psi in the z-direction were applied to Sample 11 to investigate the effect of short-term tri-axial stress loading on acoustic signatures. The tri-axial stress loading was repeated four times, consisting of 21 minutes, 23 minutes, 21 minutes, and 41 minutes. Before tri-axial stress loading and after each cycle of loading, acoustic signatures of P- and S-waves were measured from the specified locations on all six faces.

Figures 3.52 to 3.57 compare the five acoustic wave curves before tri-axial stress loading and after each cycle of tri-axial stress loading: black- before tri-axial stress loading, green- after the 1st stress loading, red- after the 2nd stress loading, blue- after the 3rd stress loading, magenta- after the 4th stress loading. It can be seen in most of these figures that after each cycle of tri-axial stress loading, P-wave and S-wave delay in arrival time, indicating certain internal structure changes rather than a simple compaction in density. Also, given longer stress loading, the acoustic waves tended to be delayed more, e.g. shifts of the magenta curve are much bigger than other colors in location 10 in Figure 3.52 and location 5 in Figure 3.57. Nonetheless, several of the wave curves are mixed, which could have suggested a competition between internal structure change and compaction in density, for example locations 7 and 11 in Figure 3.52. In consideration of these effects of tri-axial stress loading on acoustic waves, in the following CO_2 injection experiments a pre-injection stress loading was first applied for a certain time before reference acoustic signatures were measured.

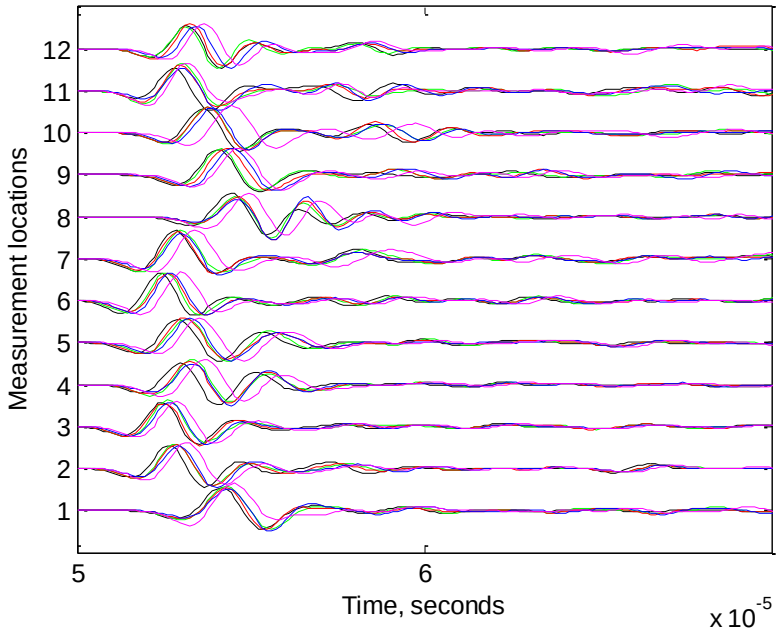

Figure 3.52. P-wave signatures measured from Surface 1 and Surface 3 of Sample 11.

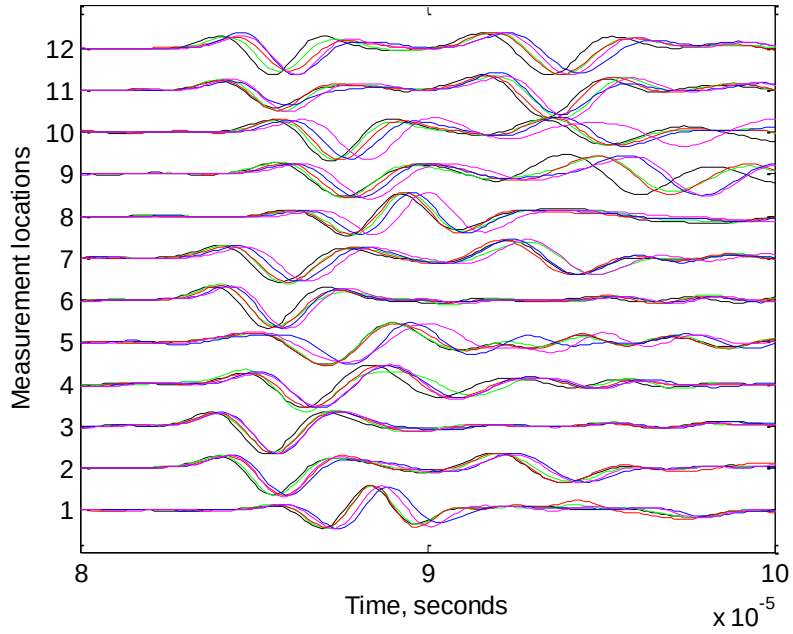

Figure 3.53. S-wave signatures measured from Surface 1 and Surface 3 of Sample 11.

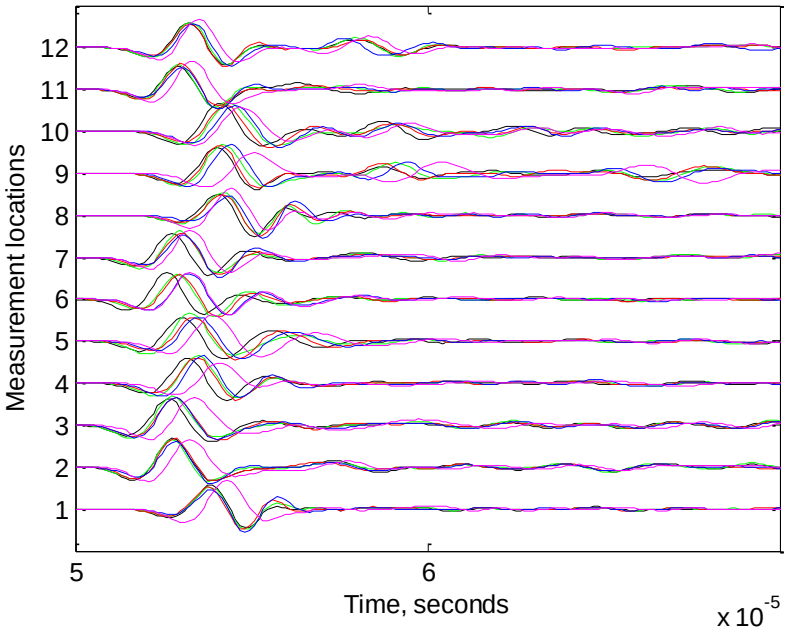

Figure 3.54. P-wave signatures measured from Surface 2 and Surface 4 of Sample 11.

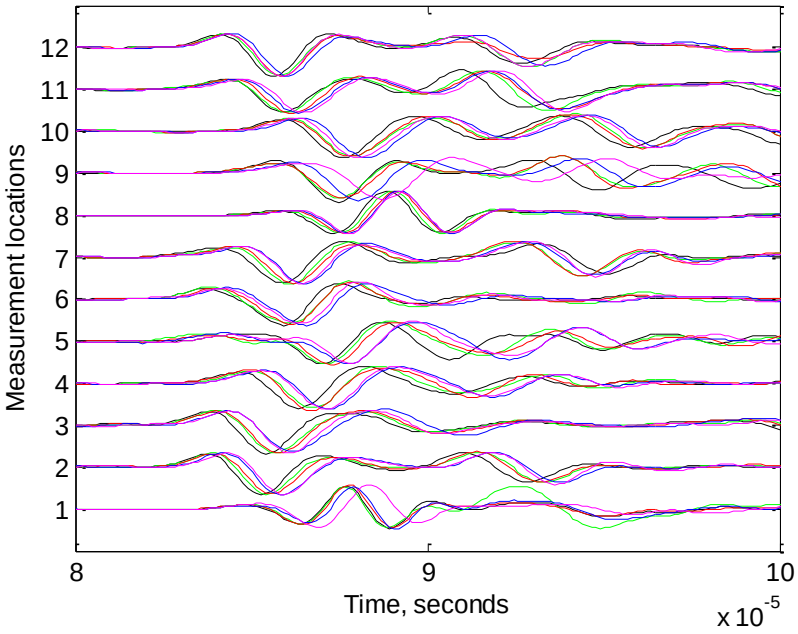

Figure 3.55. S-wave signatures measured from Surface 2 and 4 of Sample 11.

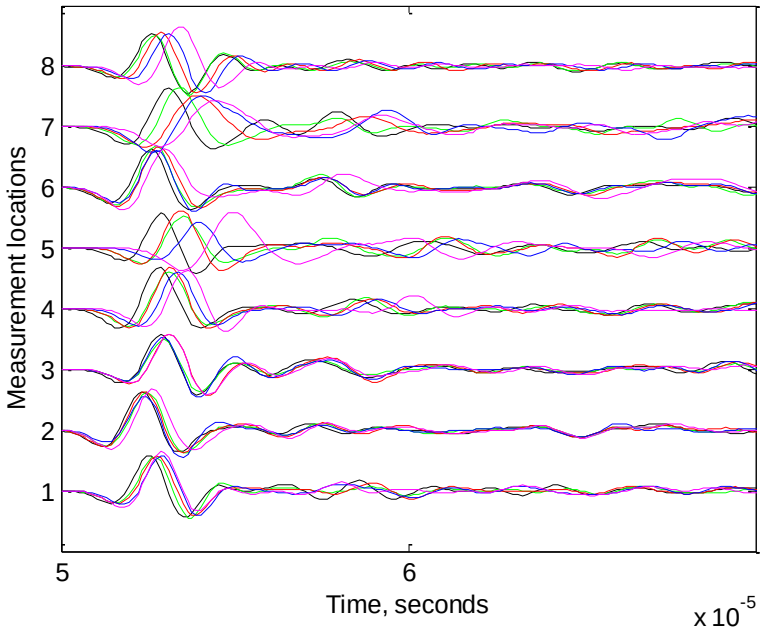

Figure 3.56. P-wave signatures measured from Surface 5 and Surface 6 of Sample 11.

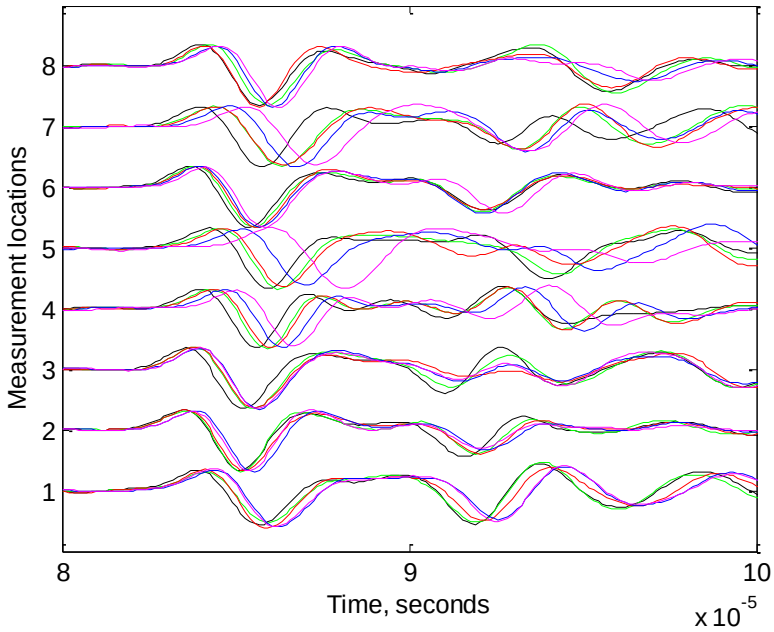

Figure 3.57. S-wave signatures measured from Surface 5 and Surface 6 of Sample 11.

Concrete Sample 28

Similar to Sample 11, we also did a comparison for acoustic wave measurements before and after applying a pre-injection tri-axial stress loading of 1000 psi in the x-direction, 1500 psi in the y-direction, and 2000 psi in the z-direction on Sample 28 for about 10 mins, as shown in Figure 3.58. The acoustic signatures are compared in Figures 3.59 through 3.64, with black and red curves measured before and after, respectively, the pre-injection stress loading. It was obvious that both P-waves and S-waves show highly consistent delay in arrival time on every measurement location. This confirms that internal structure change resulting from stress loading impedes the acoustic emission.

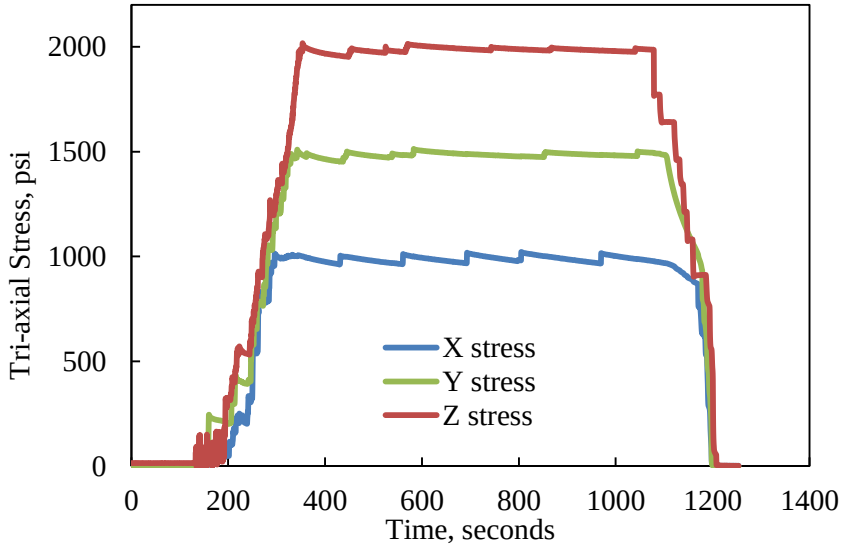

Figure 3.58. Pre-injection stress loading for Sample 28.

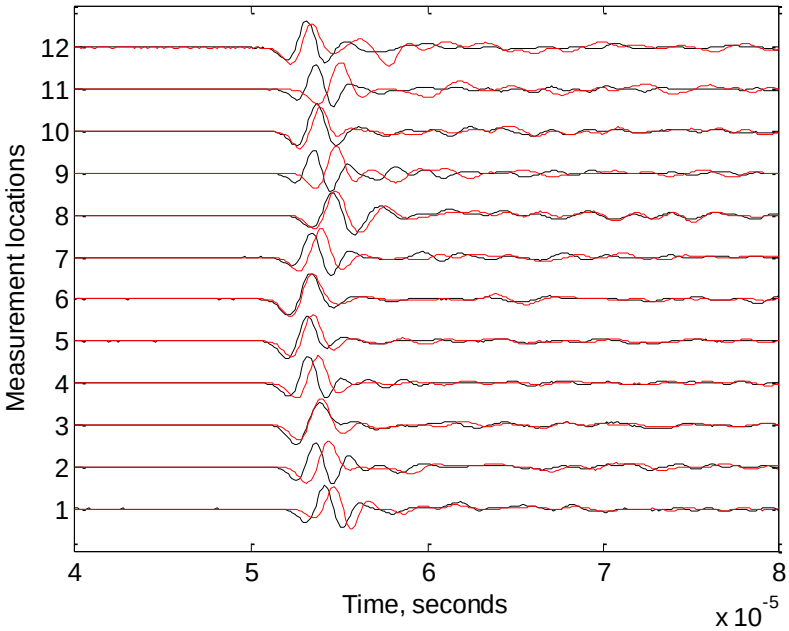

Figure 3.59. P-wave signatures measured from Surface 1 and Surface 3 of Sample 28.

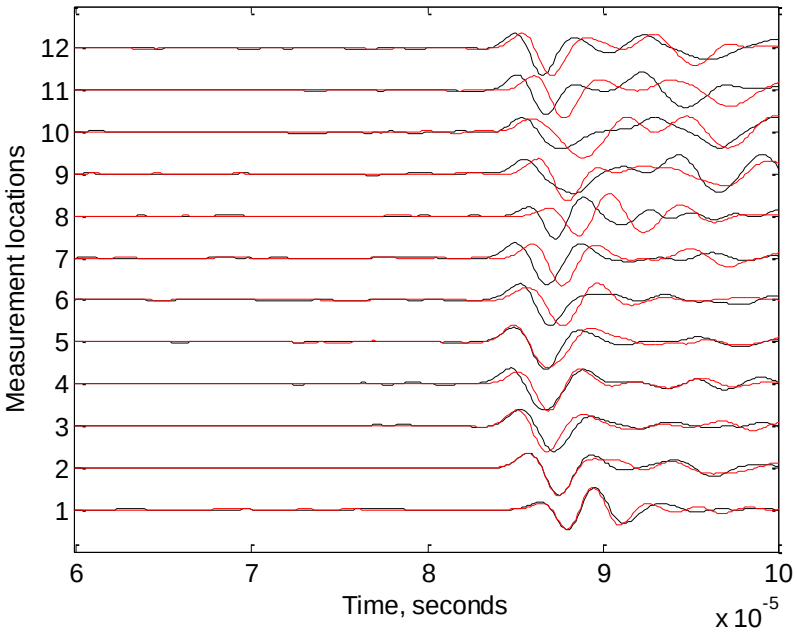

Figure 3.60. S-wave signatures measured from Surface 1 and Surface 3 of Sample 28.

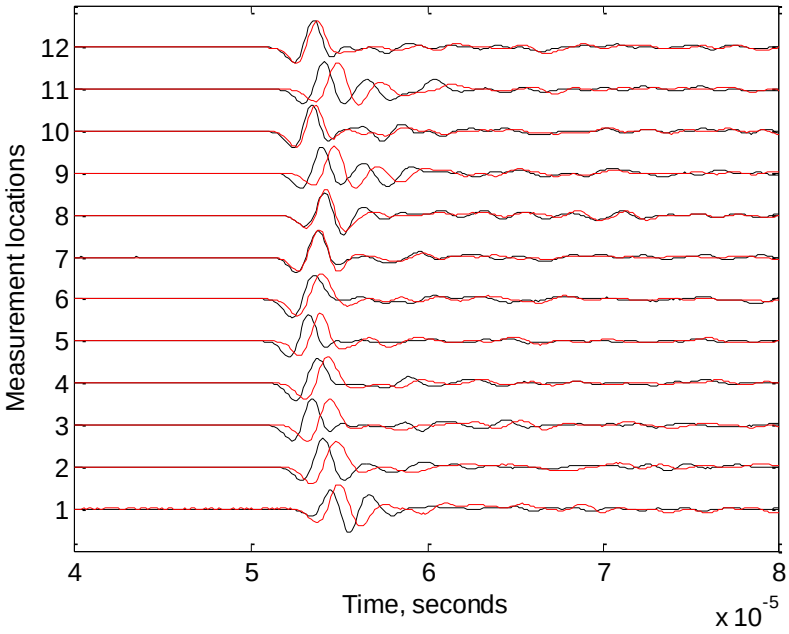

Figure 3.61. P-wave signatures measured from Surface 2 and Surface 4 of Sample 28.

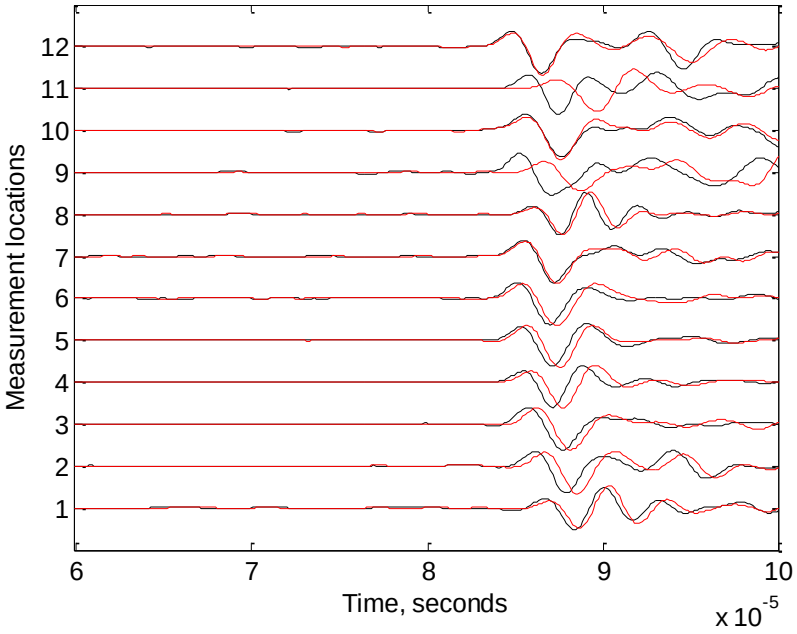

Figure 3.62. S-wave signatures measured from Surface 2 and Surface 4 of Sample 28.

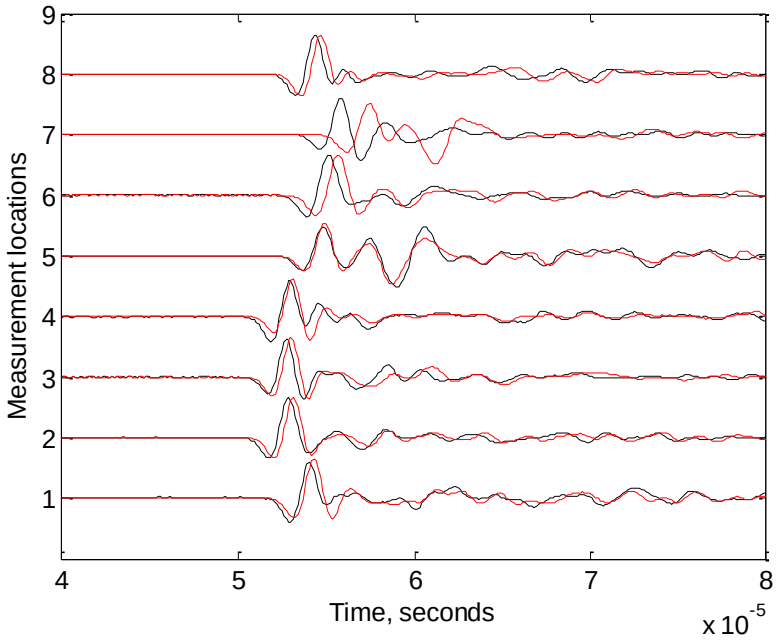

Figure 3.63. P-wave signatures measured from Surface 5 and Surface 6 of Sample 28.

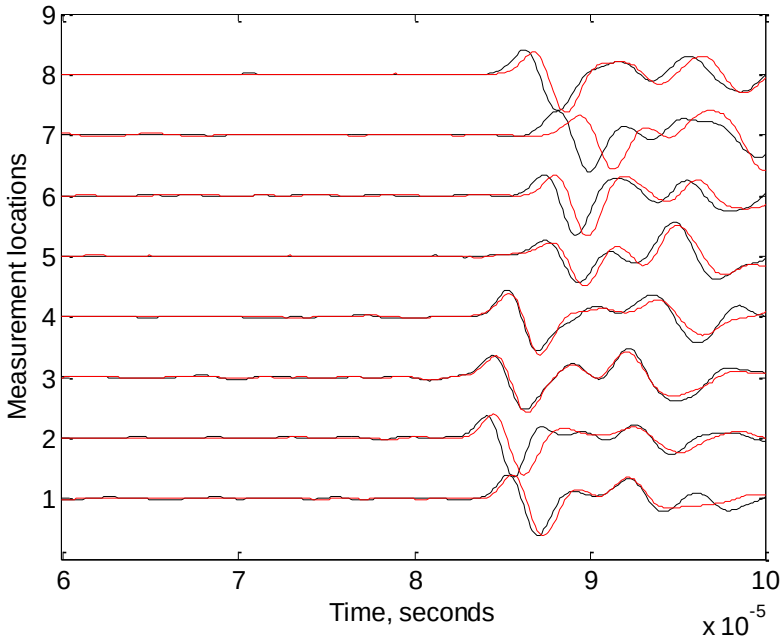

Figure 3.64. S-wave signatures measured from Surface 5 and Surface 6 of Sample 28.

After the acoustic measurements, we did the pressure decay test under no stress loading as a reference for comparison of permeability change after CO_2 injection. However, after the injection treatment, the fractures generated were too permeable for the nitrogen gas to build up to 180 psi, therefore only the pressure decay curve before CO_2 injection is shown below in Figure 3.65.

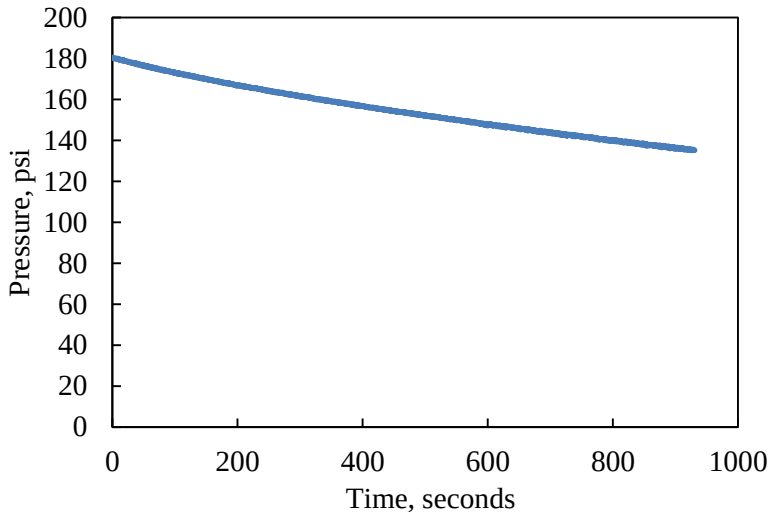

Figure 3.65. Pressure decay curve before CO_2 injection for Sample 28.

Sample 28 was then treated by injecting CO_2 into the borehole under tri-axial stress loading of 1000 psi in the x-direction, 1500 psi in the y-direction, and 2000 psi in the z-direction. The pressure and temperature profiles in the borehole are shown in Figures 3.66 and 3.67. The peak pressure when fractures were induced was 842.13 psi, and the corresponding temperature was 33.4 °C, which is above the supercritical temperature of 31.0 °C. However, the peak pressure is lower than the supercritical value of 1070.38 psi, indicating that CO_2 was in gas state when fractures were induced.

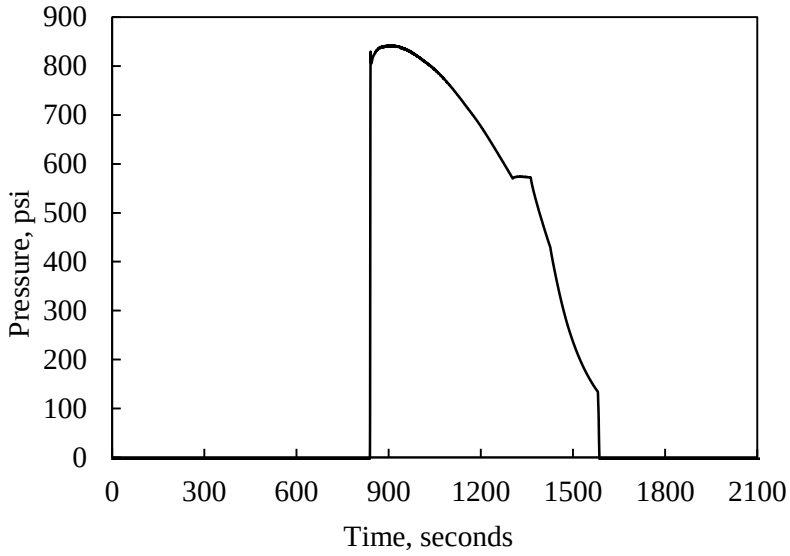

Figure 3.66. Pressure profile of CO_2 injection into Sample 28.

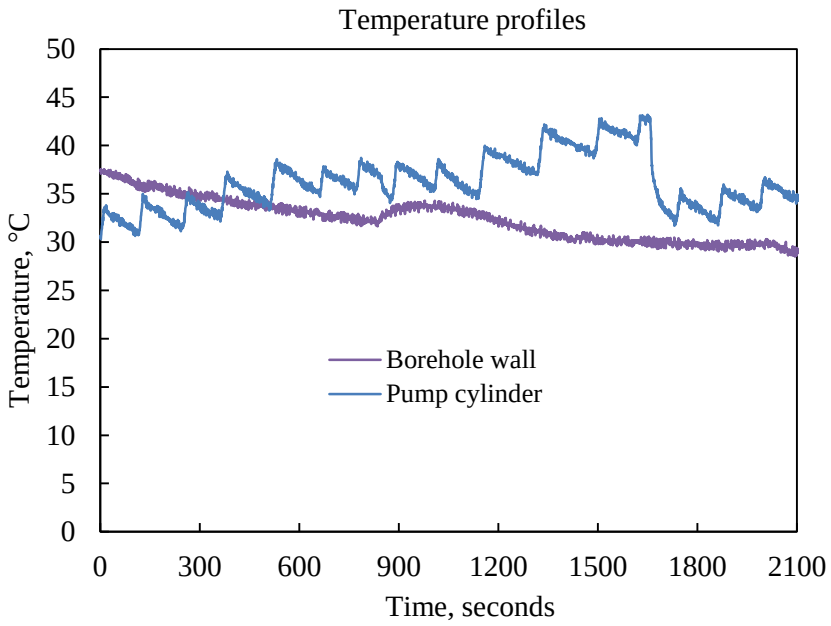

Figure 3.67. Temperature profiles during CO_2 injection into Sample 28.

Concrete Sample 29

Sample 29 was treated by injecting CO_2 under a tri-axial stress loading of 1500 psi in the x-direction, 2250 psi in the y-direction, and 3000 psi in the z-direction. Before the treatment, it was pre-loaded with the same stresses for about 15 mins, as shown in Figure 3.68. Then acoustic signatures were measured as reference for post-injection comparison, and pressure decay was carried out for pre-treatment permeability evaluation.

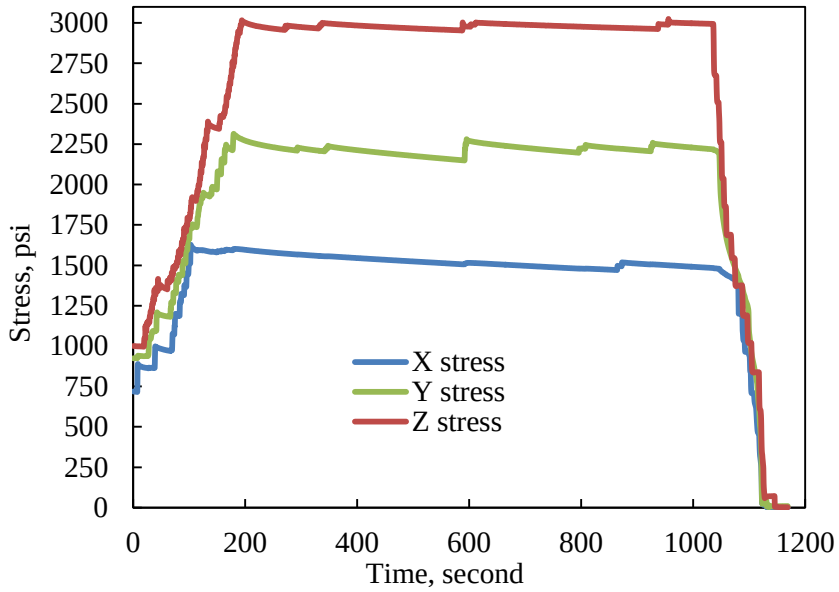

Figure 3.68. Pre-injection tri-axial stress loading for Sample 29.

Sample 29 was then treated by injecting CO_2 into borehole at a constant rate of 40ml/min under tri-axial stress loading of 1500 psi in the x-direction, 2250 psi in the y-direction, and 2000 psi in the z-direction, as shown in Figure 3.69. The injection pressure and borehole temperature profiles are shown in Figures 3.70 and 3.71. We injected three cycles of CO_2 in order to fracture Sample 29, one cycle more than Sample 27, due to higher tri-axial stress loading. These three cycles correspond to three pressure peaks in Figure 3.70. Before injecting the second and third cycles, liquid CO_2 refilled into the pump had to be heated up to 45-50 °C, which was relatively time-consuming. Since no heating source was installed for the concrete sample, the borehole temperature gradually decreased. When the third or the highest pressure peak of 2570.88 psi was achieved, the borehole temperature cooled down to 29.4 °C, lower than the supercritical temperature, thus Sample 29 was fractured by liquid CO_2.

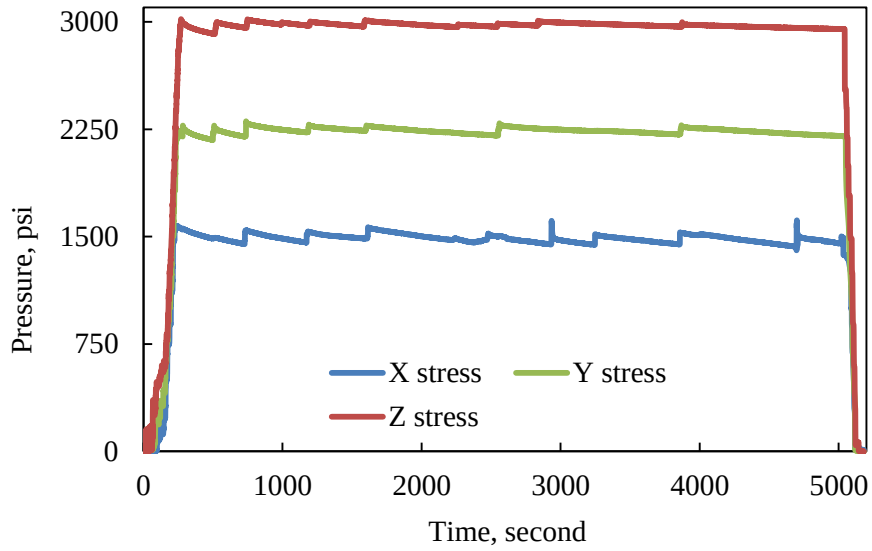

Figure 3.69. Tri-axial stress loading for CO_2 injection into Sample 29.

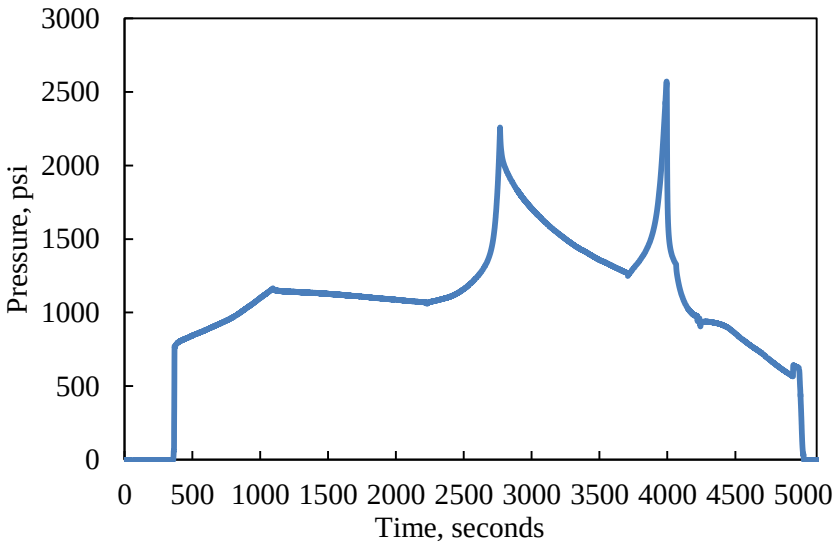

Figure 3.70. Pressure profile of CO_2 injection into Sample 29.

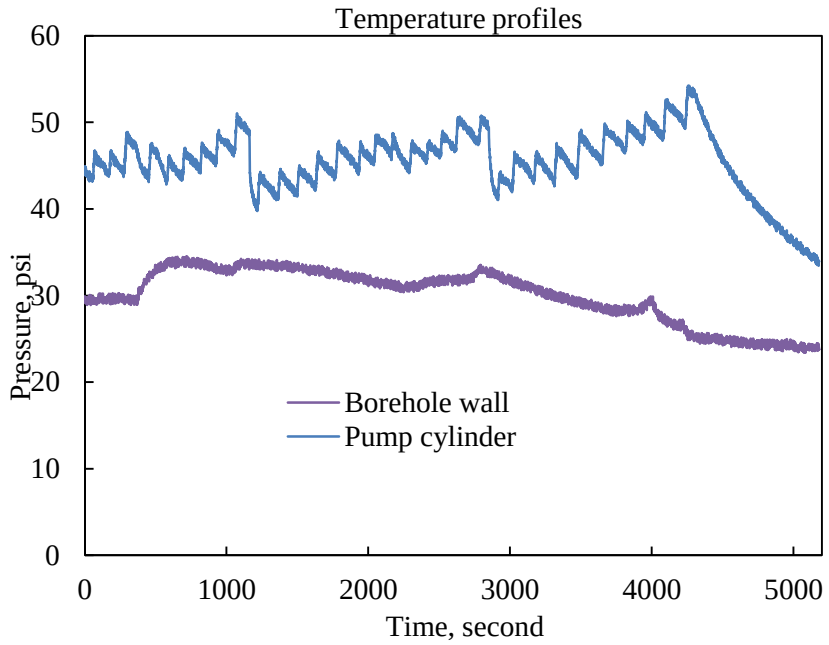

Figure 3.71. Borehole temperature profile during CO_2 injection into Sample 29.

Figure 3.72 compares the pressure decay curves measured before and after CO_2 injection. It was obvious that gas leaking rate significantly increased after CO_2 injection, due to fractures generated inside the concrete block.

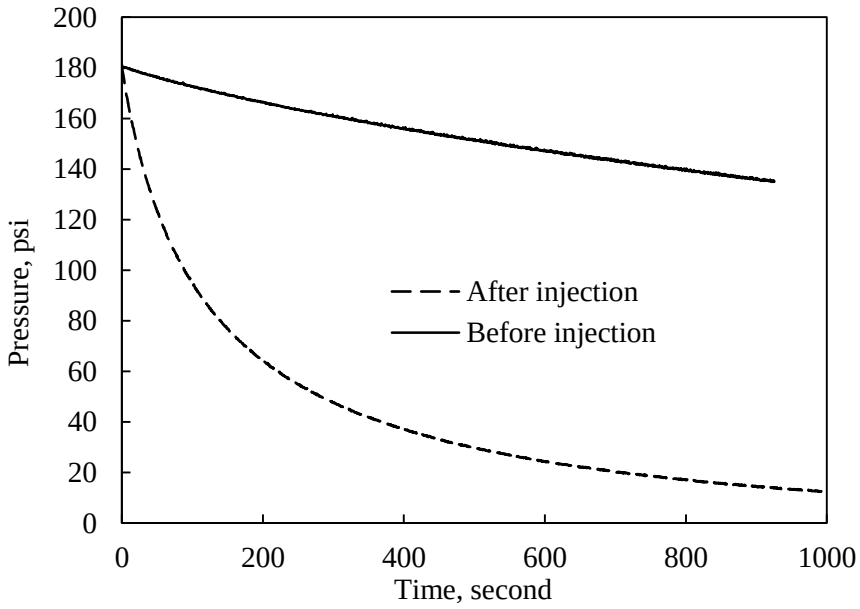

Figure 3.72. Pre- and post-injection pressure decay curves of Sample 29.

Acoustic signatures including P-waves and S-waves before (black curves) and after (red curves) CO_2 injection are compared in Figures 3.73 through 3.78. Both P-waves and S-waves show delays in arrival time, which is particularly consistent for measurement locations on Surface 1 and Surface 3. This indicates that the major fracture planes are parallel to Surface 1 and Surface 3. In other words, the fracture planes generated are perpendicular to the minimum horizontal stress in x-axis, in agreement with fracturing principles.

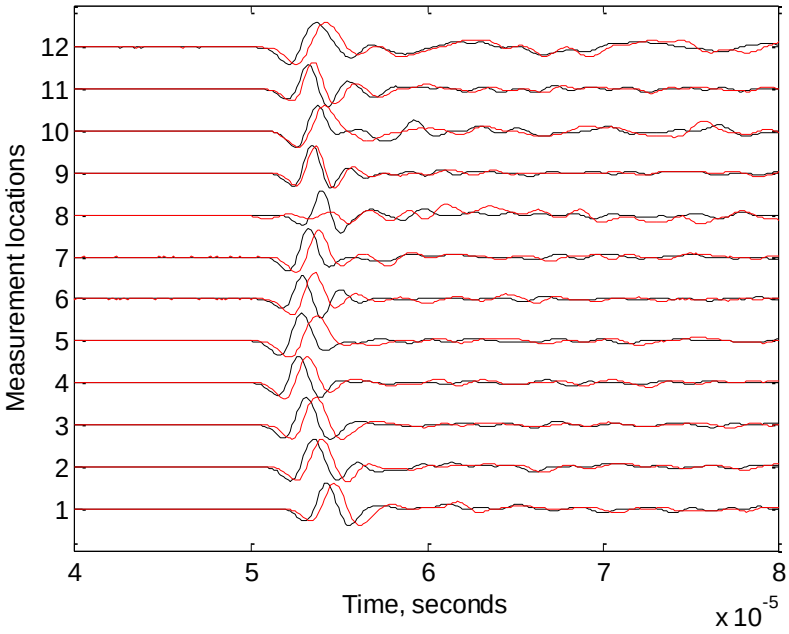

Figure 3.73. P-wave signatures measured from Surface 1 and Surface 3 of Sample 29.

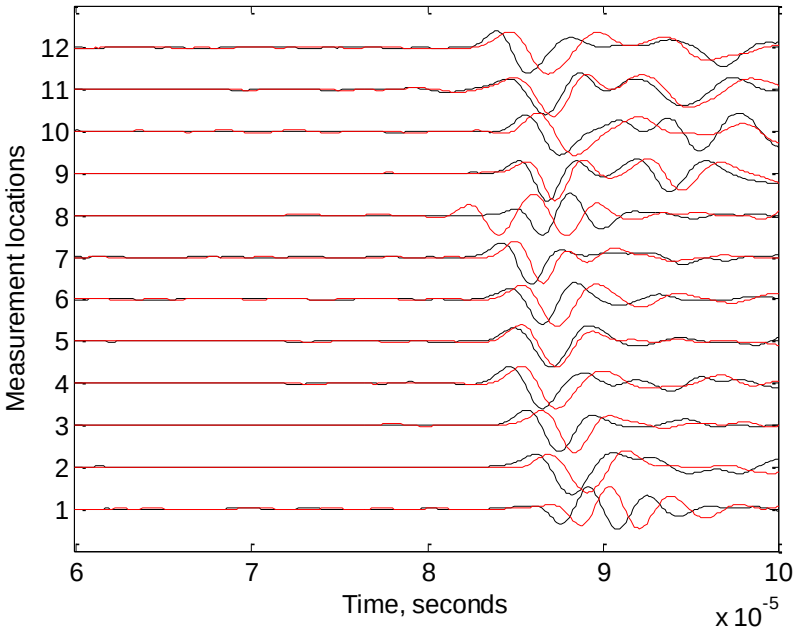

Figure 3.74. S-wave signatures measured from Surface 1 and Surface 3 of Sample 29.

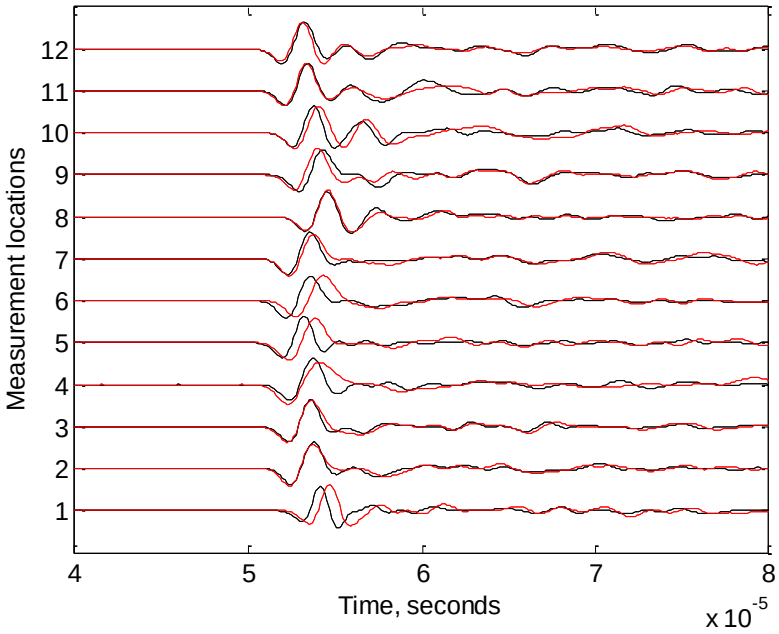

Figure 3.75. P-wave signatures measured from Surface 2 and Surface 4 of Sample 29.

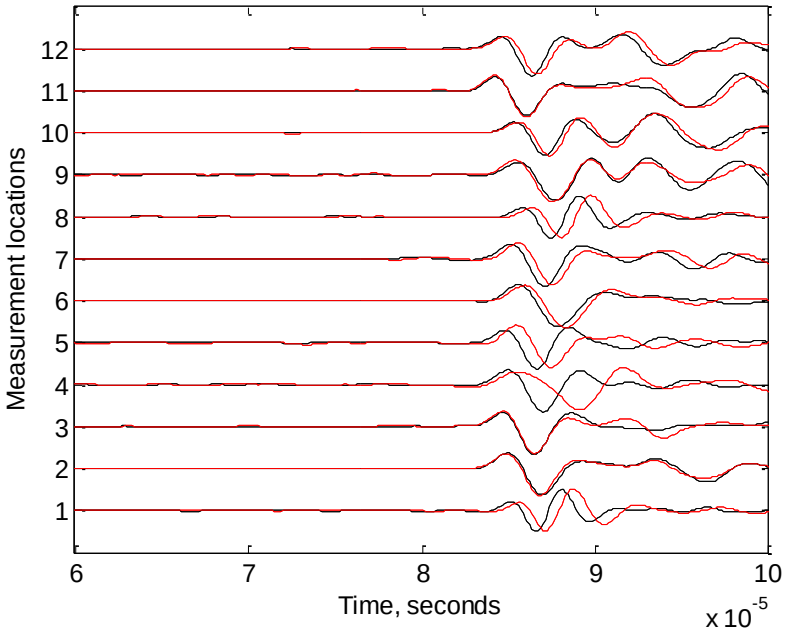

Figure 3.76. S-wave signatures measured from Surface 2 and Surface 4 of Sample 29.

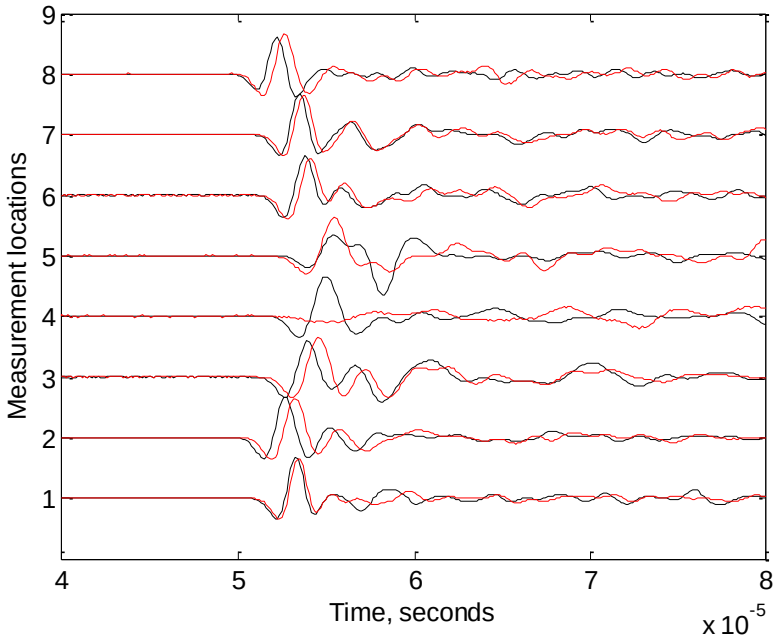

Figure 3.77. P-wave signatures measured from Surface 5 and Surface 6 of Sample 29.

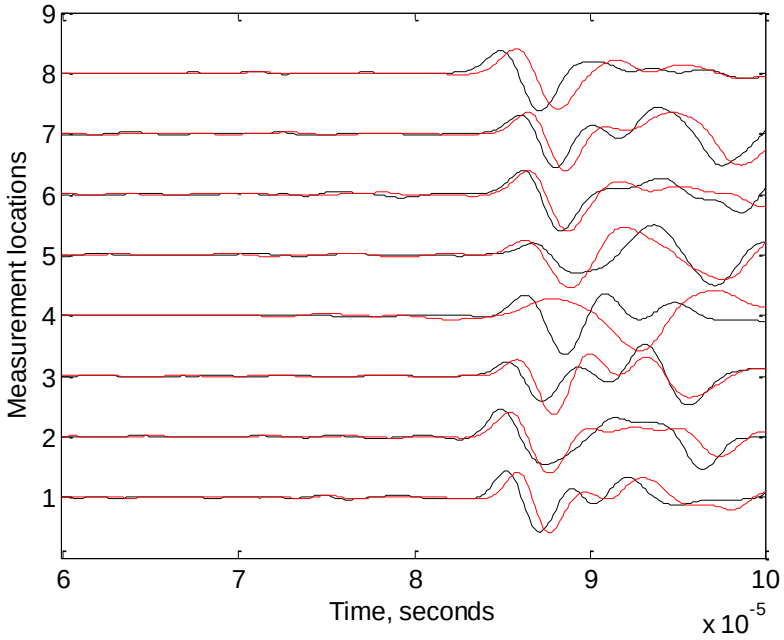

Figure 3.78. S-wave signatures measured from Surface 5 and Surface 6 of Sample 29.

Dye solution was later injected into Sample 29 to color the fracture planes. Then it was fractured by high pressure nitrogen gas, with the pressure profile shown by Figure 3.79. Gas fracturing revealed the fracture planes generated by CO_2 injection, as shown in Figure 3.80, 3.81, and 3.82. The fracture planes are almost parallel to Surface 1 and Surface 3, confirming indications obtained from acoustic measurements.

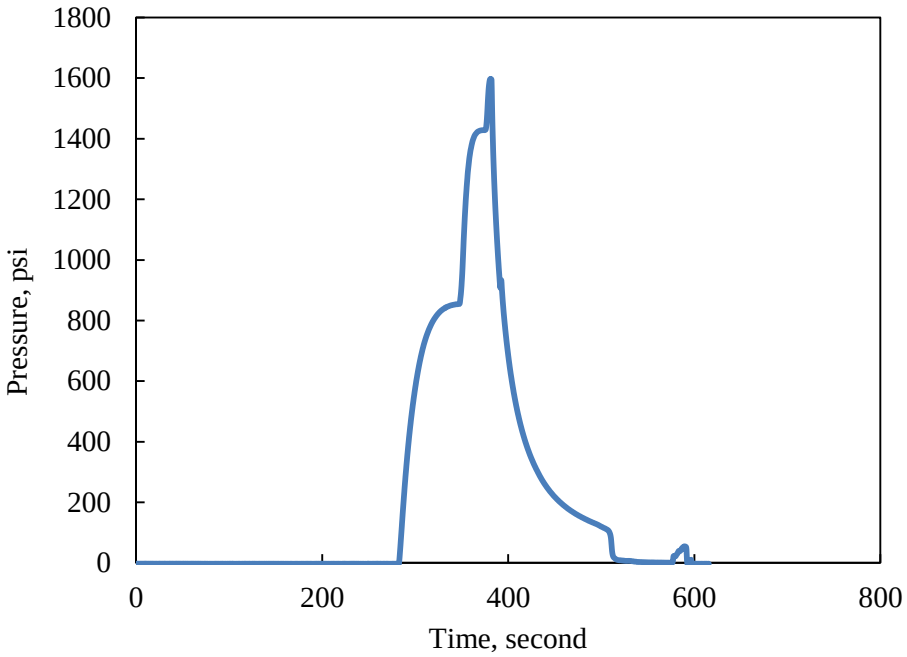

Figure 3.79. Gas fracturing of Sample 29 under tri-axial stress loading.

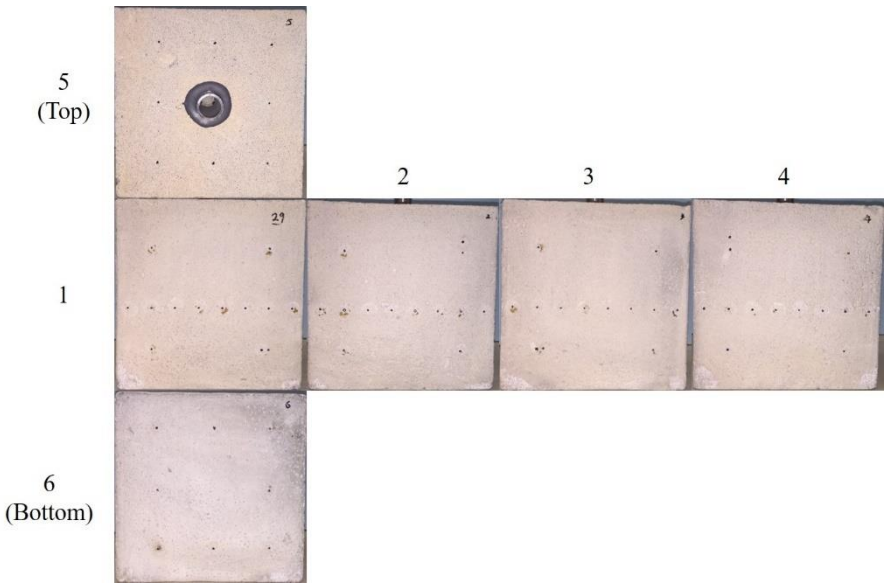

Figure 3.80. Faces of Sample 29 before CO_2 injection.

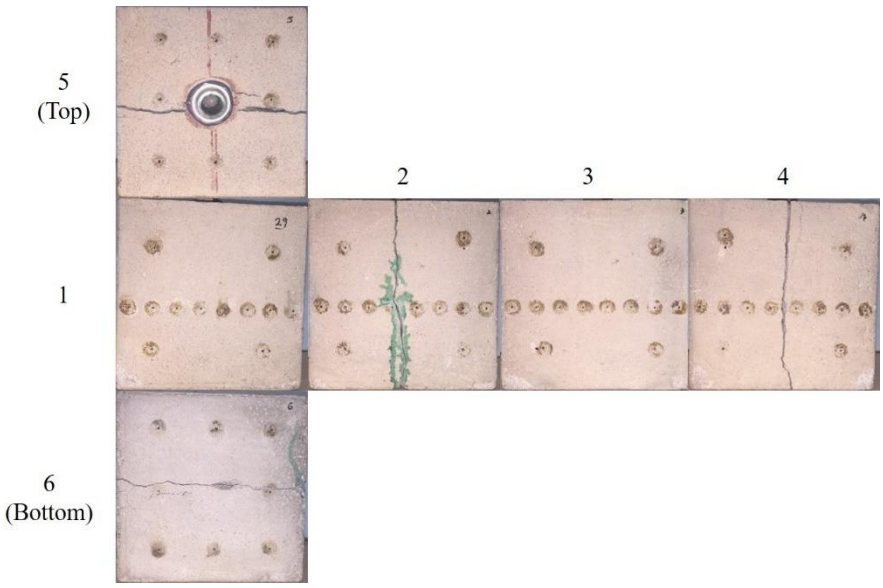

Figure 3-81. Faces of Sample 29 after gas fracturing.


Figure 3.82. Colored CO_2 injection induced fracture planes in Sample 29.

The major fracture planes primarily propagate toward Surface 2, but did not extend to the opposite side, exhibiting an asymmetric pattern around the wellbore. As we can see, the opposite side is probably protected from fracture initiation by the epoxy drape formed during the binding of the casing.

Concrete Sample 46

Sample 46 was treated by injecting CO_2 under a tri-axial stress loading of 1000 psi in the x-direction, 1500 psi in the y-direction, and 2000 psi in the z-direction. Before the treatment, it was pre-loaded with the same stresses for about 42 mins, as shown in Figure 3.83. Then

acoustic signatures were measured as reference for post-injection comparison, pressure decay was carried out for pre-treatment permeability evaluation, as shown in Figure 3.84. Before treatment, the gas leakage rate from borehole was very slow, indicating concrete samples are good analogs for caprocks.

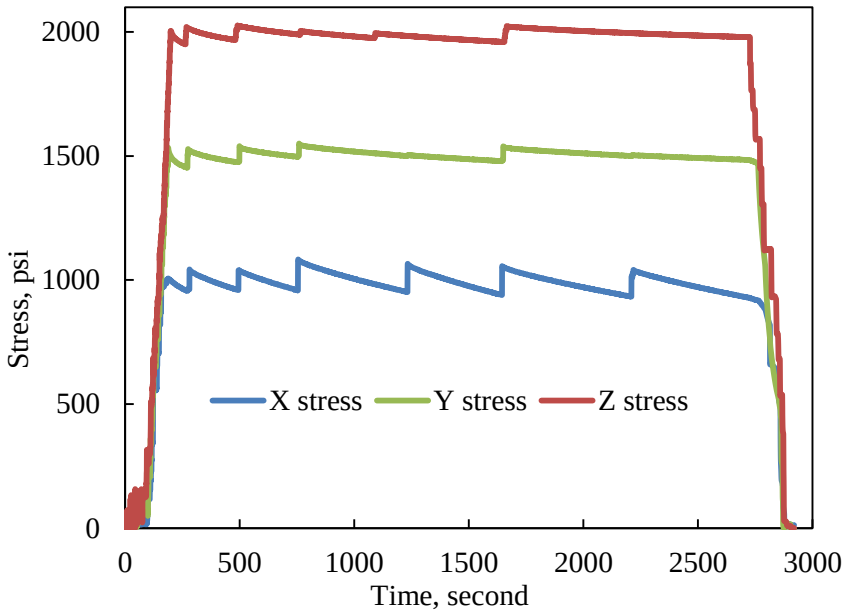

Figure 3.83. Pre-treatment stress loading for Sample 46.

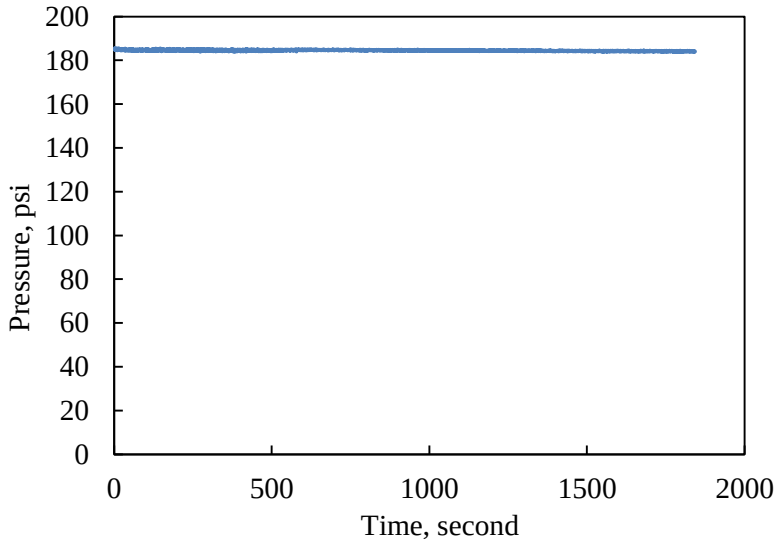

Figure 3.84. Pre-treatment pressure decay for Sample 46.

Sample 46 was fractured when the valve to the sample was opened. The peak pressure is ~810 psi and the corresponding temperature is above 30 °C, so it was a gaseous CO_2 fracturing case. Data for CO_2 injection was lost due to a file crash. Acoustic signatures before and after CO_2 injection are compared in Figure 3.85 through Figure 3.90. Both P-waves and S-waves show

delays in arrival time and changes in waveforms after CO_2 injection, indicating CO_2 injection induced fractures.

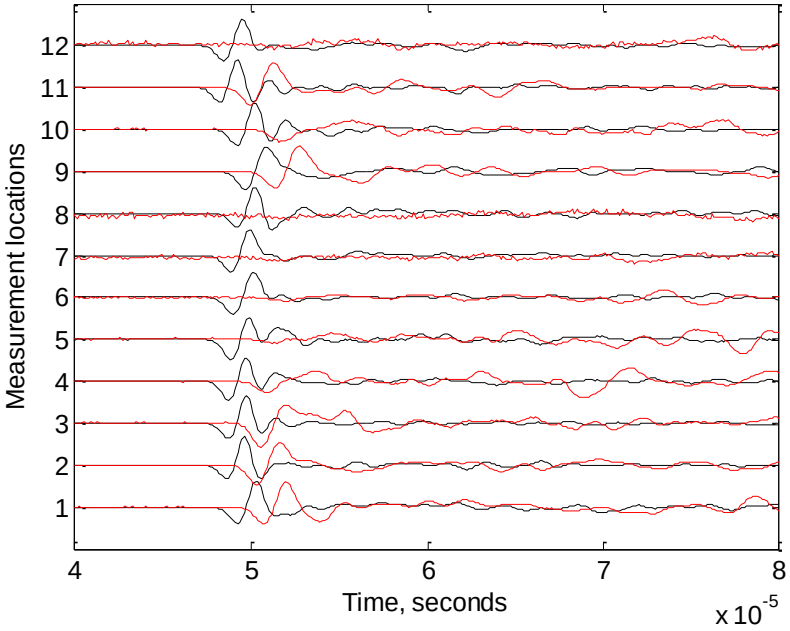

Figure 3.85. P-wave signatures measured from Surface 1 and Surface 3 of Sample 46.

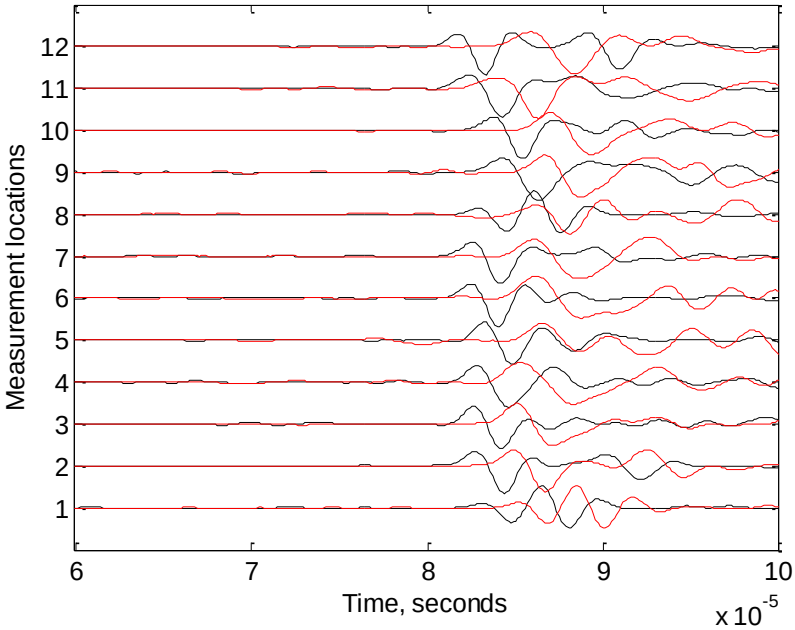

Figure 3.86. S-wave signatures measured from Surface 1 and Surface 3 of Sample 46.

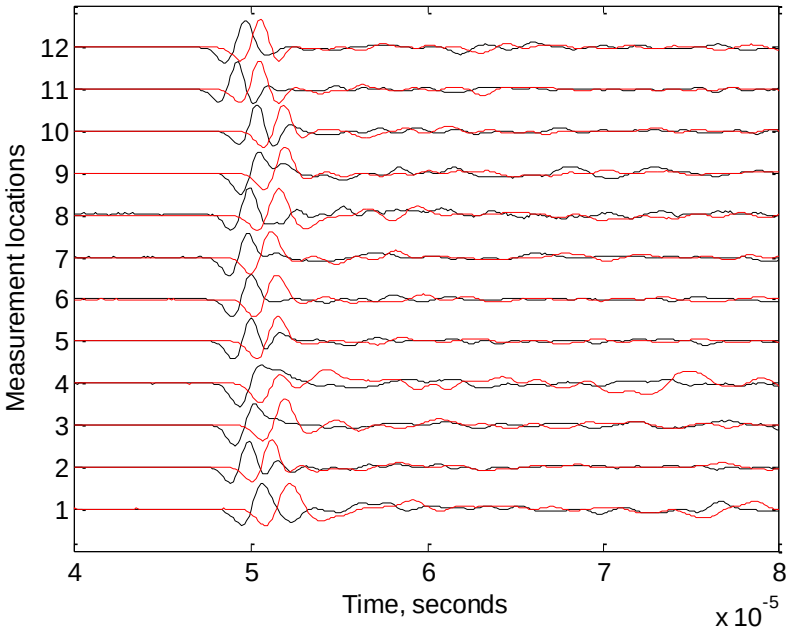

Figure 3.87. P-wave signatures measured from Surface 2 and Surface 4 of Sample 46.

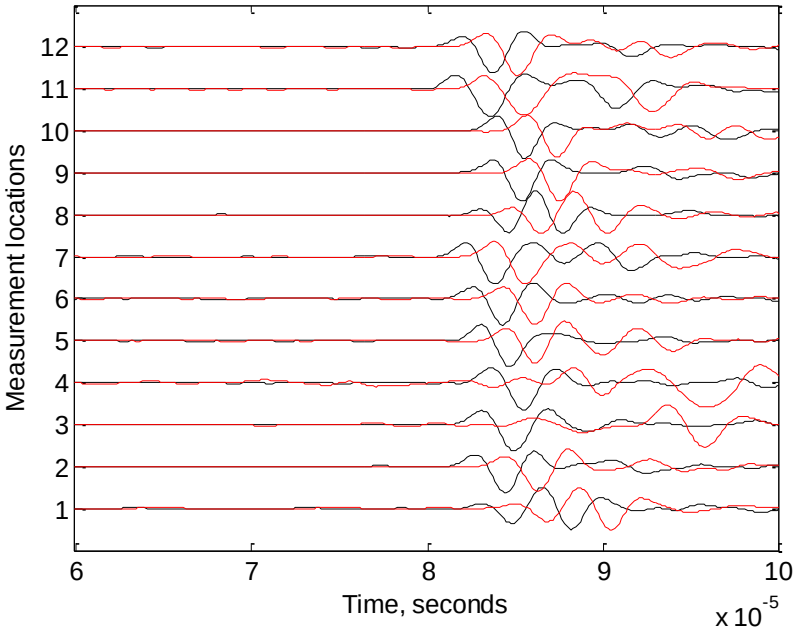

Figure 3.88. S-wave signatures measured from Surface 2 and Surface 4 of Sample 46.

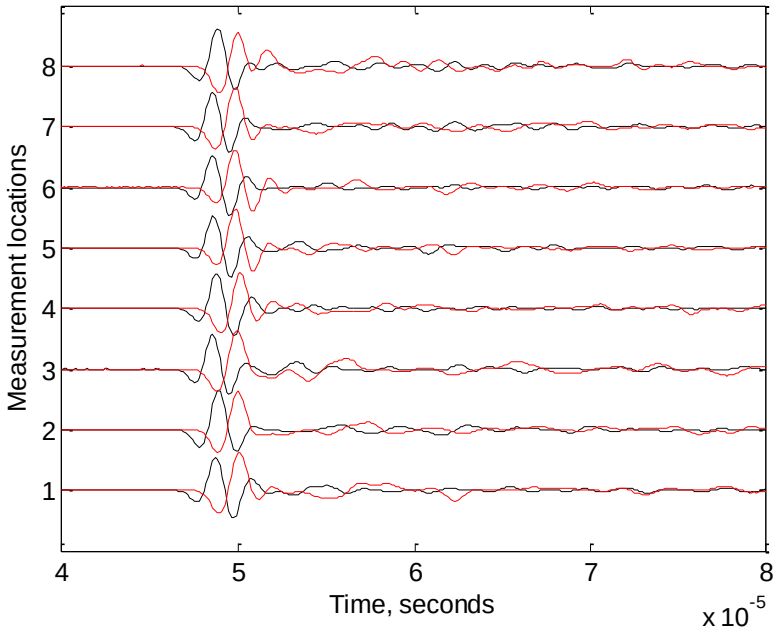

Figure 3.89. P-wave signatures measured from Surface 5 and Surface 6 of Sample 46.

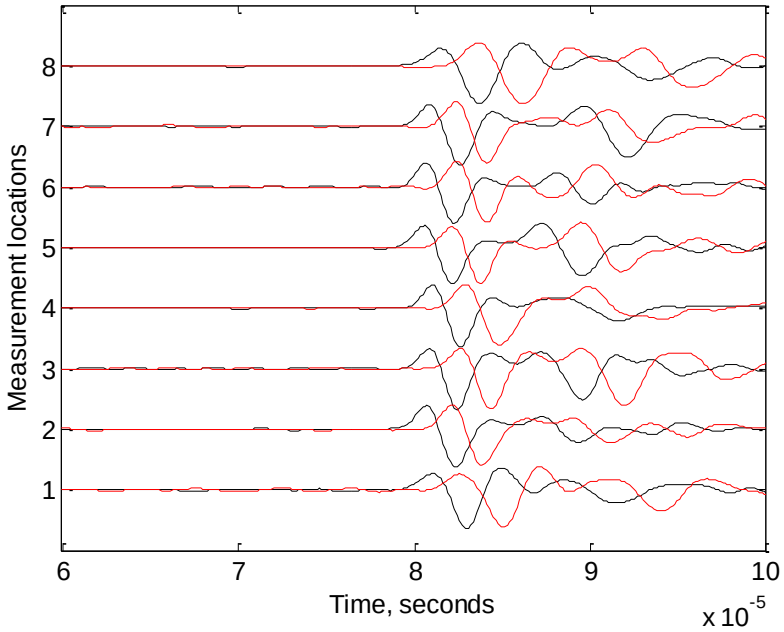

Figure 3.90. S-wave signatures measured from Surface 5 and Surface 6 of Sample 46.

Dye solution was then injected into Sample 46 to color the CO_2 injection induced fractures, and the dye solution flowed out of the block surface. Then the sample was fractured by nitrogen gas, and the pressure profile for that is shown in Figure 3.91. Coloring and gas fracturing revealed the fracture planes generated by CO_2 injection, as shown in Figures 3.92, 3.93, and 3.94. The fracture planes are perpendicular to the minimum horizontal stress direction.

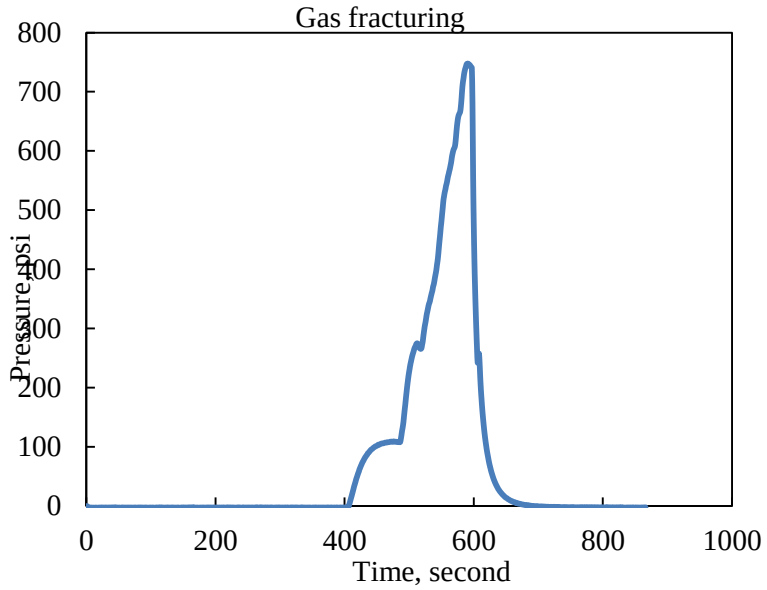

Figure 3.91. Gas fracturing after CO_2 injection into Sample 46.

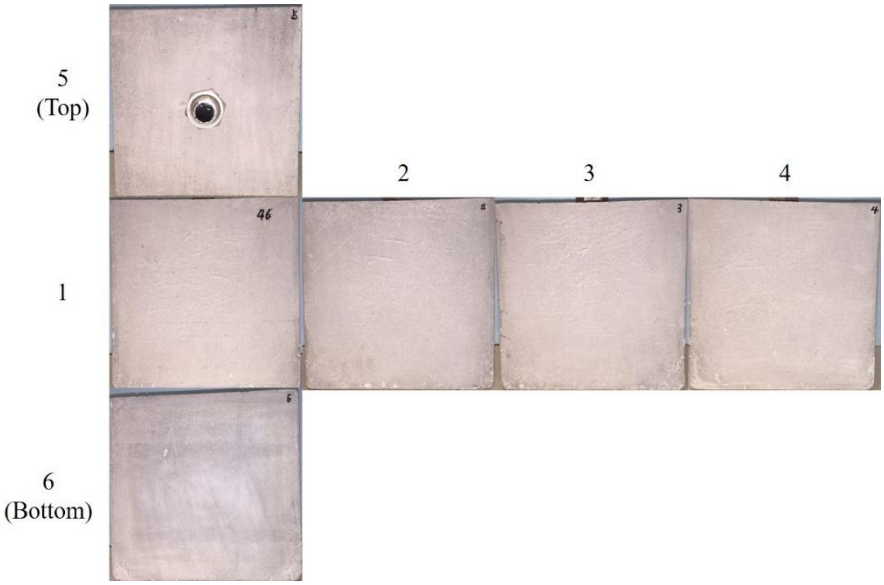

Figure 3.92. Intact surfaces of Sample 46 before treatment.

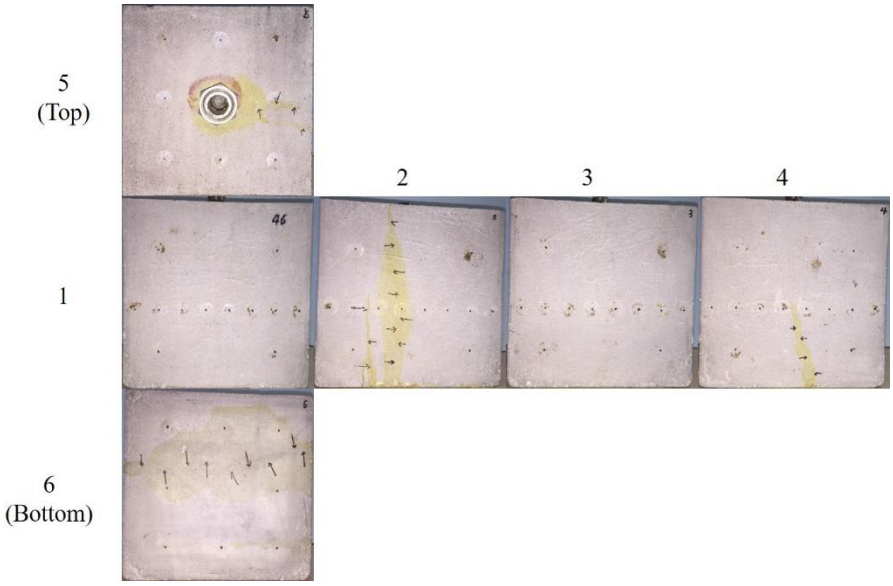

Figure 3.93. Surfaces of Sample 46 after coloring.


Figure 3.94. CO_2 injection induced fracture morphology of Sample 46 after gas fracturing.

Concrete Sample 47

Sample 47 was treated by injection CO_2 under a tri-axial stress loading of 1500 psi in the x-direction, 2250 psi in the y-direction, and 3000 psi in the z-direction. Before the treatment, it was pre-loaded with the same stresses for about 40 mins, as shown in Figure 3.95. Then acoustic signatures were measured as reference for post-injection comparison, and pressure decay was carried out for pre-treatment permeability evaluation.

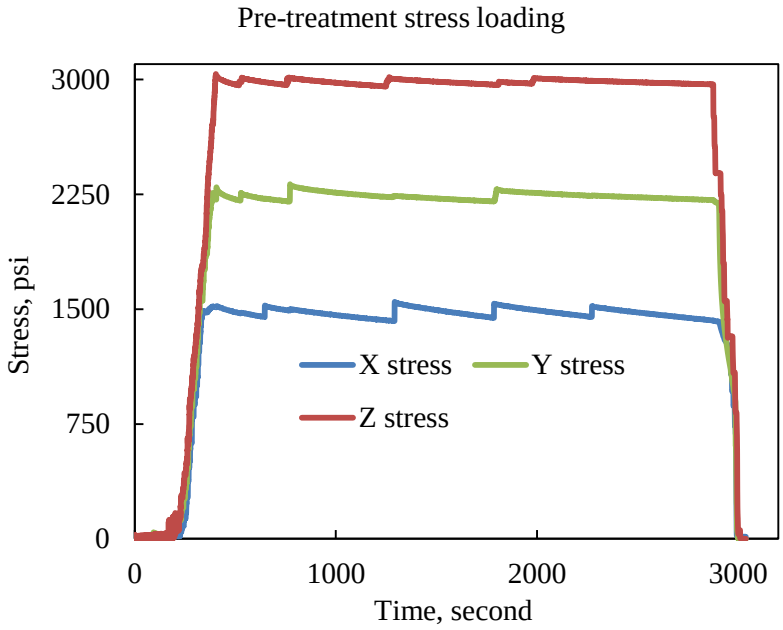

Figure 3.95. Stress loading before CO_2 injection for Sample 47.

Sample 47 was treated by injecting CO_2 at a constant rate of 100 ml/min under tri-axial stress loading of 1500 psi in the x-direction, 2250 psi in the y-direction, and 2000 psi in the z-direction, as shown in Figure 3.96. The injection pressure and borehole temperature profiles are shown in Figures 3.97 and 3.98. Two cycles of CO_2 were injected to fracture the sample. These two cycles correspond to the pressure peaks around 360 seconds and 430 seconds in Figure 3.97. The highest peak pressure is 1151.13 psi, corresponding to the borehole temperature of 35.0 °C. Both of the pressure and temperature are higher than the supercritical values, thus Sample 47 was fractured by sc-CO_2.

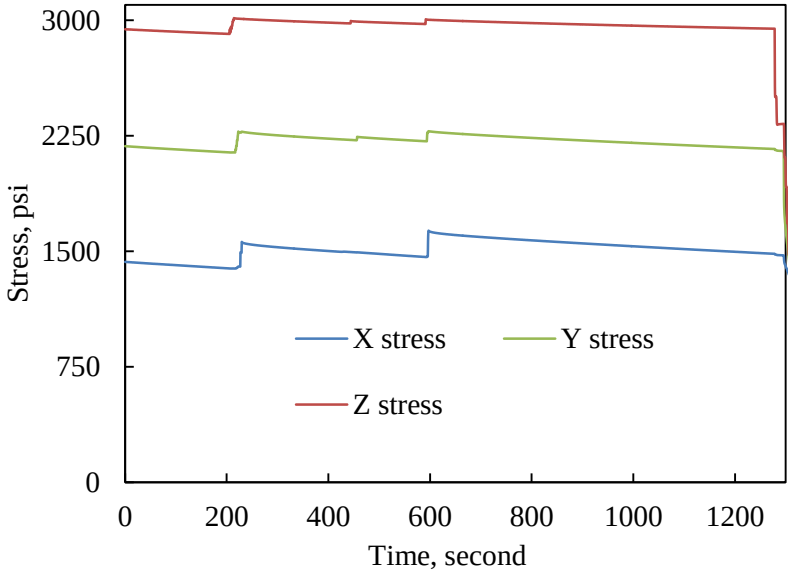

Figure 3.96. Stress loading for CO_2 injection for Sample 47.

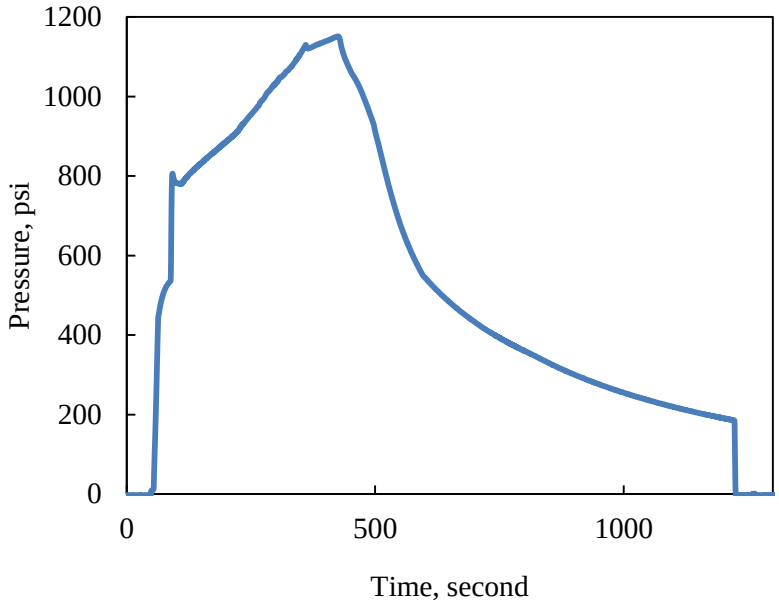

Figure 3.97. CO_2 injection pressure for Sample 47.

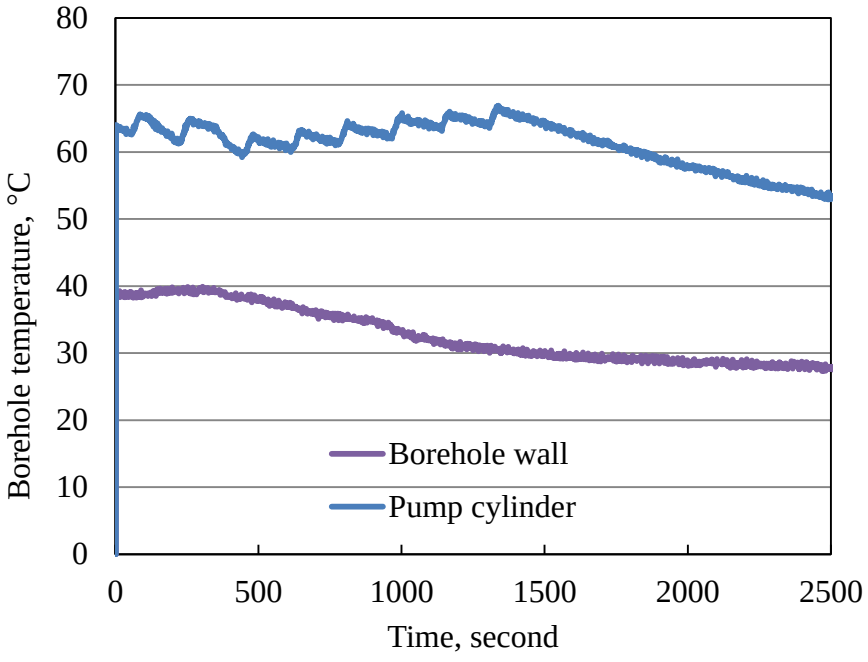

Figure 3.98. Borehole temperature during CO_2 injection into Sample 47.

Figure 3.99 compares the pressure decay curves measured before and after CO_2 injection. It was obvious that gas leakage rate significantly increased after CO_2 injection, due to fractures generated inside the concrete block.

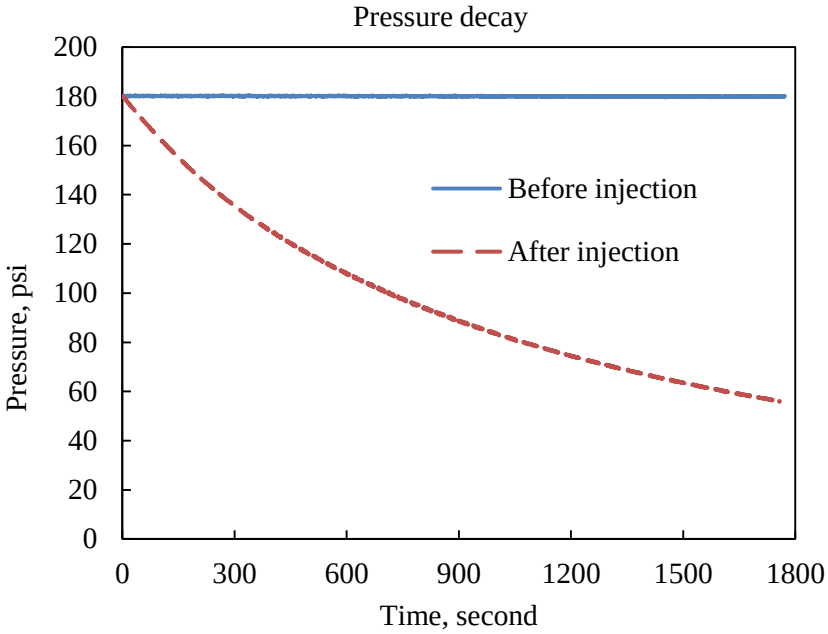

Figure 3.99. Pressure decay curves before and after treatment for Sample 47.

Acoustic signatures including P-waves and S-waves before (black curves) and after (red curves) CO_2 injection are compared in Figures 3.100 through 3.105. Both P-waves and S-waves show delays in arrival time, indicating that the fracture planes are generated inside the sample.

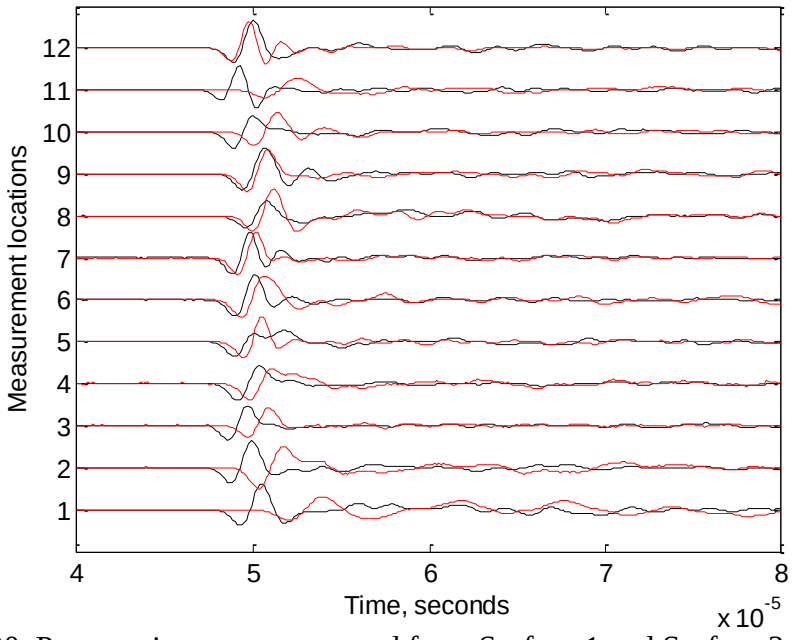

Figure 3.100. P-wave signatures measured from Surface 1 and Surface 3 of Sample 47.

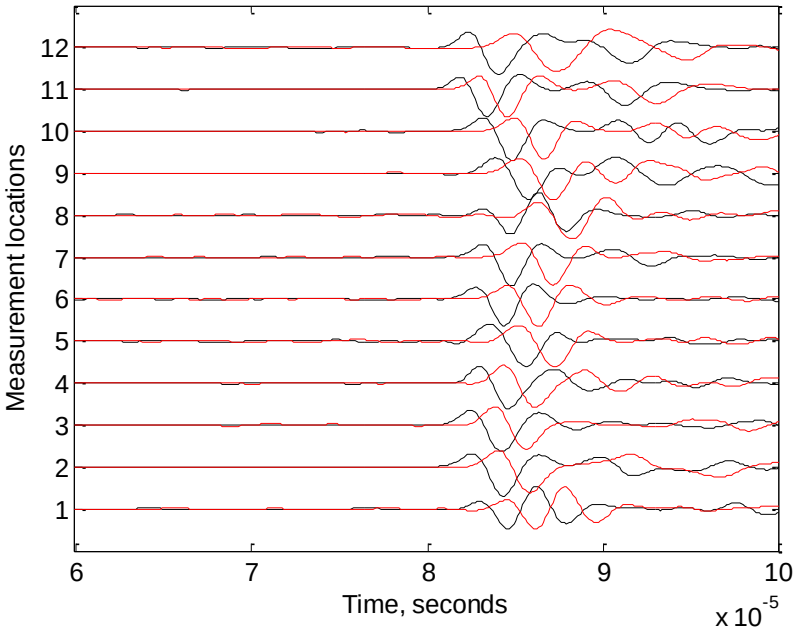

Figure 3.101. S-wave signatures measured from Surface 1 and Surface 3 of Sample 47.

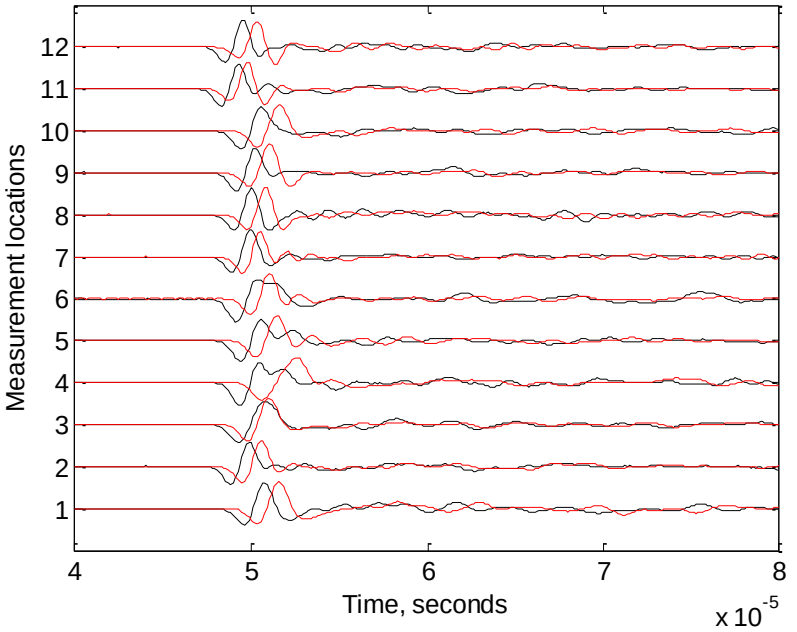

Figure 3.102. P-wave signatures measured from Surface 2 and Surface 4 of Sample 47.

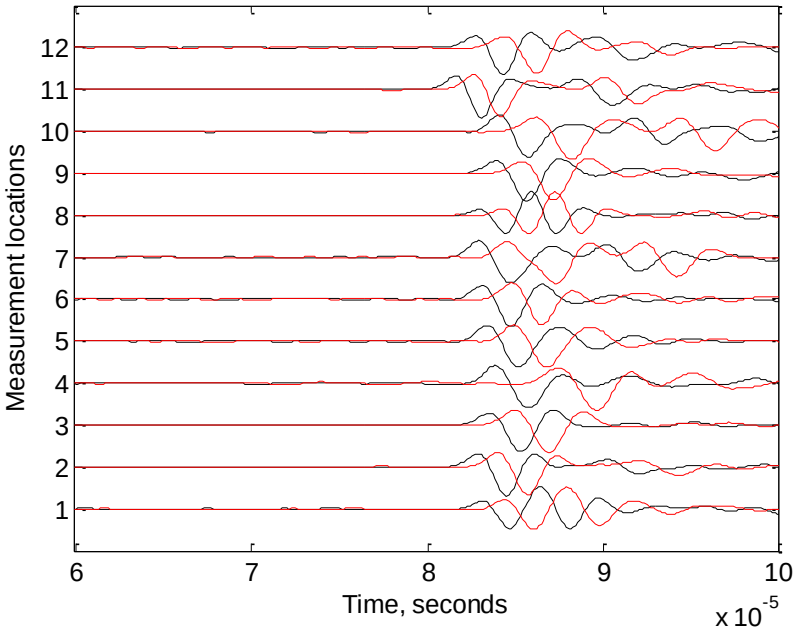

Figure 3.103. S-wave signatures measured from Surface 2 and Surface 4 of Sample 47.

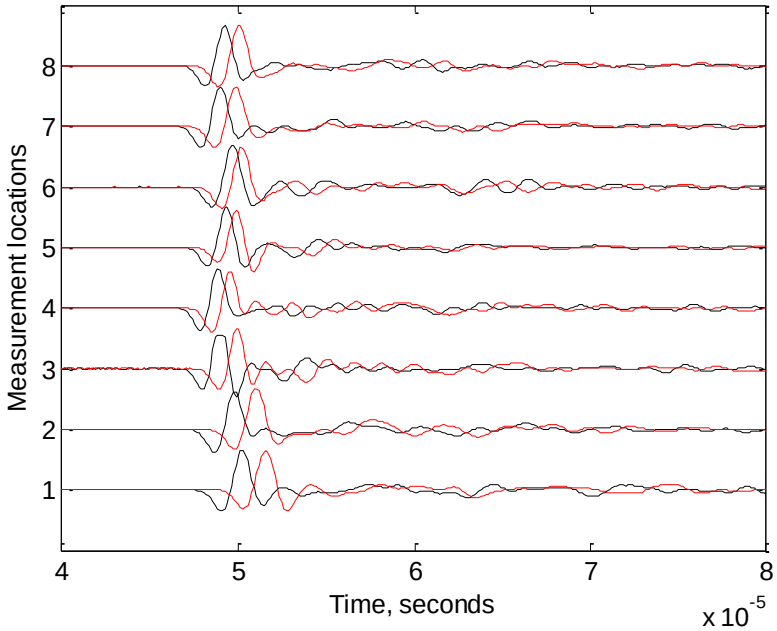

Figure 3.104. P-wave signatures measured from Surface 5 and Surface 6 of Sample 47.

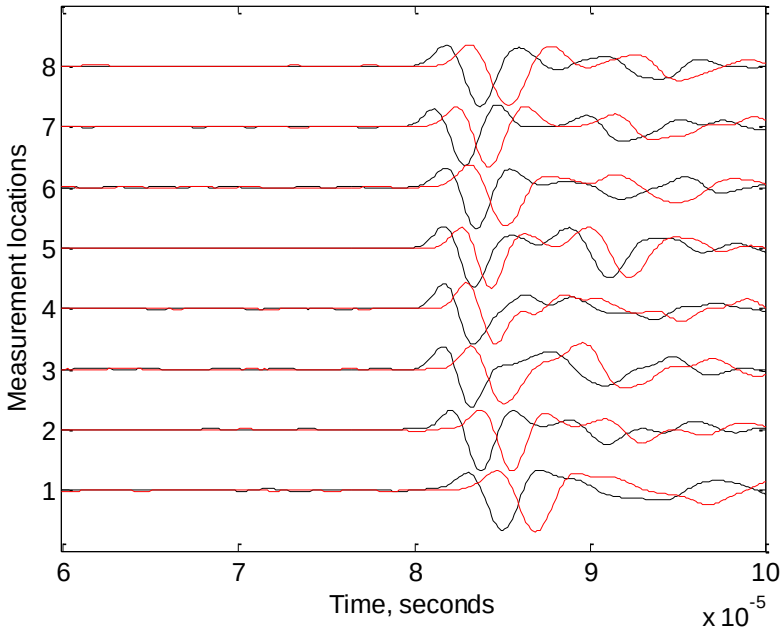

Figure 3.105. S-wave signatures measured from Surface 5 and Surface 6 of Sample 47.

Dye solution was later injected into Sample 47 to color the CO_2 injection induced fracture planes. Then, nitrogen gas was injected to break down the sample, whose pressure profile is shown in Figure 3.106. Fracture coloring and gas fracturing revealed the fracture planes generated by CO_2 injection, as shown in Figures 3.107, 3.108, and 3.109. It is clear that the fracture planes were perpendicular to the minimum horizontal stress direction.

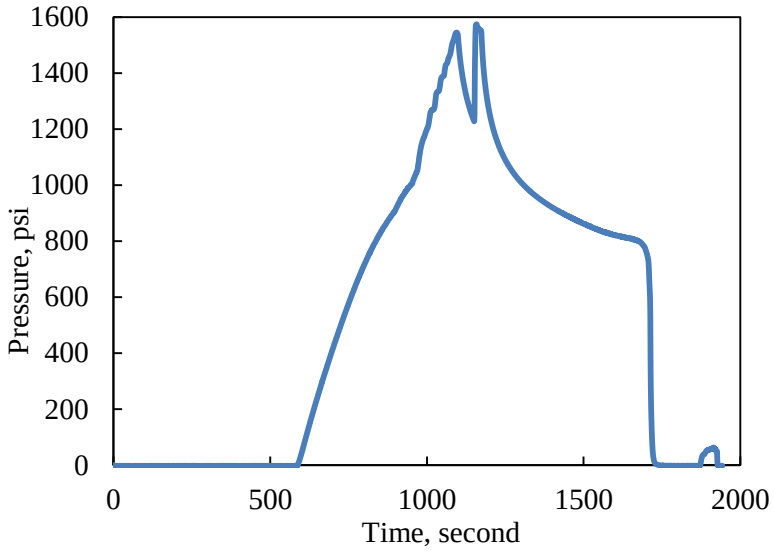

Figure 3.106. Gas fracturing pressure for Sample 47.

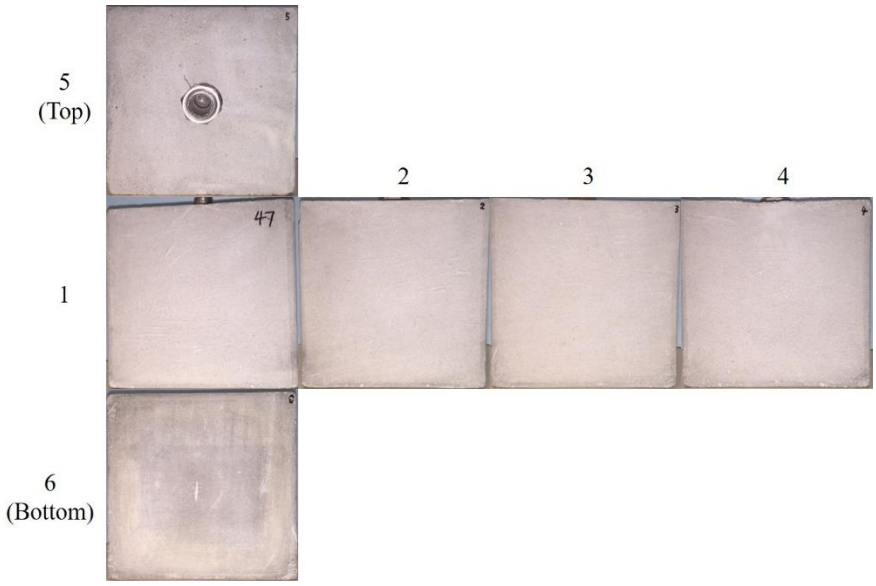

Figure 3.107. Intact surfaces of Sample 47 before treatment.

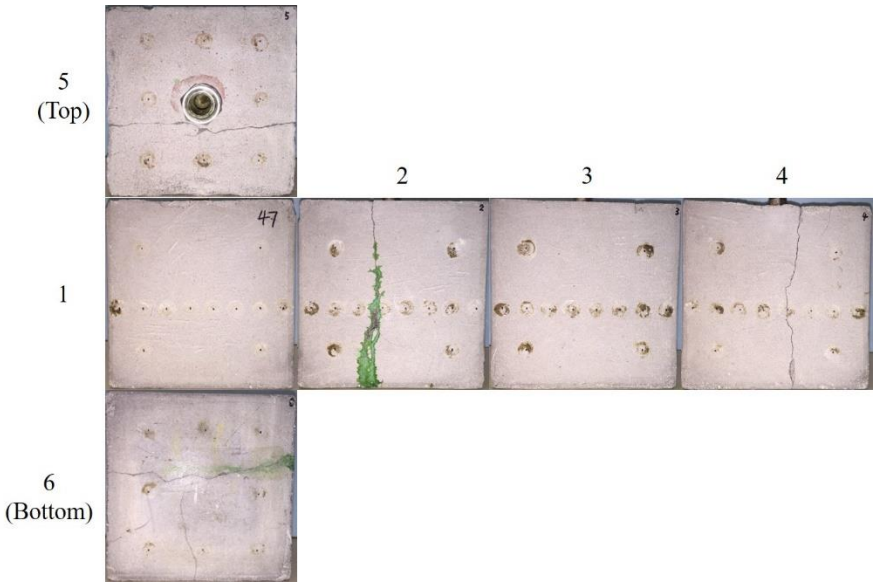

Figure 3.108. Surfaces of Sample 47 after coloring and gas fracturing.

Figure 3.109. CO_2 injection induced fracture morphology of Sample 47.

Concrete Sample 48

Sample 48 was first pre-loaded tri-axial stresses of 1000 psi in the x-direction, 1500 psi in the y-direction, and 2000 psi in the z-direction for about 42 min, then acoustic measurements and the pressure decay test were carried out. After that, CO_2 was injected at a constant rate of 40 ml/min into the sample under the same tri-axial stress loading, as shown in Figure 3.110. The peak pressure of CO_2 injection was 1021.86 psi at 912.57 seconds, shown in Figure 3.111, corresponding a temperature of 49.9 °C in Figure 3.112. Therefore, it is a gaseous CO_2 injection induced fracturing case. The injection induced fracturing generated a small stress loading response in the x-axis direction in Figure 3.110.

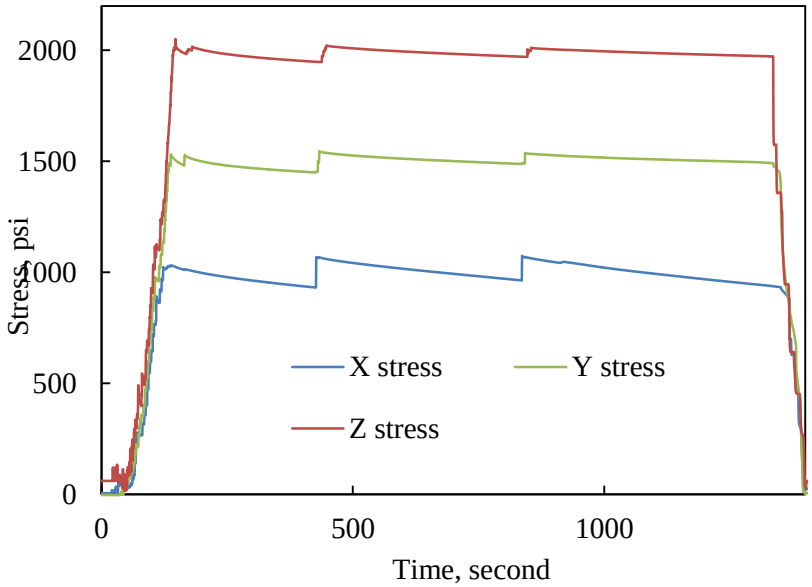

Figure 3.110. Tri-axial stress loading for CO_2 injection into Sample 48.

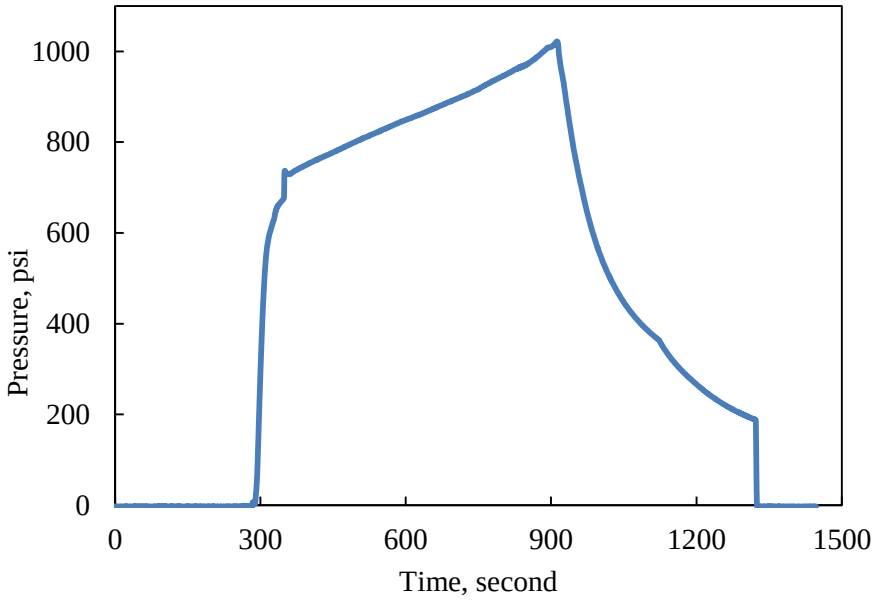

Figure 3.111. CO_2 injection pressure of Sample 48.

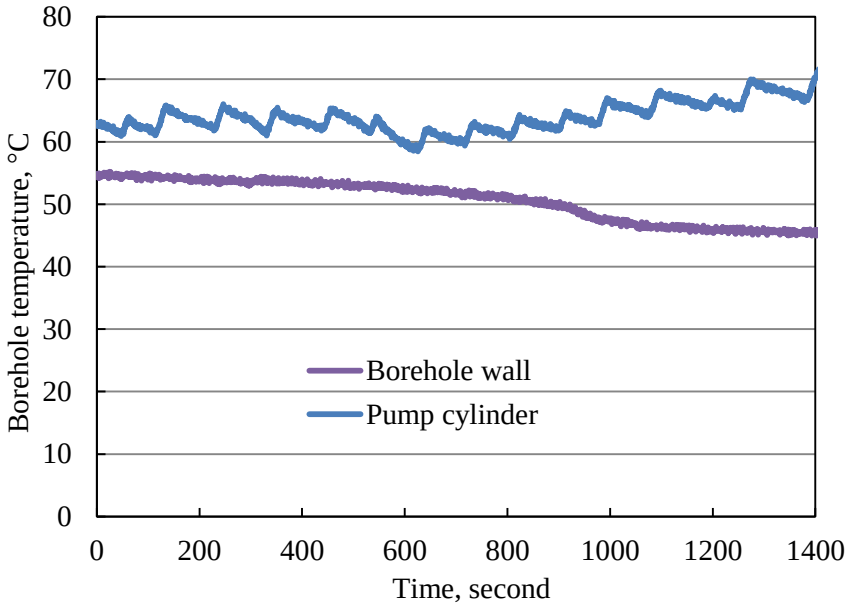

Figure 3.112. Borehole temperature profile during injection for Sample 48.

Pressure decay curves measured before and after CO_2 injection for Sample 48 are compared in Figure 3.113, which shows significant permeability increase of the concrete block due to injection induced fractures.

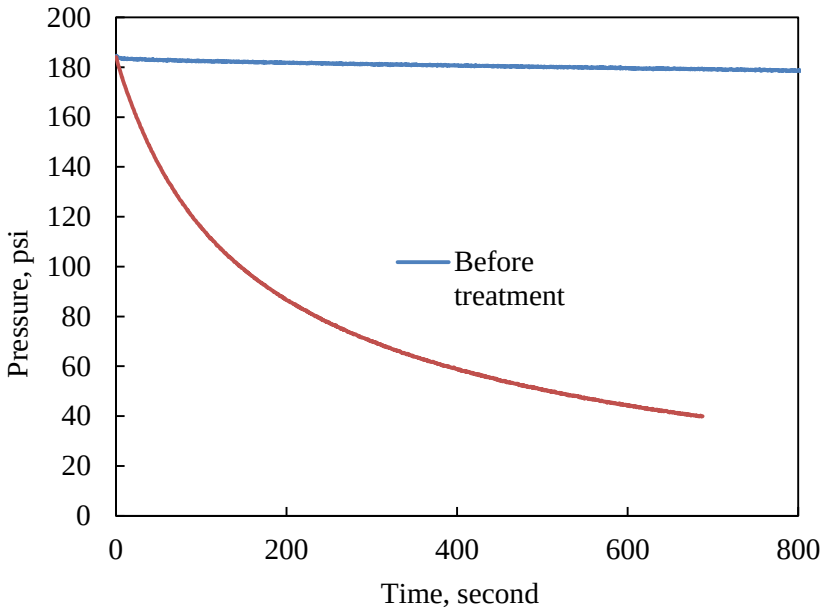

Figure 3.113. Pressure decay curves before and after CO_2 injection for Sample 48.

Acoustic signatures before and after CO_2 injection for Sample 48 are compared in Figure 3.114 through 3.119. Both P-waves and S-waves show delays in arrival time and changes in waveforms after CO_2 injection, indicating existence of injection induced fractures inside the concrete sample.

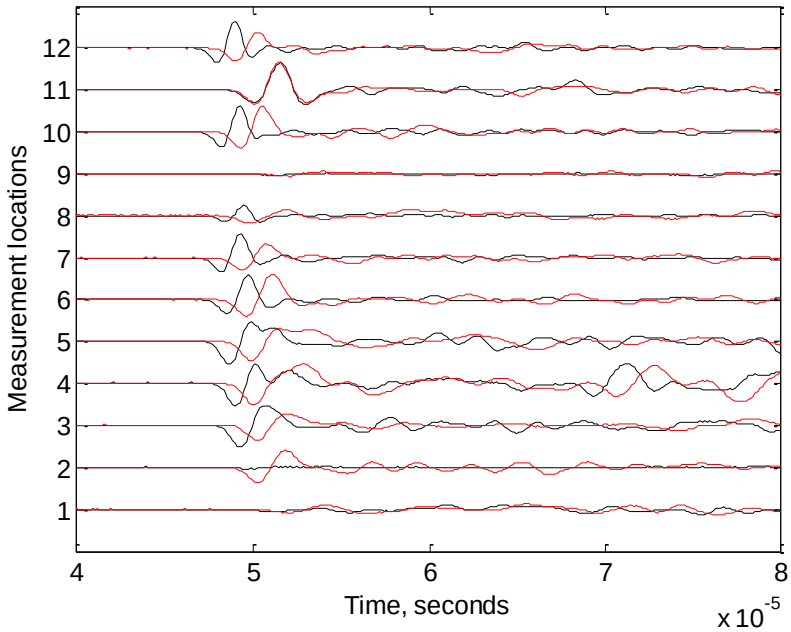

Figure 3.114. P-wave signatures measured from Surface 1 and Surface 3 of Sample 48.

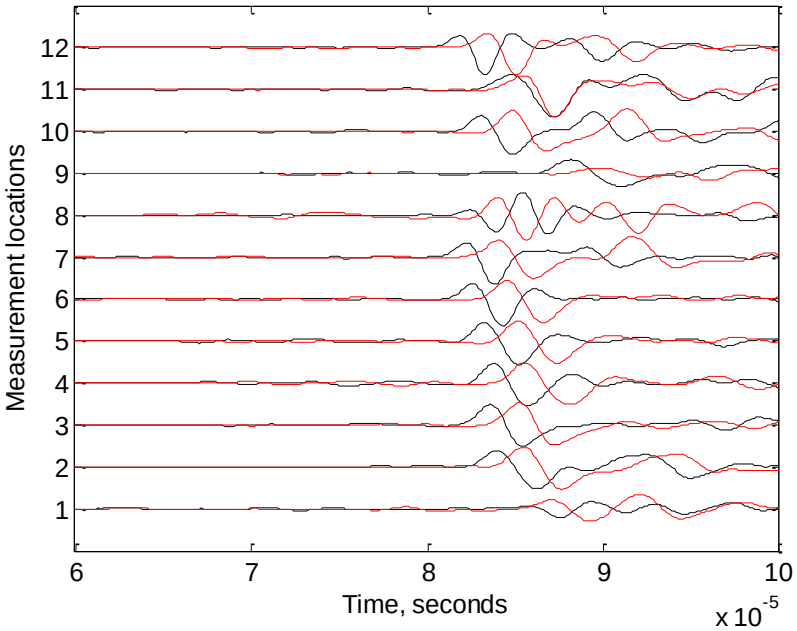

Figure 3.115. S-wave signatures measured from Surface 1 and Surface 3 of Sample 48.

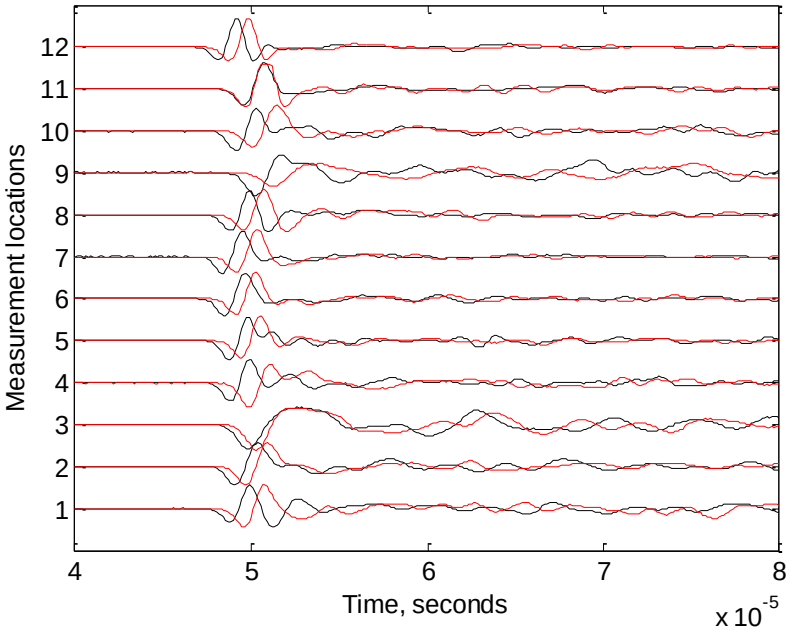

Figure 3.116. P-wave signatures measured from Surface 2 and Surface 4 of Sample 48.

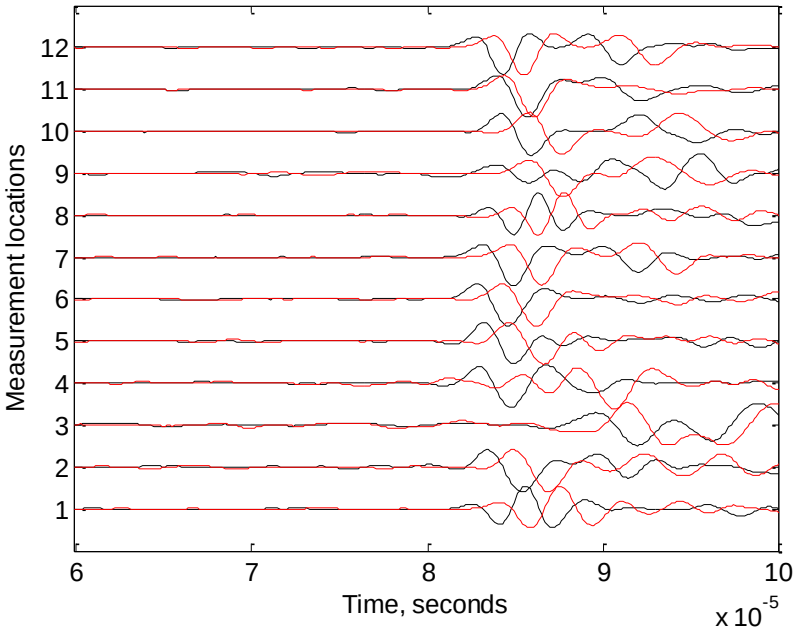

Figure 3.117. S-wave signatures measured from Surface 2 and Surface 4 of Sample 48.

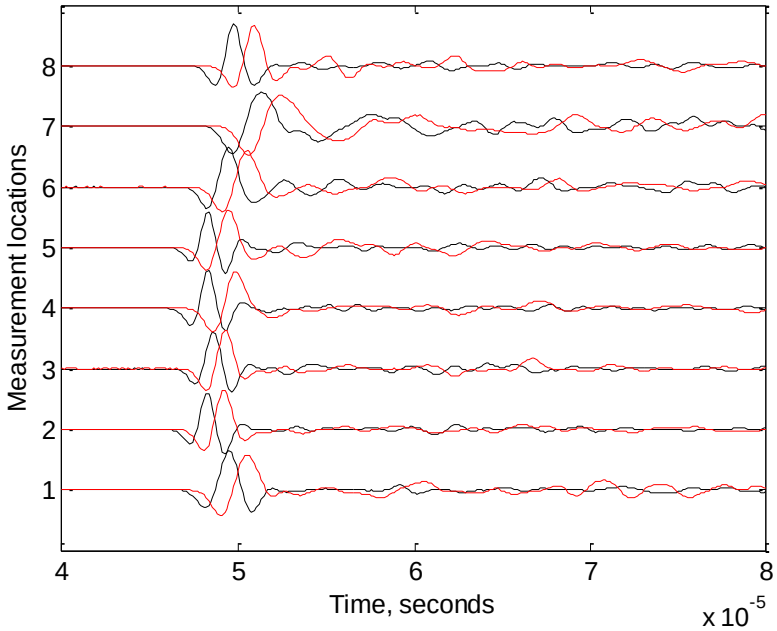

Figure 3.118. P-wave signatures measured from Surface 5 and Surface 6 of Sample 48.

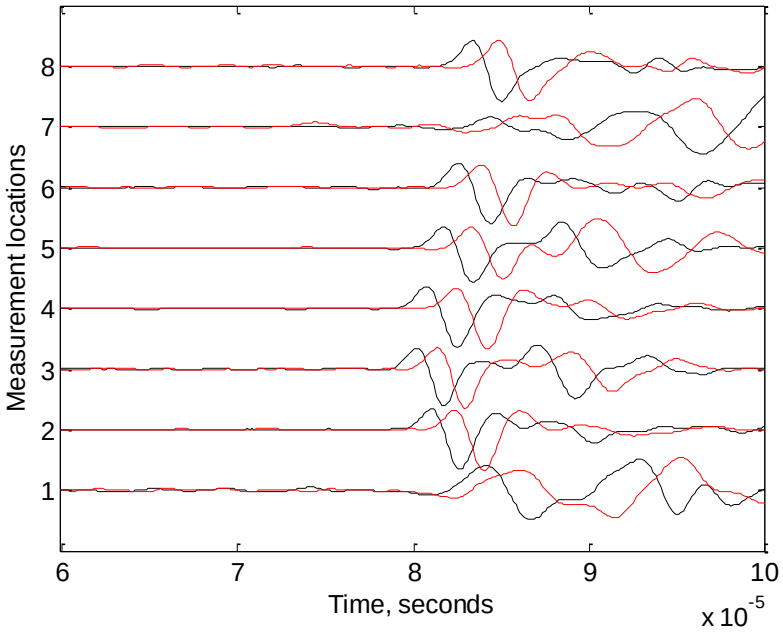

Figure 3.119. S-wave signatures measured from Surface 5 and Surface 6 of Sample 48.

Dye solution was then injected into the borehole of Sample 48 to color the CO_2 injection induced fractures, through which dye solution flowed out of the block surface. Then, the sample was fractured by injecting nitrogen gas, and the pressure profile is shown in Figure 3.120. Peak pressure of gas fracturing is 1159.99 psi at 473.07 seconds, which corresponds to a stress loading response in the x-axis direction in Figure 3.121. Coloring and gas fracturing revealed the fracture generated by CO_2 injection, as shown in Figure 3,122, 3.123, and 3.124. The major fracture planes are nearly perpendicular to the minimum horizontal stress direction.

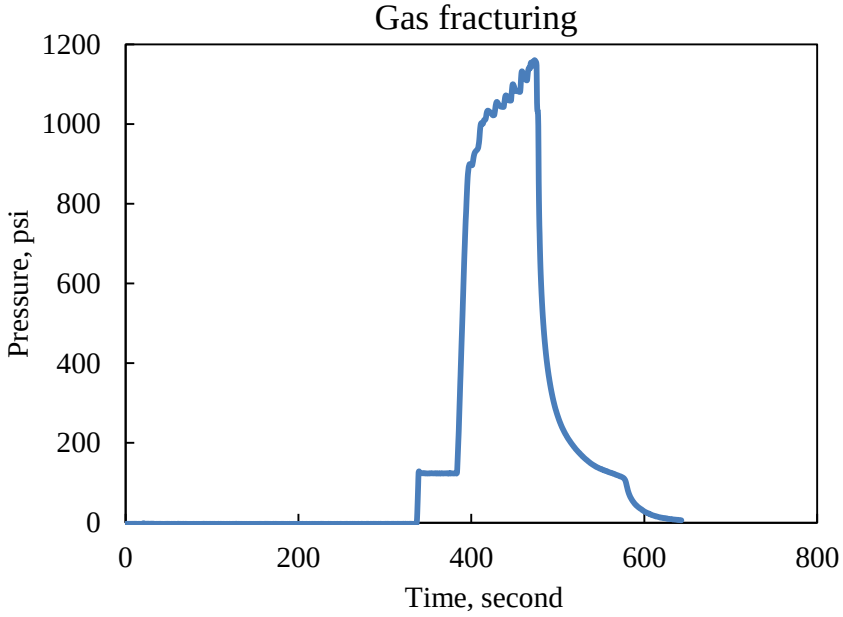

Figure 3.120. Gas fracturing pressure of Sample 48.

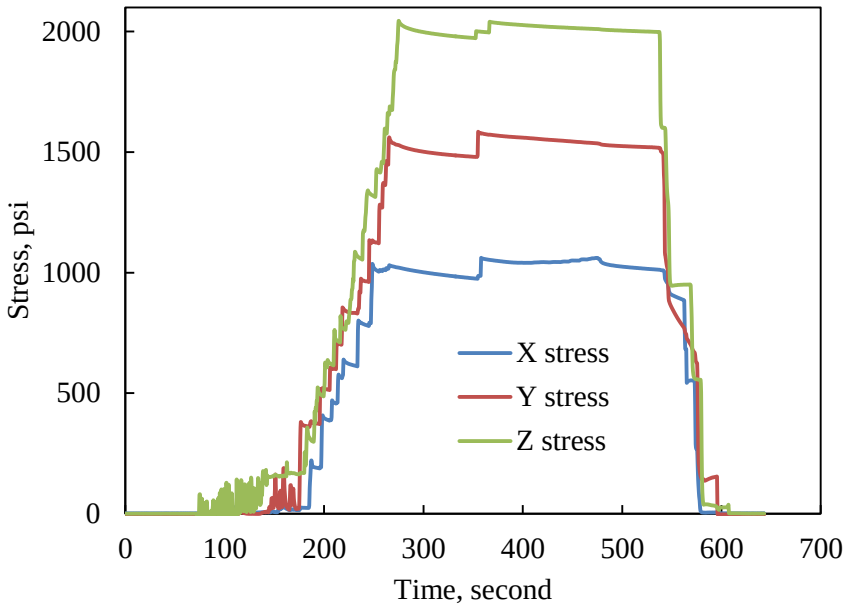

Figure 3.121. Tri-axial stress loading for CO_2 injection into Sample 48.

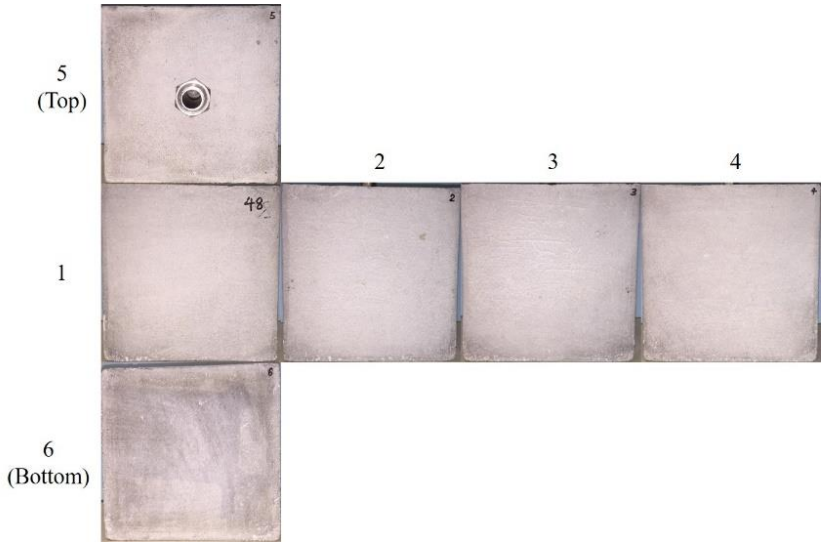

Figure 3.122. Intact surfaces of Sample 48.

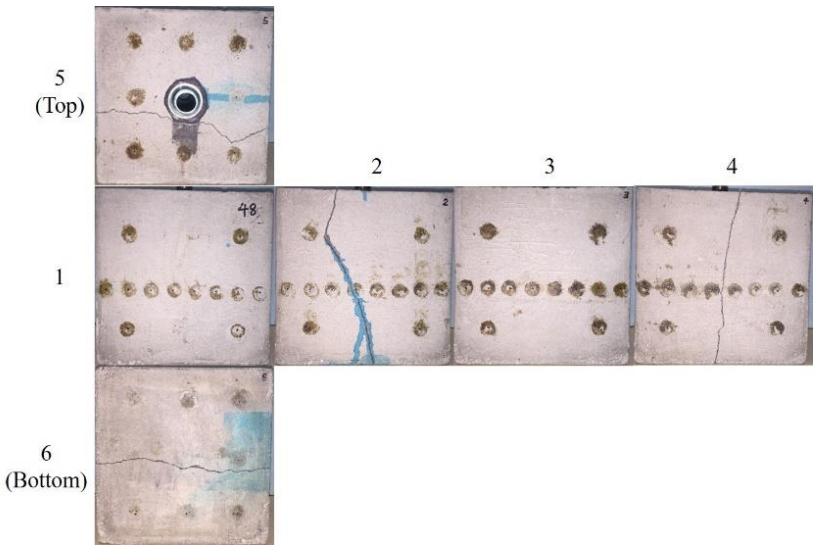

Figure 3.123. Surfaces of Sample 48 after dyeing and gas fracturing.

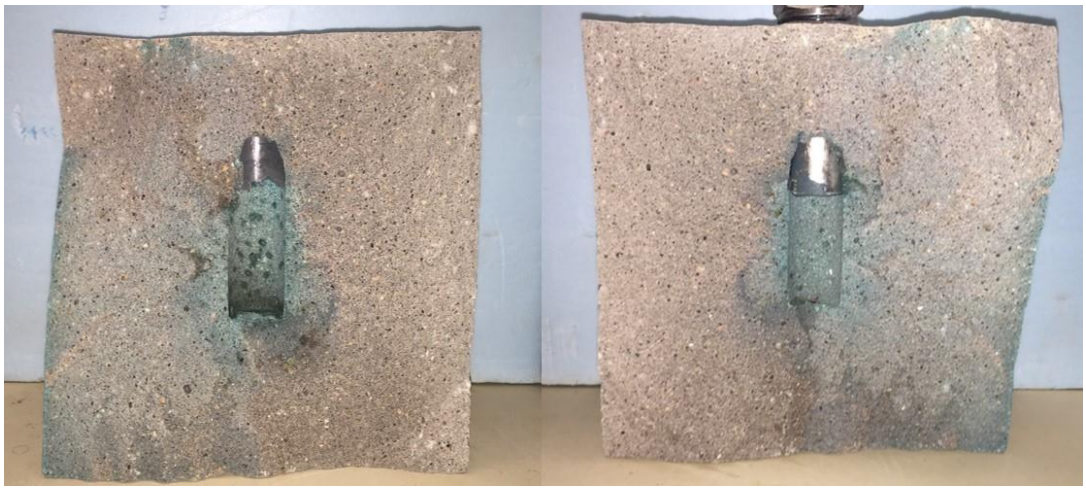
Figure 3.124. Injection induced fracture morphology of Sample 48 after dyeing and gas breakdown.

Concrete Sample 49

Sample 49 was first treated by applying a pre-injection stress loading of 1250 psi in the x-direction, 1875 psi in the y-direction, and 2500 psi in the z-direction for 43 minutes, as shown in Figure 3.125. Then, acoustic signatures were measured as reference for post-injection comparison and pressure decay was carried out for pre-treatment permeability evaluation. Afterwards, the sample was treated by injecting CO_2 under the same tri-axial stress loading, shown in Figure 3.126, at room temperature of 20 °C. The sample was unexpectedly fractured at a relatively low peak pressure of 784.70 psi at 521.08 seconds, shown in Figure 3.127, generating a stress response in the x-axis direction in Figure 3.126.

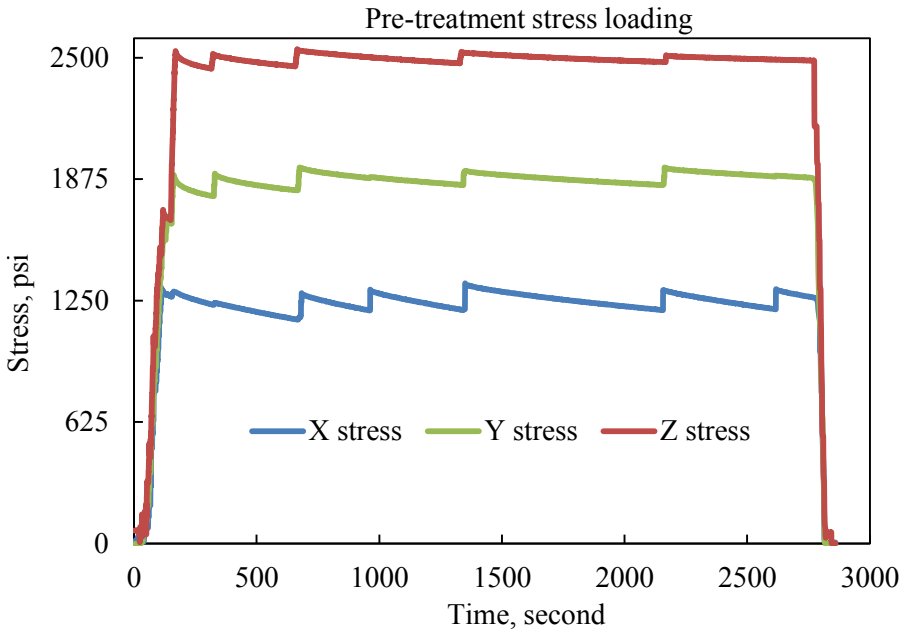

Figure 3.125. Pre-injection stress loading on Sample 49.

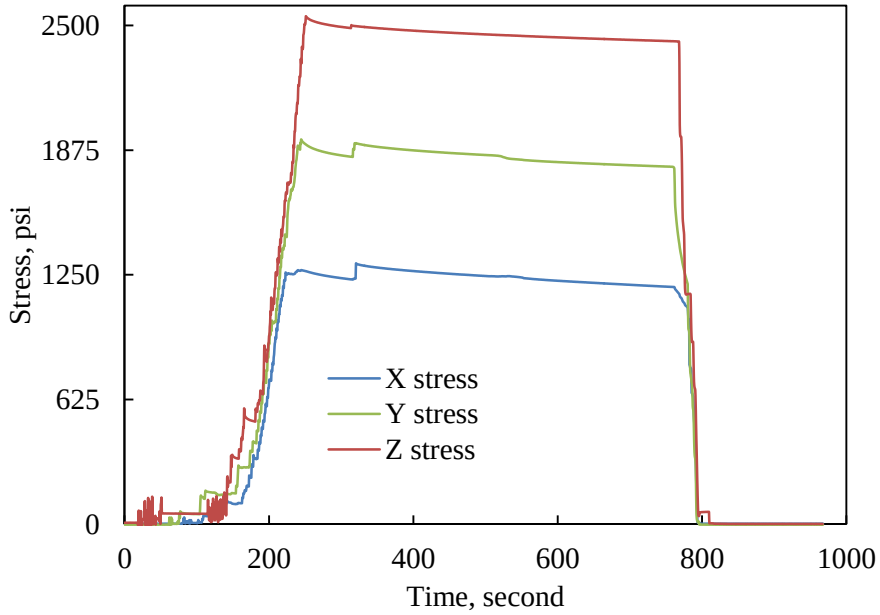

Figure 3.126. Stress loading for CO_2 injection into Sample 49.

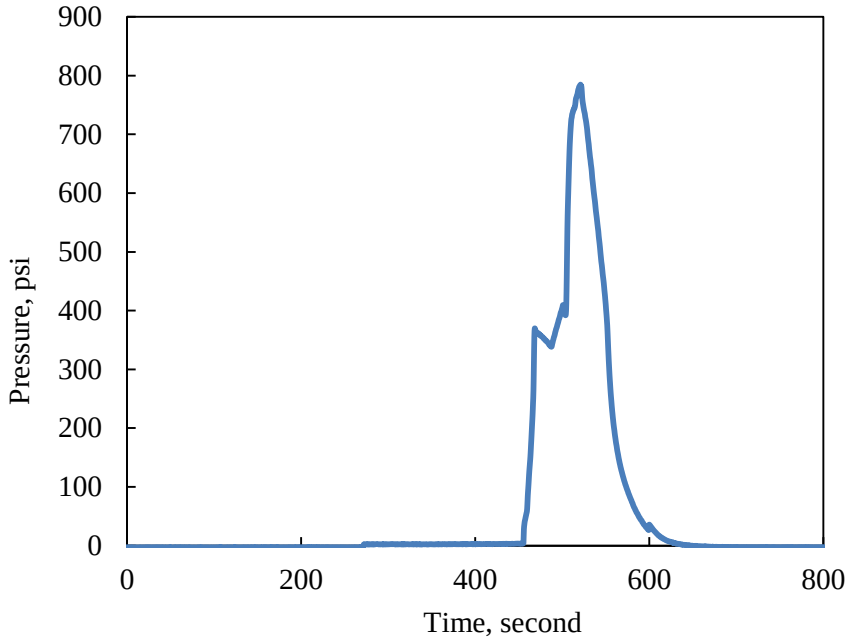

Figure 3.127. CO_2 injection pressure for Sample 49.

Figure 3.128 compares the pressure decay curves measured before and after CO_2 injection. It can be seen that gas leakage rate significantly increased after CO_2 injection, due to permeability enhancements by injection induced fractures.

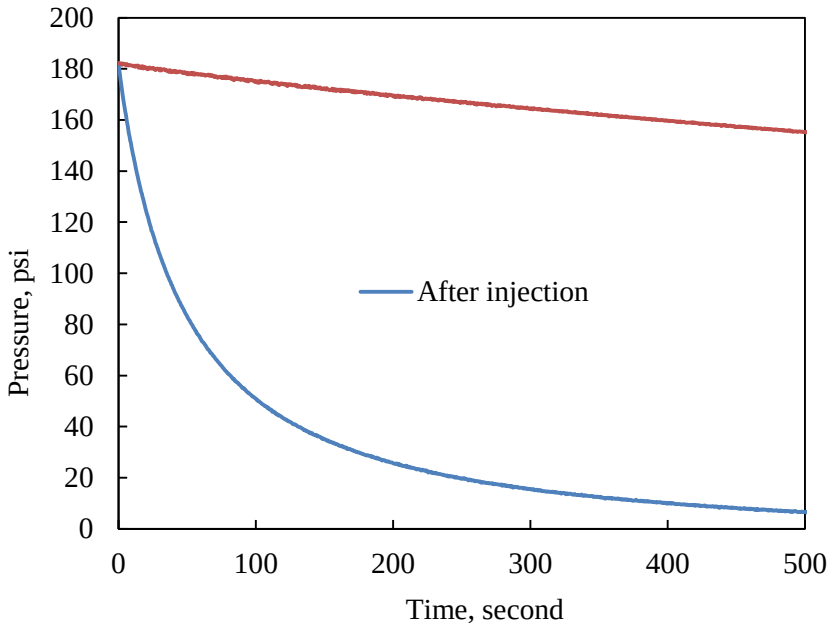

Figure 3.128. Pressure decay curves before and after CO_2 injection for Sample 49.

Acoustic signatures for Sample 49 before and after CO_2 injection are compared in Figure 3.129 through Figure 3.134. Both P-waves and S-waves show delays in arrival time and changes in

waveforms after CO_2 injection, indicating that CO_2 injection induced fractures inside the concrete block.

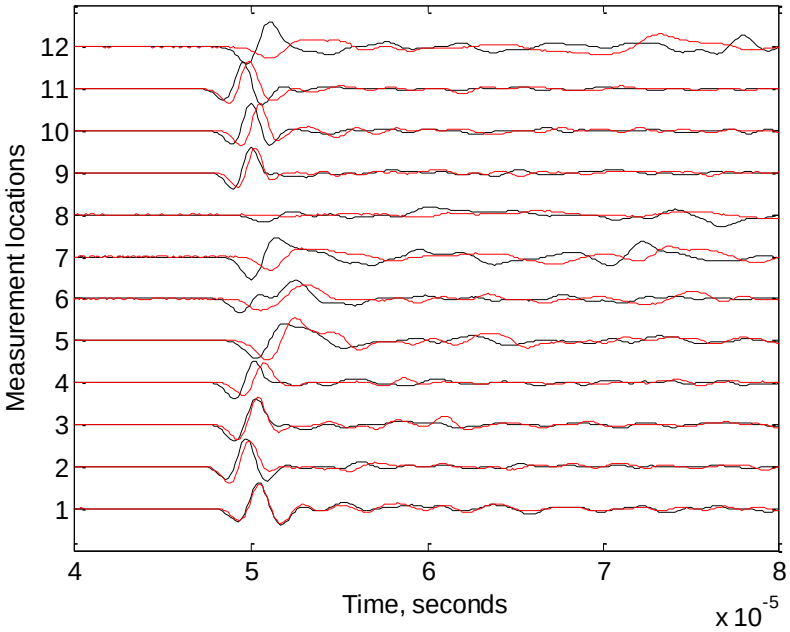

Figure 3.129. P-wave signatures measured from Surface 1 and Surface 3 of Sample 49.

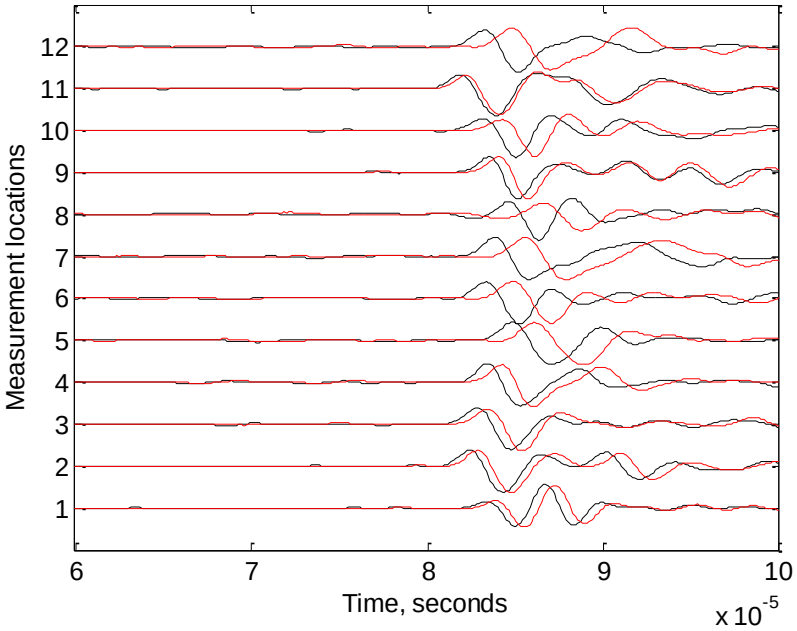

Figure 3.130. S-wave signatures measured from Surface 1 and Surface 3 of Sample 49.

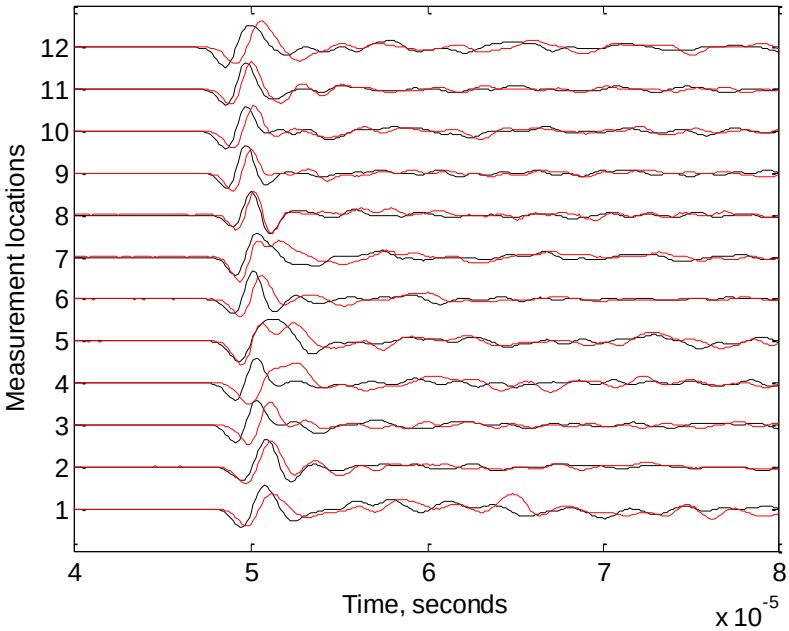

Figure 3.131. P-wave signatures measured from Surface 2 and Surface 4 of Sample 49.

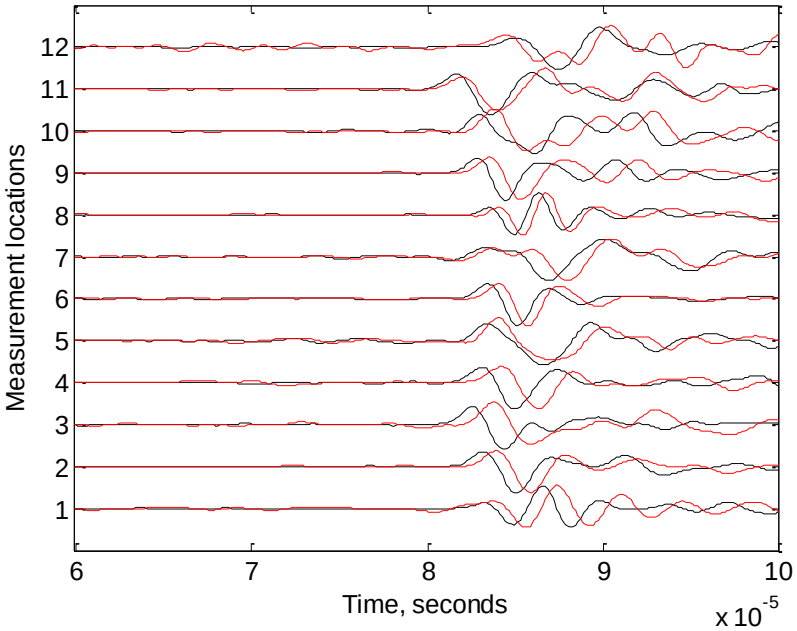

Figure 3.132. S-wave signatures measured from Surface 2 and Surface 4 of Sample 49.

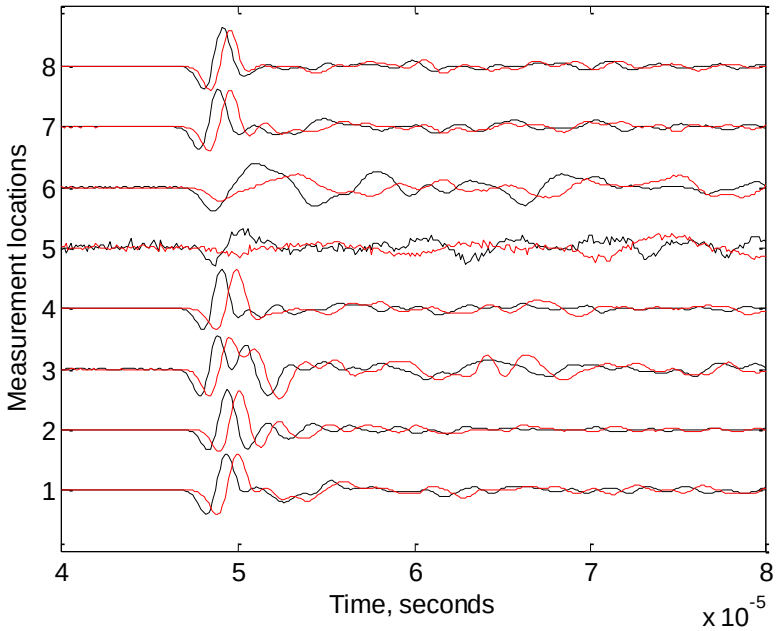

Figure 3.133. P-wave signatures measured from Surface 5 and Surface 6 of Sample 49.

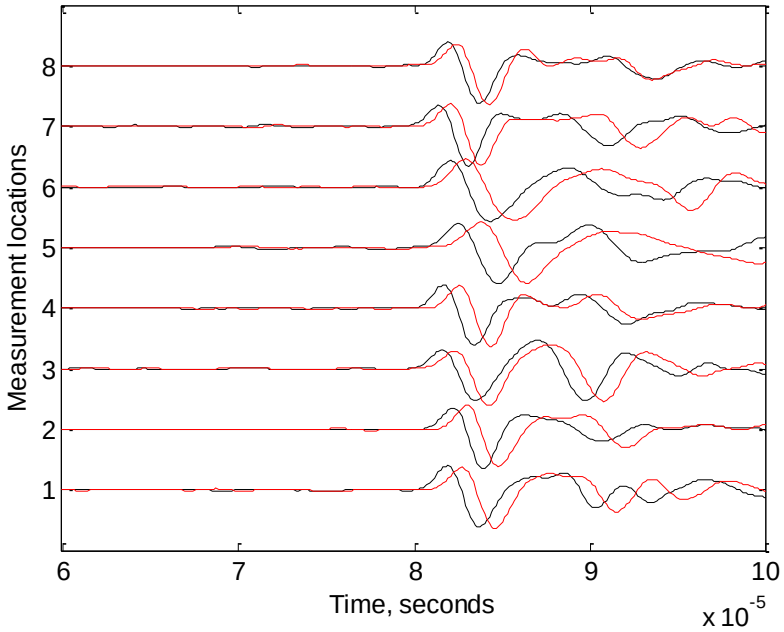

Figure 3.134. S-wave signatures measured from Surface 5 and Surface 6 of Sample 49.

Dye solution was then injected into Sample 49 to color the CO_2 injection induced fractures, and dye solution flowed out of the block surface. Then the sample was broken down by injecting nitrogen gas. Coloring and gas fracturing revealed that the major fracture planes generated by CO_2 injection are generally perpendicular to the minimum horizontal stress direction, but there is also a horizontal fracture wing generated in the edge of Surface 1 and Surface 2, as shown in Figures 3.135, 3.136, and 3.137.

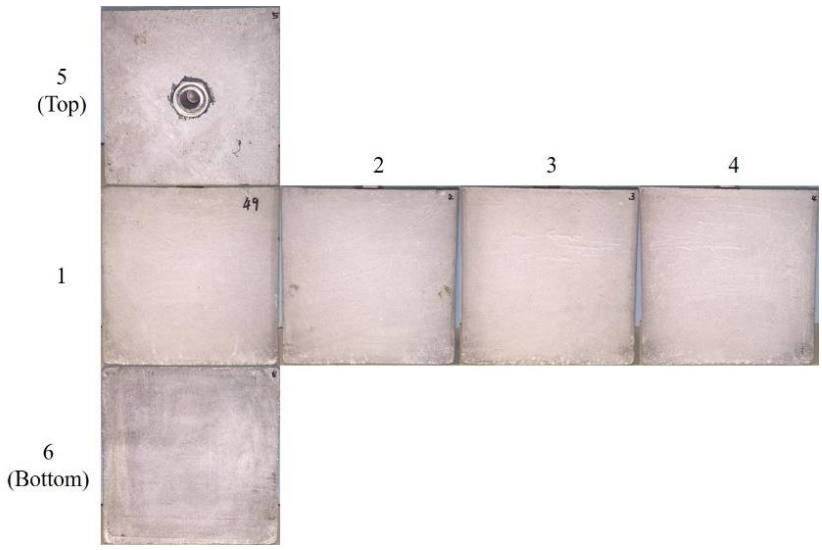

Figure 3.135. Intact surfaces of Sample 49 before treatment.

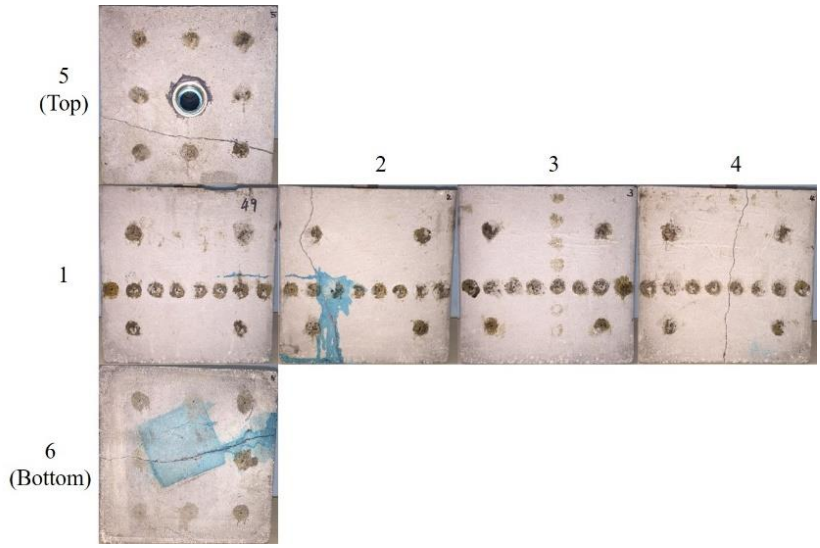

Figure 3.136. Surfaces of Sample 49 after dyeing and gas fracturing.

Figure 3.137. Injection induced fracture morphology of Sample 49 after dyeing and gas breakdown.

For the previous seven concrete samples treated, one was fractured by sc-CO_2, two by liquid CO_2, and four by gaseous CO_2. Regardless of the state of CO_2 being injected, it was concluded that high injection rates bring lower peak pressures (pulses from pump are considered as high injection rates). In addition, peak pressures are generally higher under high tri-axial stress loading conditions. Stress responses on x-axis stress loading were seen in most of these injection cases. Comparison of acoustic measurements can reflect the internal structure change of the concrete blocks. Finally, dye coloring and gas fracturing are capable of effectively capturing the morphology of CO_2 injection induced fractures inside the concrete blocks. Fracture initiation and propagation induced by CO_2 injection follow the fundamental principles of hydraulic fracturing.

We next conducted sc-CO_2 injection induced fracturing experiments on seven more concrete samples (Samples 50-56) with borehole temperature and injection pressure above the supercritical conditions. Thus all of these samples were fractured by sc-CO_2. The injection rate was kept constant at 40 ml/min for all samples. While the tri-axial stress loading level and difference were changed to investigate the effect of *in-situ* stress on the peak pressure or fracturing pressure values during CO_2 injection into these concrete samples.

Concrete Sample 50

Sample 50 was first pre-loaded with tri-axial stresses of 1250 psi in the x-direction, 1875 psi in the y-direction, and 2500 psi in the z-direction for about 40 mins, shown in Figure 3.138, then acoustic measurements and the pressure decay test were carried out.

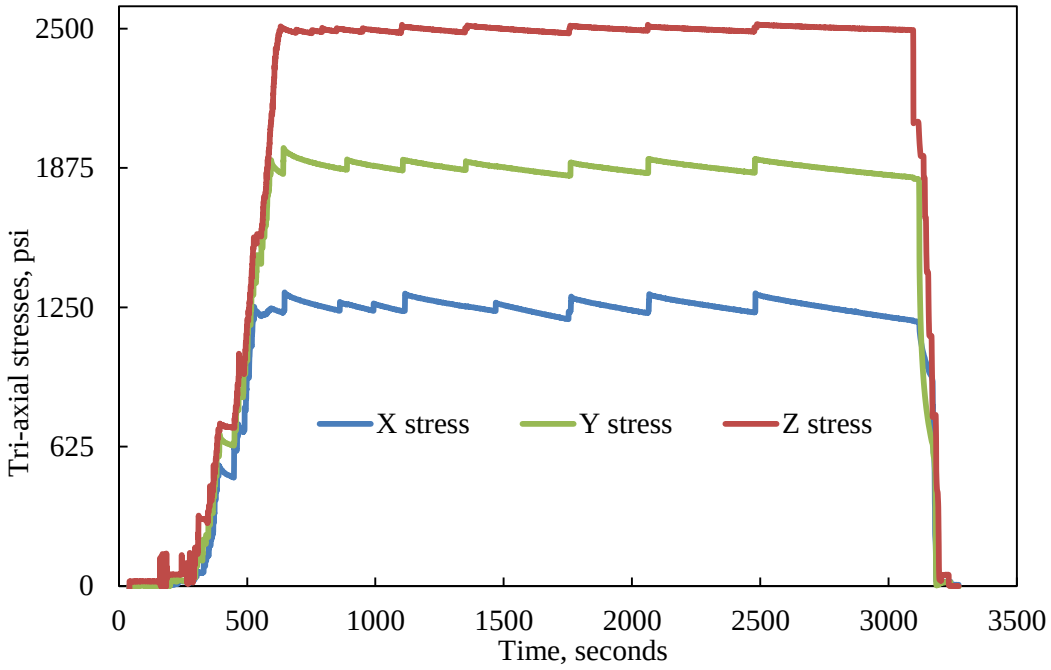

Figure 3.138. Stress loading before CO_2 injection for Sample 50.

After that, under the same tri-axial stress loading, shown in Figure 3.139, CO_2 was injected at a constant rate of 40 ml/min into the sample. Figure 3.140 shows the pressure profile during CO_2 injection. The peak pressure of CO_2 injection is 1641.23 psig at 3669 seconds, corresponding to a small stress change in the x-axis direction in Figure 3.140. The temperature when the sample was fractured was 34.44 °C in Figure 3.141, then it started decreasing at a high rate due to sc-CO_2 leakage through generated fractures and resultant vaporization.

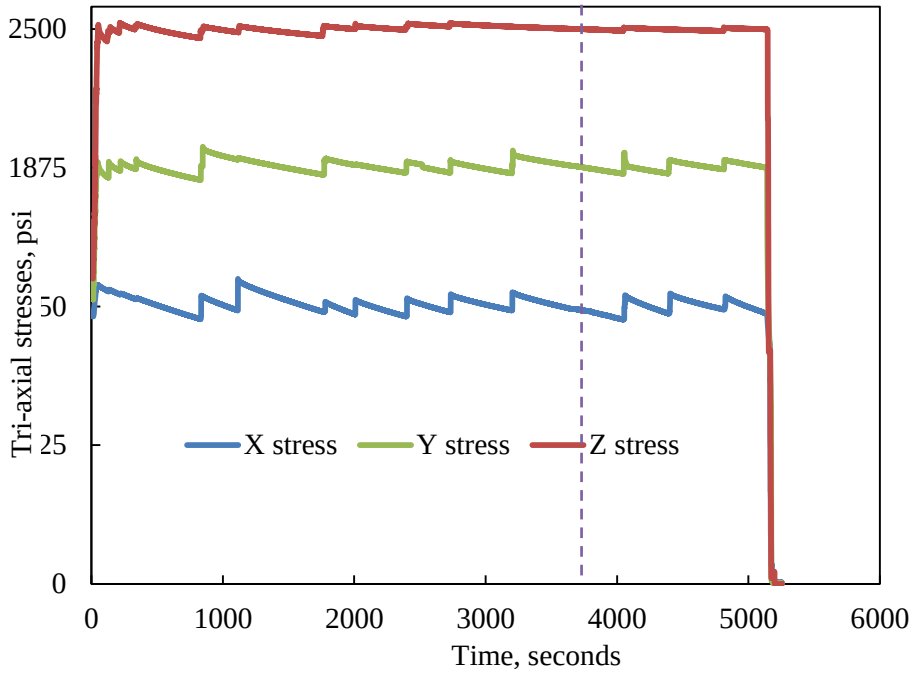

Figure 3.139. Tri-axial stress loading for CO_2 injection into Sample 50.

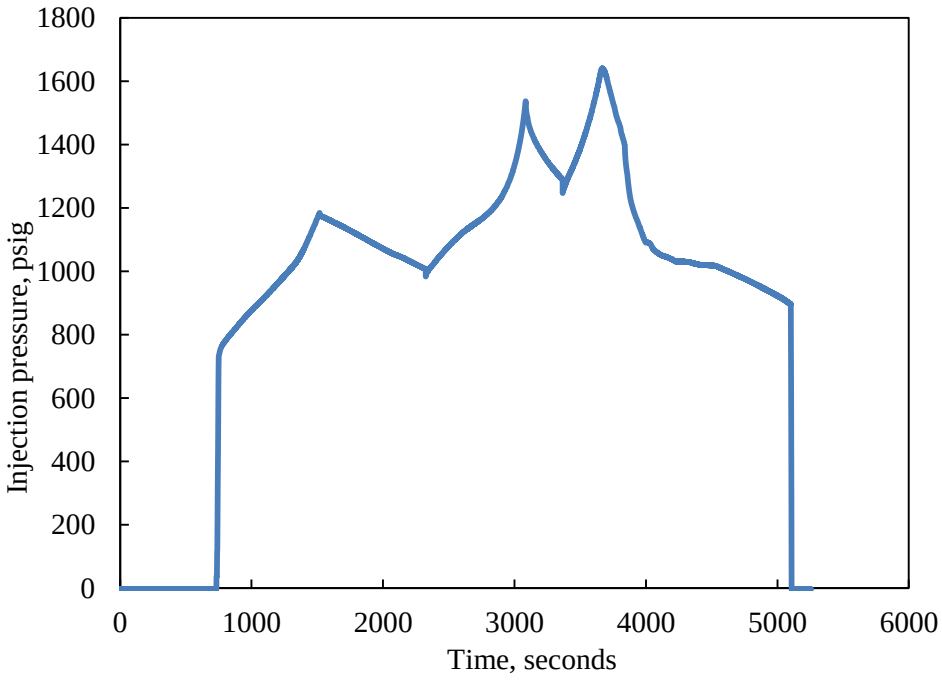

Figure 3.140. CO_2 injection pressure of Sample 50.

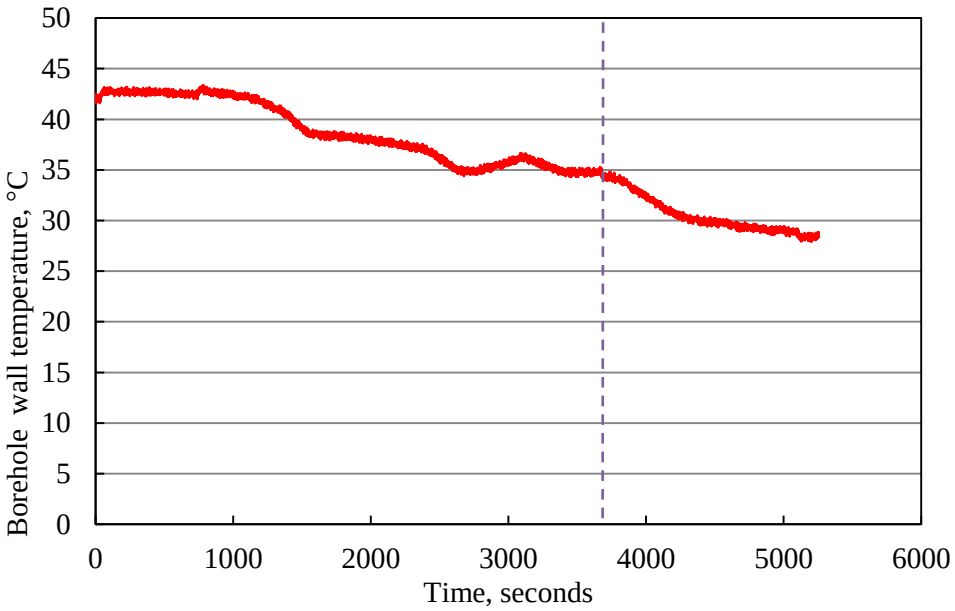

Figure 3.141. Borehole wall temperature profile during CO_2 injection into Sample 50.

Pressure decay curves measured before and after CO_2 injection for Sample 50 are compared in Figure 3.142, which shows significant permeability increase of the concrete block due to injection induced fractures.

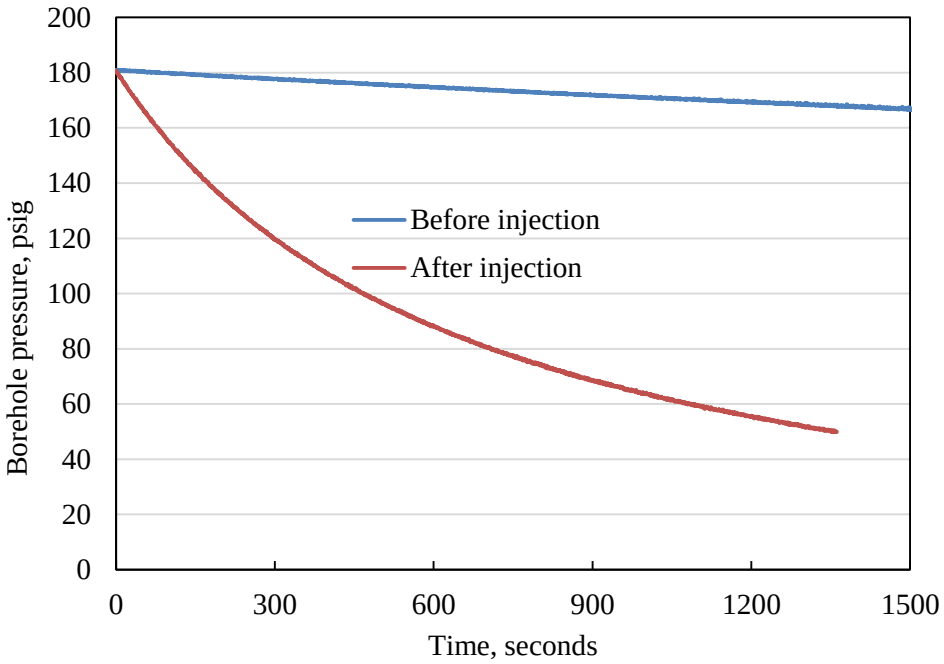

Figure 3.142. Pressure decay curves before and after treatment for Sample 50.

Figures 3.143 through Figure 3.148 compare the two acoustic wave curves measured before and after CO_2 injection: black - before injection, red - after injection. It can be seen that after

CO_2 injection both P-wave and S-wave delay in arrival time, indicating certain internal structure change rather than a simple compaction in density.

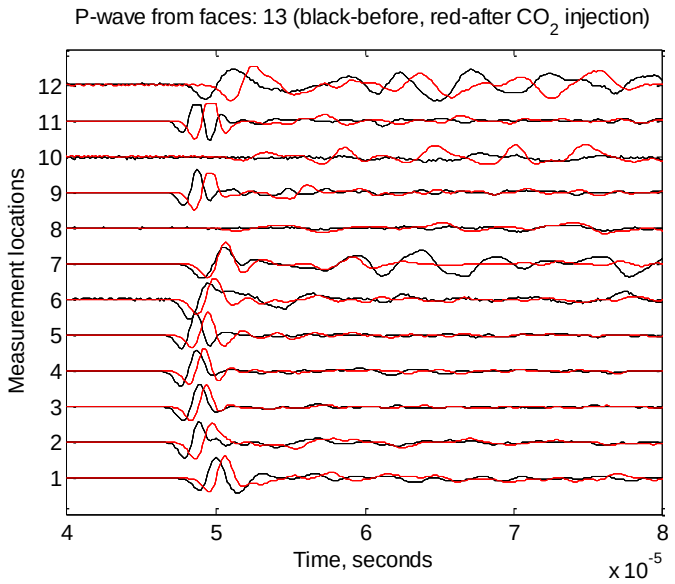

Figure 3.143. P-wave signatures measured from Surface 1 and Surface 3 of Sample 50.

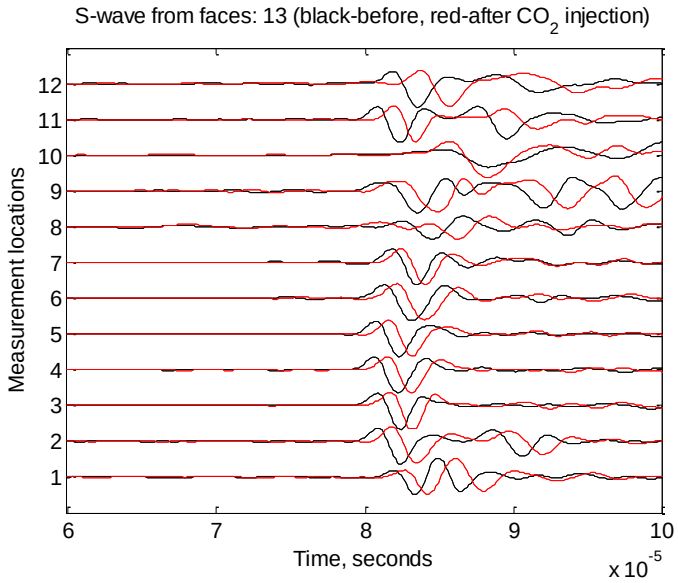

Figure 3.144. S-wave signatures measured from Surface 1 and Surface 3 of Sample 50.

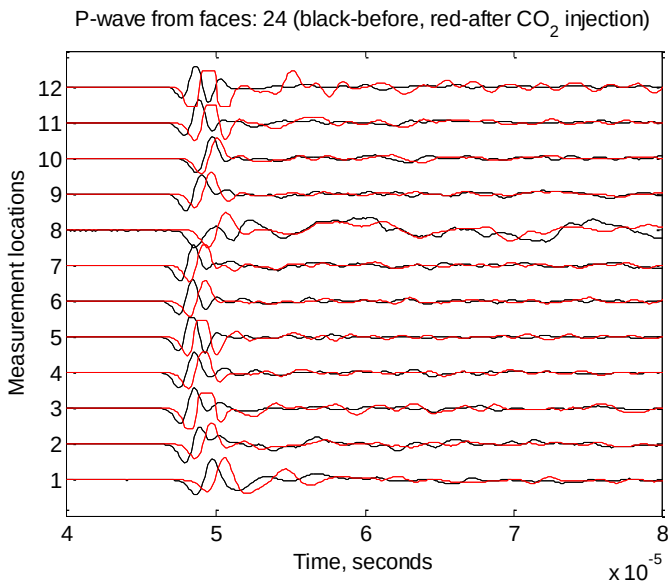

Figure 3.145. P-wave signatures measured from Surface 2 and Surface 4 of Sample 50.

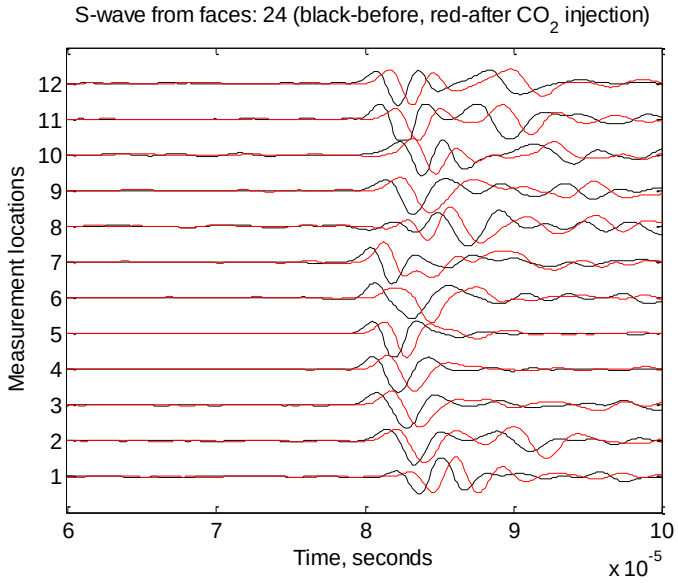

Figure 3.146. S-wave signatures measured from Surface 2 and Surface 4 of Sample 50.

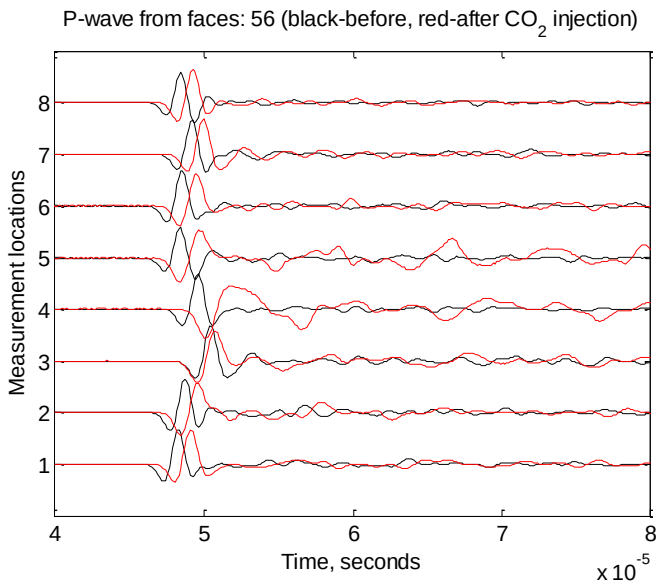

Figure 3.147. P-wave signatures measured from Surface 5 and Surface 6 of Sample 50.

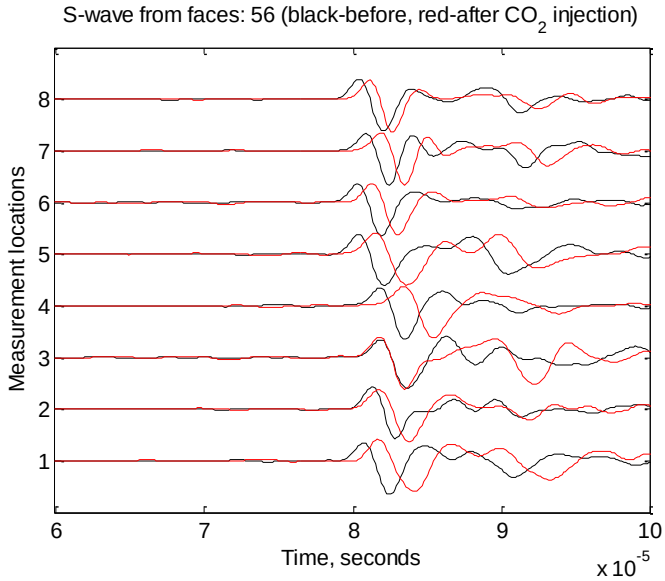

Figure 3.148. S-wave signatures measured from Surface 5 and Surface 6 of Sample 50.

Dye solution was then injected at 180 psig into Sample 50 to color the CO_2 injection induced fractures, through which dye solution flowed out of the block surface. Then, the sample was fractured by nitrogen gas. Coloring and gas fracturing revealed the fracture planes generated by CO_2 injection, as shown in Figures 3.149, 3.150, and 3.151. The fracture planes are complex in both morphology and direction, although the major fracture is roughly perpendicular to the minimum horizontal stress direction, shown in Figure 3.150 and Figure 3.151a, there is a secondary fracture dipping with angles to both x and y directions, shown in Figure 3.151b, also there a small fracture that is perpendicular to z direction, shown in Figure 3.151c.

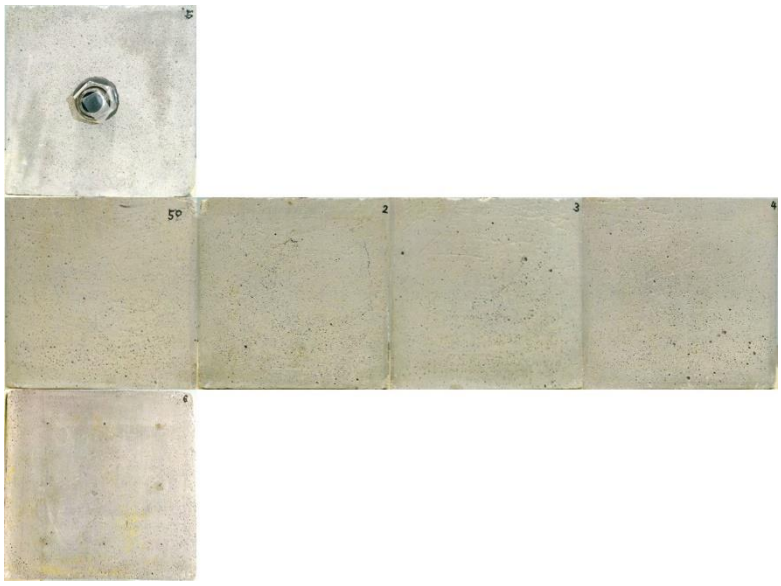

Figure 3.149. Surfaces of Sample 50 before treatment.

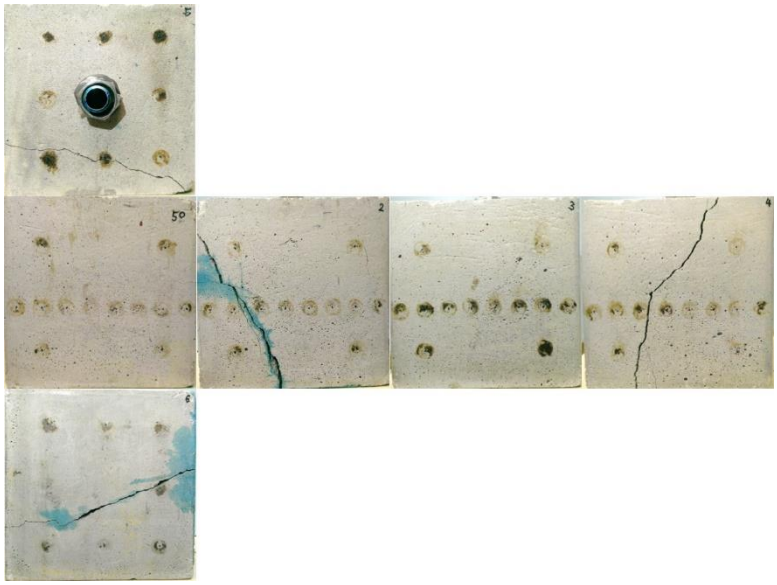

Figure 3.150. Surfaces of Sample 50 after coloring and gas fracturing.

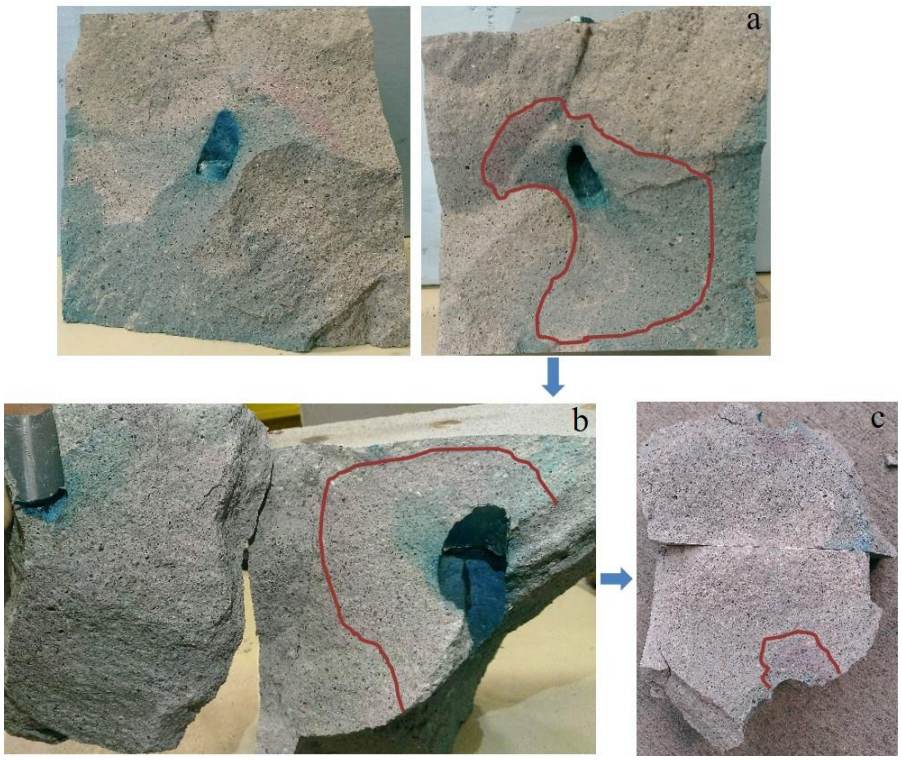

Figure 3.151. CO_2 injection induced fracture morphology of Sample 50.

Concrete Sample 51

Sample 51 was first compressed for about 45 minutes by applying a tri-axial stress loading of 1500 psi in the x-direction, 2125 psi in the y-direction, and 2750 psi in the z-direction, as shown in Figure 3.152.

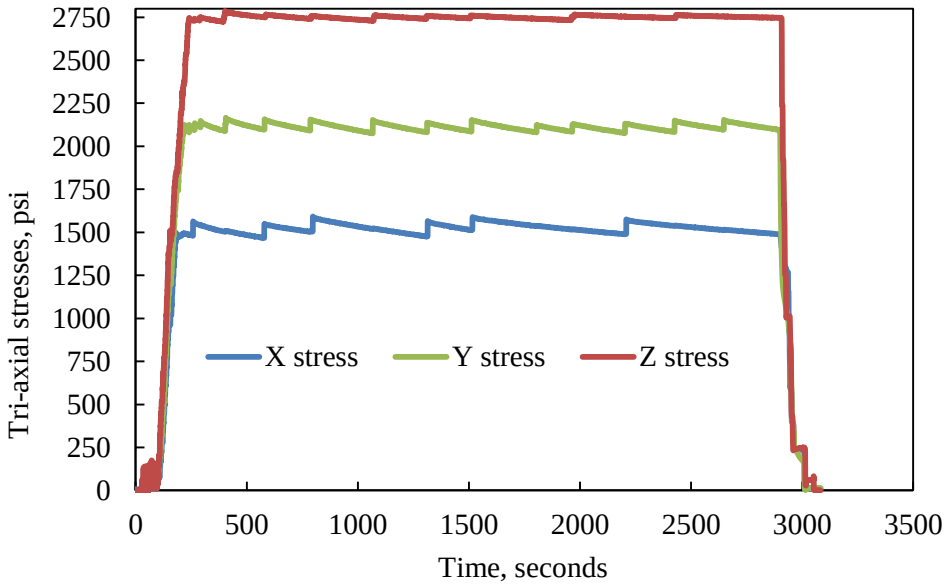

Figure 3.152. Stress loading before CO_2 injection for Sample 51.

Then, acoustic wave measurements were carried out and the pressure decay curve was measured under no stress loading as a reference for comparison of permeability change after CO_2 injection for the sample. Sample 51 was then treated by injecting CO_2 into borehole under tri-axial stress loading of 1500 psi in the x-direction, 2125 psi in the y-direction, and 2750 psi in the z-direction, shown in Figure 3.153.

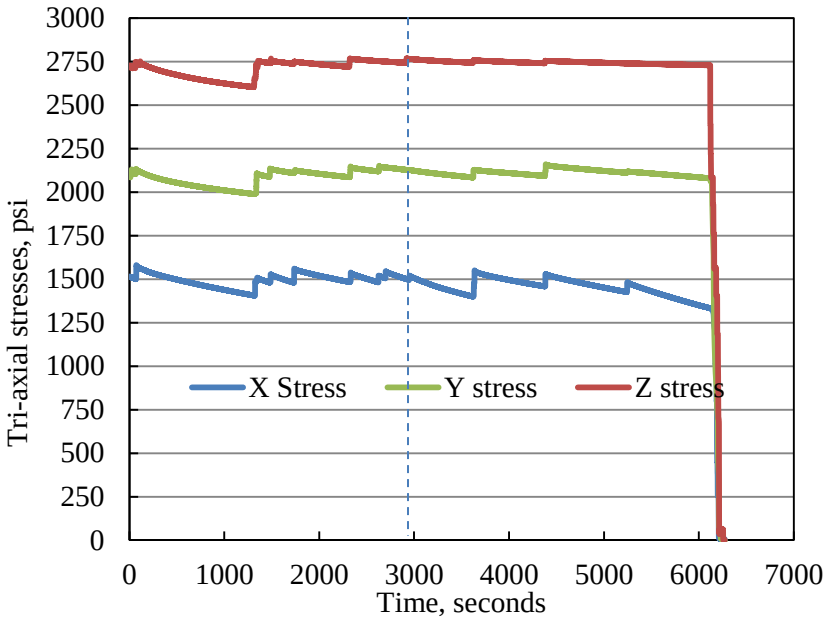

Figure 3.153. Tri-axial stress loading for CO_2 injection into Sample 51.

The pressure and temperature profiles in borehole are shown in Figures 3.154 and 3.155. The first peak pressure is 1578.02 psi at 2630 seconds, as shown in Figure 3.154. At this point, the pump stopped and started refilling, thus pressure decreased. In view of the high pressure decreasing rate, it was speculated that fractures were initiated and slow leakage occurred. But there were no obvious responses on the tri-axial stress loading and temperature profiles. The second peak pressure was 1527.36 psi at 2948 seconds, when the x-axis stress responded, as shown in Figure 3.152. Meanwhile, injection pressure quickly decreased, shown in Figure 3.154, and borehole wall temperature dropped shown in Figure 3.155, due to CO_2 leakage and resultant vaporization. The corresponding temperature at the second peak pressure is 39.12 °C, which is above the supercritical temperature of 31.0 °C.

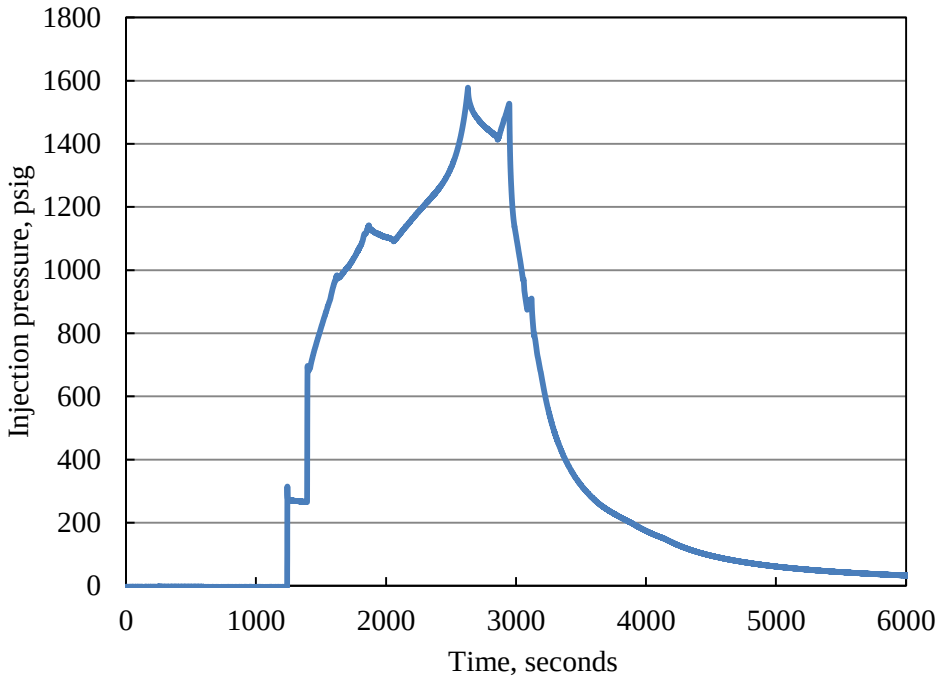

Figure 3.154. Pressure profile of CO_2 injection into Sample 51.

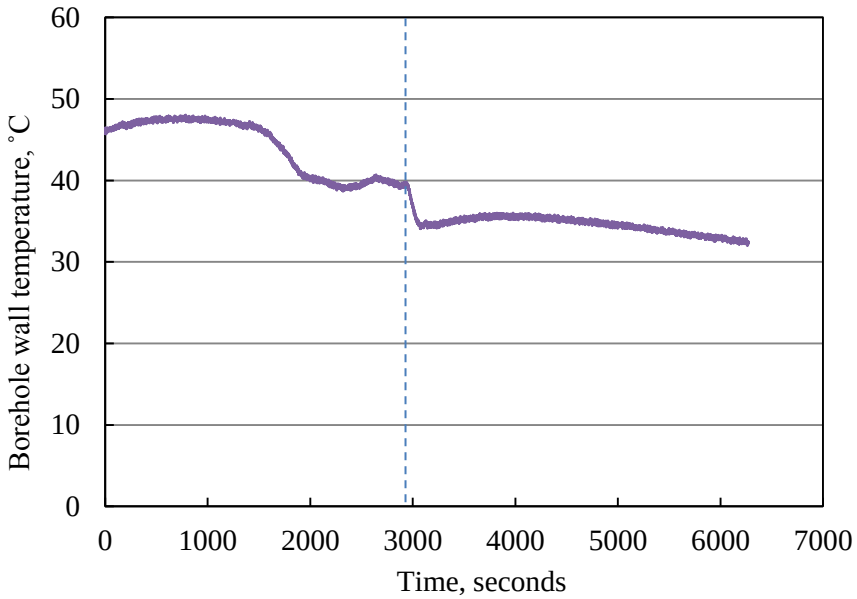

Figure 3.155. Temperature profiles during CO_2 injection into Sample 51.

Pressure decay curves measured before and after CO_2 injection for Sample 51 are compared in Figure 3.156, which shows significant permeability increase of the concrete block due to injection induced fractures.

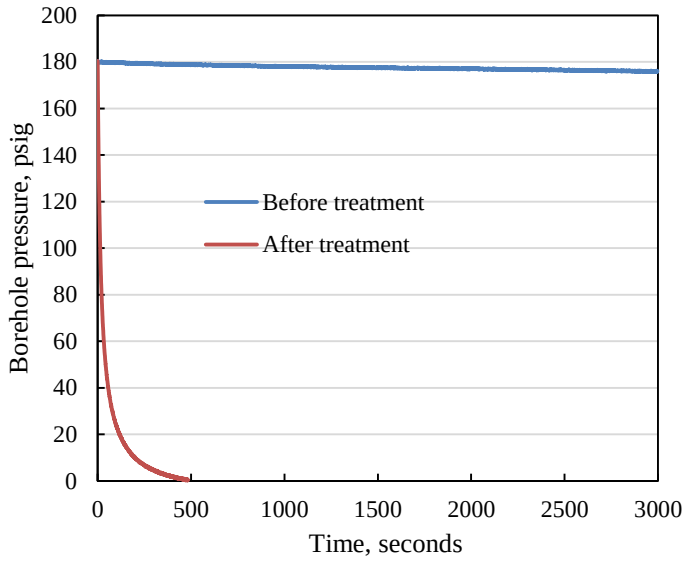

Figure 3.156. Pressure decay curves before and after treatment.

Figures 3.157 through 3.162 compare the two acoustic wave curves measured before and after CO_2 injection: black - before injection, red - after injection. It can be seen that after CO_2 injection both P-waves and S-waves delay in arrival time, indicating certain internal structure change rather than a simple compaction in density.

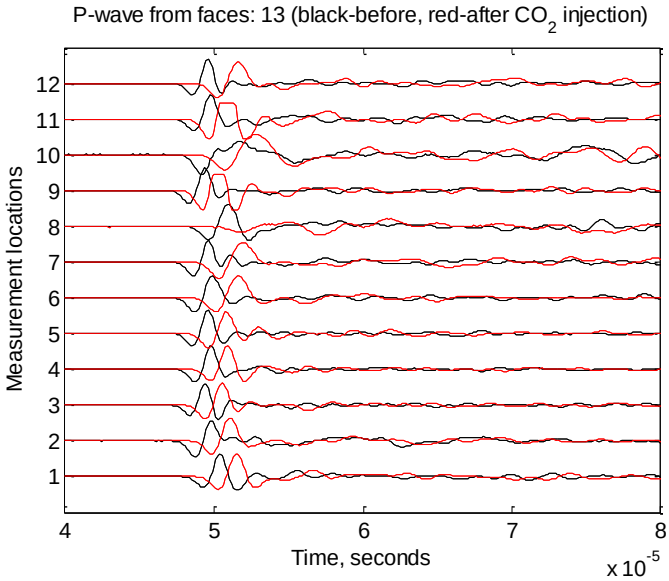

Figure 3.157. P-wave signatures measured from Surface 1 and Surface 3.

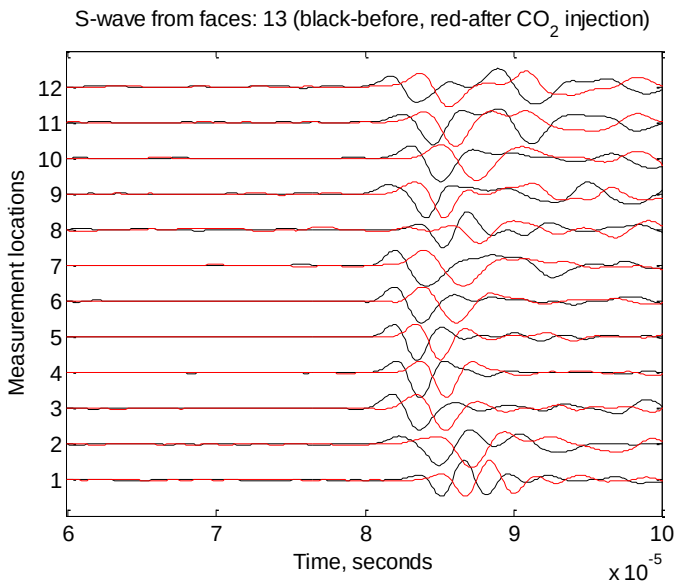

Figure 3.158. S-wave signatures measured from Surface 1 and Surface 3.

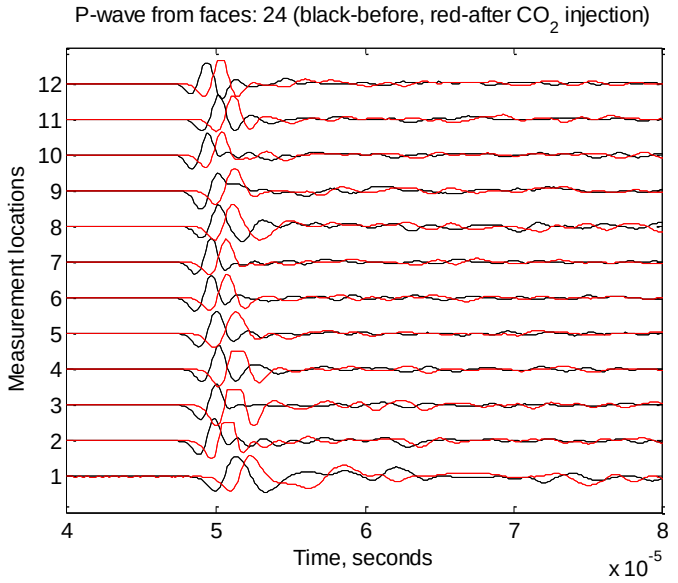

Figure 3.159. P-wave signatures measured from Surface 2 and Surface 4.

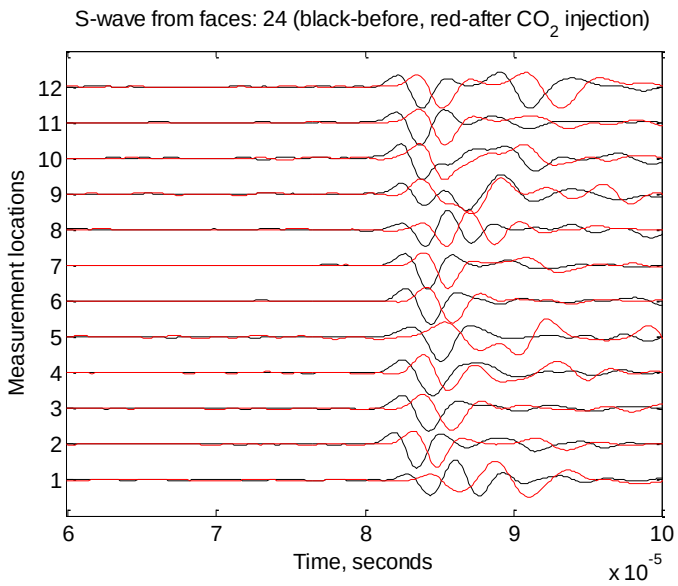

Figure 3.160. P-wave signatures measured from Surface 2 and Surface 4.

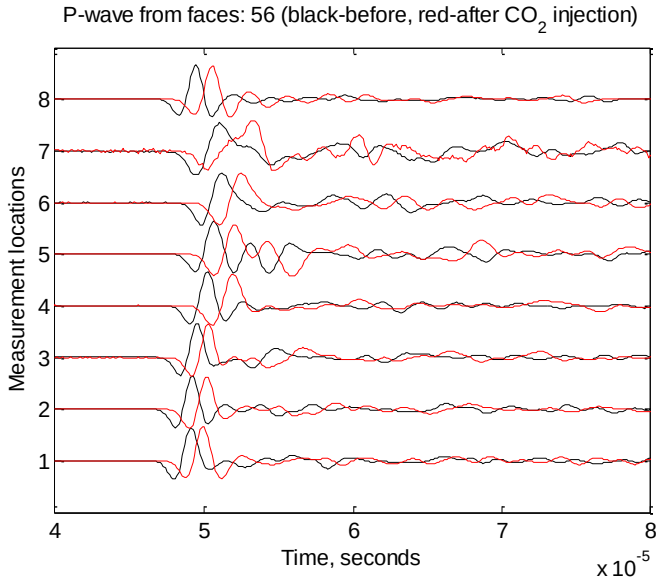

Figure 3.161. P-wave signatures measured from Surface 5 and Surface 6.

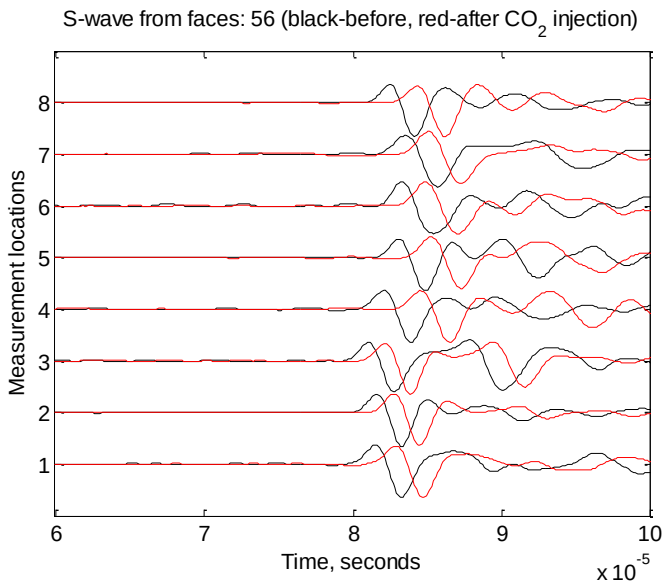

Figure 3.162. S-wave signatures measured from Surface 5 and Surface 6.

Dye solution was later injected into Sample 51 to color the CO_2 injection induced fracture planes. Then, under tri-axial stress loading, shown in Figure 3.163, high pressure nitrogen gas was used to fracture the sample. As shown in Figure 3.164, the highest pressure of 1678.62 psig was achieved at 456 seconds, corresponding to a hump on x-axis stress in Figure 3.163 51-12. Then without tri-axial stress loading, the sample was broken down by nitrogen gas at 54.82 psig, shown in Figure 3.165.

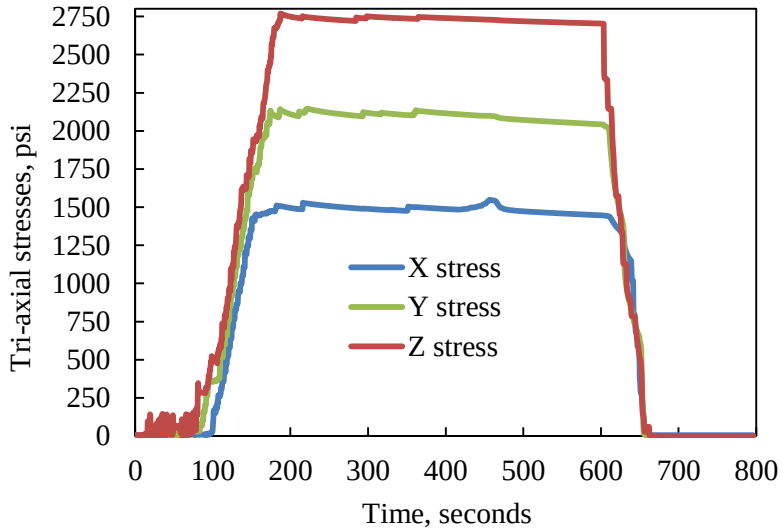

Figure 3.163. Tri-axial stress loading for gas fracturing of Sample 51.

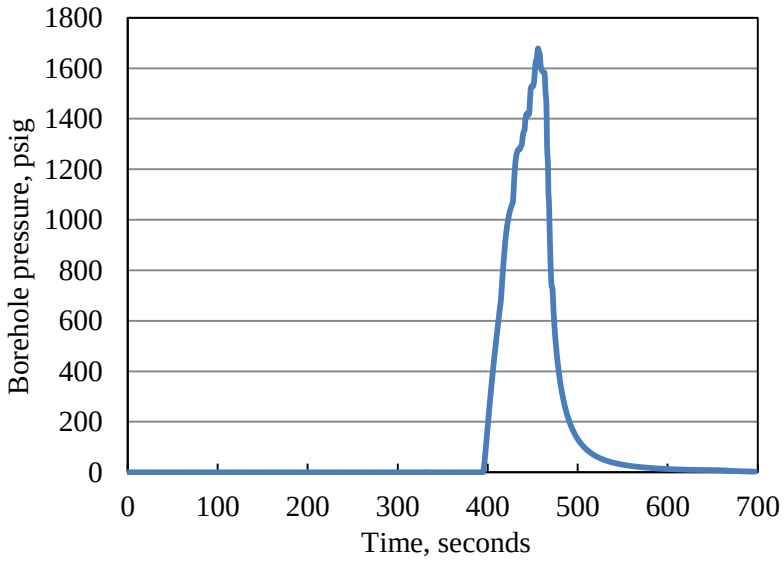

Figure 3.164. Pressure profile during gas fracturing with tri-axial stress loading.

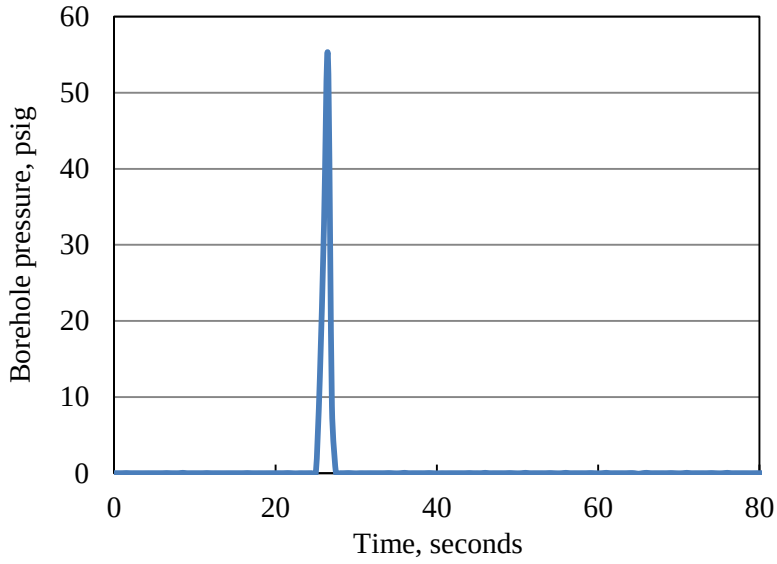

Figure 3.165. Pressure profile during gas fracturing without tri-axial stress loading.

Fracture coloring and gas fracturing revealed the fracture planes generated by CO_2 injection, as shown in Figures 3.166, 3.167, and 3.168. It is clear that the fracture planes are almost perpendicular to the minimum horizontal stress direction. The injection induced fracture planes primarily open on one side of the borehole.

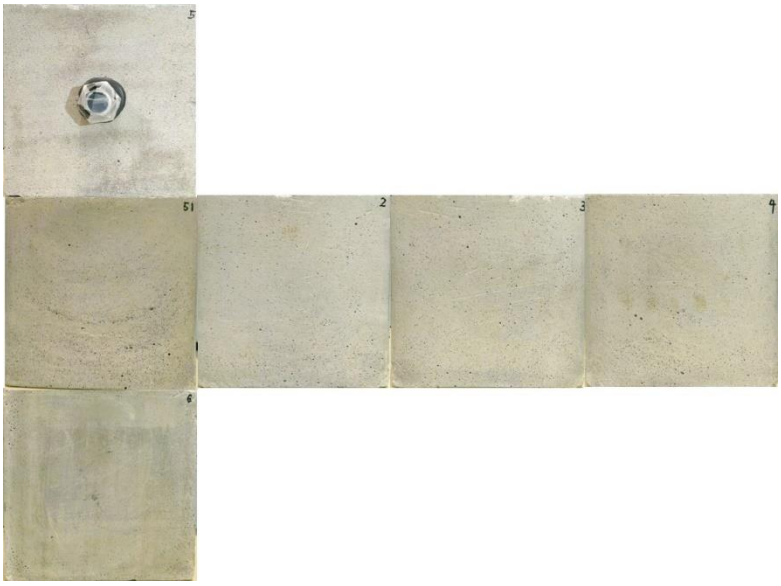

Figure 3.166. Surfaces of Sample 51 before treatment.

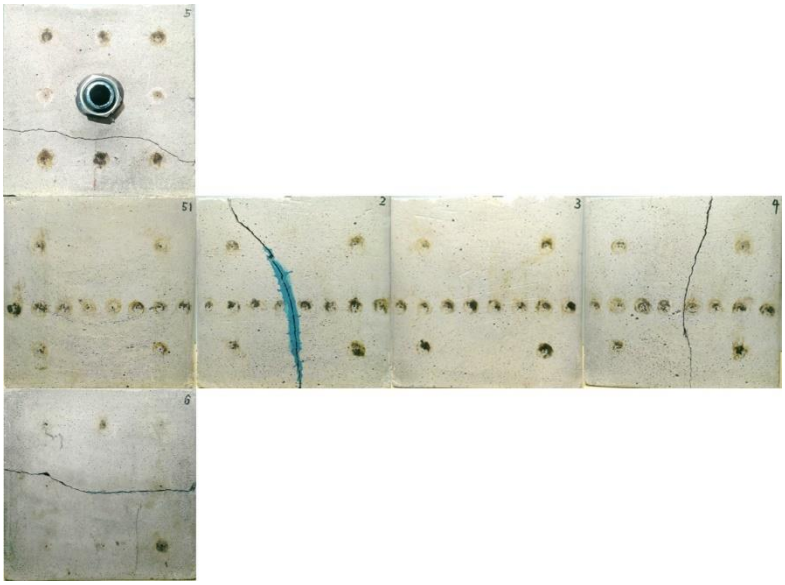

Figure 3.167. Surfaces of Sample 51 after coloring and gas fracturing.

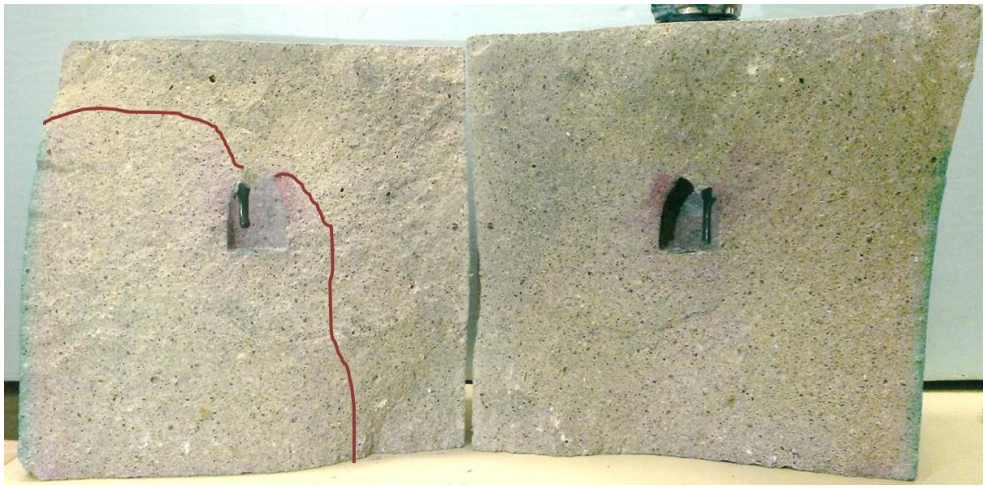

Figure 3.168. CO_2 injection induced fracture morphology of Sample 51.

Concrete Sample 52

Sample 52 was treated by injecting CO_2 under a tri-axial stress loading of 1500 psi in the x-direction, 2125 psi in the y-direction, and 2750 psi in the z-direction. Before the treatment, it was pre-loaded with the same stresses for about 40 mins, as shown in Figure 3.169. Then acoustic signatures were measured as reference for post-injection comparison, and pressure decay was carried out for pre-treatment permeability evaluation.

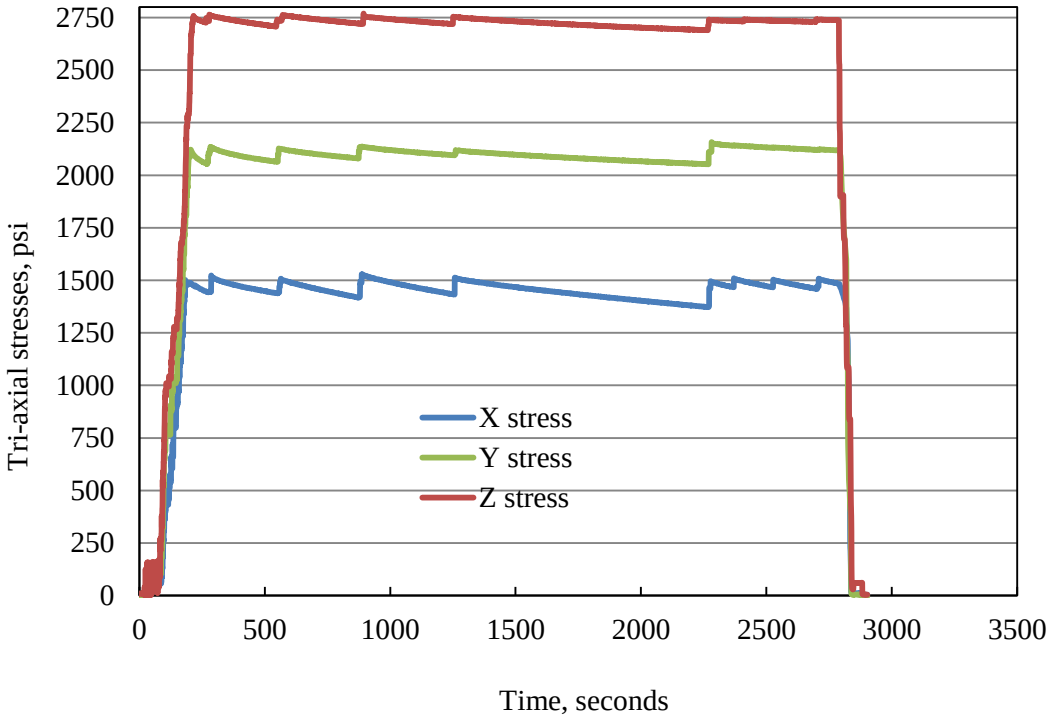

Figure 3.169. Pre-injection tri-axial stress loading for Sample 52.

Sample 52 was then treated by injecting CO_2 into borehole at a constant rate of 40 ml/min under tri-axial stress loading of 1500 psi in the x-direction, 2125 psi in the y-direction, and 2750 psi in the z-direction, as shown in Figure 3.170. The injection pressure and borehole temperature profiles are shown in Figures 3.171 and 3.172. We injected two cycles of CO_2 to fracture Sample 52. These two cycles corresponded to two pressure peaks in Figure 3.171. Since no heating source was installed for the concrete sample, the borehole temperature gradually decreased. When the highest pressure peak of 2130.17 psi was achieved, the borehole temperature was 43.40 °C, much higher than the supercritical temperature; thus, Sample 52 was fractured under supercritical conditions. At 1006 seconds when the pressure peak was reached, there was an obvious stress response on the x-axis stress loading, indicating that the major fracture planes were generated perpendicular to the x-axis. In addition, the temperature drastically dropped right after the fracturing point, due to CO_2 leakage and expansion.

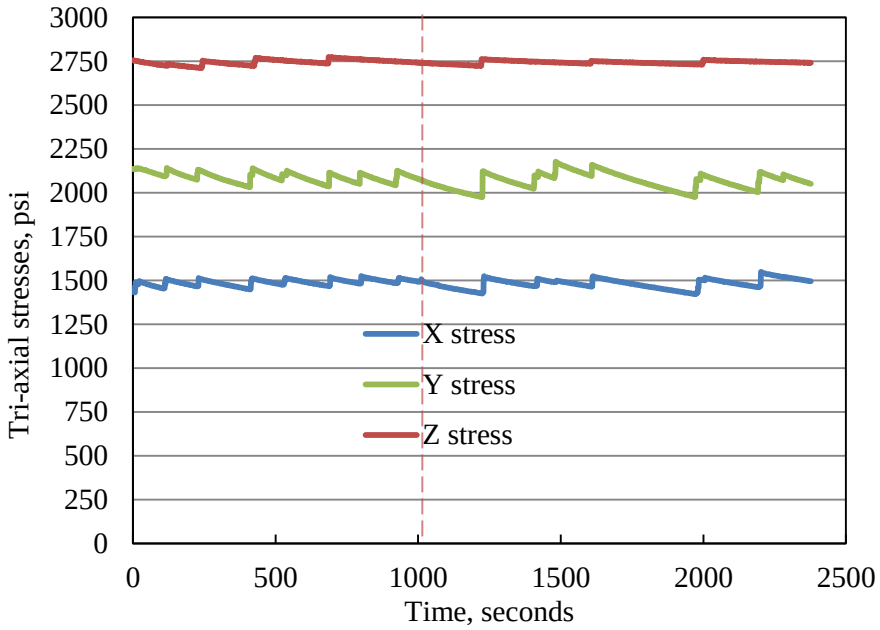

Figure 3.170. Tri-axial stress loading for CO_2 injection into Sample 52.

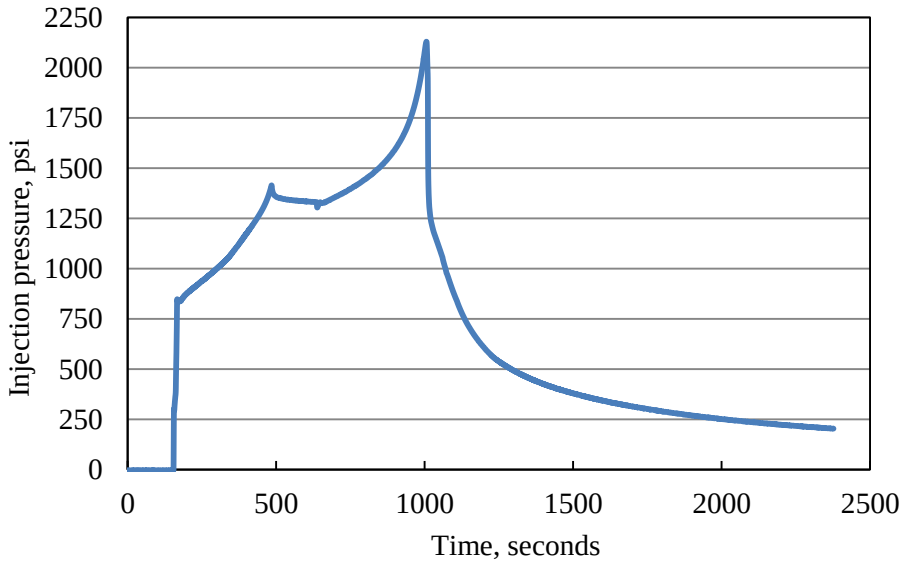

Figure 3.171. Pressure profile of CO_2 injection into Sample 52.

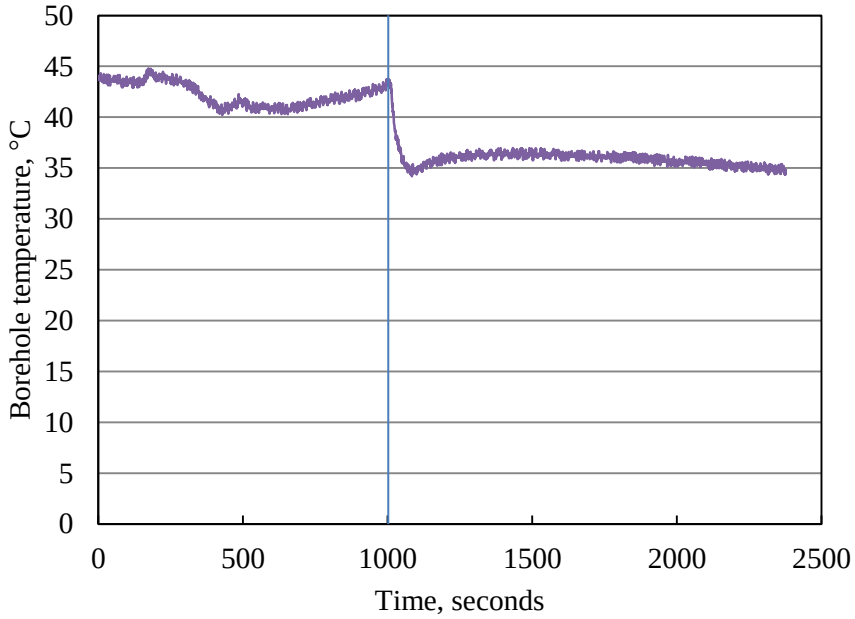

Figure 3.172. Borehole temperature profile during CO_2 injection into Sample 52.

Figure 3.173 compares the pressure decay curves measured before and after CO_2 injection. It was obvious that gas leaking rate significantly increased after CO_2 injection, due to fractures generated inside the concrete block.

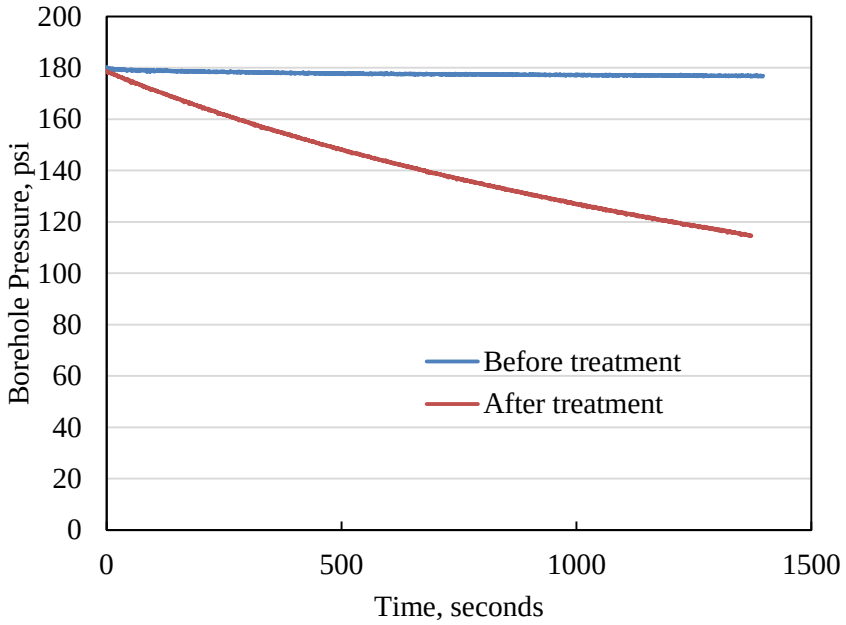

Figure 3.173. Pre- and post-injection pressure decay curves of Sample 52.

Acoustic signatures including P-waves and S-waves before (black curves) and after (red curves) CO_2 injection are compared in Figures 3.174 through Figure 3.179. Both P-waves and S-waves show delays in arrival time, indicating that the major fracture planes are parallel to Surface 1 and Surface 3. In other words, the fracture planes generated are perpendicular to the minimum horizontal stress in x-axis, in agreement with fracturing principles.

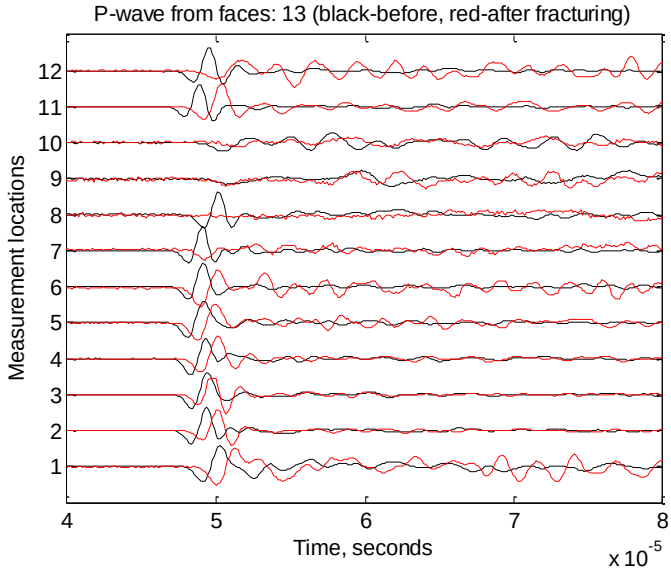

Figure 3.174. P-wave signatures measured from Surface 1 and Surface 3 of Sample 52.

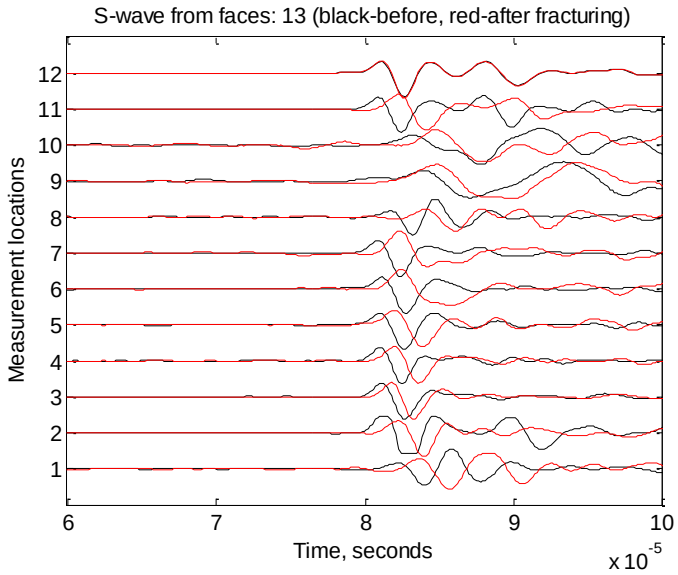

Figure 3.175. S-wave signatures measured from Surface 1 and Surface 3 of Sample 52.

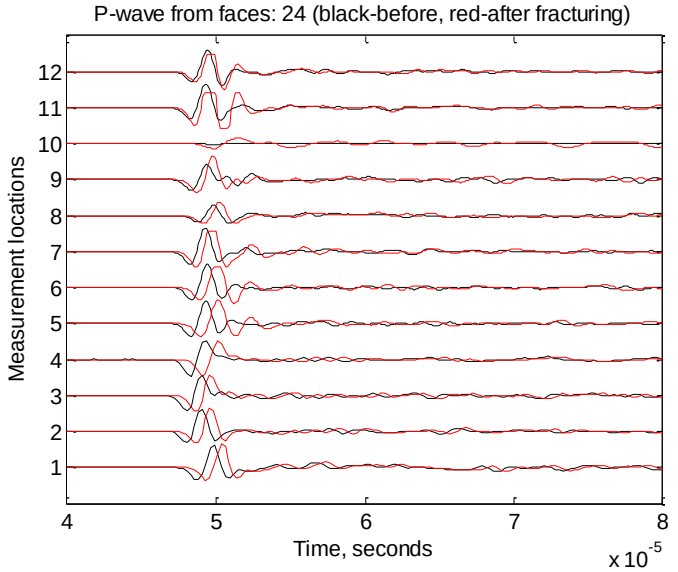

Figure 3.176. P-wave signatures measured from Surface 2 and Surface 4 of Sample 52.

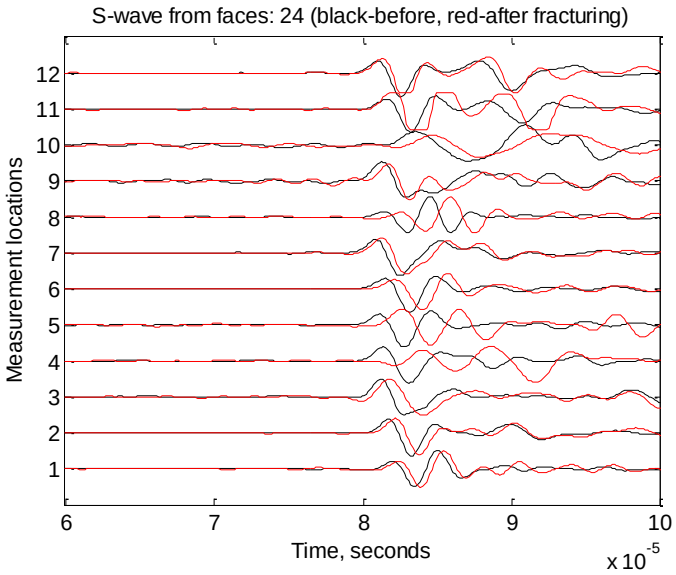

Figure 3.177. S-wave signatures measured from Surface 2 and Surface 4 of Sample 52.

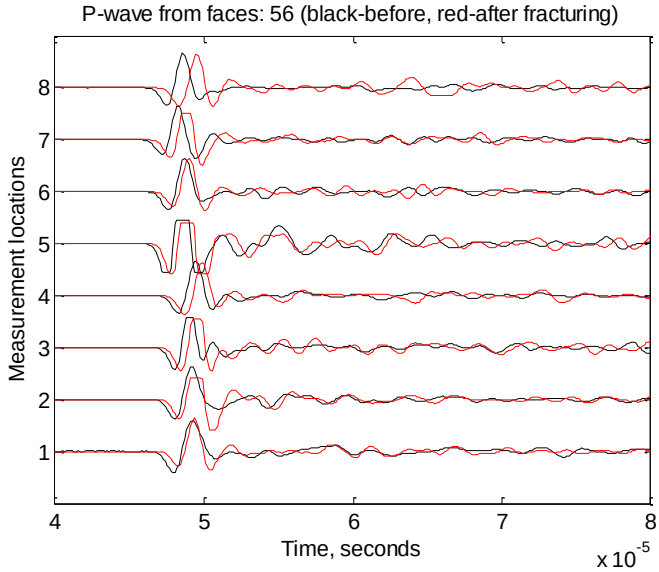

Figure 3.178. P-wave signatures measured from Surface 5 and Surface 6 of Sample 52.

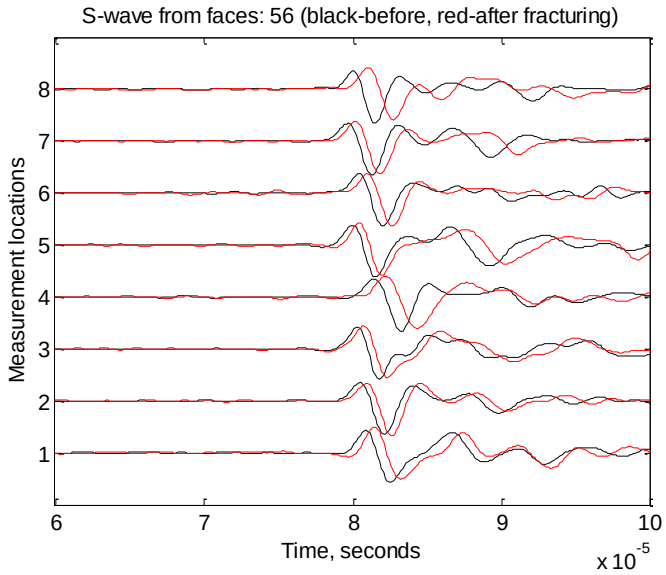

Figure 3.179. S-wave signatures measured from Surface 5 and Surface 6 of Sample 52.

Figure 3.180 is the P-wave signatures measured from Surface 2 and Surface 4 and they were plotted without adjusting the magnitude. As can be seen, locations 4, 10, 13 (middle point of locations 11 and 12), 14 (middle point of locations 4 and 5), and 15 (middle point of locations 13 and 14) have a strong interference on the P-wave transmission. Except location 10, all the other four locations are almost aligned on a straight line. These interferences suggest a major fracture plane connecting these four pulsing locations on Surface 2 and their corresponding receiving locations on Surface 4.

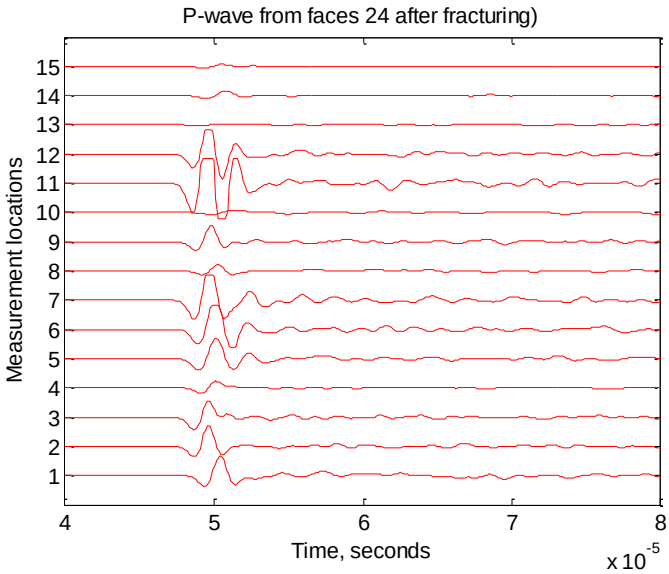

Figure 3.180. P-wave signatures measured from Surface 2 and Surface 4 of Sample 52.

Dye solution was later injected into Sample 52 to color the fracture planes. Then under tri-axial stress loading, the sample was fractured by injecting nitrogen gas, and the pressure profile is shown in Figure 3.181, in which the peak pressure 1718.55 psig. Finally, the sample was

broken down by nitrogen gas under no confining stress, and the breakdown pressure is 176.47 psig, as shown in Figure 3.182.

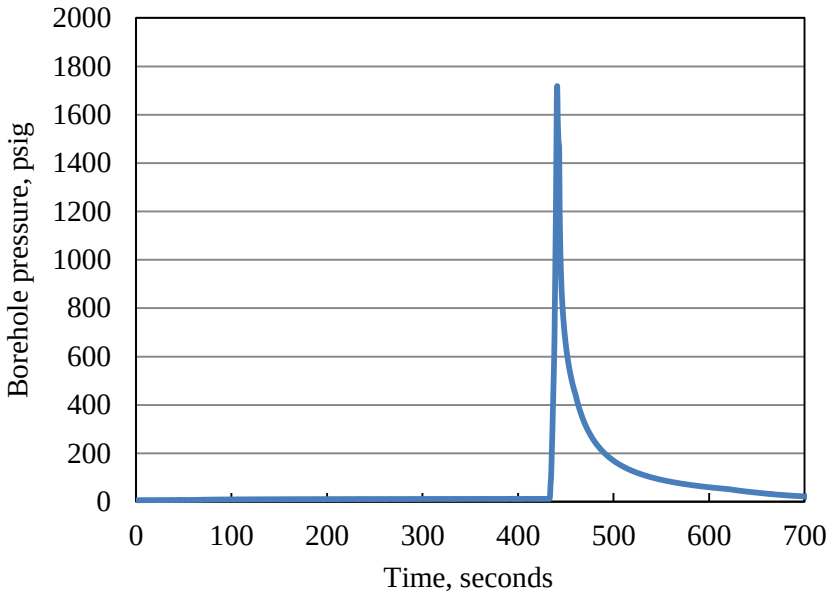

Figure 3.181. Pressure profile during gas fracturing with tri-axial stress loading for Sample 52.

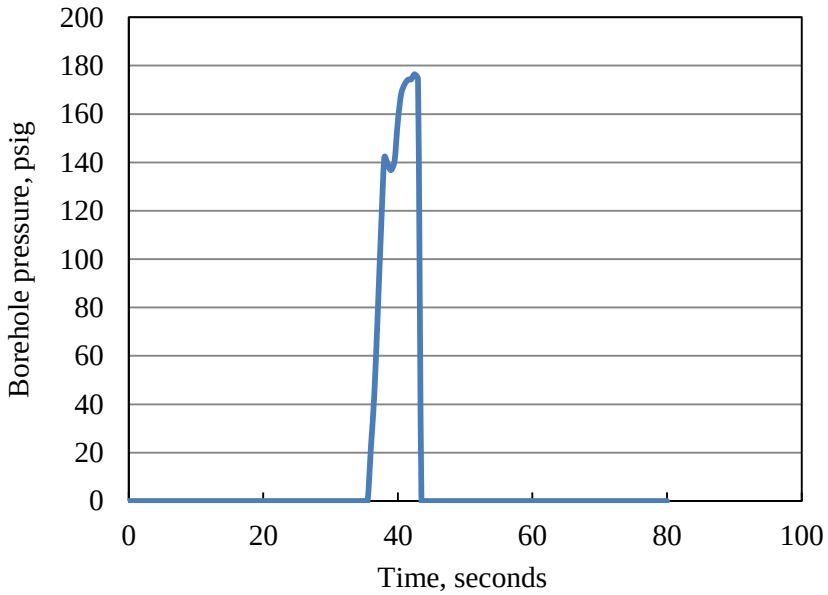

Figure 3.182. Pressure profile during gas fracturing without tri-axial stress loading for Sample 52.

Figures 3.183 and Figure 3.184 shows the faces of Sample 52 before and after dye injection; on Surface 2 there was a small leakage point near acoustic measurement location 4, and on Surface 6, a 7-inch fracture that is nearly perpendicular to the x-axis direction was clearly observed. Then the sample was fractured by high pressure nitrogen gas, which revealed the

fracture planes generated by CO_2 injection, as shown in Figure 3.185 and 3.186. The fracture planes are almost parallel to the Surface 1 and Surface 3 and pass the acoustic locations 4, 13, 14, and 15 on Surface 2 and Surface 4, confirming indications obtained from P-wave measurements.

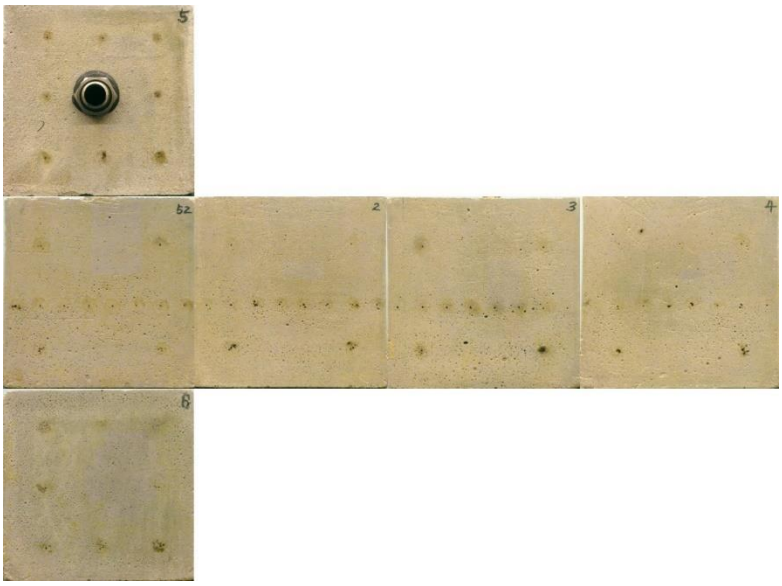

Figure 3.183. Faces of Sample 52 before treatment.

Figure 3.184. Faces of Sample 52 after dye injection.

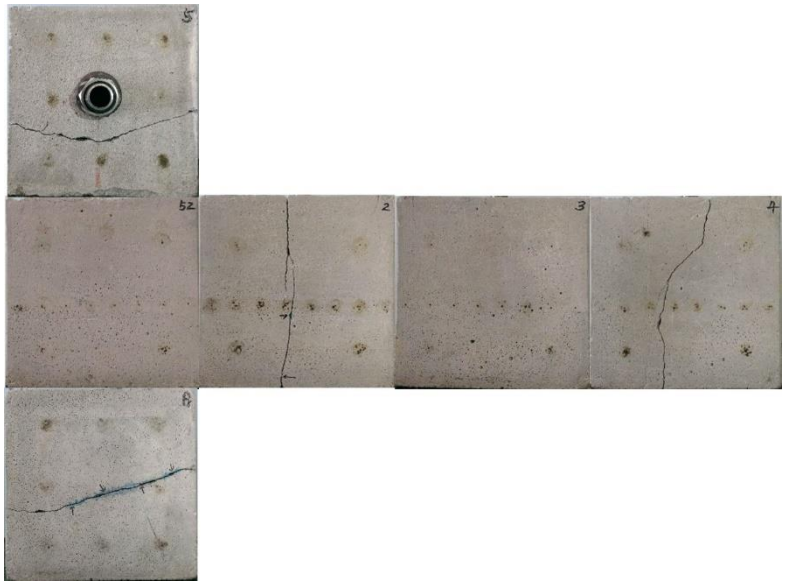

Figure 3.185. Faces of Sample 52 after gas fracturing.

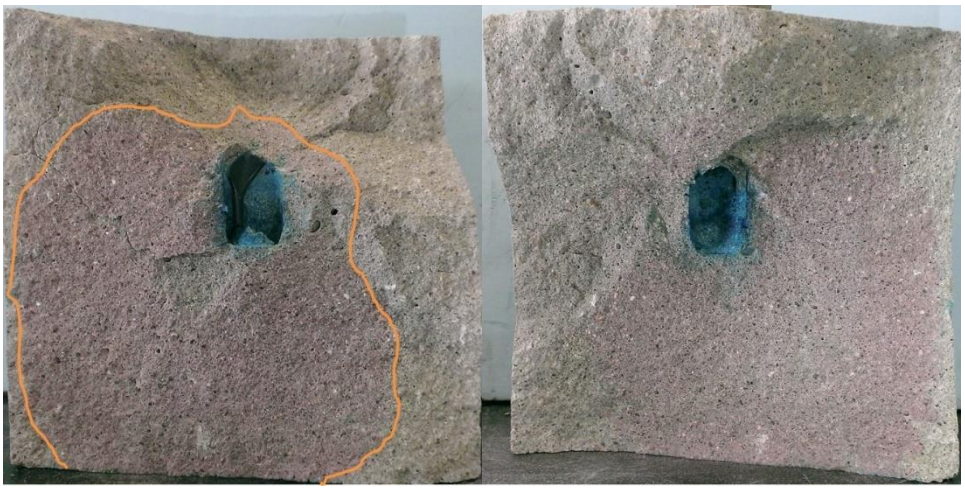
Figure 3.186. Colored CO_2 injection induced fracture planes in Sample 52.

The major fracture planes primarily propagated from the borehole toward Surface 2, but did not extend as much to the opposite side, exhibiting an asymmetric pattern around the wellbore. Also except the bottom face, the fracture did not reach much of the other faces, i.e. the major fractures are confined in the concrete block. This helps explain the relatively slow pressure decay after CO_2 injection, as compared to Samples 50 and 51.

Concrete Sample 53

Sample 53 was treated by injecting CO_2 under a tri-axial stress loading of 1000 psi in the x-direction, 1625 psi in the y-direction, and 2250 psi in the z-direction. Before the treatment, it was pre-loaded with the same stresses for about 43 mins, as shown in Figure 3.187. Then, acoustic signatures were measured as a reference for post-injection comparison and pressure decay was carried out for pre-treatment permeability evaluation.

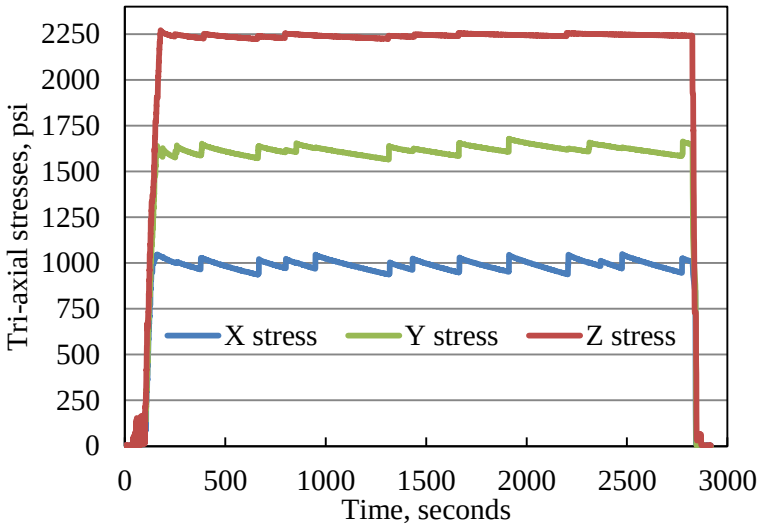

Figure 3.187. Pre-treatment stress loading for Sample 53.

Sample 53 was then treated by injecting CO_2 into borehole at a constant rate of 40 ml/min under tri-axial stress loading of 1000 psi in the x-direction, 1625 psi in the y-direction, and 2250 psi in the z-direction, as shown in Figure 3.188. The injection pressure and borehole temperature profiles are shown in Figures 3.189 and 3.190. The sample was fractured at 435 seconds when the injection pressure reached 1091.49 psi. This peak pressure corresponds to the stress responses on tri-axial stress loading in x, y, and z directions in Figure 3.188. As can be seen, x-direction stress rose while y- direction and z- direction stresses fell a little when the sample was fractured, indicating that the major fracture planes were generated perpendicular to the x-axis. When the highest pressure was achieved, the borehole temperature was 46.84 °C, much higher than the supercritical temperature, thus the sample was fractured under supercritical conditions. In addition, the temperature drastically dropped about 4 °C right after the fracturing, due to CO_2 leakage and expansion.

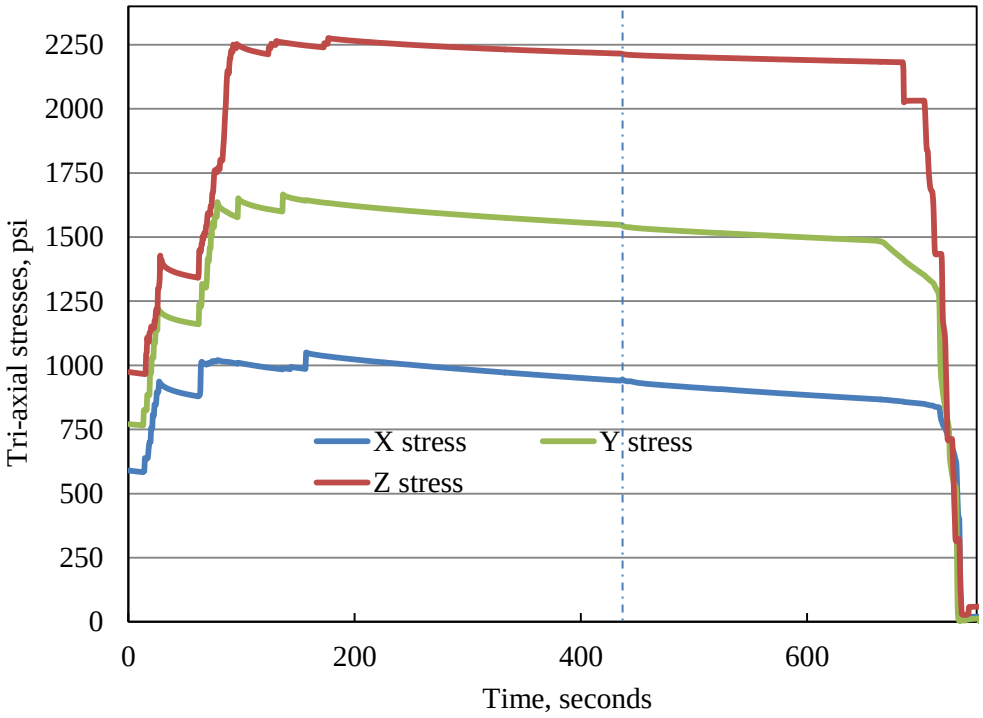

Figure 3.188. Pre-treatment pressure decay for Sample 53.

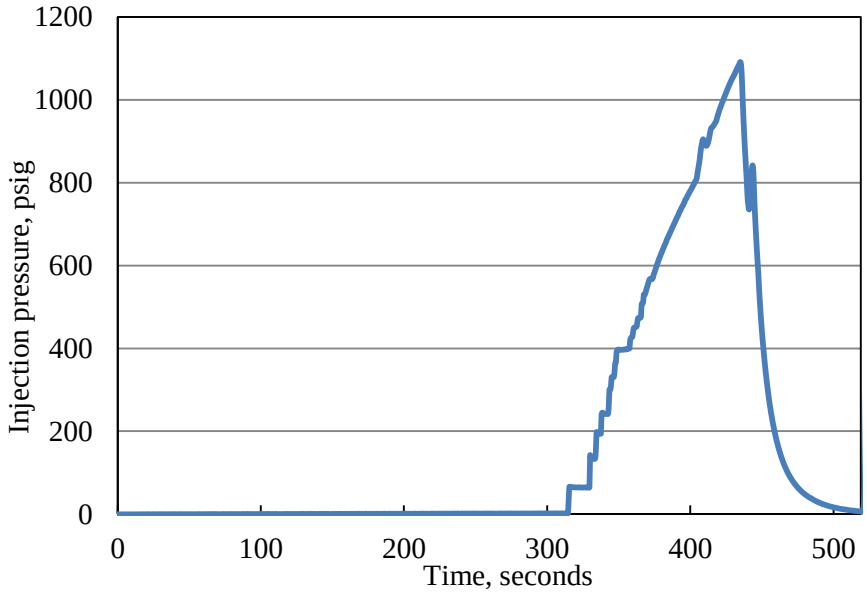

Figure 3.189. CO_2 injection pressure for Sample 53.

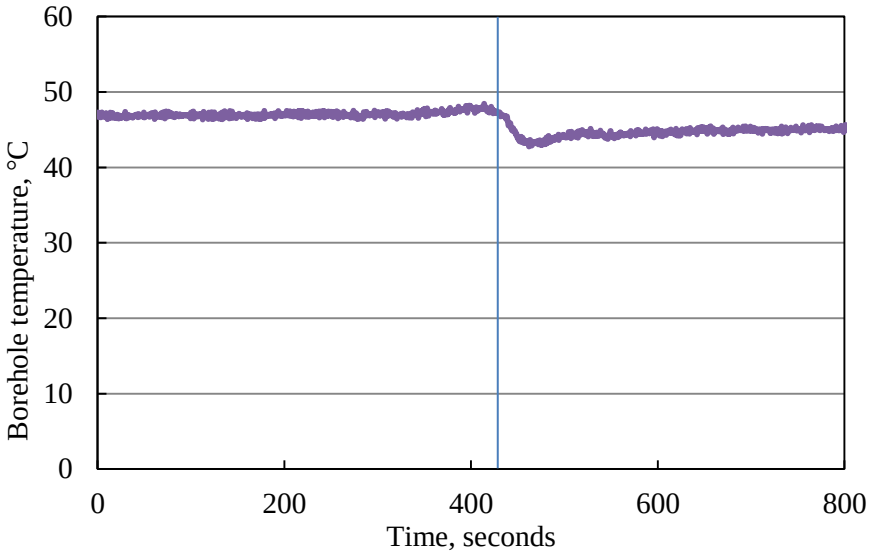

Figure 3.190. Borehole temperature during CO_2 injection.

Figure 3.191 compares the pressure decay curves measured before and after CO_2 injection. Before treatment, the gas leakage rate from borehole was very slow, indicating concrete samples as good analogs for cap rocks. After CO_2 injection, it is obvious that gas leaking rate significantly increased, due to fractures generated inside the concrete block.

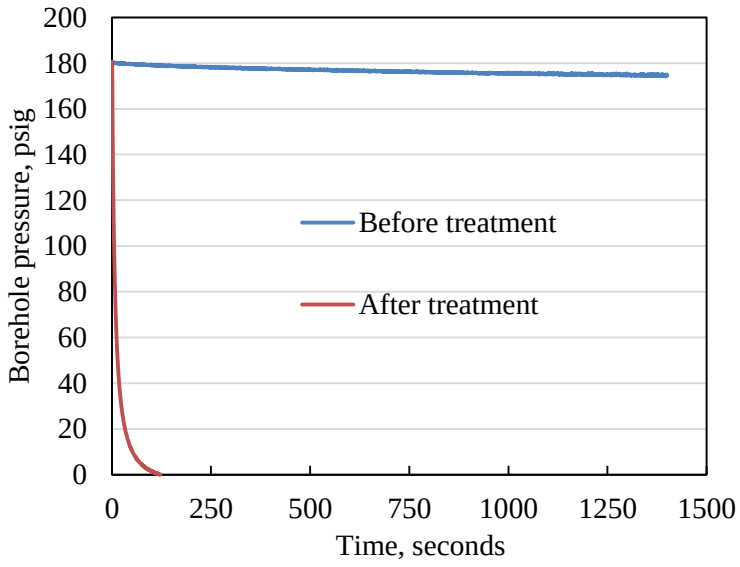

Figure 3.191. Pressure decay curves before and after CO_2 injection.

Acoustic signatures including P-waves and S-waves before (black curves) and after (red curves) CO_2 injection are compared in Figures 3.192 through 3.197. Both P-waves and S-waves show delays in arrival time, and waveforms changed, indicating fractures generated in concrete blocks.

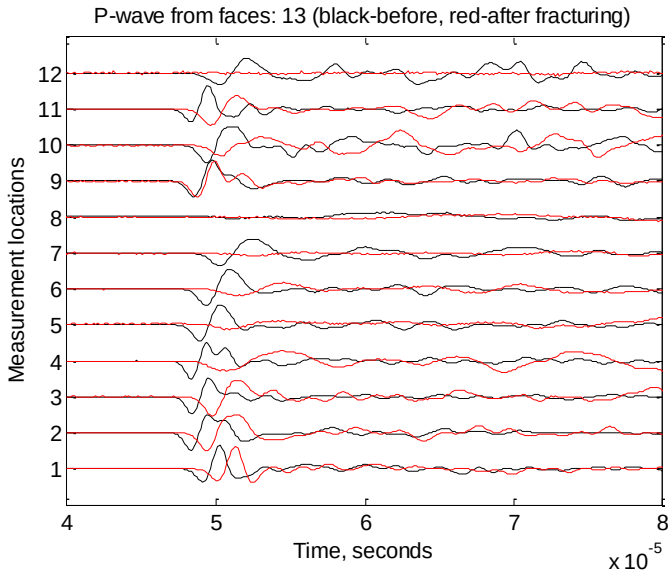

Figure 3.192. P-wave signatures measured from Surface 1 and Surface 3 of Sample 53.

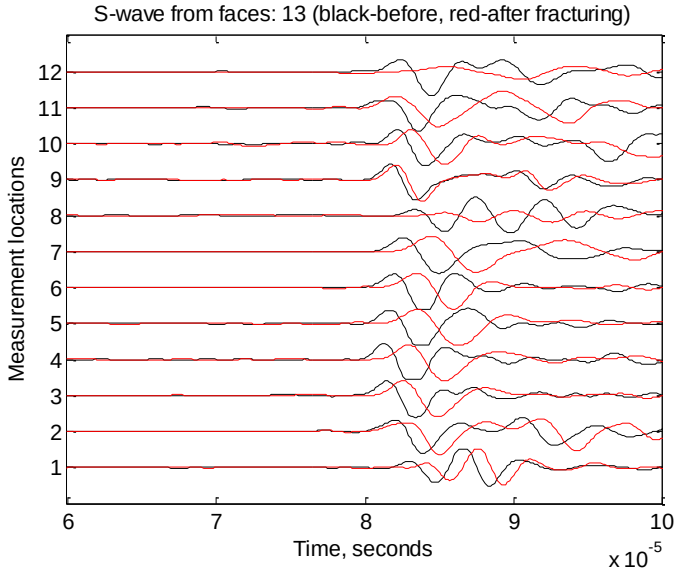

Figure 3.193. S-wave signatures measured from Surface 1 and Surface 3 of Sample 53.

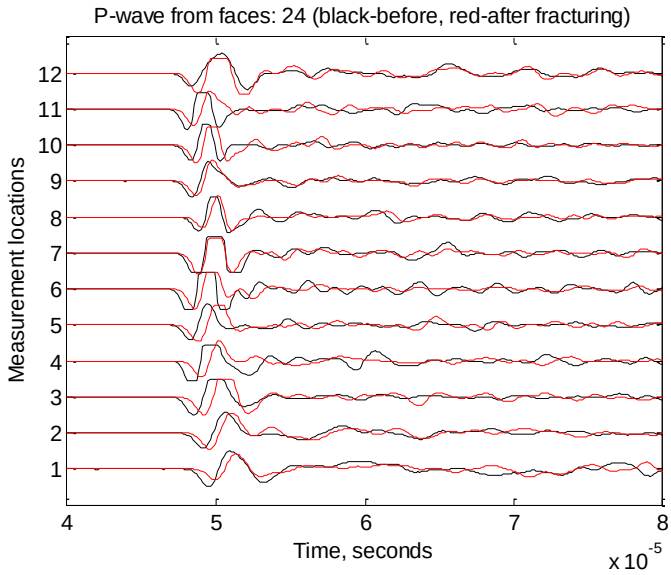

Figure 3.194. P-wave signatures measured from Surface 2 and Surface 4 of Sample 53.

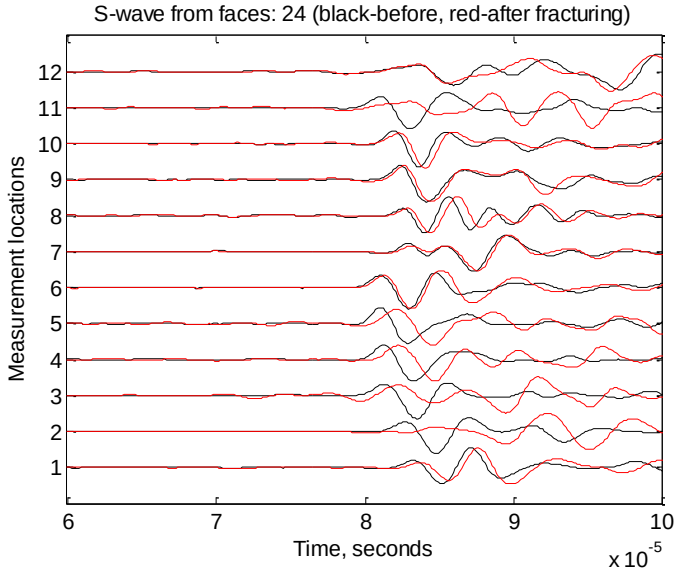

Figure 3.195. S-wave signatures measured from Surface 2 and Surface 4 of Sample 53.

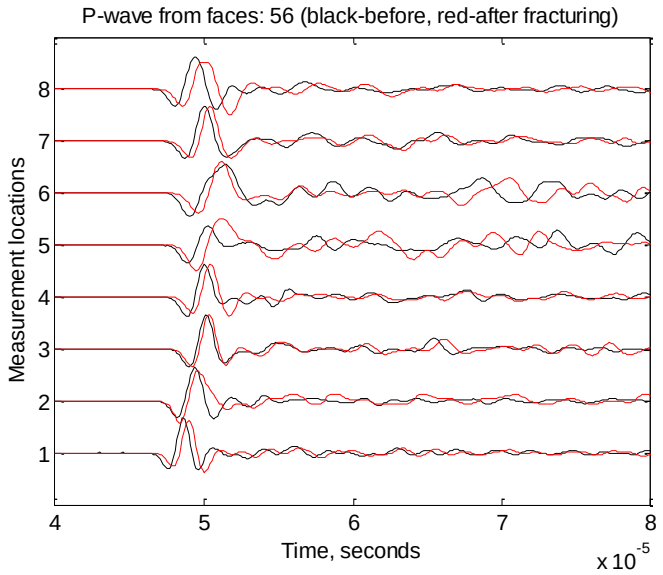

Figure 3.106. P-wave signatures measured from Surface 5 and Surface 6 of Sample 53.

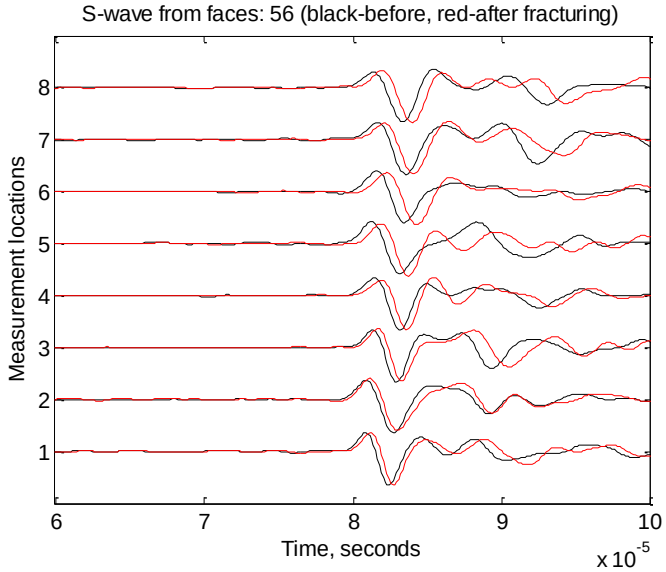

Figure 3.197. S-wave signatures measured from Surface 5 and Surface 6 of Sample 53.

Figure 3.198 is the P-wave signatures measured from Surface 2 and Surface 4 and they are plotted without adjusting the magnitude. As can be seen, P-wave measured through locations 13 (middle point of locations 11 and 12) and 14 (middle point of locations 4 and 5) on Surface 2 is strongly interfered by the fractures generated in the concrete sample. These interferences suggest a major fracture plane connecting these two pulsing locations on Surface 2 and their corresponding receiving locations on Surface 4.

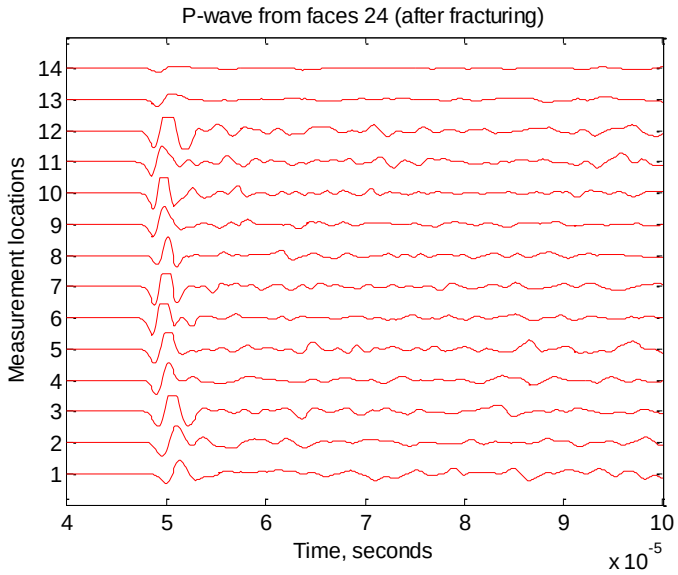

Figure 3.198. P-wave signatures measured from Surface 2 and Surface 4 of Sample 53 without adjusting the magnitude.

Dye solution was then injected into Sample 53 to color the CO_2 injection induced fractures, through which dye solution flowed out of the block surface. Then, under tri-axial stresses shown in Figure 3.199, the sample was fractured by nitrogen gas at a peak pressure of 1297.93 psig at 74 seconds with a rebound on x-axis stress. The gas fracturing pressure profile is shown in Figure 3.200. Finally, after unloading the tri-axial stresses, the fractured sample was broken down at 182.99 psig by nitrogen gas, as shown in Figure 3.201.

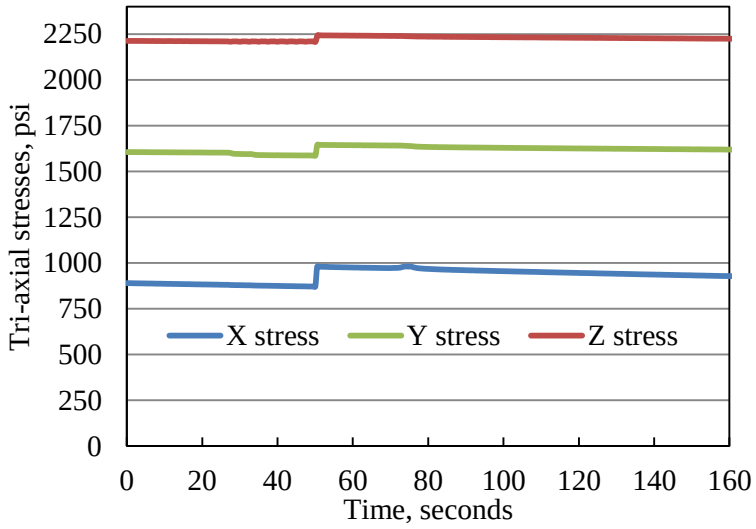

Figure 3.199. Tri-axial stress loading for gas fracturing of Sample 53.

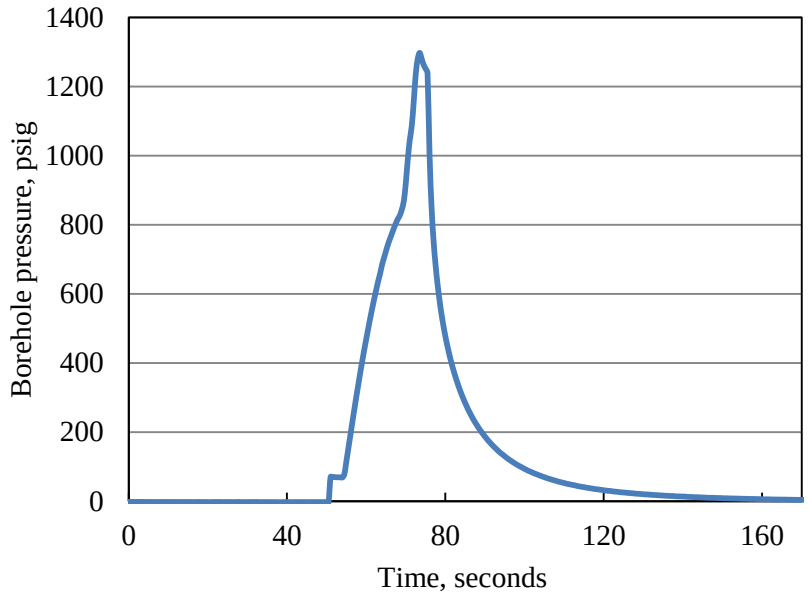

Figure 3.200. Pressure profile of gas fracturing of Sample 53 under tri-axial stress conditions.

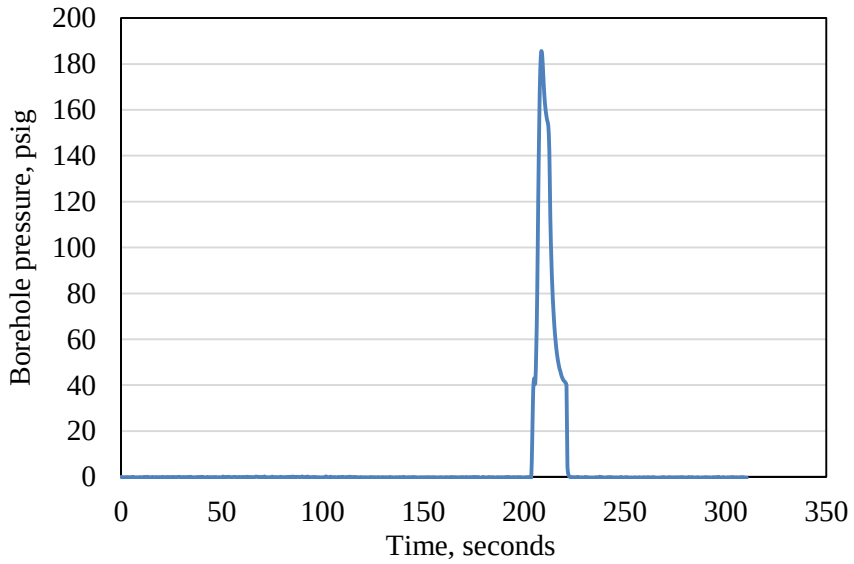

Figure 3.201. Gas fracturing of Sample 53 under no confining stress.

The surfaces of Sample 53 before CO_2 treatment are shown in Figure 3.202. During dye solution injection, dye solution leaked from Surfaces 2, 4, 5, and 6, as shown in Figure 3.203. Coloring and gas fracturing revealed the fracture planes generated by CO_2 injection, as shown in Figure 3.204 and 3.205. The CO_2 injection induced fracture planes are perpendicular to the minimum horizontal stress direction.

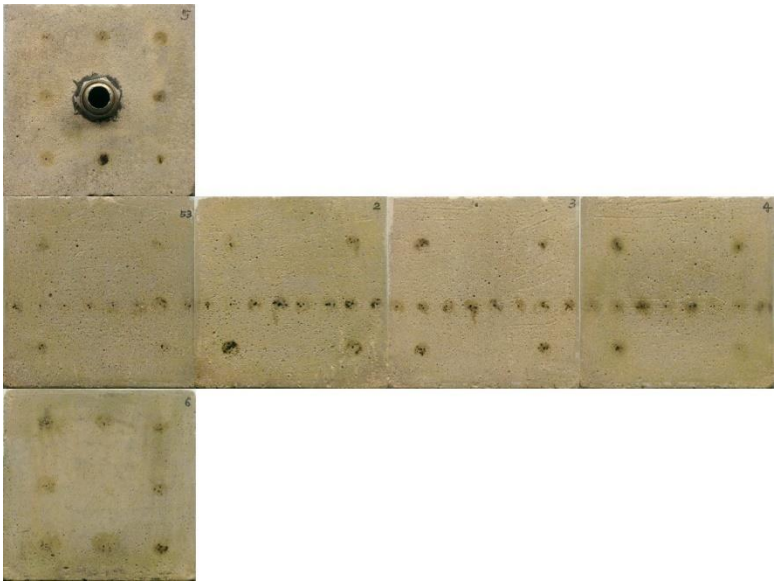

Figure 3.202. Intact surfaces of Sample 53 before treatment.

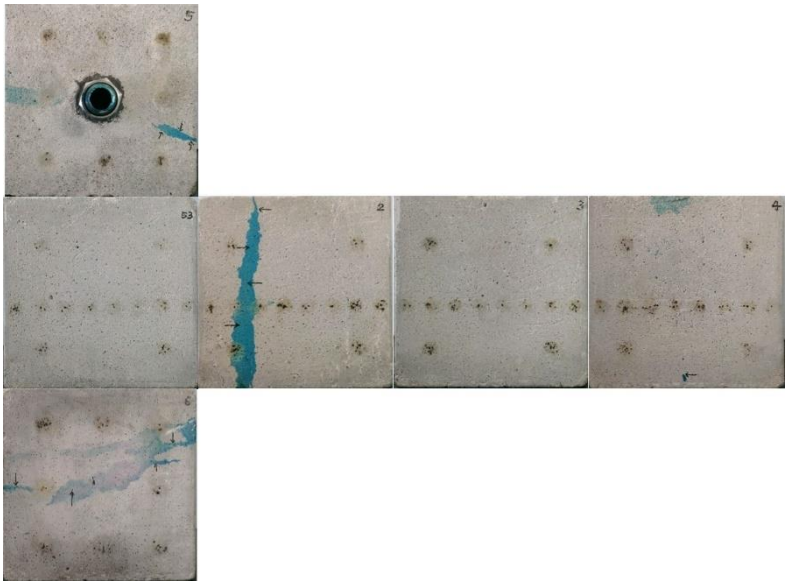

Figure 3.203. Surfaces of Sample 53 after dye injection.

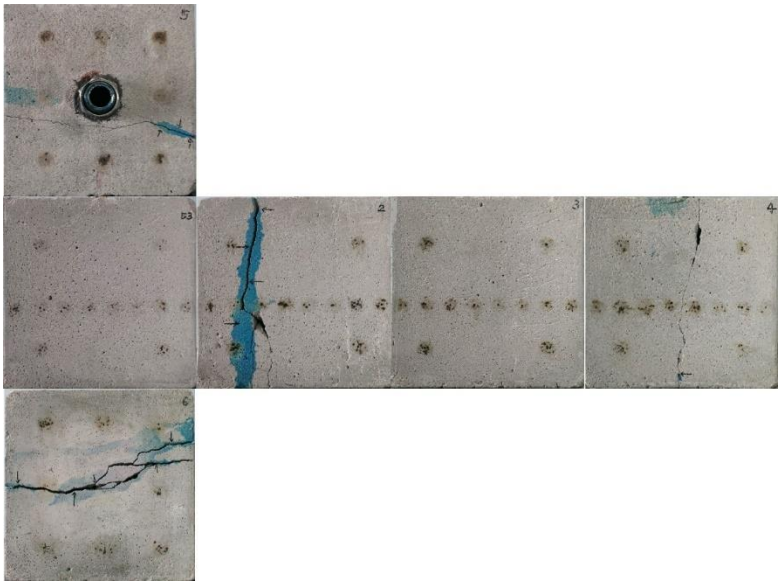

Figure 3.204. Surfaces of Sample 53 after dye injection.

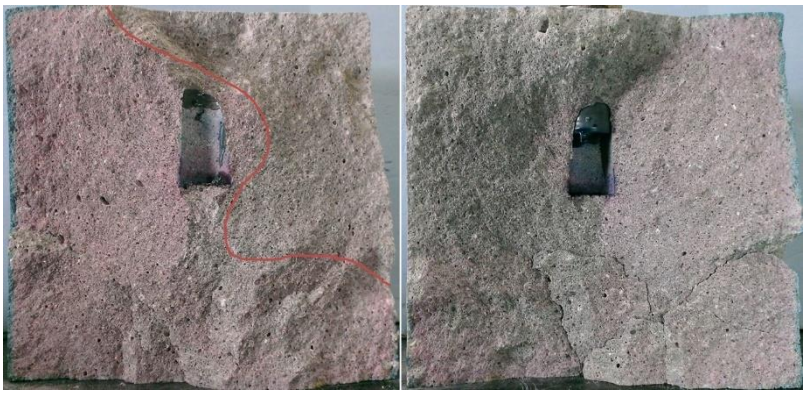

Figure 3.205. CO_2 injection induced fracture morphology of Sample 53 after gas fracturing.

Concrete Sample 54

Sample 54 was treated by injecting CO_2 under a tri-axial stress loading of 1250 psi in the x-direction, 1562 psi in the y-direction, and 1875 psi in the z-direction. Before the treatment, it was pre-loaded with the same stresses for about 41 mins, as shown in Figure 3.206. Then acoustic signatures were measured as reference for post-injection comparison, and pressure decay was carried out for pre-treatment permeability evaluation.

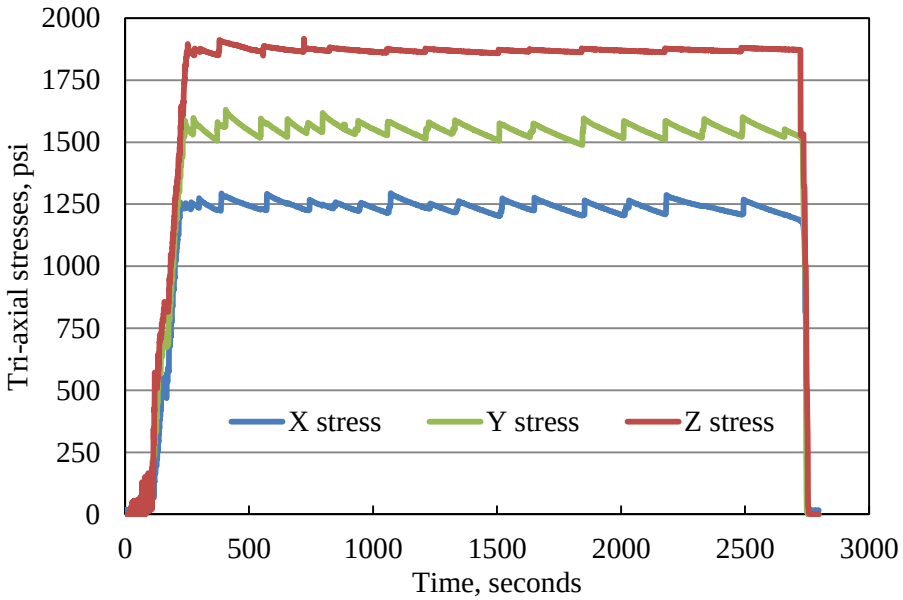

Figure 3.206. Stress loading before CO_2 injection for Sample 54.

Sample 54 was treated by injecting CO_2 at a constant rate of 40 ml/min under tri-axial stress loading of 1250 psi in the x-direction, 1562 psi in the y-direction, and 1875 psi in the z-direction, as shown in Figure 3.207. Two cycles of CO_2 were injected to fracture the sample, and these two cycles correspond to the pressure peaks around 682 s and 1217 s in Figure 3.208. The highest peak pressure is 1641.90 psi, corresponding to the borehole temperature of 44.84°C in Figure 3.209. Both pressure and temperature were higher than the supercritical values, thus Sample 54 was fractured by sc-CO_2. On the tri-axial stress loading curves, there is a slight response on y-axis, but no obvious responses can be seen on x-axis and z-axis. This suggests that the major fracture generated is not perpendicular to x-axis. Right after the fracturing point, borehole temperature significantly dropped to -7.91°C, due to rapid vaporization of sc-CO_2.

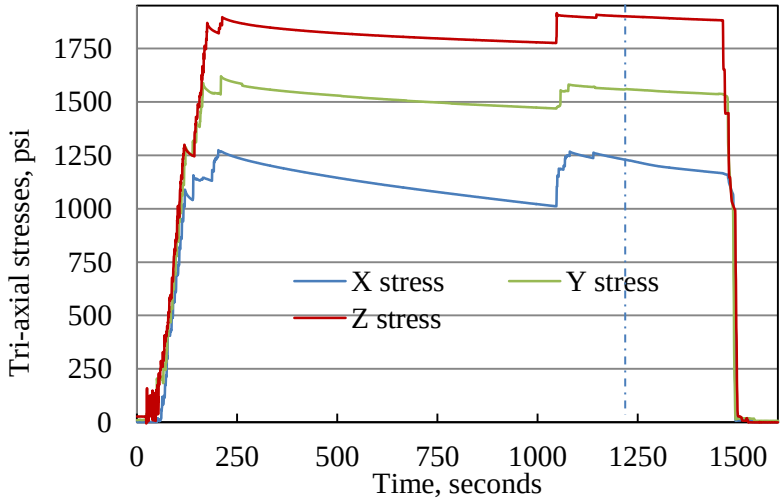

Figure 3.207. Stress loading for CO_2 injection into Sample 54.

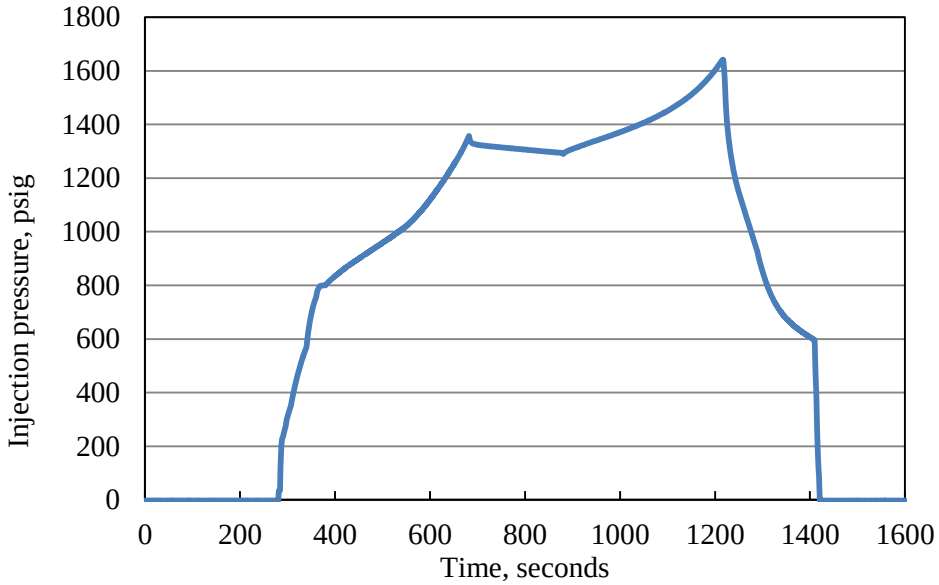

Figure 3.208. CO_2 injection pressure for Sample 54.

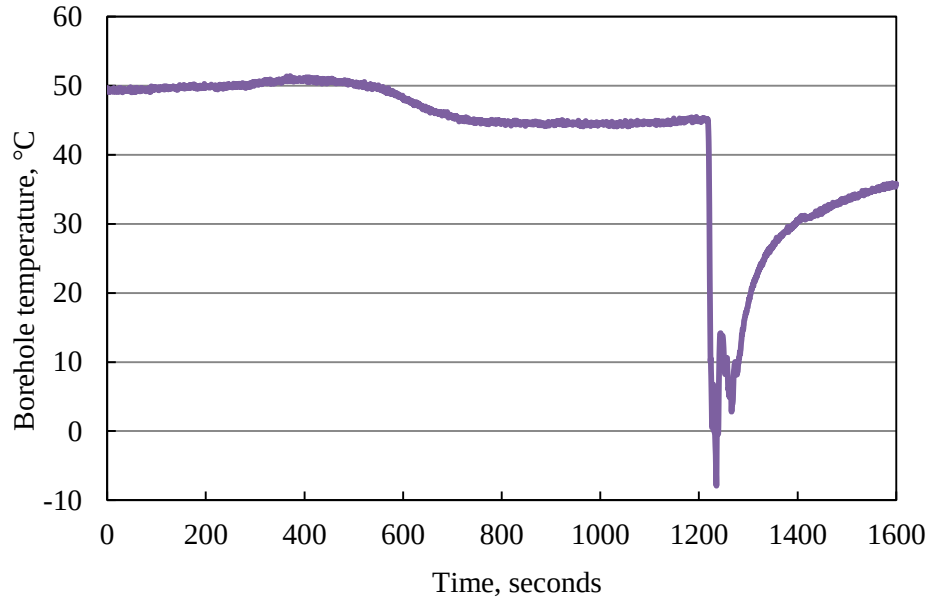

Figure 3.209. Borehole temperature during CO_2 injection into Sample 54.

Figure 3.210 compares the pressure decay curves measured before and after CO_2 injection. It is obvious that gas leaking rate significantly increased after CO_2 injection, due to fractures generated inside the concrete block.

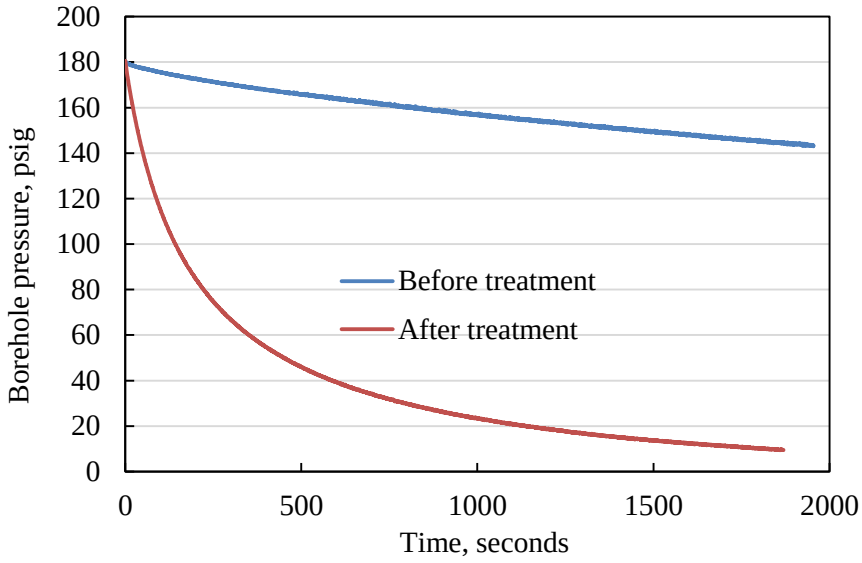

Figure 3.210. Pressure decay curves before and after treatment for Sample 54.

Acoustic signatures including P-waves and S-waves before (black curves) and after (red curves) CO_2 injection are compared in Figures 3.211 through 3.216. The results for Sample 54 here are mixed.

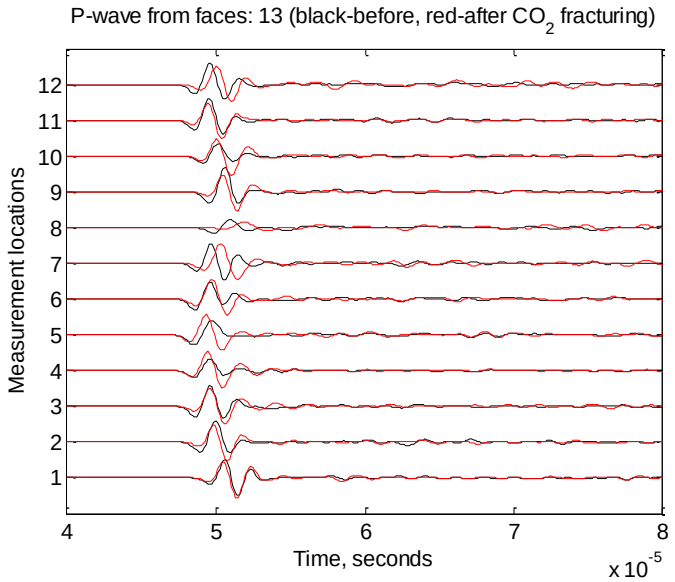

Figure 3.211. P-wave signatures measured from Surface 1 and Surface 3 of Sample 54.

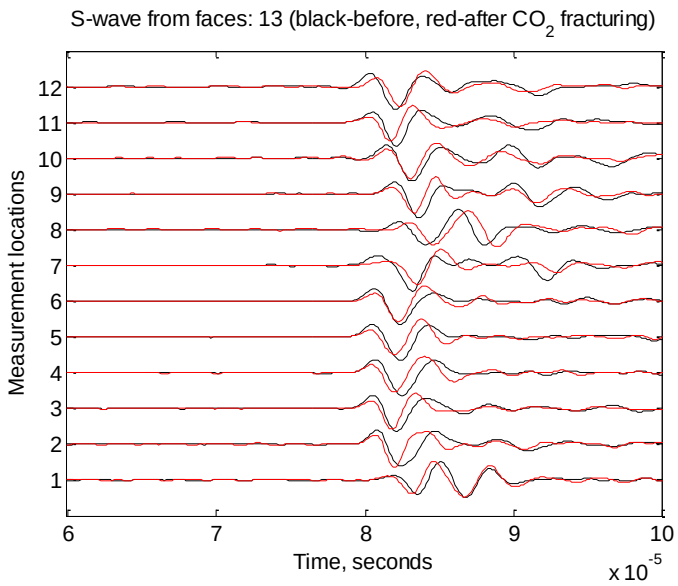

Figure 3.212. S-wave signatures measured from Surface 1 and Surface 3 of Sample 54.

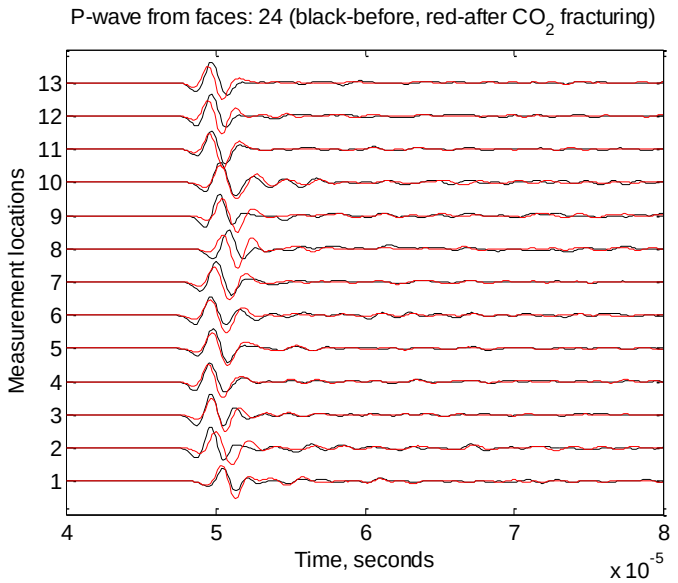

Figure 3.213. P-wave signatures measured from Surface 2 and Surface 4 of Sample 54.

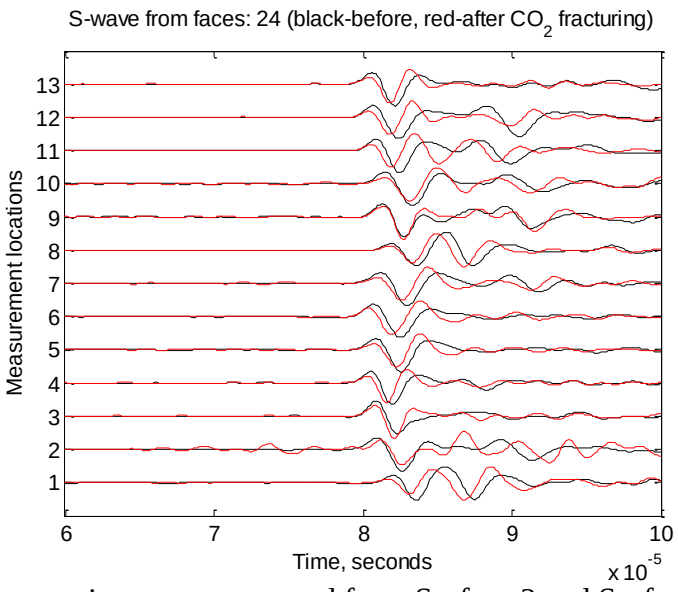

Figure 3.214. S-wave signatures measured from Surface 2 and Surface 4 of Sample 54.

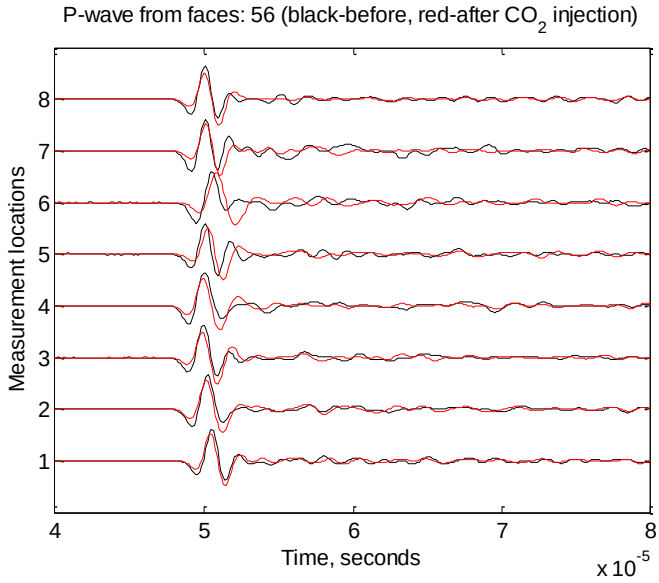

Figure 3.215. P-wave signatures measured from Surface 5 and Surface 6 of Sample 54.

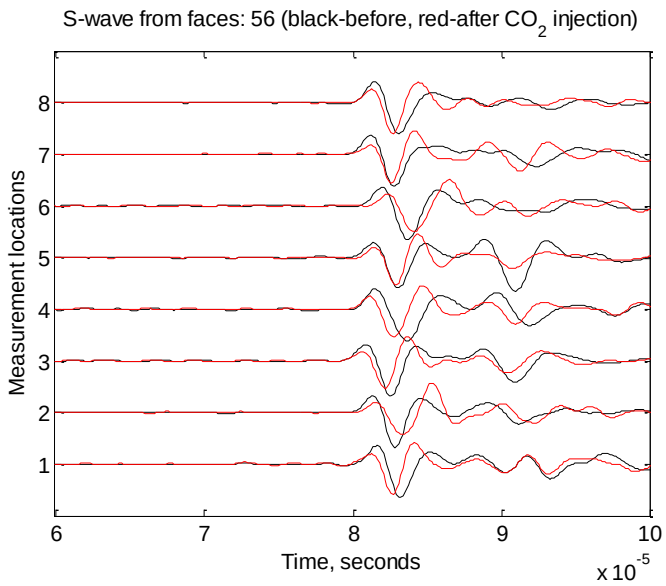

Figure 3.216. S-wave signatures measured from Surface 5 and Surface 6 of Sample 54.

Dye solution was later injected into Sample 54 to color the CO_2 injection induced fracture planes. Then under tri-axial stresses, shown in Figure 3.217, nitrogen gas was injected to break down the sample and the pressure profile for that is shown in Figure 3.218. The highest fracturing pressure was 1614.31 psig. Finally, the sample was broken down at 302.02 psig by injecting nitrogen gas under no tri-axial stresses, shown in Figure 3.219.

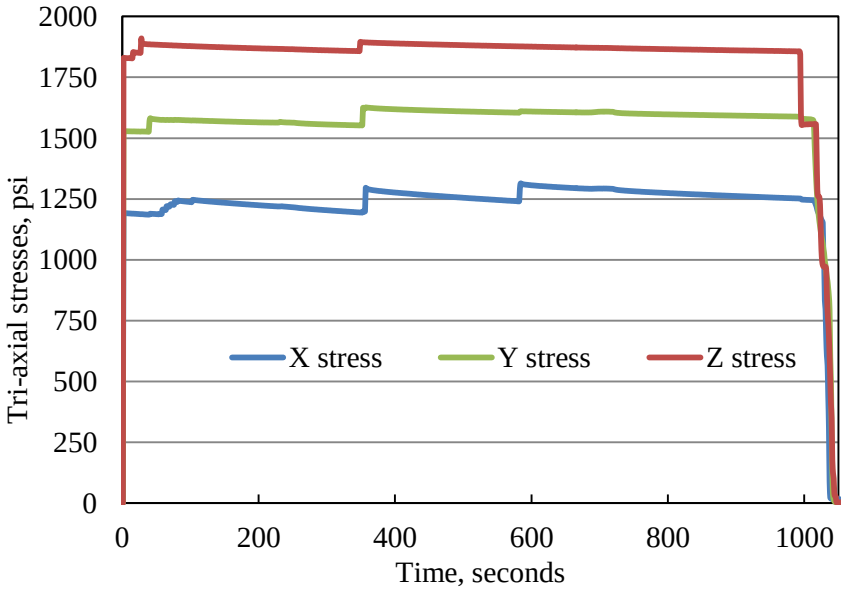

Figure 3.217. Stress loading for gas fracturing of Sample 54.

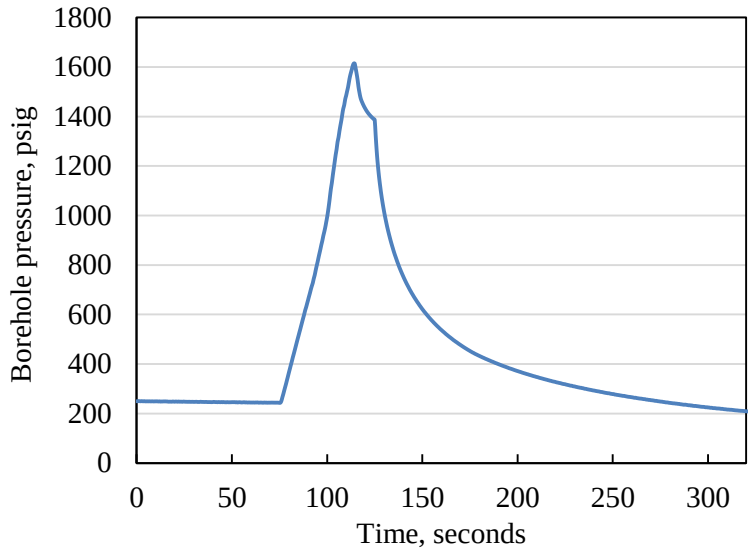

Figure 3.218. Gas fracturing pressure for Sample 54 under tri-axial stresses.

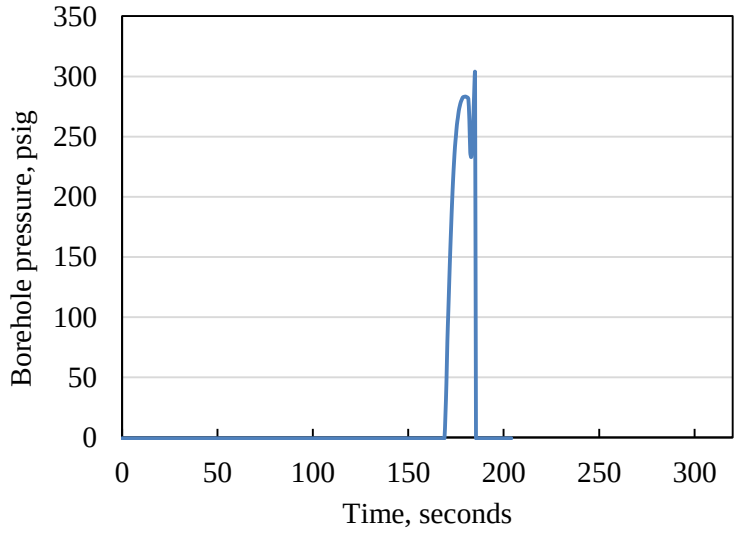

Figure 3.219. Gas fracturing pressure for Sample 54 under no tri-axial stresses.

Fracture coloring and gas fracturing revealed the fracture planes generated by CO_2 injection, as shown before Figure 3.220 and after in Figures 3.221 and 3.222. It is clear that the fracture planes are dipping from the top surface with angles to both x-axis and y-axis directions. The fracture planes extend through the top surface, but are highly confined in the concrete sample.

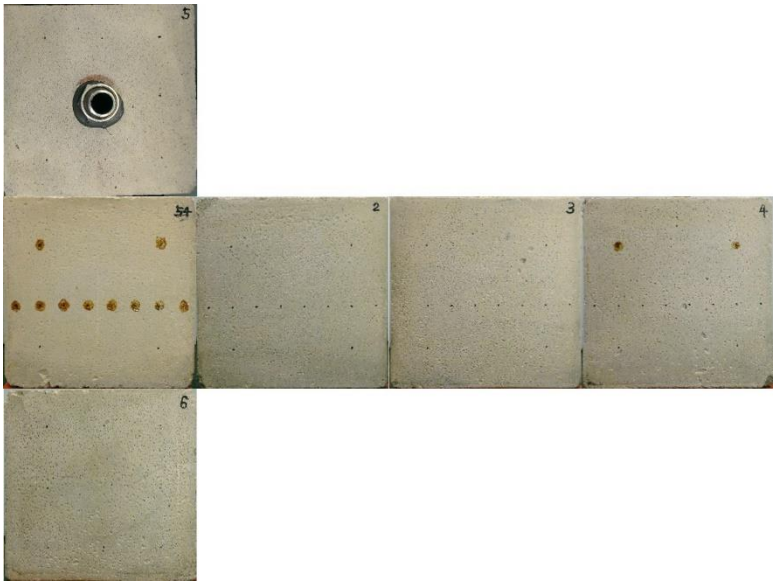

Figure 3.220. Intact surfaces of Sample 54 before treatment.

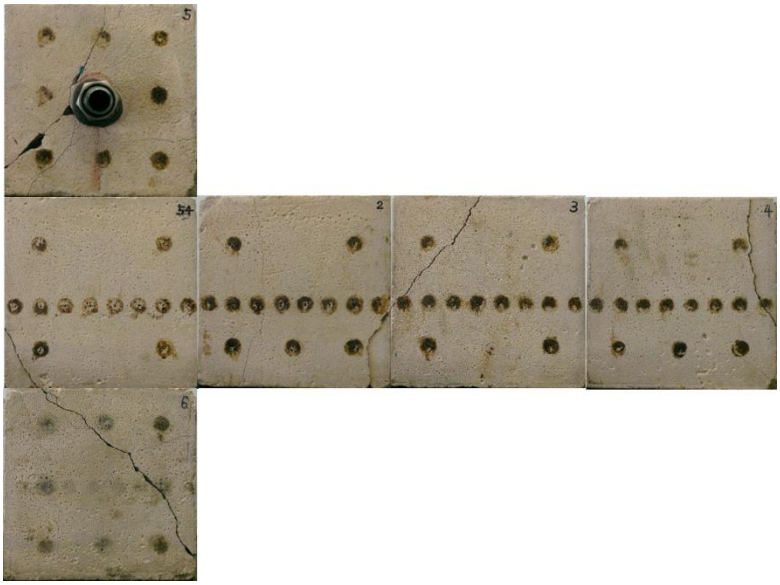

Figure 3.221. Surfaces of Sample 54 after coloring and gas fracturing.

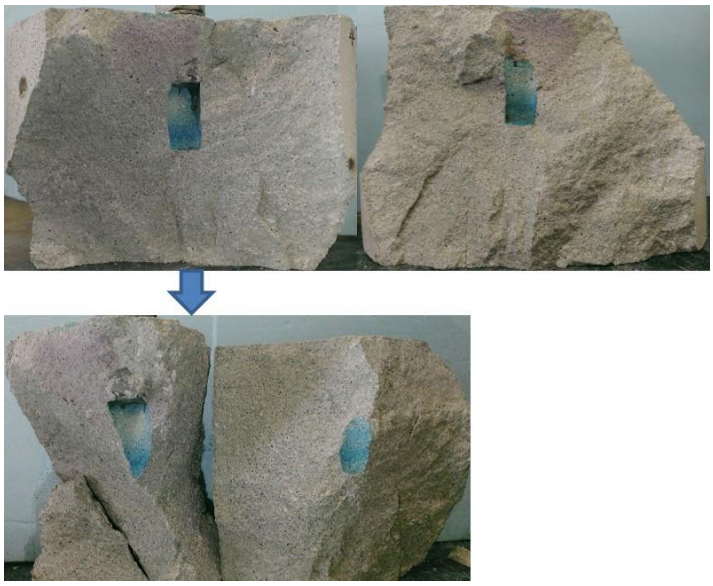

Figure 3.222. CO_2 injection induced fracture morphology of Sample 54.

Concrete Sample 55

Sample 55 was first pre-loaded tri-axial stresses of 1250 psi in the x-direction, 2187 psi in the y-direction, and 3125 psi in the z-direction for about 40 mins, as shown in Figure 3.223. Then acoustic measurements and a pressure decay test were carried out. After that, CO_2 was injected at a constant rate of 40 ml/min into the sample under the same tri-axial stress loading, as shown in Figure 3.224. We injected two cylinders of CO_2 into the sample, corresponding to two pressure peaks of 1066.47 psig and 1195.53 psig at 1009 seconds and 1475 seconds, respectively, in Figure 3.225. The first peak was achieved when the first cylinder of CO_2 ran out. Then the cylinder was refilled with CO_2 and heated up, during which the borehole pressure decreased due to CO_2 leakage through the concrete matrix. The second peak is the pressure CO_2 broke through the concrete sample (fracture initiation and propagation). It was achieved during the injection of the second cylinder of CO_2 and the temperature was 39.86 °C. Thus, the CO_2 in borehole was in a supercritical state before it broke through the concrete block. After breakthrough, the borehole temperature instantly dropped several degrees, as shown in Figure 3.226. In Figure 3.224, on the x-axis stress loading, the CO_2 injection induced fracturing generated a small stress response at the breakthrough point.

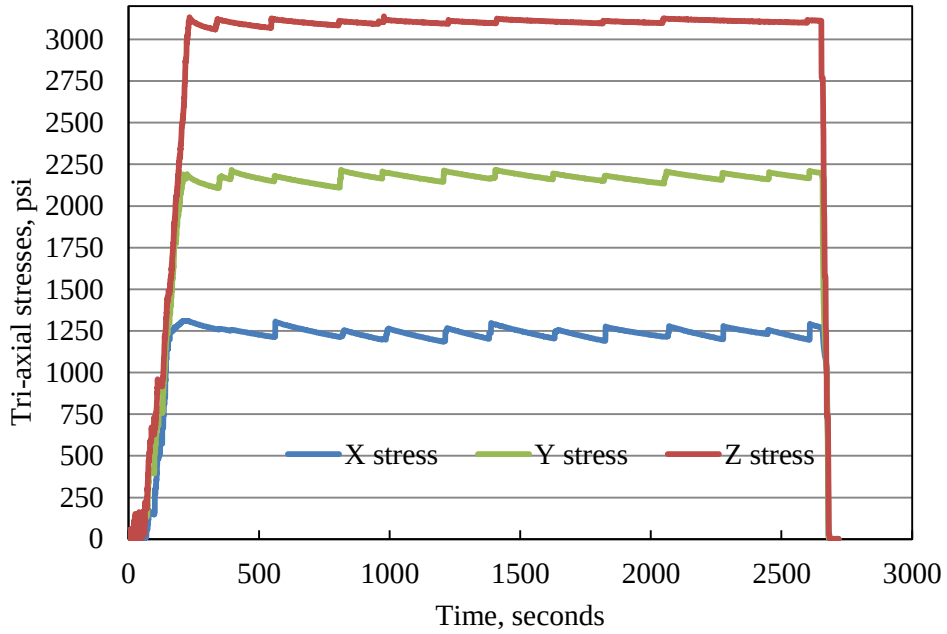

Figure 3.223. Tri-axial stress loading before CO_2 injection into Sample 55.

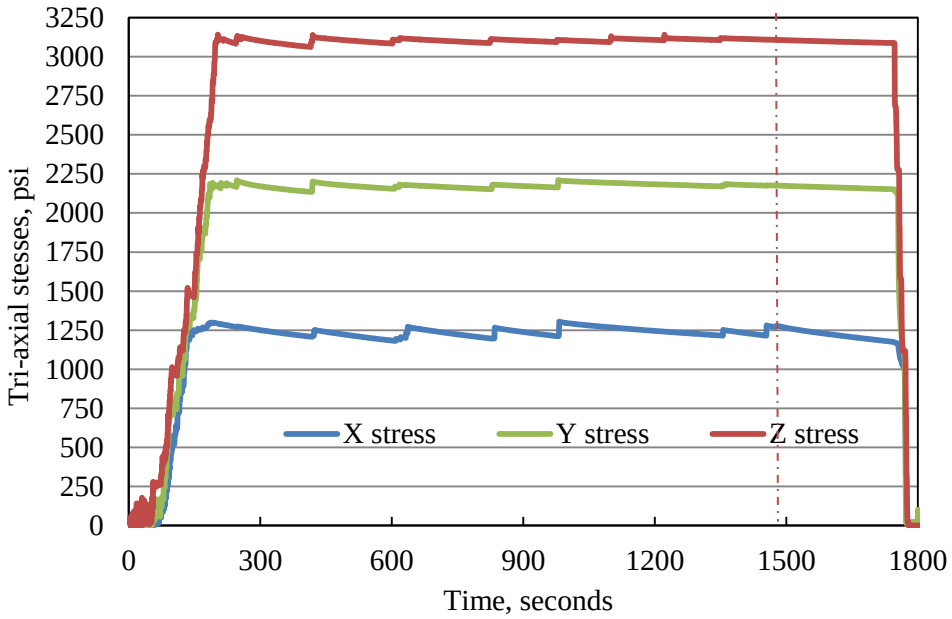

Figure 3.224. Tri-axial stress loading for CO_2 injection into Sample 55.

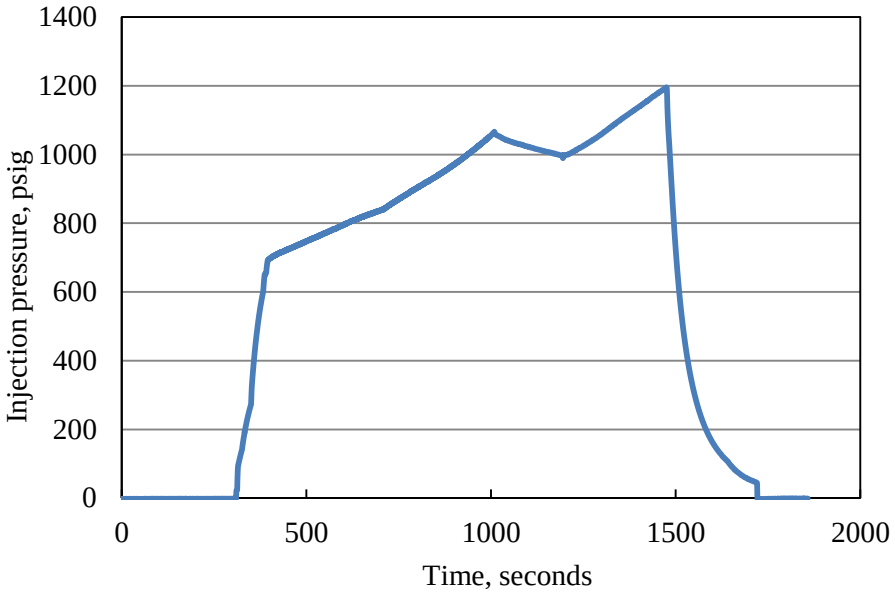

Figure 3.225. CO_2 injection pressure of Sample 55.

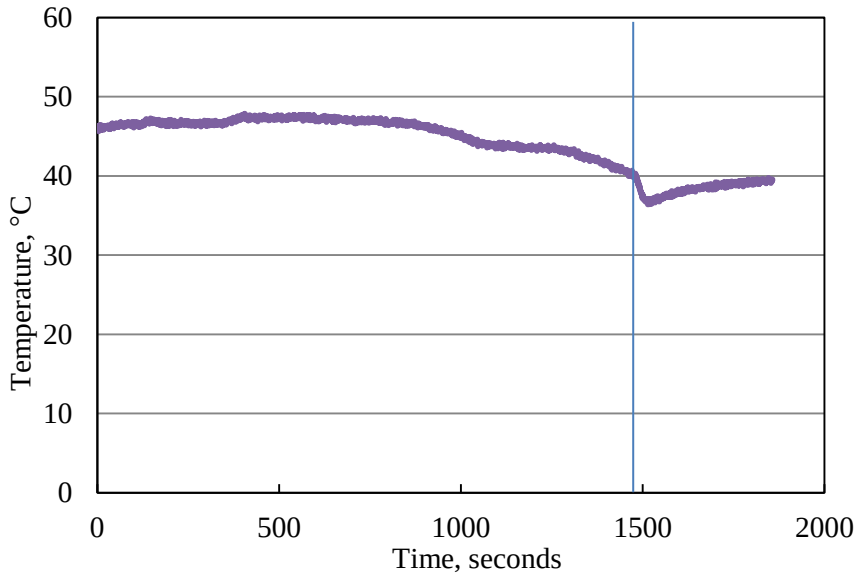

Figure 3.226. Borehole temperature profile during injection for Sample 55.

Pressure decay curves measured before and after sc-CO_2 injection for Sample 55 were compared in Figure 3.227, which shows significant permeability enhancement of the concrete block due to injection induced fractures.

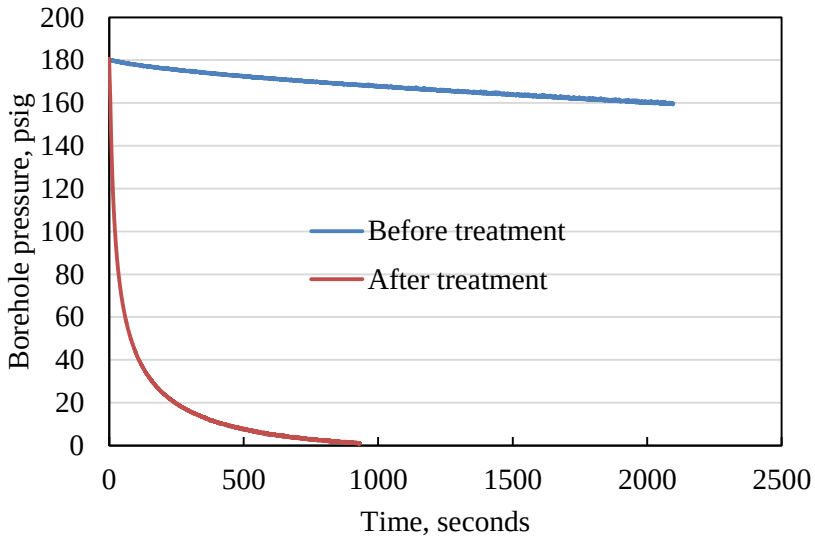

Figure 3.227. Pressure decay curves before and after CO_2 injection for Sample 55.

Acoustic signatures before and after CO_2 injection for Sample 55 are compared in Figures 3.228 through 3.233. Both P-waves and S-waves show delays in arrival time and changes in waveforms after CO_2 injection, indicating existence of injection induced fractures inside the concrete sample.

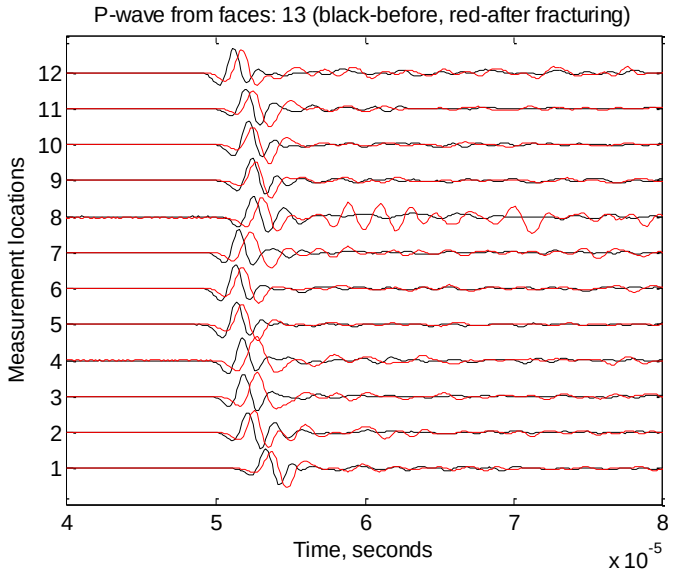

Figure 3.228. P-wave signatures measured from Surface 1 and Surface 3 of Sample 55.

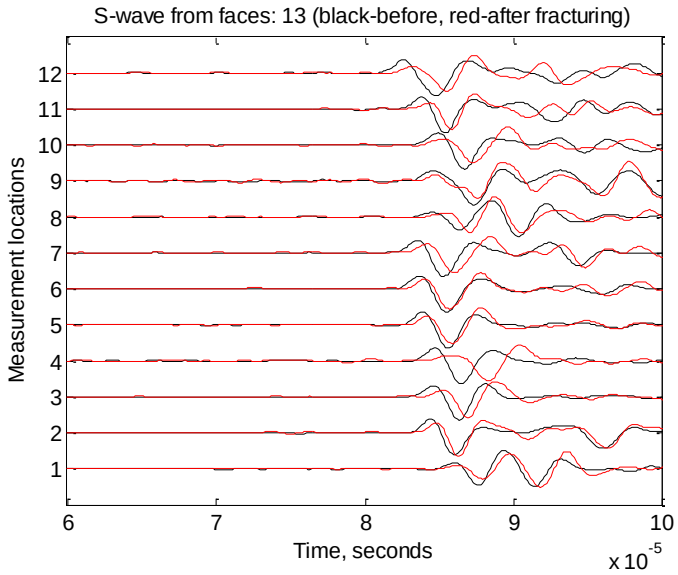

Figure 3.229. S-wave signatures measured from Surface 1 and Surface 3 of Sample 55.

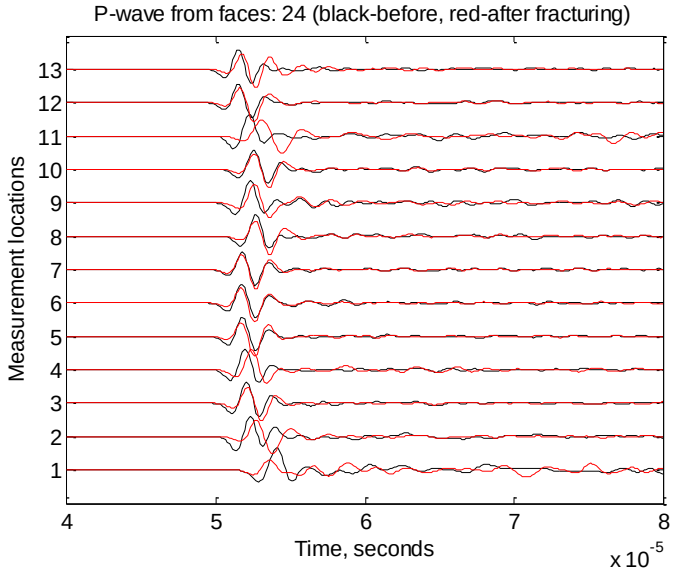

Figure 3.230. P-wave signatures measured from Surface 2 and Surface 4 of Sample 55.

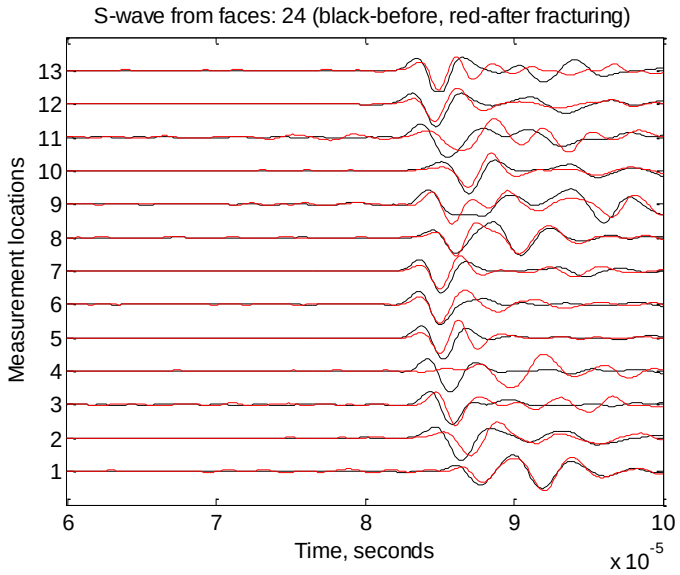

Figure 3.231. S-wave signatures measured from Surface 2 and Surface 4 of Sample 55.

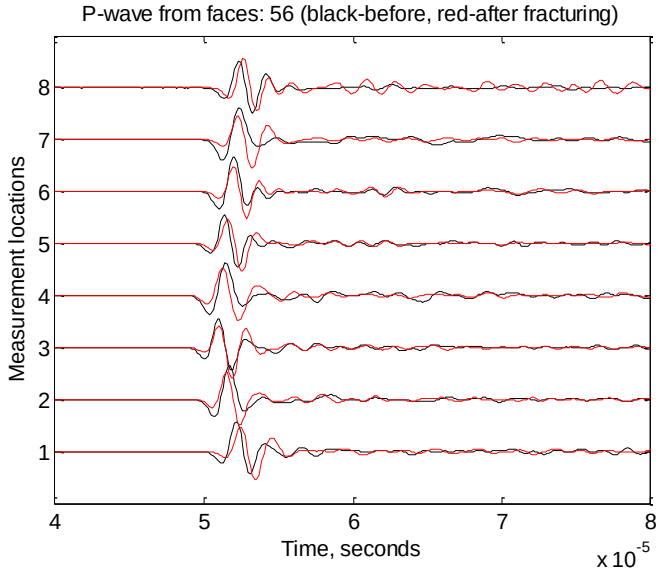

Figure 3.232. P-wave signatures measured from Surface 5 and Surface 6 of Sample 55.

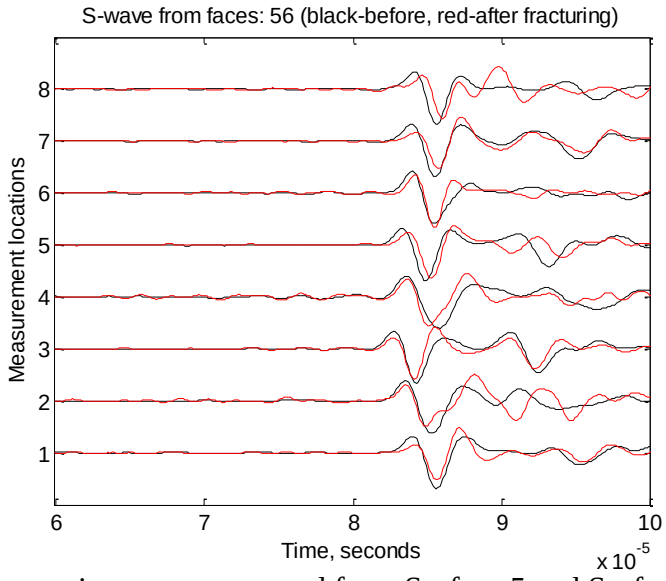

Figure 3.233. S-wave signatures measured from Surface 5 and Surface 6 of Sample 55.

Dye solution was then injected into the borehole of Sample 55 to color the CO_2 injection induced fractures, through which dye solution flowed out of the block surface. Then, under tri-axial stress loading, shown in Figure 3.234, the sample was fractured by injecting nitrogen gas, and the pressure profile is shown in Figure 3.235. Peak pressure of gas fracturing is 974.76 psi at 353 seconds, which corresponds to a stress loading response in the x-axis direction in Figure 3.234. Finally, the sample was broken down by nitrogen gas under no confining stress, and the breakdown pressure is 112.31 psig, as shown in Figure 3.236.

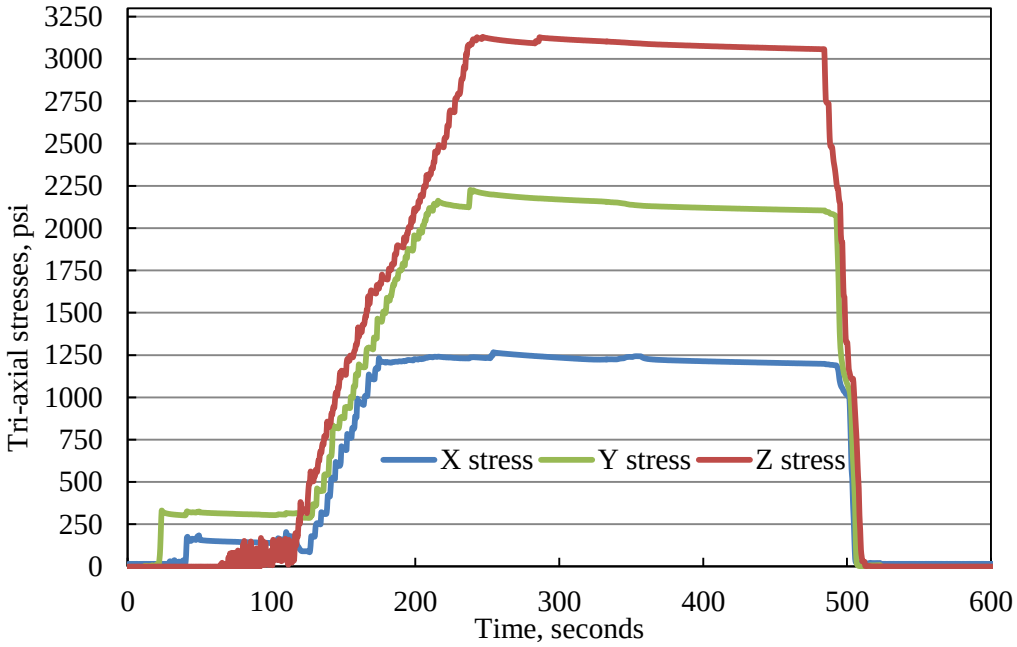

Figure 3.234. Tri-axial stress loading for CO_2 injection into Sample 55.

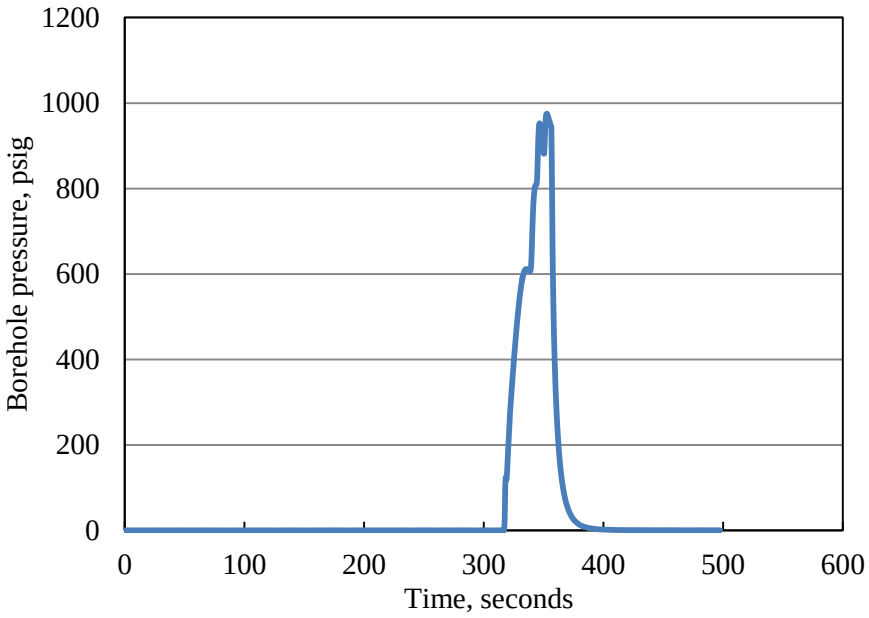

Figure 3.235. Gas fracturing pressure of Sample 55 under tri-axials tress loading.

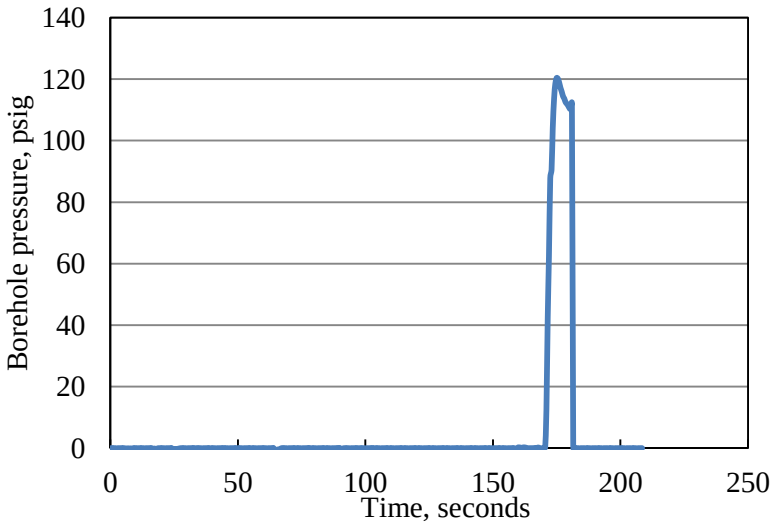

Figure 3.236. Gas fracturing pressure of Sample 55 without tri-axial stress loading.

Coloring and gas fracturing revealed the fracture generated by CO_2 injection, as shown before and after in Figures 3.237 and 3.238 and in Figure 3.239. The major fracture planes are nearly perpendicular to the minimum horizontal stress direction.

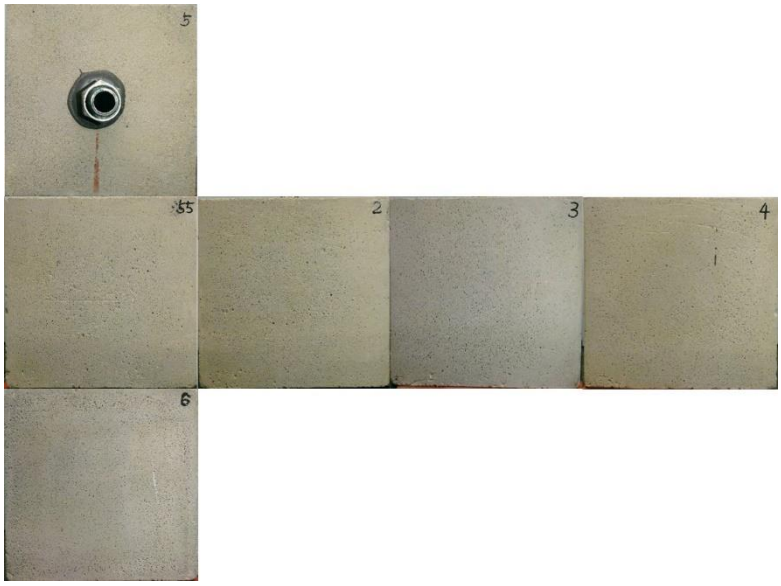

Figure 3.237. Intact surfaces of Sample 55.

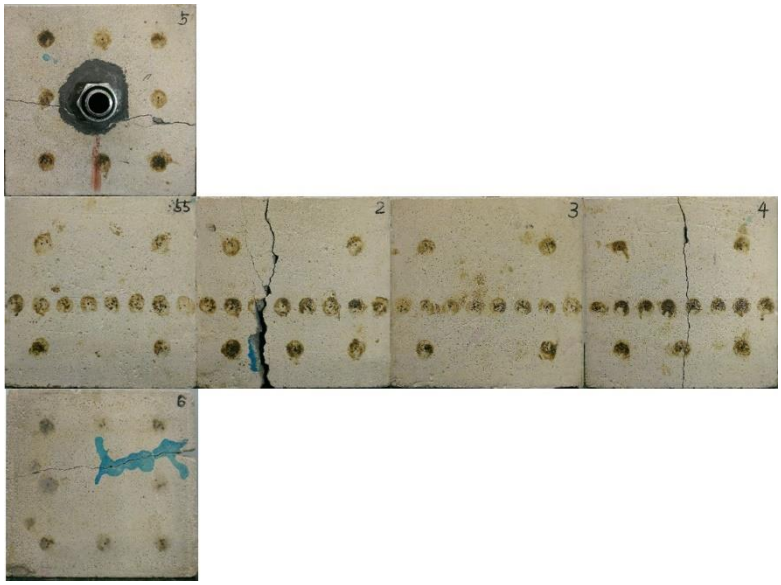

Figure 3.238. Surfaces of Sample 55 after dyeing and gas fracturing.

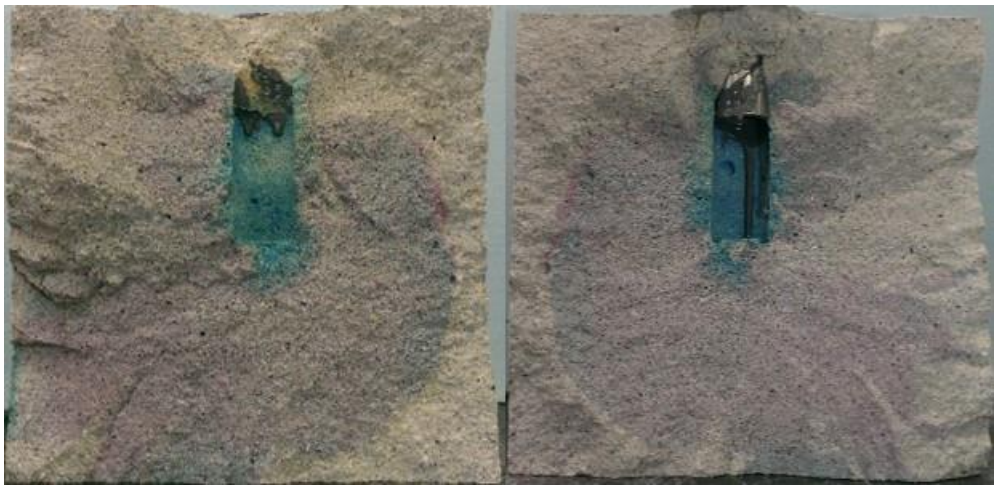

Figure 3.239. CO_2 injection induced fracture morphology of Sample 55 after dyeing and gas breakdown.

Concrete Sample 56

Sample 56 was first treated by applying a pre-injection stress loading of 1250 psi in the x-direction, 1562 psi in the y-direction, and 1875 psi in the z-direction for 43 minutes, as shown in Figure 3.240. Then, acoustic signatures were measured as reference for post-injection comparison and pressure decay was carried out for pre-treatment permeability evaluation. Afterwards, the sample was treated by injecting CO_2 under the same tri-axial stress loading, shown in Figure 3.241. Two cylinders of CO_2 were pumped, thus there were two peaks on the pressure profile in Figure 3.242. The second peak of 1218.29 psig at 764 seconds is lower than the first one of 1289.79 psig at 477 seconds; also the second peak did not spike as the first one did. It was speculated that at the first peak fractures were initiated, and the injection of the second cylinder further propagated the fractures. The temperatures at these two pressure peaks were 44.68°C and 40.93°C, respectively, shown in Figure 3.243. In Figure 3.241, there were no obvious stress responses at either 477 seconds or 764 seconds.

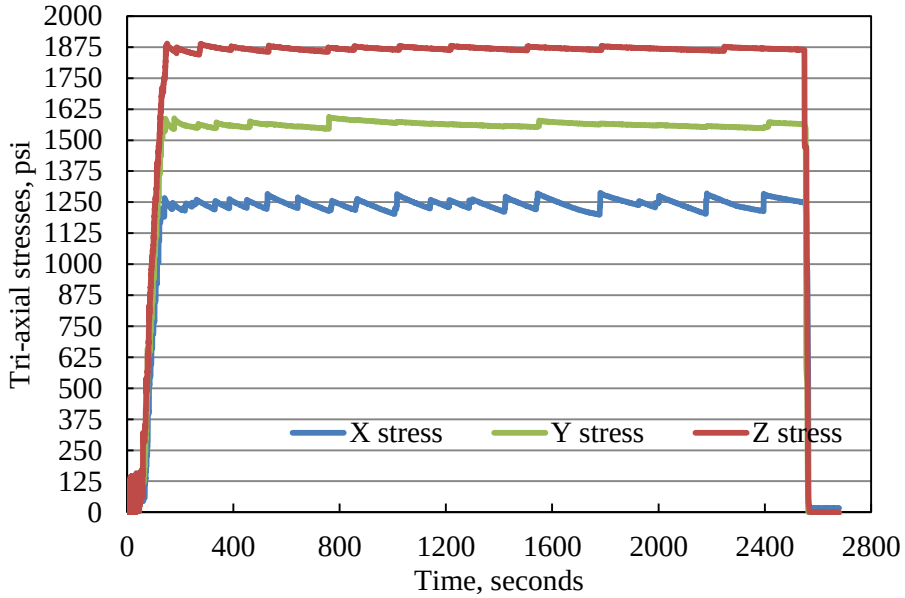

Figure 3.240. Pre-injection stress loading on Sample 56.

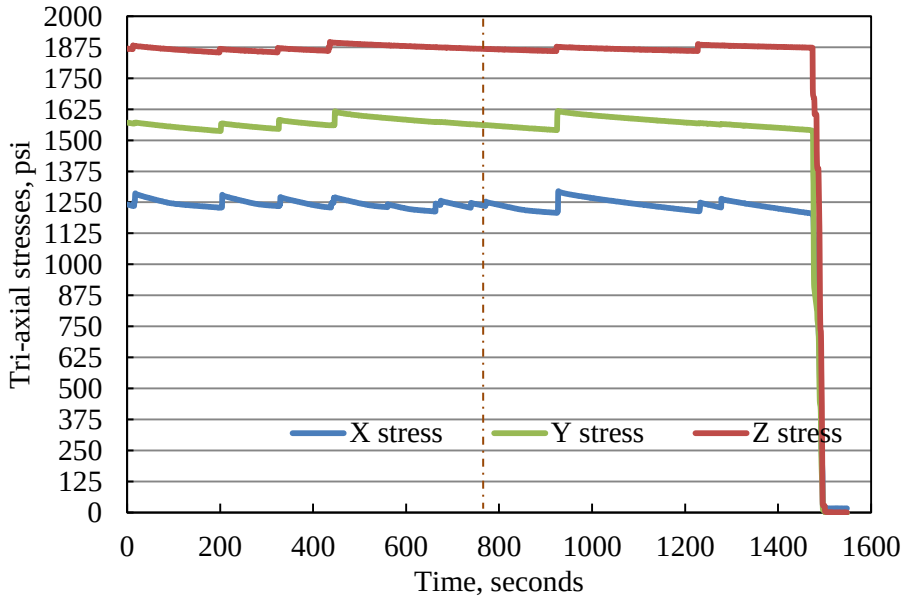

Figure 3.241. Stress loading for CO_2 injection into Sample 56.

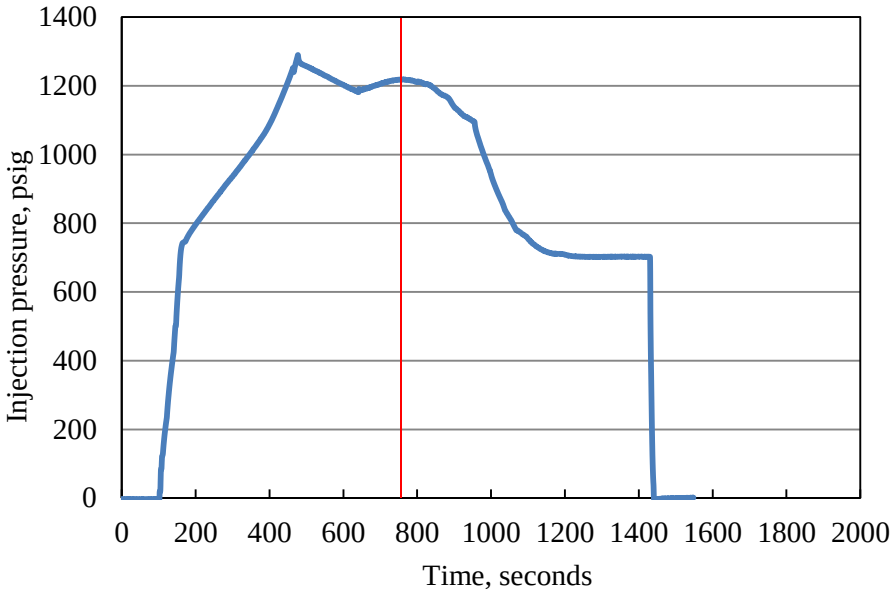

Figure 3.242. CO_2 injection pressure for Sample 56.

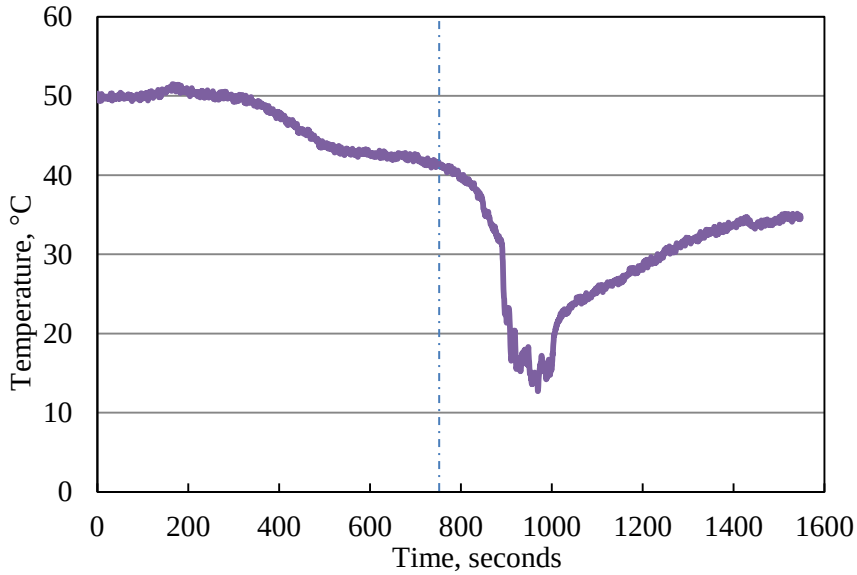

Figure 3.243. Borehole temperature during CO_2 injection into Sample 56.

Figure 3.244 compares the pressure decay curves measured before and after CO_2 injection. It is clear that the pressure decay curve after fracturing almost overlaps with that before fracturing, indicating that the CO_2 injection induced fractures are highly confined inside the sample and did not effectively propagate to the surface of the concrete block. Also from the injection pressure profile in Figure 3.241, it can be seen that after 1200 seconds, the borehole pressure leveled out at about 702 psi, i.e. the tri-axial stresses and the tensile strength equilibrated with the CO_2 pressure at high level. This is different from most of the other CO_2 fracturing experiments, where borehole pressure kept decreasing to very low values.

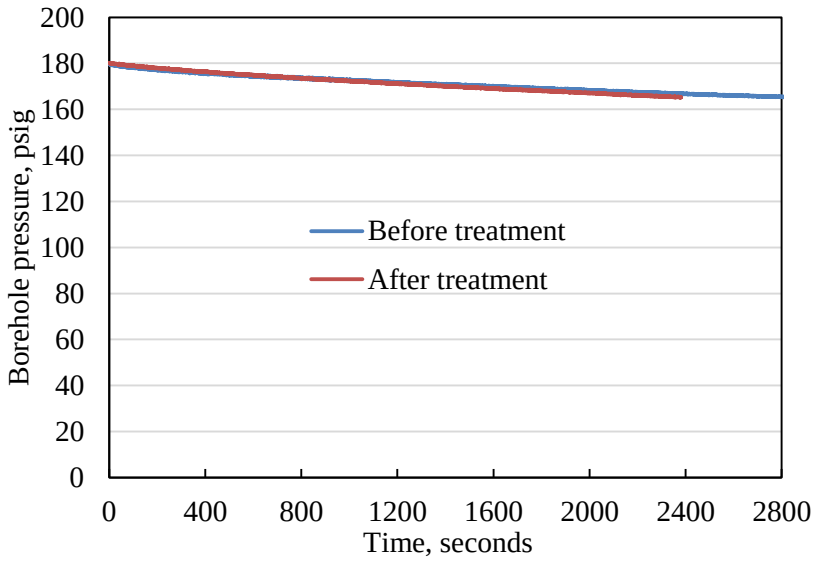

Figure 56-3.244. Pressure decay curves before and after CO_2 injection for Sample 56.

Acoustic signatures for sample 56 before and after CO_2 injection are compared in Figures 3.245 through 3.250. Both P-waves and S-waves show delays in arrival time and changes in waveforms after CO_2 injection, indicating that CO_2 injection induced fractures inside the concrete block.

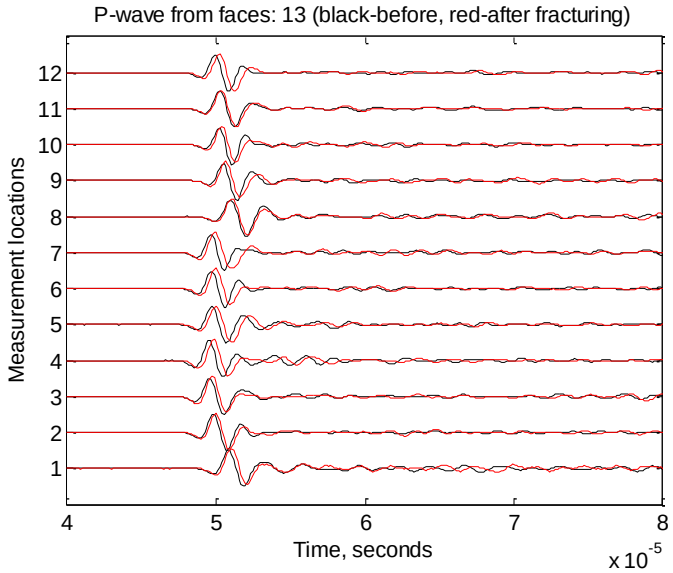

Figure 3.245. P-wave signatures measured from Surface 1 and Surface 3 of Sample 56.

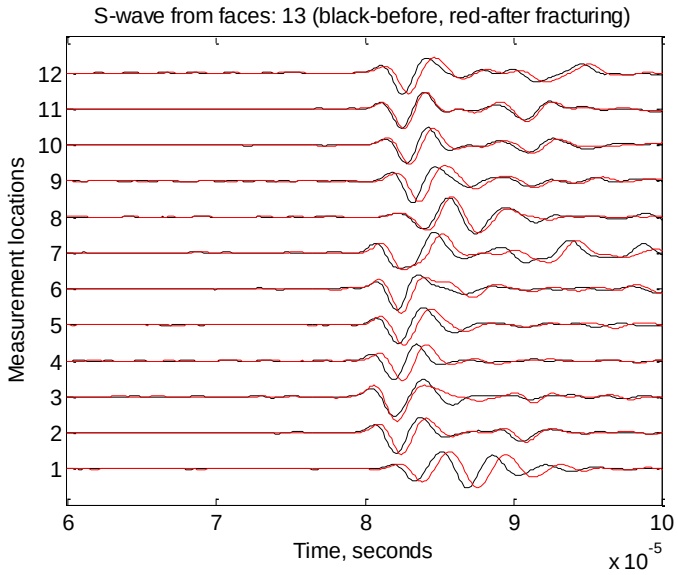

Figure 3.246. S-wave signatures measured from Surface 1 and Surface 3 of Sample 56.

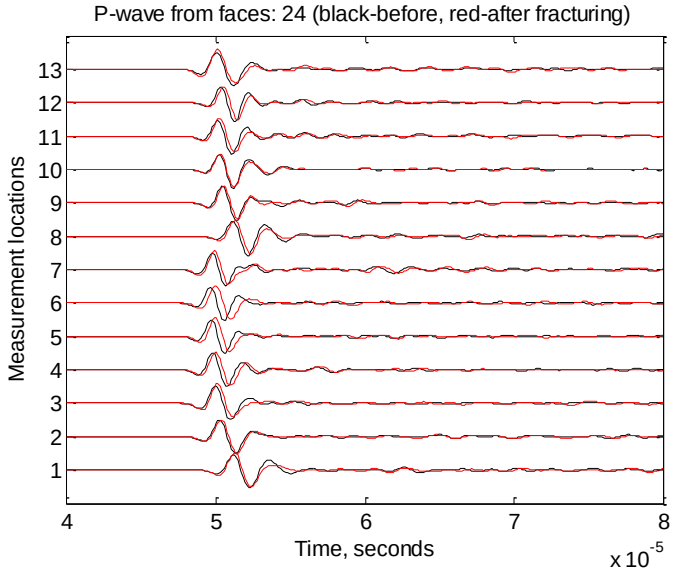

Figure 3.247. P-wave signatures measured from Surface 2 and Surface 4 of Sample 56.

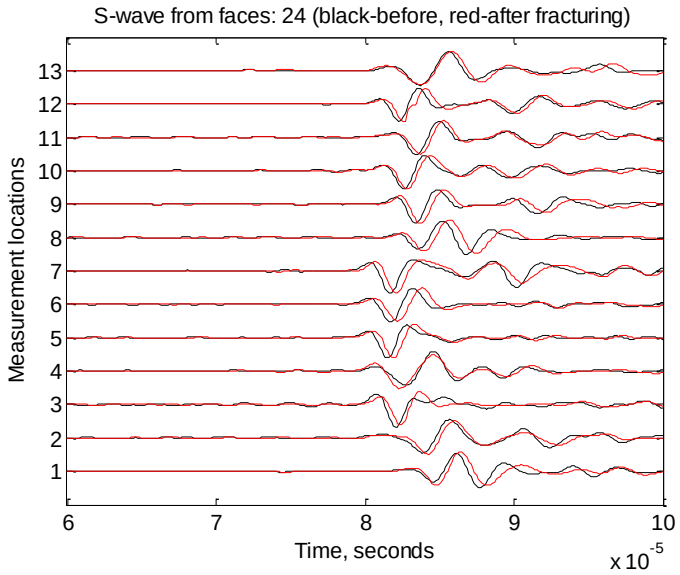

Figure 3.248. S-wave signatures measured from Surface 2 and Surface 4 of Sample 56.

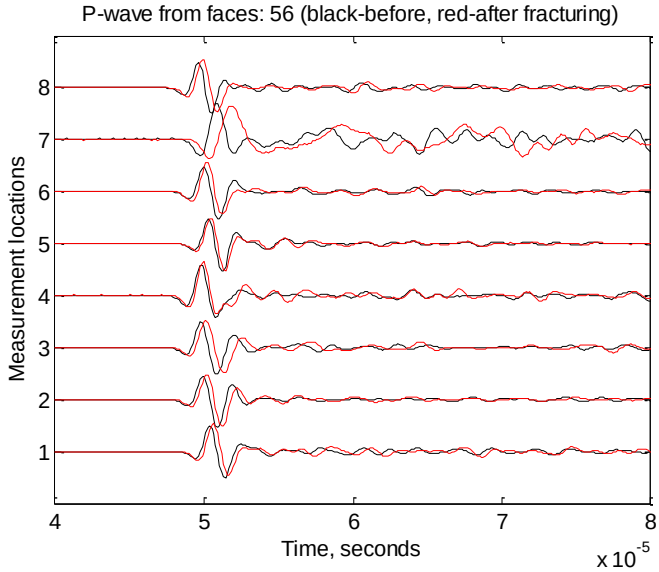

Figure 3.249. P-wave signatures measured from Surface 5 and Surface 6 of Sample 56.

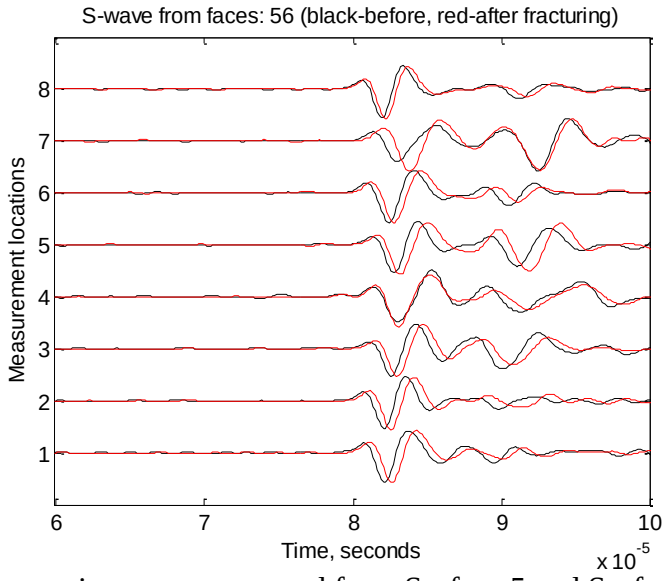

Figure 3.250. S-wave signatures measured from Surface 5 and Surface 6 of Sample 56.

Dye solution was then injected into Sample 56 to color the CO_2 injection induced fractures, however no dye solution was observed flowing out of the block surface. Thus, it can be inferred that there are no fractures propagating through the concrete block. Then the sample was fractured by high pressure nitrogen gas under tri-axial stress conditions, shown in Figure 3.251. The gas pressure reached a peak of 1447.19 psig, shown in Figure 3.252, much higher than the CO_2 breakthrough pressure. At the fracturing point, x-axis stress rose up a little while y-axis and z-axis stresses slightly dropped, shown in Figure 3.251. Finally, the concrete sample was broken down at 220.81 psig under no confining stress by injecting nitrogen gas, shown in Figure 3.253.

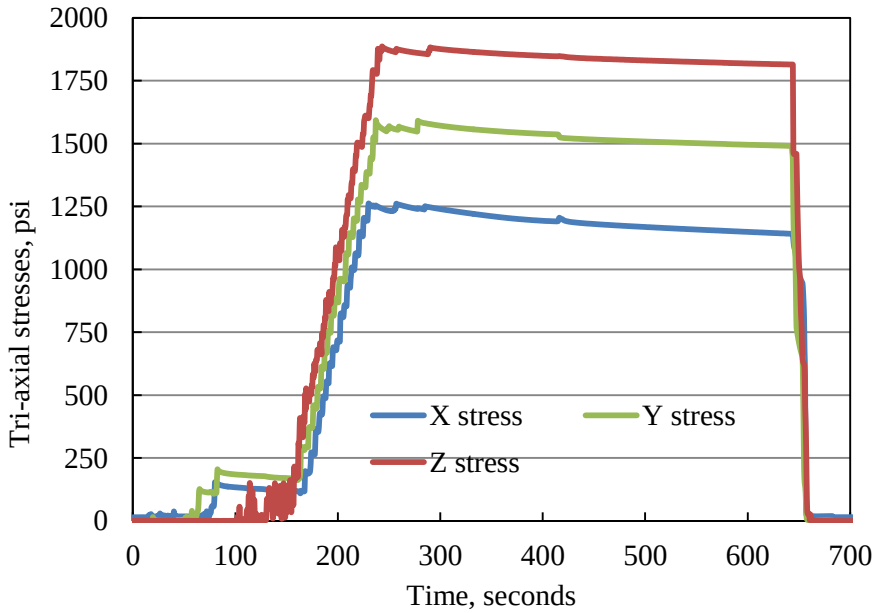

Figure 3.251. Stress loading for gas fracturing of Sample 54.

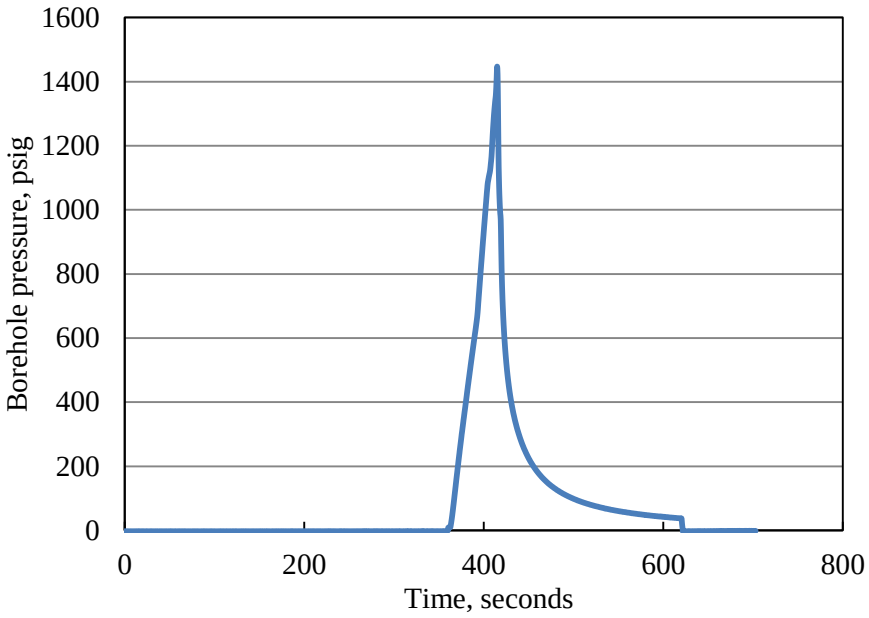

Figure 3.252. Gas fracturing pressure of Sample 55 under tri-axials stress loading.

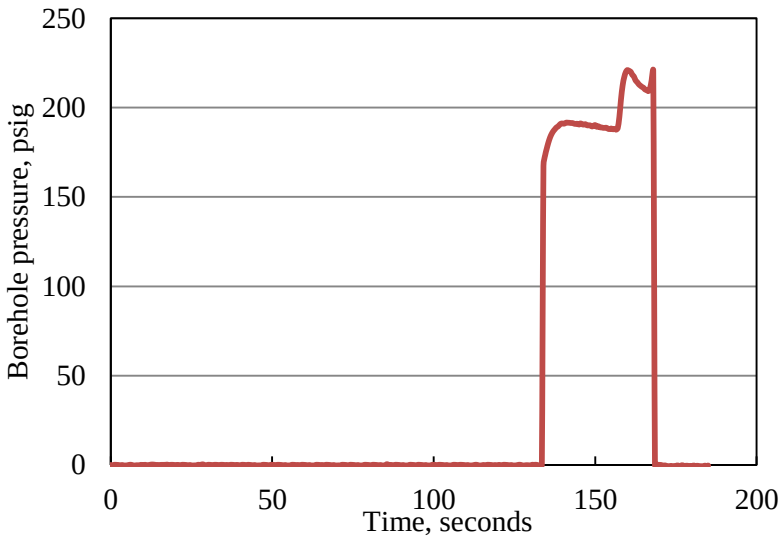

Figure 3.253. Gas fracturing pressure of Sample 56 without tri-axials stress loading.

Dyeing and gas fracturing revealed the fractures induced by CO_2 injection. As shown before and after in Figures 3.254 and 3.255, after in Figure 3.256, gas fracturing there consists of one major fracture propagating perpendicular to the x-axis direction. CO_2 injection induced fractures are very small in size, and the other major fracture plane nearly perpendicular to the z-axis direction. Figure 3.256 presents the CO_2 injection induced fractures colored by dye solution, it can be seen that the induced fractures are very small in length and are highly confined near the wellbore. These small fractures contribute little to the permeability of the concrete block, thus pressure decay after fracturing is almost the same as that before. Considering that pressure dropped remarkably before 1200 seconds and leveled out around 702 psig afterwards during the CO_2 injection as well as the gas fracturing pressure is much

higher than CO_2 peak pressures, it can be deduced that the tensile strength of this concrete block is extremely high, thus preventing the fracture propagation throughout the block during the CO_2 injection.

Figure 3.254. Intact surfaces of Sample 56 before treatment.

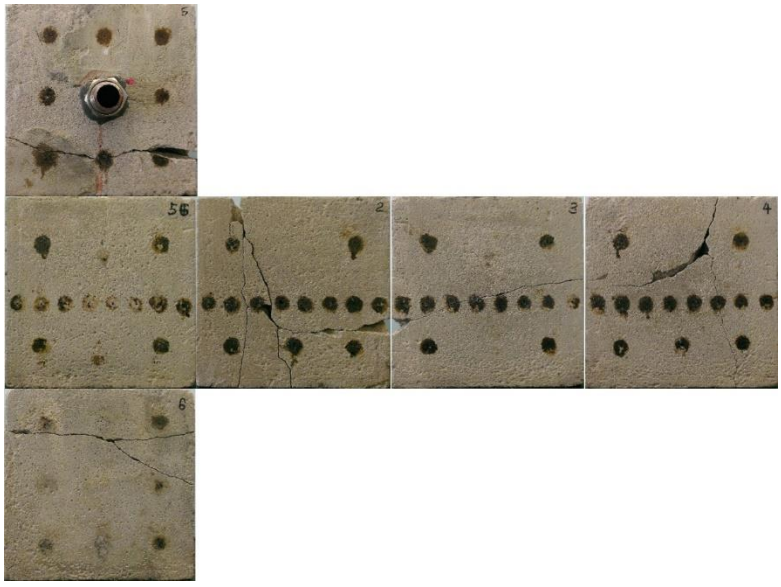

Figure 3.255. Surfaces of Sample 56 after dyeing and gas fracturing.

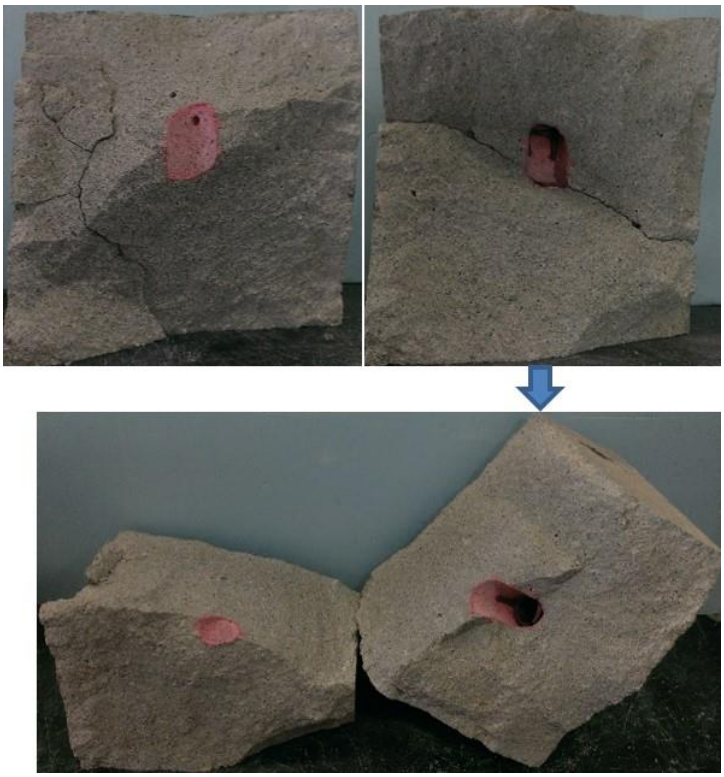

Figure 3.256. Injection induced fracture morphology of Sample 56 after dyeing and gas breakdown.

Generally, peak pressures during CO_2 injection increase with elevating tri-axial stress levels, and increase of stress difference among the axes reduces the CO_2 fracturing pressures. Also, as the tri-axial stresses increase, the observed fracture lengths colored by dye get shorter and the fracture planes become more and more confined to the wellbore. By increasing the stress difference among axes, the CO_2 injection induced fractures become larger, as is also indicated by the decreasing gas N_2 fracturing pressures under both confined and unconfined conditions. In a word, higher tri-axial stresses confine the development of injection induced fractures more to the wellbore, while larger stress differences are favorable for generation of fractures.

In our next experiments, we conducted sc-CO_2 injection induced fracturing experiments on three concrete samples (Samples 57-59) with pre-existing hydraulic fractures on x-z surface near the wellbore, where the borehole temperature and injection pressure were above supercritical conditions. Then, we conducted sc-CO_2 injection induced fracturing experiments on two water saturated concrete samples (Samples 62-63) with borehole temperature and injection pressure above supercritical conditions. The injection rate was kept constant at 10 ml/min or 40 ml/min. The tri-axial stress loading levels and differences were changed to investigate the effect of *in-situ* stress on the peak pressure or fracturing pressure values during CO_2 injection into these samples.

Concrete Sample 57

Sample 57 was treated by injecting CO_2 under a tri-axial stress loading of 1260 psi in the x-direction, 1562 psi in the y-direction, and 1875 psi in the z-direction. Before the treatment, it was pre-loaded with the same stresses of xyz=1500 psi for about 40 minutes, as shown in Figure 3.257. Then acoustic signatures were measured as reference for post-injection comparison, and pressure decay was carried out for pre-treatment permeability evaluation.

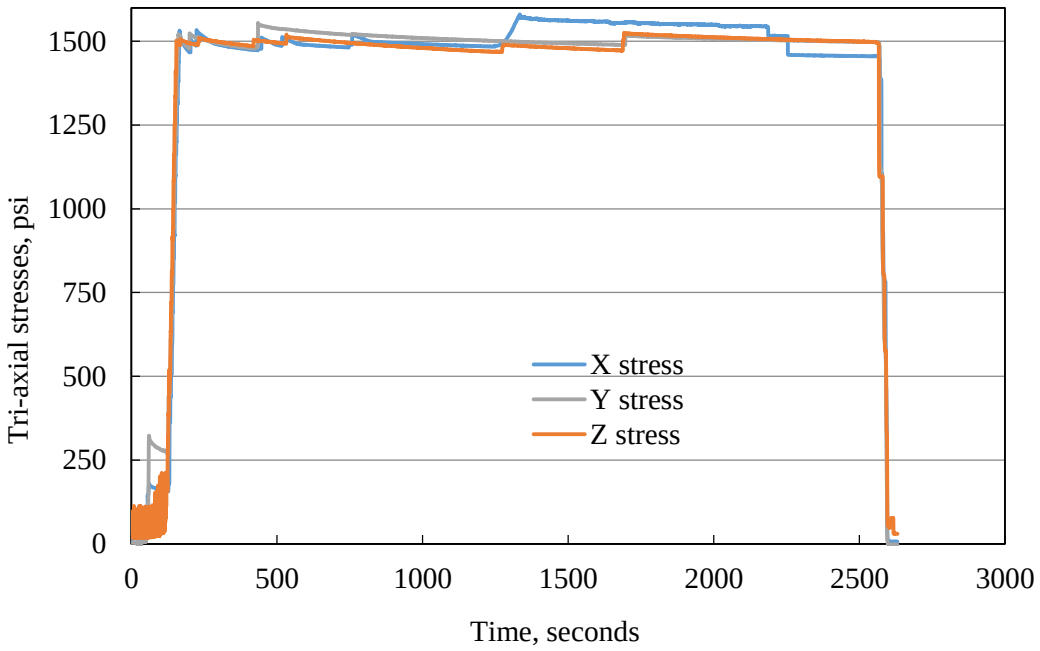

Figure 3.257. Pre-injection tri-axial stress loading for Sample 57.

Sample 57 was then treated by injecting red dye into the borehole to make a seeding fracture on the xz surface at a constant rate of 1.0 ml/min under tri-axial stress of 1500 psi in the x-direction, 1000 psi in the y-direction, and 2000 psi in the z-direction, as shown in Figure 3.259. The injection pressure and borehole temperature profiles are shown in Figures 3.259 and 3.260. The temperature for water injection was around 21 ºC since it was conducted at room temperature. The highest pressure peak of 1346 psi was achieved at 980 seconds and the pump was stopped at the same time. After the peak pressure, an obvious stress response on the y-axis stress loading at 988 seconds, indicating that the seed fracture planes were generated perpendicular to the y-axis.

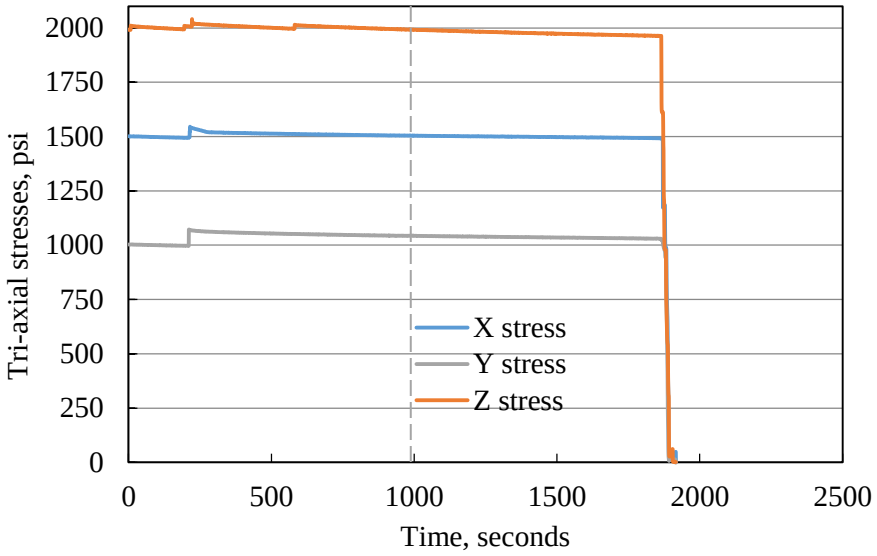

Figure 3.258. Tri-axial stress loading for water injection into Sample 57.

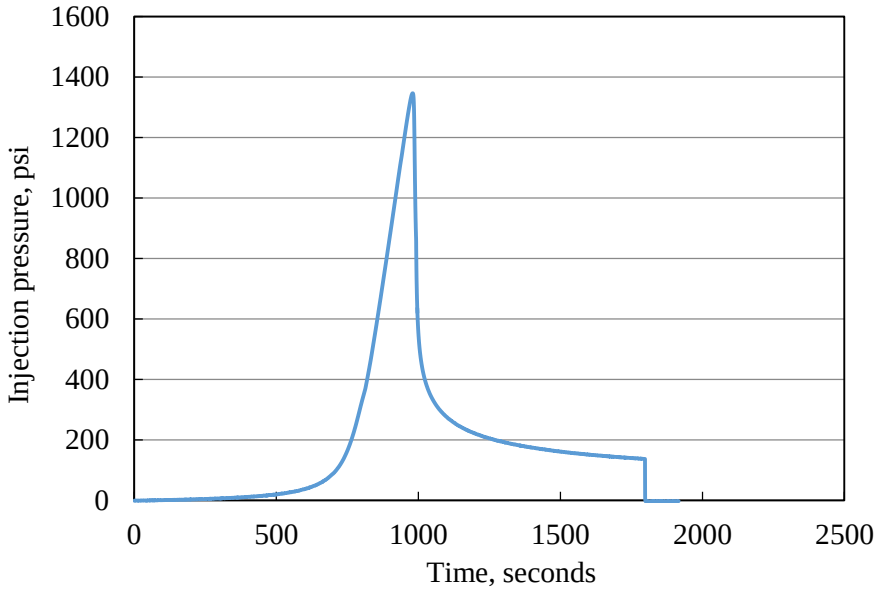

Figure 3.259. Pressure profile for water injection into Sample 57.

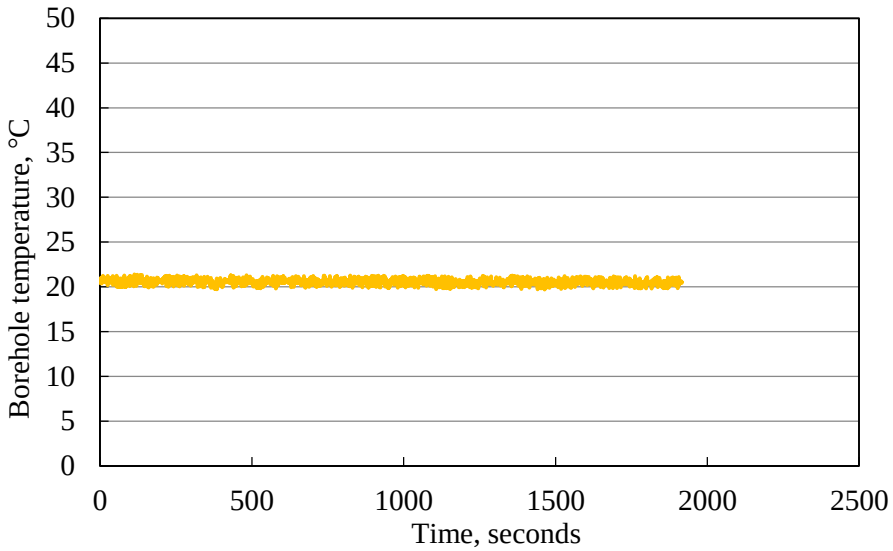

Figure 3.260. Borehole temperature profile during water injection into Sample 57.

After water injection, the Sample 57 was heated at 60 ℃ for more than 8 hours to dry the sample and dye the seed fracture. Then, acoustic signatures were measured as reference for post-injection comparison, and pressure decay was carried out for pre-treatment permeability evaluation. Next, the sample was re-heated to 60 ℃ and treated by injecting CO_2 into the borehole at a constant rate of 10 ml/min under tri-axial stress loading of 1250 psi in the x-direction, 1562 psi in the y-direction, and 1875 psi in the z-direction, as shown in Figure 3.261. The injection pressure and borehole temperature profiles are shown in Figure 3.262 and 3.263. We injected one cycle of CO_2 to fracture Sample 57. Since no heating source was installed for the concrete sample, the borehole temperature gradually decreased. When the highest pressure peak of 1548.94 psi was achieved at 55.5 seconds, the borehole temperature was 44.23°C, much higher than the supercritical temperature, thus Sample 57 was fractured under supercritical conditions. There is a very small stress response on the y-axis stress loading around 58.5 seconds, after the pressure peak was reached, indicating that the major fracture planes were generated perpendicular to the y-axis. Thus, the sc-CO_2 induced fracture should be the extension of the seed fracture induced at the beginning. In addition, the temperature drastically dropped right after the fracturing point, due to CO_2 leakage and expansion.

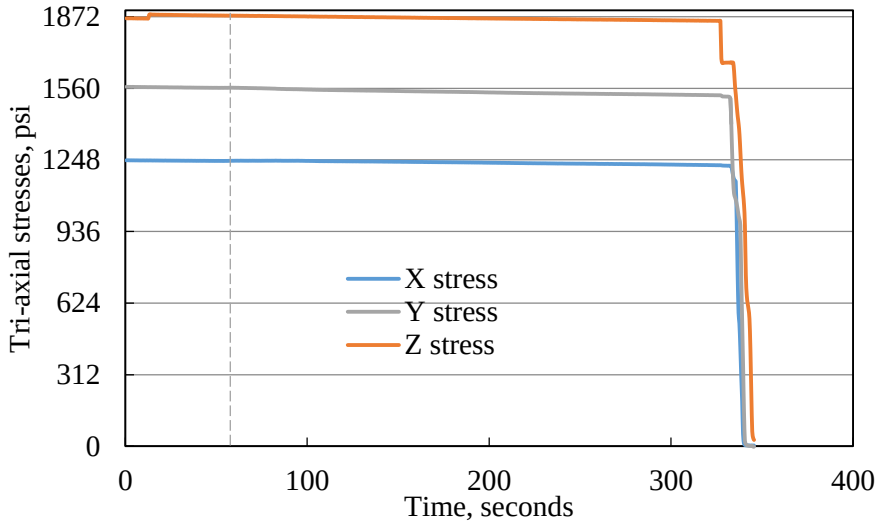

Figure 3.261. Tri-axial stress loading for sc-CO_2 injection into Sample 57.

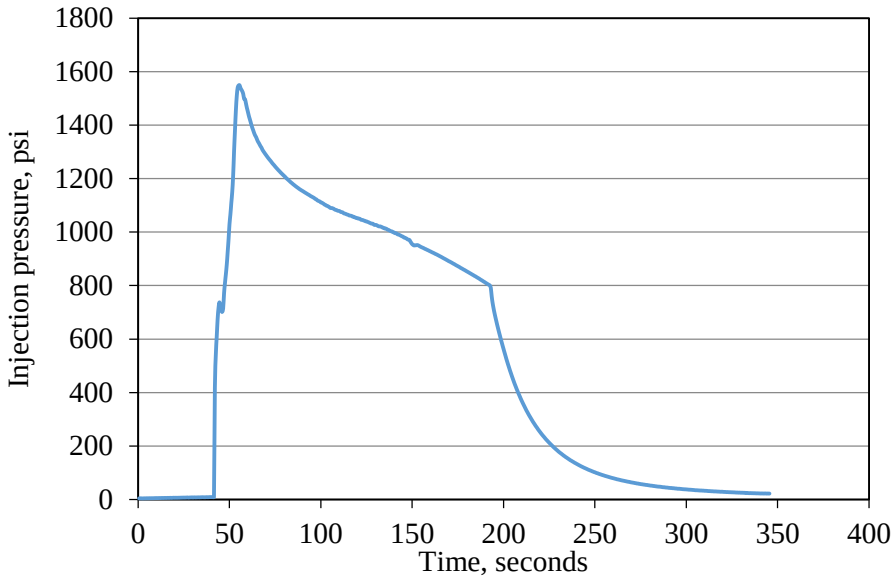

Figure 3.262. Pressure profile of sc-CO_2 injection into Sample 57.

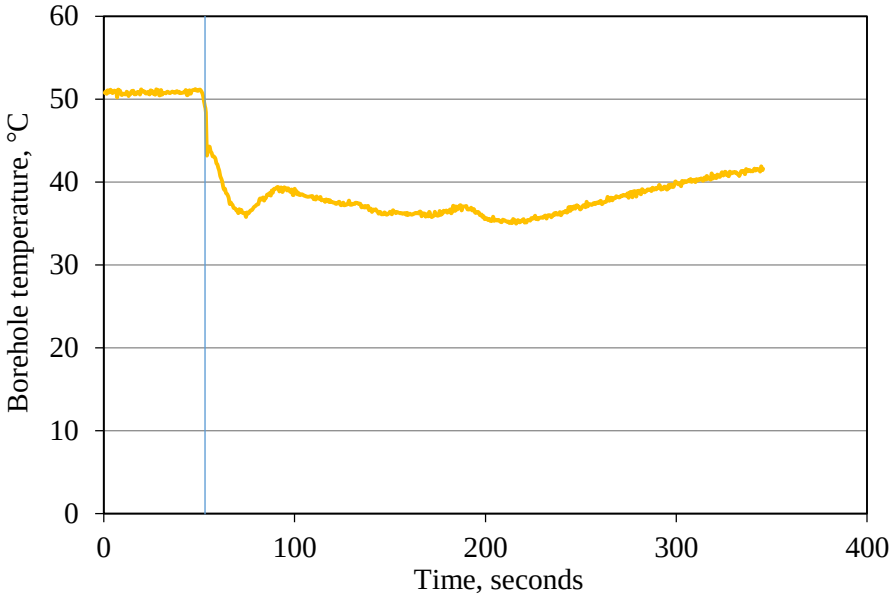

Figure 3.263. Borehole temperature profile during sc-CO_2 injection into Sample 57.

The gas leakage rate is not obvious after water injection, since the water induced fracture is very small compared to the borehole area as shown in Figure 3.264. But, the gas leakage rate significantly increased after CO_2 injection, due to fractures generated inside the concrete block.

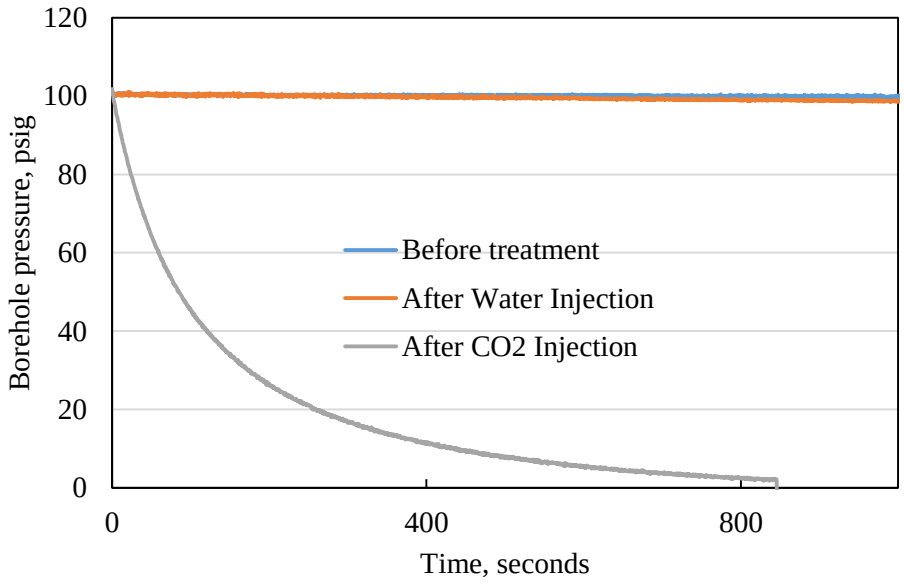

Figure 3.264. Pre- and post-injection pressure decay curves for Sample 52.

Acoustic signatures including P-waves and S-waves before and after dye injection and after CO_2 injection are compared in Figures 3.265 through 3.270. Both P-waves and S-waves show slight delays in arrival time, indicating that the major fracture planes are parallel to Surface 1 and Surface 3, Surface 2 and Surface 4, and Surface 5 and Surface 6. In general, the fracture planes generated

are perpendicular to the minimum horizontal stress, which is the x-direction, in agreement with fracturing principles. But the seeding fracture was generated before sc-CO_2 injection, and the seeding fracture is parallel to the minimum horizontal stress. This leads to CO_2 flow in seeding fracture first, and the CO_2 induced fracture turns its direction at its end - the fracture planes are complex in Sample 57.

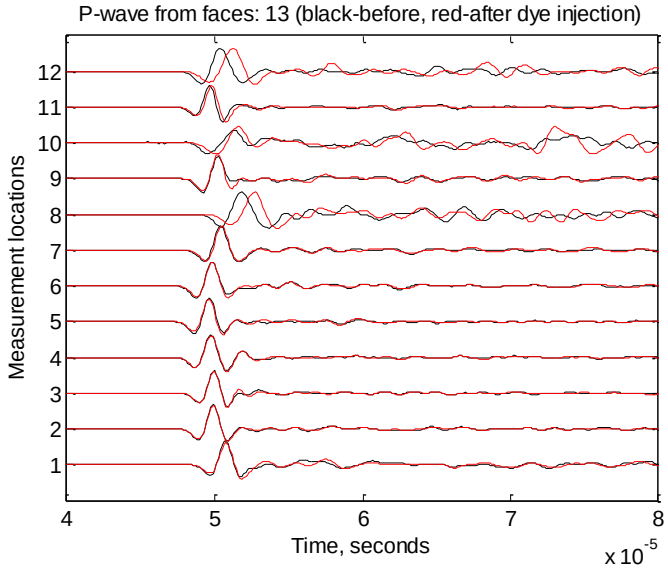

(a)

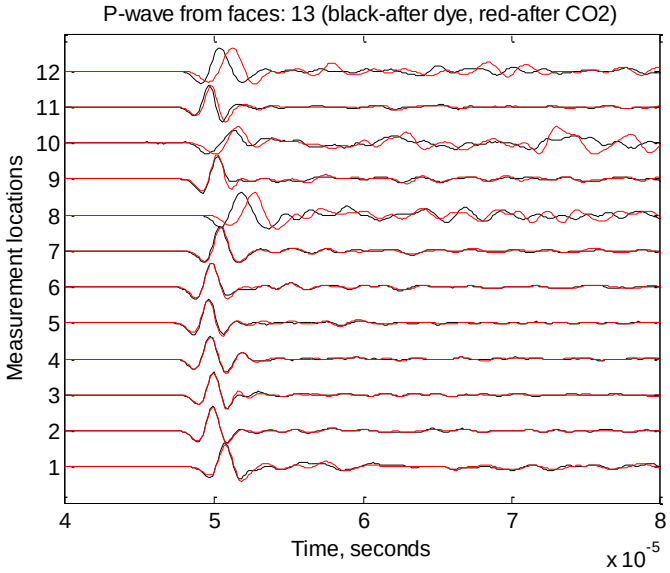

(b)

Figure 3.265. P-wave signatures measured from Surface 1 and Surface 3 of Sample 57.

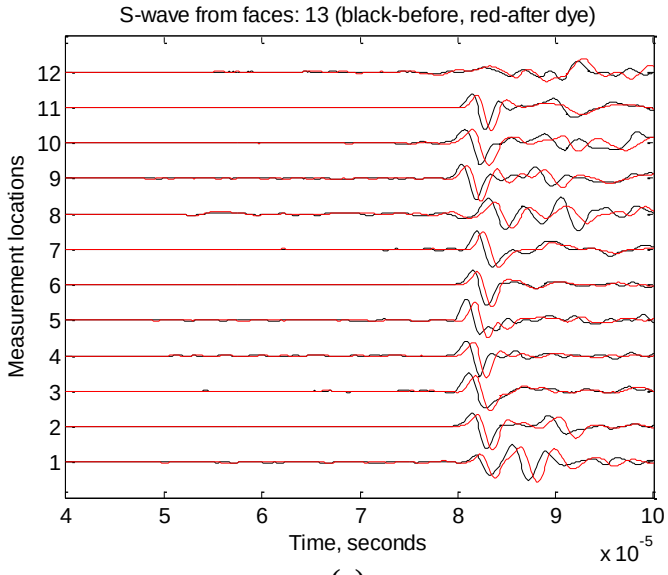

(a)

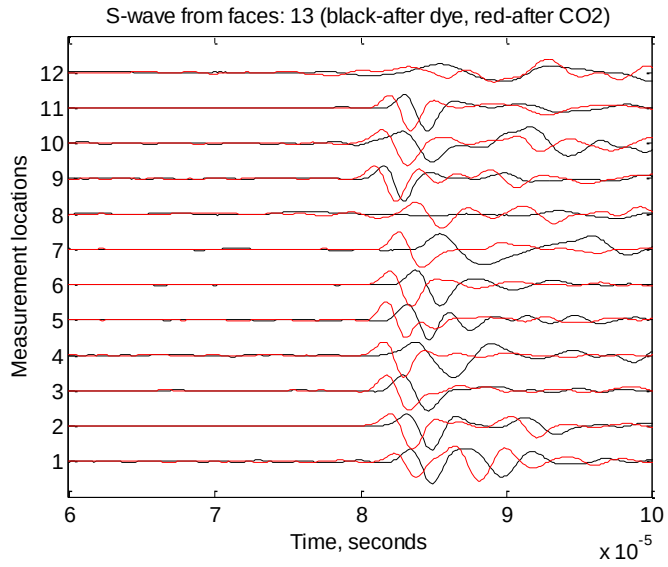

(b)

Figure 3.266. S-wave signatures measured from Surface 1 and Surface 3 of Sample 57.

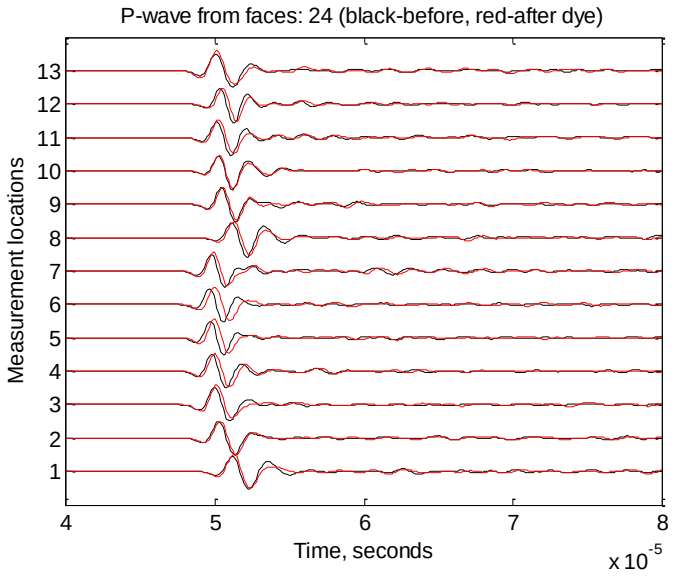

(a)

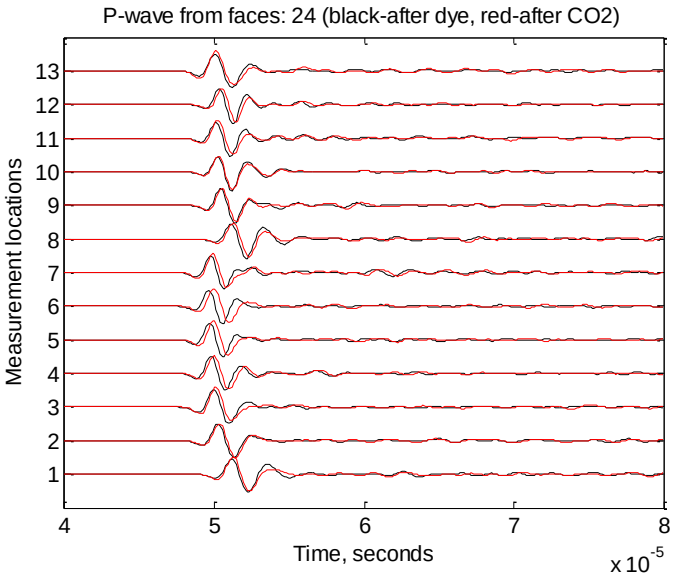

(b)

Figure 3.267. P-wave signatures measured from Surface 2 and Surface 4 of Sample 57.

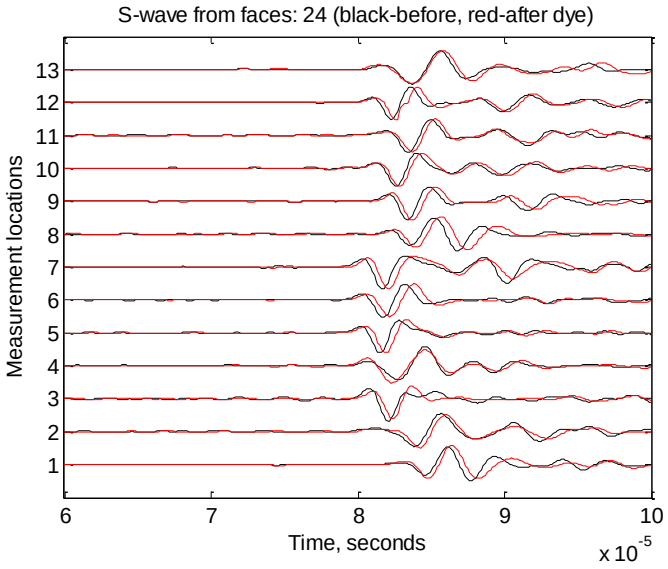

(a)

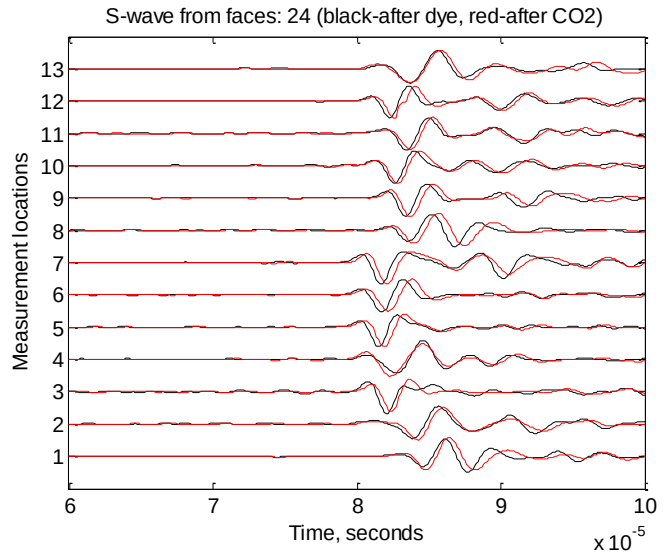

(b)

Figure 3.268. S-wave signatures measured from Surface 2 and Surface 4 of Sample 57.

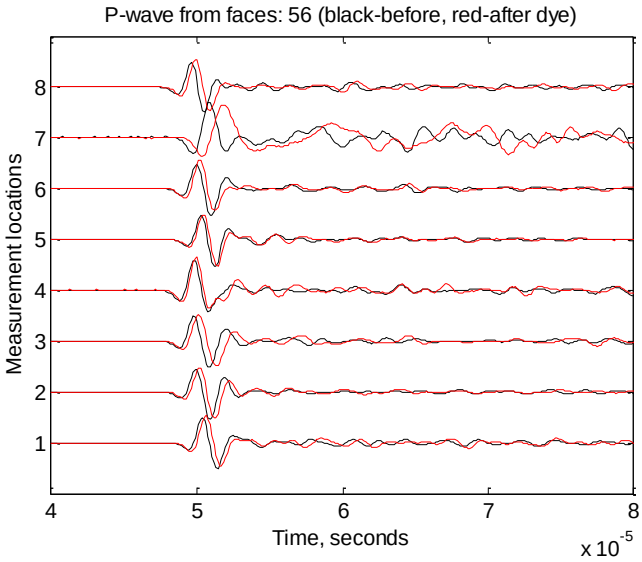

(a)

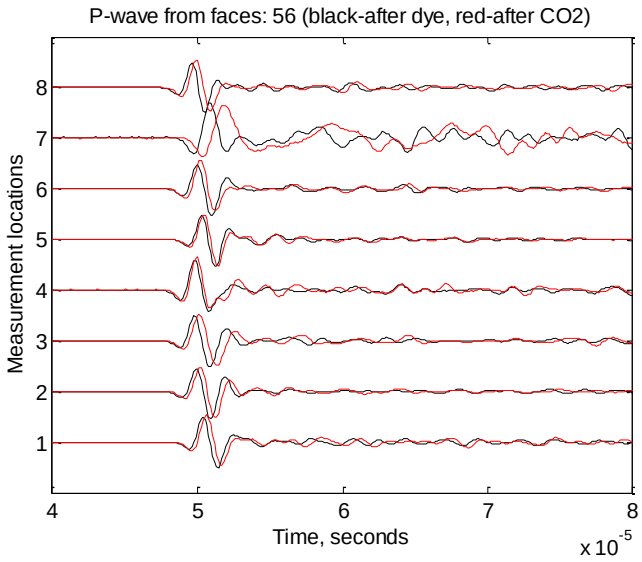

(b)

Figure 3.269. P-wave signatures measured from Surface 5 and Surface 6 of Sample 57.

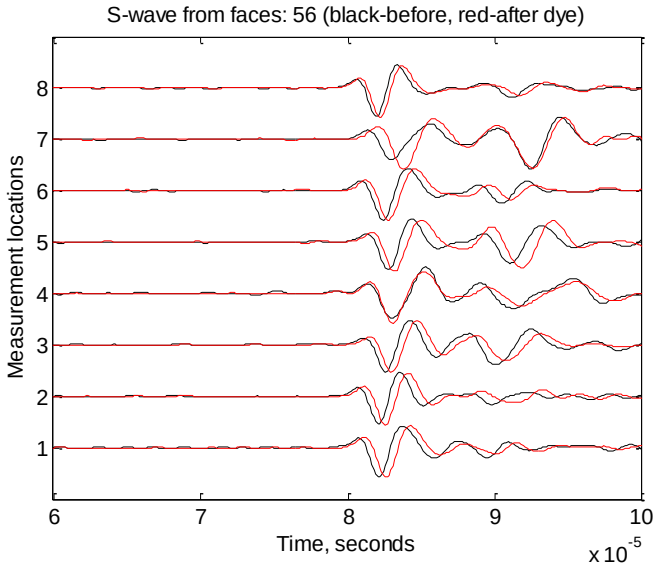

(a)

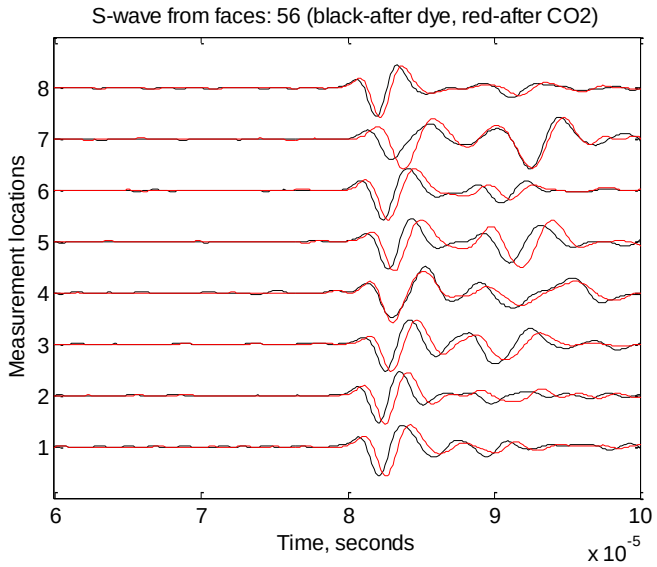

(b)

Figure 3.270. S-wave signatures measured from Surface 5 and Surface 6 of Sample 57.

Green dye solution was later injected into Sample 57 to color the fracture planes. Then, under tri-axial stress loading, shown in Figure 3.270, the sample was fractured by injecting nitrogen gas. The pressure profile is shown in Figure 3.271. The peak pressure is 1473.3 psig and the pressure mostly is stable above 1400 psi from 65-78 seconds. During that time, there are very small pressure peaks on all three axes. Finally, the sample was broken down by nitrogen gas under no confining stress, and the breakdown pressure is 461.24 psig, as shown in Figure 3.272.

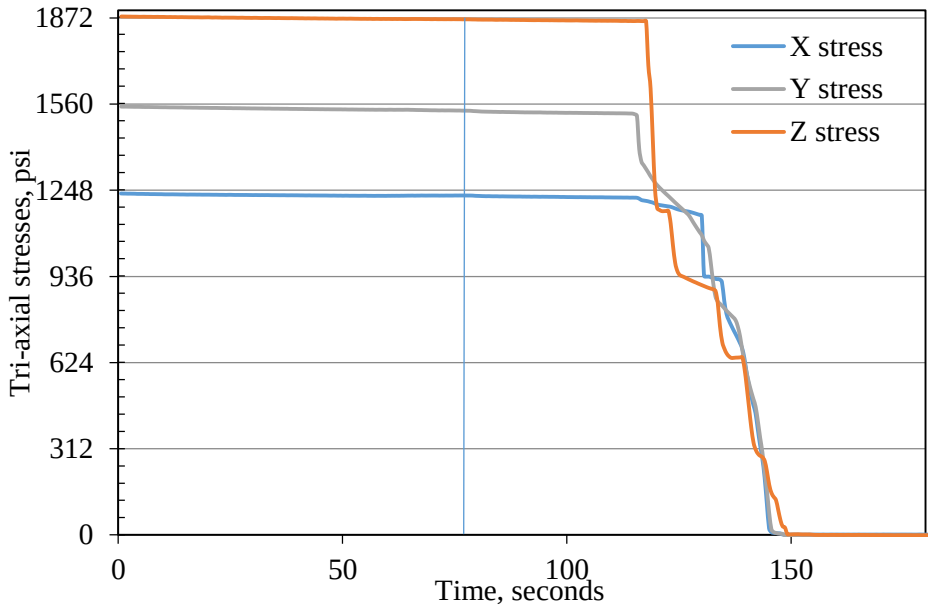

Figure 3.270 Tri-axial stresses for gas fracturing of Sample 57.

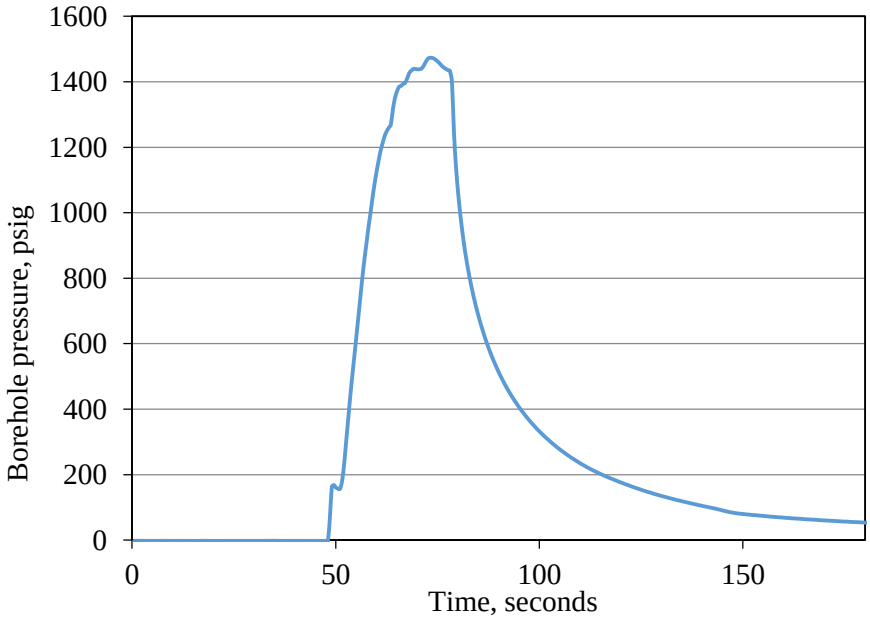

Figure 3.271. Pressure profile during gas fracturing with tri-axial stress loading of Sample 57.

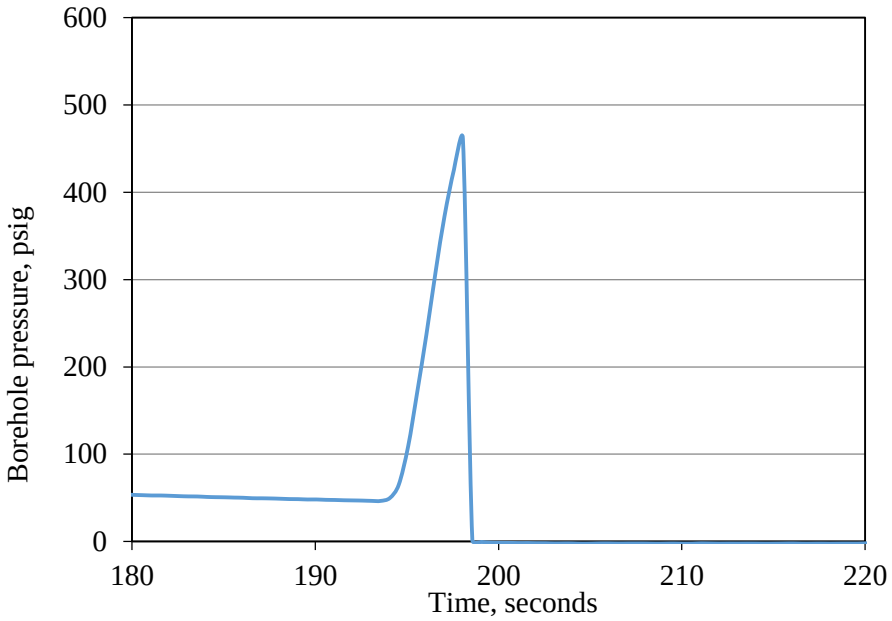

Figure 3.272. Pressure profile during gas fracturing without tri-axial stress loading of Sample 57.

Figure 3.273 shows the surfaces of Sample 57 after CO_2 injection. There is no leakage point or fractures on the surfaces after dye injection. And there is only a small leakage point near acoustic measurement location 11 on Surface 2 that can be observed. Then, the sample was fractured by high pressure nitrogen gas, which revealed the fracture planes generated by CO_2 injection, as shown in Figure 3.274. The major fracture planes are approximately parallel to Surface 5 and Surface 6, and pass the acoustic locations 4 and 5 on Surface 1, location 11 on Surface 2, locations 4 and 9 on Surface 3, locations 10 on Surface 4, locations 7 and 8 on Surface 5. But there are small fractures that are perpendicular to the major fracture. So the fracture system is complex in Sample 57, confirming indications obtained from acoustic measurements.

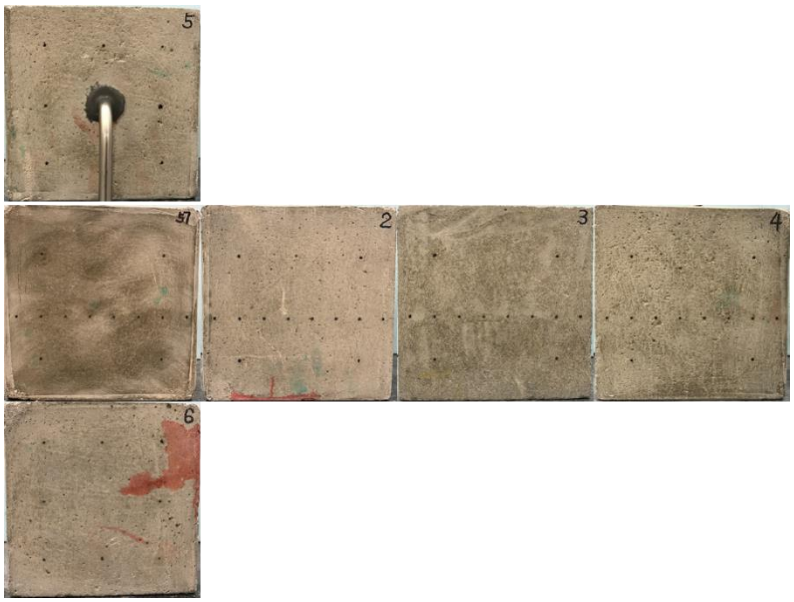

Figure 3.273. Faces of Sample 57 after sc-CO_2 injection.

Figure 3.274. Surfaces of Sample 57 after gas fracturing.

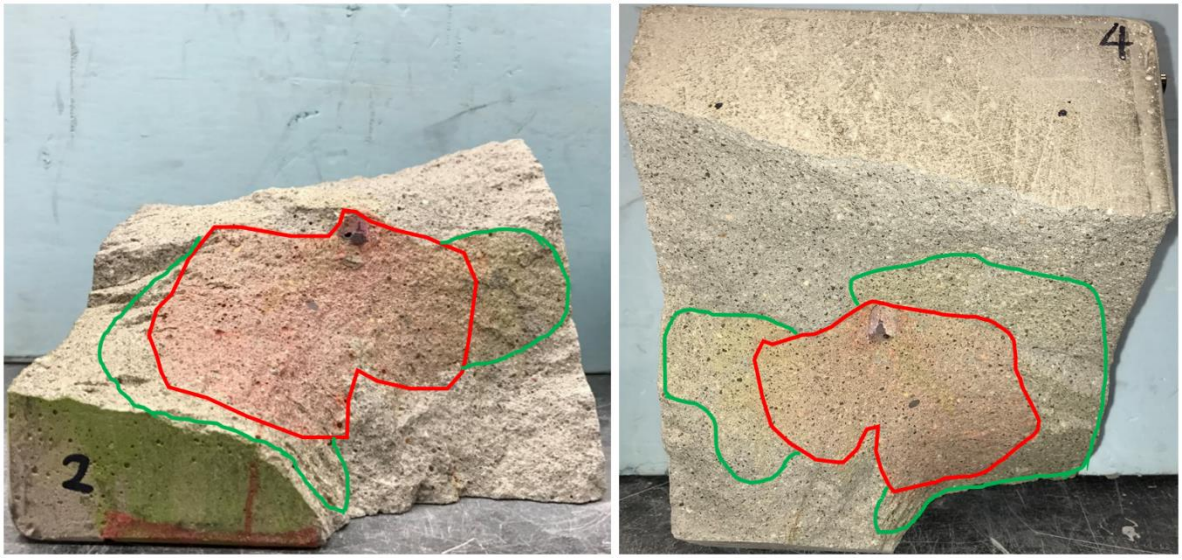

Figure 3.275. Colored water and CO_2 injection induced fracture planes in Sample 57.

(a)

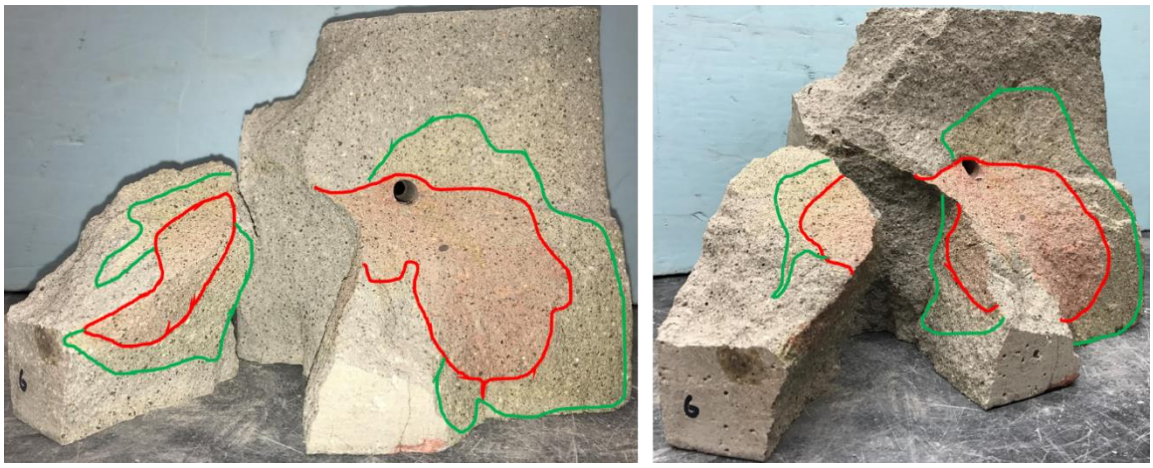

(b)

Figure 3.276. Colored water and CO_2 injection induced small branch fracture planes in Sample 57.

During dye injection, the major fracture plane (red color) primarily propagated from the borehole on the horizontal plane and the major fracture was confined in the concrete block as shown in Figures 3.275 and 3.276. For sc-CO_2 injection, the CO_2 induced fracture first expanded on the major fracture plane and then some small fractures ware generated, which are parallel to Surface 2 and Surface 4. These small fractures induced by CO_2 are perpendicular to the minimum horizontal stress in the x-direction, in agreement with fracturing principles. Injected CO_2 will first flow in the seeding fracture and generate new fractures under the influence of tri-axial stresses.

Concrete Sample 58

Sample 58 was treated by injecting CO_2 under a tri-axial stress loading of 1250 psi in the x-direction, 2187 psi in the y-direction, and 3125 psi in the z-direction. Before the treatment, it was pre-loaded with the stresses of 1500 psi in all three directions for about 40 mins, as shown in Figure 3.277. Then acoustic signatures were measured as reference for post-injection comparison, and pressure decay was carried out for pre-treatment permeability evaluation.

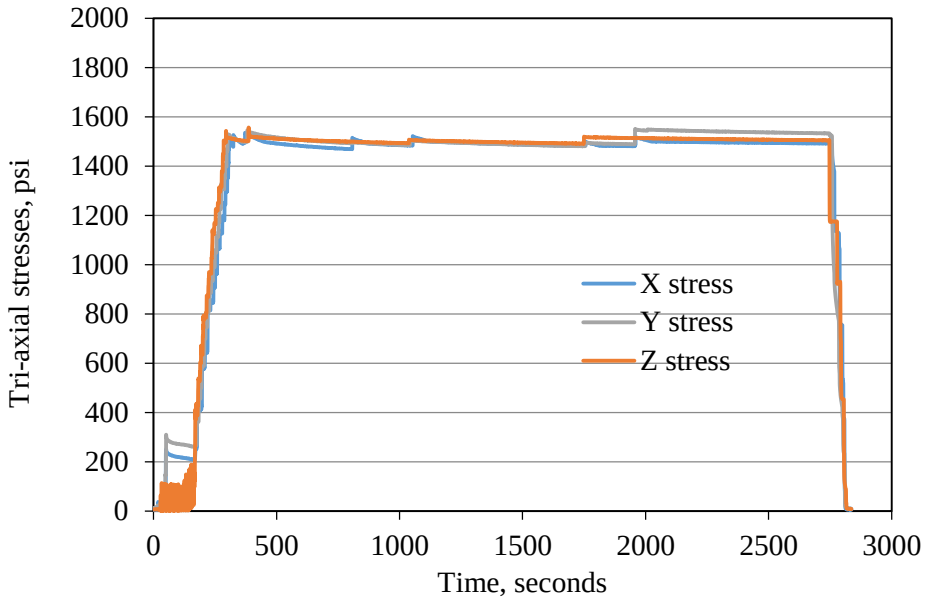

Figure 3.277. Pre-treatment stress loading for Sample 58.

Sample 58 was then treated by injecting blue dye into the borehole to make a seeding fracture on the xz-surface at a constant rate of 2.0 ml/min under tri-axial stress of 1500 psi in the x-direction, 1000 psi in the y-direction, and 2000 psi in the z-direction, as shown in Figure 3.278. The injection pressure and borehole temperature profiles are shown in Figures 3.279 and 3.280. The temperature for water injection was around 21 ℃ since it was conducted at room temperature. The highest pressure peak of 1807.2 psi was achieved around 508 seconds and the pressure kept stable above 1800 psi from 500 to 515 seconds. In this period, a small stress response on the x and y-axis stress loading can be seen in Figure 3.278, indicating that the seeding fracture planes were generated perpendicular to the x-axis and y-axis. But after the peak pressure, the dye flowed out from the epoxy near the well head.

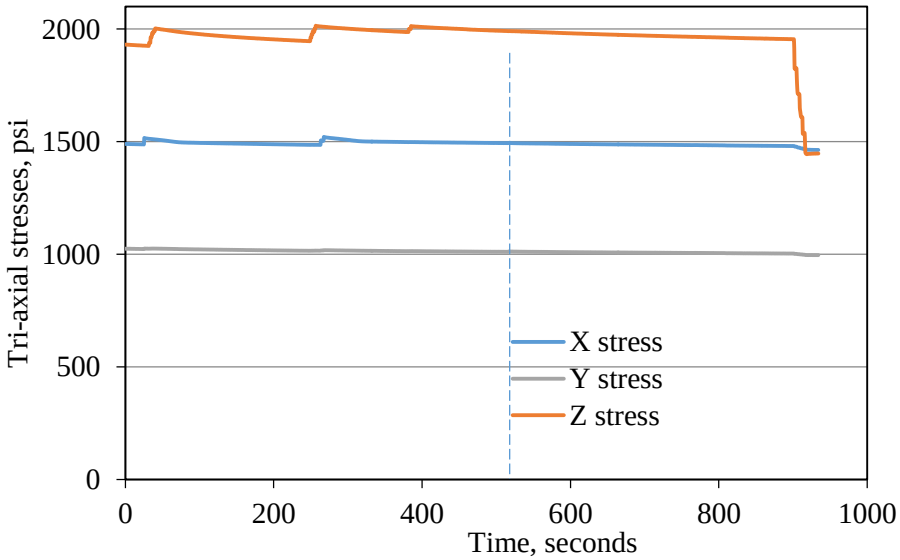

Figure 3.278. Water injection pressure decay for Sample 58.

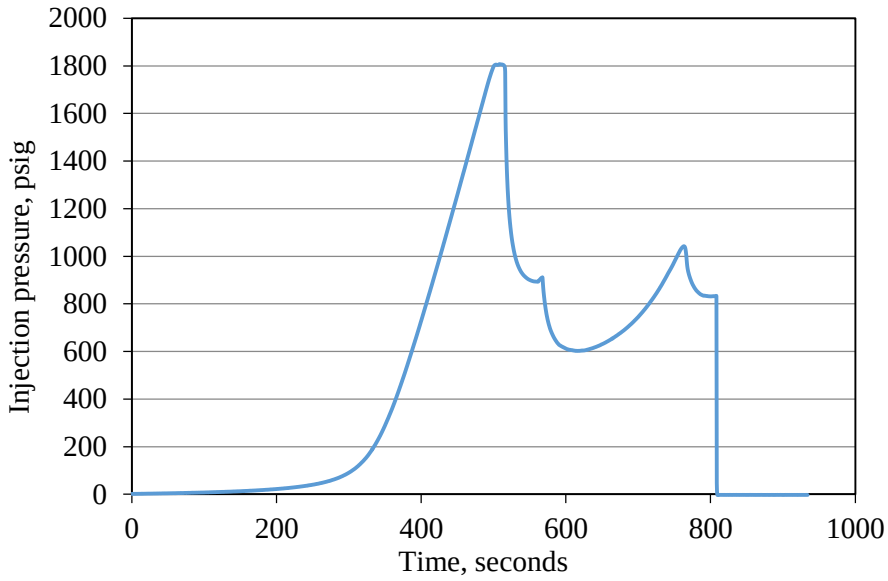

Figure 3.279. Water injection pressure for Sample 58.

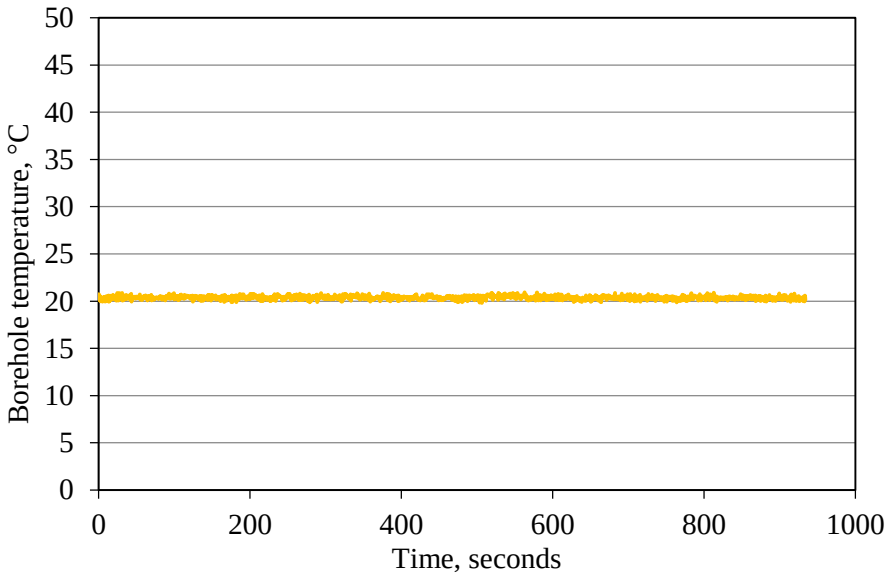

Figure 3.280. Borehole temperature during water injection for Sample 58.

Figure 3.281 compares the pressure decay curves before and after CO_2 injection. Before treatment, the gas leakage rate from borehole was very slow, indicating the concrete samples were good analogs for cap rocks. Since the fractures generated inside the concrete block expanded to the wellhead, the gas leakage rate significantly increased after water injection. Thus, this sample can't be used for the sc-CO_2 injection experiment.

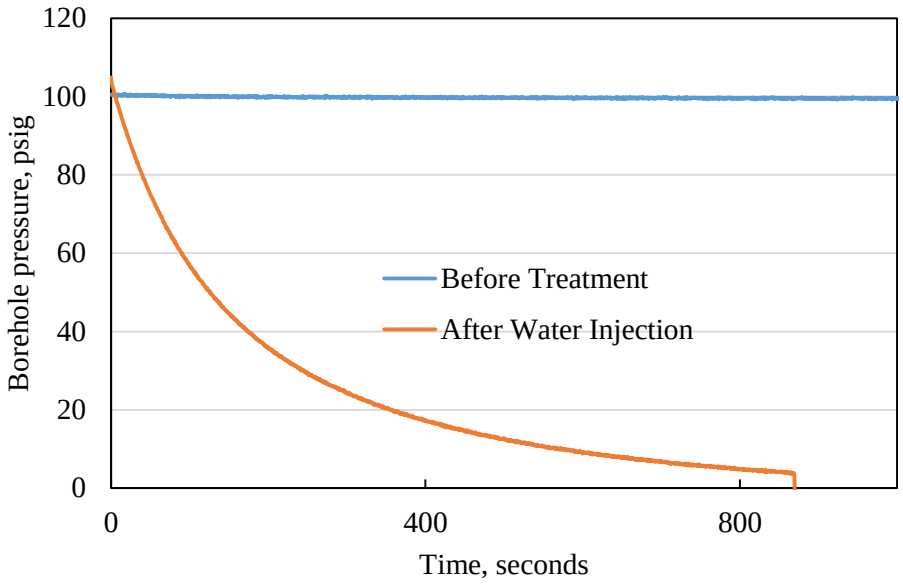

Figure 3.281. Pressure decay curves before and after CO_2 injection.

Acoustic signatures including P-waves and S-waves before (black curves) and after (red curves) CO_2 injection are compared in Figures 3.282 through 3.287. Both P-waves and S-waves show little delays in arrival time and waveforms.

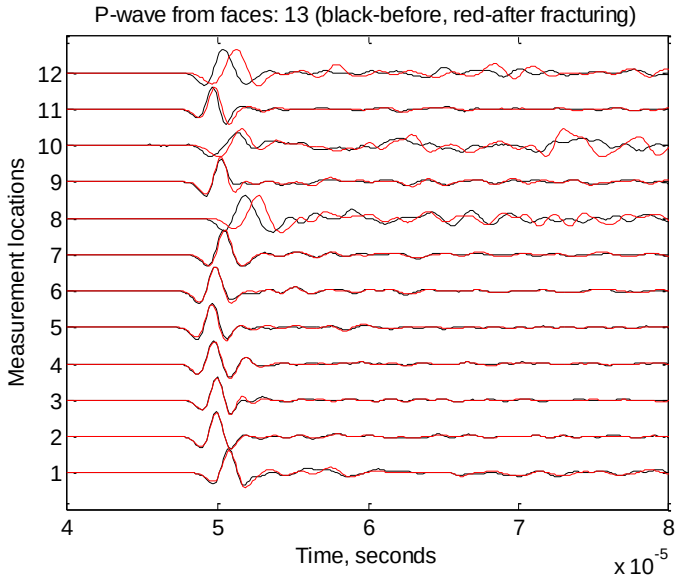

Figure 3.282. P-wave signatures measured from Surface 1 and Surface 3 of Sample 58.

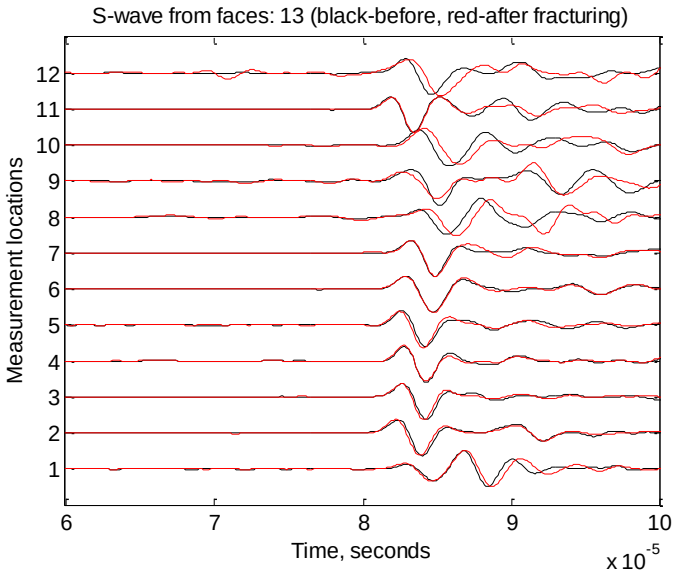

Figure 3.283. S-wave signatures measured from Surface 1 and Surface 3 of Sample 58.

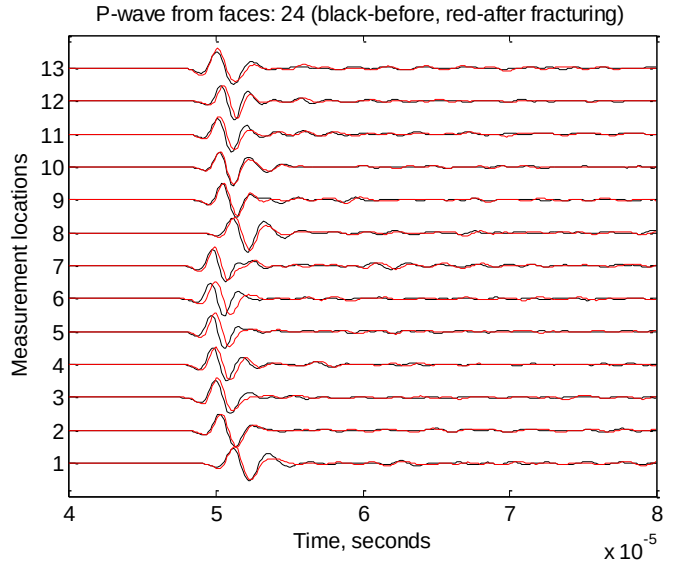

Figure 3.284. P-wave signatures measured from Surface 2 and Surface 4 of Sample 58.

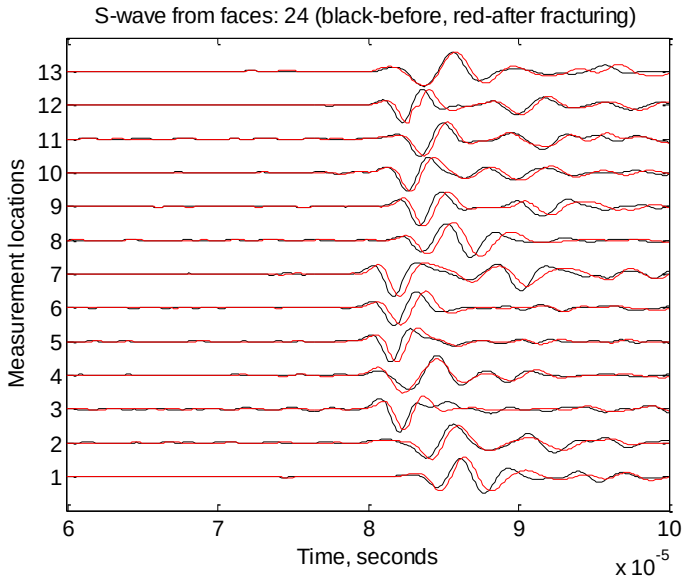

Figure 3.285. S-wave signatures measured from Surface 2 and Surface 4 of Sample 58.

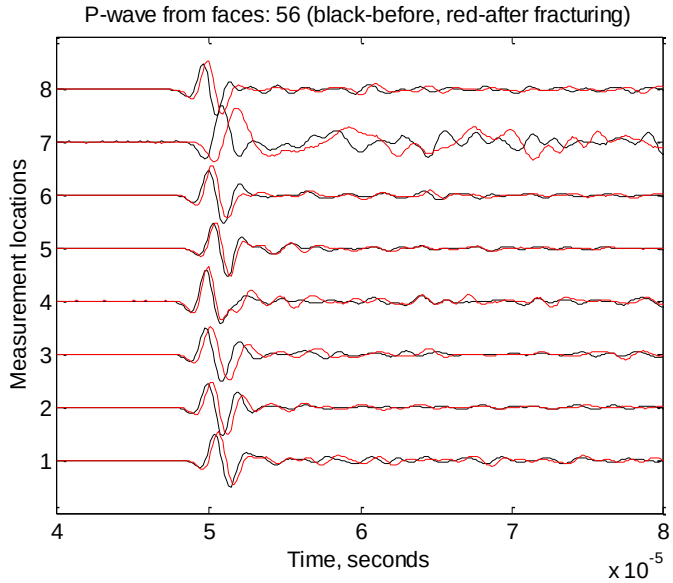

Figure 3.286. P-wave signatures measured from Surface 5 and Surface 6 of Sample 58.

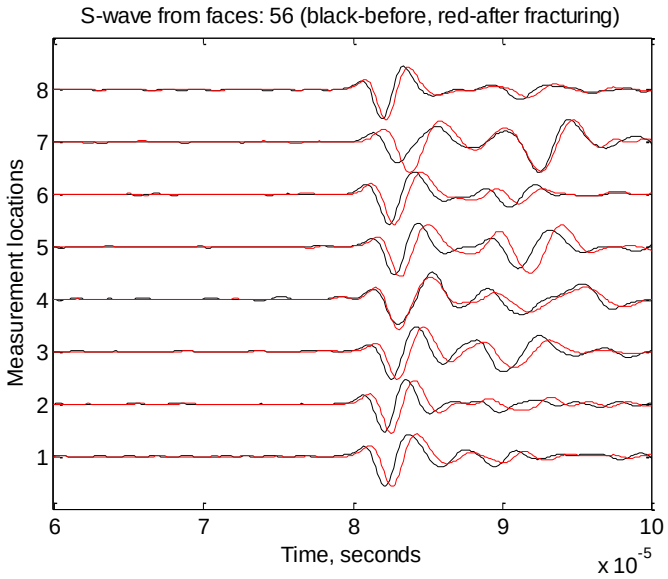

Figure 3.287. S-wave signatures measured from Surface 5 and Surface 6 of Sample 58.

During dye solution injection, dye solution leaked from Surface 2, Surface 4, Surface 5, and Surface 6 of Sample 58, as shown in Figure 3.288.

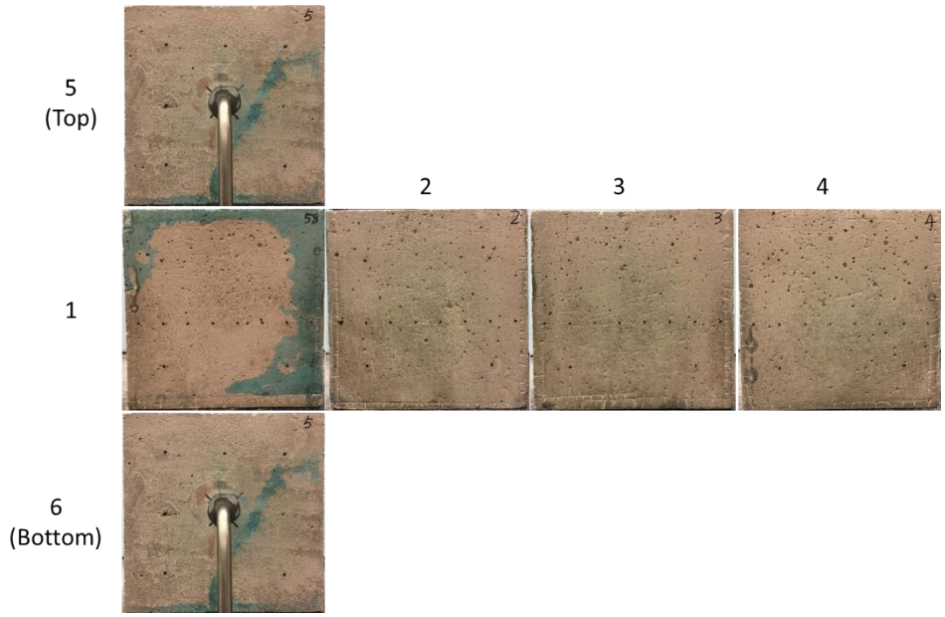

Figure 3.288. Surfaces of Sample 58 after dye injection.

Concrete Sample 59

Sample 59 was treated by injecting CO_2 under a tri-axial stress loading of 1250 psi in the x-direction, 1875 psi in the y-direction, and 2500 psi in the z-direction. Before the treatment, it was pre-loaded with the stresses of 1500 psi in all three directions for about 40 mins, as shown in Figure

3.289. Then, acoustic signatures were measured as a reference for post-injection comparison, and pressure decay was carried out for pre-treatment permeability evaluation.

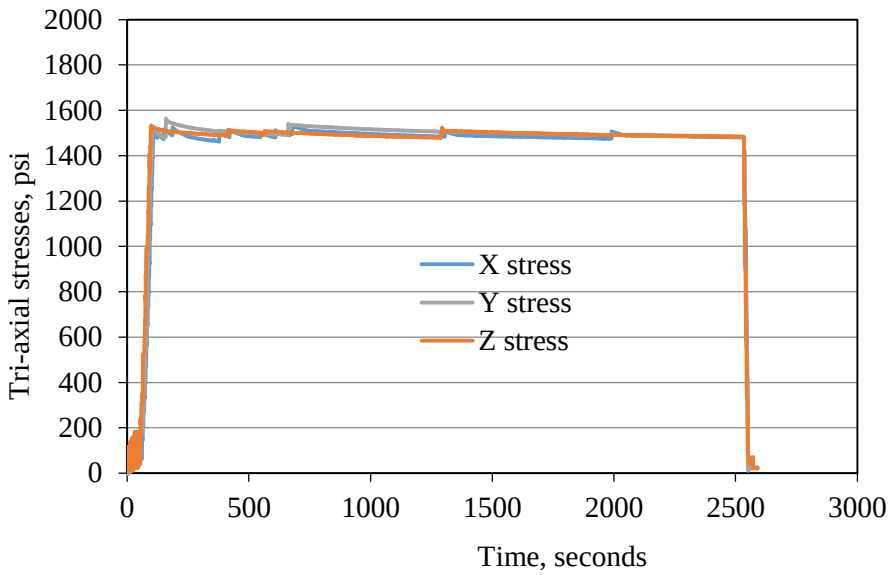

Figure 3.289. Pre-injection tri-axial stress loading for Sample 59.

Sample 59 was then treated by injecting red dye into the borehole to make a seeding fracture on the zx-surface at a constant rate of 1.0 ml/min under tri-axial stress of 1500 psi in the x-direction, 1000 psi in the y-direction, and 2000 psi in the z-direction, as shown in Figure 3.290. The injection pressure and borehole temperature profiles are shown in Figure 3.291 and 3.292. The temperature for water injection was around 21 ℃ since it was conducted at room temperature. The highest pressure peak of 1928.17 psi was achieved at 934 seconds and the pump was stopped at the same time. After the peak pressure, no obvious stress response on the tri-axial stress loading was observed and the pressure decreased slowly after stopping injection, indicating that the seed fracture planes were very small compared to the borehole area.

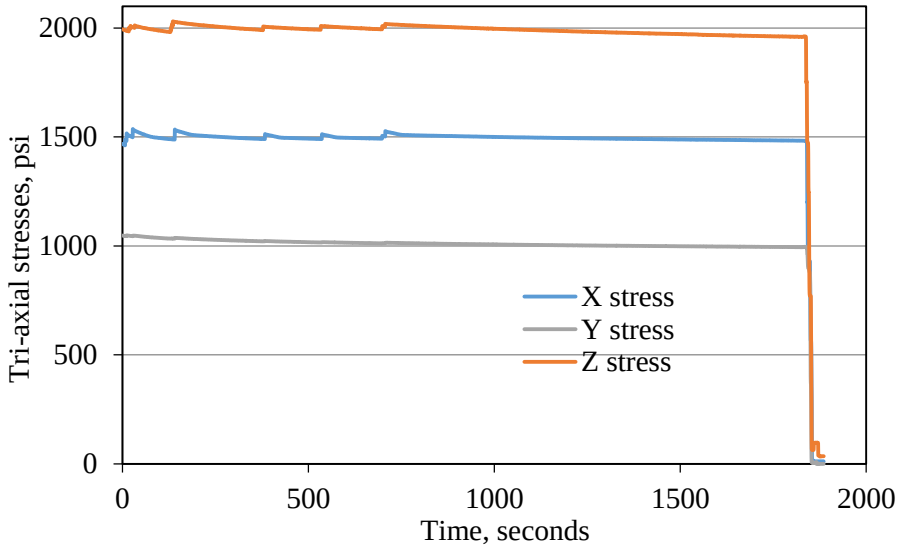

Figure 3.290. Tri-axial stress loading for water injection into Sample 59.

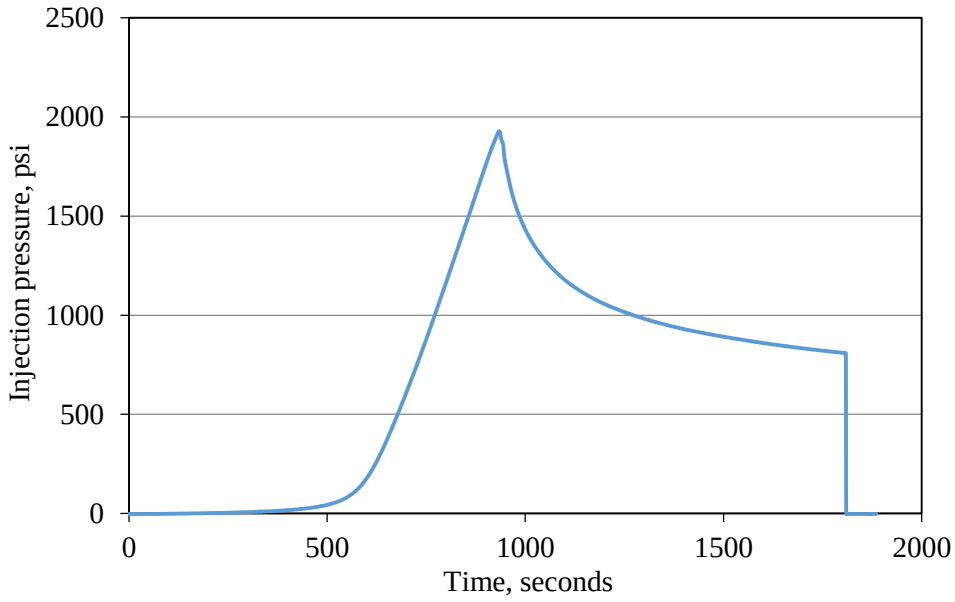

Figure 3.291. Pressure profile of water injection into Sample 59.

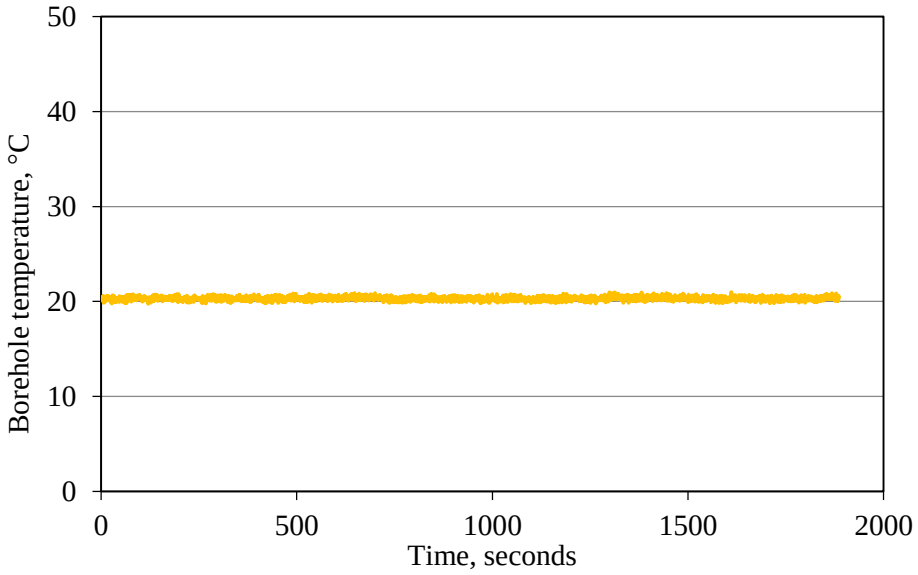

Figure 3.292. Borehole temperature profile during water injection into Sample 59.

After water injection, the Sample 59 was heated at 60 ℃ for more than 8 hours to dry the sample and dye the seed fracture. Then acoustic signatures were measured as reference for post-injection comparison, and pressure decay was carried out for pre-treatment permeability evaluation.

Then, the sample was reheated to 60℃, and treated by injecting CO_2 into borehole at a constant rate of 10 ml/min under tri-axial stress loading of 1250 psi in the x-direction, 1875 psi in the y-direction, and 2500 psi in the z-direction, as shown in Figure 3.293. The injection pressure and borehole temperature profiles are shown in Figures 3.294 and 3.295. We injected one cycle of CO_2 to fracture Sample 59. At beginning, the valve was opened slowly, so the borehole pressure

increased from 0 to about 1300 psi and the temperature decreased. After that, the borehole pressure and temperature slowly increased. When the highest pressure peak of 1761.44 psi was achieved at 725.5 seconds, the borehole temperature was 41.87 °C, much higher than the supercritical temperature. Thus, Sample 59 was fractured under supercritical conditions. There is an obvious stress response on the x-axis stress loading around the 727.5 seconds after the pressure peak was reached, indicating that the major fracture planes were generated perpendicular to the y-axis. At the same time, there was a small stress response on the y-axis stress loading around the 727.5 seconds. In addition, the temperature drastically dropped right after the fracturing point, due to CO_2 leakage and expansion.

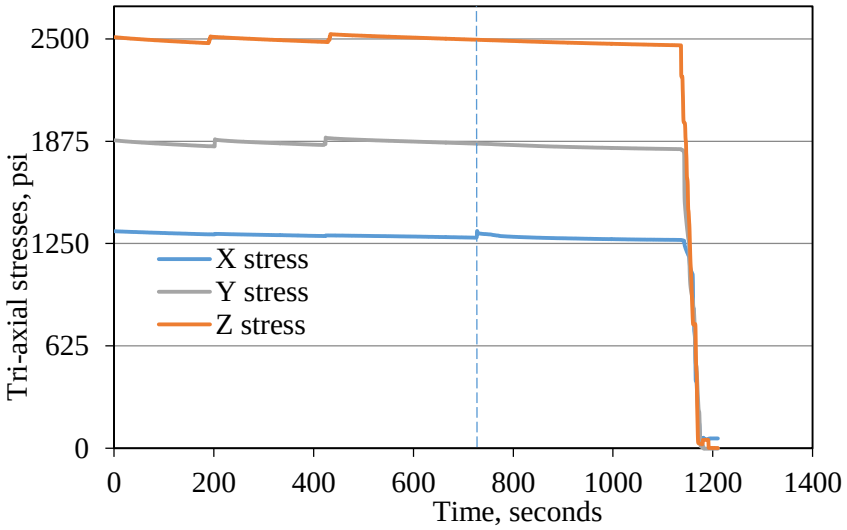

Figure 3.293. Tri-axial stress loading for Sc-CO_2 injection into Sample 59.

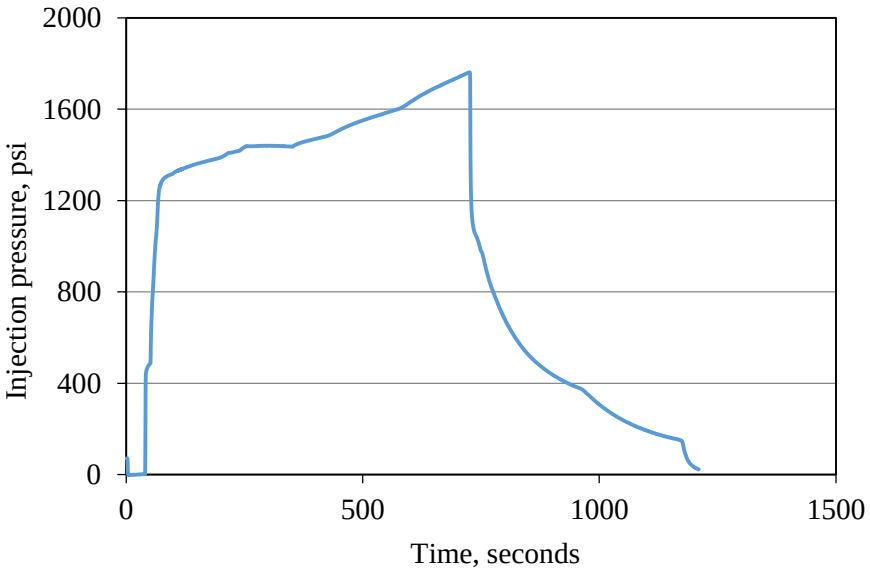

Figure 3.294. Pressure profile of Sc-CO_2 injection into Sample 59.

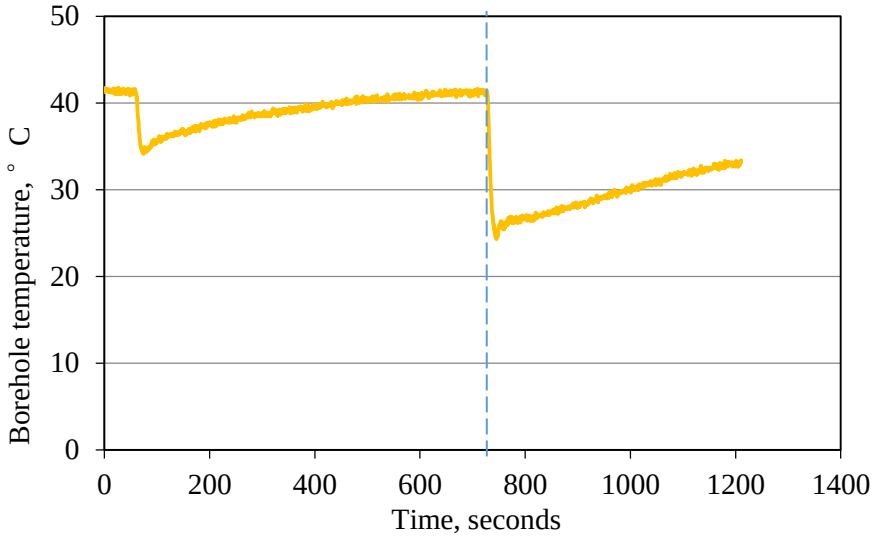

Figure 3.295. Borehole temperature profile during cc-CO_2 injection into Sample 59.

The gas leakage rate is not obvious after the water injection, since the water induced fracture is very small compared to the borehole area. But the gas leakage rate significantly increased after CO_2 injection, due to fractures generated inside the concrete block that propagated to the surface, as shown in Figure 3.296.

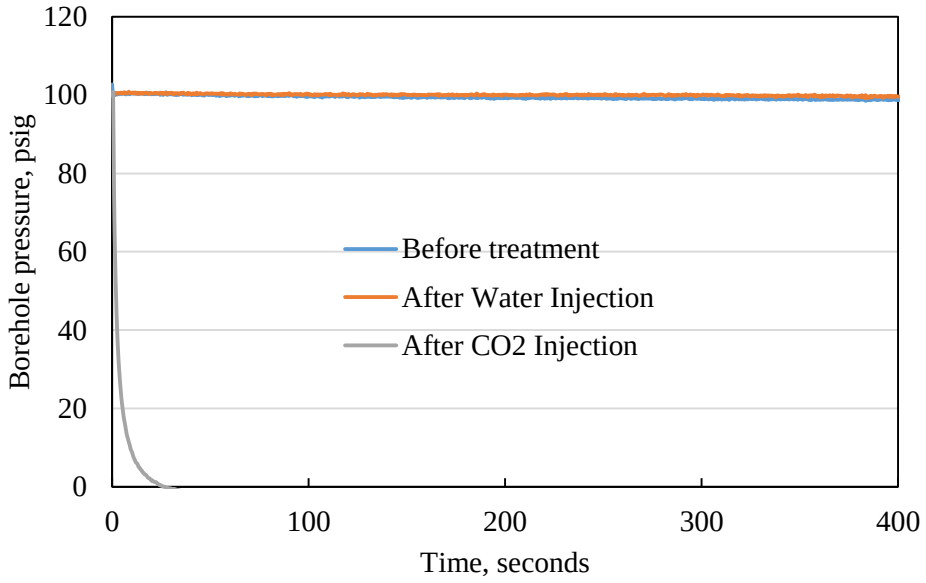

Figure 3.296. Pre- and post-injection pressure decay curves of Sample 59.

Acoustic signatures including P-waves and S-waves before (black curves) and after (red curves) CO_2 injection are compared in Figures 3.297 through 3.302. Both P-waves and S-waves show delays in arrival time, especially on Surface 1 and Surface 3, indicating that the major fracture planes are parallel to Surface 1 and Surface 3. In other words, the fracture planes generated are perpendicular to the minimum horizontal stress in x-axis, in agreement with fracturing principles.

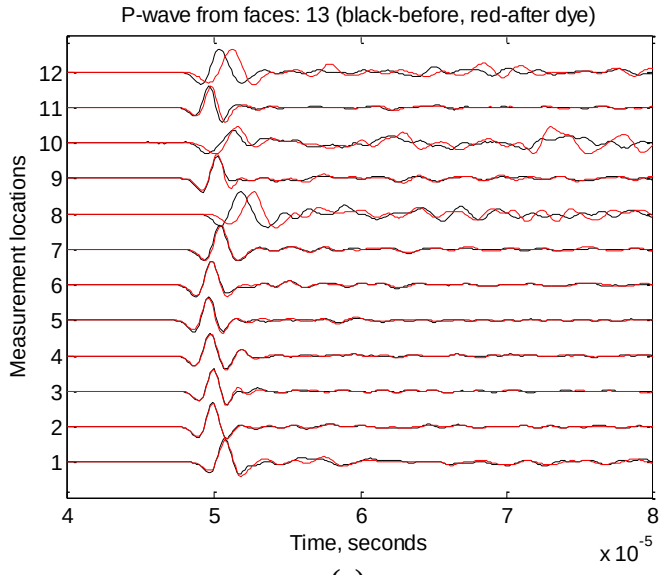

(a)

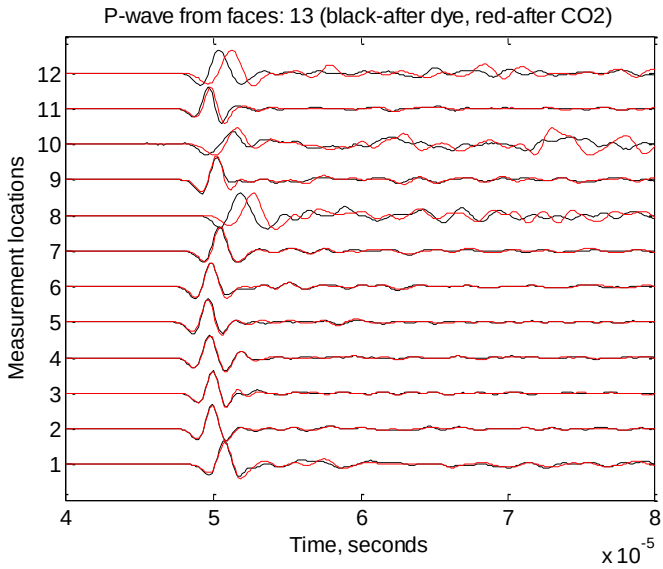

(b)

Figure 3.297. P-wave signatures measured from Surface 1 and Surface 3 of Sample 59.

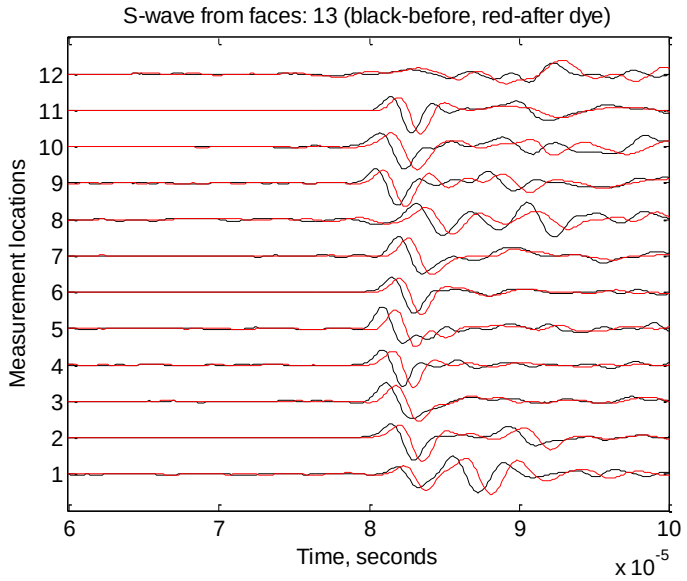

(a)

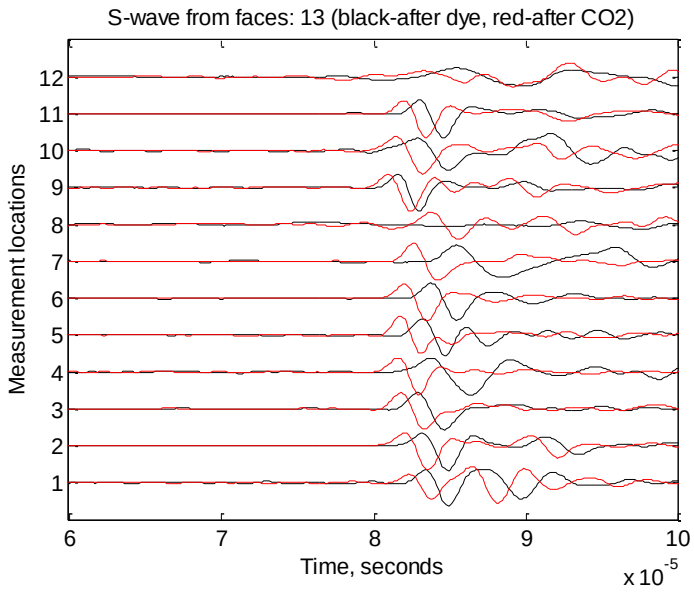

(b)

Figure 3.298. S-wave signatures measured from Surface 1 and Surface 3 of Sample 59.

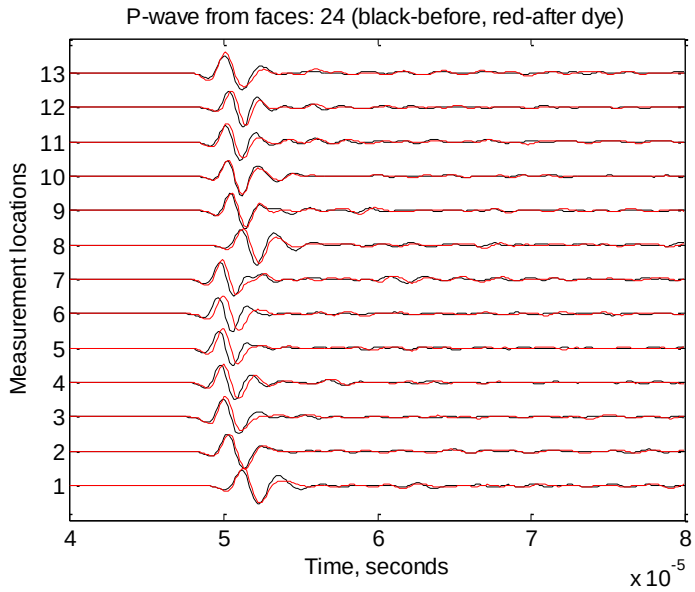

(a)

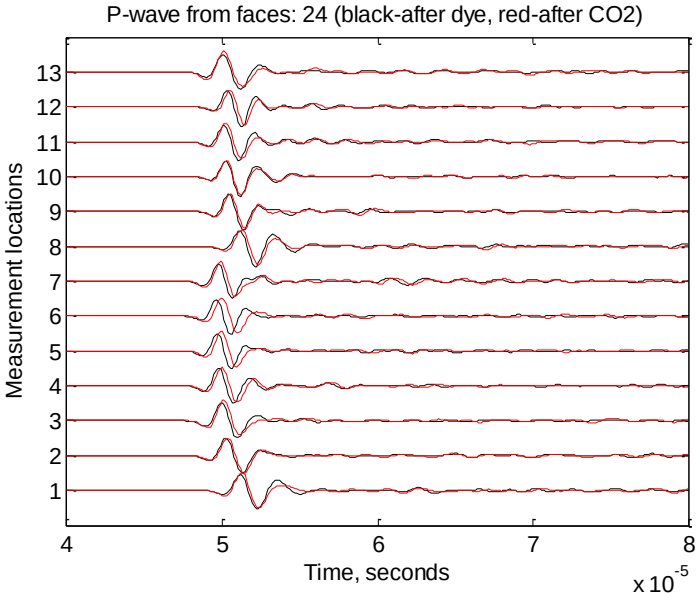

(b)

Figure 3.299. P-wave signatures measured from Surface 2 and Surface 4 of Sample 59.

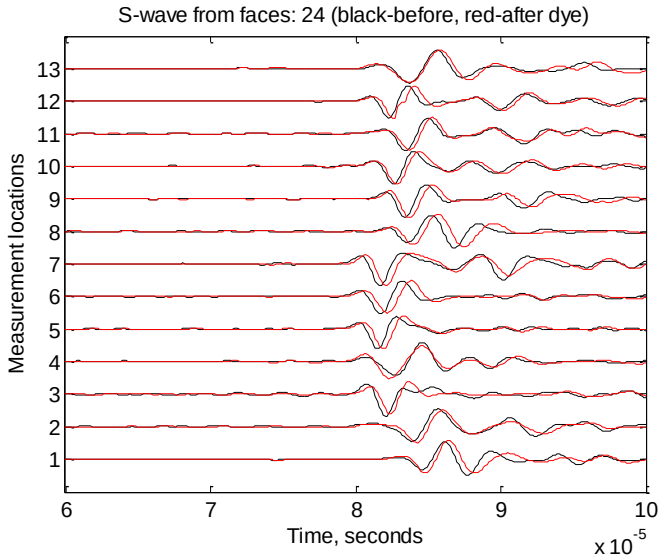

(a)

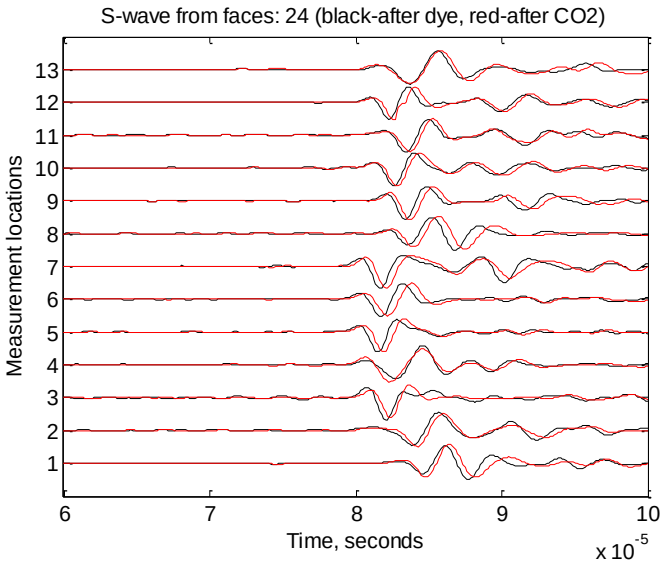

(b)

Figure 3.300. S-wave signatures measured from Surface 2 and Surface 4 of Sample 59.

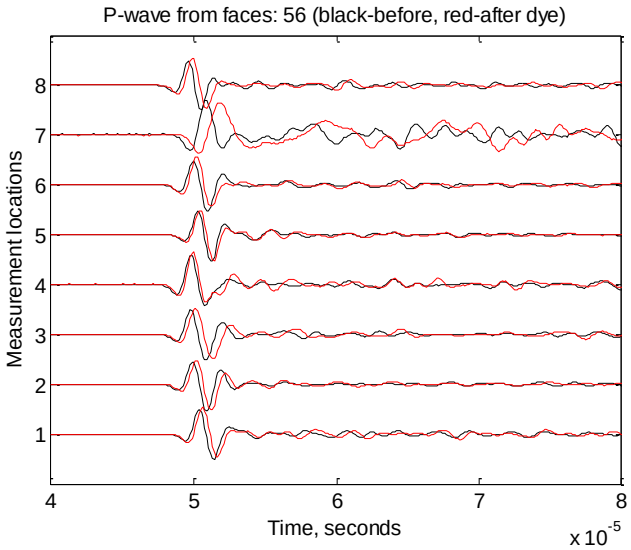

(a)

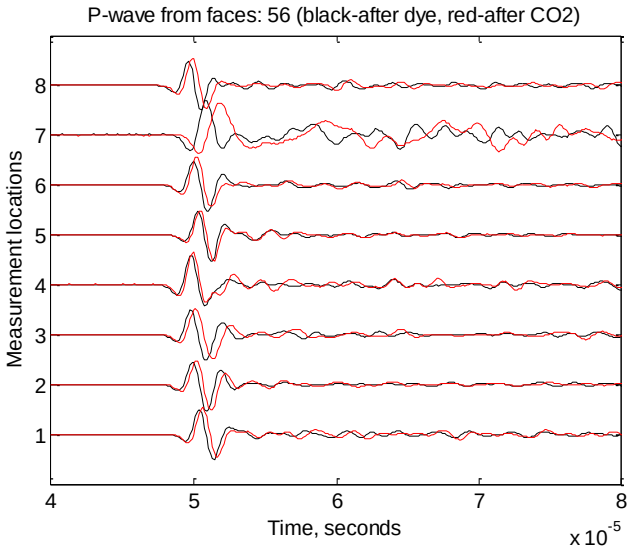

(b)

Figure 3.301. P-wave signatures measured from Surface 5 and Surface 6 of Sample 59.

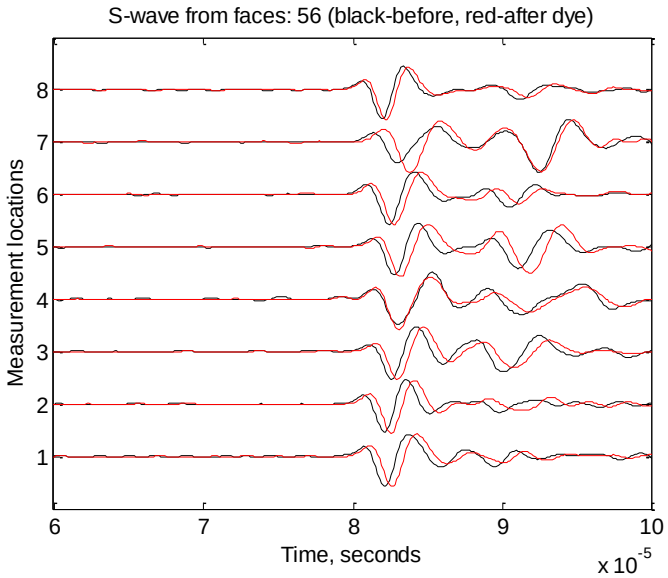

(a)

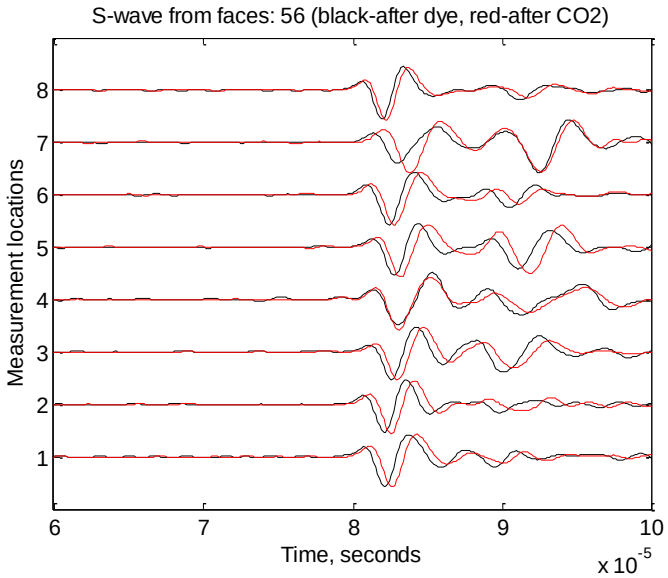

(b)

Figure 3.302. S-wave signatures measured from Surface 5 and Surface 6 of Sample 59.

Red dye solution was later injected into Sample 59 to color the fracture planes. Then under tri-axial stress loading, shown in Figure 3.303, the sample was fractured by injecting nitrogen gas, and the pressure profile is shown in Figure 3.304, in which the peak pressure reached at 1557.69 psig around 109 seconds. At the same time, there were very small pressure peaks both on x- and y-axes. Finally, the sample was broken down by nitrogen gas under no confining stress, and the breakdown pressure was 114.69 psig, as shown in Figure 3.305.

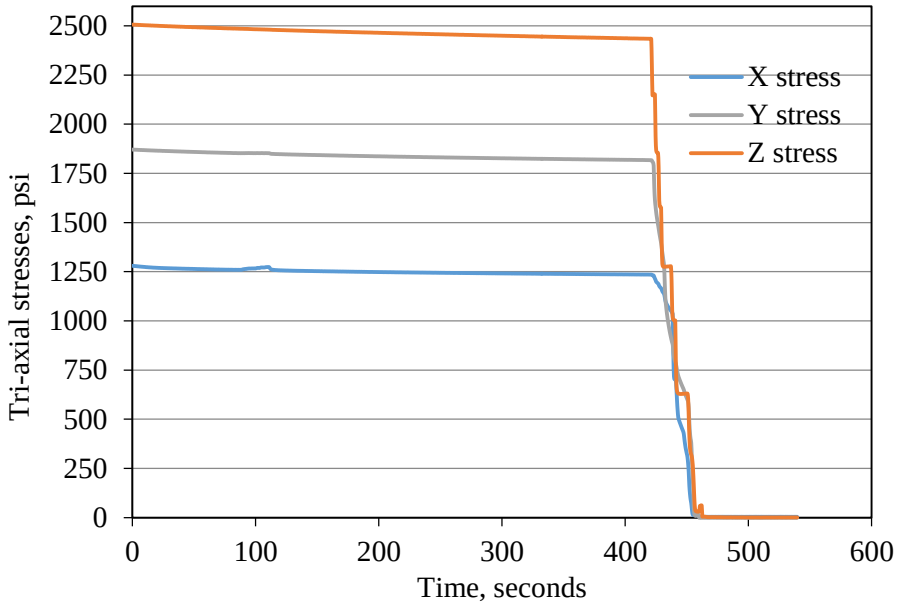

Figure 3.303 Tri-axial stresses for gas fracturing of Sample 59.

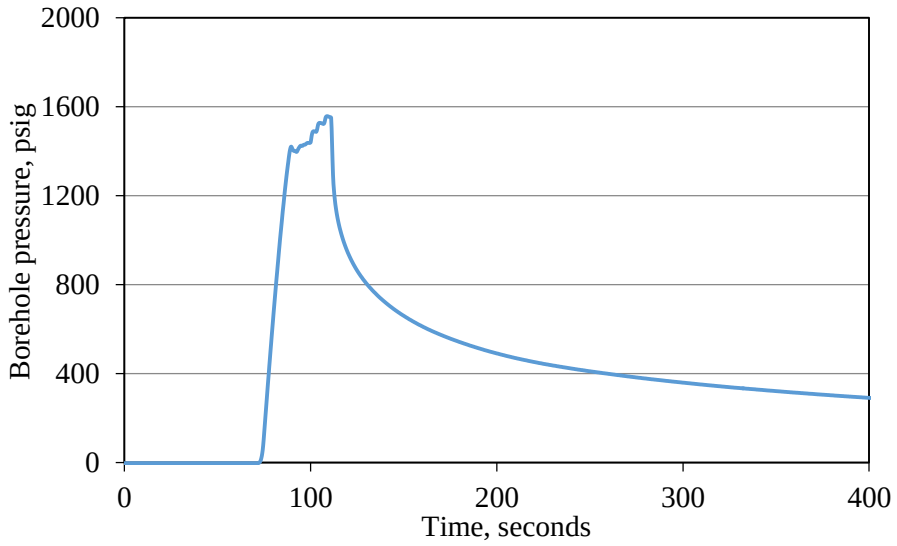

Figure 3.304. Pressure profile during gas fracturing with tri-axial stress loading of Sample 59.

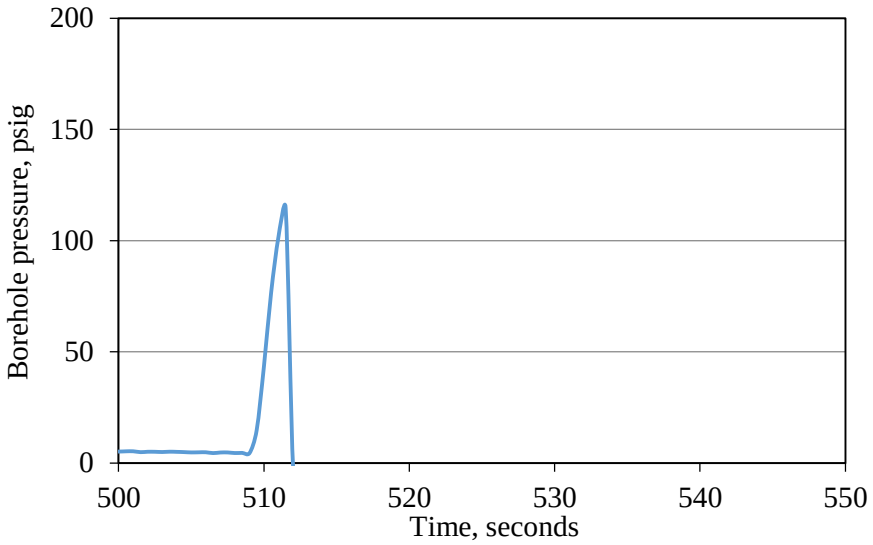

Figure 3.305. Pressure profile during gas fracturing without tri-axial stress loading of Sample 59.

There are no obvious fractures after dye water injection. Figure 3.306 shows the surfaces of Sample 59 after CO_2 injection, on Surface 2 there is an obvious fracture that is perpendicular to the x-axis direction. This fracture can also be observed on Surface 5 and Surface 6. During the red dye injection, the dye flowed out of this fracture. Then, the sample was fractured by high pressure nitrogen gas, which revealed the fracture planes generated by CO_2 injection, as shown in Figure 3.307 and 3.308. The fracture planes are almost parallel to the Surface 1 and Surface 3 and pass the acoustic location 4 on Surface 2 and Surface 4, confirming indications obtained from P-wave measurements.

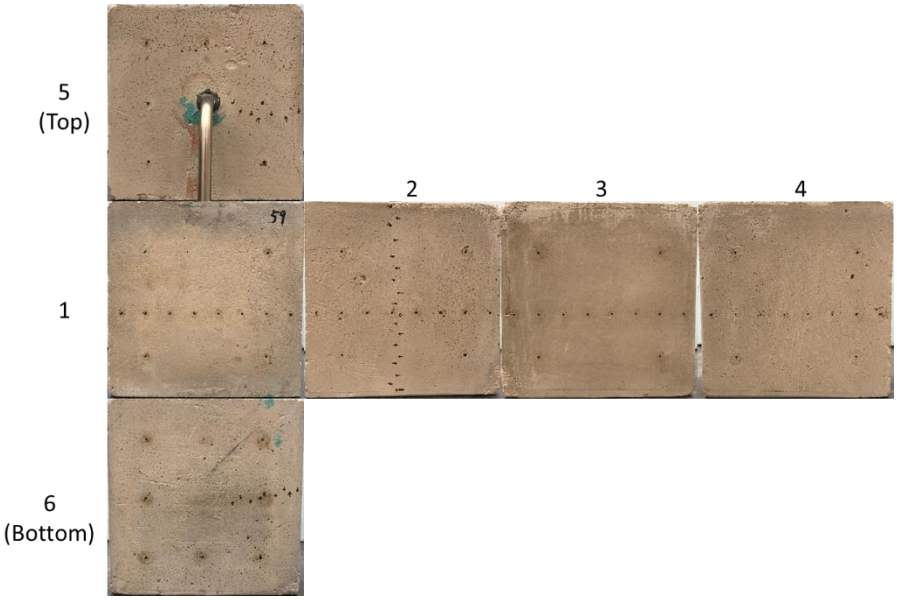

Figure 3.306. Faces of Sample 59 after Sc-CO_2 injection.

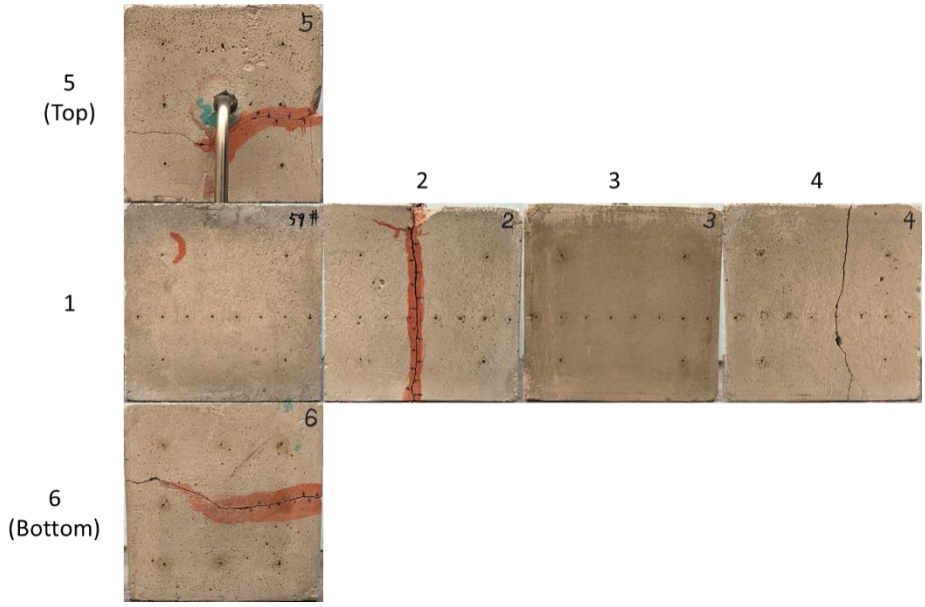

Figure 3.307. Faces of Sample 59 after gas fracturing.

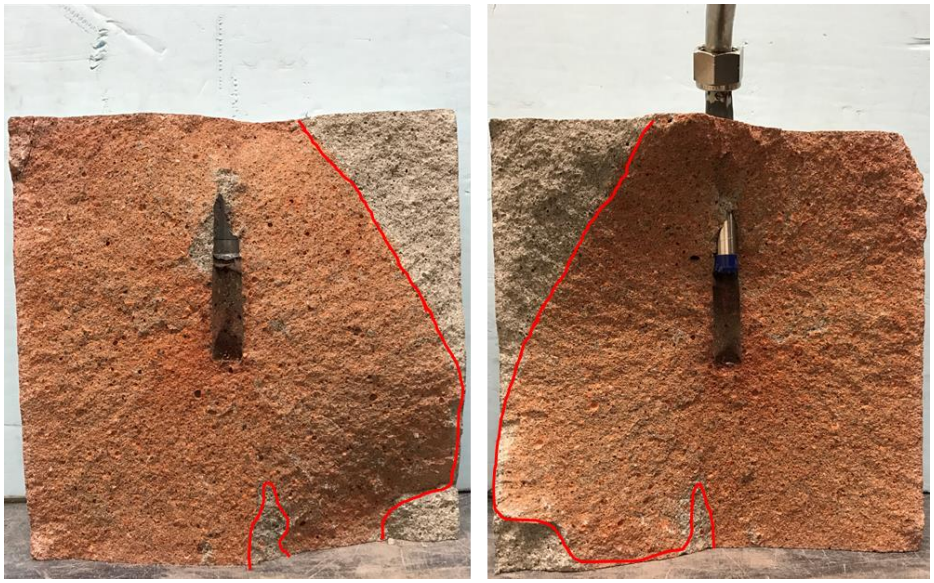
Figure 3.308. Colored water and CO_2 injection induced fracture planes in Sample 59.

No obvious seeding fracture (green color) can be observed in Figure 3.308. Fractures induced by CO_2 are perpendicular to the minimum horizontal stress, the x-direction, in agreement with fracturing principles.

Concrete Sample 62

Sample 62 was first pre-loaded with tri-axial stresses of 1250 psi in the x-direction, 1875 psi in the y-direction, and 2500 psi in the z-direction for about 45 minutes, shown in Figure 3.309, and then acoustic measurements and a pressure decay test were carried out.

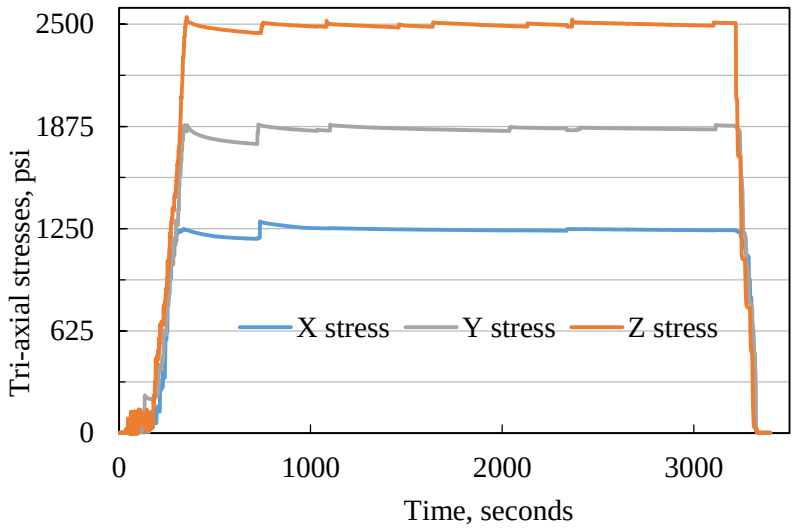

Figure 3.309. Stress loading before CO_2 injection for Sample 62.

After that, under the same tri-axial stress loading, shown in Figure 3.310, CO_2 was injected at a constant rate of 40 ml/min into the sample. Figure 3.311 presents the pressure profile during CO_2 injection. The peak pressure of CO_2 injection is 2070.9 psig at 2469.6 seconds, corresponding to a small stress bump in the x-direction in Figure 3.310. The temperature when the sample was fractured was 36.67 °C in Figure 3.311, then it sharply decreased to 23.5 °C due to sc-CO_2 leakage through generated fractures and resultant expansion and vaporization.

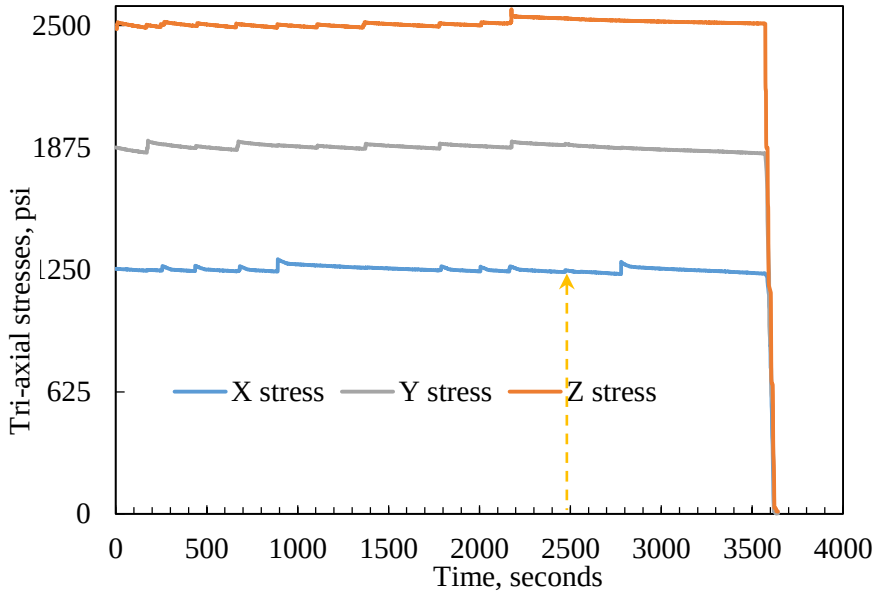

Figure 3.310. Tri-axial stress loading for CO_2 injection into Sample 62.

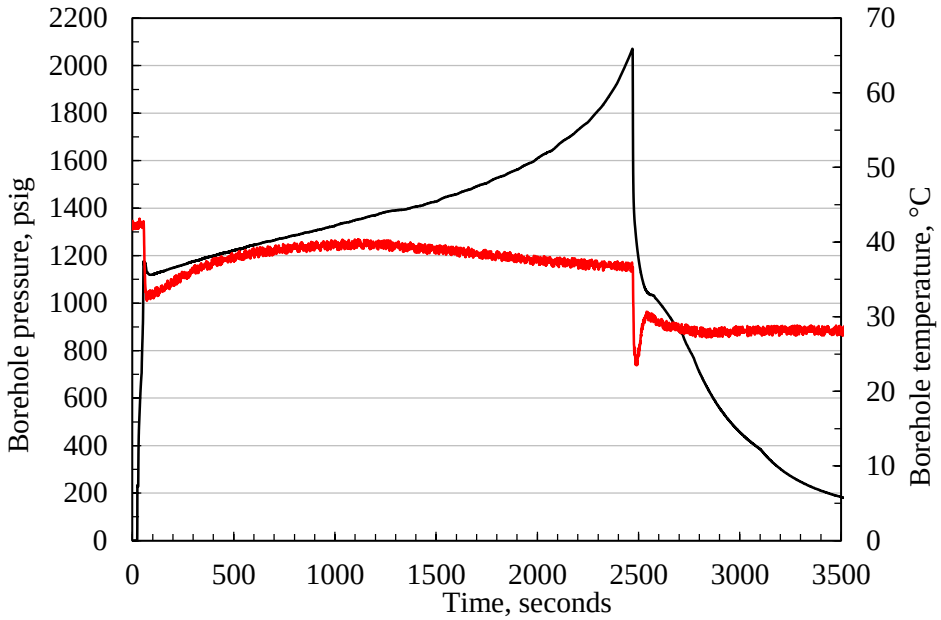

Figure 3.311. CO_2 injection pressure and temperature of Sample 62.

Pressure decay curves measured before and after CO_2 injection for Sample 62 are compared in Figure 3.312, which shows significant permeability increase of the concrete block due to injection induced fractures.

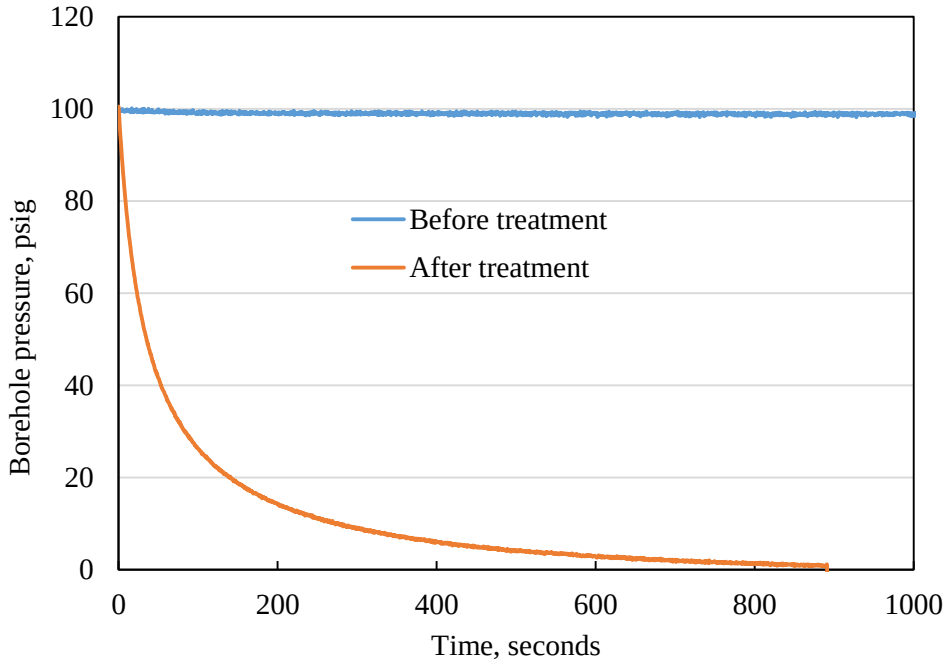

Figure 3.312. Pressure decay curves before and after treatment for Sample 62.

Figures 3.313 through 3.318 compare the two acoustic wave curves measured before and after CO_2 injection: black - before injection, red - after injection. It can be seen that after CO_2 injection both

P-waves and S-waves delay in arrival time, indicating fracture generation inside the concrete block.

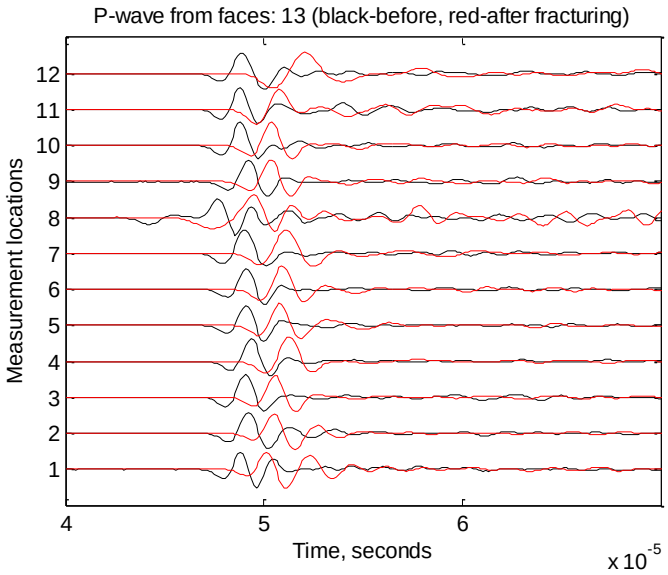

Figure 3.313. P-wave signatures measured from Surface 1 and Surface 3 of Sample 62.

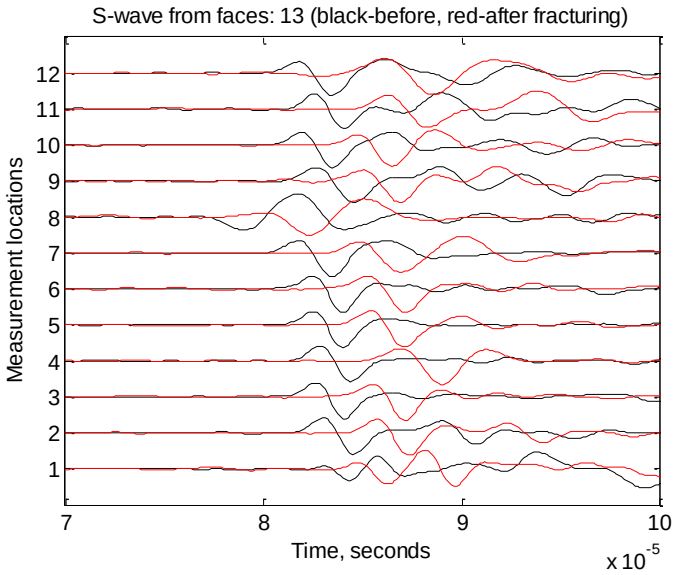

Figure 3.314. S-wave signatures measured from Surface 1 and Surface 3 of Sample 62.

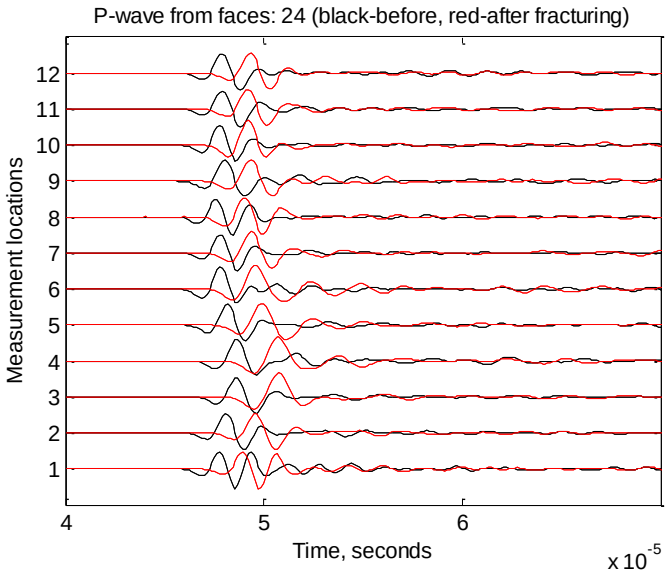

Figure 3.315. P-wave signatures measured from Surface 2 and Surface 4 of Sample 62.

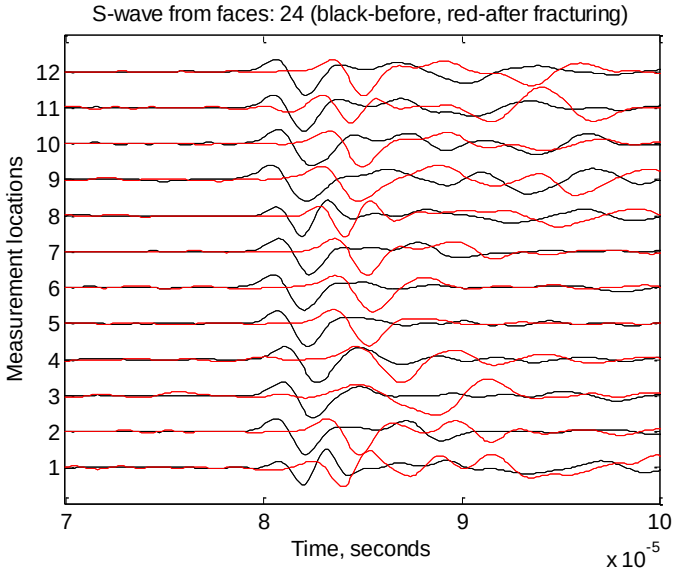

Figure 3.316. S-wave signatures measured from Surface 2 and Surface 4 of Sample 62.

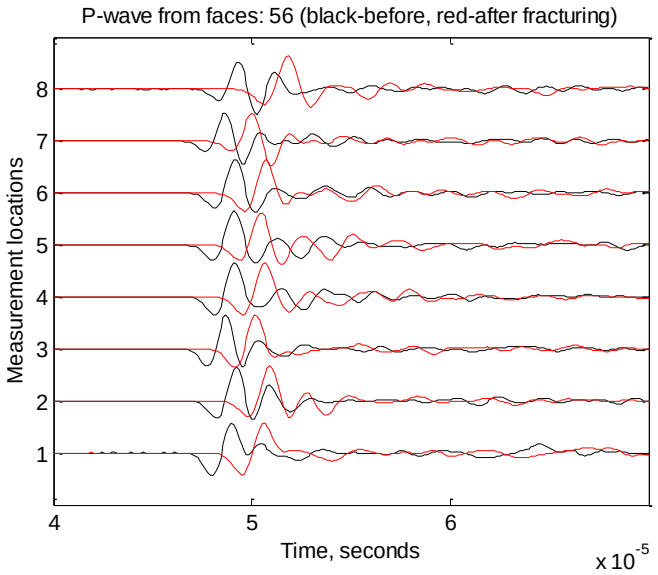

Figure 3.317. P-wave signatures measured from Surface 5 and Surface 6 of Sample 62.

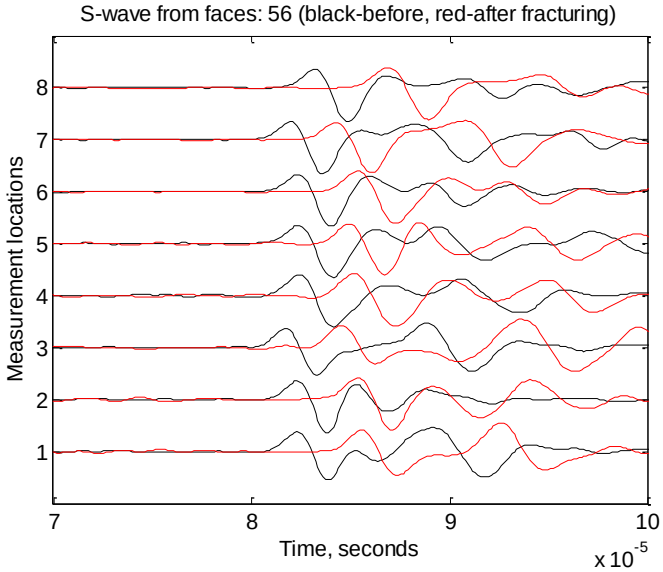

Figure 3.318. S-wave signatures measured from Surface 5 and Surface 6 of Sample 62.

Dye solution was then injected at ~70 psig into Sample 62 to color the CO_2 injection induced fractures, through which dye solution flowed and out at the block surface. Then, the sample was fractured by nitrogen gas under tri-axial stresses. The tri-axial loading and nitrogen gas pressure profiles are shown in Figures 3.319 and 3.320, respectively. The concrete sample was broken down by pressurizing nitrogen gas to 1521.3 psig at 390.1 seconds, shown in Figure 3.320, corresponding to a small heave on x-stress and small drops on y- and z-stress, shown in Figure 3.319. Stress responses suggest that the major gas fracture opened against the minimum horizontal stress.

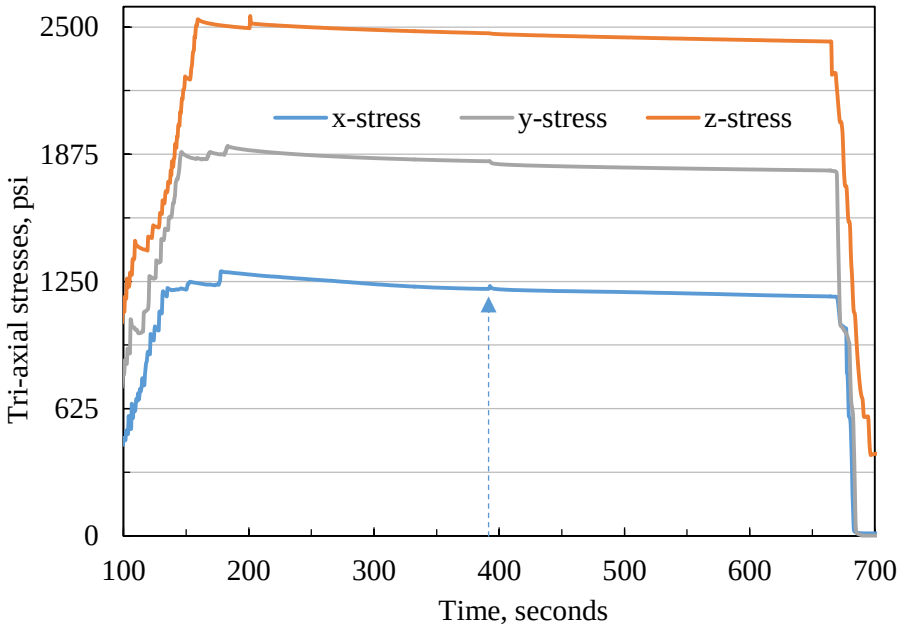

Figure 3.319. Tri-axial stresses for gas fracturing of Sample 62.

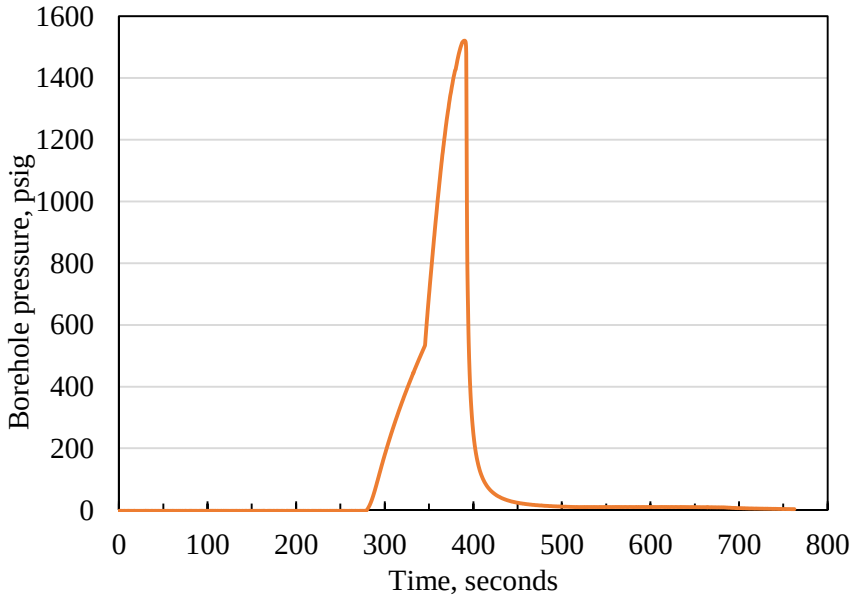

Figure 3.320. Gas fracturing pressure profile of Sample 62.

Coloring and gas fracturing revealed the fracture planes induced by CO_2 injection, as shown in Figure 3.321 before, and Figures 3.322 Figure 3.323 after. The fracture plane, circular around the openhole section, is generally perpendicular to the minimum horizontal stress direction and is simple in both morphology and direction. There are no secondary fractures observed.

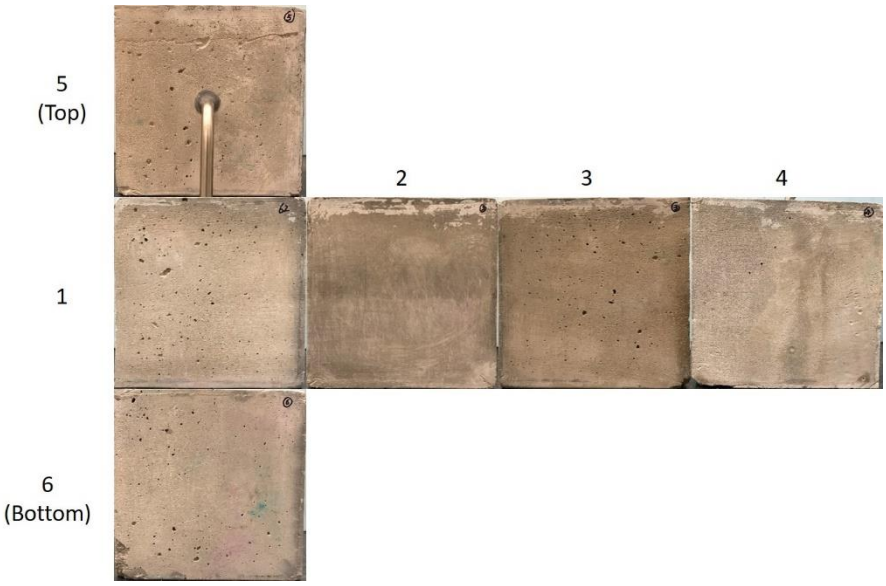

Figure 3.321. Surfaces of Sample 62 before treatment.

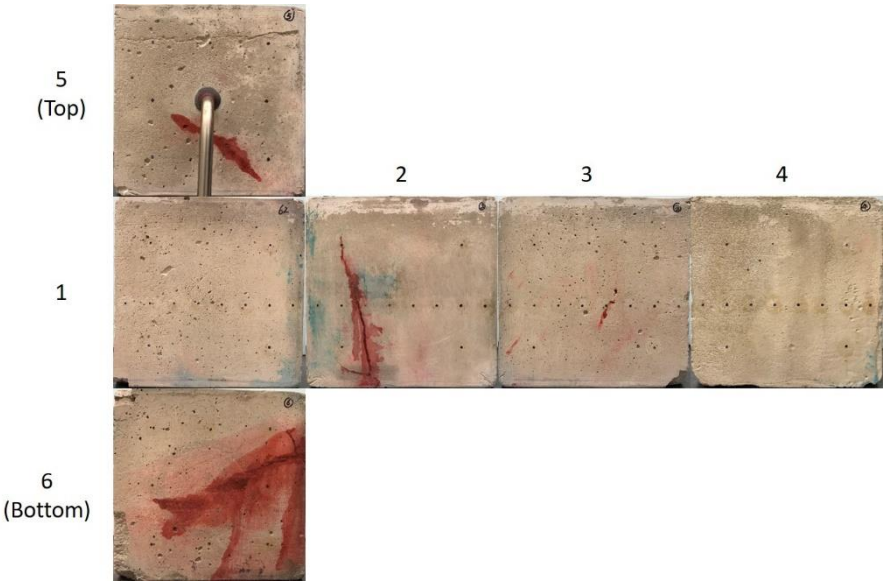

Figure 3.322. Surfaces of Sample 62 after coloring.


Figure 3.323. CO_2 injection induced fracture morphology of Sample 62 (opened from Surface 2).

Concrete Sample 63

Sample 63 was first compressed for about 45 minutes by applying a tri-axial stress loading of 1248 psi in the x-direction, 1560 psi in the y-direction, and 1872 psi in the z-direction, as shown in Figure 3.324.

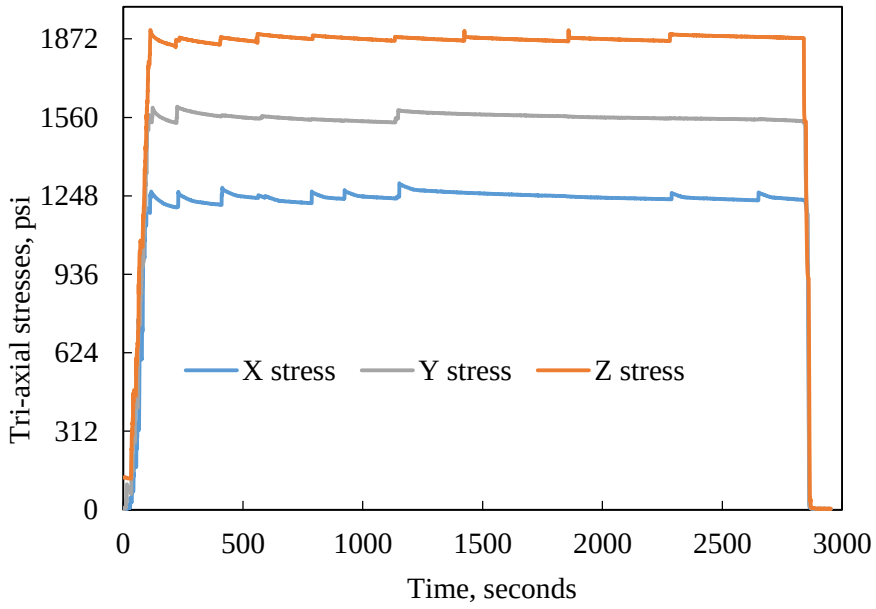

Figure 3.324. Stress loading before CO_2 injection for Sample 63.

Then acoustic wave measurements were then carried out and pressure decay curve was measured under no stress loading as a reference for comparison of permeability change after CO_2 injection for the sample. Sample 63 was then treated by injecting CO_2 into borehole under tri-axial stresses of 1248 psi in the x-direction, 1560 psi in the y-direction, and 1872 psi in the z-direction, shown in Figure 3.325.

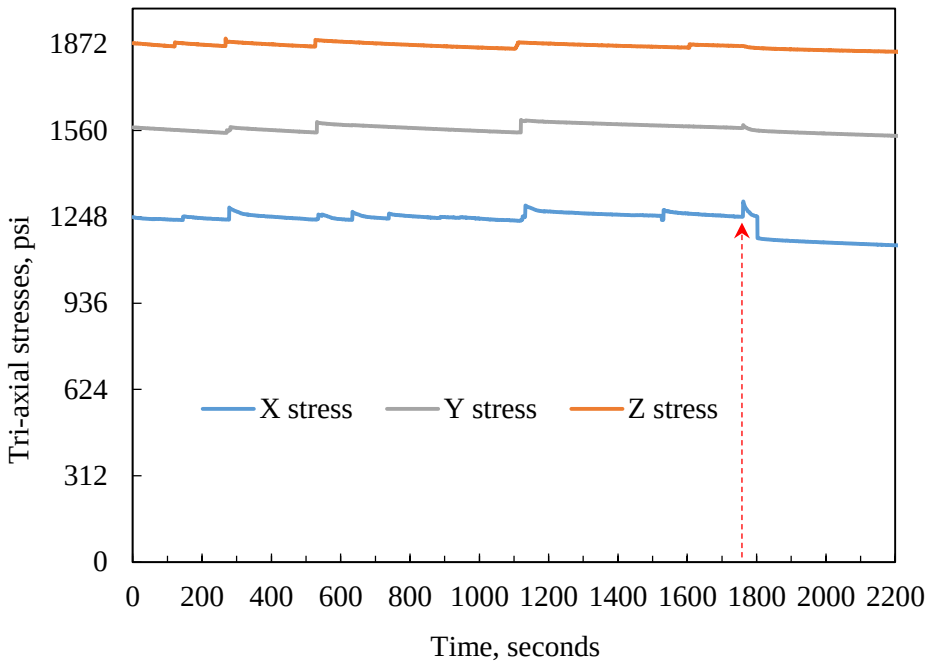

Figure 3.325. Tri-axial stress loading for CO_2 injection into Sample 63.

The pressure and temperature profiles in borehole are shown in Figure 3.326. The first peak pressure is 1141.6 psig at 78.5 seconds as the valve from the pump to the borehole was completely opened. In view of the sharp temperature and pressure drop, it is speculated that fractures were initiated and slow leakage occurred. But, there are no obvious responses on tri-axial stress loading. After this point, pumping started, thus pressure steadily increased. The second peak pressure is 1402.6 psi at 1757.0 seconds, when the x- and y-stresses responded, as shown in Figure 3.326. Meanwhile, injection pressure drastically dropped and borehole wall temperature decreased due to CO_2 leakage and resultant expansion and vaporization. The corresponding temperature at the second peak pressure is 39.3 °C, which is above the supercritical temperature of 31.0 °C.

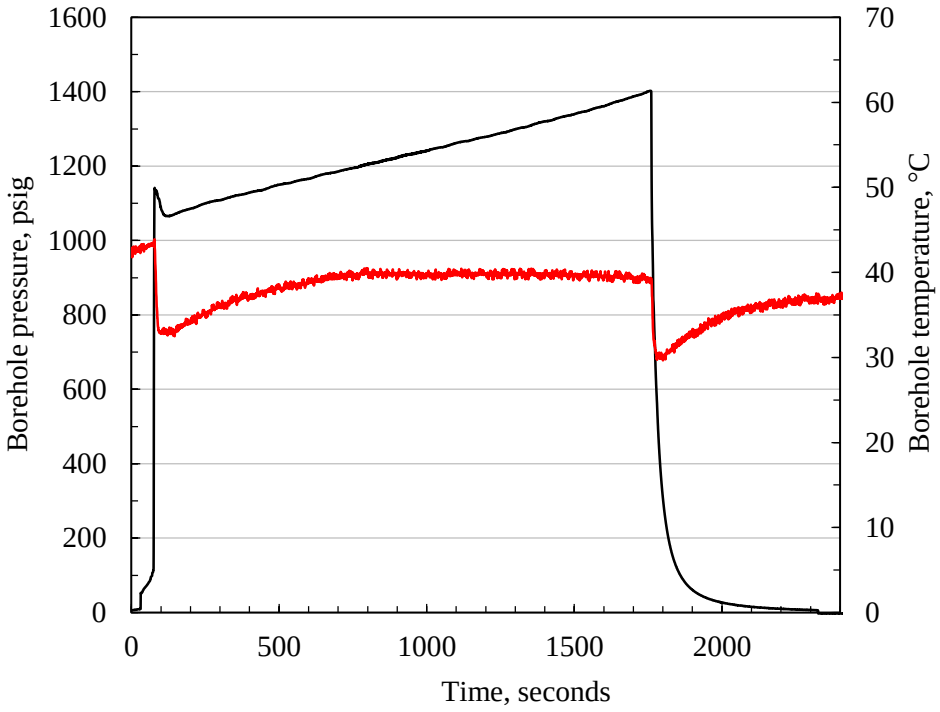

Figure 3.326. Pressure and temperature profiles of CO_2 injection into Sample 63.

Pressure decay measured before CO_2 injection for Sample 63 is shown in Figure 3.327, which shows very low permeability for the water saturated concrete block. After CO_2 injection, the induced fracture is too conductive so that the borehole pressure cannot be built to 100 psig.

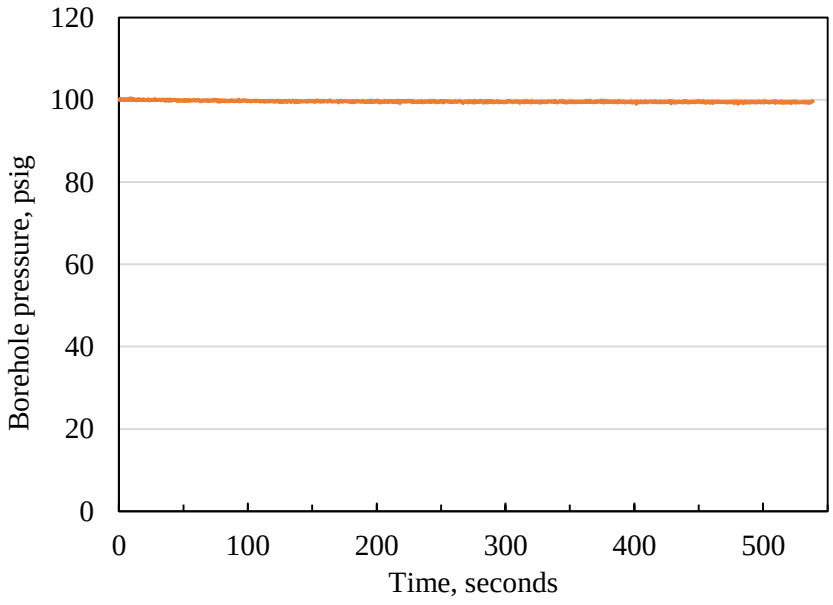

Figure 3.327. Pressure decay curve before treatment.

Seeing that the CO_2 injection induced fractures have reached the concrete surface, post-treatment acoustic emission tests, dye injection and gas fracturing were not conducted.

As shown in Figure 3.328, before treatment, and Figure 3.329, after treatment, it is clear that the induced fracture planes, almost perpendicular to the minimum horizontal stress direction, opened symmetrically on both sides of the borehole. Sample 63 was broken off by hand, as shown in Figure 3.330. The induced fracture propagated radially from the openhole section to the outer surface with slightly rugged planes.

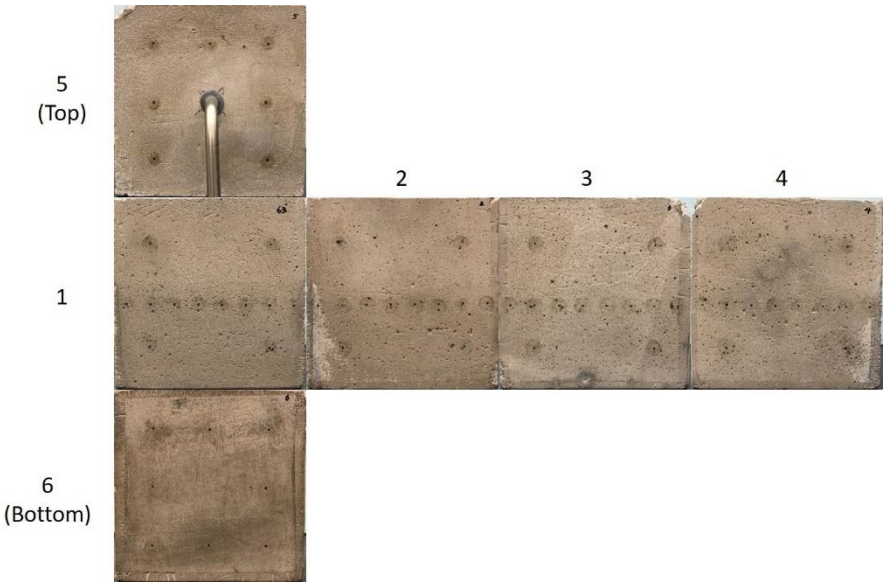

Figure 3.328. Surfaces of Sample 63 before treatment.

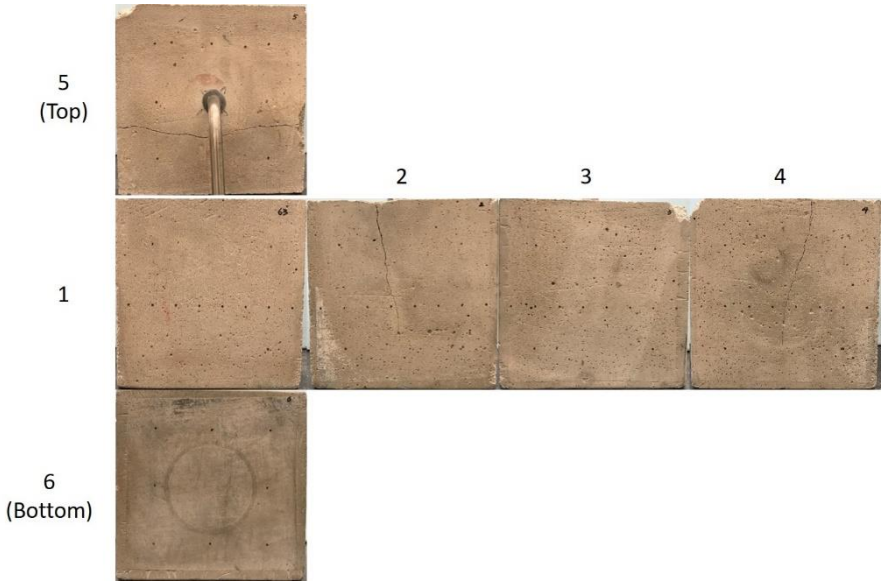

Figure 3.329. Surfaces of Sample 63 after coloring and gas fracturing.

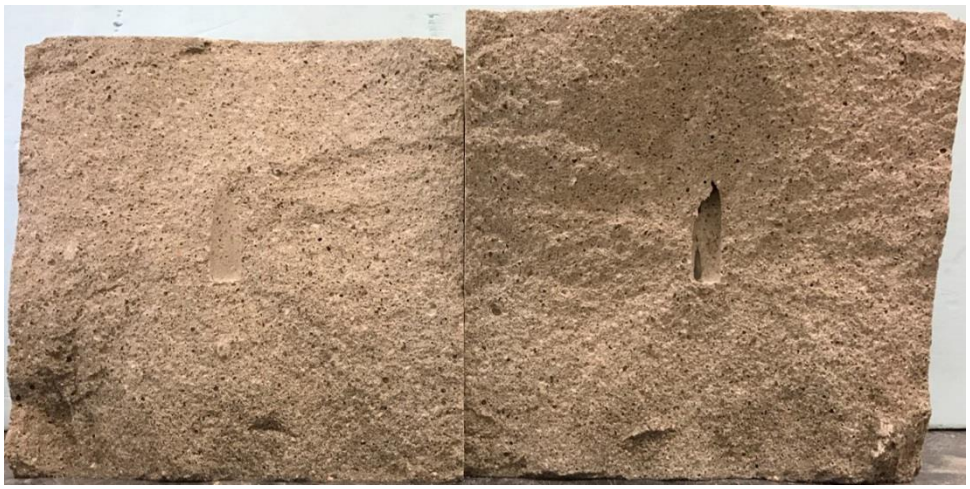

Figure 3.330. CO_2 injection induced fracture morphology of Sample 63 (opened from Surface 2).

For samples with seeding fractures (Sample 57 and Sample 59), peak pressures during CO_2 injection increase with elevating stress difference. By increasing the directional stress differences, the CO_2 injection induced fractures become larger, as is indicated by the decreasing gas N_2 fracturing pressures under both confined and unconfined conditions. Larger stress differences are favorable for generation of fractures. The sc-CO_2 induced fracture should be the extension of the seed fracture generated at the beginning. In addition, the temperature drastically dropped right after the fracturing point, due to CO_2 leakage and expansion.

For samples without seeding fractures and saturated with water (Sample 62 and Sample 63), peak pressures during CO_2 injection decrease with elevating tri-axial stress levels.

Water Saturated Samples

Samples 64, 65 and 66 are water saturated samples and went through the same experimental procedures as Samples 62 and 63, which have been covered above. Although the fracture morphology is different for each individual sample, all of these samples have delayed acoustic signal arrival time and changed wave forms, shown in Figure 3.331.

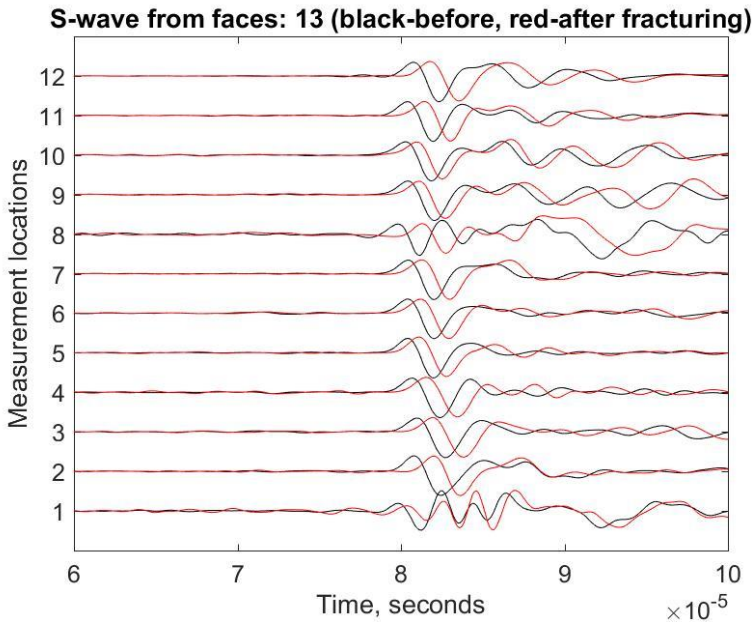

Figure 3.331: Typical acoustic measurements of water saturated samples (Sample 65 face 13).

Composite Samples

The composite samples are simplified versions of CO_2 injection into a high permeability zone which is surrounded by a low permeability sealing formation. For the composite samples, the high permeability balls in the center have lower strength, so they may be fractured easier than normal concrete samples. Composite Sample 67 failed due to leaking from side faces. Composite Sample 68 shows higher overall permeability with a visible decline during the pressure decay test, compared to normal concrete samples without an observable decline in a short period of time. The peak injection pressure (1214.33 psi) is within a reasonable range when compared to other concrete samples fractured with same stress condition (1250 psi in the x-direction, 2187 psi in the y-direction, and 2125 psi in the z-direction). Sample 68 has shown significant arrival delay in acoustic measurement, shown in Figure 3. and

Figure 3.. The fracturing plane is basically vertical and perpendicular to the minimum horizontal stress direction, shown in Figure 3.. It can be clearly distinguished that the high permeability ball in the center of Sample 68 has acted as a pressure equalizer within low permeability shell, since the dye color sufficiently and evenly filled the fracture plane within the ball boundary.

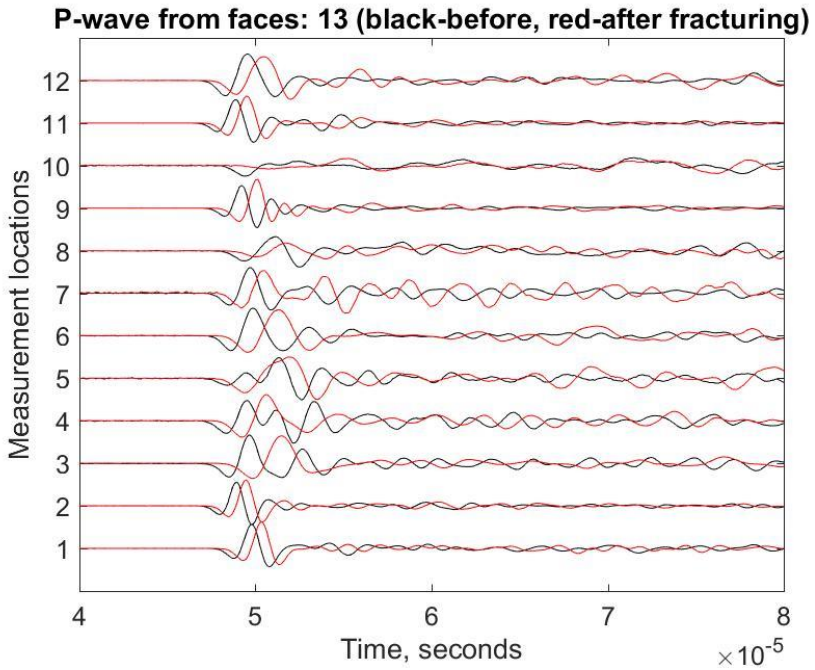

Figure 3.332: P-wave signature measured from Surface 1 and Surface 3 of Sample 68.

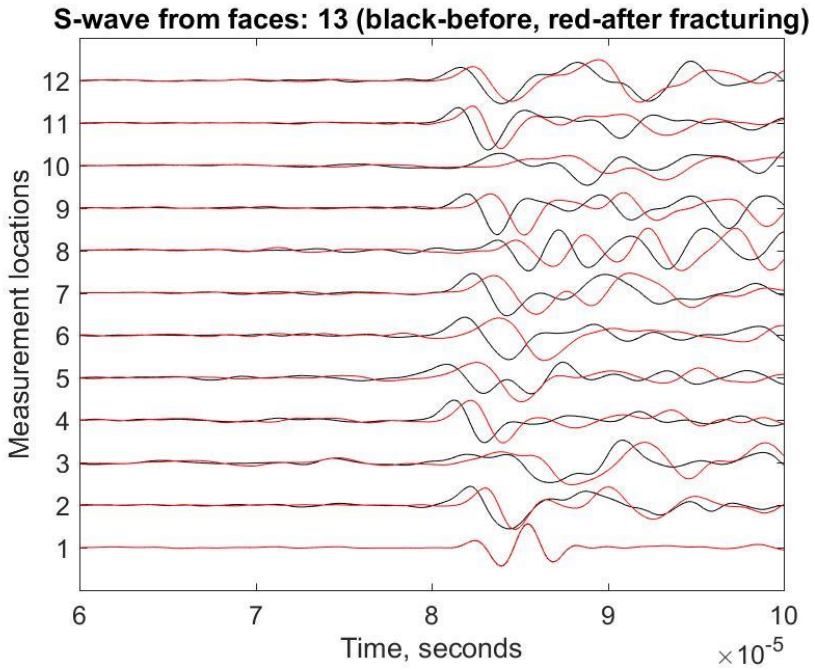

Figure 3.333: S-wave signature measured from Surface 1 and Surface 3 of Sample 68.

Figure 3.334: Colored CO_2 injection induced fracture planes in Sample 68. Note that the shape of high permeability ball is clearly distinguishable after dye injection.

In the following composite samples, boreholes were drilled to 4.5" of depth and casings were epoxied to 3.5" of depth. Thus the open-hole section is 1" long and locates at the center of the sample.

Composite Sample 69

Composite Sample 69 was subjected to stress condition of 1250 psi in the x-direction, 1875 psi in the y-direction, and 2500 psi in the z-direction. During CO_2 injection, the borehole pressure gradually increased to 1497 psi and then started to decline, as shown in Figure 3.335. Since the decline rate is relatively slow, it is very difficult to judge whether Sample 69 was fractured or not. Then at time around 4300 seconds, a new cycle of injection started. And this time, borehole pressure reached 1505 psi and then leaking was obvious. The borehole temperature dropped about 20 °C after leaking.

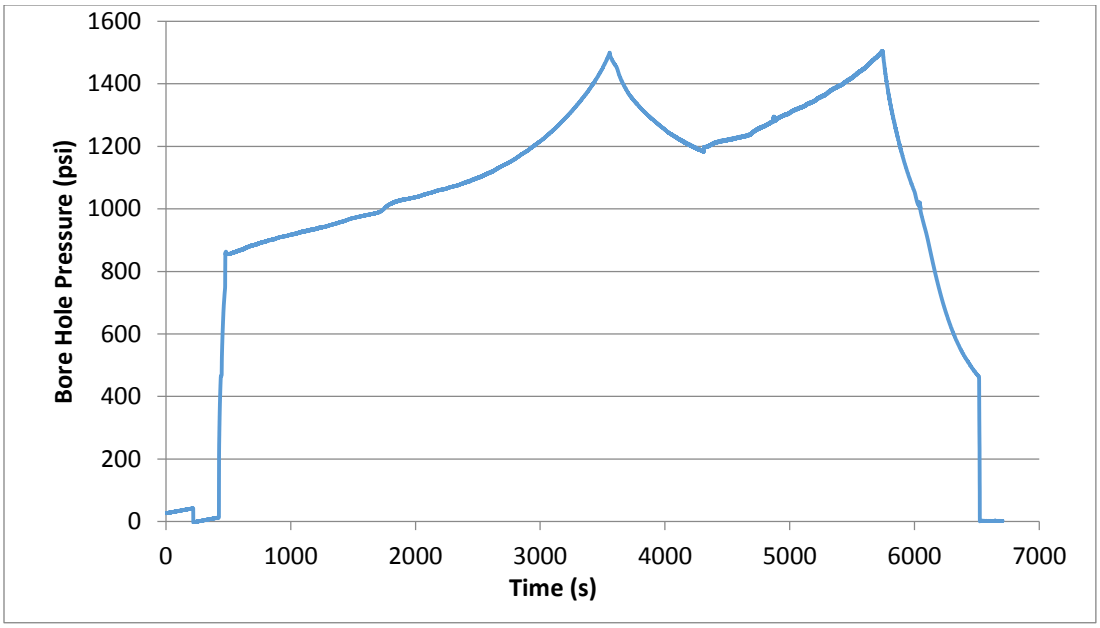

Figure 3.335: Borehole pressure during CO_2 injection test of Sample 69.

However, the acoustic measurement didn't show the obvious delay between measurements before and after CO_2 injection test. The post gas break-down pictures of fracture profile, shown in Figures 3.336 and 3.337 shows no CO_2 injection fractures reaching any surface but a leaking path in the near wellbore/casing region, which is not on the path of any acoustic measurement points.

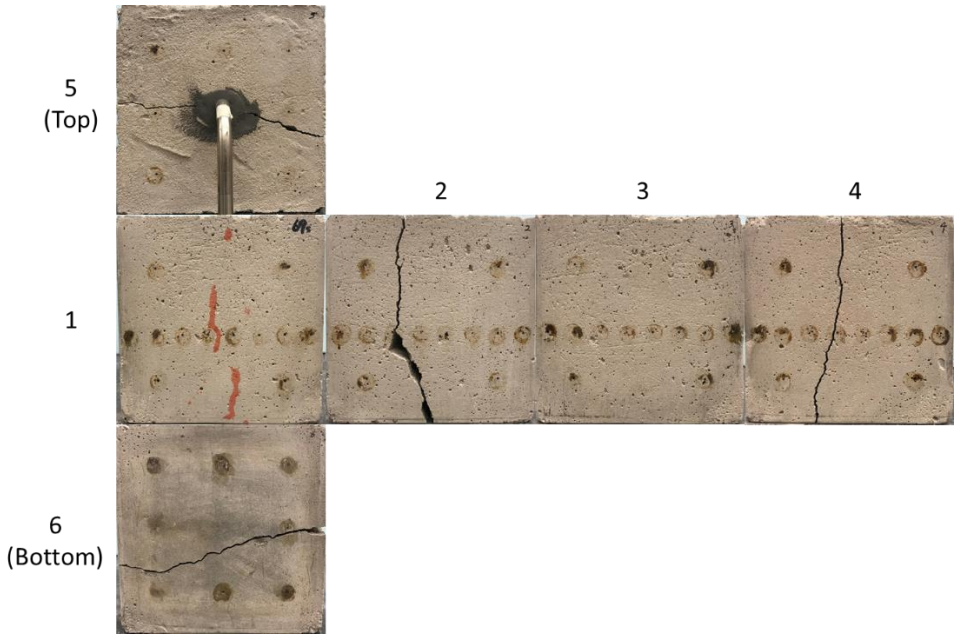

Figure 3.336. Surfaces of Sample 69 after dye injection and gas break-down.

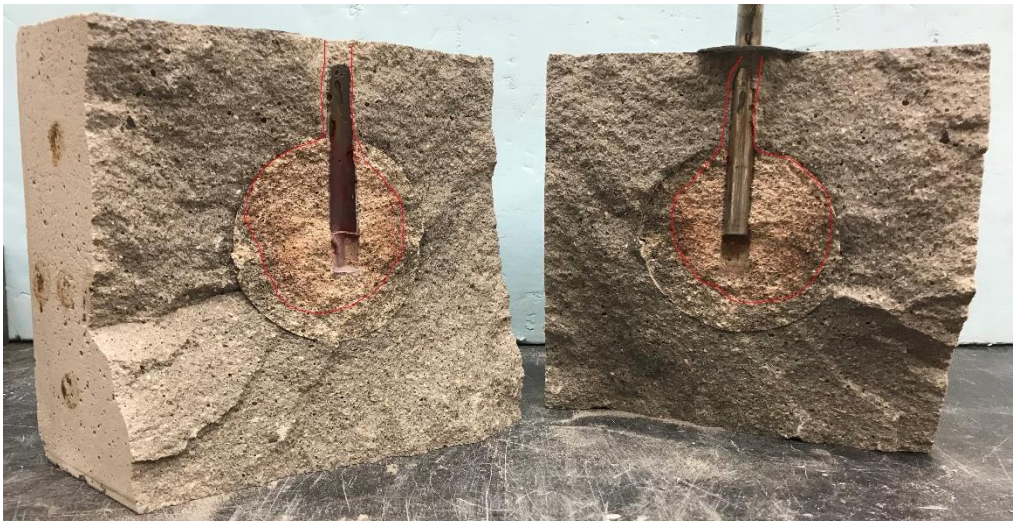

Figure 3.337. Fracture profile inside Sample 69.

Composite Sample 70 was subjected to stress condition of 1250 psi in the x-direction, 1562 psi in the y-direction, and 1875 psi in the z-direction. During CO_2 injection, the borehole pressure curve did not show a distinguished fracturing pressure, as shown in Figure 3.338. The injection rate was raised up to 100 ml/min around 900 seconds, resulting in a small hump between 900 seconds to 1100 seconds. Once the injection stopped (at 1150 seconds), the borehole pressure dropped at significant speed. The borehole temperature dropped about 13 °C after leaking.

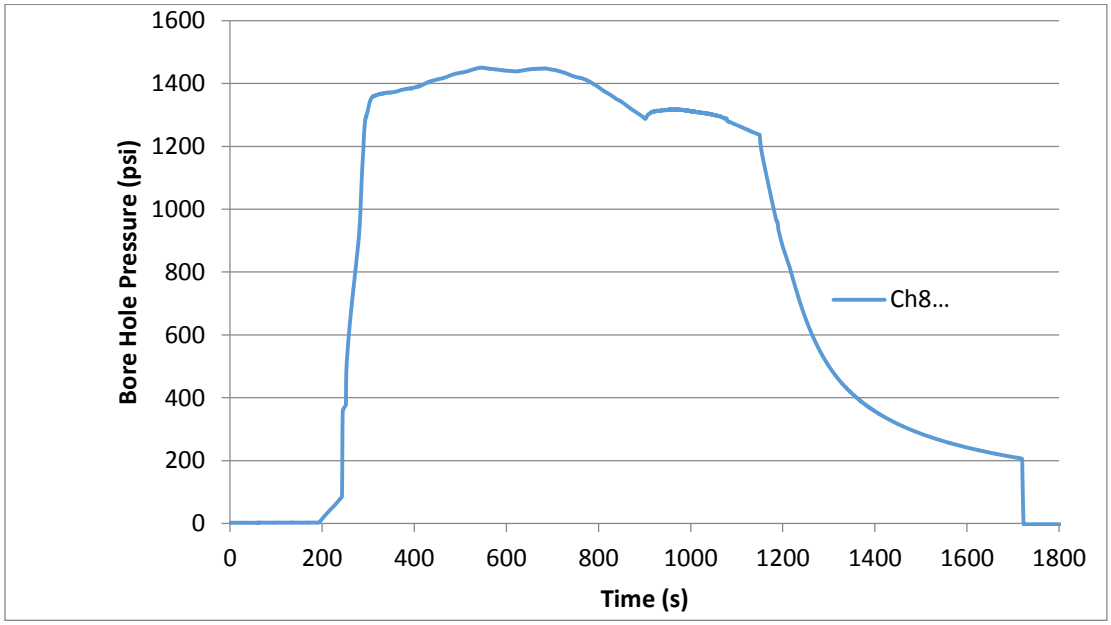

Figure 3.338. Borehole pressure during CO_2 injection test of Sample 70.

The acoustic measurement showed an obvious delay and wave form change for both P- and S-waves, as in Figure 3.339. There is no visible leaking of dye solution on any surface after dye

injection as shown in Figure 3.340. The fracture profile after sample break-down agrees with the points with more delay in acoustic measure.

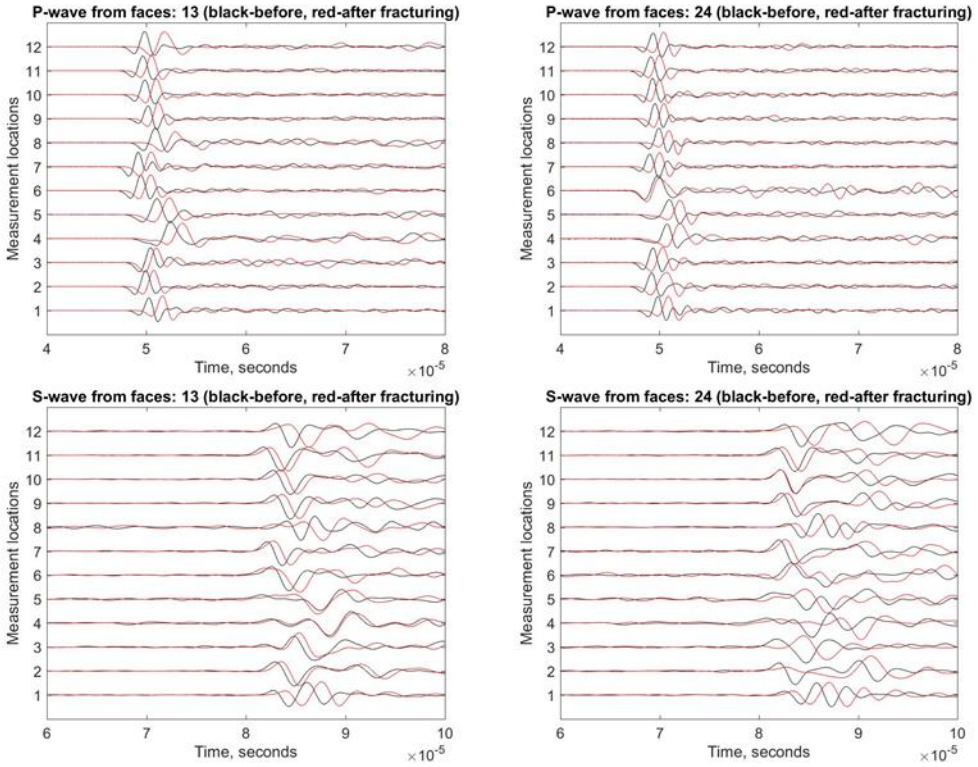

Figure 3.339: Acoustic measurement of Sample 70.

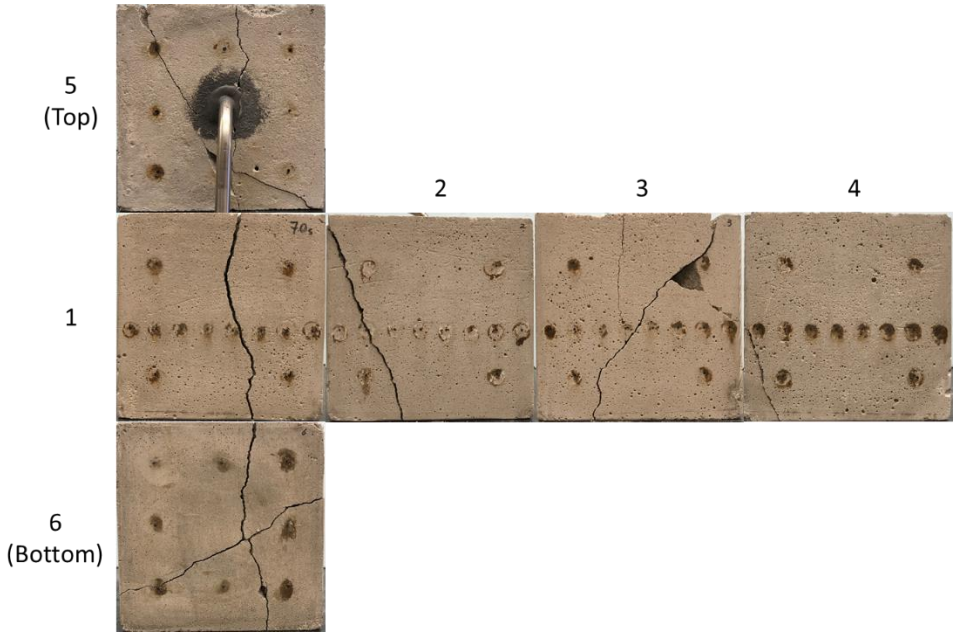

Figure 3.340: Surfaces of Sample 70 after dye injection and gas break-down.

Samples with pre-existing seeding fracture

Both of the samples (Samples 60 and 61) went through water fracturing first to create a relatively small-size fracture perpendicular to y-direction before CO_2 induced fracture (presumably perpendicular to x-direction). The idea of this type of experiment was to investigate whether the newly created fracture (i.e. induced by supercritical CO_2) will follow existing fracture pathways (induced by water). The faces of these two samples after gas fracturing are shown in Figure 3.341 and Figure 3.342. Both of these samples show a deviated fracture plane from the direction perpendicular to x-direction.

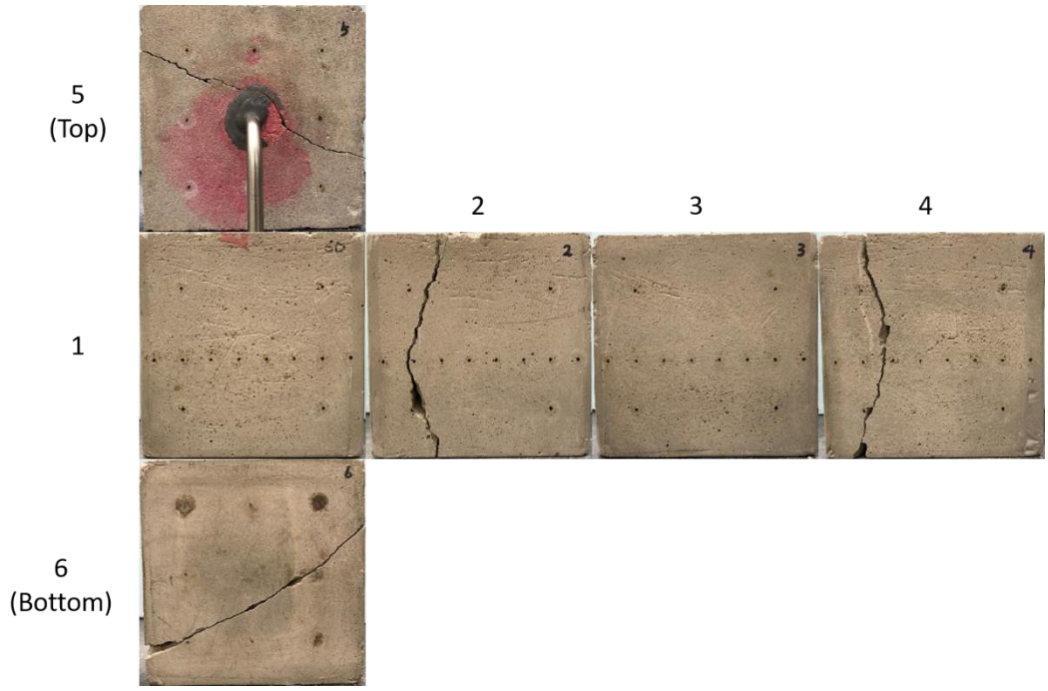

Figure 3.341 : Faces of Sample 60 after gas fracturing.

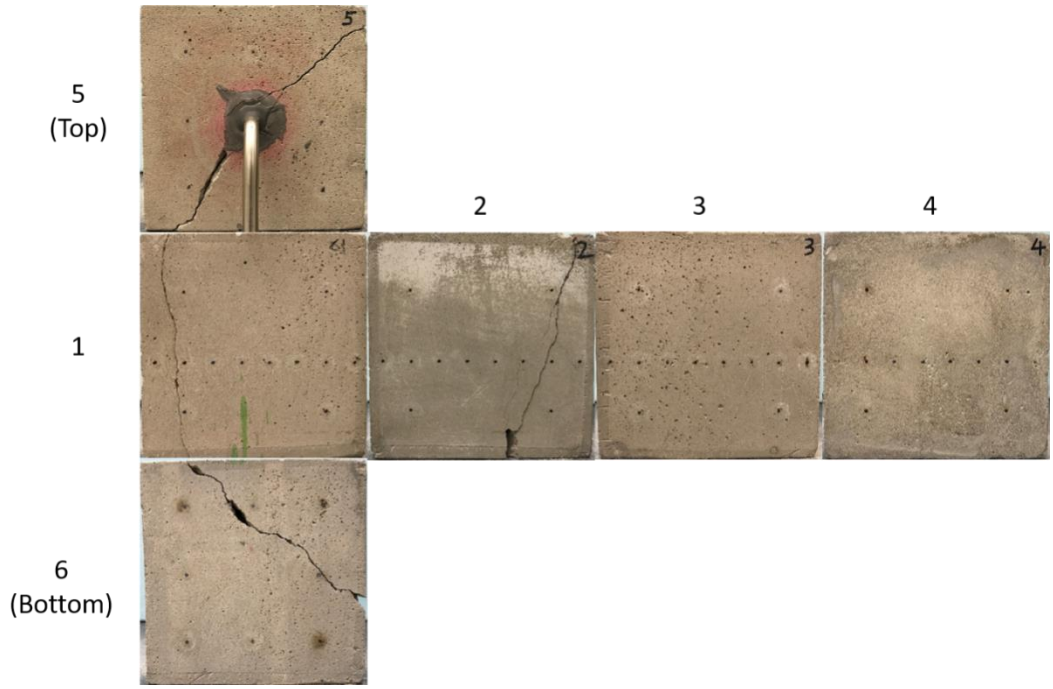

Figure 3.342： Faces of Sample 61 after gas fracturing.

Although sc-CO_2 induced fractures in these samples are deviated, none of these two samples shows new fractures will follow the direction the pre-existing fractures grow in, as shown in Figure 3.343 and 3.344. This might due to the pre-existing fractures being closed under the confining stress. However, their existence changed the local stress distribution, so the new fractures were deviated. Sample 61 clearly shows a water induced fracture that grows perpendicular to y-direction from the wellbore in Figure 3.345.

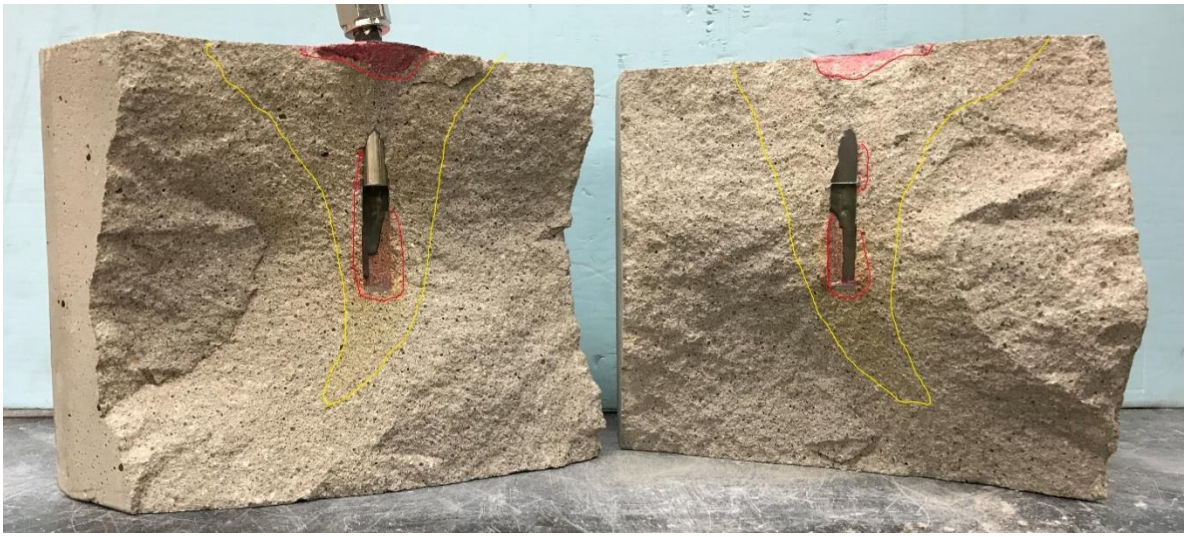
Figure 3.343: Colored water and CO_2 injection induced fracture planes in Sample 60.

3.344: Colored water and CO_2 injection induced fracture planes in Sample 61.

Figure 3.345: Water induced fracture that is perpendicular to y-direction in Sample 61.

Shale Samples

We acquired real shale rock chunks from the CEMEX Lyons, CO, cement plant, which excavates the Niobrara shale outcrop as raw material to manufacture Portland cement. In total, from the chunks, we have five 8-inch shale blocks cut, within which natural or preexisting fractures were observed. The sample borehole is 4.5-inch deep with a diameter of 0.7-inch and a 2-inch uncased

bottom section. By varying the tri-axial stresses, we injected CO_2 into four fractured shale samples and slick water into one sample to investigate initiation, propagation, patterns and morphology of injection induced fractures.

The experimental procedure for CO_2 injection into shale samples is detailed below. The injection rate was kept constant at 40 ml/min for all samples. Tri-axial stress loading level and difference were varied to investigate the effect of *in-situ* stress on the breakdown pressure during CO_2 injection. We first pre-heated the shale samples in an oven to a desired temperature, we then set up the sample in the tri-axial loading frame with injection pipelines connected. Afterwards, sc-CO_2 is pumped into the borehole until the sample is fractured. Depending on the borehole pressure when the samples were fractured, CO_2 in the borehole could be either in the supercritical state or the gas state. For these experiments, the procedures varied but generally consist of:

1. Surface cleaning and well bore installation.
2. Take pictures of the sample surfaces.
3. Pre-injection acoustic emission measurements.
4. Pressure decay under no stress loading using 100 psi nitrogen gas.
5. CO_2 injection until sample fractures.
6. Take pictures if obvious fractures were generated on sample surfaces.
7. Post-injection acoustic emission measurements.
8. Pressure decay under no stress loading using 100 psi nitrogen gas.
9. Fracture coloring by pressurizing dye solution into the sample.
10. Heat the sample to dry dye solution if necessary.
11. Gas fracturing under tri-axial stresses loading.
12. Take pictures of the internal fracture planes and sample surfaces.

Shale Sample 1

Shale Sample 1 was fractured by sc-CO_2 under tri-axial stresses of 1600 psi in the x-direction, 2100 psi in the y-direction, and 2600 psi in the z-direction. Before injection, acoustic measurements and a pressure decay test were carried out as reference for post-injection comparison. After that, under the same tri-axial stress loading, shown in Figure 3.346, sc-CO_2 was injected at a constant rate of 40 ml/min into the sample. Figure 3.347 shows the pressure profile for Shale Sample 1 during CO_2 injection and Figure 3.348 shows the temperature profile. The breakdown pressure for CO_2 injection is 1300.1 psig at 1135.6 seconds, corresponding to an obvious bump on the x-stress and slight drops on y- and z-stress in Figure 3.346. The temperature when the sample was fractured was 37.4 °C in Figure 3.348, then it sharply dropped to 29.4 °C due to sc-CO_2 leakage through generated fractures and resultant vaporization.

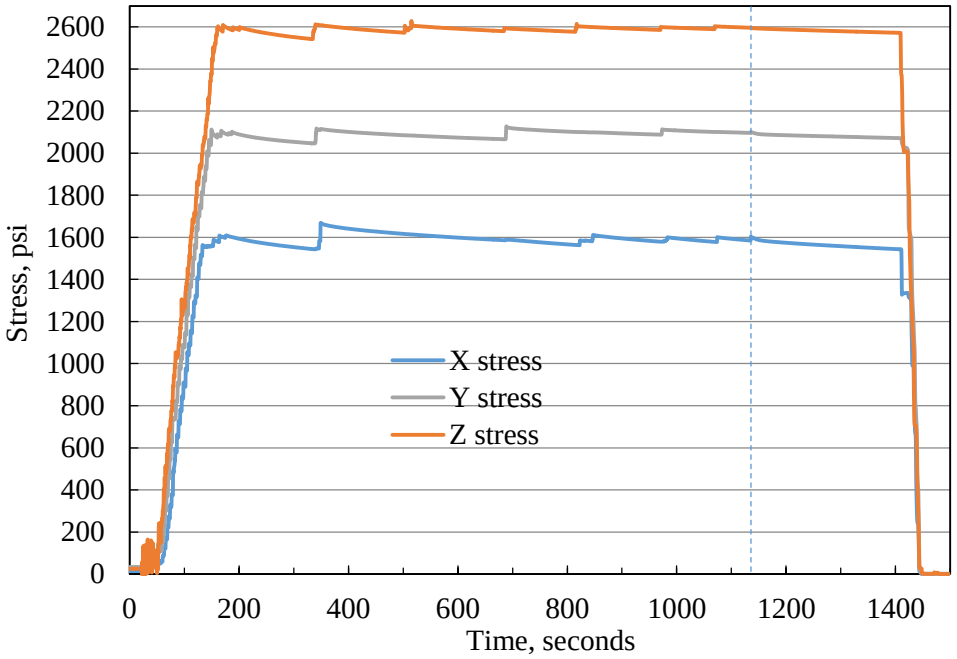

Figure 3.346. Tri-axial stress loading for CO_2 injection into Shale Sample 1.

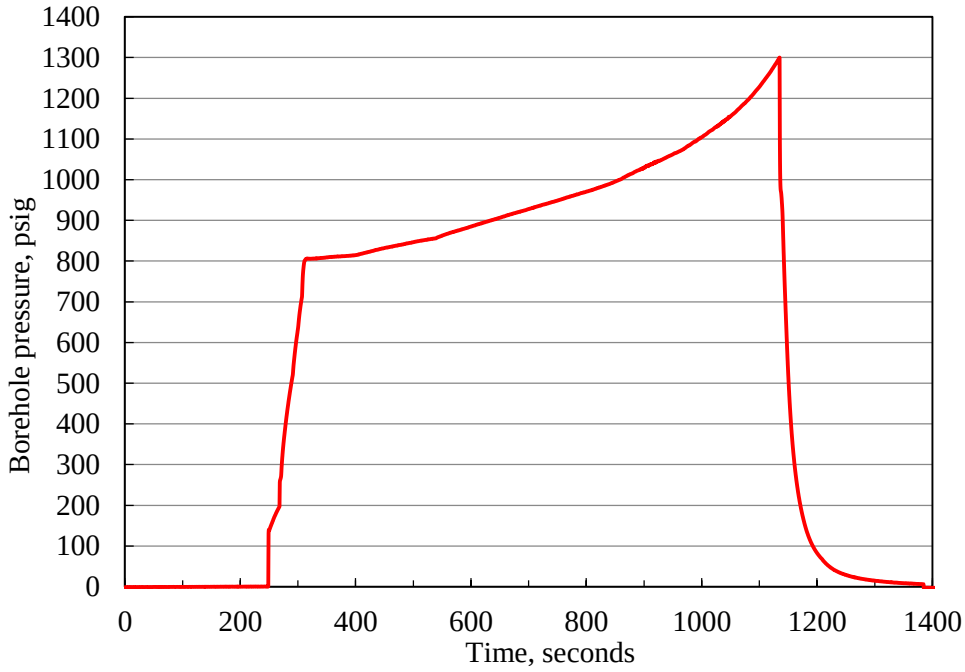

Figure 3.347. CO_2 injection pressure of Shale Sample 1.

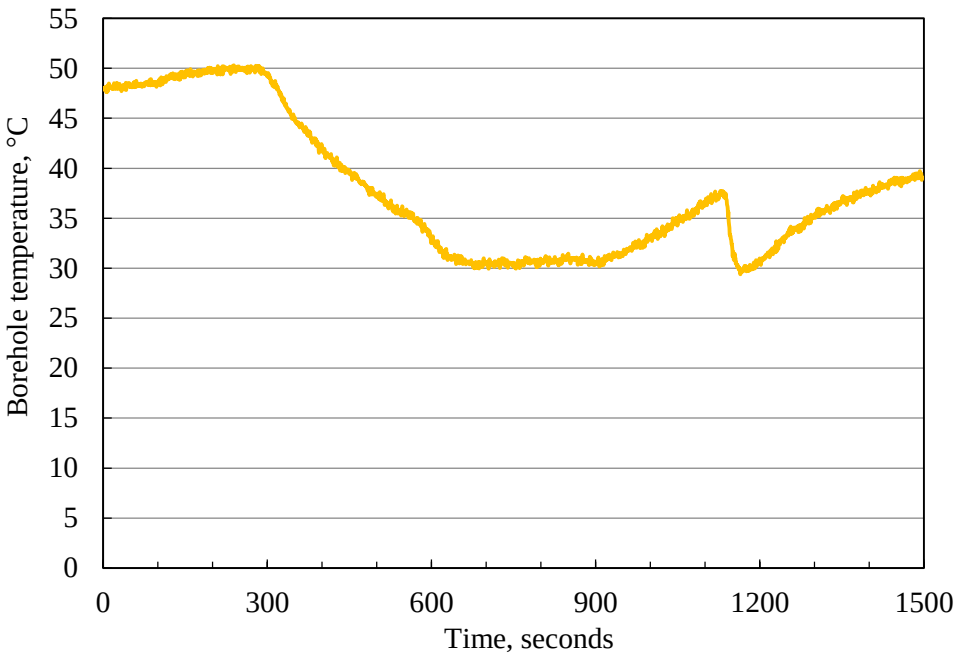

Figure 3.348. Borehole wall temperature profile during CO_2 injection into Shale Sample 1.

Pressure decay curves measured before and after CO_2 injection for Shale Sample 1 are compared in Figure 3.349, which shows significant permeability increase of the shale block due to injection induced fractures.

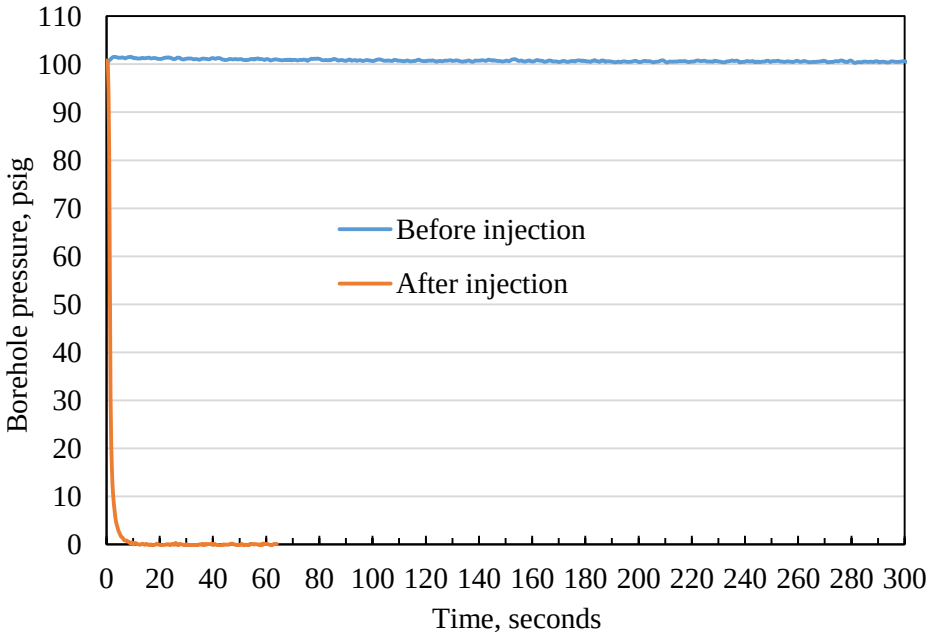

Figure 3.349. Pressure decay curves before and after treatment for Shale Sample 1.

Figures 3.350 to 3.355 compare the two acoustic wave curves measured before and after CO_2 injection: black - before injection, red - after injection. It can be seen that after sc-CO_2 injection both P-waves and S-waves at most of the measurement locations delay in arrival time and the

normalized waveforms change, indicating certain internal structure change rather than a simple compaction in density.

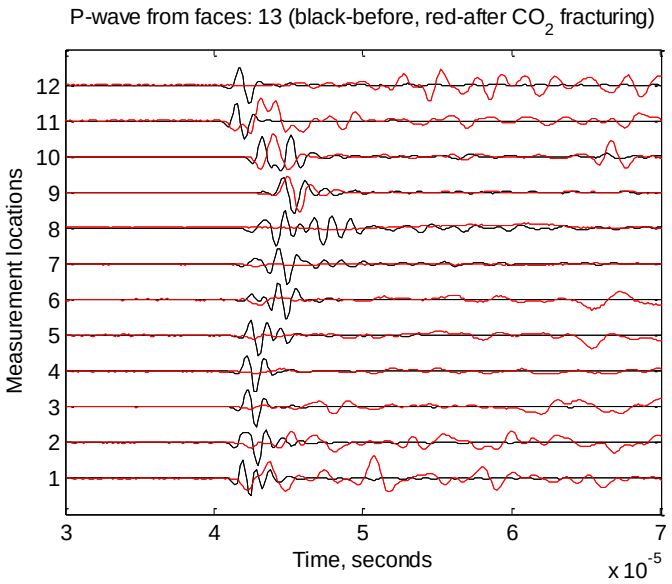

Figure 3.350. P-wave signatures measured from Surface 1 and Surface 3 of Shale Sample 1.

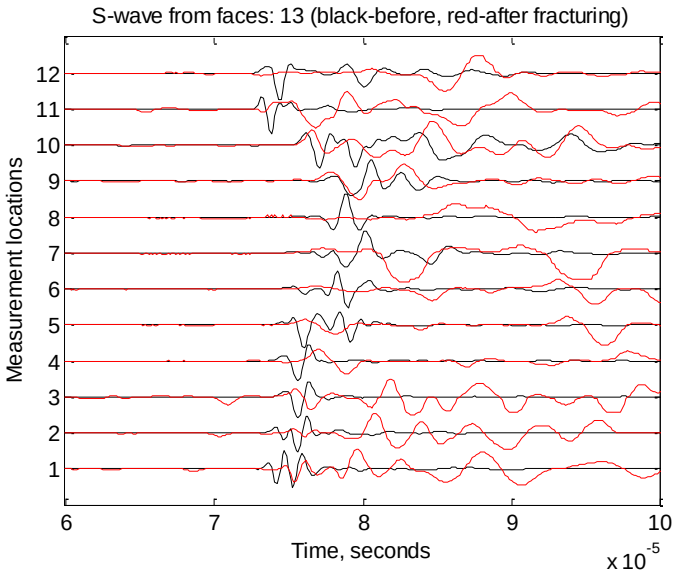

Figure 3.351. S-wave signatures measured from Surface 1 and Surface 3 of Shale Sample 1.

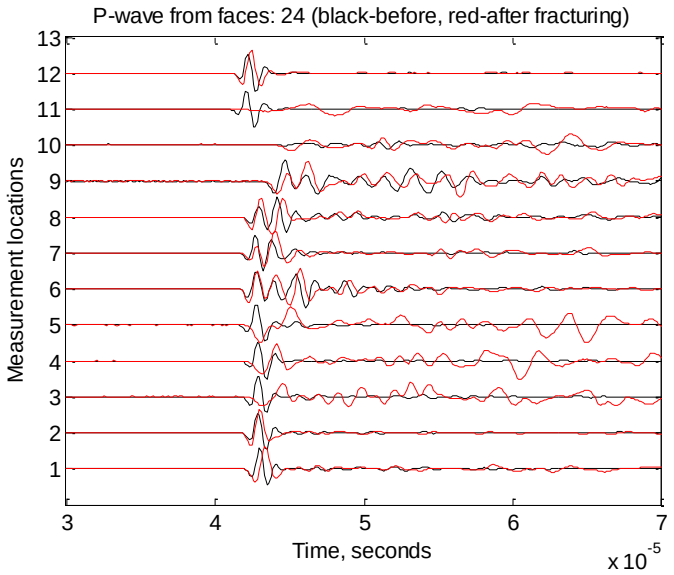

Figure 3.352. P-wave signatures measured from Surface 2 and Surface 4 of Shale Sample 1.

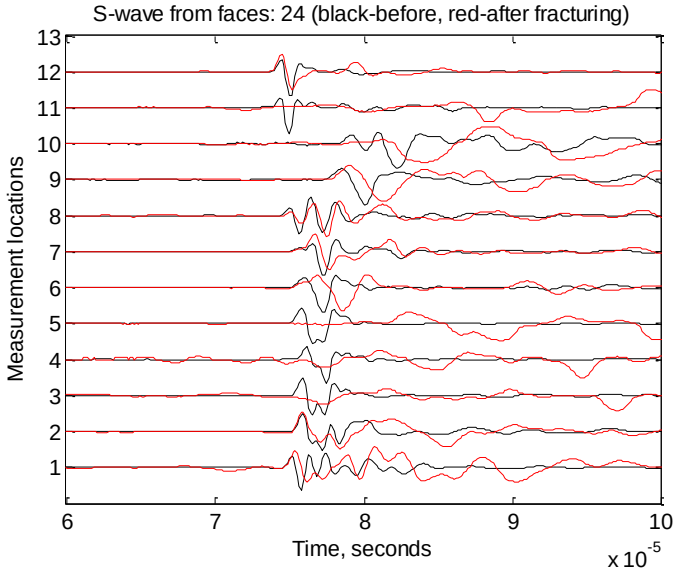

Figure 3.353. S-wave signatures measured from Surface 2 and Surface 4 of Shale Sample 1.

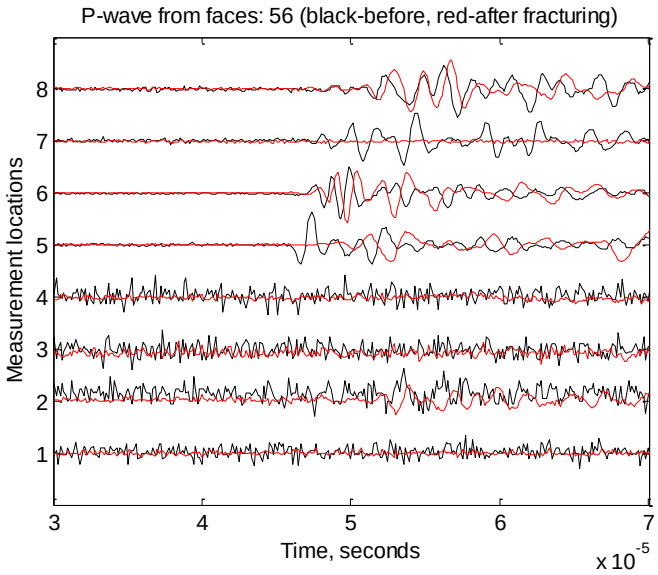

Figure 3.354. P-wave signatures measured from Surface 5 and Surface 6 of Shale Sample 1.

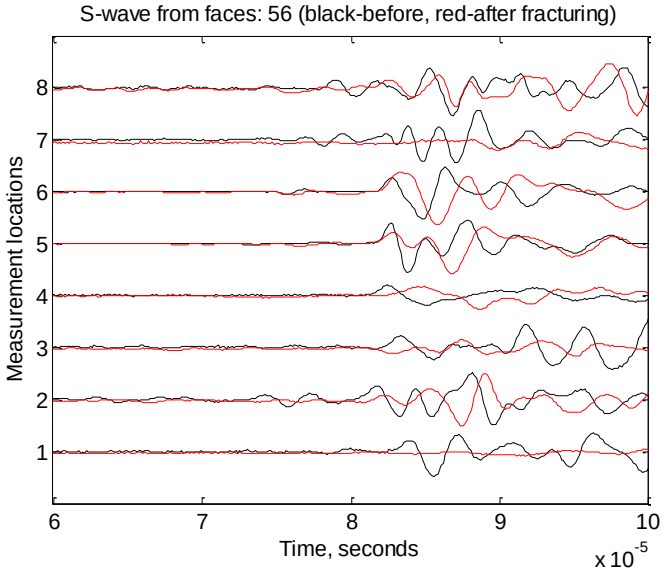

Figure 3.355. S-wave signatures measured from Surface 5 and Surface 6 of Shale Sample 1.

Dye solution was then injected at about 70 psig into Shale Sample 1 to color the CO_2 injection induced fractures, through which dye solution flowed out of the block surface within tens of seconds. Then, the sample was fractured under tri-axial stress loading by nitrogen gas. The tri-axial stress and pressure profiles are shown in Figures 3.356 and 3.357, respectively. Under tri-axial stress loading, Shale Sample 1 was fractured with a peak pressure of 1448.0 psig at 369.6 seconds, shown in Figure 3.357, corresponding to slight bumps on x- and y-stress and a slight drop on z-stress in Figure 3.356, indicating major fractures opening against x- and y-stress. By further unloading the tri-axial stress, the sample broke down at 81.7 psig.

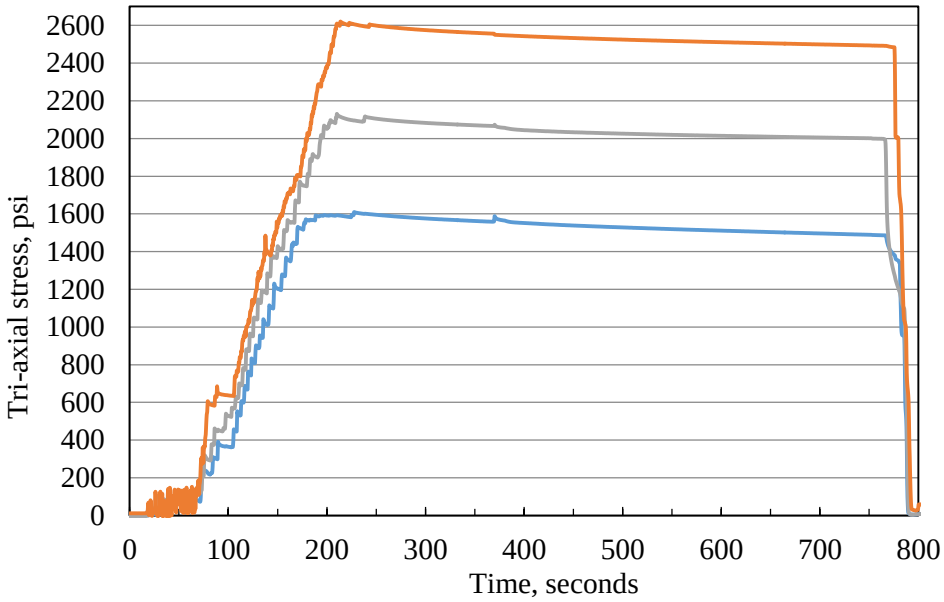

Figure 3.356. Tri-axial stresses for nitrogen gas fracturing.

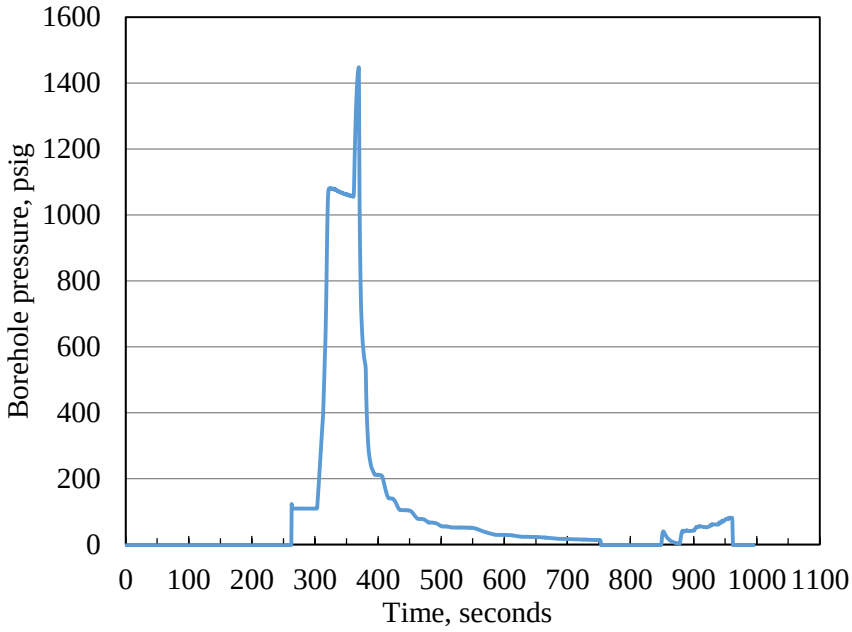

Figure 3.357. Pressure profile of gas fracturing and unconfined breakdown.

Before any treatment, the faces of Shale Sample 1 are shown in Figure 3.358. After the CO_2 injection, the shale sample faces are shown in Figure 3.359. It is obvious that after injection, vertical fractures that are generally perpendicular to the minimum horizontal stress (x-stress) appear on Face 2 and 6.

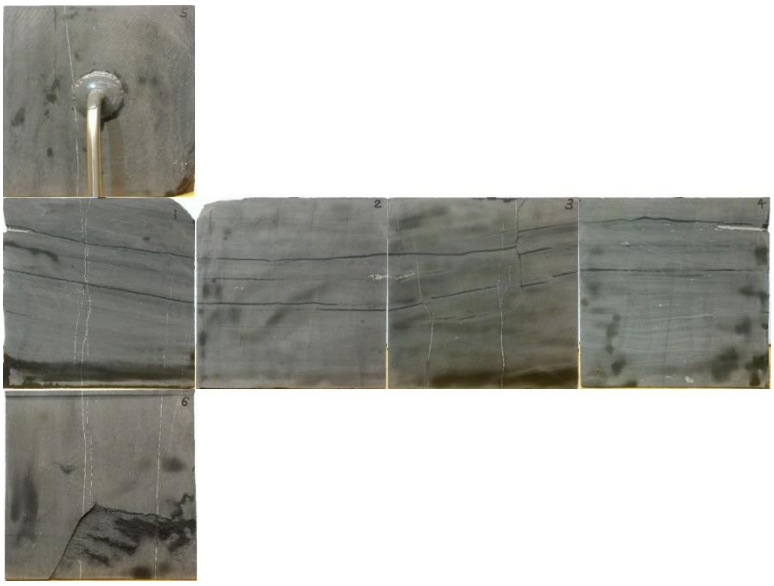

Figure 3.358. Surfaces of Shale Sample 1 before treatment.

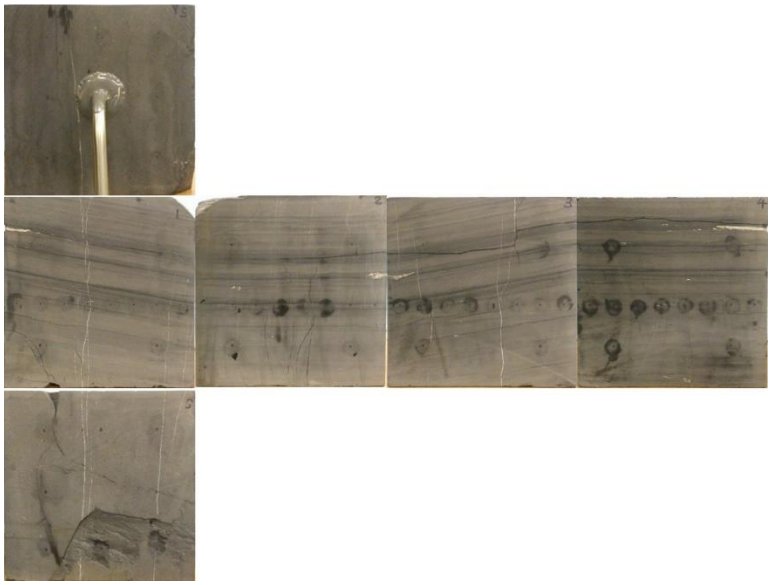

Figure 3.359. Surfaces of Shale Sample 1 after injection.

Coloring and gas fracturing revealed the fracture planes generated by sc-CO_2 injection, as shown in Figures 3.360 and 3.361, respectively. Coloring further developed the visible contrast of the sc-CO_2 injection induced fractures from the shale matrix. There is only one big fracture induced by sc-CO_2 injection, and the fracture plane is sinuous rather than straight. Generally, it is generated in a circular shape around the open hole section. The distinction between sc-CO_2 fracture and nitrogen gas fracture is quite clear, as can be identified from the transition of the relatively smooth to ragged region. There are no secondary fractures seen in the picture except that nitrogen gas created an additional fracture along the bedding interface.

Figure 3.360. Sample faces after dye injection.

Figure 3.361. Sc-CO_2 injection induced fracture morphology of Shale Sample 1 after coloring and gas fracturing.

Shale Sample 2

For Shale Sample 2, acoustic wave measurements and a pressure decay were first conducted under no stress loading as a reference for comparison of permeability change after CO_2 injection for the sample. Shale Sample 2 was then treated by injecting CO_2 into borehole under tri-axial stress loading of 1100 psi in the x-direction, 1600 psi in the y-direction, and 2100 psi in the z-direction, shown in Figure 3.362.

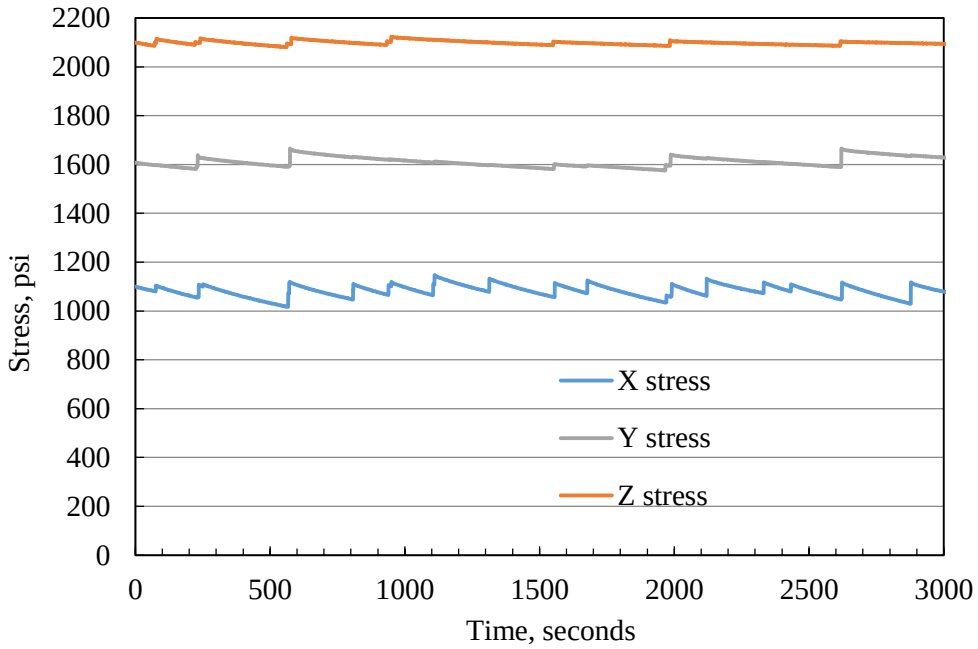

Figure 3.362. Tri-axial stress loading for CO_2 injection into Shale Sample 2.

The borehole pressure and temperature profiles are shown in Figures 3.363 and 3.364. The first peak pressure is 953.6 psig at 191.1 seconds, as achieved by opening the valve to allow sc-CO_2 to flow from the pump to the borehole. The temperature was 46.2 °C. After this point, the pump ran at 10 ml/min while the borehole pressure kept decreasing fast. Then, the pump rate was increased to 40 ml/min, and the rate of pressure decreasing slowed down. We then increased the pump rate to 80 ml/min, which turned the pressure profile up and reached a second peak of 727.2 psig at 907.6 seconds when the pump ran out of CO_2. The valve was immediately closed and the pump was refilled and heated, during which borehole pressure decreased to 220.4 psig at 1608.6 seconds. In view of the high pressure decreasing rate, it was speculated that fractures were initiated and leakage occurred. At this point, the valve was reopened and pumping restarted at 80 ml/min, and the third peak pressure is 769.3 psig at 1687.6 seconds. After that the second pump of CO_2, injection was stopped, leaving the pressure to decrease until 3000 seconds. During the whole injection process, there are no obvious responses on tri-axial stress loading in Figure 3.362. However, borehole wall temperature shows obvious decreases at the moments when the first and the third pressure peaks were achieved, due to CO_2 leakage and resultant vaporization. Since the pressure peaks are below the supercritical pressure, Shale Sample 2 was fractured by gaseous CO_2.

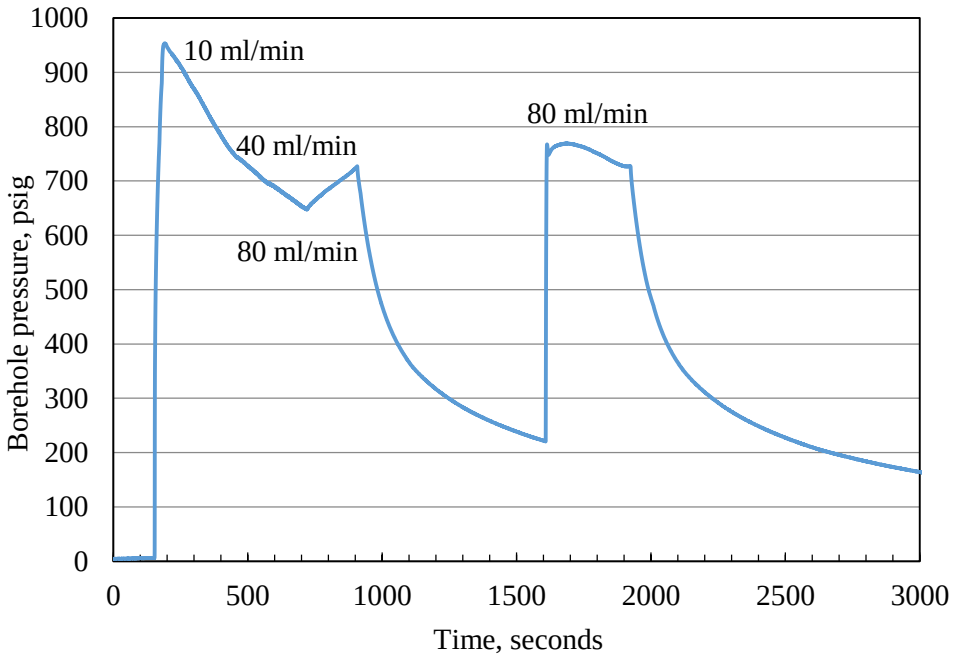

Figure 3.363. Pressure profile of CO_2 injection into Shale Sample 2.

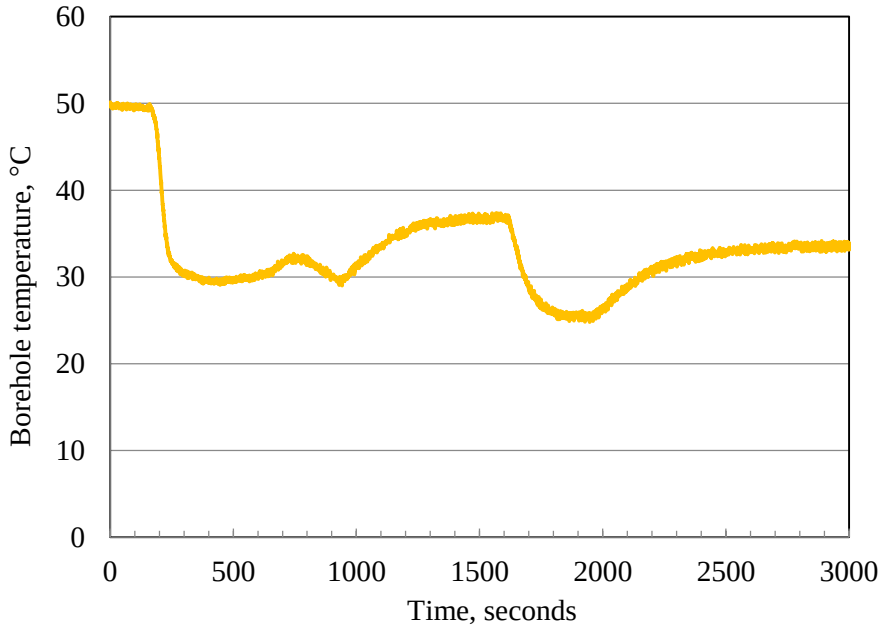

Figure 3.364. Temperature profiles during CO_2 injection into Shale Sample 2.

Pressure decay curves measured before and after CO_2 injection for Shale Sample 2 are compared in Figure 3.365, which shows obvious permeability increase of the shale block due to injection induced fractures. As compared to Shale Sample 1, the decreasing rate, however, is much slower, indicating that the induced fractures are much smaller or more confined than those generated in Shale Sample 1.

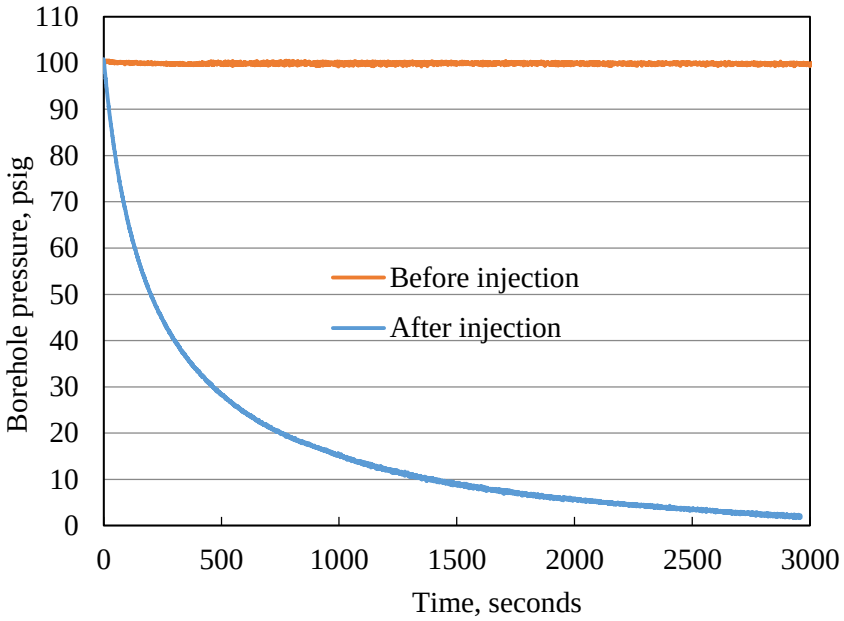

Figure 3.365. Pressure decay curves before and after CO_2 injection.

Figure 3.366 through 3.371 compare the two acoustic wave curves measured before and after CO_2 injection: black - before injection, red - after injection. It can be seen from Figure 3.366 that after CO_2 injection P-wave signatures measured from Surfaces 1 and Surface 3 showed slight delays in arrival time at location: 5-8, 10 and 12, indicating that induced fractures exist across the pathway of these measurement locations. Nonetheless, on Figure 3.367, S-wave signatures remain almost the same, which means that these fractures are tightly closed, or the fracture width is very small; this is consist with the pressure decay test. P-wave and S-wave signatures measured from Surfaces 2 and Surface 4 and Surfaces 5 and Surface 6 show no obvious changes, implying that there are no fractures induced or induced fractures are very tight.

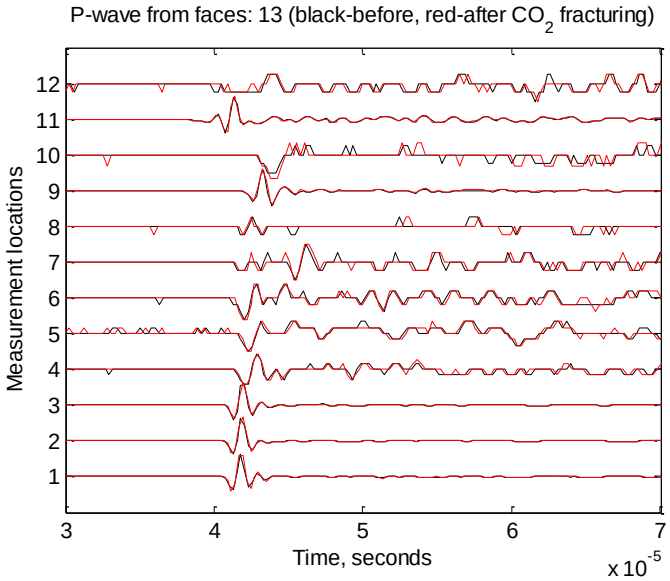

Figure 3.366. P-wave signatures measured from Surfaces 1 and Surface 3.

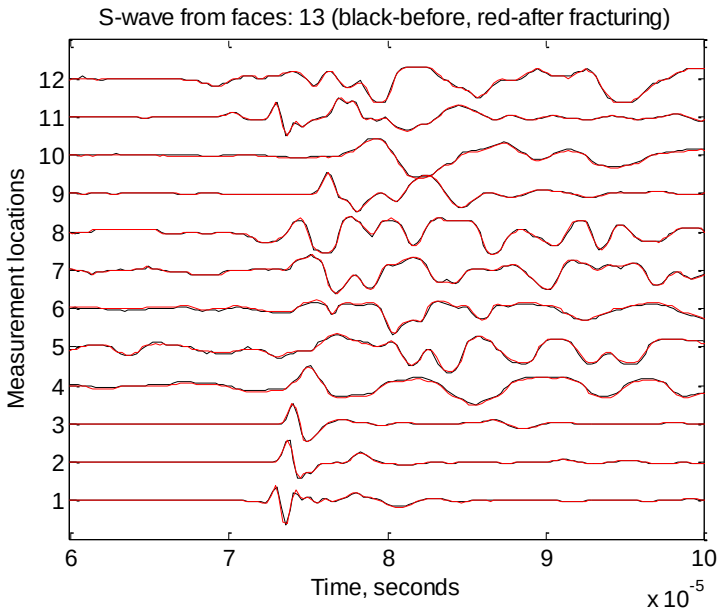

Figure 3.367. S-wave signatures measured from Surfaces 1 and Surface 3.

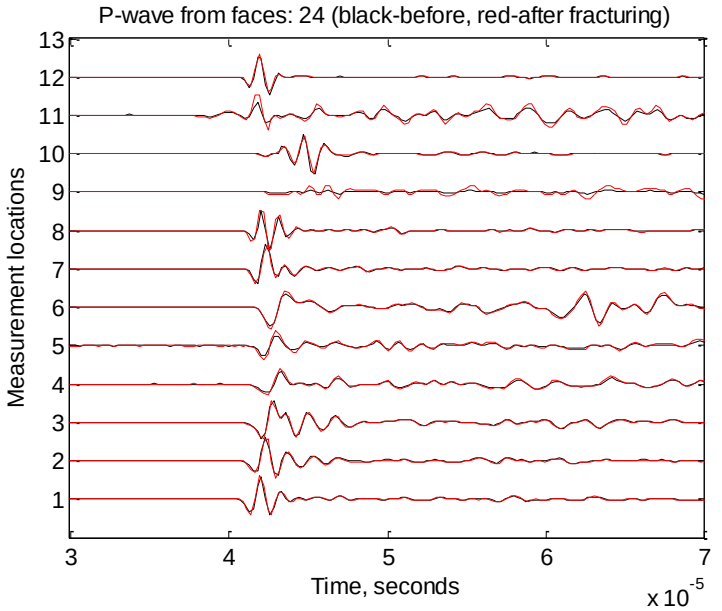

Figure 3.368. P-wave signatures measured from Surfaces 2 and Surface 4.

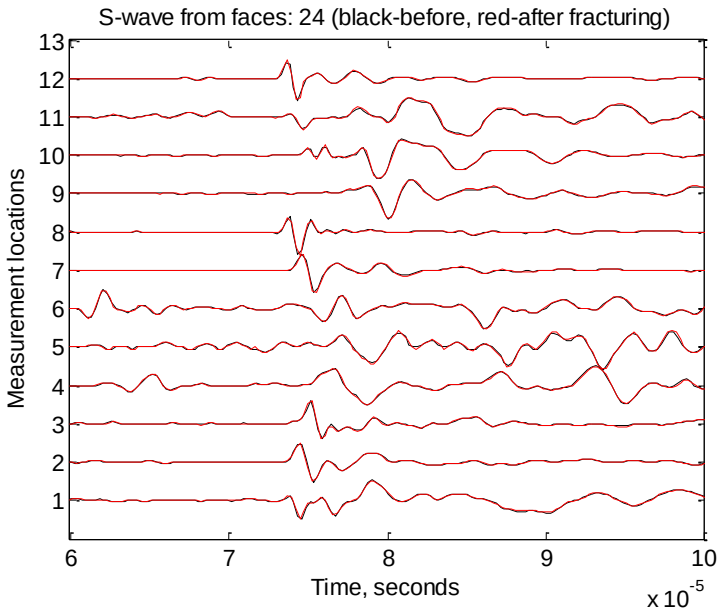

Figure 3.369. S-wave signatures measured from Surfaces 2 and Surface 4.

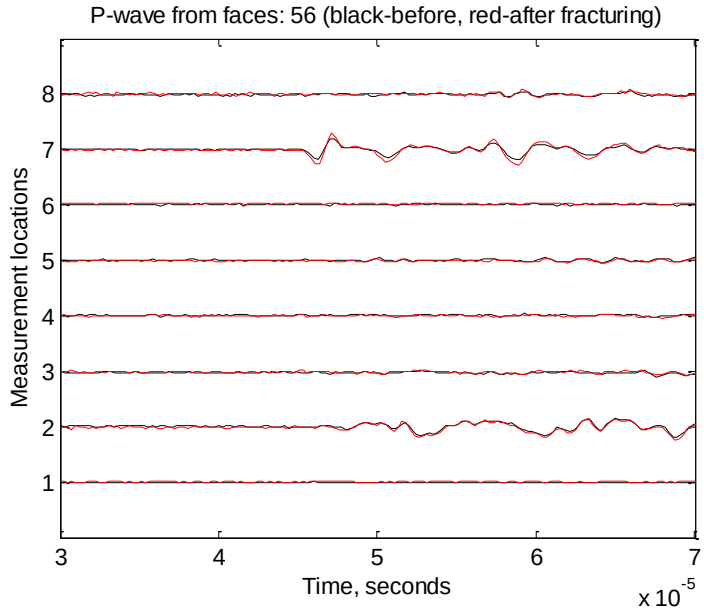

Figure 3.370. P-wave signatures measured from Surfaces 5 and Surface 6.

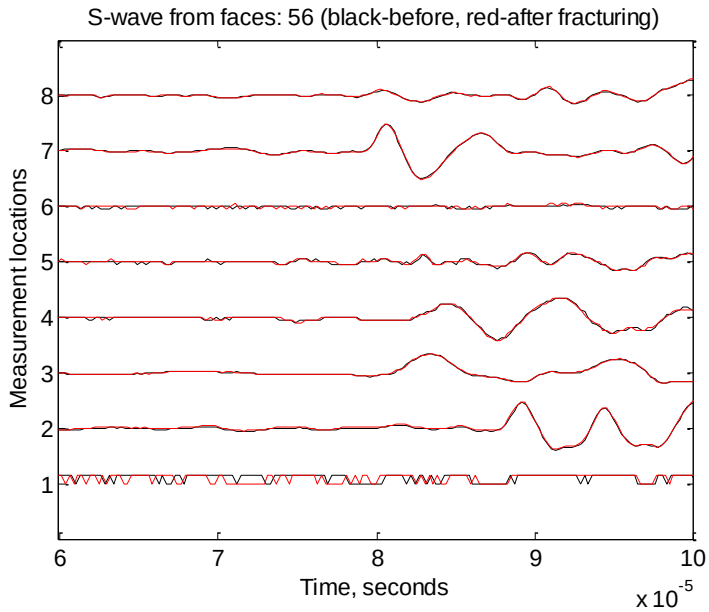

Figure 3.371. S-wave signatures measured from Surfaces 5 and Surface 6.

Comparison of the faces of Shale Sample 2 before, shown in Figure 3.372, and after, shown in Figure 3.373, CO_2 injection does not show any new fractures on all six faces.

Figure 3.372. Surfaces of Shale Sample 2 before CO_2 injection.

Figure 3.373. Surfaces of Shale Sample 2 after CO_2 injection.

We then used a bubbling agent to detect the leaking points while pressurizing the borehole to ~50 psig with nitrogen gas; leaking points appeared on Surface 1 and Surface 2, as shown in Figure 3.374.

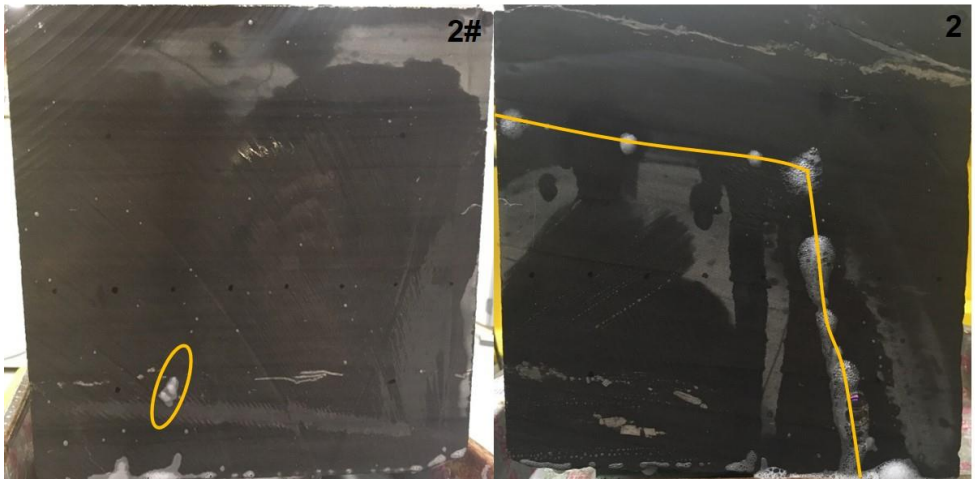

Figure 3.374. Leaking points on Faces 1 and 2 after CO_2 injection.

Dye solution was later injected into Shale Sample 2 to color the CO_2 injection induced fracture planes. Then, under tri-axial stress loading, shown in Figure 3.375, high pressure nitrogen gas was used to fracture the sample. As shown in Figure 3.376, two pressure peaks of 1715.5 and 1590.0 psig were achieved at 161.1 and 471.1 seconds, respectively. This two pressure peaks caused humps on both x- and y-axis stresses in Figure 3.375, meaning that there are gas fractures generated perpendicular or angular to both x- and y-axis. Then, without tri-axial stress loading, the sample was broken down by nitrogen gas at 96.4 psig, shown in Figure 3.377.

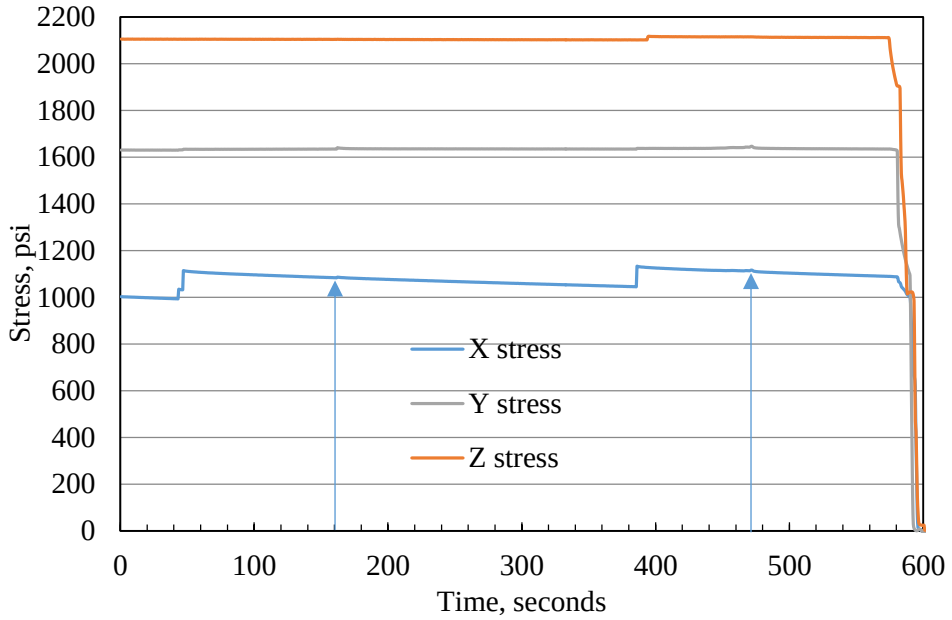

Figure 3.375. Tri-axial stress loading for gas fracturing of Shale Sample 2.

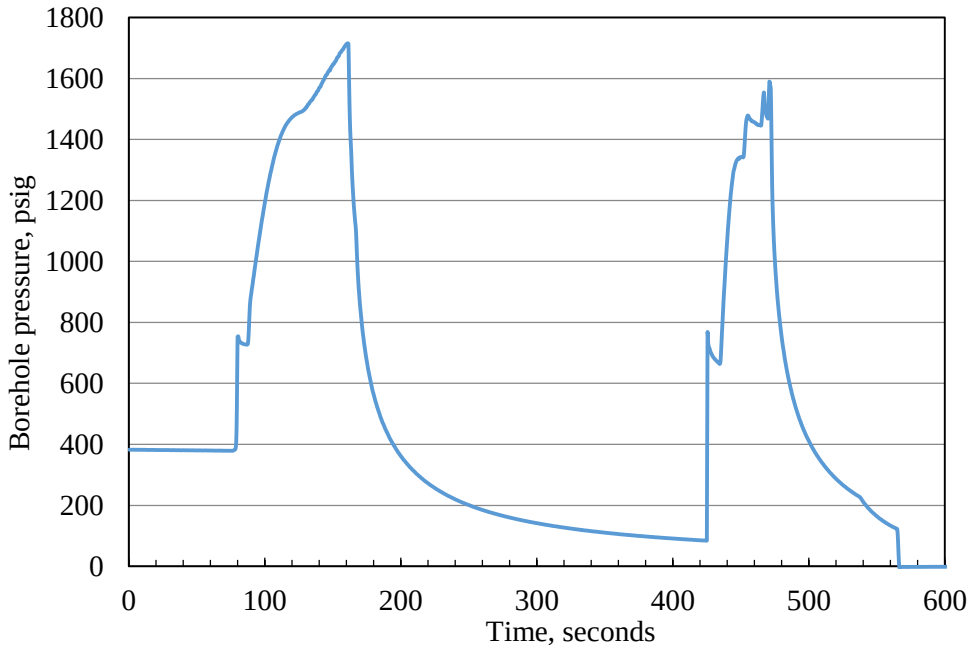

Figure 3.376. Pressure profile during gas fracturing with tri-axial stress loading.

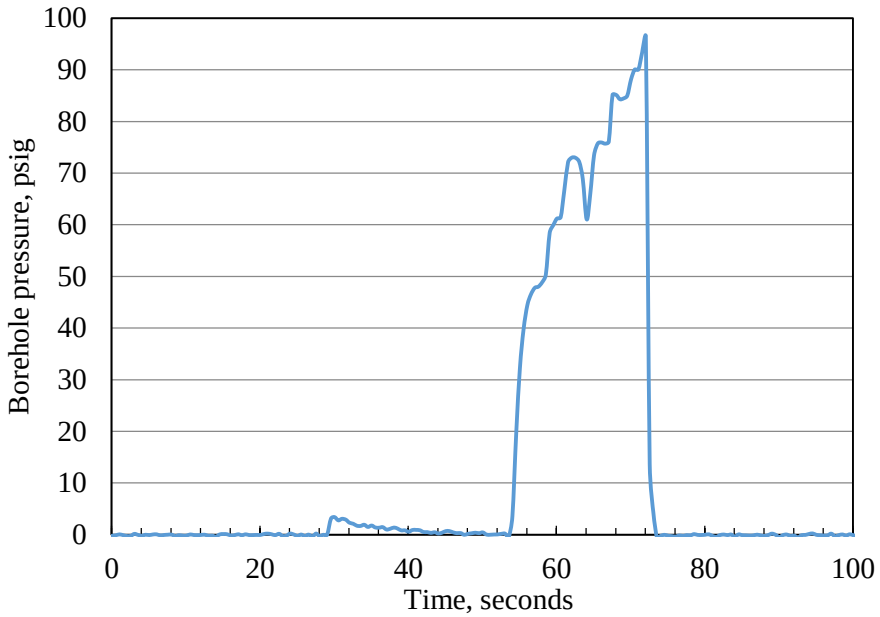

Figure 3.377. Pressure profile during gas fracturing without tri-axial stress loading.

As shown in Figure 3.378, blue dye did not penetrate deep into the rock sample, indicating that the induced fractures are too tight for liquid to flow into. The gas fracture planes, in agreement with the acoustic signatures, propagated along the bubbling traces, which are preexisting fractures, as can be clearly identified in Figure 3.378. It is obvious that when there are unfilled preexisting fractures, CO_2 would preferentially flow into and extend these fractures.

Figure 3.378. CO_2 injection induced fracture morphology of Shale Sample 2.

Shale Sample 3

Shale Sample 3 was found to be of high permeability due to existence of several fractures crossing through the shale block. To better model the fractured reservoir, we first injected epoxy into the

preexisting fractures through the borehole to seal them. Epoxy was seen seeping out of several points on the block surface and then injection was stopped. Residual epoxy in the borehole was washed out by rinsing the borehole with acetone for five times. The epoxy has a nominal tensile strength of 2500 psi after curing for 12 hours. After injecting the epoxy, we left Shale Sample 3 under room conditions to cure for 5 days. Figure 3.379 compared the pressure decay curves before and after the epoxy treatment of preexisting fractures in Shale Sample 3, showing that the fractures connecting to the borehole have been successfully sealed, at least in the near borehole region.

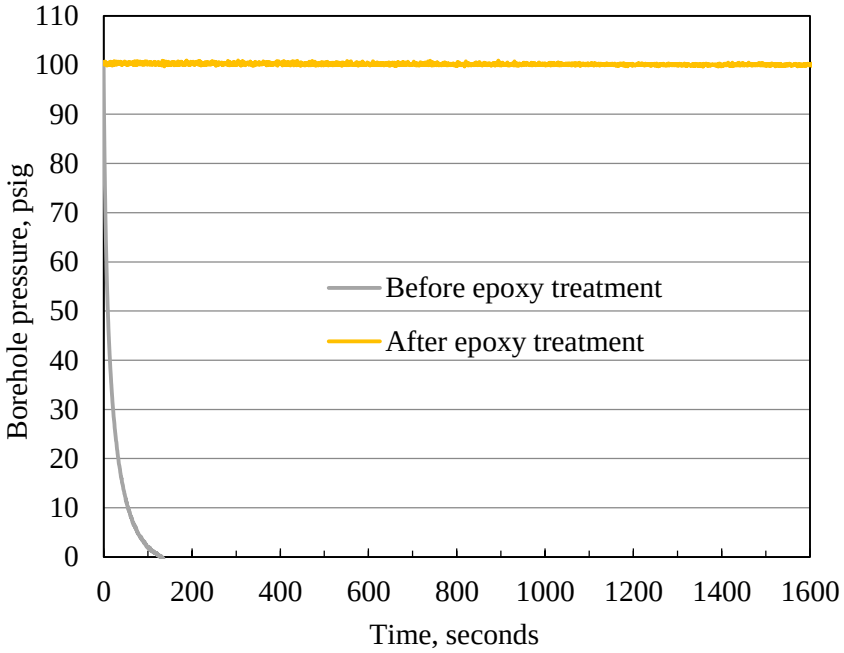

Figure 3.379. Pressure decay curves before and after epoxy treatment of fractures inside Sample 3.

Shale Sample 3 was fractured by injecting sc-CO_2 under a tri-axial stress loading of 1100 psi in the x-direction, 1600 psi in the y-direction, and 2100 psi in the z-direction, shown in Figure 3.380. Before the treatment, acoustic signatures were measured as reference for post-injection comparison, and pressure decay was carried out as well.

The injection pressure and borehole temperature profiles are shown in Figures 3.381 and 3.382. We injected two cycles of CO_2 to fracture Shale Sample 3, corresponding to two pressure peaks in Figure 3.381. At the beginning, after opening valve at 608.2 seconds, the borehole pressure rose to 766.4 psig. Then, the injection rate was set at 40 ml/min and soon the pressure tended to level out. Thereafter the injection rate was increased to 80 ml/min, as sc-CO_2 ran out, the first pressure peak of 1392.5 psig was achieved at 1138.5 seconds, and the borehole temperature was 39.7 °C. The pump was refilled and heated, and then injection continued at 80 ml/min. Borehole pressure reached the second peak of 1109.7 psig at 1722.5 seconds with borehole temperature of 35.4°C. On the temperature profile in Figure 3.382, there are two small drops corresponding to these two injection cycles. On the stress profiles, there are no obvious responses at these two moments, indicating that no big new fractures were created or the sc-CO_2 just leaked off through the preexisting fractures sealed by epoxy.

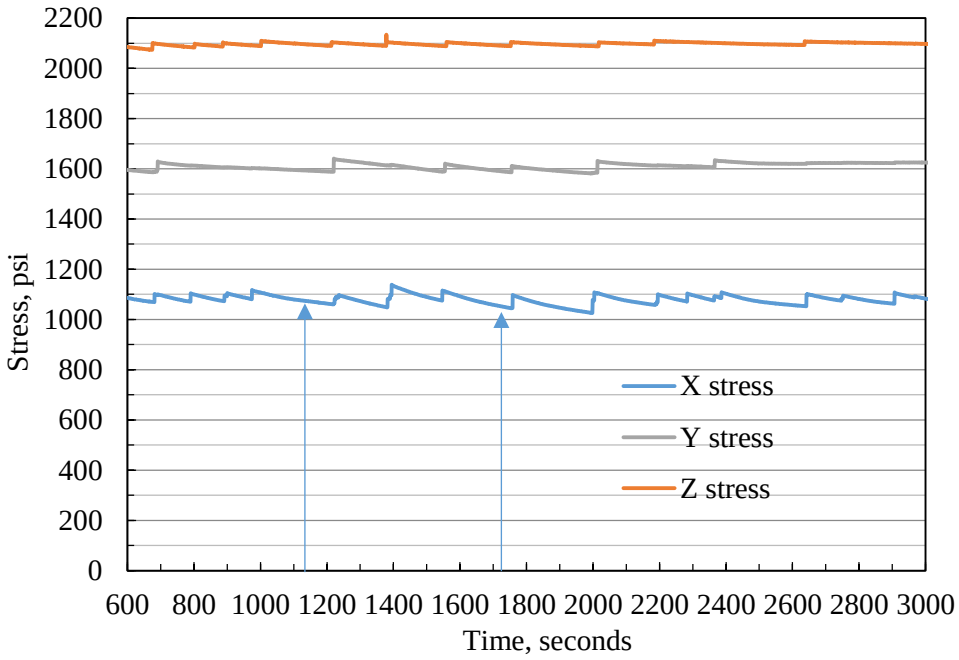

Figure 3.380. Tri-axial stress loading for Sc-CO_2 injection into Shale Sample 3.

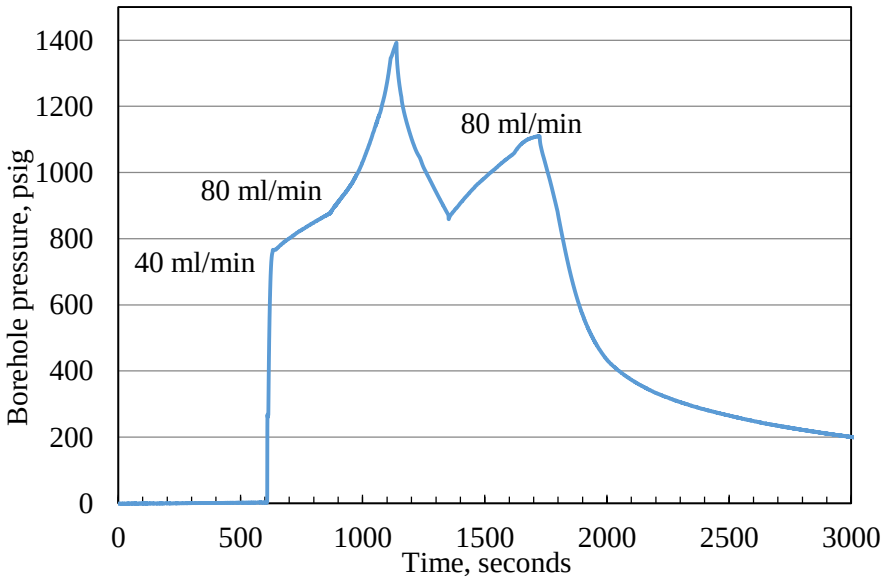

Figure 3.381. Pressure profile of CO_2 injection into Shale Sample 3.

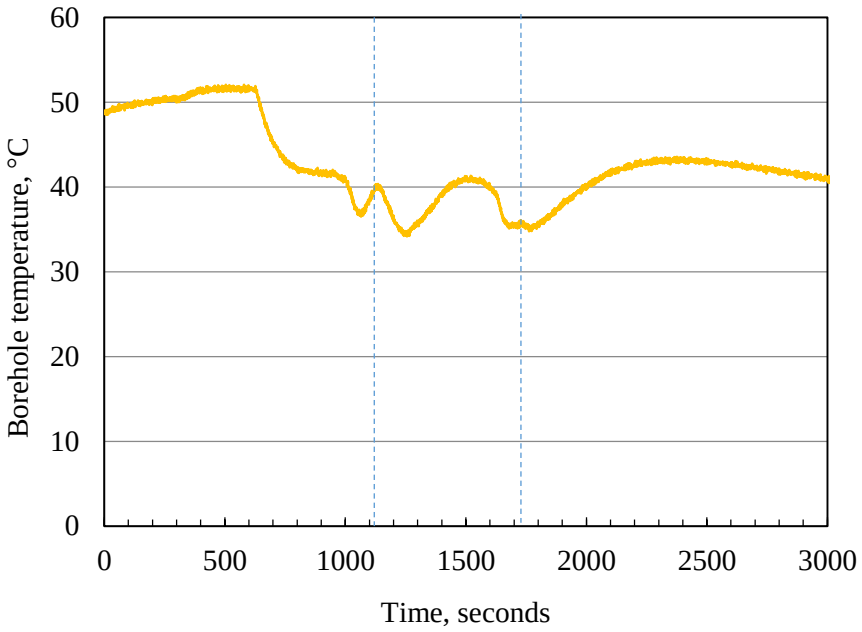

Figure 3.382. Borehole temperature profile during CO_2 injection into Shale Sample 3.

Figure 3.383 compares the pressure decay curves measured before and after CO_2 injection. It is obvious that the gas leakage rate significantly increased after CO_2 injection, due to fractures generated inside the shale block.

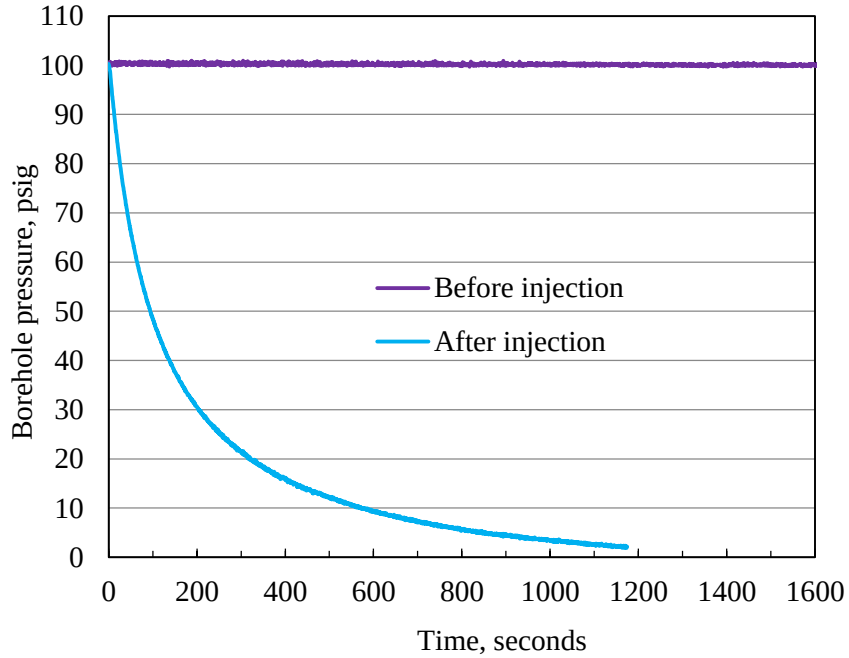

Figure 3.383. Pre- and post-injection pressure decay curves of Shale Sample 3.

Acoustic signatures including P-waves and S-waves before epoxy treatment (blue curves), after epoxy treatment but before CO_2 injection (black curves), and after CO_2 injection (red curves) are

compared in Figures 3.384 through 3.389. Compared to blue curves, acoustic signatures of black curves were significantly magnified in waveform and at many locations the wave arrived much earlier after epoxy treatment. That is because fluid epoxy filled the preexisting fractures and solidified, facilitating the propagation of the acoustic signals. Hence, epoxy treatment successfully sealed most of the preexisting fractures inside the block. After CO_2 injection, at many locations, the acoustic waveforms waned again and arrival time got delayed, indicating that sealed fractures were reopened or new fractures were created on their transmission pathway.

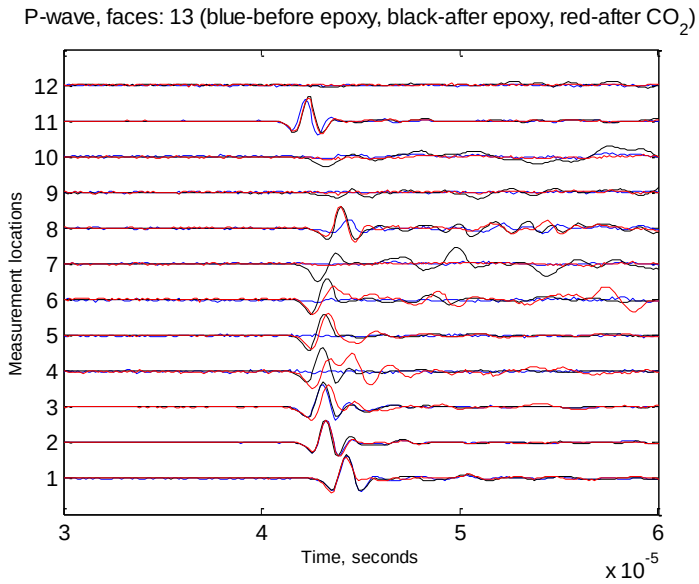

Figure 3.384. P-wave signatures measured from Surface 1 and Surface 3 of Shale Sample 3.

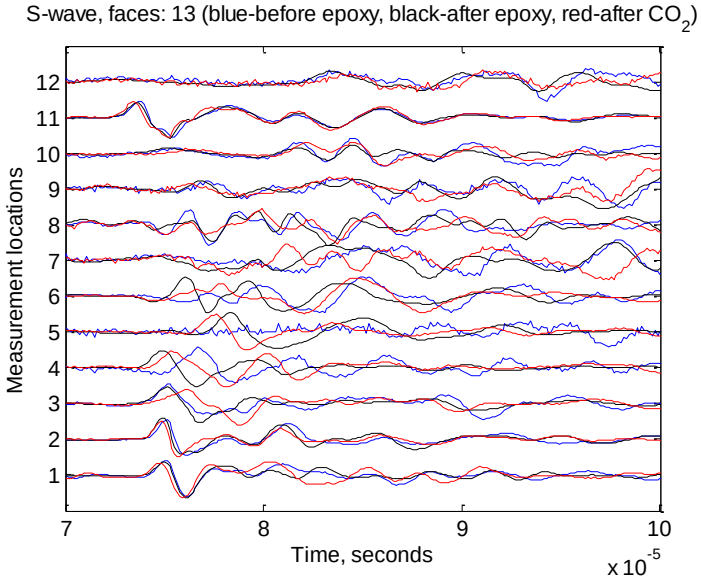

Figure 3.385. S-wave signatures measured from Surfaces 1 and Surface 3 of Shale Sample 3.

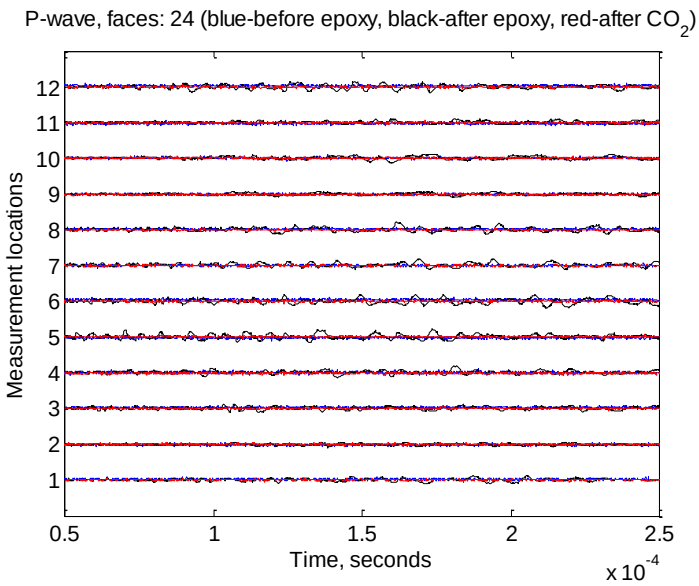

Figure 3.386. P-wave signatures measured from Surfaces 2 and Surface 4 of Shale Sample 3.

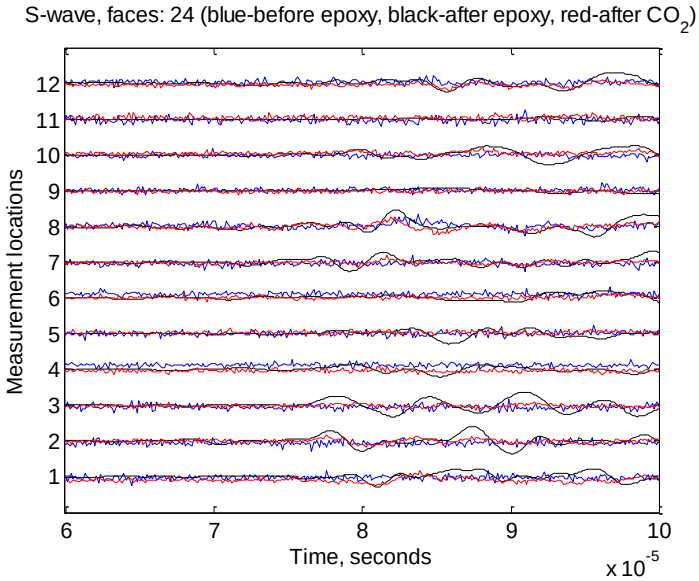

Figure 3.387. S-wave signatures measured from Surfaces 2 and Surface 4 of Shale Sample 3.

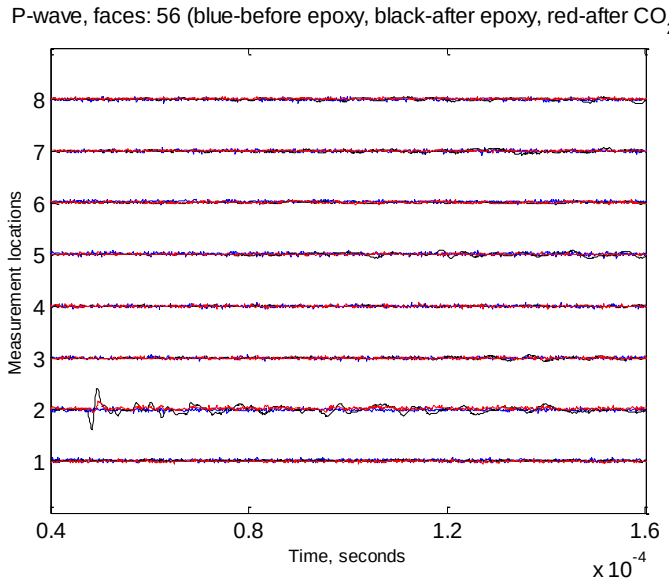

Figure 3.388. P-wave signatures measured from Surfaces 5 and Surface 6 of Shale Sample 3.

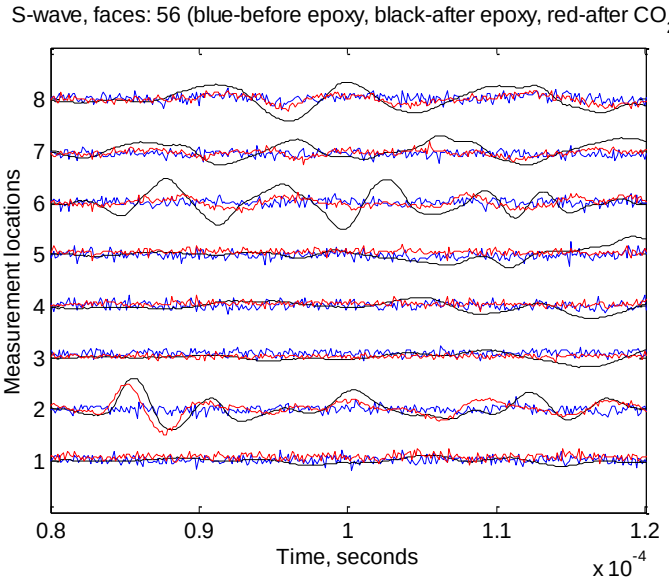

Figure 3.389. S-wave signatures measured from Surfaces 5 and Surface 6 of Shale Sample 3.

Dye solution was later injected into Shale Sample 3 to color the fracture planes. Then under tri-axial stress loading, shown in Figure 3.390, the sample was fractured by high pressure nitrogen gas, and the pressure profile is shown in Figure 3.391, in which the peak pressure is 2263.8 psig at 627.1 seconds. The gas fracturing caused a bump on x-stress, meaning that new gas fracture planes were created perpendicular to x axis. Finally, the sample was broken down by nitrogen gas under no confining stress, and the breakdown pressure is 131.0 psig, as shown in Figure 3.392.

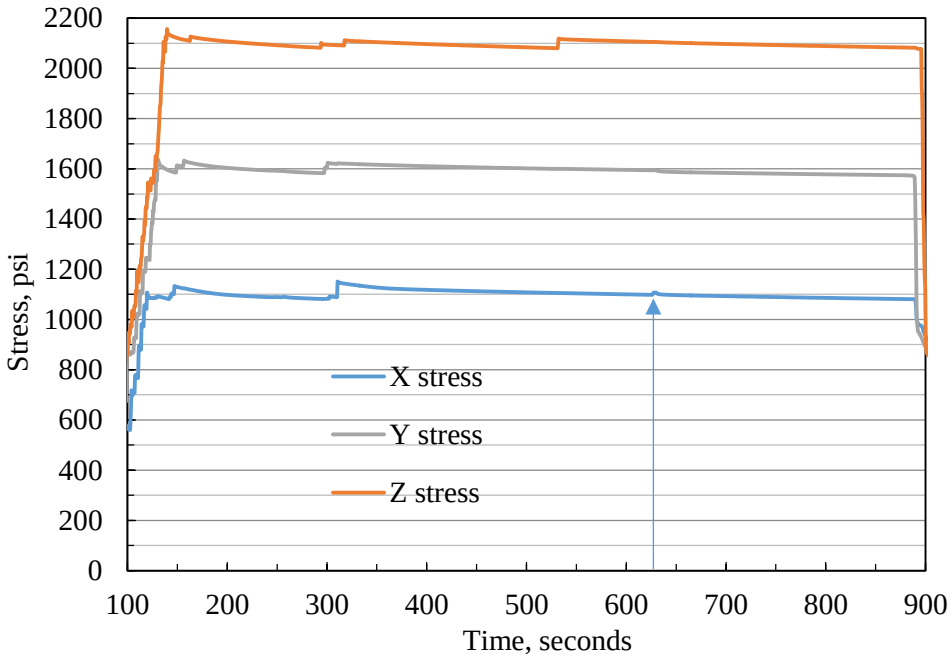

Figure 3.390. Tri-axial stress loading for gas fracturing.

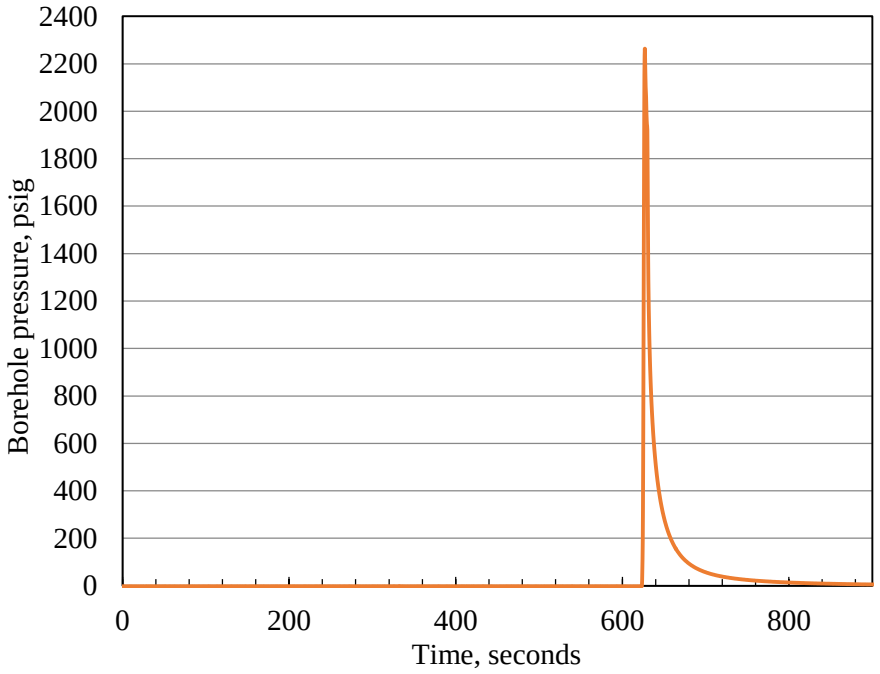

Figure 3.391. Pressure profile during gas fracturing with tri-axial stress loading.

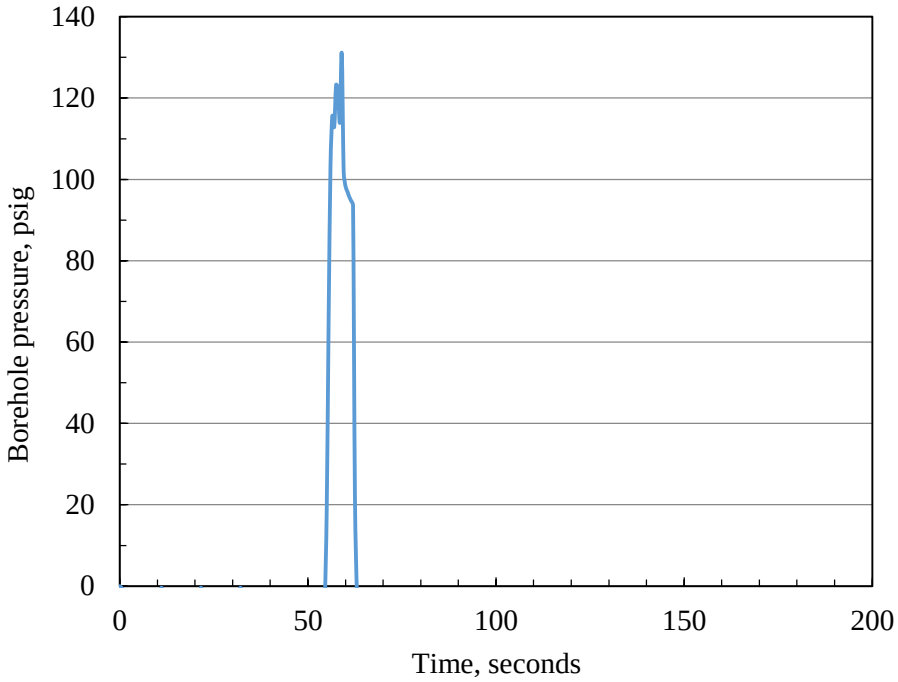

Figure 3.392. Pressure profile during gas fracturing without tri-axial stress loading.

Figure 3.393 shows the faces of Shale Sample 3 before any treatment. A lot of fractures can be seen already existing vertically along the x-, y-, and z-axis, also it can be noticed that there are more preexisting fractures on Surfaces 1, 3, 5, and 6 than Surfaces 2 and 4. Figure 3.394 shows the faces of Shale Sample 3 after epoxy treatment and CO_2 injection. Epoxy stains can be seen on Surface 1 and Surface 4, but it seems that no new fractures have been created on the surface. After dye injection, purple color appears on Surfaces 1, 3, and 6 in Figure 3.395. Generally, these leaking points are all preexisting fractures.


Figure 3.393. Faces of Shale Sample 3 before any treatment.

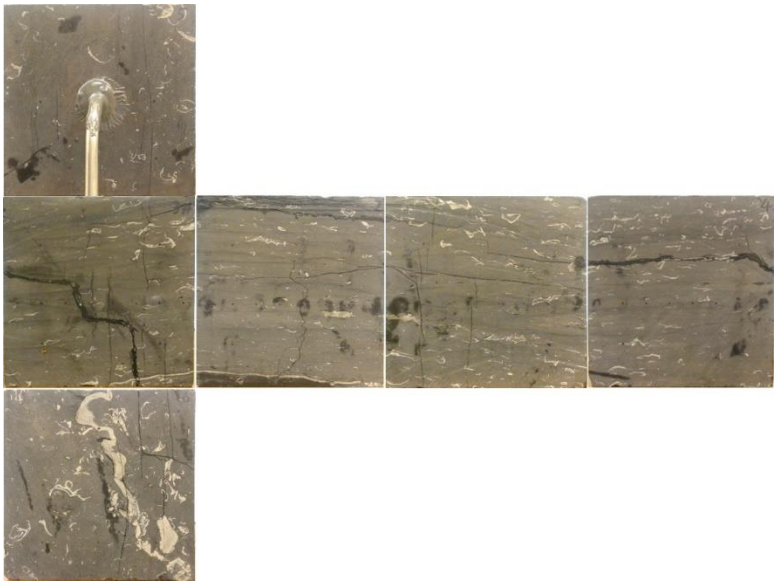

Figure 3.394. Faces of Shale Sample 3 after epoxy treatment and CO_2 injection.

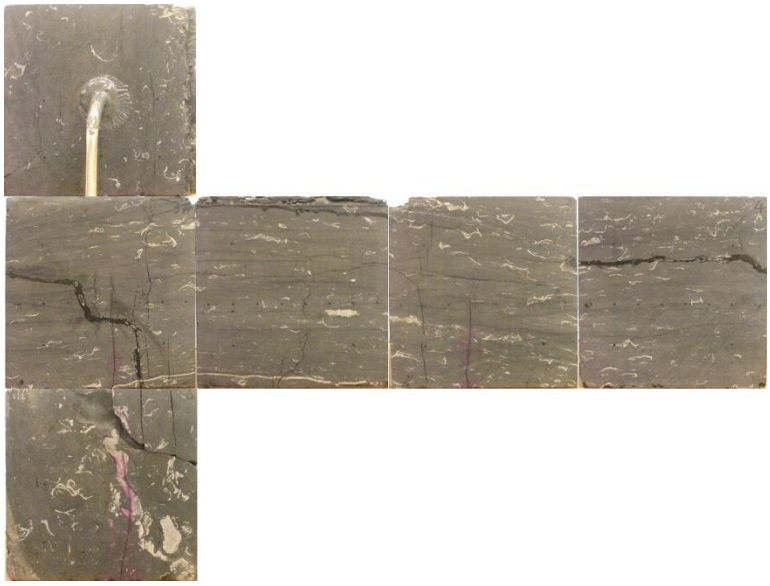

Figure 3.395. Faces of Shale Sample 3 after dye injection.

Then the sample was fractured by high pressure nitrogen gas, which revealed the fracture planes inside the sample, as shown in Figure 3.396, based on which several aspects of the experiments are made clear. Note that the top halves (a and b) were opened from Surface 1, a was broken into c, which was further broken into d. First, one preexisting fracture and one interface that have been bonded by epoxy are identified, as circled by the black dashed lines. Basically, the preexisting fracture corresponds to the epoxy stains on Surface 1, and the interface corresponds to that on Surface 4 in Figure 3.395. Second, sc-CO_2 injection induced fractures preferentially initiated and propagated in the preexisting fractures, even if they are bonded with epoxy, as evidenced by the purple color over all epoxy stained areas. The possible reasons for sc-CO_2 breaking through the epoxy bonded fractures are that the preexisting fracture planes are not clean or consolidated enough to enable the nominal tensile strength of 2500 psi with the epoxy solution. And then, under a

relatively small stress difference of 500 psi, they are still weak planes to be split. Third, the small colored fracture plane perpendicular to Surfaces 1 and 3 at the bottom in Figure 3.396c is a new fracture induced by sc-CO_2 injection under tri-axial stress loading, because there are no epoxy stains on it. Nitrogen gas fracturing further extended these induced fractures and opened other preexisting fractures, which are either parallel or perpendicular to the minimum horizontal stress (x-axis). Therefore, under a stress difference of 500 psi, preexisting fractures, even being weakly bonded, still dominate the sc-CO_2 injection induced fracturing process.

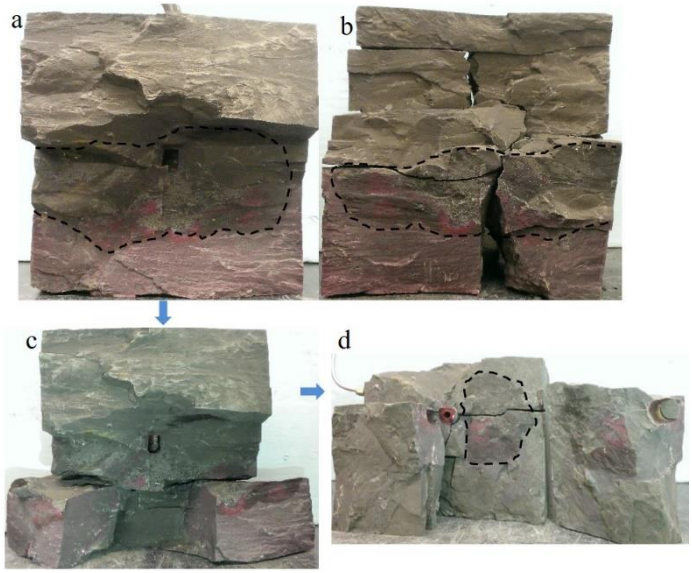

Figure 3.396. Colored CO_2 injection induced fracture planes in Shale Sample 3.

Shale Sample 4

Similar to Shale Sample 3, Shale Sample 4 also has a lot of fractures, which resulted in high permeability. We employed the same procedure as that for Shale Sample 3 to seal the preexisting fractures in Shale Sample 4. Epoxy flowed out of several locations along the preexisting horizontal fractures, which are perpendicular to the z-axis. Figure 3.397 compares the pressure decay curves before and after the epoxy treatment of preexisting fractures in Shale Sample 4, showing that the fractures connecting to the borehole, at least in the near borehole region, have been successfully sealed. Then, acoustic signatures were measured as reference for post-injection comparison, and pressure decay was carried out for pre-treatment permeability evaluation.

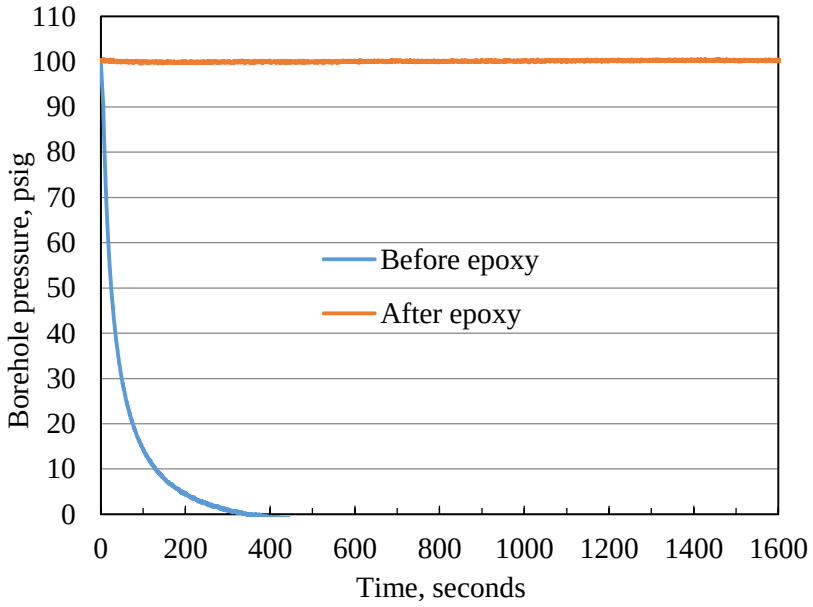

Figure 3.397. Pressure decay curves before and after epoxy treatment for Shale Sample 4.

Shale Sample 4 was then treated by injecting CO_2 into the borehole under tri-axial stress loading of 1200 psi in the x-direction, 2100 psi in the y-direction, and 3000 psi in the z-direction, as shown in Figure 3.398. The injection pressure and borehole temperature profiles are shown in Figure 3.399. After completely opening the valve, Shale Sample 4 was fractured at 114.6 seconds when the borehole pressure reached 804.3 psig at 54.0 °C. This peak pressure corresponds to no obvious responses on tri-axial stress loading in Figure 3.398, indicating that the gaseous CO_2 fracturing primarily occurred along preexisting fracture planes. In addition, the temperature drastically dropped about 7 °C right after the fracturing, due to CO_2 leakage and expansion.

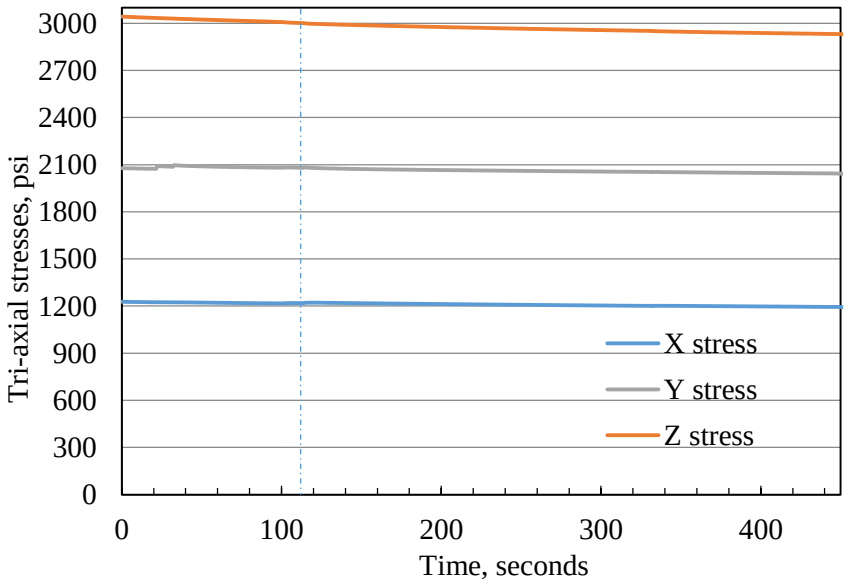

Figure 3.398. Tri-axial stress loading for CO_2 injection into Shale Sample 4.

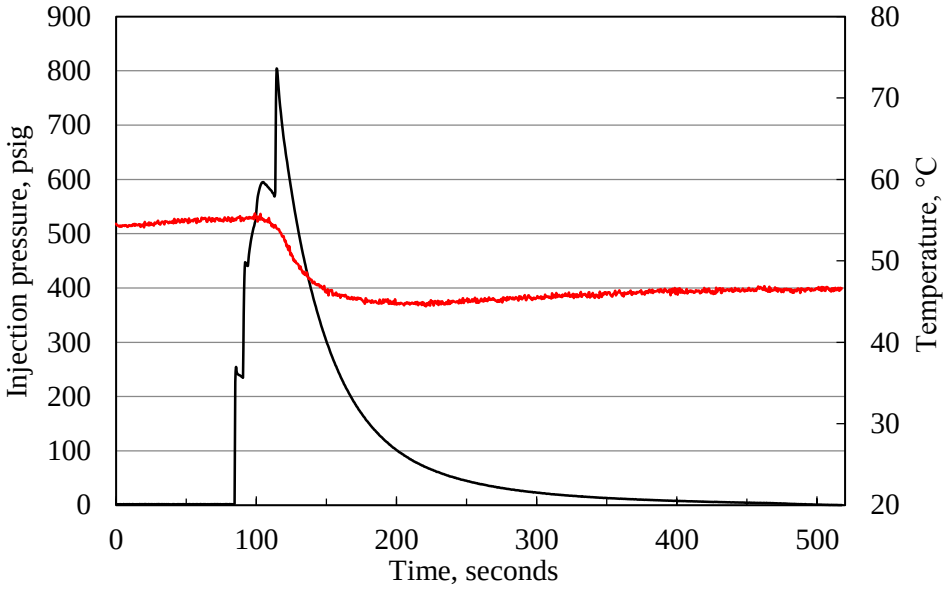

Figure 3.399. CO_2 injection pressure and temperature profiles for Shale Sample 4.

Figure 3.400 compares the pressure decay curves measured before and after CO_2 injection. After CO_2 injection, it is obvious that gas leak-off happened instantaneously; to increase the borehole pressure to 100 psig needed very high flow rate from the nitrogen gas cylinder.

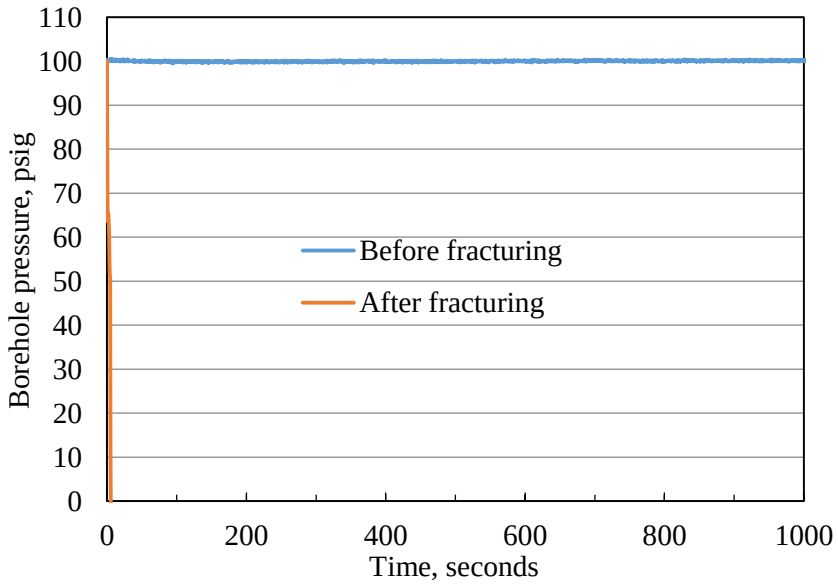

Figure 3.400. Pressure decay curves before and after CO_2 injection.

Acoustic signatures including P-waves and S-waves before epoxy treatment (blue curve), after epoxy treatment but before CO_2 injection (black curves), and after CO_2 injection (red curves) are compared in Figures 3.401 through 3.406. After epoxy treatment, acoustic signatures (black curves) were significantly magnified in waveform at almost all measurement locations, indicating that epoxy had filled and solidified most major preexisting fractures that affected the acoustic signal transmission. Also, the signal arrival time was shifted earlier at many locations after epoxy

treatment. After CO_2 injection, at many locations, the arrival time got delayed and regular waveforms waned or even disappeared, particularly for signals transmitting across Surfaces 5 and Surface 6, indicating that sealed fracture planes that are perpendicular to z-axis were reopened.

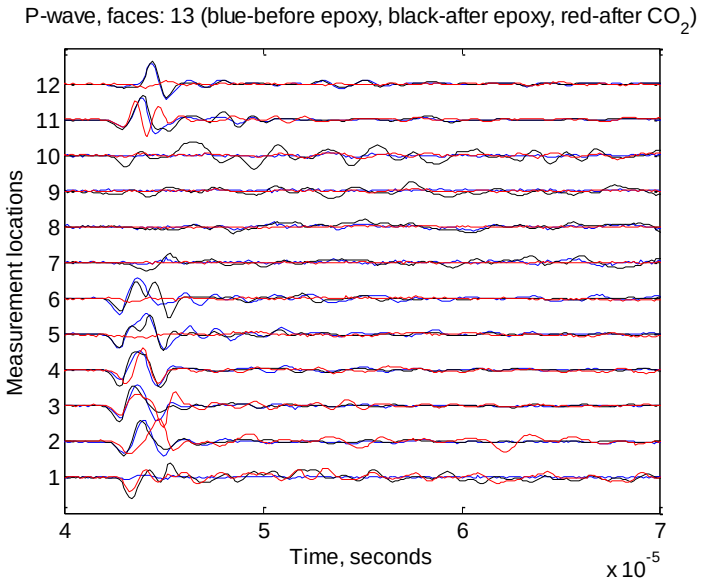

Figure 3.401. P-wave signatures measured from Surfaces 1 and Surface 3 of Shale Sample 4.

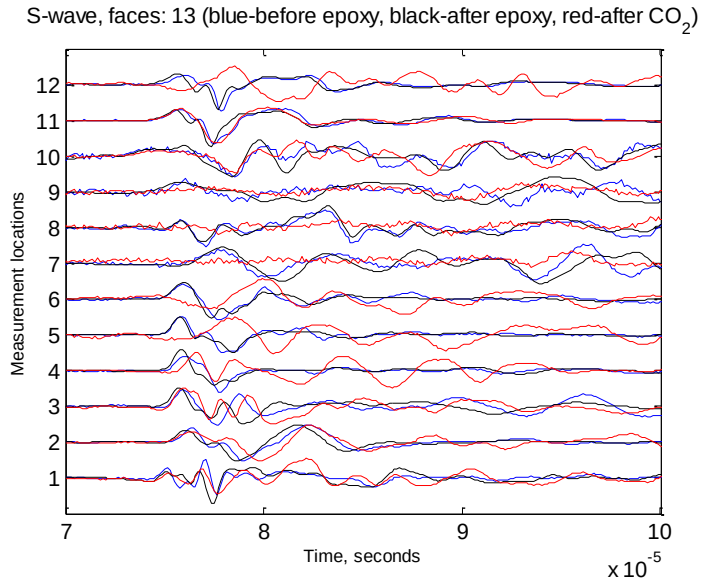

Figure 3.402. S-wave signatures measured from Surfaces 1 and Surface 3 of Shale Sample 4.

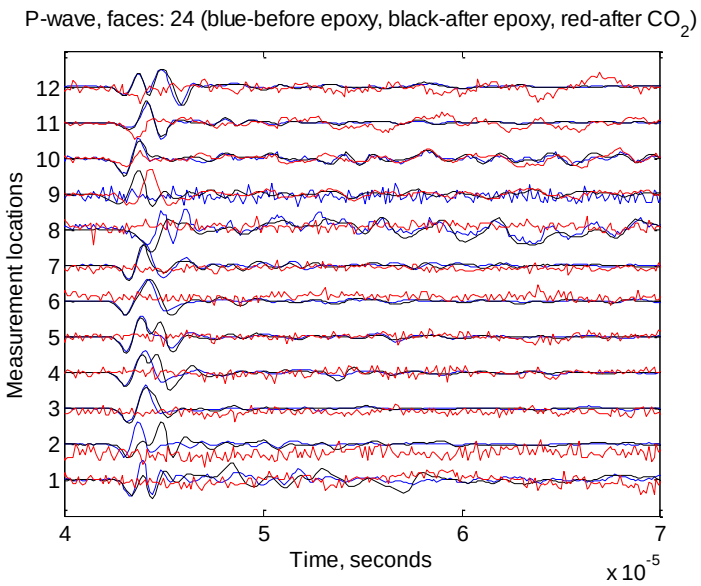

Figure 3.403. P-wave signatures measured from Surfaces 2 and Surface 4 of Shale Sample 4.

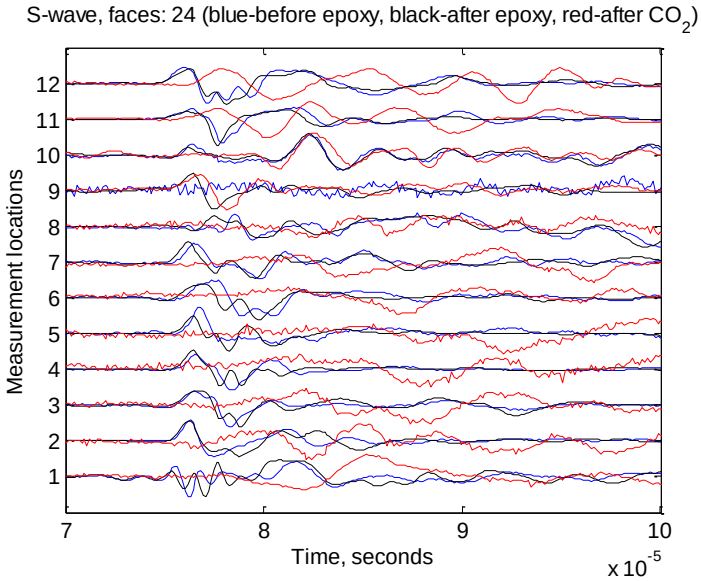

Figure 3.404. S-wave signatures measured from Surfaces 2 and Surface 4 of Shale Sample 4.

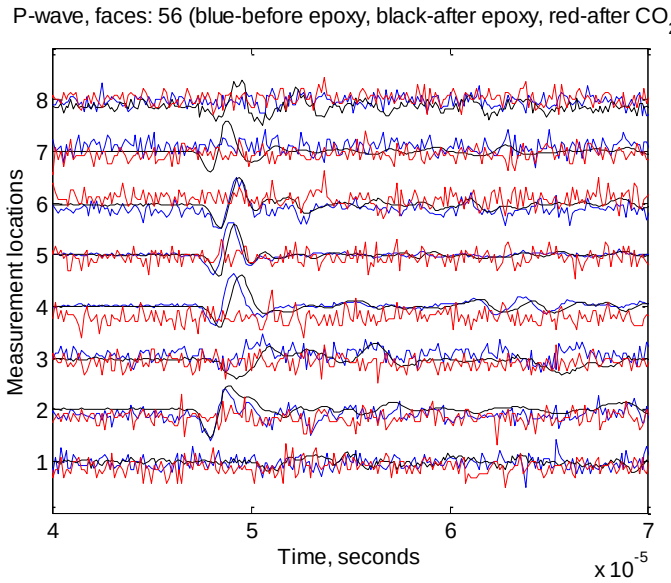

Figure 3.405. P-wave signatures measured from Surfaces 5 and Surface 6 of Shale Sample 4.

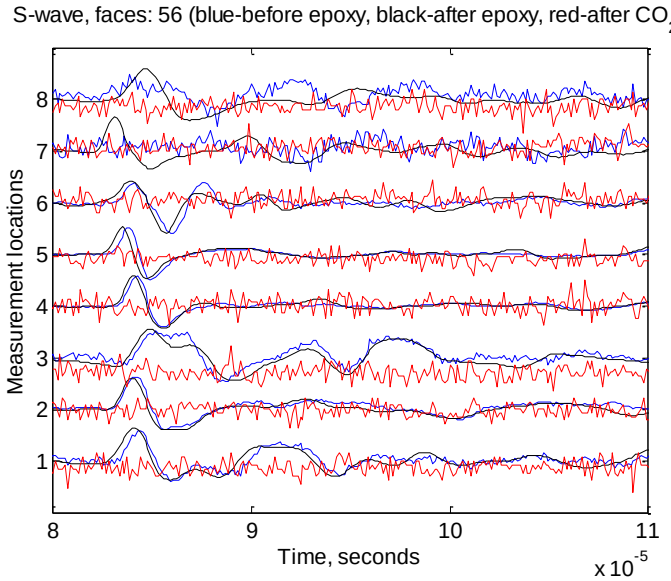

Figure 3.406. S-wave signatures measured from Surfaces 5 and Surface 6 of Shale Sample 4.

Dye solution was then injected into Shale Sample 4 to color the CO_2 injection induced fractures, through which dye solution automatically flowed out of the block surface driven by gravity. Then under tri-axial stresses, shown in Figure 3.407, the sample was fractured by nitrogen gas at a peak pressure of 1803.3 psig at 321.5 seconds with obvious rebounds on x- and y-stress and a drop on z-stress. The gas fracturing pressure profile is shown in Figure 3.408. Finally, after unloading the tri-axial stresses, the fractured sample was broken down at 70.6 psig by nitrogen gas, as shown in Figure 3.409.

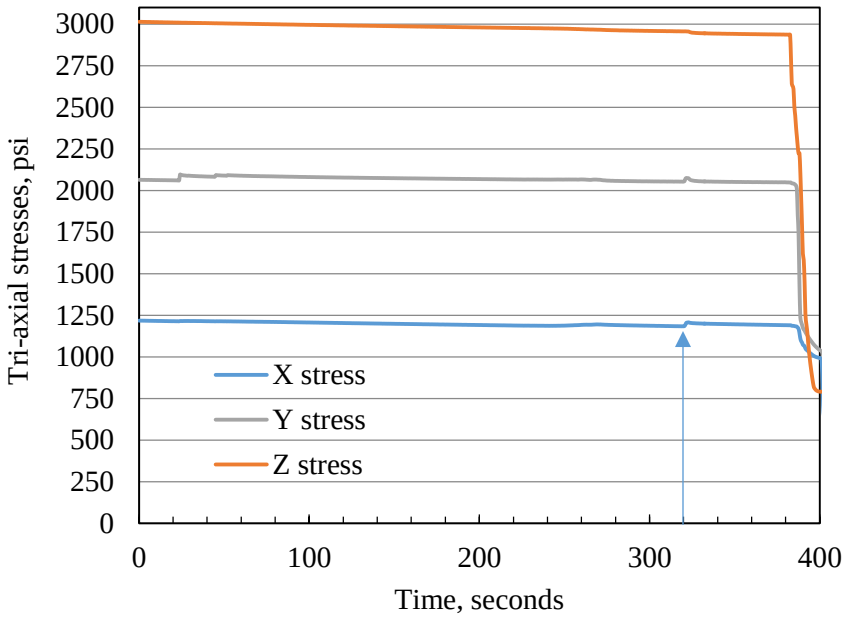

Figure 3.407. Tri-axial stress loading for gas fracturing of Shale Sample 4.

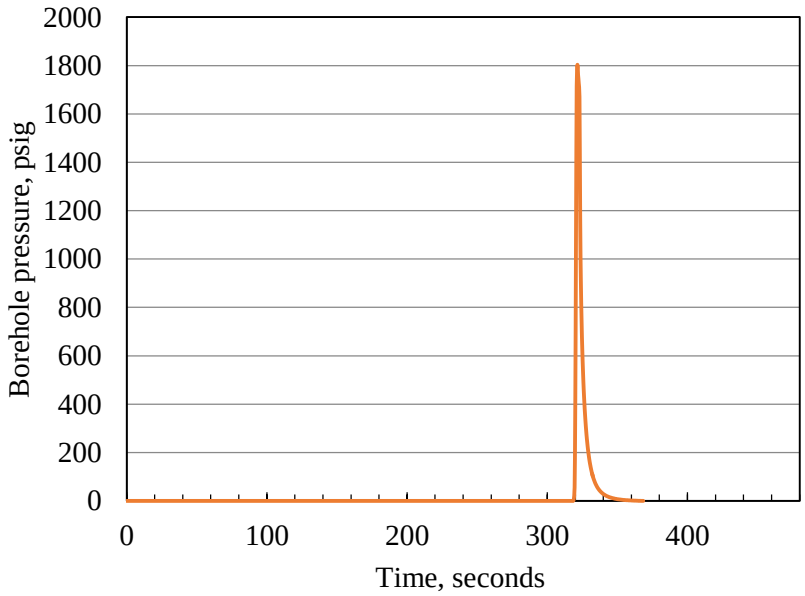

Figure 3.408. Pressure profile of gas fracturing of Shale Sample 4 under tri-axial stress conditions.

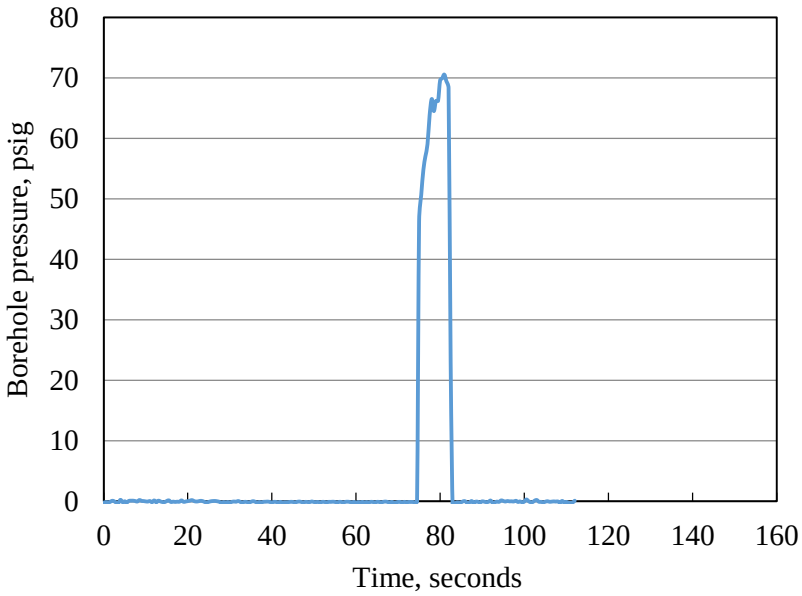

Figure 3.409. Gas fracturing of Shale Sample 4 under no confining stress.

The faces of Shale Sample 4 before and after CO_2 injection are shown in Figure 3.410 and 3.411. On the lower halves of Surfaces 1 and 3, new fractures were generated. Whereas on other faces, no big new fractures can be seen, only preexisting fractures were extended and widened, for example, the one on the lower half of Surface 4.

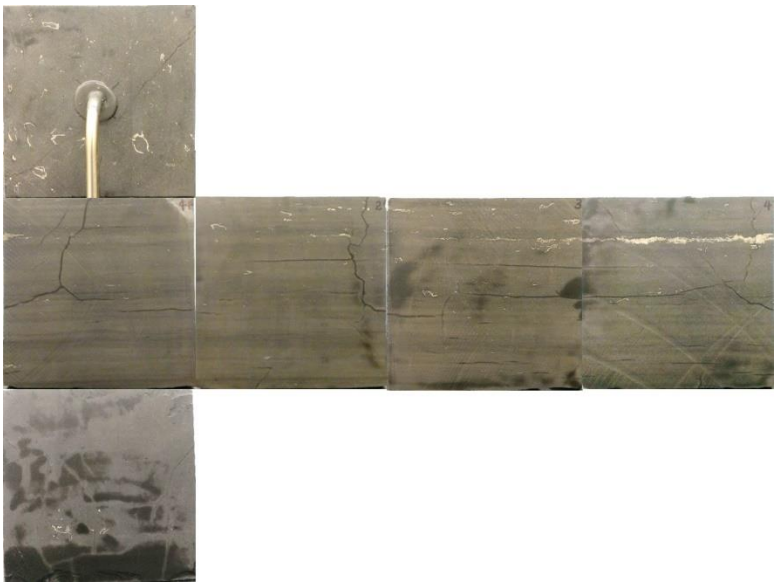
Figure 3.410. Intact surfaces of Shale Sample 4 before any treatment.

Figure 3.411. Surfaces of Shale Sample 4 after CO_2 injection.

We then tried to inject dye solution, which, without any pressurization, automatically flowed out of the continuous preexisting horizontal fractures in the middle of the sample and the new downturned fractures on the lower halves of Surfaces 1 and 3, shown in Figure 3.412.

Figure 3.412. Surfaces of Shale Sample 4 after dye injection and gas fracturing.

The sample was later broken down by nitrogen gas fracturing under no tri-axial stresses, as shown in Figure 3.413, which was taken by placing the borehole to the left and opening Surface 2. As can be seen from the cross-section, the epoxy had covered the whole horizontal fracture plane at the middle of the z-axis. However, differently from newly cracked planes, as fingers slightly rubbed this fracture plane, the surface smeared very easily, meaning that this preexisting fracture was generated long time ago and had been severely weathered. Furthermore, this weathered fracture plane should be responsible for the failing of epoxy consolidation, which did not effectively

prevent the CO_2 break through. Purple color all over the horizontal plane verified that CO_2 preferentially reopened this weakly bonded plane. In the lower picture of Figure 3.413, there is a newly created fracture, which is nearly perpendicular to the y-axis. This fracture has no epoxy stains but was colored with dye solution. Along its tip, gas fracturing further reached the bottom of Surface 6. These observations suggest that CO_2 injection induced fractures preferentially initiate and propagate in the weakly bonded preexisting fractures, even if they are opening against the maximum vertical z-stress; meanwhile, under the high stress difference of 900 psi, new fractures can be induced against the horizontal stress directions. That is, both weakly bonded preexisting fractures and in-situ stress with high contrast dominate the CO_2 injection induced fracturing process.

Figure 3.413. Fracture morphology of Shale Sample 4 after gas breakdown.

Shale Sample 5

Shale Sample 5 was fractured by injecting a synthetic slick water which consisted of 0.1 wt% HPAM, 2% KCl, and red dye. At 20 °C, the viscosity of this synthetic slick water, measured with a rotating cylinder viscometer, is 1.8 mPa·s. We also tried to seal the preexisting fractures in Shale Sample 5 by injecting epoxy, nonetheless it turned out that instead of sealing the fractures, epoxy treatment widened the fractures, as indicated by the increasing pressure decay rate in Figure 3.414. Epoxy was seen seeping out of the block surface and it was injected twice; both of these increased the fracture permeability. It is postulated that injected epoxy shrank as it solidified inside the preexisting fractures, while the fracture planes were severely weathered with removable fines, which undermined the consolidation effect of epoxy.

Acoustic signatures were measured as reference for post-injection comparison, and pressure decay was carried out for pre-treatment permeability evaluation.

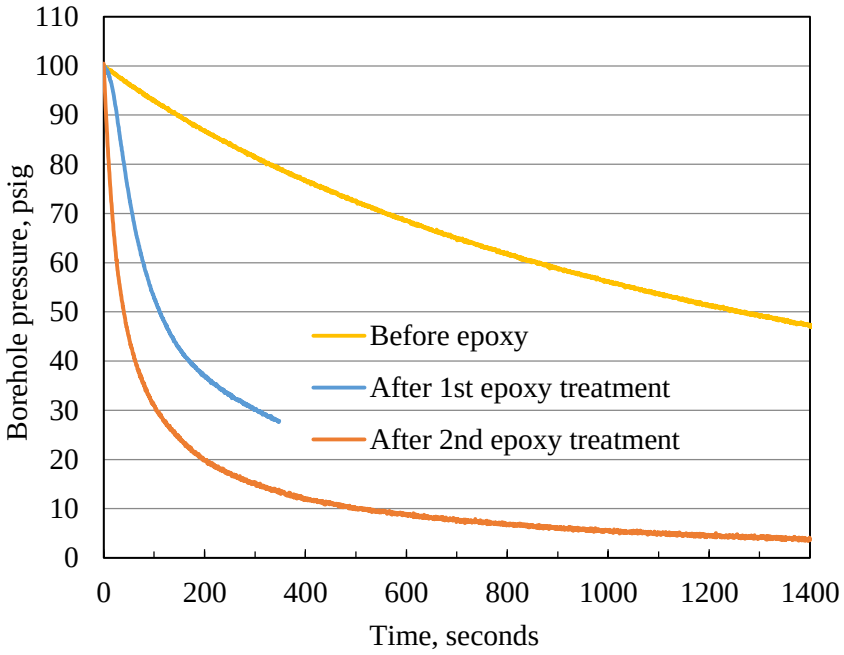

Figure 3.414. Pressure decay curves before and after epoxy treatment for Shale Sample 5.

Shale Sample 5 was fractured by injecting the synthetic slick water at 1 ml/min under a tri-axial stress loading of 1100 psi in the x-direction, 1600 psi in the y-direction, and 2100 psi in the z-direction, shown in Figure 3.415. Figure 3.416 shows the borehole pressure profile during the slick water injection. Injection started at 1 ml/min, and pressure reached the first peak of 521.3 psig and tended to level out at 1281.1 seconds. Ten seconds later, the pump was stopped to allow pressure decline. Seeing that borehole pressure leveled out near 100 psig, we restarted the pump at 1 ml/min, and the pressure reached the highest peak of 1602.5 psig at 2352.6 seconds. After 10 seconds, the pump was again stopped. Unexpectedly, a file corrupted around 2900 seconds and the data acquisition system was restarted. This caused the data gaps in both Figure 3.412 and 3.413. As pressure leveled out near 180 psig, the pump was restarted at 1 ml/min. A small peak of 309.7 psig was achieved at 3462.2 seconds, and then pressure slowly decreased, indicating the fracture propagation stage. Later, we increased the injection rate to 10 ml/min, and a pressure peak of 434.7 psig was reached at 4156.2 seconds. In tens of seconds, fluid leak-off was observed on the sample surface and the pump was stopped. On the tri-axial stress curves, there are slight responses on x-, y-, and z-stress corresponding to the last pressure peak, while all other peaks including the highest one did not bring about obvious responses. It suggested that probably only the last peak created new fractures or extended preexisting fractures, whereas all other peaks only broke through the weakly bonded preexisting fractures. In comparison with Shale Samples 1-4 fractured by CO_2, slick water fracturing needs extra hundreds of psi to break down the sample, even though Shale Sample 5 has more permeable fractures than the others.

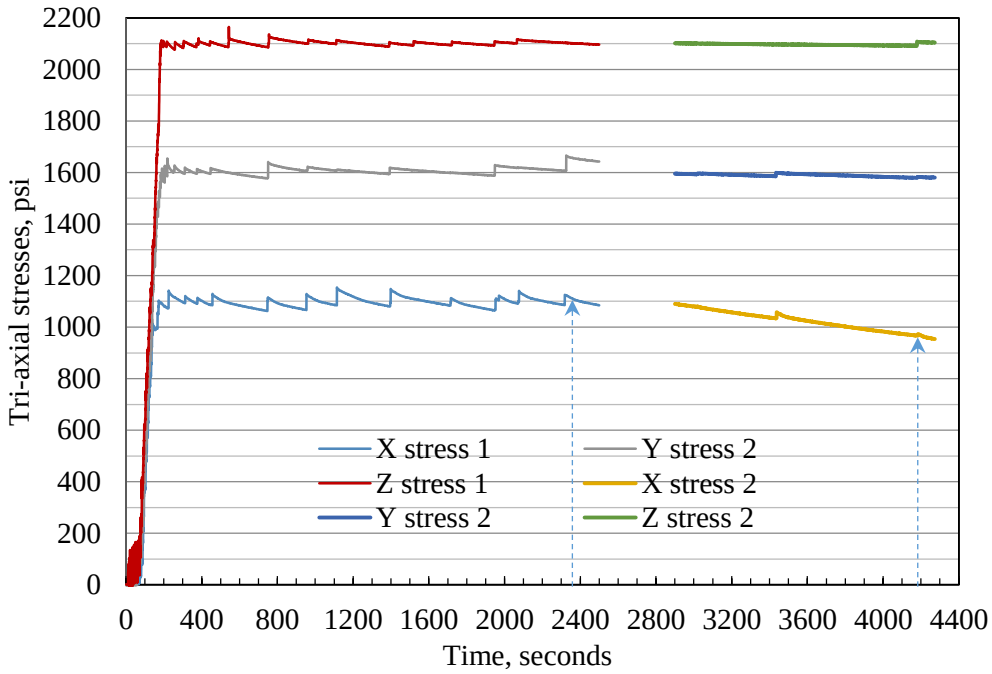

Figure 3.415. Stress loading for slick water injection into Shale Sample 5.

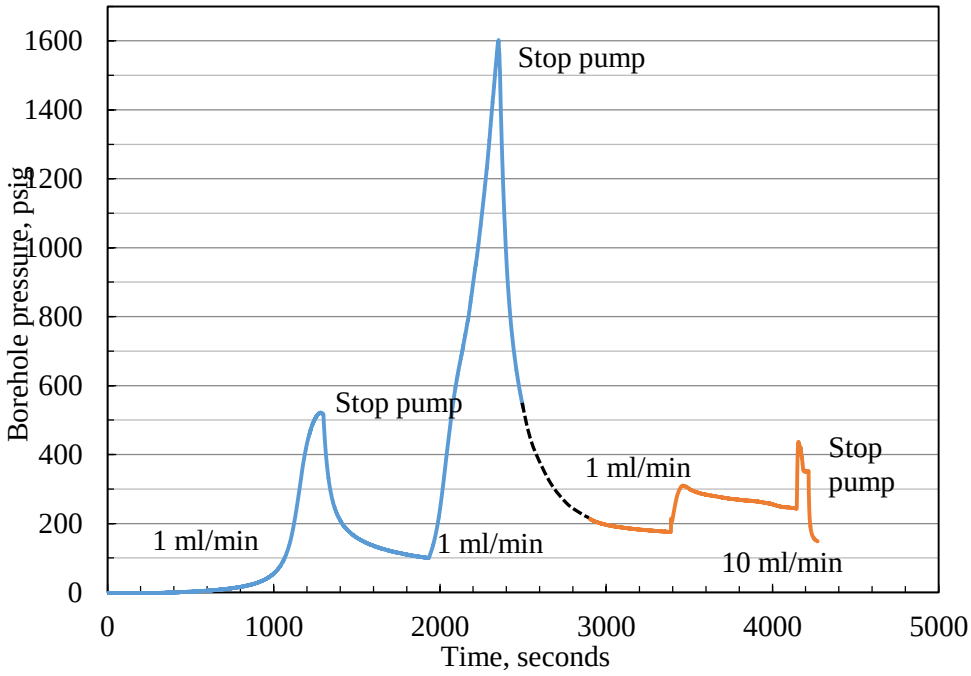

Figure 3.416. Slick water injection pressure for Shale Sample 5.

Figure 3.417 compares the pressure decay curves measured before and after slick water injection. It is obvious that gas leaking rate significantly increased after slick water fracturing, due to fractures reopened or generated inside the shale block.

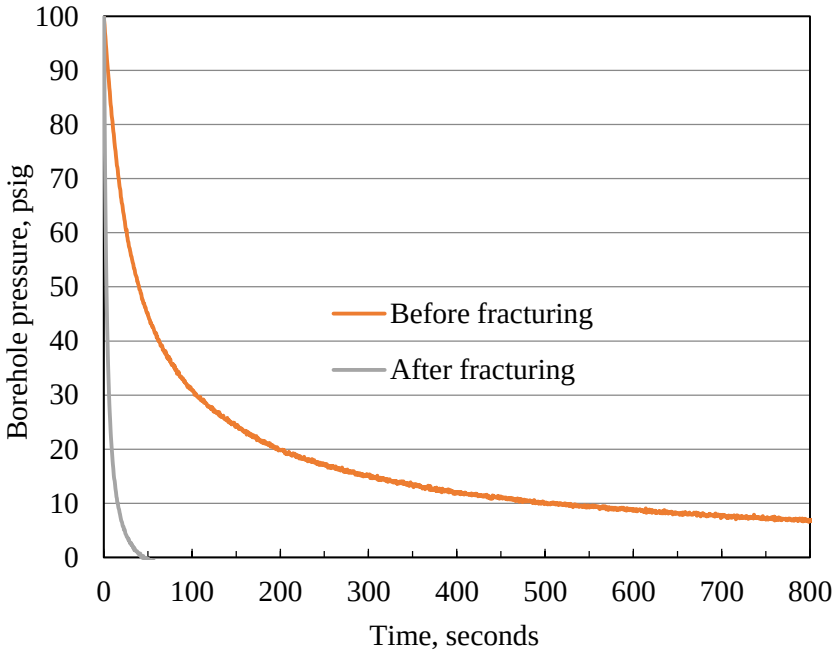

Figure 3.417. Pressure decay curves before and after slick water fracturing for Shale Sample 5.

Acoustic signatures including P-waves and S-waves before epoxy treatment (blue curves), after epoxy treatment but before fracturing (black curves) and after slick water fracturing (red curves) are compared in Figures 3.418 through 3.423. The results before and after epoxy treatment for Shale Sample 5 are somewhat mixed; waveforms are generally improved after epoxy treatment, but for arrival time, some are delayed and some are shifted earlier, the latter of which indicates widening of preexisting fractures. This agrees with the accelerated pressure decay after epoxy treatments. After slick water fracturing, most of the locations showed arrival time delays and collapsed acoustic signals, which are similar to those before epoxy treatment. This indicates that the preexisting fractures sealed by epoxy were reopened or extended, or there were some new fractures generated.

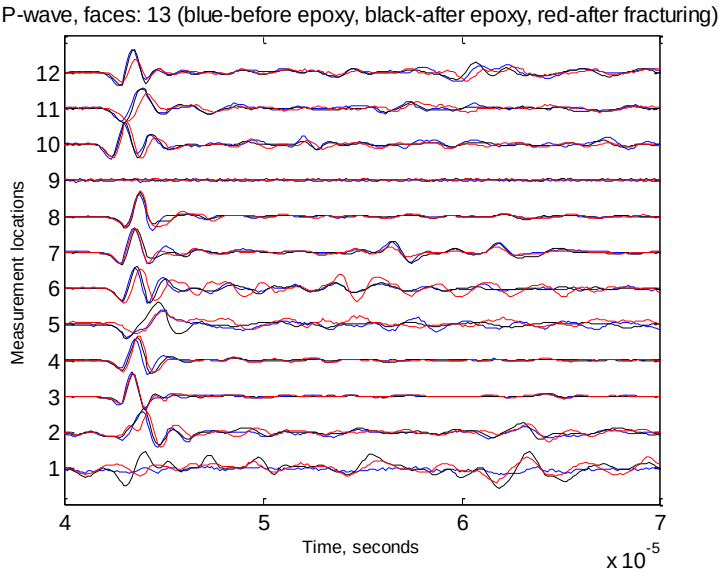

Figure 3.418. P-wave signatures measured from Surfaces 1 and Surface 3 of Shale Sample 5.

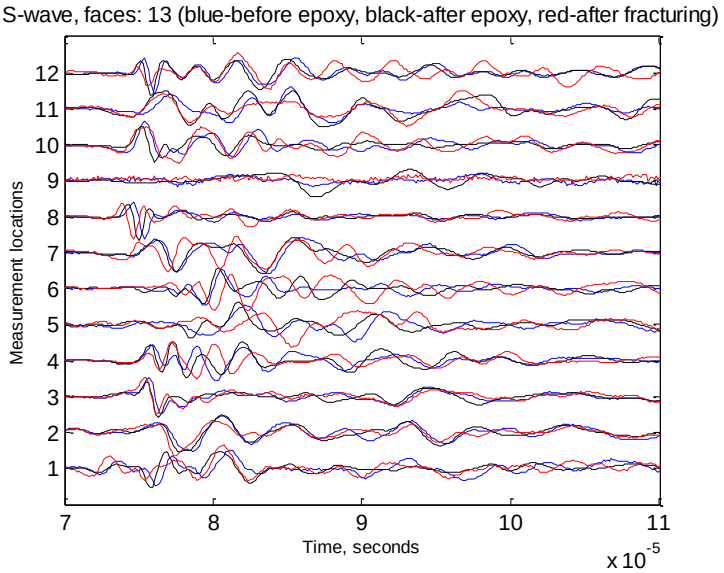

Figure 3.419. S-wave signatures measured from Surfaces 1 and Surface 3 of Shale Sample 5.

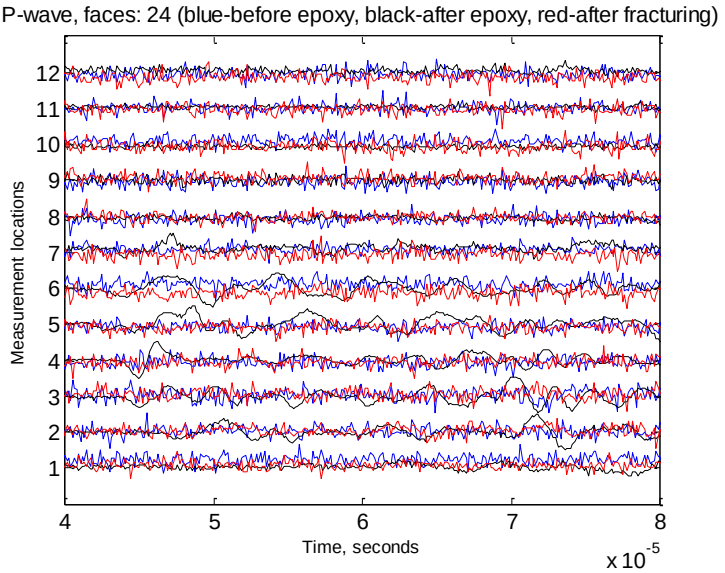

Figure 3.420. P-wave signatures measured from Surfaces 2 and Surface 4 of Shale Sample 5.

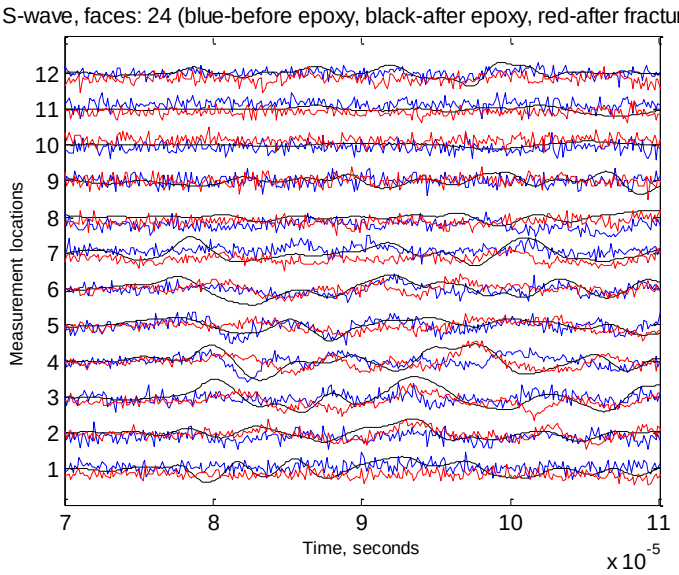

Figure 3.421. S-wave signatures measured from Surfaces 2 and Surface 4 of Shale Sample 5.

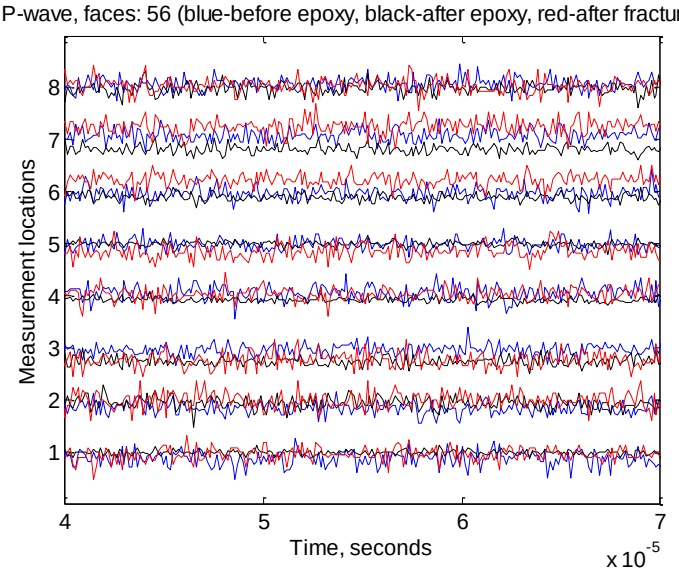

Figure 3.422. P-wave signatures measured from Surfaces 5 and Surface 6 of Shale Sample 5.

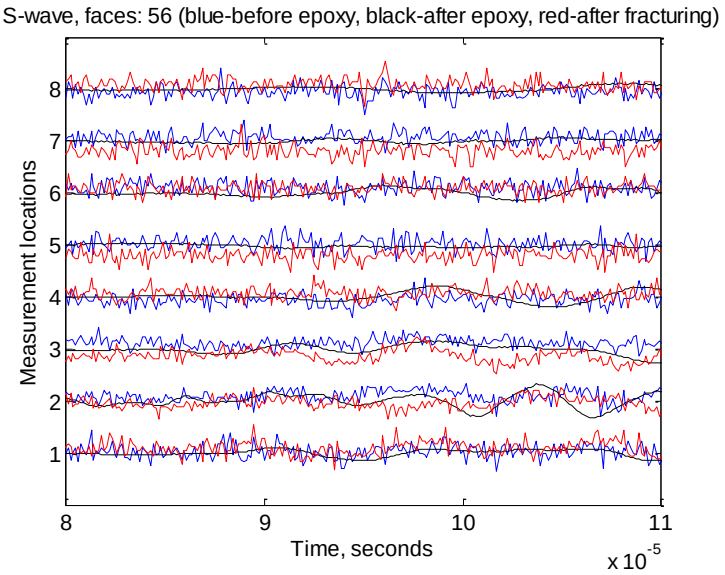

Figure 3.423. S-wave signatures measured from Surfaces 5 and Surface 6 of Shale Sample 5.

Then under tri-axial stresses, shown in Figure 3.424, nitrogen gas was injected to break down the sample, of which the pressure profile is shown in Figure 3.425. The break down pressure is 1316.4 psig at 683.6 seconds. Finally, the sample was broken down at 116.3 psig by injecting nitrogen gas under no tri-axial stresses, shown in Figure 3.426.

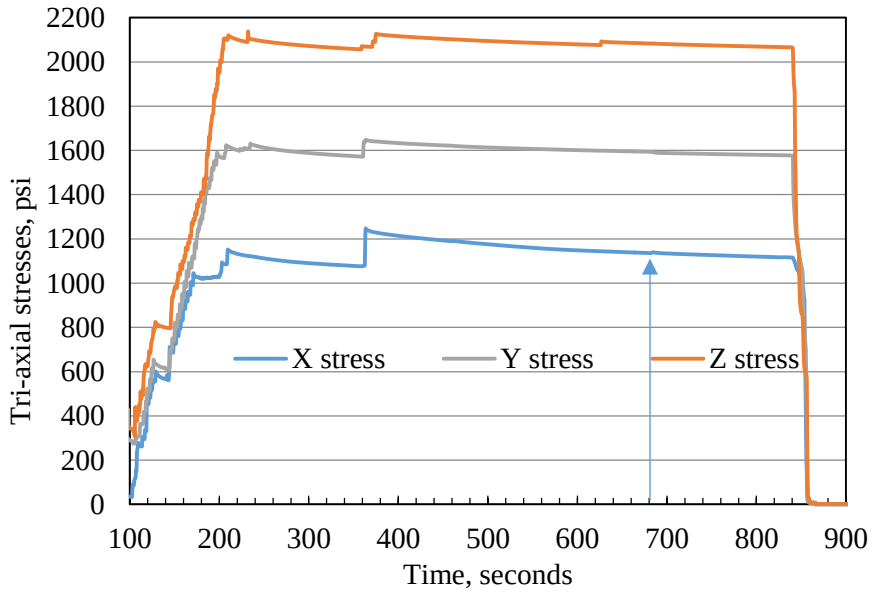

Figure 3.424. Stress loading for nitrogen gas fracturing of Shale Sample 5.

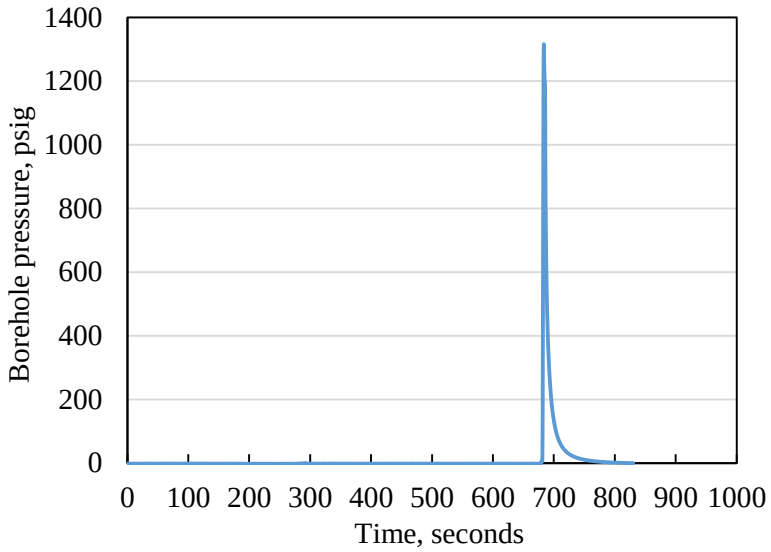

Figure 3.425. Nitrogen gas fracturing pressure for Shale Sample 5 under tri-axial stresses.

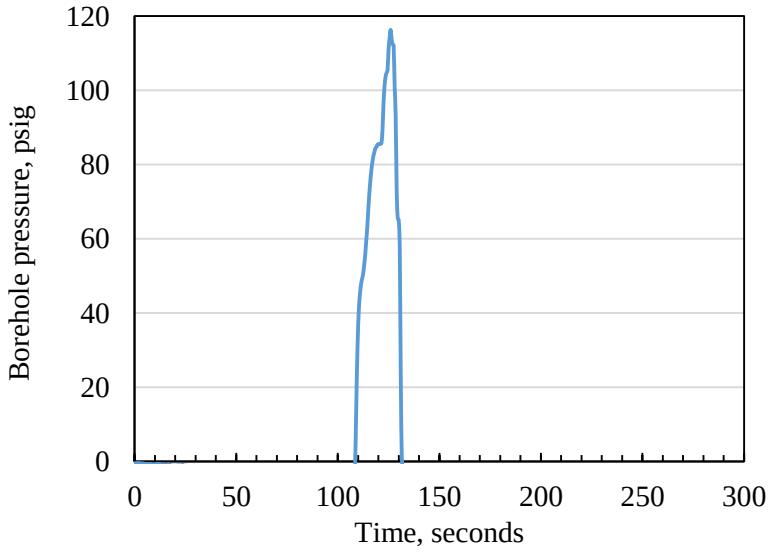

Figure 3.426. Nitrogen gas fracturing pressure for Shale Sample 5 under no tri-axial stresses.

As compared with original surfaces in Figure 3.427, there are no noticeable new fractures generated by slick water injection in Figure 3.428. After fracturing, purple slick water appeared on Surfaces 1, 3, 4, and 5 along preexisting fractures.

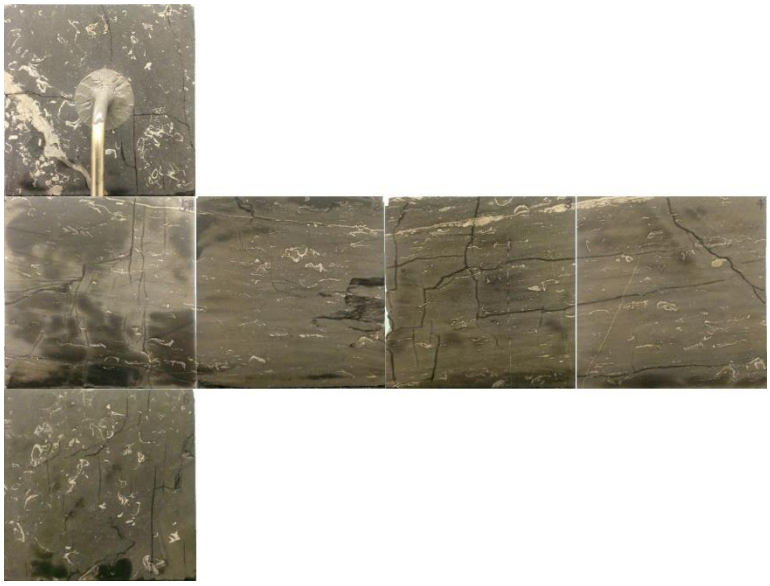

Figure 3.427. Intact surfaces of Shale Sample 5 before treatment.

Figure 3.428. Surfaces of Shale Sample 5 after slick water and gas fracturing.

As shown in Figure 3.429, epoxy covered the fractures near the borehole (darker areas), which are also colored by slick water, verifying that slick water preferentially flowed into epoxy bonded preexisting fractures. The other fracture planes without color were created by nitrogen gas fracturing; they are generally perpendicular to the x- and y-stress directions. Similar to Shale Sample 2 and Shale Sample 3, with a stress difference of 500 psi, preexisting fractures dominated the fracturing initiation and propagation.

Figure 3.429. Slick water fracture morphology of Shale Sample 5 after gas break down.

Generally, breakdown pressures for supercritical or gas CO_2 injection induced fracturing are much lower than that that of slick water fracturing under tri-axial stress loading. Raising tri-axial stress levels tended to increase the break down pressure and increase of stress difference among the axes and reduce the CO_2 breakdown pressures. In the presence of preexisting fracturing that were weakly bonded by epoxy, injected CO_2, either supercritical or gas, preferentially reopened these fractures and continued to extend them. Given a higher stress difference, new fractures were generated in addition to the preexisting ones. When the direction of the minimum horizontal stress is not perpendicular to the preexisting fracture planes, tri-axial stress loading and preexisting weak fractures compete against each other for the dominance of the injection induced fracturing process.

All results for concrete samples fractured by brine injection (4.0 wt% KCl) / CO_2 injection as well as shale samples fractured by gas/supercritical CO_2 and slick water in laboratory are briefly summarized in Table 3.1 for both concrete (denoted as C) and shale (denoted as S) samples.

Table 3.1. Summary of brine/CO_2 injection induced fracturing on concrete and shale samples

Rock sample	Tri-axial stresses x:y:z psi	Injection rate ml/min	Peak pressure psi, & temperature °C	Stress response	Acoustic emission delay	Gas N_2 fracturing psi	Borehole depth and colored fracture
C32 Brine	500:750:1000	100	458.29	Not obvious	No AE	Unc.-244	4” Rugged vertical plane, top ▽
C33 Brine	500:750:1000	200	453.24	Not obvious	No AE	Con.-450 Unc.-293	6” angled plane, bottom ▵
C37 Brine	500:750:1000	40	1097.04	Strong	No AE	Unc.-420	No dyeing
C38 Brine	500:750:1000	20	898.30	Obvious	No AE	Con.-667 Unc.-217	4” Turning fracture plane
C39 Brine	1000:1500:2000	40	1656.26	Obvious	Delayed	Con.-1381 Unc.-257	4” small circular plane slightly deviates from center

C40 Brine	1000:1500:2000	40	2424.13	Obvious	Delayed	Con.-1165 Unc.-543	4” turning and irregular at center
C27 LCO_2	1000:1500:2000	40	1145.40 29.22	Strong	No AE	Unc.-33	4”, sharp, smooth vertical plane, Temp. (-13.82 °C)
C28 GCO_2	1000:1500:2000	100	842.13 33.41	Not obvious	Delayed	No	4” Gas leakage around wellhead
C29 LCO_2	1500:2250:3000	40	2570.88 29.32	Obvious	Delayed	Con.-1597	4” Sharp, smooth plane on one side of borehole
46 GCO_2	1000:1500:2000	Pulse pump	~809 ~30	No data	Delayed	Con.-748	4” Injection data file corrupted.
C47 $ScCO_2$	1500:2250:3000	100	1151.13 35.05	Not obvious	Delayed	Con.-1574	4” Higher GN fracturing pressure
C48 GCO_2	1000:1500:2000	40	1021.86 49.86	Obvious	Delayed	Con.-1160	4” higher GN fracturing pressure
C49 GCO_2	1250:1875:2500	Pulse pump	784.70 19.48	Obvious	Delayed	Unc.-216	4” CO_2 leaking
C50 $ScCO_2$	1250:1875:2500	40	1641.23 34.44	Slight	Delayed	NA, fast leakage	4”, 13” on face 2&6, multiple rugged fracture planes, >1/2 of the cross section
C51 $ScCO_2$	1500:2125:2750	40	1527.36 39.12	Obvious	Delayed	Con. 1679 Unc. 55	4”, 11” on face 2&6, single fracture on one side of the wellbore, ~1/2 of the cross section
C52 $ScCO_2$	1500:2125:2750	40	2130.17 43.40	Obvious	Delayed	Con. 1719 Uncon. 176	4”, 5” on face 2 & 6, Single smooth plane on one side of borehole, ~1/2 of the cross section
C53 $ScCO_2$	1000:1625:2250	40	1091.49 46.84	Obvious	Delayed	Con. 1298 Uncon. 183	4”, 18” on face 2, 4, 5, and 6; single rugged fracture, ~3/4 of the cross section
C54 $ScCO_2$	1250:1562:1875	40	1641.90 44.84	Not obvious	Mixed	Con. 1614 Unc. 302	4”, 0.5” on face 5, small fan upward from wellbore 2” wide, ~1/16 of the cross section

C55 $ScCO_2$	1250:2187:3125	40	1195.53 39.86	Slight	Delayed	Con. 975 Unc. 112	4”, 7” on face 2&4, single circular around wellbore 7.5” wide, ~2/3 of the cross section
C56 $ScCO_2$	1250:1562:1875	40	1289.79 44.68	Not obvious	Delayed	Con. 1447 Unc. 221	0”, highly confined near wellbore <0.5” wide
C57 $ScCO_2$	1250:1562:1875	10	1548.94 44.23	Slight	Delayed	Con. 1473.3 Unc.461.24	4” , CO_2 induced fracture change direction at the end of seeding fracture
C58 $ScCO_2$	1250:2187:3125	10	-	-	-	-	4”, failed due to leaking at well head
C59 $ScCO_2$	1250:1875:2500	10	1761.44 41.87	Obvious	Delayed	Con. 1557.69 Unc.114.69	4”, no obvious seeding fracture; CO_2 induced fracture is perpendicular to the minimum stress
C60 $ScCO_2$	1250:1562:1875	10	1798.14 39.38	Obvious	Delayed	Con. 1447.188 Unc. 243.87	4”, very short seeding fracture; CO_2 induced fracture is perpendicular to the minimum stress
C61 $ScCO_2$	1250:1875:2500	10	2139.80 41.58	Obvious	Delayed	Con. 2320.568 Unc. 258.05	4”, visible seeding fracture in $\perp$y-stress; CO_2 induced fracture is perpendicular to the minimum stress
C62 $ScCO_2$	1250:1875:2500	10	2070.9 36.67	Obvious	Delayed	Con. 1521.3 Unc.131.8	4”, CO_2 induced fracture is perpendicular to the minimum stress

C63 $ScCO_2$	1500:2125:2750	10	1402.6 39.3	Obvious	Delayed	Con. 1521.3 Unc.-	4", CO_2 induced fracture is perpendicular to the minimum stress and expanded to surface
C64 $ScCO_2$	1250:2187:3125	10	1579.03 43.67	Not obvious	Delayed	Con. 1539.9 Unc.297.5	4", CO_2 induced fracture is 30°from the minimum stress and expanded to surface
C65 $ScCO_2$	1250:1562:1875	10	1151.35 53.68	Obvious	Delayed	Con. 1448.57 Unc.603.9	4", CO_2 induced fracture is subvertical from the minimum stress and expanded to surface
C66 $ScCO_2$	1000:1625:2250	10	1241.88 33.9	Not obvious	Delayed	Con. - Unc.-	4", CO_2 induced fracture is perpendicular to the minimum stress and expanded to surface
C67 $ScCO_2$	1250:1875:2500	10	-	-	-	-	4.5", failed due to fractures on samples
C68 $ScCO_2$	1250:2187:3125	10	1214.33 -	Not obvious	Delayed	Con. 1447.41 Unc. 293.98	4.5", CO_2 induced fracture is almost perpendicular to the minimum stress and expanded to surface
C69 $ScCO_2$	1250:1875:2500	10	1505.19 53.7	Obvious	Small delay	Con. 1965.80 Unc. 592.50	4.5", CO_2 induced fracture is perpendicular to min stress plane in high perm core. Leaking in near wellbore region in low perm shell

C70 $ScCO_2$	1250:1562:1875	10	1450.398 55.7	Not obvious	Delayed	Con. 1875.04 Unc. 833.37	4.5", CO_2 induced fracture is not completely perpendicular to min stress plane
S1 $ScCO_2$	1600:2100:2600	40	1300.1 37.4	Obvious	Delayed	Con. 1448.0 Unc. 81.7	Big vertical and sinuous fracture around borehole, ⊥x-stress
S2 GCO_2	1100:1600:2100	80	953.6 46.2	Not obvious	Delayed	Con. 1715.5 Unc. 96.4	Tiny fractures connected to unbonded pre-existing fractures and interfaces
S3 $ScCO_2$	1100:1600:2100	80	1392.5 39.7	Not obvious	Delayed	Con. 2263.8 Unc. 131.0	Reopened big weakly epoxy bonded fracture ⊥y-stress, and a small new fracture ⊥x-stress
S4 GCO_2	1200:2100:3000	Pulse pump	804.3 54.0	Not obvious	Delayed	Con. 1803.3 Unc. 70.6	Reopened big weakly epoxy bonded interface ⊥z-stress, and a new fracture ⊥y-stress
S5 slick water	1100:1600:2100	1	1602.5 20.0	Not obvious	Delayed	Con. 1316.4 Unc. 116.3	Reopened big weakly epoxy bonded fracture ⊥y-stress, and a small one ⊥y-stress
S6 GCO_2	500:1000:1500	Pulse pump	604.6 38.7	Obvious	Delayed	Con. 761.8 Unc. 69.0	Opened big preexisting horizontal fracture first, then plane turned to the vertical direction, nearly ⊥x-stress
Note: Con & Unc - confined & unconfined gas N_2 fracturing, AE - Acoustic emission measurements.							

CO_2 induced fractures on normal concrete samples with various confining stress conditions

During hydraulic fracturing process, the rock will usually fail due to tensile and shear failure. To determine the rock failure type, it is essential to calculate the stress conditions at the borehole wall.

According to the Kirsch solution, the principal stresses at failure points on borehole wall (two points located in the horizontal plane in the direction of maximum horizontal stress) can be calculated as following.

$$\sigma_r = P_w \tag{3.1}$$

$$\sigma_\theta = 3\sigma_h - \sigma_H - P_w \tag{3.2}$$

$$\sigma_z = \sigma_v - 2\nu(\sigma_H - \sigma_h) \tag{3.3}$$

where, σ_r is the stress along radial direction; σ_θ is the stress along the tangential direction; σ_z is the stress in vertical direction; σ_v, σ_H, σ_h are vertical, maximum and minimum horizontal stresses in far field, respectively; P_w is the wellbore pressure; and ν is the Poisson's ratio.

With the stress condition of the failure points determined, we can further apply the tensile and shear failure criteria. The selected tensile failure criterion is adopted from Haimson and Fairhurst (1967), which is developed for permeable rocks:

$$p_b = \frac{3\sigma_h - \sigma_H + \sigma_t - \eta P_p}{2-\eta} \tag{3.4}$$

where, σ_t is the tensile strength of the rock; P_p is the pore pressure; and η is a function of Biot's number α and Poisson's ratio ν:

$$\eta = \frac{\alpha(1-2\nu)}{1-\nu} \tag{3.5}$$

The selected shear failure criterion is the Mogi-Coulomb criterion. It can be expressed as:

$$\tau_{oct} = k + m\sigma_{oct} \tag{3.6}$$

where, τ_{oct} is the octahedral shear stress; σ_{oct} is the octahedral normal stress; k and m are Mogi-Coulomb intercept and slope, which depend on the material. The octahedral stresses can be calculated using following equations:

$$\tau_{oct} = \frac{1}{3}\sqrt{(\sigma_1 - \sigma_2)^2 + (\sigma_1 - \sigma_3)^2 + (\sigma_2 - \sigma_3)^2} \tag{3.7}$$

$$\sigma_{oct} = \frac{1}{3}(\sigma_1 + \sigma_2 + \sigma_3) \tag{3.8}$$

where, σ_1, σ_2, and σ_3 are principal stresses.

Samples C27 – C29, C46 – 56 in Table 3.1 are used in this section. The tensile strength for concrete samples is 418 psi and Poisson's ratio is 0.243 as reported in the second quarterly report. The Biot's number is assumed to be 0.8. The results after checking against the tensile failure criterion show that only C29, C52 and possibly C50 have experienced the borehole pressure greater than

predicted breakdown pressure, as shown in Figure 3.430. This indicates in most of these concrete samples, the fractures initiated by shear failure.

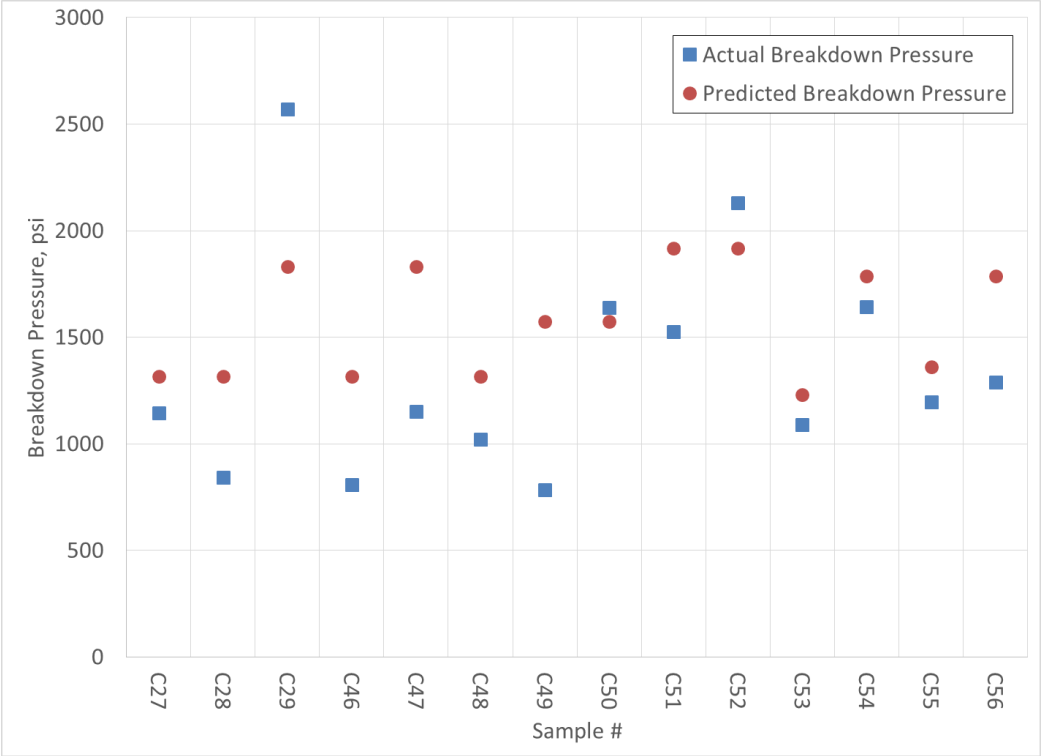

Figure 3.430: Comparison between actual and predicted breakdown pressure for CO_2 induced fractures on normal concrete samples.

The rest of selected samples are then checked against the shear failure criterion. After calculating the local principal stress condition and the octahedral stresses, the results can be shown in Figure 3.431. The Mogi – Coulomb intercept is 154.47 psi and the slope is 0.3439.

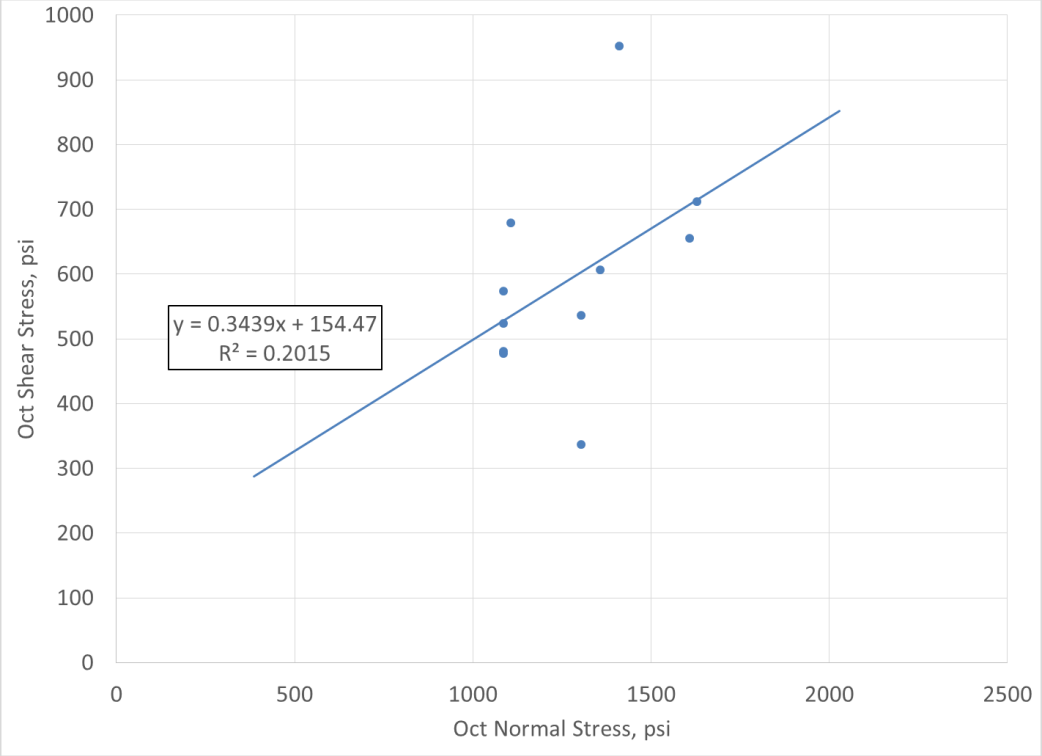

Figure 3.431: Mogi – Coulomb failure envelope determined from selected concrete samples with CO2 injection induced fracturing.

Influence of pre-existing fractures on CO_2 induced fracture initiation

Samples 57-61 contains pre-existing brine induced fractures in the direction that is perpendicular to the CO_2 induced fractures. The CO_2 induced fractures are in the direction of yz-plane, while the brine induced fractures are in the xz-plane. The results show that the closed (without any proppants) transvers pre-existing fractures have little to no effect on the fracture initiation pressure, while the fracture morphology changes significantly. Due to the existence of pre-existing fractures, the CO_2 induced fractures deviate from the Y-Z plane and become tilted, as shown in Figure 3.432, creating much more complicated morphology.

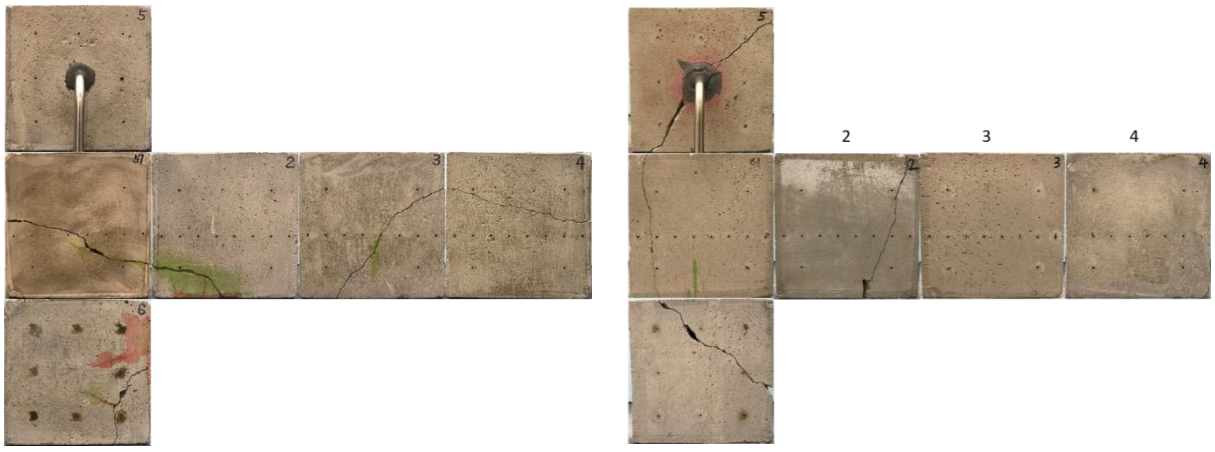

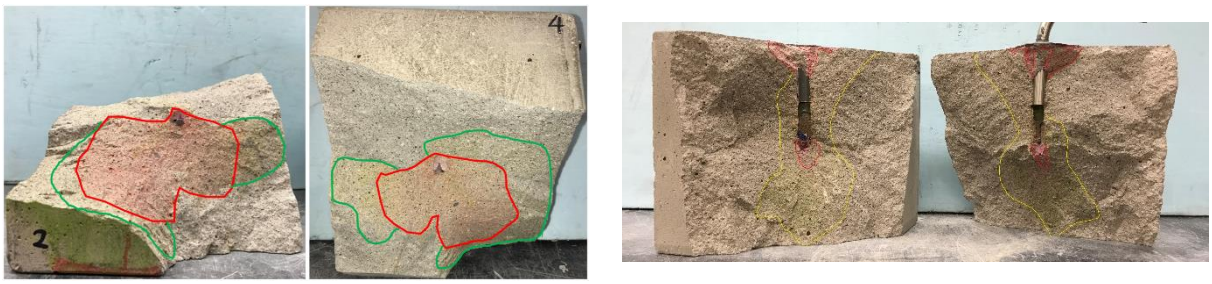

Sample #57 Sample #61

Figure 3.432: Observed fractures distribution (first row: surfaces; second row: inside) of Samples 57 and 61 (Red color indicates pre-existing transverse fractures. Green and yellow colors indicate CO_2 induced fractures).

Influence of water saturation on CO_2 induced fracture initiation

Samples 62 – 66 are water saturated concrete samples. The results show that the extent of CO_2 induced fractures are generally limited to a relative small area when compared to dry samples, as shown in Figure 3.433. This is probably due to the existence of water in pores. The dual phase fluid effect will reduce the relative permeability of CO_2 thus limit the area that injected CO_2 can reach. Therefore, the elevated pressure is contained within smaller region. The CO_2 fracturing in water saturated samples behaves much similar to brine induced fracturing.

Sample 62 Sample 64

Figure 3.433: Fracture morphology (colored in red) of water saturated Samples 62 and 64.

Influence of composite samples during CO_2 induced fractures initiation

Samples 68 – 70 are composite concrete samples with a high permeability and low strength spherical core in the center. Compared to other concrete samples fractured under the same stress condition, the breakdown pressures of composite samples are noticeably lower. The fracture profile shows very clear that the spherical core is acting a pressure equalizer during fracturing process. The fracture usually can fully separate the core into halves. Once the injected fluid getting into the outer shell, the fracture will usually favor one side instead of another, as shown in Figure 3.434. After a closer inspection, a small deviation in fracturing plane at the boundary of spherical core is noticed, although the fracture still lies in y-z plane (i.e. stress condition still dominates the direction of fracture). This is probably due to the weak bonding between outer shell and spherical

core, fluid leaks along the boundary and then the fluid finds another weak spot before further fracturing the outer concreter shell.

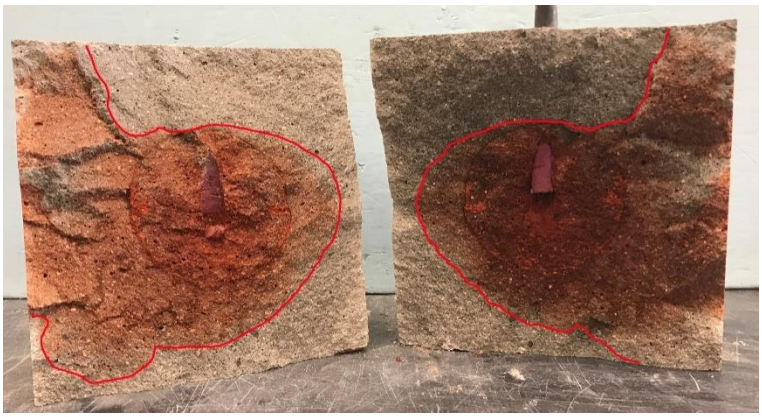

Figure 3.434: Fracture morphology of composite sample #68.

Difference of breakdown pressure between CO_2 and brine induced fracturing

Break down pressure of injection with different fluids were compared. Figure 3.435 shows the significant difference of breakdown pressure for injection CO_2 and brine in terms of viscosity. The results here are for samples under confining stress of 1000-15000-2000 psi. It is worth noting that the breakdown pressure for CO_2 induced fracturing is generally around the minimum horizontal stress, i.e. the tensile strength is not important in CO_2 induced fracturing when defects of rocks are presenting. A possible reason for this may be some small drilling induced cracks around wellbore may only allow CO_2 to enter due to the low viscosity and low interfacial tension. Once the CO_2 enters these small cracks, it only need to overcome the friction and minimum horizontal stress to propagate existing defects instead of initiating a new fracture.

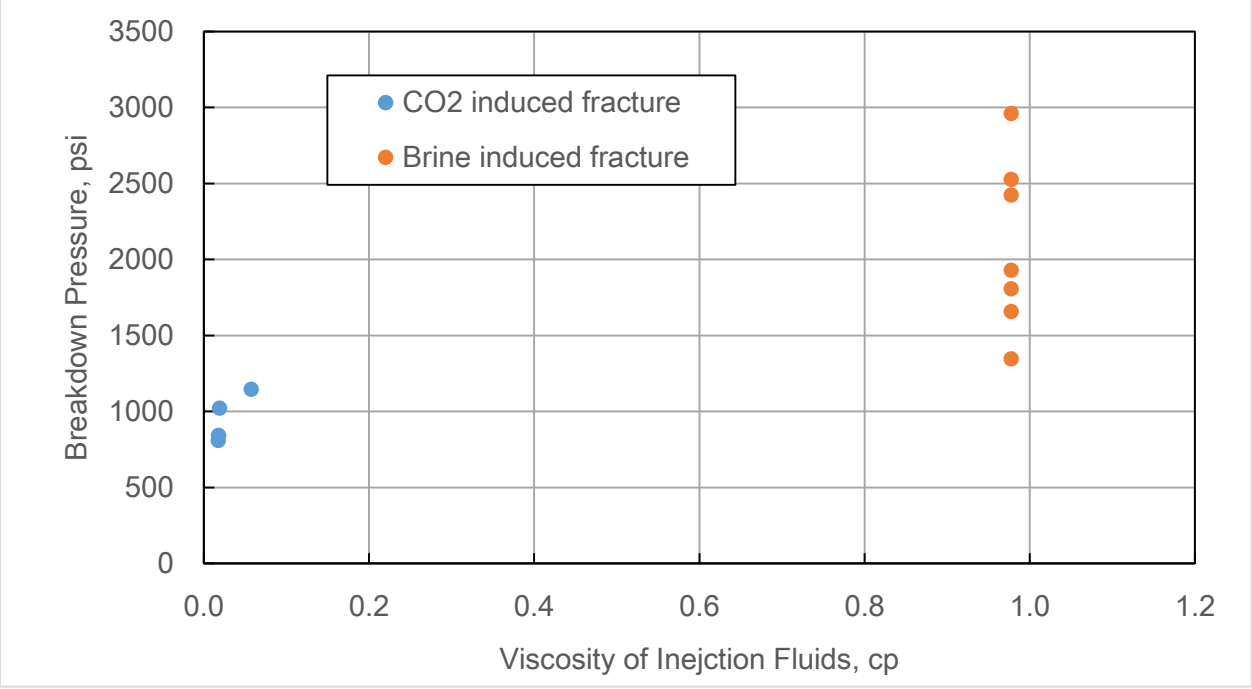

Figure 3.435: Breakdown pressure from different viscosity of injected fluids for concrete samples under stress condition of 1000-1500-2000 psi.

Confining stress relative magnitude on fracture orientation

The fracture orientation under different confining stress were also study. During the fracturing process, the orientation of fractures is mostly dominated by confining stress (or in-situ stress in field application). For most samples with confining stress differential (difference between confining stress in different direction) is large, the fracture planes all lie in y-z plane (which is perpendicular to the minimum horizontal stress), as shown in Figure 3.436. However, when the stress differential, especially the difference between two directions with smallest stresses, is small, the fracture orientation is dominated not only by the stress direction, but also magnitude of confining stress, tensile strength of the rock, and break down pressure, as shown in Figure 3.437 and Figure 3.438.

One finding is that when the stress differential is larger than the tensile strength of rock samples and maximum stress is much higher than break down pressure, the fracture plane will be perpendicular to the minimum horizontal stress direction; otherwise the fracture plane will deviate from the aforementioned direction. Smaller stress differential in two horizontal stresses (assuming the vertical stress is the largest) will cause the fracture plane to deviate in horizontal direction. When vertical stress is smaller or similar to break down pressure, the fracture plane will tilt in the vertical direction.

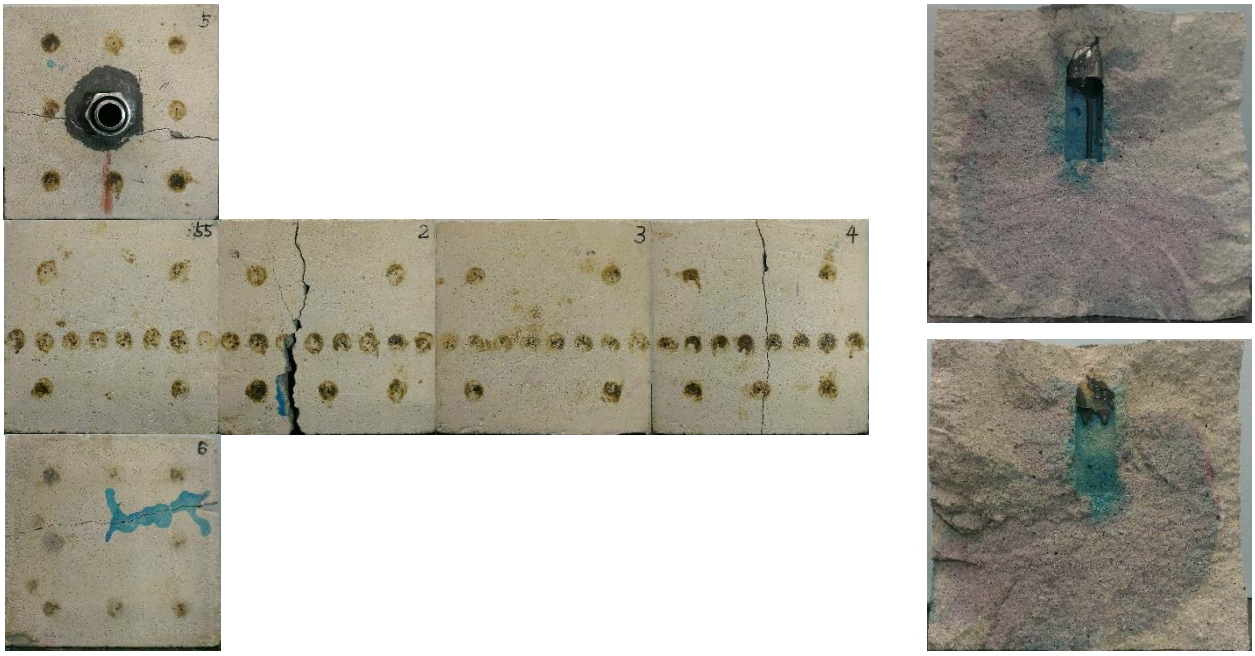

Figure 3.436: Fracture profile of Sample 55, with confining stress of 1250-2187-3125 psi. The left shows the outer surface of Sample 55 after fracturing. The right shows the fracture surface after Sample 55 is broken into two halves. Note that the fracture plane is almost perfectly in-line with y-z plane.

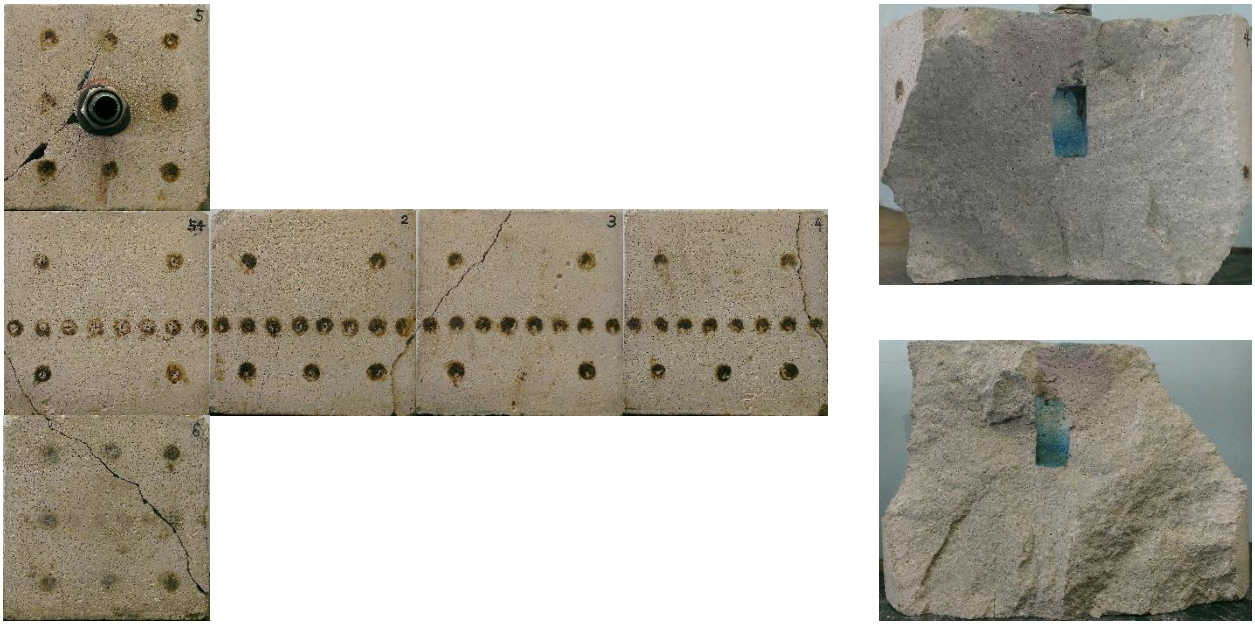

Figure 3.437: Fracture profile of Sample 54, with confining stress of 1250-1562-1875 psi. The left shows the outer surface of Sample 54 after fracturing. The right shows the fracture surface. Note that the fracture plane is deviated from y-z plane.

Figure 3.438: Fracture profile of Sample 38, with confining stress of 500-750-1000 psi. The left shows the outer surface of Sample 38 after fracturing. The right shows the fracture surface. Due to the low magnitude of confining stress and small stress differential, the fracture plane is relatively arbitrarily distributed.

Comparison of fracturing Marcellus shale blocks using water and liquid CO_2 under true triaxial stress with imaging

Fracturing of shale using different fracture fluids is expected to yield different results. When fracturing, the fracturing fluid will invade the medium, controlled by the medium permeability, pressure, and the viscosity of the fracturing fluid. This invasion tends to reduce the breakdown pressure (Hubbert and Willis, 1957). This is supported by lab studies including Zoback et al (1977) and Haimson and Fairhurst (1969), who used fluids having differing viscosities and pressurization rates. In cubes of brittle shale, Zhang et al. (2017) compared the use of water, liquid CO_2, and sc-CO_2 as fracturing fluids. Using liquid CO_2 as the fracturing fluid resulted in a breakdown pressure of about one half that using water, and when sc-CO_2 was used, another 15% reduction in breakdown pressure was achieved. This is in order of their declining viscosities.

It has been noticed that as the viscosity of the fracturing fluid decreases, the fracture morphology becomes more complex. In microscale examinations of macroscale fracturing granite using hydraulic oil, water and sc-CO_2, fractures formed using the more viscous hydraulic oil and water tended to go through grains, whereas fractures formed using the less viscous sc-CO_2 tended to go around grains (Chen et al. (2015). With the least viscous sc-CO_2, microscale examination showed that fractures were the most tortuous and branched. At the larger laboratory scale, fractures formed in shale samples using slickwater and gel under a variety of conditions resulted in different fracturing behaviors Wang et al (2015). The lower viscosity slickwater with low differential horizontal stress did not form a main fracture but opened the natural fracture system. A simple fracture was formed in addition to some opening of the natural fracture system however with the viscous cross-linked gel. Using a higher horizontal differential stress and slickwater resulted in a simple fracture. It was also noticed that the less viscous slickwater fractures were more easily hampered by discontinuities.

Based on these studies, it was hypothesized that fracturing brittle Marcellus shale blocks under moderate horizontal stress differential using water and sc-CO_2 would result in markedly different fractures formed. The CO_2-stimulated sample would be expected to have a lower breakdown pressure, and a rougher surface. Because our samples did not have a significant natural fracture system inside, that was thought not to be important here.

Method

The LBNL true triaxial X-ray transparent frame was used in this test (Figure 3.439). A 6” x 2.5” x 2.5” (15 cm x 6.25 cm x 6.25 cm) rock block is placed on the bottom platen and between 4 “moon-shaped” (round on the outside, flat on the inside) platens. These platens have a series of holes and tubes machined into them to control the fluid pressure on the outside of the sample (here set to atmospheric pressure). An elastomer sleeve with eight through-going steel feet is then stretched around the assembly and attached to the bottom platen. The sleeve is attached to the top platen and the entire assembly is placed in the pressure vessel. A confining pressure can be applied around the outer sides of the sample using a fluid connected to a high-pressure syringe pump. Axial stress is applied using a jack on the inside of the lower platen. The steel feet that protrude trough the elastomer sleeve are arranged such that they are actuated by rods protruding through the vessel wall. Four feet actuate one “moon”, and on the opposite side, four feet actuate another moon. Four

of these rods are in contact with hydraulic jacks on the top resisted by massive steel rings and controlled using high pressure syringe pumps and the other four are directly resisted by the support rings. In this way, three independent stresses can be applied to the sample. The space between the support rings (window in Figure 3.439b.) is composed of X-ray transparent materials allowing visualization of the fracturing process.

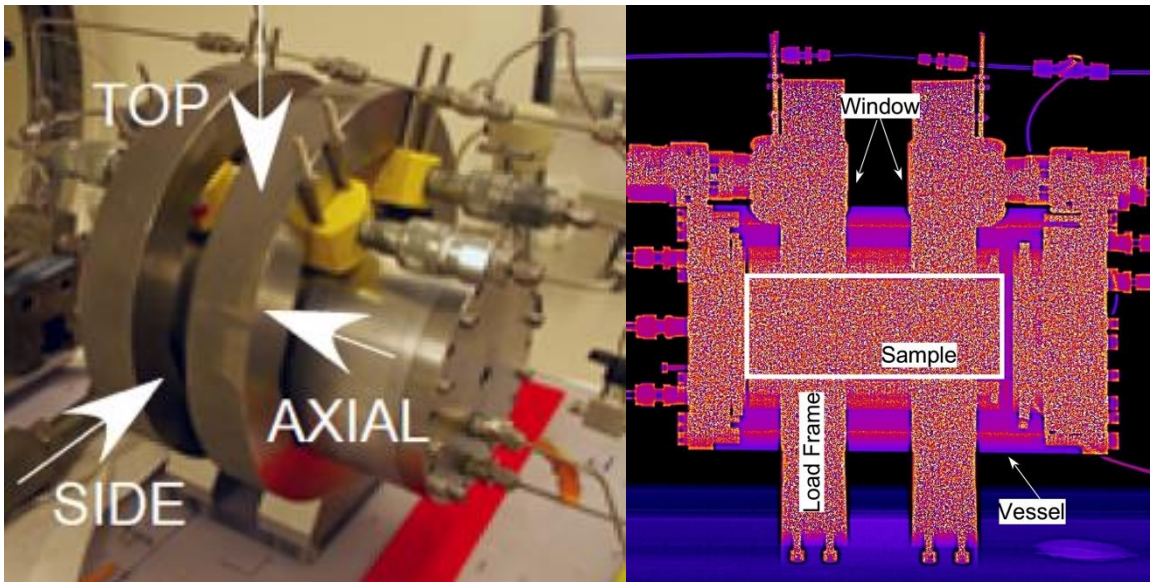

a. b.

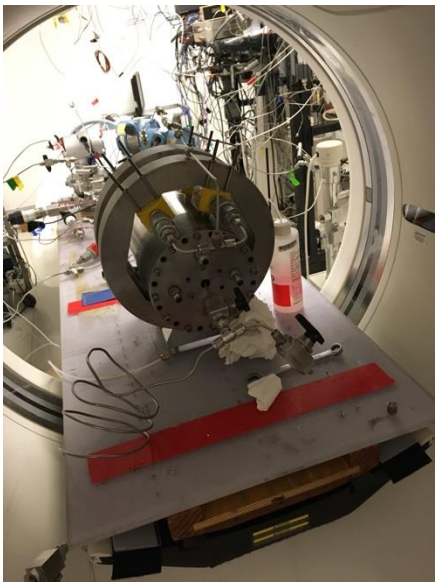

c.

Figure 3.439. The LBNL true-triaxial X-ray transparent frame. a. Ortho-view showing how stresses are applied in general. b. Linear X-ray scan of the triaxial cell showing the sample location, the X-ray window, the frame, and the vessel. c. image of the cell on the X-ray table.

Samples

Three blocks of Marcellus shale were obtained from Kocurek Industries, and machined into the 6” x 2.5” x 2.5” blocks. These were CT scanned prior to use to look for flaws (Figure 3.440). In Figure 3.440, higher density regions (likely carbonate-rich) are indicated by the lighter colors in the grey scale images and in purple in the color images. Two of the blocks were similar, and were selected for further testing.

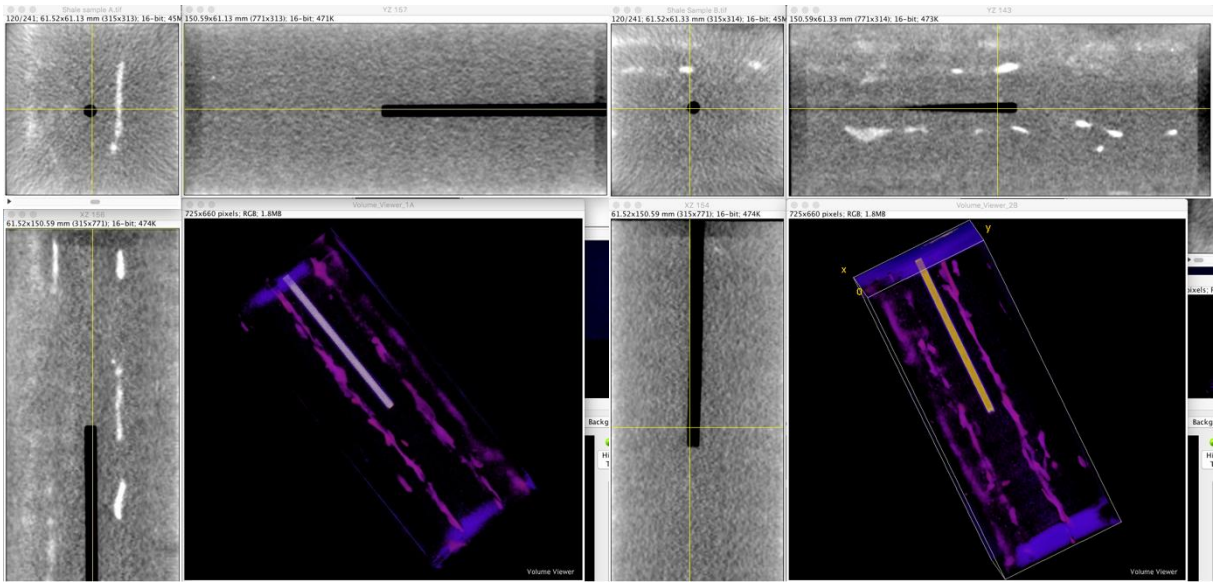

Figure 3.440. left – Shale sample A, right – Shale sample B.

Prior to assembly, a 1/8 inch hole was drilled into the center of the shale samples along the center long axis. A 1/8 inch stainless steel tube was epoxied in the hole leaving some space at the bottom of the hole. This allows the stimulation fluid to be applied to the center of the sample, which is in the X-ray window.

Test Set Up

Once the sample was appropriately assembled in the triaxial cell, the cell was set up in the frame. The frame was then set and aligned on the X-ray computed tomography table. The stresses were slowly brought up to 1000 psi along the long axis, 1000 psi along the direction parallel to the natural bedding, and 2000 psi in the other direction, such that a stress-controlled fracture would propagate against the natural bedding. Once set up, an initial set of CT scans of the region between the frames was collected.

The fracturing fluids were applied using a Quizix Q 5210 displacement pump. This pump has nanoliter/min resolution and extremely fine control. Pump rates were adjusted as needed, although typically on the order of 0.05 mL/minute.

The water fracturing test was performed first, and pressurization was accomplished by slowly flowing water into the sample center. The stimulation pressure was initially brought to 1000 psi to start the test. Since the applied stresses were on this order of magnitude, this was considered safe. A few very small leaks (not visible over 30 minutes) were encountered during this test, resulting in a nonuniform pressure increase (Figure 3.441). Since the breakdown pressure was the desired

information from the test, leaks were rapidly assessed and fittings tightened, and the test continued. CT scans were taken regularly in an attempt to observe the fracturing. During the water stimulation, 29 sets of scans were collected.

The same set of conditions were applied for the CO_2 stimulation, except that most of the leaks had been fixed, allowing a more uniform loading (Figure 3.441). In all, 35 sets of CT scans were collected during this test.

In both tests, the pressure increased against the unfractured shale until the breakdown pressure was achieved. Following that, the pressures fell dramatically as the fluid accessed the atmospheric pressure condition on the outer edge. In the case of the CO_2 stimulation, the breakdown was audible and energetic. The breakdown pressure for the water stimulation was 3230 psi and for the CO2 stimulation was 3570 psi.

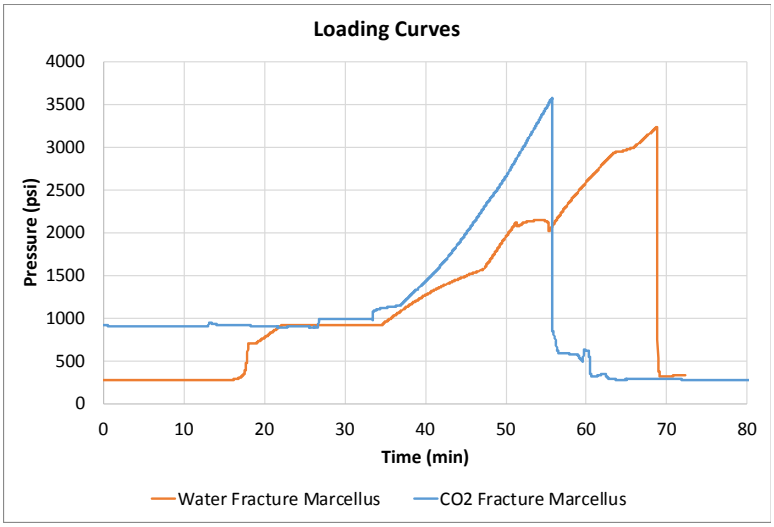

Figure 3.441. Loading curves for water stimulation (orange) and CO_2 stimulation (blue). The breakdown pressure for the water stimulation was 3230 psi and for the CO2 stimulation was 3570 psi.

Post Stimulation Analysis

The water stimulation sample was removed from the apparatus in a single piece. Following that, a fluorescent dye was injected into the fracture and allowed to dry. Traces of the dye and the fracture trace on the intact block are shown in Figure 3.442. The sample was pried open and the fracture faces examined both under white light and UV light (Figure 3.443). The dye had reached most of the accessible fracture with the exception of the lower portion. The upper left corner in the leftmost figure shows where the two rock pieces were held together. There is some curvature to the fracture, which may be due to some uneven loading, or stress direction changes during stimulation.

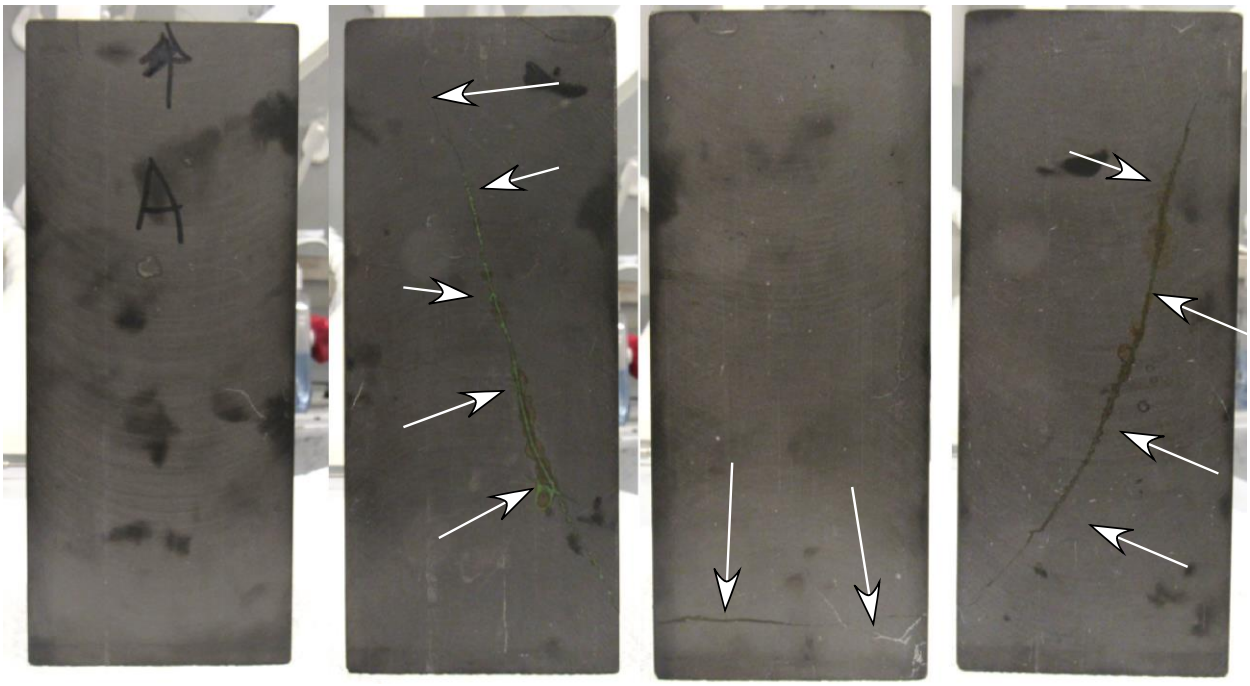

Figure 3.442. Four sides of the water stimulation block with fracture traces identified.

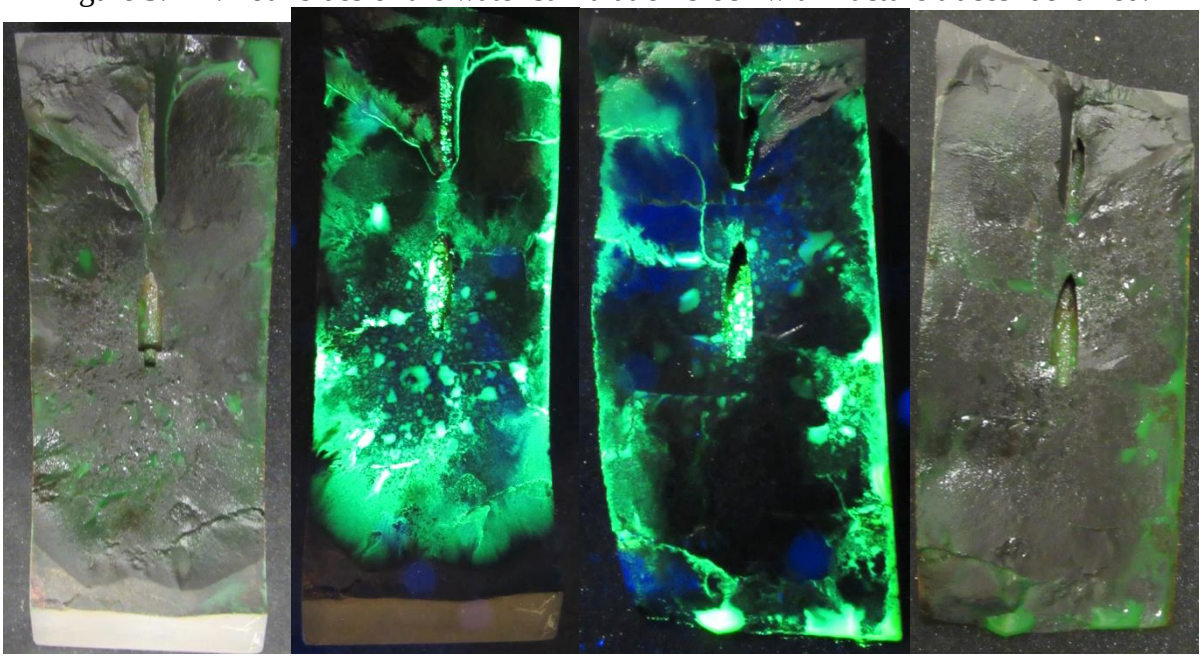

Figure 3.443. Fracture faces of the water stimulation block. The outer two images are under white light, and the inner two are under UV illumination.

The CO_2 stimulated block was separated into 2 halves by the stimulation, which was accompanied by an audible pop. The fracture trace for this reassembled block is shown in Figure 3.444, and the trace is fairly planar (Figure 3.445).

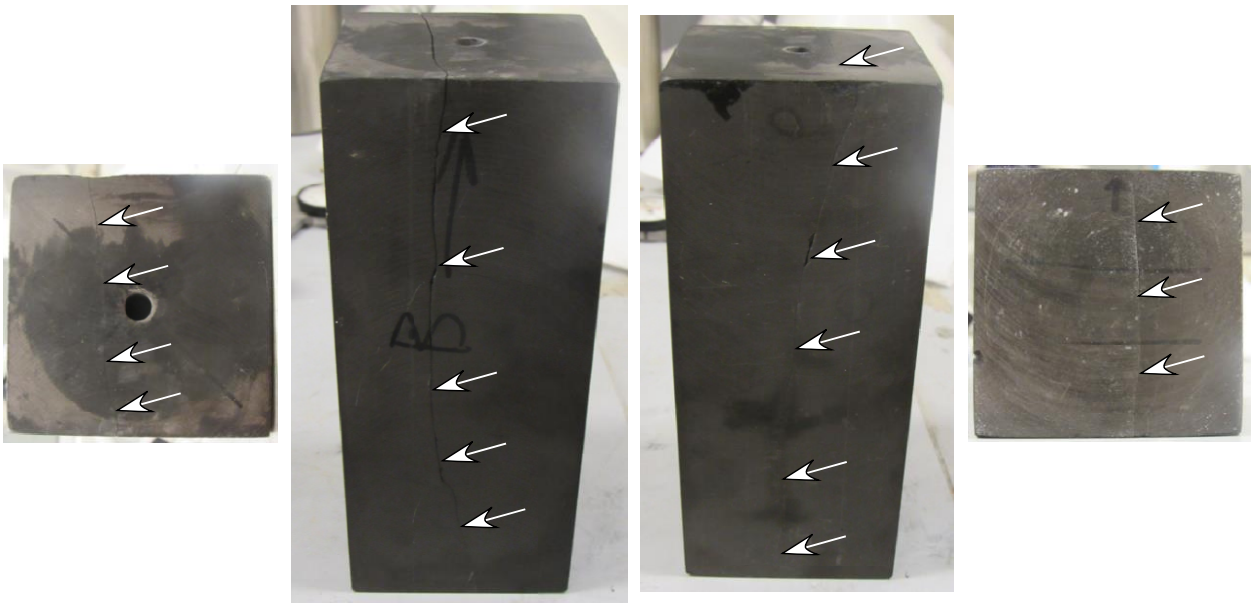

Figure 3.444. Reassembled CO_2 stimulated block with fracture trace identified. From left to right – top, side1, side 2, and bottom.

Figure 3.445. The exposed fracture faces from the CO_2 stimulated block.

Close visual and photographic examination of all fracture faces revealed no significant texture difference between the two blocks.

Remarks

Although two samples are not adequate to draw significant conclusions, the following observations are noted:

1. The breakdown pressures in our tests did not increase with increasing viscosity, and both breakdown pressures are roughly similar. In this respect, our tests contrast with the work of Zhang

et al. (2017) who showed the breakdown pressure decreasing with decreasing viscosity. This may be due to the very low permeability of the shale not allowing invasion of either fluid into the matrix over the experiment timeframe. A longer soak may have allowed more CO_2 to be absorbed allowing lower breakdown for mechanical reasons.

2. The texture of the fracture surfaces for the 2 tests was similar. It was not apparent that either fracture went through any grains, or if they did, they did so similarly. The samples used have very small grain size. If the fractures went through grains, it may not have been noticed.

3. The fracture in the water stimulation case was not planar. We surmise that this is from nonuniform loading, but this is conjecture. It is not likely to be bedding, since the fracture is perpendicular to bedding.

4. The fractures were small, and have not been extractable from the X-ray CT data as of this time. With a uniform medium, fractures as small as 10 microns can often be detected in spite of the ~ 200 micron pixel size. A sufficient number of scans have been collected to allow further analysis.

Task 4: Development of CO_2 flow and geomechanics-coupled mathematical models and numerical schemes for modeling fracturing growth and propagation in storage formations and caprocks

Background - TOUGH2-CSM Fluid and Heat Flow Formulation and Simplified Geomechanical Formulation

The TOUGH2-CSM fluid and heat flow formulation is based on the TOUGH2 formulation (Pruess *et al.*, 1999) of mass and energy conservation equations that govern fluid and heat flow in general multiphase, multicomponent, multi-porosity systems. The conservation equations for mass and energy can be written in differential form as:

$$\frac{\partial M^k}{\partial \mathrm{t}} = \nabla \cdot \bar{F}^k + q^k \tag{4.1}$$

where M^k is conserved quantity k per unit volume, q^k is source or sink per unit volume, and $\bar{F}^k$ is flux.

Mass per unit volume is a sum over phases:

$$M^k = \phi \sum_l S_l \rho_l X_l^k \tag{4.2}$$

where ϕ is porosity, subscript l denotes a phase, S is phase saturation, ρ is mass density, and X is mass fraction of component k. Energy per unit volume accounts for internal energy in rock and fluid and is the following:

$$M^{N+1} = (1-\phi) C_r \rho_r T + \phi \sum_l S_l \rho_l U \tag{4.3}$$

where ρ_r is rock density, C_r is rock specific heat, T is temperature, U is phase specific internal energy, and N is the number of mass components with energy as conserved species N+1.

Fluid advection is described with a multiphase extension of Darcy's law; in addition, there is diffusive mass transport in all phases. Advective mass flux is a sum over phases:

$$\bar{F}_{adv}^k = \sum_l \bar{F}_l X_l^k \tag{4.4}$$

and phase flux, $\bar{F}_l$, is given by Darcy's law:

$$\bar{F}_l = -k \frac{k_{rl}\rho_l}{\mu_l} \left(\nabla P + \nabla P_{c,l} - \rho_l \bar{g} \right) \tag{4.5}$$

where k is absolute permeability, k_r is phase relative permeability, μ is phase viscosity, P is pore pressure, P_c is phase capillary pressure, and $\bar{g}$ is gravitational acceleration. The pressure in phase l:

$$P_l = P + P_{c,l} \tag{4.6}$$

is relative to a reference phase, which is the gaseous phase. Diffusive mass flux is given by:

$$\bar{F}^k_{dis} = \sum_l \rho_l \bar{\bar{D}}^k_l \nabla X^k_l \tag{4.7}$$

where $\bar{\bar{D}}^k_l$ is the dispersion tensor. Heat flux occurs by conduction and convection, the latter including sensible as well as latent heat effects, and includes conductive and convective components:

$$\bar{F}^{N+1} = -\lambda \Delta T + \sum_l h_l \bar{F}_l \tag{4.8}$$

where λ is thermal conductivity and h_l is phase l specific enthalpy.

The description of thermodynamic conditions is based on the assumption of local equilibrium of all phases. Fluid and formation parameters can be arbitrary nonlinear functions of the primary thermodynamic variables.

The TOUGH2-CSM simplified geomechanical formulation is based on the linear theory of elasticity applied to multi-porosity non-isothermal (thermo-multi-poroelastic) media. The first two fundamental relations in this theory are the relation between the strain tensor and the displacement vector $\boldsymbol{u}$:

$$\bar{\bar{\epsilon}} = \frac{1}{2}(\nabla \bar{u} + \nabla \bar{u}^t) \tag{4.9}$$

and the static equilibrium equation, which is an expression of momentum conservation:

$$\nabla \cdot \bar{\bar{\tau}} + \bar{F}_b = 0 \tag{4.10}$$

where $\bar{F}_b$ is the body force.

The last fundamental relation in this theory is the relation between the stress and strain tensors, Hooke's law for a thermo-multi-poroelastic material (Winterfeld and Wu, 2014):

$$\bar{\bar{\tau}} - h(\bar{P}, \bar{T}) = \lambda \epsilon_v + 2G\bar{\bar{\epsilon}} \tag{4.11}$$

$$h(\bar{P}, \bar{T}) = \sum_j \left(\alpha_j P_j + 3\beta K \omega_j \left(T_j - T_{ref} \right) \right) \tag{4.12}$$

where the subscript j refers to a porous continuum, ω is the porous continuum volume fraction, G is shear modulus, and λ is the Lamé parameter, α is Biot's coefficient, T_{ref} is reference temperature for a thermally unstrained state, K is bulk modulus, and β is linear thermal expansion coefficient. The volumetric strain, ϵ_v, is the trace of the strain tensor and also the divergence of the displacement vector:

$$\epsilon_v = \epsilon_{xx} + \epsilon_{yy} + \epsilon_{zz} = \nabla \cdot \bar{u} = \frac{\partial u_x}{\partial x} + \frac{\partial u_y}{\partial y} + \frac{\partial u_z}{\partial z} \tag{4.13}$$

We substitute Equations 4.9 and Equation 4.11 into Equation 4.10 to obtain:

$$\epsilon_v \nabla\lambda + \nabla G \cdot (\nabla\bar{u} + \nabla\bar{u}^t) + (\lambda + \mathrm{G})\nabla\epsilon_v + G\nabla^2\bar{u} + \nabla h(\bar{P},\bar{T}) + \bar{F}_b = 0 \tag{4.14}$$

We assume rock properties are constant. Then, Equation 4.14 reduces to the thermo-multi-poroelastic version of the Navier equation:

$$(\lambda + \mathrm{G})\nabla\epsilon_v + G\nabla^2\bar{u} + \nabla h(\bar{P},\bar{T}) + \bar{F}_b = 0 \tag{4.15}$$

We take the divergence of Equation 4.15 to obtain:

$$(\lambda + 2\mathrm{G})\nabla^2\epsilon_v + \nabla^2 h(\bar{P},\bar{T}) + \nabla \cdot \bar{F}_b = 0 \tag{4.16}$$

We take the trace of Equation 4.11 and obtain a relation between mean stress, volumetric strain, pore pressures, and temperatures:

$$K\epsilon_v = \tau_m - h(\bar{P},\bar{T}) \tag{4.17}$$

Finally, we substitute Equations 4.17 into Equation 4.16 and obtain an equation relating mean stress, pore pressures, temperatures, and body force - the Mean Stress equation:

$$\frac{3(1-\nu)}{1+\nu}\nabla^2\tau_m - \frac{2(1-2\nu)}{1+\nu}\nabla^2 h(\bar{P},\bar{T}) + \nabla \cdot \bar{F}_b = 0 \tag{4.18}$$

The Mean Stress equation is the geomechanical equation for the TOUGH2-CSM simplified geomechanical formulation. This equation is added to the TOUGH2-CSM fluid and heat flow equations with mean stress as an additional primary variable and volumetric strain as an additional property.

Derivation of Stress Tensor Component Equations in Cartesian Coordinates

In this project, we extend the TOUGH2-CSM simplified geomechanical formulation to calculate the entire stress tensor rather than just the mean stress. The thermo-multi-poroelastic Navier equation, Equation 4.15, is a vector equation with a right hand side of zero. Consequently, each component of that equation is zero:

$$(\lambda + \mathrm{G})\frac{\partial\epsilon_v}{\partial \mathrm{x}} + G\nabla^2 u_x + \frac{\partial h(\bar{P},\bar{T})}{\partial \mathrm{x}} + F_{b,x} = 0 \tag{4.19}$$

$$(\lambda + \mathrm{G})\frac{\partial\epsilon_v}{\partial \mathrm{y}} + G\nabla^2 u_y + \frac{\partial h(\bar{P},\bar{T})}{\partial \mathrm{y}} + F_{b,y} = 0 \tag{4.20}$$

$$(\lambda + \mathrm{G})\frac{\partial\epsilon_v}{\partial \mathrm{z}} + G\nabla^2 u_z + \frac{\partial h(\bar{P},\bar{T})}{\partial \mathrm{z}} + F_{b,z} = 0 \tag{4.21}$$

Differentiating Equation 4.19 by *x* and eliminating strains and displacements in favor of stresses using Equations 4.9, 4.11, and 4.17 yields an equation containing the xx-normal stress component, mean stress, pore pressures, and temperatures:

$$\frac{2\nu-1}{2(1+\nu)}\frac{\partial^2 h(\bar{P},\bar{T})}{\partial x^2}+\frac{3}{2(1+\nu)}\frac{\partial^2 \tau_m}{\partial x^2}+\frac{1}{2}\nabla^2\left[\tau_{xx}-\frac{3\nu}{1+\nu}\tau_m+\frac{2\nu-1}{1+\nu}h(\bar{P},\bar{T})\right]+\frac{\partial F_{b,x}}{\partial \mathrm{x}}=0 \tag{4.22}$$

Differentiating Equation 4.20 by *y* and performing the same elimination as above yields an equation containing the yy-normal stress component, mean stress, pore pressures, and temperatures:

$$\frac{2\nu-1}{2(1+\nu)}\frac{\partial^2 h(\bar{P},\bar{T})}{\partial y^2}+\frac{3}{2(1+\nu)}\frac{\partial^2 \tau_m}{\partial y^2}+\frac{1}{2}\nabla^2\left[\tau_{yy}-\frac{3\nu}{1+\nu}\tau_m+\frac{2\nu-1}{1+\nu}h(\bar{P},\bar{T})\right]+\frac{\partial F_{b,y}}{\partial \mathrm{y}}=0 \tag{4.23}$$

Differentiating Equation 4.21 by *z* and performing the same elimination as above yields an equation containing the zz-normal stress component, mean stress, pore pressures, and temperatures:

$$\frac{2\nu-1}{2(1+\nu)}\frac{\partial^2 h(\bar{P},\bar{T})}{\partial z^2}+\frac{3}{2(1+\nu)}\frac{\partial^2 \tau_m}{\partial z^2}+\frac{1}{2}\nabla^2\left[\tau_{zz}-\frac{3\nu}{1+\nu}\tau_m+\frac{2\nu-1}{1+\nu}h(\bar{P},\bar{T})\right]+\frac{\partial F_{b,z}}{\partial \mathrm{z}}=0 \tag{4.24}$$

Differentiating Equation 4.20 by *x*, differentiating Equation 4.19 by *y*, averaging the two, and performing the same elimination as above yields an equation containing the xy-shear stress component, mean stress, pore pressures, and temperatures:

$$\frac{2\nu-1}{2(1+\nu)}\frac{\partial^2 h(\bar{P},\bar{T})}{\partial \mathrm{x}\,\partial \mathrm{y}}+\frac{3}{2(1+\nu)}\frac{\partial^2 \tau_m}{\partial \mathrm{x}\,\partial \mathrm{y}}+\frac{1}{2}\nabla^2\tau_{xy}+\frac{1}{2}\left(\frac{\partial F_{b,y}}{\partial \mathrm{x}}+\frac{\partial F_{b,x}}{\partial \mathrm{y}}\right)=0 \tag{4.25}$$

Differentiating Equation 4.20 by *z*, differentiating Equation 4.21 by *y*, averaging the two, and performing the same elimination as above yields an equation containing the yz-shear stress component, mean stress, pore pressures, and temperatures:

$$\frac{2\nu-1}{2(1+\nu)}\frac{\partial^2 h(\bar{P},\bar{T})}{\partial \mathrm{y}\,\partial \mathrm{z}}+\frac{3}{2(1+\nu)}\frac{\partial^2 \tau_m}{\partial \mathrm{y}\,\partial \mathrm{z}}+\frac{1}{2}\nabla^2\tau_{yz}+\frac{1}{2}\left(\frac{\partial F_{b,z}}{\partial \mathrm{y}}+\frac{\partial F_{b,y}}{\partial \mathrm{z}}\right)=0 \tag{4.26}$$

Differentiating Equation 4.21 by *x*, differentiating Equation 4.19 by *z*, averaging the two, and performing the same elimination as above yields an equation containing the xz-shear stress component, mean stress, pore pressures, and temperatures:

$$\frac{2\nu-1}{2(1+\nu)}\frac{\partial^2 h(\bar{P},\bar{T})}{\partial \mathrm{x}\,\partial \mathrm{z}}+\frac{3}{2(1+\nu)}\frac{\partial^2 \tau_m}{\partial \mathrm{x}\,\partial \mathrm{z}}+\frac{1}{2}\nabla^2\tau_{xz}+\frac{1}{2}\left(\frac{\partial F_{b,z}}{\partial \mathrm{x}}+\frac{\partial F_{b,x}}{\partial \mathrm{z}}\right)=0 \tag{4.27}$$

The normal stress tensor components are obtained from Equations 4.22-4.24, and the shear stress tensor components are obtained from Equations 4.25-4.27. Each of these equations consists of the Laplacian of the stress tensor component plus various derivatives of the terms (mean stress, body force, and the pore pressure-temperature term (Equation 4.13)) that appear in the Mean Stress

equation. This feature, as will be shown later, enables efficient calculation of stress tensor components after mean stress and associated primary variables are solved for.

Stress Tensor Initialization in Cartesian Coordinates

The stress tensor is initialized at the beginning of a simulation. We assume there are no shear stresses and normal stresses have z-direction dependence only. In addition, pore pressure is in hydrostatic equilibrium. Then, the static equilibrium equation (Equation 4.10) for the normal z-direction stress is:

$$\frac{\partial \tau_{zz}}{\partial z} + F_{b,z} = 0 \tag{4.28}$$

We integrate Equation 4.28 from a reference elevation, at which normal stresses and pressure are specified, to a given elevation to get the normal z-direction stress there:

$$\tau_{zz} = \tau_{zz,0} - \int_{z_0}^{z} F_{b,z} dz \tag{4.29}$$

We obtain the following from applying the above assumptions to the x- and y-direction normal stress equations (Equations 4.22 and 4.23):

$$\frac{\mathrm{d}^2}{\mathrm{d}z^2}\left[\tau_{xx} - \frac{3\nu}{1+\nu}\tau_m + \frac{2\nu-1}{1+\nu}h(\bar{P},\bar{T})\right] = 0 \tag{4.30}$$

$$\frac{d^2}{dz^2}\left[\tau_{yy} - \frac{3\nu}{1+\nu}\tau_m + \frac{2\nu-1}{1+\nu}h(\bar{P},\bar{T})\right] = 0 \tag{4.31}$$

Equations 4.30 and 4.31 are integrated twice to yield:

$$\tau_{xx} - \frac{3\nu}{1+\nu}\tau_m + \frac{2\nu-1}{1+\nu}h(\bar{P},\bar{T}) = D_1(z - z_0) + D_2 \tag{4.32}$$

$$\tau_{yy} - \frac{3\nu}{1+\nu}\tau_m + \frac{2\nu-1}{1+\nu}h(\bar{P},\bar{T}) = E_1(z - z_0) + E_2 \tag{4.33}$$

where D_i and E_i are constants of integration. Constants with subscript *2* are evaluated at the reference conditions and the normal x- and y-direction stresses are obtained from solving Equations 4.32 and 4.33 simultaneously:

$$\tau_{xx} = \frac{D_2+\nu E_2}{1-\nu} + \frac{D_1+\nu E_1}{1-\nu}(z - z_0) + \frac{\nu}{1-\nu}\tau_{zz} - \frac{2\nu-1}{1-\nu}h(\bar{P},\bar{T}) \tag{4.34}$$

$$\tau_{yy} = \frac{E_2+DE_2}{1-\nu} + \frac{E_1+D_1}{1-\nu}(z - z_0) + \frac{\nu}{1-\nu}\tau_{zz} - \frac{2\nu-1}{1-\nu}h(\bar{P},\bar{T}) \tag{4.35}$$

Constants with subscript *1* are evaluated from the condition that the ratio of vertical to horizontal stress change is given at the reference point:

$$\lim_{z\to z_0} \frac{\tau_{xx}-\tau_{xx,0}}{\tau_{zz}-\tau_{zz,0}} = R_{xz} \tag{4.36}$$

$$\lim_{z\to z_0} \frac{\tau_{yy}-\tau_{yy,0}}{\tau_{zz}-\tau_{zz,0}} = R_{yz} \tag{4.37}$$

where R_{xz} and R_{yz} are the x- and y-direction ratios, respectively. This yields the following for the D_1 and E_1 constants of integration:

$$D_1 = \left.\frac{\nu R_{yz} F_{b,z} - F_{b,z} R_{xz} + F_{b,z}\nu - (2\nu-1)\gamma}{1+\nu}\right|_{z_0} \tag{4.38}$$

$$E_1 = \left.\frac{\nu R_{xz} F_{b,z} - F_{b,z} R_{yz} + F_{b,z}\nu - (2\nu-1)\gamma}{1+\nu}\right|_{z_0} \tag{4.39}$$

where:

$$\gamma = -\frac{\partial h(\bar{P},\bar{T})}{\partial z} \tag{4.40}$$

Derivation of Stress Tensor Component Equations in rz-Coordinates

In the previous two sections, stress tensor component equations and stress tensor initialization have been presented in Cartesian coordinates. In this section and the next, we consider stress tensor components in rz-coordinates. The displacement vector in these coordinates is:

$$\bar{u} = u_r\hat{e}_r + u_\theta\hat{e}_\theta + u_z\hat{e}_z \tag{4.41}$$

where $\hat{e}_i$ is the unit vector in direction *i*. In rz-coordinates, there is no displacement in or dependence on the θ-direction, so the strain tensor becomes:

$$\bar{\bar{\epsilon}} = \frac{1}{2}(\nabla\bar{u} + \nabla\bar{u}^t) = \begin{bmatrix} \frac{\partial u_r}{\partial r} & 0 & \frac{1}{2}\left(\frac{\partial u_r}{\partial z} + \frac{\partial u_z}{\partial r}\right) \\ 0 & \frac{u_r}{r} & 0 \\ \frac{1}{2}\left(\frac{\partial u_r}{\partial z} + \frac{\partial u_z}{\partial r}\right) & 0 & \frac{\partial u_z}{\partial z} \end{bmatrix} \tag{4.42}$$

The Means Stress equation, Equation 4.18, and the Navier equation, Equation 4.16, can both be written using the gradient and Laplacian operators in rz-coordinates with the volumetric strain given by:

$$\epsilon_v = \epsilon_{rr} + \epsilon_{\theta\theta} + \epsilon_{zz} = \nabla\cdot\bar{u} = \frac{\partial u_r}{\partial r} + \frac{u_r}{r} + \frac{\partial u_z}{\partial z} \tag{4.43}$$

Hooke's law also has the same form in rz-coordinates as in Cartesian. The Navier equation z-component in rz-coordinates is the same as that for Cartesian ones (Equation 4.21) and that

component's z-derivative (Equation 4.24) yields z-direction normal stress and strain as before. We next rearrange Equation 4.43 to obtain:

$$\epsilon_v - \epsilon_{zz} = \epsilon_{rr} + \epsilon_{\theta\theta} = \frac{\partial u_r}{\partial r} + \frac{u_r}{r} = \frac{1}{r}\frac{\partial (r u_r)}{\partial r} \tag{4.44}$$

We integrate Equation 4.44 from the radial center to radius *r* along constant *z* to obtain:

$$u_r(r,z) = \frac{1}{r}\int_0^r \xi\big(\epsilon_v(\xi,z) - \epsilon_{zz}(\xi,z)\big)d\xi \tag{4.45}$$

The radial component of the displacement vector and its r-derivative yield the following strains:

$$\epsilon_{rr} = \frac{\partial u_r}{\partial r} \tag{4.46}$$

$$\epsilon_{\theta\theta} = \frac{u_r}{r} \tag{4.47}$$

The rz-shear stress is obtained from the z-component of the equilibrium equation in rz-coordinates with no dependence on the θ-direction:

$$\frac{\partial \tau_{rz}}{\partial r} + \frac{\partial \tau_{zz}}{\partial z} + \frac{\tau_{rz}}{r} + F_z = 0 \tag{4.48}$$

We rearrange Equation 4.48 and integrate from the radial center to radius *r* along constant *z* to obtain:

$$\tau_{rz}(r,z) = -\frac{1}{r}\int_0^r \xi\left(\frac{\partial \tau_{zz}(\xi,z)}{\partial z} + F_z(\xi,z)\right)d\xi \tag{4.49}$$

Stress Tensor Initialization in rz-Coordinates

The stress tensor is initialized at the beginning of a simulation. We assume there are no shear stresses and normal stresses have z-direction dependence only. In addition, pore pressure is in hydrostatic equilibrium. Then, the static equilibrium equation for the normal z-direction stress is given by Equation 4.28 and the Mean Stress equation becomes:

$$\frac{3(1-\nu)}{1+\nu}\frac{\mathrm{d}^2}{\mathrm{d}z^2}\tau_m - \frac{2(1-2\nu)}{1+\nu}\frac{\mathrm{d}^2}{\mathrm{d}z^2}h(\bar{P},\bar{T}) + \frac{\mathrm{d}}{\mathrm{d}z}F_{b,z} = 0 \tag{4.50}$$

We substitute Equation 4.28 in Equation 5.40 to remove the body force term:

$$\frac{3(1-\nu)}{1+\nu}\frac{\mathrm{d}^2}{\mathrm{d}z^2}\tau_m - \frac{2(1-2\nu)}{1+\nu}\frac{\mathrm{d}^2}{\mathrm{d}z^2}h(\bar{P},\bar{T}) - \frac{\mathrm{d}^2}{\mathrm{d}z^2}\tau_{zz} = 0 \tag{4.51}$$

Equation 4.51 is integrated twice to yield:

$$\frac{3(1-\nu)}{1+\nu}\tau_m - \frac{2(1-2\nu)}{1+\nu}h(\bar{P},\bar{T}) - \tau_{zz} = F_1(z-z_0) + F_2 \tag{4.52}$$

The constant with subscript *2* is evaluated at the reference conditions and the constant with subscript *1* is evaluated from the condition that the ratio of vertical to mean stress change is given at the reference point:

$$\lim_{z\to z_0} \frac{\tau_{zz}-\tau_{zz,0}}{\tau_m-\tau_{m,0}} = R_{zm} \tag{4.53}$$

where R_{zm} is that ratio. This yields the following for the subscript *1* constant of integration:

$$F_1 = -\frac{3(1-\nu)}{1+\nu}\frac{F_{b,z}}{R_{zm}} + \frac{2(1-2\nu)}{1+\nu}\gamma + F_{b,z}\Big|_{z_0} \tag{4.54}$$

We use Equation 4.17 and Hooke's law to express the strain difference in the integrand of Equation 4.45 as:

$$\epsilon_v - \epsilon_{zz} = \frac{3(1-\nu)\left(\tau_m - h(\bar{P},\bar{T})\right) - (1+\nu)\left(\tau_{zz} - h(\bar{P},\bar{T})\right)}{3(1-2\nu)K} \tag{4.55}$$

The numerator of Equation 4.55 is equal to the left hand side of Equation 4.52 multiplied by $(1+\nu)$. Then:

$$\epsilon_v - \epsilon_{zz} = \frac{(1+\nu)F_1(z-z_0)+(1+\nu)F_2}{3(1-2\nu)K} \tag{4.56}$$

Substituting Equation 4.56 into 4.45 and integrating along constant z gives the initial displacement vector r-component:

$$u_r(r,z) = \frac{r}{2}\frac{(1+\nu)F_1(z-z_0)+(1+\nu)F_2}{3(1-2\nu)K} \tag{4.57}$$

Equations 4.46 and 4.47 give the initial normal radial and angular strains, respectively, which are equal and only depend on *z*:

$$\epsilon_{rr} = \epsilon_{\theta\theta} = \frac{(1+\nu)F_1(z-z_0)+(1+\nu)F_2}{6(1-2\nu)K} \tag{4.58}$$

Finite Difference Approximation to Coupled Fluid and Heat Flow and Geomechanical Equations in Cartesian Coordinates

Our simulator's mass, energy, and momentum conservation equations are discretized in space using the integral finite difference method (Narasimhan and Witherspoon, 1976). In this method, the simulation domain is subdivided into Cartesian grid blocks and the conservation equations (Equation 4.1 for fluid components and energy, Equations 4.18 and 4.22-4.27 for momentum) are integrated over grid block volume, V_n, with flux terms expressed as an integral over grid block surface, Γ_n, using the divergence theorem:

$$\frac{d}{dt}\int_{V_n} M^k dV = \int_{\Gamma_n} \bar{F}^k \cdot \hat{n} d\Gamma + \int_{V_n} q^k dV \tag{4.59}$$

Volume integrals are replaced with volume averages:

$$\int_{V_n} M^k dV = M_n^k V_n \tag{4.60}$$

and surface integrals with discrete sums over surface averaged segments:

$$\int_{\Gamma_n} \bar{F}^k \cdot \hat{n} d\Gamma = \sum_m A_{nm} \bar{F}_{nm}^k \tag{4.61}$$

where subscript *n* denotes an averaged quantity over volume V_n, A_{nm} is the area of a surface segment common to volumes V_n and V_m, and double subscript *nm* denotes an averaged quantity over area A_{nm}. The definitions of the geometric parameters used in this discretization are shown in Figure 4.1.

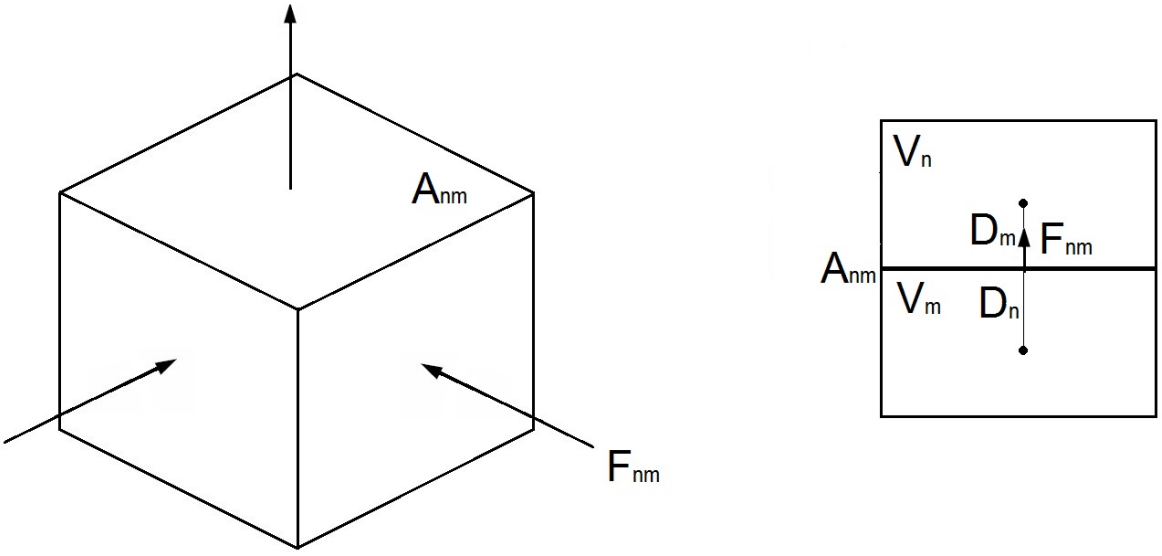

Figure 4.1. Parameter definitions for the integral finite difference method. The figure on the right shows two neighboring grid blocks and the interface between them.

Strictly speaking, the integrals in Equations 4.59-4.61 apply to control volumes with fixed geometry. Due to the addition of the geomechanical equations to our formulation, control volume geometry is no longer fixed. We introduce strain dependence into the volumes, areas, and distances that arise when the integrals in Equations 4.59-4.61 are evaluated and perform the integrations over the fixed unstrained Cartesian grid. The strain dependence terms are appended to the storage, flux, and generation terms in these equations. Volume depends on volumetric strain:

$$V_n = V_{n,0}(1 - \epsilon_v) \tag{4.62}$$

Direction *i* distance depends on normal strain:

$$d_i = d_{i,0}(1 - \epsilon_{ii}) \tag{4.63}$$

Direction *ij* area depends on normal strain in each direction:

$$A_{ij} = A_{ij,0}\left(1 - \epsilon_{ii} - \epsilon_{jj}\right) \tag{4.64}$$

where subscript 0 refers to an unstrained quantity.

The details of the finite difference approximation for the mass and energy conservation equations have been developed elsewhere (Pruess et al., 1999) and in this section, the finite difference approximation for the geomechanical equations is developed.

Our geomechanical formulation was derived for constant rock properties (Young's modulus and Poisson's ratio). However, geological formations consist of strata with differing rock properties. In such composite systems, properties and fluxes are continuous at the interfaces between strata and we apply that to derive finite difference approximations valid for rock properties varying in this manner. We obtain momentum fluxes for our geomechanical equations by "factoring" a divergence operator out of each equation. Then, the geomechanical equations (Equations 4.18 and 4.22-4.27) can be written as:

$$\nabla \cdot \bar{\psi}_k = 0 \tag{4.65}$$

where $\bar{\psi}_k$ is the momentum flux and subscript *k* refers to the specific geomechanical equation (*ms* for mean stress, *zz* for normal zz-stress, *xz* for xz-shear stress, etc.). The mean stress and normal and shear stress momentum fluxes are the following:

$$\bar{\psi}_{ms} = \frac{3(1-\upsilon)}{1+\upsilon}\nabla\tau_m + \bar{F}_b - \frac{2(1-2\upsilon)}{1+\upsilon}\nabla h(\bar{P},\bar{T}) \tag{4.66}$$

$$\bar{\psi}_{xx} = \left[\frac{2\upsilon-1}{1+\upsilon}\frac{\partial h(\bar{P},\bar{T})}{\partial x} + \frac{3}{1+\upsilon}\frac{\partial \tau_m}{\partial x} + 2F_{b,x}\right]\hat{\imath} + \nabla\left[\tau_{xx} - \frac{3}{1+\upsilon}\tau_m + \frac{2\upsilon-1}{1+\upsilon}h(\bar{P},\bar{T})\right] \tag{4.67}$$

$$\bar{\psi}_{yy} = \left[\frac{2\upsilon-1}{1+\upsilon}\frac{\partial h(\bar{P},\bar{T})}{\partial y} + \frac{3}{1+\upsilon}\frac{\partial \tau_m}{\partial y} + 2F_{b,y}\right]\hat{\jmath} + \nabla\left[\tau_{yy} - \frac{3}{1+\upsilon}\tau_m + \frac{2\upsilon-1}{1+\upsilon}h(\bar{P},\bar{T})\right] \tag{4.68}$$

$$\bar{\psi}_{zz} = \left[\frac{2\upsilon-1}{1+\upsilon}\frac{\partial h(\bar{P},\bar{T})}{\partial z} + \frac{3}{1+\upsilon}\frac{\partial \tau_m}{\partial z} + 2F_{b,z}\right]\hat{k} + \nabla\left[\tau_{zz} - \frac{3}{1+\upsilon}\tau_m + \frac{2\upsilon-1}{1+\upsilon}h(\bar{P},\bar{T})\right] \tag{4.69}$$

$$\bar{\psi}_{xy} = \left[\frac{\partial h(\bar{P},\bar{T})}{\partial y} + \frac{3}{2(1+\upsilon)}\frac{\partial\left(\tau_m - h(\bar{P},\bar{T})\right)}{\partial y} + F_{b,y}\right]\hat{\imath} + \left[\frac{\partial h(\bar{P},\bar{T})}{\partial x} + \frac{3}{2(1+\upsilon)}\frac{\partial\left(\tau_m - h(\bar{P},\bar{T})\right)}{\partial x} + F_{b,x}\right]\hat{\jmath} + \nabla\tau_{xy} \tag{4.70}$$

$$\bar{\psi}_{xz} = \left[\frac{\partial h(\bar{P},\bar{T})}{\partial z} + \frac{3}{2(1+\upsilon)}\frac{\partial\left(\tau_m - h(\bar{P},\bar{T})\right)}{\partial z} + F_{b,z}\right]\hat{\imath} + \left[\frac{\partial h(\bar{P},\bar{T})}{\partial x} + \frac{3}{2(1+\upsilon)}\frac{\partial\left(\tau_m - h(\bar{P},\bar{T})\right)}{\partial x} + F_{b,x}\right]\hat{k} + \nabla\tau_{xz} \tag{4.71}$$

$$\bar{\psi}_{yz} = \left[\frac{\partial h(\bar{P},\bar{T})}{\partial z} + \frac{3}{2(1+\upsilon)}\frac{\partial\left(\tau_m - h(\bar{P},\bar{T})\right)}{\partial z} + F_{b,z}\right]\hat{\jmath} + \left[\frac{\partial h(\bar{P},\bar{T})}{\partial y} + \frac{3}{2(1+\upsilon)}\frac{\partial\left(\tau_m - h(\bar{P},\bar{T})\right)}{\partial y} + F_{b,y}\right]\hat{k} + \nabla\tau_{yz} \tag{4.72}$$

The finite difference approximations for momentum conservation are obtained by integrating the momentum flux over grid block volume, V_n, with those terms expressed as an integral over grid block surface, Γ_n, using the divergence theorem, and approximating the surface integrals as discrete sums over surface averaged segments from Equation 4.61:

$$\sum_m A_{nm}\bar{\psi}_k \cdot \hat{n} = 0 \tag{4.73}$$

Consider two adjacent grid blocks, whose nodes are denoted by *n* and *m* and with different rock properties, shown in Figure 4.2. The interface common to the grid blocks is denoted by **int** and a

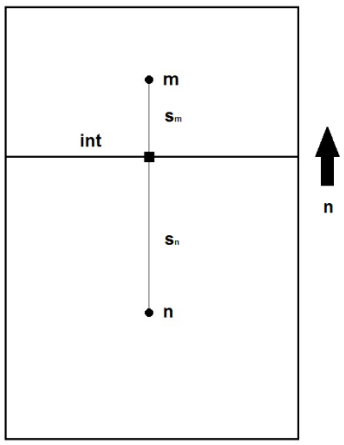

Figure 4.2. Two adjacent grid blocks, *n* and *m*, with interface, **int**, distances, **s**, and normal, **n**.

node is located there, **s** refers to the distance between the grid block node and the interface node, and **n** denotes the direction of the normal vector at the interface. We associate primary variables (pressures, temperatures, and stresses) and rock properties with the *n* and *m* nodes and only primary variables with the interface node. We obtain two sets of finite difference approximations for the momentum fluxes at the interface, one calculated using properties and primary variables at the *m* node and primary variables at the interface node, and the other using properties and primary variables at the *n* node and primary variables at the interface node. These fluxes are equal:

$$\bar{\psi}_k \cdot \hat{n} = \bar{\psi}_{k,n} \cdot \hat{n} = \bar{\psi}_{k,m} \cdot \hat{n} \tag{4.74}$$

The two equal expressions for the mean stress flux are the following:

$$\bar{\psi}_{ms,m} \cdot \hat{n} = \frac{3(1-\upsilon_m)}{1+\upsilon_m}\frac{\tau_{m,m} - \tau_{m,int}}{s_m} + \bar{F}_{b,m} \cdot \hat{n} - \frac{2(1-2\upsilon_m)}{1+\upsilon_m}\frac{h(\bar{P},\bar{T})_m - h(\bar{P},\bar{T})_{m,int}}{s_m} \tag{4.75}$$

$$\bar{\psi}_{ms,n} \cdot \hat{n} = \frac{3(1-\upsilon_n)}{1+\upsilon_n} \frac{\tau_{m,int} - \tau_{m,n}}{s_n} + \bar{F}_{b,n} \cdot \hat{n} - \frac{2(1-2\upsilon_n)}{1+\upsilon_n} \frac{h(\bar{P},\bar{T})_{n,int} - h(\bar{P},\bar{T})_n}{s_n} \tag{4.76}$$

In Equation 4.75, the gradient terms are approximated as the value at the grid block node minus the value at the interface node divided by the distance between them; in Equation 4.76, the gradient terms are approximated as the value at the interface node minus the value at the grid block node divided by the distance between them. The body force terms are evaluated at the specified node. The function $h(\bar{P},\bar{T})$ with a single subscript is evaluated using the primary variables and rock properties of the node denoted by the subscript; the function $h(\bar{P},\bar{T})$ with a subscript followed by *int* is evaluated using the primary variables at the interface node and rock properties of the node denoted by the subscript. We eliminate $\tau_{m,int}$ from Equations 4.75 and 4.76 and solve for the mean stress flux:

$$\bar{\psi}_{ms} \cdot \hat{n} = \frac{\tau_{m,m} - \tau_{m,n} + \frac{(1+\upsilon_m)s_m}{3(1-\upsilon_m)} \bar{F}_{b,m} \cdot \hat{n} + \frac{(1+\upsilon_n)s_n}{3(1-\upsilon_n)} \bar{F}_{b,n} \cdot \hat{n} - \frac{2(1-2\upsilon_m)}{3(1-\upsilon_m)} \left(h(\bar{P},\bar{T})_m - h(\bar{P},\bar{T})_{m,int}\right) - \frac{2(1-2\upsilon_n)}{3(1-\upsilon_n)} \left(h(\bar{P},\bar{T})_{n,int} - h(\bar{P},\bar{T})_n\right)}{\frac{(1+\upsilon_m)s_m}{3(1-\upsilon_m)} + \frac{(1+\upsilon_n)s_n}{3(1-\upsilon_n)}} \tag{4.77}$$

Then, $\tau_{m,int}$ is obtained from Equation 4.75 (or 4.76):

$$\tau_{m,int} = \tau_{m,m} + \frac{(1+\upsilon_m)s_m}{3(1-\upsilon_m)} \left(\bar{F}_{b,m} \cdot \hat{n} - \frac{2(1-2\upsilon_m)}{(1+\upsilon_m)s_m} \left(h(\bar{P},\bar{T})_m - h(\bar{P},\bar{T})_{m,int}\right) - \bar{\psi}_{ms} \cdot \hat{n} \right) \tag{4.78}$$

The two equal expressions for the xx-normal stress flux are the following:

$$\bar{\psi}_{xx,m} \cdot \hat{n} = \frac{1}{2} \frac{\tau_{xx,m} - \tau_{xx,int}}{s_m} + \frac{3(\hat{\imath} \cdot \hat{n} - \upsilon_m)}{2(1+\upsilon_m)} \frac{\tau_{m,m} - \tau_{m,int}}{s_m} + F_{b,x,m} \hat{\imath} \cdot \hat{n} + \frac{(2\upsilon_m - 1)(1+\hat{\imath} \cdot \hat{n})}{2(1+\upsilon_m)} \frac{h(\bar{P},\bar{T})_m - h(\bar{P},\bar{T})_{m,int}}{s_m} \tag{4.79}$$

$$\bar{\psi}_{xx,n} \cdot \hat{n} = \frac{1}{2} \frac{\tau_{xx,int} - \tau_{xx,n}}{s_n} + \frac{3(\hat{\imath} \cdot \hat{n} - \upsilon_n)}{2(1+\upsilon_n)} \frac{\tau_{m,int} - \tau_{m,n}}{s_n} + F_{b,x,n} \hat{\imath} \cdot \hat{n} + \frac{(2\upsilon_n - 1)(1+\hat{\imath} \cdot \hat{n})}{2(1+\upsilon_n)} \frac{h(\bar{P},\bar{T})_{n,int} - h(\bar{P},\bar{T})_n}{s_n} \tag{4.80}$$

We use the same type of approximations for gradient, body force terms, and the function $h(\bar{P},\bar{T})$ as for the mean stress flux. In Cartesian coordinates, the approximation for the x-derivative would be the same as the approximation for the gradient if the normal vector points in the x-direction, and the approximation for the x-derivative would be zero if the normal vector points in another direction. We eliminate $\tau_{xx,int}$ from Equations 4.79 and 4.80 and solve for the xx-normal stress flux:

$$\bar{\psi}_{xx} \cdot \hat{n} = \frac{\begin{array}{c} \tau_{xx,m} - \tau_{xx,n} + \frac{3(\hat{\imath} \cdot \hat{n} - \upsilon_m)}{(1+\upsilon_m)} \left(\tau_{m,m} - \tau_{m,int}\right) + \frac{3(\hat{\imath} \cdot \hat{n} - \upsilon_n)}{(1+\upsilon_n)} \left(\tau_{m,int} - \tau_{m,n}\right) + \\ \frac{(2\upsilon_m - 1)(1+\hat{\imath} \cdot \hat{n})}{(1+\upsilon_m)} \left(h(\bar{P},\bar{T})_m - h(\bar{P},\bar{T})_{m,int}\right) + \frac{(2\upsilon_n - 1)(1+\hat{\imath} \cdot \hat{n})}{(1+\upsilon_n)} \left(h(\bar{P},\bar{T})_{n,int} - h(\bar{P},\bar{T})_n\right) + 2s_m F_{b,x,m} \hat{\imath} \cdot \hat{n} + 2s_n F_{b,x,n} \hat{\imath} \cdot \hat{n} \end{array}}{2(s_m + s_n)} \tag{4.81}$$

Then, $\tau_{xx,int}$ is obtained from Equation 4.79 (or 4.80):

$$\tau_{xx,int} = \tau_{xx,m} + \frac{3(\hat{\imath}\cdot\hat{n}-\upsilon_m)}{(1+\upsilon_m)}\left(\tau_{m,m} - \tau_{m,int}\right) + 2s_m F_{b,x,m}\hat{\imath}\cdot\hat{n} + \frac{(2\upsilon_m-1)(1+\hat{\imath}\cdot\hat{n})}{(1+\upsilon_m)}\left(h(\bar{P},\bar{T})_m - h(\bar{P},\bar{T})_{m,int}\right) - 2s_m\bar{\psi}_{xx}\cdot\hat{n} \tag{4.82}$$

The two equal expressions for the yy-normal stress flux are the following:

$$\bar{\psi}_{yy,m}\cdot\hat{n} = \frac{1}{2}\frac{\tau_{yy,m}-\tau_{yy,int}}{s_m} + \frac{3(\hat{\jmath}\cdot\hat{n}-\upsilon_m)}{2(1+\upsilon_m)}\frac{\tau_{m,m}-\tau_{m,int}}{s_m} + F_{b,y,m}\hat{\jmath}\cdot\hat{n} + \frac{(2\upsilon_m-1)(1+\hat{\jmath}\cdot\hat{n})}{2(1+\upsilon_m)}\frac{h(\bar{P},\bar{T})_m - h(\bar{P},\bar{T})_{m,int}}{s_m} \tag{4.83}$$

$$\bar{\psi}_{yy,n}\cdot\hat{n} = \frac{1}{2}\frac{\tau_{yy,int}-\tau_{yy,n}}{s_n} + \frac{3(\hat{\jmath}\cdot\hat{n}-\upsilon_n)}{2(1+\upsilon_n)}\frac{\tau_{m,int}-\tau_{m,n}}{s_n} + F_{b,y,n}\hat{\jmath}\cdot\hat{n} + \frac{(2\upsilon_n-1)(1+\hat{\jmath}\cdot\hat{n})}{2(1+\upsilon_n)}\frac{h(\bar{P},\bar{T})_{n,int} - h(\bar{P},\bar{T})_n}{s_n} \tag{4.84}$$

We use the same type of approximations for gradient, body force terms, and the function $h(\bar{P},\bar{T})$ as for the mean stress flux. In Cartesian coordinates, the approximation for the y-derivative would be the same as the approximation for the gradient if the normal vector points in the y-direction, and the approximation for the y-derivative would be zero if the normal vector points in another direction. We eliminate $\tau_{yy,int}$ from Equations 4.83 and 4.84 and solve for the yy-normal stress flux:

$$\bar{\psi}_{yy}\cdot\hat{n} = \frac{\begin{array}{c}\tau_{yy,m}-\tau_{yy,n}+\frac{3(\hat{\jmath}\cdot\hat{n}-\upsilon_m)}{(1+\upsilon_m)}(\tau_{m,m}-\tau_{m,int})+\frac{3(\hat{\jmath}\cdot\hat{n}-\upsilon_n)}{(1+\upsilon_n)}(\tau_{m,int}-\tau_{m,n})+ \\ \frac{(2\upsilon_m-1)(1+\hat{\jmath}\cdot\hat{n})}{(1+\upsilon_m)}(h(\bar{P},\bar{T})_m-h(\bar{P},\bar{T})_{m,int})+\frac{(2\upsilon_n-1)(1+\hat{\jmath}\cdot\hat{n})}{(1+\upsilon_n)}(h(\bar{P},\bar{T})_{n,int}-h(\bar{P},\bar{T})_n)+2s_mF_{b,y,m}\hat{\jmath}\cdot\hat{n}+2s_nF_{b,y,n}\hat{\jmath}\cdot\hat{n}\end{array}}{2(s_m+s_n)} \tag{4.85}$$

Then, $\tau_{yy,int}$ is obtained from Equation 4.83 (or 4.84):

$$\tau_{yy,int} = \tau_{yy,m} + \frac{3(\hat{\jmath}\cdot\hat{n}-\upsilon_m)}{(1+\upsilon_m)}\left(\tau_{m,m} - \tau_{m,int}\right) + 2s_m F_{b,y,m}\hat{\jmath}\cdot\hat{n} + \frac{(2\upsilon_m-1)(1+\hat{\jmath}\cdot\hat{n})}{(1+\upsilon_m)}\left(h(\bar{P},\bar{T})_m - h(\bar{P},\bar{T})_{m,int}\right) - 2s_m\bar{\psi}_{yy}\cdot\hat{n} \tag{4.86}$$

The two equal expressions for the zz-normal stress flux are the following:

$$\bar{\psi}_{zz,m}\cdot\hat{n} = \frac{1}{2}\frac{\tau_{zz,m}-\tau_{zz,int}}{s_m} + \frac{3(\hat{k}\cdot\hat{n}-\upsilon_m)}{2(1+\upsilon_m)}\frac{\tau_{m,m}-\tau_{m,int}}{s_m} + F_{b,z,m}\hat{k}\cdot\hat{n} + \frac{(2\upsilon_m-1)(1+\hat{k}\cdot\hat{n})}{2(1+\upsilon_m)}\frac{h(\bar{P},\bar{T})_m - h(\bar{P},\bar{T})_{m,int}}{s_m} \tag{4.87}$$

$$\bar{\psi}_{zz,n}\cdot\hat{n} = \frac{1}{2}\frac{\tau_{zz,int}-\tau_{zz,n}}{s_n} + \frac{3(\hat{k}\cdot\hat{n}-\upsilon_n)}{2(1+\upsilon_n)}\frac{\tau_{m,int}-\tau_{m,n}}{s_n} + F_{b,k,n}\hat{k}\cdot\hat{n} + \frac{(2\upsilon_n-1)(1+\hat{k}\cdot\hat{n})}{2(1+\upsilon_n)}\frac{h(\bar{P},\bar{T})_{n,int} - h(\bar{P},\bar{T})_n}{s_n} \tag{4.88}$$

We use the same type of approximations for gradient, body force terms, and the function $h(\bar{P},\bar{T})$ as for the mean stress flux. In Cartesian coordinates, the approximation for the y-derivative would

be the same as the approximation for the gradient if the normal vector points in the z-direction, and the approximation for the z-derivative would be zero if the normal vector points in another direction. We eliminate $\tau_{zz,int}$ from Equations 4.87 and 4.88 and solve for the zz-normal stress flux:

$$\bar{\psi}_{zz}\cdot\hat{n}=\frac{\tau_{zz,m}-\tau_{zz,n}+\frac{3(\hat{k}\cdot\hat{n}-\upsilon_m)}{(1+\upsilon_m)}(\tau_{m,m}-\tau_{m,int})+\frac{3(\hat{k}\cdot\hat{n}-\upsilon_n)}{(1+\upsilon_n)}(\tau_{m,int}-\tau_{m,n})+\frac{(2\upsilon_m-1)(1+\hat{k}\cdot\hat{n})}{(1+\upsilon_m)}(h(\bar{P},\bar{T})_m-h(\bar{P},\bar{T})_{m,int})+\frac{(2\upsilon_n-1)(1+\hat{k}\cdot\hat{n})}{(1+\upsilon_n)}(h(\bar{P},\bar{T})_{n,int}-h(\bar{P},\bar{T})_n)+2s_mF_{b,z,m}\hat{k}\cdot\hat{n}+2s_nF_{b,z,n}\hat{k}\cdot\hat{n}}{2(s_m+s_n)} \tag{4.89}$$

Then, $\tau_{zz,int}$ is obtained from Equation 4.87 (or 4.88):

$$\tau_{zz,int}=\tau_{zz,m}+\frac{3(\hat{k}\cdot\hat{n}-\upsilon_m)}{(1+\upsilon_m)}\left(\tau_{m,m}-\tau_{m,int}\right)+2s_mF_{b,z,m}\hat{k}\cdot\hat{n}+\frac{(2\upsilon_m-1)(1+\hat{k}\cdot\hat{n})}{(1+\upsilon_m)}\left(h(\bar{P},\bar{T})_m-h(\bar{P},\bar{T})_{m,int}\right)-2s_m\bar{\psi}_{zz}\cdot\hat{n} \tag{4.90}$$

The two equal expressions for the xy-shear stress flux are the following:

$$\bar{\psi}_{xy,m}\cdot\hat{n}=\frac{\tau_{xy,m}-\tau_{xy,int}}{s_m}+\left[\frac{2\upsilon_m-1}{2(1+\upsilon_m)}\frac{\partial h(\bar{P},\bar{T})_m}{\partial y}+\frac{3}{2(1+\upsilon_m)}\frac{\partial\tau_{m,m}}{\partial y}+F_{b,y,m}\right]\hat{\imath}\cdot\hat{n}+\left[\frac{2\upsilon_m-1}{2(1+\upsilon_m)}\frac{\partial h(\bar{P},\bar{T})_m}{\partial x}+\frac{3}{2(1+\upsilon_m)}\frac{\partial\tau_{m,m}}{\partial x}+F_{b,x,m}\right]\hat{\jmath}\cdot\hat{n} \tag{4.91}$$

$$\bar{\psi}_{xy,n}\cdot\hat{n}=\frac{\tau_{xy,int}-\tau_{xy,n}}{s_n}+\left[\frac{2\upsilon_n-1}{2(1+\upsilon_n)}\frac{\partial h(\bar{P},\bar{T})_n}{\partial y}+\frac{3}{2(1+\upsilon_n)}\frac{\partial\tau_{m,n}}{\partial y}+F_{b,y,n}\right]\hat{\imath}\cdot\hat{n}+\left[\frac{2\upsilon_n-1}{2(1+\upsilon_n)}\frac{\partial h(\bar{P},\bar{T})_n}{\partial x}+\frac{3}{2(1+\upsilon_n)}\frac{\partial\tau_{m,n}}{\partial x}+F_{b,x,n}\right]\hat{\jmath}\cdot\hat{n} \tag{4.92}$$

We use the same type of approximation for gradient, body force terms, and the function $h(\bar{P},\bar{T})$ as for the mean stress flux. Approximations for the other derivatives are discussed below. We eliminate $\tau_{xy,int}$ from Equations 4.91 and 4.92 and solve for the xy-shear stress flux:

$$\bar{\psi}_{xy,m}\cdot\hat{n}=\frac{\tau_{xy,m}-\tau_{xy,n}+s_m\left[\frac{2\upsilon_m-1}{2(1+\upsilon_m)}\frac{\partial h(\bar{P},\bar{T})_m}{\partial y}+\frac{3}{2(1+\upsilon_m)}\frac{\partial\tau_{m,m}}{\partial y}+F_{b,y,m}\right]\hat{\imath}\cdot\hat{n}+s_m\left[\frac{2\upsilon_m-1}{2(1+\upsilon_m)}\frac{\partial h(\bar{P},\bar{T})_m}{\partial x}+\frac{3}{2(1+\upsilon_m)}\frac{\partial\tau_{m,m}}{\partial x}+F_{b,x,m}\right]\hat{\jmath}\cdot\hat{n}+s_n\left[\frac{2\upsilon_n-1}{2(1+\upsilon_n)}\frac{\partial h(\bar{P},\bar{T})_n}{\partial y}+\frac{3}{2(1+\upsilon_n)}\frac{\partial\tau_{m,n}}{\partial y}+F_{b,y,n}\right]\hat{\imath}\cdot\hat{n}+s_n\left[\frac{2\upsilon_n-1}{2(1+\upsilon_n)}\frac{\partial h(\bar{P},\bar{T})_n}{\partial x}+\frac{3}{2(1+\upsilon_n)}\frac{\partial\tau_{m,n}}{\partial x}+F_{b,x,n}\right]\hat{\jmath}\cdot\hat{n}}{s_m+s_n} \tag{4.93}$$

Then, $\tau_{xy,int}$ is obtained from Equation 4.91 (or 4.92):

$$\tau_{xy,int} = \tau_{xy,m} + s_m \left[\frac{2\upsilon_m - 1}{2(1+\upsilon_m)} \frac{\partial h(\bar{P},\bar{T})_m}{\partial y} + \frac{3}{2(1+\upsilon_m)} \frac{\partial \tau_{m,m}}{\partial y} + F_{b,y,m}\right] \hat{\imath} \cdot \hat{n} + s_m \left[\frac{2\upsilon_m - 1}{2(1+\upsilon_m)} \frac{\partial h(\bar{P},\bar{T})_m}{\partial x} + \frac{3}{2(1+\upsilon_m)} \frac{\partial \tau_{m,m}}{\partial x} + F_{b,x,m}\right] \hat{\jmath} \cdot \hat{n} - \bar{\psi}_{xy} \cdot \hat{n} \tag{4.94}$$

In Equations 4.91 and 4.92, the derivatives in the brackets are in a direction perpendicular to the unit vector just outside the bracket; for example, the first such bracket has y-direction derivatives with a unit vector in the x-direction just outside the bracket. These derivatives are evaluated as the difference between interfacial values on opposite grid block faces divided by the distance between them. Figure 4.3 shows a grid block with two opposite faces denoted by *A* and *B*. The

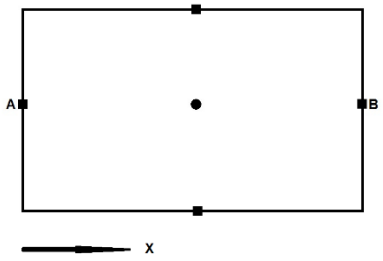

Figure 4.3. Grid block with interior node, square interfacial nodes, and two adjacent faces denoted by *A* and *B*. Direction along *A* and *B* is denoted as x-direction.

derivative of a function, *F*, associated with a grid block is approximated as the following:

$$\frac{\partial F}{\partial x} \approx \frac{F_B - F_A}{d_{AB}} \tag{4.95}$$

where d_{AB} is the distance between faces *A* and *B* in Figure 4.3.

The two equal expressions for the xz-shear stress flux are the following:

$$\bar{\psi}_{xz,m} \cdot \hat{n} = \frac{\tau_{xz,m} - \tau_{xz,int}}{s_m} + \left[\frac{2\upsilon_m - 1}{2(1+\upsilon_m)} \frac{\partial h(\bar{P},\bar{T})_m}{\partial z} + \frac{3}{2(1+\upsilon_m)} \frac{\partial \tau_{m,m}}{\partial z} + F_{b,z,m}\right] \hat{\imath} \cdot \hat{n} + \left[\frac{2\upsilon_m - 1}{2(1+\upsilon_m)} \frac{\partial h(\bar{P},\bar{T})_m}{\partial x} + \frac{3}{2(1+\upsilon_m)} \frac{\partial \tau_{m,m}}{\partial x} + F_{b,x,m}\right] \hat{k} \cdot \hat{n} \tag{4.96}$$

$$\bar{\psi}_{xz,n} \cdot \hat{n} = \frac{\tau_{xz,int} - \tau_{xz,n}}{s_n} + \left[\frac{2\upsilon_n - 1}{2(1+\upsilon_n)} \frac{\partial h(\bar{P},\bar{T})_n}{\partial z} + \frac{3}{2(1+\upsilon_n)} \frac{\partial \tau_{m,n}}{\partial z} + F_{b,z,n}\right] \hat{\imath} \cdot \hat{n} + \left[\frac{2\upsilon_n - 1}{2(1+\upsilon_n)} \frac{\partial h(\bar{P},\bar{T})_n}{\partial x} + \frac{3}{2(1+\upsilon_n)} \frac{\partial \tau_{m,n}}{\partial x} + F_{b,x,n}\right] \hat{k} \cdot \hat{n} \tag{4.97}$$

We use the same type of approximation for gradient, body force terms, and the function $h(\bar{P},\bar{T})$ as for the mean stress flux as well as the approximations for the other derivatives discussed above. We eliminate $\tau_{xz,int}$ from Equations 4.96 and 4.97 and solve for the xz-shear stress flux:

$$\bar{\psi}_{xz,m}\cdot\hat{n}=\frac{\tau_{xz,m}-\tau_{xz,n}+s_m\left[\frac{2\upsilon_m-1}{2(1+\upsilon_m)}\frac{\partial h(\bar{P},\bar{T})_m}{\partial z}+\frac{3}{2(1+\upsilon_m)}\frac{\partial \tau_{m,m}}{\partial z}+F_{b,z,m}\right]\hat{\imath}\cdot\hat{n}+s_m\left[\frac{2\upsilon_m-1}{2(1+\upsilon_m)}\frac{\partial h(\bar{P},\bar{T})_m}{\partial x}+\frac{3}{2(1+\upsilon_m)}\frac{\partial \tau_{m,m}}{\partial x}+F_{b,x,m}\right]\hat{k}\cdot\hat{n}+s_n\left[\frac{2\upsilon_n-1}{2(1+\upsilon_n)}\frac{\partial h(\bar{P},\bar{T})_n}{\partial z}+\frac{3}{2(1+\upsilon_n)}\frac{\partial \tau_{m,n}}{\partial z}+F_{b,z,n}\right]\hat{\imath}\cdot\hat{n}+s_n\left[\frac{2\upsilon_n-1}{2(1+\upsilon_n)}\frac{\partial h(\bar{P},\bar{T})_n}{\partial x}+\frac{3}{2(1+\upsilon_n)}\frac{\partial \tau_{m,n}}{\partial x}+F_{b,x,n}\right]\hat{k}\cdot\hat{n}}{s_m+s_n} \tag{4.98}$$

Then, $\tau_{xz,int}$ is obtained from Equation 4.96 (or 4.97):

$$\tau_{xz,int}=\tau_{xz,m}+s_m\left[\frac{2\upsilon_m-1}{2(1+\upsilon_m)}\frac{\partial h(\bar{P},\bar{T})_m}{\partial z}+\frac{3}{2(1+\upsilon_m)}\frac{\partial \tau_{m,m}}{\partial z}+F_{b,z,m}\right]\hat{\imath}\cdot\hat{n}+s_m\left[\frac{2\upsilon_m-1}{2(1+\upsilon_m)}\frac{\partial h(\bar{P},\bar{T})_m}{\partial x}+\frac{3}{2(1+\upsilon_m)}\frac{\partial \tau_{m,m}}{\partial x}+F_{b,x,m}\right]\hat{k}\cdot\hat{n}-\bar{\psi}_{xz}\cdot\hat{n} \tag{4.99}$$

The two equal expressions for the yz-shear stress flux are the following:

$$\bar{\psi}_{yz,m}\cdot\hat{n}=\frac{\tau_{yz,m}-\tau_{yz,int}}{s_m}+\left[\frac{2\upsilon_m-1}{2(1+\upsilon_m)}\frac{\partial h(\bar{P},\bar{T})_m}{\partial z}+\frac{3}{2(1+\upsilon_m)}\frac{\partial \tau_{m,m}}{\partial z}+F_{b,z,m}\right]\hat{\jmath}\cdot\hat{n}+\left[\frac{2\upsilon_m-1}{2(1+\upsilon_m)}\frac{\partial h(\bar{P},\bar{T})_m}{\partial y}+\frac{3}{2(1+\upsilon_m)}\frac{\partial \tau_{m,m}}{\partial y}+F_{b,y,m}\right]\hat{k}\cdot\hat{n} \tag{4.100}$$

$$\bar{\psi}_{yz,n}\cdot\hat{n}=\frac{\tau_{yz,int}-\tau_{yz,n}}{s_n}+\left[\frac{2\upsilon_n-1}{2(1+\upsilon_n)}\frac{\partial h(\bar{P},\bar{T})_n}{\partial z}+\frac{3}{2(1+\upsilon_n)}\frac{\partial \tau_{m,n}}{\partial z}+F_{b,z,n}\right]\hat{\jmath}\cdot\hat{n}+\left[\frac{2\upsilon_n-1}{2(1+\upsilon_n)}\frac{\partial h(\bar{P},\bar{T})_n}{\partial y}+\frac{3}{2(1+\upsilon_n)}\frac{\partial \tau_{m,n}}{\partial y}+F_{b,y,n}\right]\hat{k}\cdot\hat{n} \tag{4.101}$$

We use the same type of approximation for gradient, body force terms, and the function $h(\bar{P},\bar{T})$ as for the mean stress flux as well as the approximations for the other derivatives discussed above. We eliminate $\tau_{yz,int}$ from Equations 4.100 and 4.101 and solve for the yz-shear stress flux:

$$\bar{\psi}_{yz,m}\cdot\hat{n}=\frac{\tau_{yz,m}-\tau_{yz,n}+s_m\left[\frac{2\upsilon_m-1}{2(1+\upsilon_m)}\frac{\partial h(\bar{P},\bar{T})_m}{\partial z}+\frac{3}{2(1+\upsilon_m)}\frac{\partial \tau_{m,m}}{\partial z}+F_{b,z,m}\right]\hat{\jmath}\cdot\hat{n}+s_m\left[\frac{2\upsilon_m-1}{2(1+\upsilon_m)}\frac{\partial h(\bar{P},\bar{T})_m}{\partial y}+\frac{3}{2(1+\upsilon_m)}\frac{\partial \tau_{m,m}}{\partial y}+F_{b,y,m}\right]\hat{k}\cdot\hat{n}+s_n\left[\frac{2\upsilon_n-1}{2(1+\upsilon_n)}\frac{\partial h(\bar{P},\bar{T})_n}{\partial z}+\frac{3}{2(1+\upsilon_n)}\frac{\partial \tau_{m,n}}{\partial z}+F_{b,z,n}\right]\hat{\jmath}\cdot\hat{n}+s_n\left[\frac{2\upsilon_n-1}{2(1+\upsilon_n)}\frac{\partial h(\bar{P},\bar{T})_n}{\partial y}+\frac{3}{2(1+\upsilon_n)}\frac{\partial \tau_{m,n}}{\partial y}+F_{b,y,n}\right]\hat{k}\cdot\hat{n}}{s_m+s_n} \tag{4.102}$$

Then, $\tau_{yz,int}$ is obtained from Equation 4.100 (or 4.101):

$$\tau_{yz,int}=\tau_{yz,m}+s_m\left[\frac{2\upsilon_m-1}{2(1+\upsilon_m)}\frac{\partial h(\bar{P},\bar{T})_m}{\partial z}+\frac{3}{2(1+\upsilon_m)}\frac{\partial \tau_{m,m}}{\partial z}+F_{b,z,m}\right]\hat{\jmath}\cdot\hat{n}+s_m\left[\frac{2\upsilon_m-1}{2(1+\upsilon_m)}\frac{\partial h(\bar{P},\bar{T})_m}{\partial y}+\frac{3}{2(1+\upsilon_m)}\frac{\partial \tau_{m,m}}{\partial y}+F_{b,y,m}\right]\hat{k}\cdot\hat{n}-\bar{\psi}_{yz}\cdot\hat{n} \tag{4.103}$$

The finite difference method employed here for the geomechanical equations yields an integral of

those momentum fluxes over the grid block surface that is approximated as a discrete sum over surface averaged segments. Grid block surface segments are common to another grid block or border the surroundings. For the latter grid blocks, we conceptualize the surroundings as consisting of grid blocks that are reflections of the ones that contain these surface segments and we assume the surroundings are at the grid block's initial state.

Finite Difference Approximation to Coupled Fluid and Heat Flow and Geomechanical Equations in rz-Coordinates

The finite difference approximations for the fluid and heat flow, mean stress, and the stress tensor normal zz-component equations in rz-coordinates mirror those in Cartesian coordinates. The integral for displacement vector r-component (Equation 4.44) is approximated by a summation:

$$u_r(j) = \frac{1}{r_j}\sum_i \xi_i\left(\epsilon_{v,i} - \epsilon_{zz,i}\right)\Delta\xi_i \tag{4.104}$$

where subscript *i* is over a row of grid blocks up to the grid block denoted by subscript *j*. The θθ-normal strain is obtained from:

$$\epsilon_{\theta\theta}(j) = \frac{u_r(j)}{r_j} \tag{4.105}$$

The rr-normal strain is then obtained from the definition of volumetric strain:

$$\epsilon_{rr} = \epsilon_v - \epsilon_{\theta\theta} - \epsilon_{zz} \tag{4.106}$$

The integral for rz-shear stress (Equation 4.49) is also approximated by a summation:

$$\tau_{rz}(j) = -\frac{1}{r_j}\sum_i \xi_i \left(\frac{\partial \tau_{zz}(i)}{\partial z} + F_z(i)\right)\Delta\xi_i \tag{4.107}$$

The zz-normal stress z-derivative in the integrand of Equation 4.107 is approximated using Equation 4.95.

Conservation Equation Solution in Cartesian Coordinates

Our simulator's governing equations consist of Equation 4.59 (fluid and heat flow), Equation 4.18 (mean stress), and Equations 4.22-4.27 (normal and shear stress components). Each governing equation has a primary variable associated with it, and this is summarized in Table 4.1. Because mean stress is a primary variable only two out of the three normal stress components need to be solved for.

Table 4.1. Cartesian coordinate equations and associated primary variables for *N* mass components.

Equation	**Associated Primary Variables**
Conservation of mass	Pressure, *N*-1 mass fractions
Conservation of energy	Temperature
Mean stress	Mean stress
Normal stresses	xx, yy, zz normal stresses
Shear stresses	xy, yz, xz shear stresses

This set of equations is nonlinear and is expressed in residual form as:

$$\bar{R}\left(\bar{x}^{j+1}\right) = 0 \tag{4.108}$$

where $\bar{x}^{j+1}$ is the primary variable vector at time level *j+1*. Equation 4.108 is solved by the Newton-Raphson method. The Newton-Raphson method is an iterative procedure used to solve systems of non-linear equations. Denoting iteration number by subscript *p*, the following system of equations result from applying the Newton-Raphson method to Equation 4.108:

$$\bar{\bar{J}}\left(\bar{x}_p^{j+1}\right)\left(\bar{x}_p^{j+1} - \bar{x}_p^{j}\right) = -\bar{R}\left(\bar{x}_p^{j+1}\right) \tag{4.109}$$

where the Jacobian matrix, $\bar{\bar{J}}\left(\bar{x}_p^{j+1}\right)$, is defined as:

$$\left[\bar{\bar{J}}\left(\bar{x}_p^{j+1}\right)\right]_{ij} = \frac{\partial R_i\left(\bar{x}_p^{j+1}\right)}{\partial x_j} \tag{4.110}$$

Elements of the Jacobian matrix are approximated by numerical differentiation:

$$\frac{\partial R_i\left(\bar{x}_p^{j+1}\right)}{\partial x_j} \approx \frac{R_i\left(x_j+\delta_j, \bar{x}_p^{j+1}(\forall i \neq j)\right) - R_i\left(\bar{x}_p^{j+1}\right)}{\delta_j} \tag{4.111}$$

where δ_j is the increment for primary variable x_j. The iteration is converged when all residuals are less than a prescribed tolerance:

$$R_i\left(\bar{x}_p^{j+1}\right) \leq \delta_{tol} \tag{4.112}$$

where δ_{tol} is a vector of tolerances.

The Newton-Raphson method is applied to these governing equations in a sequential manner. First, conservation of mass, energy, and the Mean Stress equation are solved. Solution of these equations yields pressure, mass fractions, temperature, and mean stress. The Jacobian sub-matrix size for this step in the solution is two plus the number of mass components. Normal and shear stresses are

solved for next. Equations 4.22-4.27 consist of the Laplacian of the stress tensor component plus terms that appear in the Mean Stress equation. Because of this, the Jacobian sub-matrix size for each of these equations is one and their residual functions are linear, which results in Newton-Raphson convergence in one iteration. Figure 4.4 shows a flow chart for this solution sequence.

Our simulator is massively parallel, with domain partitioning using the METIS and ParMETIS packages (Karypsis and Kumar, 1998; Karypsis and Kumar, 1999). Each processor computes Jacobian matrix elements for its own grid blocks, and exchange of information between processors uses MPI (Message Passing Interface) and allows calculation of Jacobian matrix elements associated with inter-block connections across domain partition boundaries. The Jacobian matrix is solved in parallel using an iterative linear solver from the Aztec package (Tuminaro *et al.,* 1999).

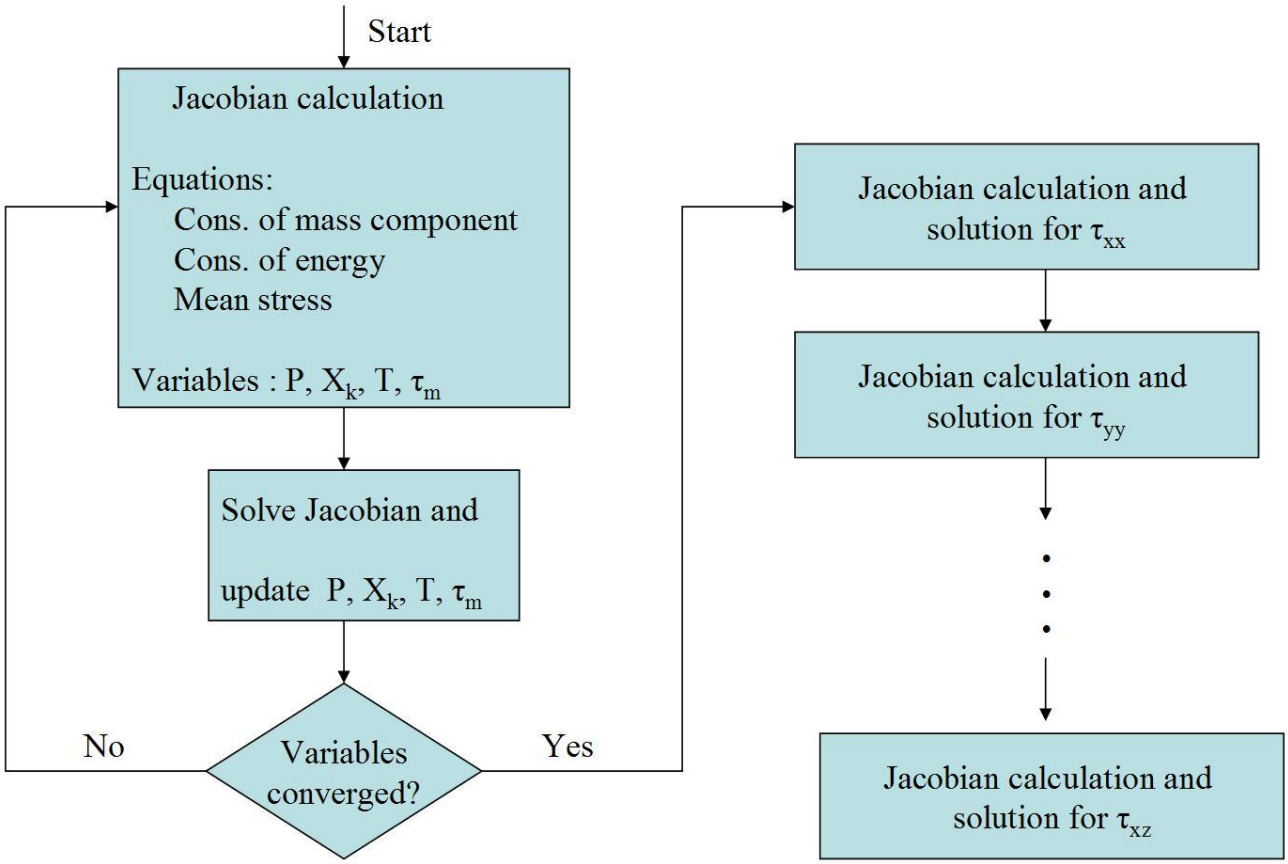

Figure 4.4. Flow chart for solution of simulator governing equations in Cartesian coordinates.

Conservation Equation Solution in rz-Coordinates

The governing equations and associated primary variables for rz-coordinates are summarized in Table 4.2.

Table 4.2. rz-Coordinate equations and associated primary variables for *N* mass components.

Equation	Associated Primary Variables
Conservation of mass	Pressure, *N*-1 mass fractions
Conservation of energy	Temperature
Mean stress	Mean stress
Normal stresses	rr, θθ, zz normal stresses
Shear stress	rz shear stress

This set of equations is also nonlinear and is solved by the Newton-Raphson method. First, conservation of mass, energy, and the Mean Stress equation are solved. Solution of these equations yields pressure, mass fractions, temperature, and mean stress. The Jacobian sub-matrix size for this step in the solution is two plus the number of mass components. The zz-normal stress is solved for next, with Jacobian sub-matrix size of one. Next, the r-component of the displacement vector is calculated, which yields the rr- and θθ-stresses. Finally, the rz-shear stress is calculated. Figure 4.5 shows a flow chart for this solution sequence.

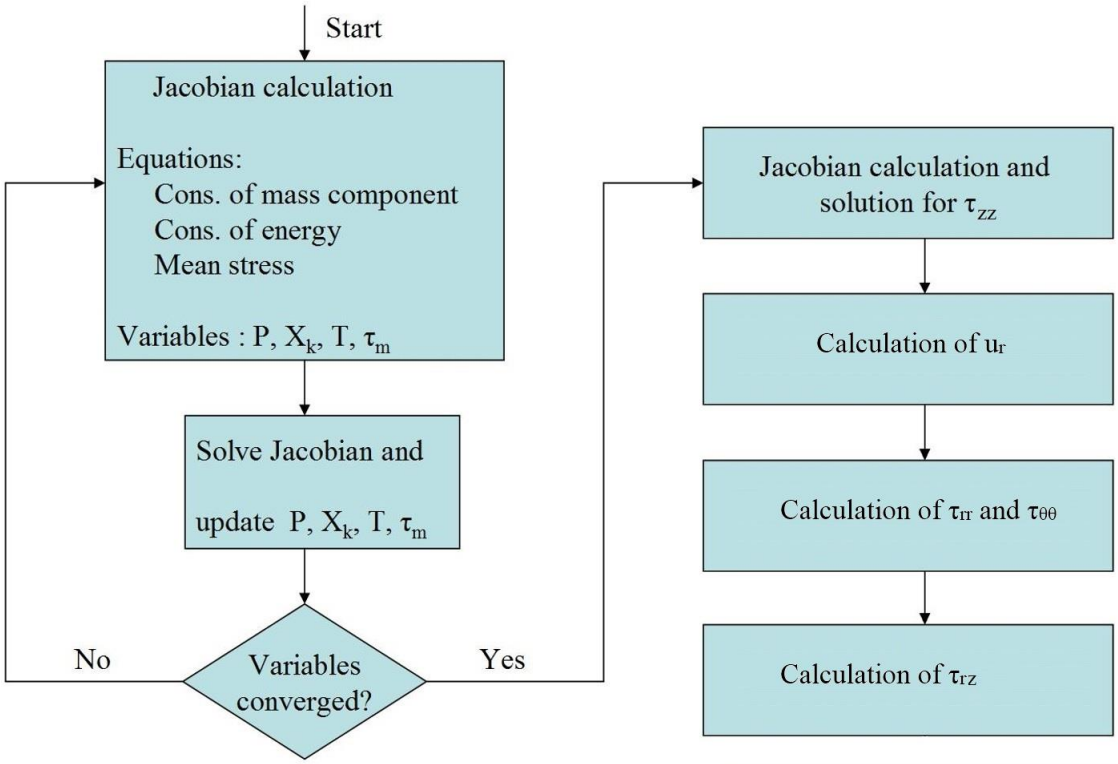

Figure 4.5. Flow chart for solution of simulator governing equations in rz-coordinates.

Task 5.0: Incorporation of CO_2 injection-enhanced property and fracture correlations/models into reservoir simulators

Determination of constitutive correlations for fracture initiation, and growth and propagation

We did a literature survey to determine suitable correlations for fracture initiation, growth, and propagation. Some of the papers that contained significant information about addressing that are outlined below.

Rinaldi et al. (2014) discussed the geomechanical modeling of fault responses during carbon dioxide injection, and focused on the integrity of the sealing caprock. The fault zone reactivation was simulated using a Mohr–Coulomb criterion for failure. When the strain on the fault zone is greater than a critical value, the fault will rupture and allow flow through it. Fault permeability depended on geomechanics (stress or strain) and they simulated leakage through a fault zone as a permeability change during fault reactivation. This work was done using the TOUGH-FLAC simulator.

Pan et al. (2013) simulated coupled multiphase fluid flow and hydraulic fracturing during deep underground CO_2 injection. Fluid flow was modeled using the TOUGH2 simulator and hydraulic fracturing was modeled using the rock-discontinuous-cellular-automaton (RDCA) method. In this method, fractures are modeled explicitly as discrete cracks or fractures having two rough surfaces, with fluid-filled voids. Fluids can flow along the fractures and their aperture depends on effective stress within the fracture. The fracture tip is represented by mathematical shape functions to model the high-gradient stress field there. There are two criteria for fracturing, one based on toughness and another based on the Mohr–Coulomb model. The toughness-based one includes mixed Mode I (extension) and Mode II (shear) fracture propagation, and the Mohr–Coulomb one is modified to enable both shear and tensile failure.

Cappa et al. (2011) discussed the coupling between mechanical deformation and fluid flow in fault zones and described modeling approaches for this. Faults were represented by zero-thickness mechanical interfaces, by an equivalent continuum using solid elements, and by a combination of solid elements and ubiquitous-joints oriented as weak planes. Fluid pressures required for fault reactivation was derived from the effective stress law and the Coulomb failure criterion.

Vilarassa et al. (2010) studied the reactivation of fractures and the creation of new ones in the caprock seal of a saline aquifer undergoing CO_2 injection. Failure consists of two types, shear failure and hydraulic fracturing. The latter would occur when fluid pressure exceeds the least compressive principal stress, a conservative assumption that allows for a safety factor; the former would occur, for a random fracture random orientation when the deviatoric stress invariant exceeds a yield function.

Kim and Hosseini (2014) proposed equations that incorporate pore-pressure/stress coupling and thermal stress effects to calculate the maximum pressure limit before reactivation of preexisting fractures for normal-, reverse-, and strike-slip faulting stress regimes. The basis for these equations

is the Mohr-Coulomb failure criterion plus expressions for the horizontal and vertical stresses.

Martinez et al. (2013) introduce a joint model to describe reactivation of caprock fractures during injection of CO_2. Their model assumes equally spaced anisotropic joint sets with non-linear normal stiffness and linear shear stiffness. Normal displacement of the joints is mapped into a dynamically evolving effective anisotropic permeability tensor, and assumes a cubic law for fracture permeability as a function of joint aperture.

Karimnezhad et al. (2013) developed a three-dimensional geomechanical finite element model to investigate the effects of CO_2 injection on the caprock and to estimate the risk of caprock failure. Their criteria were Mohr-Coulomb for shear failure and zero minimum effective principal stress for tensile failure.

Lei et al. (2015) incorporated a mechanical module based on the extended Biot consolidation model into the thermal–hydrodynamic simulator TOUGH2, resulting in a THM simulation program called TOUGH2Biot.A finite element method was employed to discretize space for rock mechanical calculation and the Mohr-Coulomb failure criterion was used as the rock shear-slip failure criterion.

Sayedi et al. (2009) developed a numerical tool to model caprock damage and fault reactivation due to a rise in reservoir pressure. Shear failure was modeled using the Coulomb criterion and vertical and horizontal cracking occurred when the respective effective stresses were zero. Flow in the fracture was modeled by jointed elements and was dependent on fracture aperture size.

Garipov et al. (2014) present a fully implicit method for coupled fluid flow and geomechanical deformation in fractured porous media. They consider the relationships between fracture aperture and normal stress, and fracture aperture and permeability. These relationships are critical in modeling flow in induced and naturally occurring fractures.

Rutqvist et al. (2007) couple fluid flow and geomechanical fault slip (fault reactivation) analysis to estimate the maximum sustainable injection pressure during geological sequestration of CO_2. Two approaches for shear-slip analysis were used in their coupled calculations, a continuum one and a discrete one. In their continuum analysis the potential for shear slip was evaluated by studying the time evolution of the in situ stresses and assessing the potential for shear slip using a failure criterion. In the case of discrete fault analysis, both the extent and magnitude of shear slip was calculated using special fault mechanical elements. Both of these approaches will be considered in developing our fault reactivation model.

Goodarzi et al. (2012) developed a geomechanical assessment model of CO_2 injection which couples the flow and geomechanical models, and incorporates dynamic injection-induced fracture growth. This type of fracture growth model is in contrast to another common approach, which is to use stress-dependent permeability for modeling fractures.

LBNL has also conducted literature review and selected the approach that will be used and implemented into TOUGH-FLAC for the analysis of fracture initiation and propagation. A pragmatic approach involving a cohesive crack model for fracture propagation will be

implemented using the existing FLAC3D strain-hardening-softening ubiquitous joint model or alternative FLAC3D interfaces that are characterized by Coulomb sliding and/or tensile bonding.

Modification of TOUGH2-CSM to model stress-dependent fracture initiation, and growth and propagation

We selected the Mohr-Coulomb criterion as one of our models for the determination of shear failure in faults and in caprock. This criterion specifies a linear failure envelope that depends on the effective normal and shear stresses acting on a plane in the material. Failure would occur when the following is satisfied:

$$\tau \geq \mu\sigma' + C_0 \tag{5.1}$$

where τ is the shear stress acting on a plane in the material, σ' is the effective normal stress acting on that plane, μ is the coefficient of friction, and C_0 is called the cohesion.

The effective normal and shear stresses in Equation 5.1 are calculated from the effective stress tensor. For materials whose plane of weakness can have any orientation, such as caprock, we derive the additional equations to implement this rock failure mode.

We select our coordinate system to be aligned with the principal effective stresses. Then, the effective stress tensor is:

$$\bar{\bar{\sigma}}' = \sigma'_{xx}\hat{\imath}\hat{\imath} + \sigma'_{yy}\hat{\jmath}\hat{\jmath} + \sigma'_{zz}\hat{k}\hat{k} \tag{5.2}$$

The normal vector to an arbitrary plane of weakness is:

$$\hat{n} = n_x\hat{\imath} + n_y\hat{\jmath} + n_z\hat{k} \tag{5.3}$$

The effective traction on the weakness plane face is the dot product of its normal vector with the effective stress tensor:

$$\bar{\bar{\sigma}}' \cdot \hat{n} = n_x\sigma'_{xx}\hat{\imath} + n_y\sigma'_{yy}\hat{\jmath} + n_z\sigma'_{zz}\hat{k} \tag{5.4}$$

This effective traction vector has a normal component, whose magnitude is:

$$\sigma' = (\bar{\bar{\sigma}}' \cdot \hat{n}) \cdot \hat{n} = n_x^2\sigma'_{xx} + n_y^2\sigma'_{yy} + n_z^2\sigma'_{zz} \tag{5.5}$$

The shear component is obtained by subtracting the normal component from the effective traction, and the magnitude of the shear component is:

$$\tau = |\bar{\bar{\sigma}}' \cdot \hat{n} - [(\bar{\bar{\sigma}}' \cdot \hat{n}) \cdot \hat{n}]\hat{n}| = (\sigma'_{xx} - \sigma'_{zz})^2 n_x^2 + \left(\sigma'_{yy} - \sigma'_{zz}\right)^2 n_y^2 - \Big((\sigma'_{xx} - \sigma'_{zz})n_x^2 + \left(\sigma'_{yy} - \sigma'_{zz}\right)n_y^2\Big)^2 \tag{5.6}$$

Let the x-direction be that of maximum principal effective stress, the z-direction be that of minimum principal effective stress, and consider the plane determined by those two directions, in which there is no dependence on the normal yy-component effective stress. Equations 5.5 and 5.6 are combined to yield a relation between effective normal and shear stress for that plane:

$$\tau^2 + \left(\sigma - \frac{\sigma'_{xx}+\sigma'_{zz}}{2}\right)^2 = \frac{\left(\sigma'_{xx}-\sigma'_{zz}\right)^2}{4} \tag{5.7}$$

Equation 5.7 is that for a circle, called the Mohr circle, whose center is the average of the maximum and minimum principal effective stresses (at zero shear stress) and whose radius is the difference between those effective stresses. Failure occurs when the Mohr-Coulomb failure line (Equation 5.1) is tangent to the Mohr circle, which occurs when:

$$C_0 = -\frac{\sigma'_{xx}+\sigma'_{zz}}{2}\mu + \frac{\sigma'_{xx}-\sigma'_{zz}}{2}\sqrt{1+\mu^2} \tag{5.8}$$

For a fault with a given orientation, the normal vector to the plane of weakness is given. The normal effective stress on that plane is calculated from the effective stress tensor and Equation 5.5, and the shear stress on that plane is calculated from the effective stress tensor and Equation 5.6. If that point lies above the Mohr-Coulomb envelope, the fault is said to have failed; if below, the fault is stable.

In general the coordinate system will not be aligned with the principal effective stresses. Consequently, we must calculate the principal effective stresses, which are the eigenvalues of the effective stress tensor. Denoting the effective stress tensor elements by a_{ij}, the eigenvalues satisfy:

$$det\begin{bmatrix} a_{11}-\lambda & a_{12} & a_{13} \\ a_{21} & a_{22}-\lambda & a_{23} \\ a_{31} & a_{32} & a_{33}-\lambda \end{bmatrix} = 0 \tag{5.9}$$

Equation 5.9 is a cubic equation in terms of the three effective stress tensor invariants, denoted by I_k, that satisfy:

$$-\lambda^3 + I_1\lambda^2 - I_2\,\lambda + I_3 = 0 \tag{5.10}$$

Equation 5.10 is solved analytically:

$$\lambda_k = \frac{I_1}{3} + 2\sqrt{-\frac{p}{3}}\cos\left(\frac{1}{3}\cos^{-1}\left(\frac{3q}{2p}\sqrt{-\frac{p}{3}}\right) - \frac{2\pi k}{3}\right); k = 0,1,2 \tag{5.11}$$

where:

$$p = \frac{3I_2 - I_1^2}{3} \tag{5.12}$$

$$q = -\frac{2I_1^3 - 9I_1I_2 + 27I_3}{27} \tag{5.13}$$

The eigenvectors of the effective stress tensor are the principal directions, n_j, and are calculated from:

$$\begin{bmatrix} a_{11} - \lambda_k & a_{12} & a_{13} \\ a_{21} & a_{22} - \lambda_k & a_{23} \\ a_{31} & a_{32} & a_{33} - \lambda_k \end{bmatrix} \begin{bmatrix} n_x \\ n_y \\ n_z \end{bmatrix} = 0 \tag{5.14}$$

We also formulated a caprock fracturing model. Caprock is said to fracture when the minimum effective stress is negative or less than the tensile strength:

$$\sigma'_{min} < -\sigma_{tens} \tag{5.15}$$

When the Equation 5.15 inequality is satisfied, a single fracture is assumed to have been generated in the grid block. The normal to the fracture face is the minimum stress direction, given by:

$$\hat{n} = A\hat{\imath} + B\hat{\jmath} + C\hat{k} \tag{5.16}$$

We define a local Cartesian coordinate system starting with this normal. The other two directions ($\hat{l}$ and $\hat{m}$) are in the fracture plane, with one having no gravitational component (where gravity is in the k-direction) and the other perpendicular to these two:

$$\hat{l} = \frac{\hat{k} \times \hat{n}}{|\hat{k} \times \hat{n}|} = \frac{-B\hat{\imath} + A\hat{\jmath}}{\sqrt{A^2 + B^2}} \tag{5.17}$$

$$\hat{m} = \frac{\hat{l} \times \hat{n}}{|\hat{l} \times \hat{n}|} = \frac{AC\hat{\imath} + BC\hat{\jmath} - (A^2 + B^2)\hat{k}}{\sqrt{A^2 + B^2}} \tag{5.18}$$

The coordinate transformation from global to local coordinates is:

$$\begin{bmatrix} A & B & C \\ \frac{AC}{\sqrt{A^2+B^2}} & \frac{BC}{\sqrt{A^2+B^2}} & -\sqrt{A^2 + B^2} \\ \frac{-B}{\sqrt{A^2+B^2}} & \frac{A}{\sqrt{A^2+B^2}} & 0 \end{bmatrix} \begin{bmatrix} \hat{\imath} \\ \hat{\jmath} \\ \hat{k} \end{bmatrix} = \begin{bmatrix} \hat{n} \\ \hat{m} \\ \hat{l} \end{bmatrix} \tag{5.19}$$

The permeability of the fracture is isotropic:

$$k_{fr} = \frac{w^2}{12} \tag{5.20}$$

where *w* is the fracture width. The Darcy velocity in local coordinates, with flow only in the fracture plane (no n-direction component), is:

$$\bar{v} = \frac{k_{fr}}{\mu}\nabla \mathrm{P} = \frac{k_{fr}}{\mu}\left[(\nabla \mathrm{P} \cdot \hat{m})\hat{m} + (\nabla \mathrm{P} \cdot \hat{l})\hat{l}\right] \tag{5.21}$$

Transforming the pressure gradient from local to Cartesian coordinates using Equation 5.19 and only retaining the pressure gradient derivatives that are aligned with their unit vectors yields:

$$\bar{v} = \frac{k_{fr}}{\mu}\nabla \mathrm{P} = \frac{k_{fr}}{\mu}\left[(1-A^2)\frac{\partial \mathrm{P}}{\partial \mathrm{x}}\hat{\imath} + (1-B^2)\frac{\partial \mathrm{P}}{\partial \mathrm{y}}\hat{\jmath} + (1-C^2)\frac{\partial \mathrm{P}}{\partial \mathrm{z}}\hat{k}\right] \tag{5.22}$$

The isotropic fracture permeability is then transformed to Cartesian directional components as:

$$k_{f,x} = (1-A^2)k_{fr} \tag{5.23}$$

$$k_{f,y} = (1-B^2)k_{fr} \tag{5.24}$$

$$k_{f,z} = (1-C^2)k_{fr} \tag{5.25}$$

Grid block directional permeability is a weighted sum of fracture and rock permeability. For the x-direction, for example, flow is conceptualized to occur in parallel through the fracture and through the rock. The rock flow area is the area of the grid block face and the fracture flow area is the product of fracture width and the directional fracture height. This can be written as:

$$k_x = \frac{k_{m,x}A_{m,x}+k_{f,x}A_{f,x}}{A_{m,x}+A_{f,x}} \approx k_{m,x} + \frac{k_{f,x}A_{f,x}}{A_{m,x}} \tag{5.26}$$

where subscript m refers to the rock and fracture flow area is assumed to be much less than rock flow area. The area for fracture flow is the fracture width times the grid block height projected along the x-direction. The corresponding y- and z-direction permeabilities are:

$$k_y = \frac{k_{m,y}A_{m,y}+k_{f,y}A_{f,y}}{A_{m,y}+A_{f,y}} \approx k_{m,y} + \frac{k_{f,y}A_{f,y}}{A_{m,y}} \tag{5.27}$$

$$k_z = \frac{k_{m,z}A_{m,z}+k_{f,z}A_{f,z}}{A_{m,z}+A_{f,z}} \approx k_{m,z} + \frac{k_{f,z}A_{f,z}}{A_{m,z}} \tag{5.28}$$

The generation of a fracture also changes overall grid block porosity, which is the sum of fracture and rock pore volumes divided by the sum of fracture and rock bulk volumes. We assume fracture volume, the product of fracture width and fracture face area, is much less than rock volume:

$$\phi = \frac{\phi_m V_m + V_f}{V_m + V_f} \approx \phi_m + \frac{V_f}{V_m} \tag{5.29}$$

Fracture width is given by the following expression from Goodarzi et al. (2012):

$$w = \frac{4(1-\nu^2)h_f}{E}(P - \sigma_{min}) \quad (5.30)$$

Since fractures are primarily vertical, we assume fracture height, h_f, is the grid block z-direction height.

Fluid flow into a fracture causes the fracture front to propagate. Fracture front propagation is governed by the stress intensity factor at the fracture tip, given by:

$$K_I = \frac{G}{4(1-\nu)}\left(\frac{2\pi}{r}\right)^{\frac{1}{2}} w(r) \quad (5.31)$$

where r is the normal distance from the fracture front (Yew, 1992). The distance the fracture front propagates is given by the following (Mastrojannis et al., 1980):

$$d = d_{max}\left(\frac{K_I - K_{IC}}{K_{IC}}\right)^n \quad (5.32)$$

where K_{IC} is rock toughness, a physical property, and d_{max} and n are parameters.

Modification of TOUGH-FLAC to model stress-dependent fracture initiation, and growth and propagation

LBNL has selected an approach for modeling stress depend fracture permeability of fractured reservoirs, based on observations at the In Salah CO_2 storage project, where permeability enhancement within the fractured sandstone reservoir was observed. The model is based on the FLAC3D ubiquitous joint model, extended for the modeling of permeability changes induced by changes in effective normal stress across fracture as well permeability changes caused by shearing along fractures.

Task 6.0: Concept and flow-mechanics coupled model validation, including using field data of stress and rock deformation measurement

TOUGH2-CSM Model

We provide problems for verification of our stress tensor component calculation techniques for Cartesian and rz-coordinates. These problems are matches of analytical solutions, those obtained from the literature, or simulations of experiments conducted in Task 3.

Displacement from uniform load on semi-infinite elastic medium

Given a semi-infinite elastic medium, the displacement caused by a uniform load acting on its surface over a circular area of radius *a* is given by Timoshenko and Goodier (1951) as:

$$w(r) = \begin{matrix} \frac{4(1-\nu^2)pr}{\pi E}\left[\int_0^{\frac{\pi}{2}}\sqrt{1-\frac{r^2}{a^2}sin^2\theta}d\theta\right], r < a \\ \frac{4(1-\nu^2)pr}{\pi E}\left[\int_0^{\frac{\pi}{2}}\sqrt{1-\frac{a^2}{r^2}sin^2\theta}d\theta - \left(1-\frac{a^2}{r^2}\right)\int_0^{\frac{\pi}{2}}\frac{d\theta}{\sqrt{1-\frac{a^2}{r^2}sin^2\theta}}\right], r > a \end{matrix} \quad (6.1)$$

where *p* is the load, *w(r)* is displacement at a radius *r* from the center of the circle, and the integrals in the brackets are elliptic integrals of the first and second kind. The normal z-direction stress along the z-axis at the center of the circle is:

$$\tau_{zz} = p\left[-1+\frac{z^3}{(a^2+z^2)^{\frac{3}{2}}}\right] \quad (6.2)$$

The normal rr- and θθ-stresses along the z-axis at the center of the circle are:

$$\tau_{rr} = \tau_{\theta\theta} = \frac{p}{2}\left[-(1+2\upsilon)+\frac{2(1+\upsilon)z}{(a^2+z^2)^{\frac{1}{2}}}-\frac{z^3}{(a^2+z^2)^{\frac{3}{2}}}\right] \quad (6.3)$$

We used this analytical solution to verify calculation of normal stress tensor components. We approximated the semi-infinite medium as a large rectangular parallelepiped 194 m in the x- and y- directions and 1320 m in the z-direction. We subdivided this medium into a 200x200x800 Cartesian grid. Grid block x- and y-direction length in the vicinity of the areal center was 0.1 m and increased further away from it. Grid block z-direction length was 0.2 m in the vicinity of the surface and increased further away from it. The load was located on the surface and at the areal center and had a 1.0 m radius. Because our grid was Cartesian, we approximated the circular load area as 314 squares of radius 0.1 m, shown in Figure 6.1. The rest of the medium's surface had no load exerted on it.

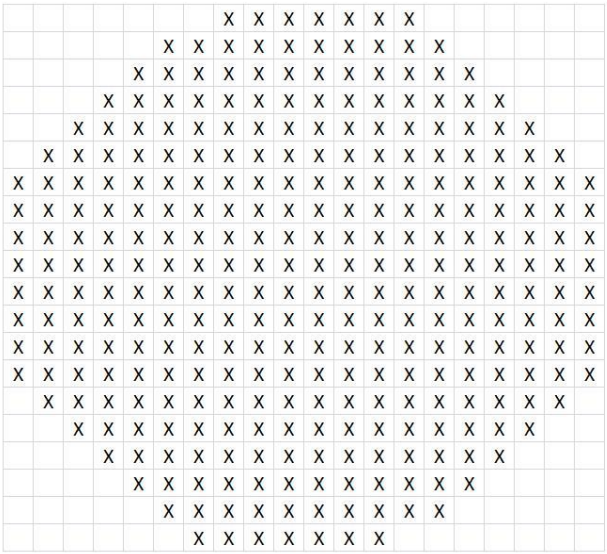

Figure 6.1. Approximation of loaded 1.0 m radius circle by 314 square grid blocks of length 0.1 m.

Our geomechanical formulation requires boundary conditions for mean stress and those stress tensor components that are calculated. We specified a mean stress of 0.48 MPa and a normal z-direction stress (the load) of 0.6 MPa over the loaded area. The equal x- and y-direction normal stresses were then 0.42 MPa. There is no fluid or heat flow in this problem. The displacement, *w*, caused by the load is the change of the medium's overall length in the direction of the applied load, given by:

$$w = \sum D_{0,z}\, \epsilon_{zz} \tag{6.4}$$

where $D_{0,z}$ is z-direction grid block unstrained length and the sum is over a *z*-direction column of grid blocks. The z-direction normal strain is calculated from Hooke's law:

$$\epsilon_{zz} = \frac{1}{E}\Big(\tau_{zz} - \nu\big(\tau_{xx} + \tau_{yy}\big)\Big) \tag{6.5}$$

The analytical and simulated displacements are shown in Figure 6.2 and those for the z-direction normal stresses are shown in Figure 6.3. In both cases, they are hardly distinguishable.

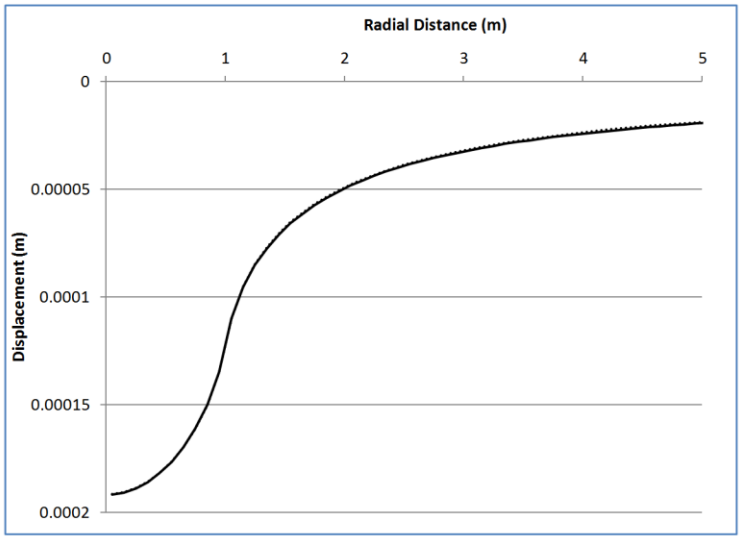

Figure 6.2. Analytical (solid line) and simulated (dotted line) displacements for semi-infinite medium subjected to circular load.

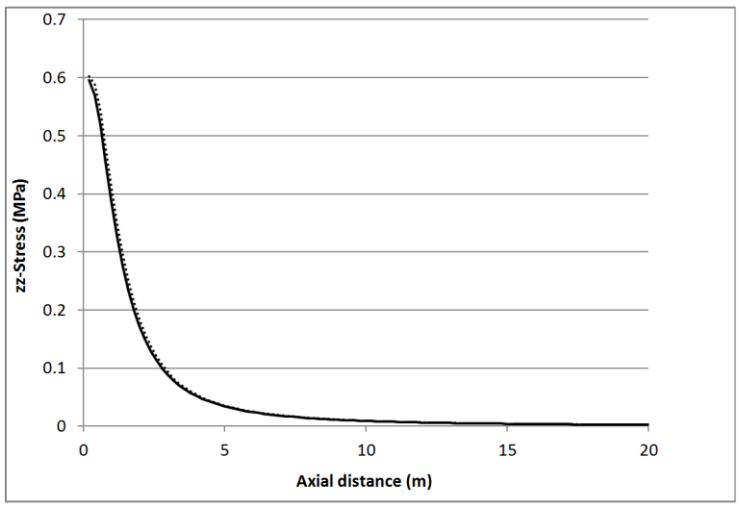

Figure 6.3. Analytical (solid line) and simulated (dotted line) z-direction normal stresses for semi-infinite medium subjected to circular load.

We also used this analytical solution to verify our rz-coordinate geomechanical formulation. We approximated the semi-infinite medium as a cylinder with 50 m radius and 54 m height. We subdivided this medium into an 800x1600 grid. Grid block radius increased logarithmically from the center and grid block z-direction length was 0.01 m for a number of layers starting at the top layer, with z-direction length increasing by an increment for subsequent blocks of layers. The loaded circle was located at the top layer with a 1.0 m radius. The analytical and simulated displacements are shown in Figure 6.4 and normal stresses for the z- and r-directions are shown in Figures 6.5 and 6.6, respectively. In all cases, the analytical solution and simulation are hardly distinguishable.

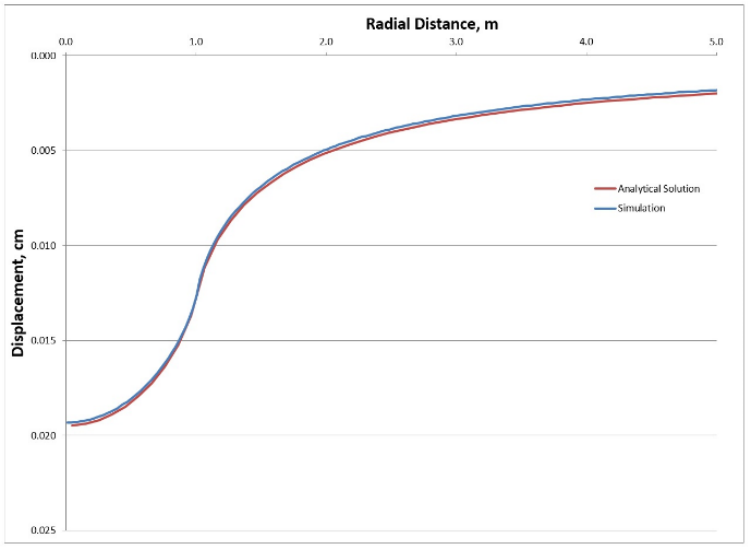

Figure 6.4. Analytical (solid line) and simulated (dotted line) displacements in rz-coordinates for semi-infinite medium subjected to circular load.

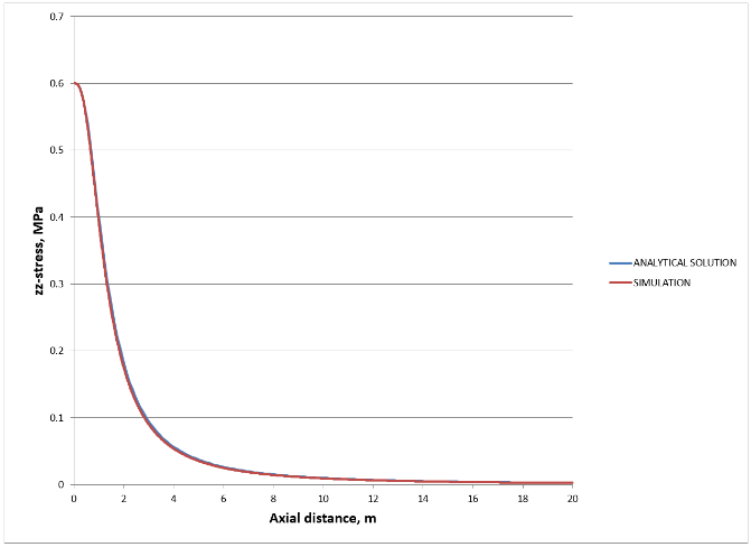

Figure 6.5. Analytical (solid line) and simulated (dotted line) z-direction normal stresses in rz-coordinates for semi-infinite medium subjected to circular load.

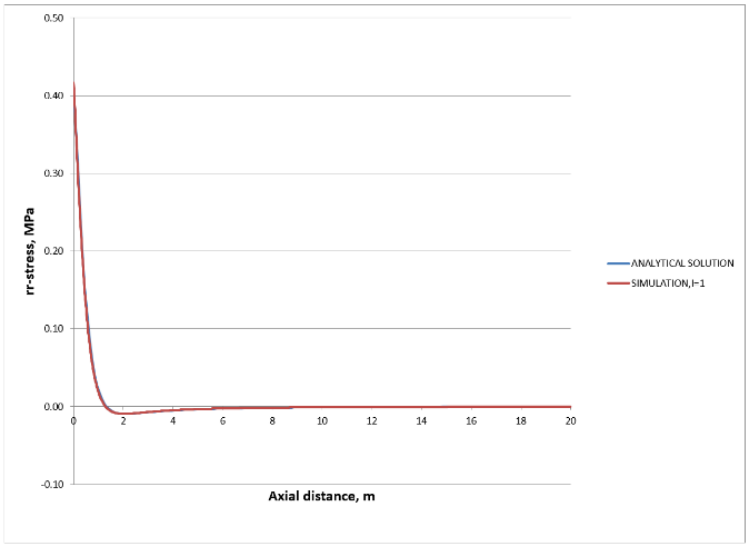

Figure 6.6. Analytical (solid line) and simulated (dotted line) r-direction normal stresses in rz-coordinates for semi-infinite medium subjected to circular load.

Two-dimensional Mandel-Cryer effect

Consider a fluid-filled poroelastic material with a constant compressive force applied to the top and bottom. There is an instantaneous compression and uniform pore pressure increase due to the force. Afterwards, the material is allowed to drain laterally. Drainage is accompanied by a decrease in pore pressure near the edges and the material there becomes less stiff, resulting in a load transfer to the center and a pore pressure there that reaches a maximum and then declines. This pore pressure behavior is the Mandel-Cryer effect (Mandel, 1953) and Abousleiman *et al.* (1996) derived an analytical solution to it. We use this analytical solution to verify our coupled fluid flow and geomechanics simulator.

Our simulation domain is 1000 m square and is subdivided into a uniform Cartesian 200x200 grid. Rock properties are the following: porosity is 0.094, permeability is 10^{-13} m^2, Young's modulus is 5.0 GPa, Poisson's ratio is 0.25, and the Biot coefficient is 1.0.

We first simulate the compression and next the drainage. The initial unstrained state is pore pressure and normal stress components at 2.0 MPa. The compressive portion of the simulation, with an imposed mean stress of 5.0 MPa at the top and bottom, is run until equilibrium is reached. After compression, the pore pressure has increased to 3.28 MPa and the mean stress becomes 5.0 MPa throughout the simulation domain. Because the lateral boundaries are free, the x- and y-direction effective stresses are zero, so the normal stresses in those directions are 3.28 MPa, and the normal z-direction stress is therefore 8.44 MPa.

In the drainage portion of the simulation, the initial pore pressure (2.0 MPa) is imposed at the lateral boundaries. Because the effective stresses at those boundaries are zero, the x- and y-direction normal stresses there also equal the initial pore pressure. The normal z-direction stresses at the top and bottom remain at 8.44 MPa. The drainage simulation is run for 100,000 seconds with 100 second time steps. Figure 6.7 shows the match of centerline pore pressure with the

analytical solution. The displacements in the x- and z- directions are calculated from the normal strains in a similar manner as the displacement calculation from the previous example problem. The applied stress causes the system to contract in the z-direction and expand in the x-direction. The expansion, shown in Figure 6.8, is matched almost perfectly and the match of the contraction, shown in Figure 6.9, shows only a small deviation from the analytical solution at early times.

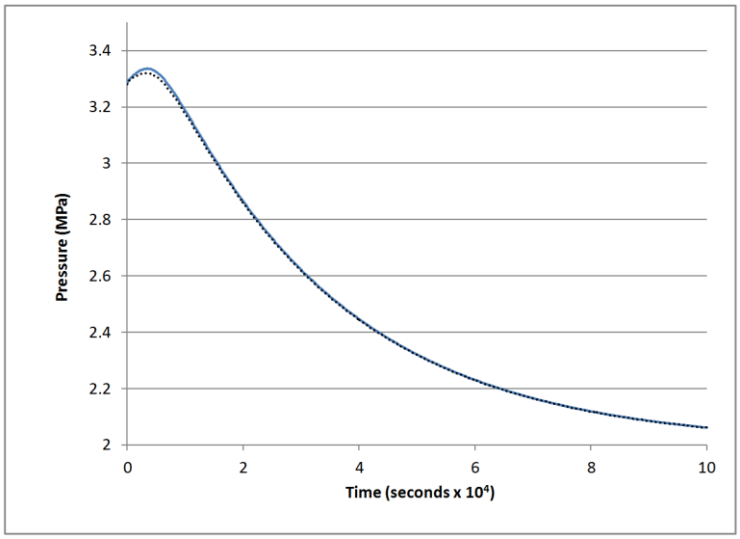

Figure 6.7. Match of simulated centerline pore pressure (dotted line) with analytical solution (solid line) for Mandel-Cryer effect.

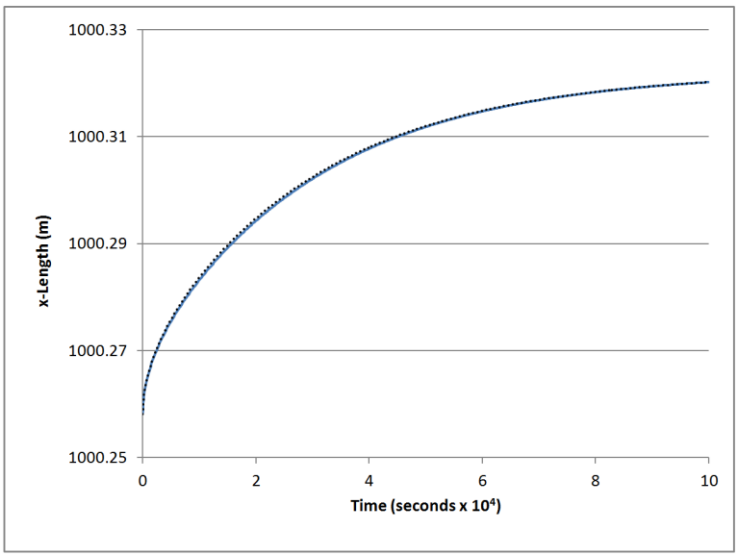

Figure 1.8. Match of simulated x-direction displacement (dotted line) with analytical solution (solid line) for Mandel-Cryer effect.

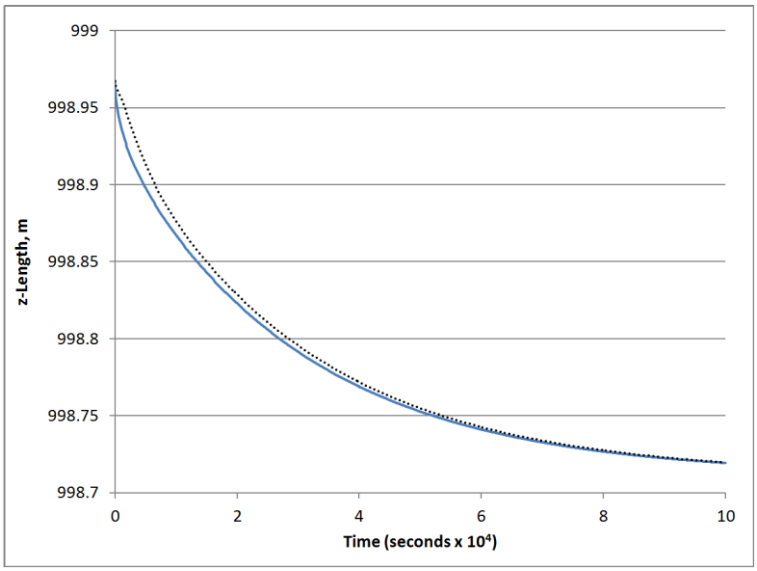

Figure 6.9. Match of simulated z-direction displacement (dotted line) with analytical solution (solid line) for Mandel-Cryer effect.

Stress tensor calculation in Cartesian coordinates

We ran a sample problem to test our stress tensor calculations. The simulation volume was a rectangular parallelepiped 671x671x61 m and subdivided into a uniform 11x11x10 grid (*I*, *J*, and *K* index dimensions, respectively). Rock properties such as porosity and permeability were constant. There was a single water phase that was initially in hydrostatic equilibrium. Normal stress components were initialized by the procedure described in Task 4 and initial shear stresses were zero. Water was injected into the center of the volume at a constant rate for three years. Figure 6.10a shows the pressure xy-cross section at K=6 and Figure 6.10b shows the pressure xz-cross section at J=6 after three years. The xy-cross section shows the expected radial symmetry and the xz-cross section is a superposition of the z-direction hydrostatic gradient and pressurization from the injection. Figure 6.11a shows the xx-stress component xy-cross section at K=5 and Figure 6.11b shows the xx-stress component xz-cross section at J=6 after three years. These show similar behavior to pressure, as does the yy- and zz-stress components.

Figure 6.12a shows the xy-shear stress component xy-cross section at K=5 and Figure 6.12b shows the xy-shear stress component xz-cross section at J=9 after three years. The xy-shear stress component depends on xy-cross derivatives of pressure and mean stress. In the xy-plane, these cross derivatives have their extremum at 45º to the coordinate axes, hence the four "blobs" of high shear stress in Figure 6.12a. These blobs are widest at the axial middle where fluid is injected and decrease axially away from there, as shown in Figure 6.12b. It should be noted that the scales in these two figures differ by a factor of ten.

Figure 6.13a shows the yz-shear stress component xy-cross section at K=6 and Figure 6.13b shows the yz-shear stress component xz-cross section at J=9 after three years. The yz-shear stress component depends on yz-cross derivatives of pressure and mean stress. In the xy-plane, these cross derivatives have their extremum along the x-axis, hence the two "blobs" of high shear stress in Figure 6.13a. These blobs are widest away from the axial middle where fluid is injected, due to

the drop off of potential and stress away from the axial center, as shown in Figure 6.13b. The lack of axial symmetry in Figure 6.13b is due to the contribution of gravity to pressure and mean stress. Also, it should be noted that the scales in these two figures differ by a factor of 0.7.

Figure 6.14a shows the xz-shear stress component xy-cross section at K=5 and Figure 6.14b shows the xz-shear stress component yz-cross section at I=9 after three years. The xz-shear stress component depends on xz-cross derivatives of pressure and mean stress. In the xy-plane, these cross derivatives have their extremum along the y-axis, hence the two "blobs" of high shear stress in Figure 6.14a. These blobs are widest away from the axial middle where fluid is injected, due to the drop off of potential and stress away from the axial center, as shown in Figure 6.14b. The lack of axial symmetry in Figure 6.14b is due to the contribution of gravity to pressure and mean stress. Also, it should be noted that the scales in these two figures differ by a factor of 12.5. These results are similar to the yz-shear stress component ones, rotated ninety degrees, and result from the circular pressure and mean stress profiles in the xy-plane.

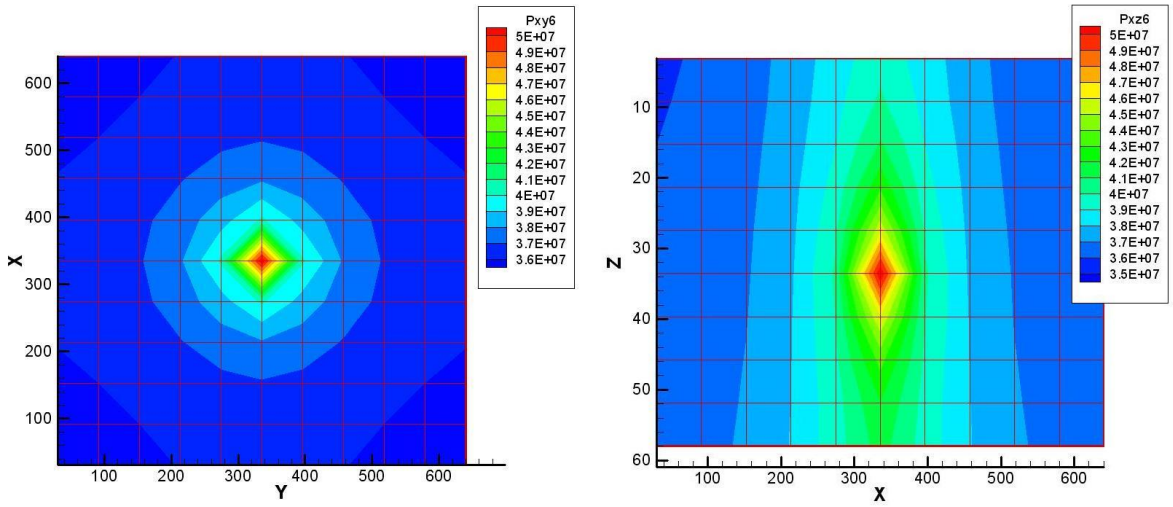

(a) (b)

Figure 6.10. Pressure cross sections for xy-plane, K=6 (a) and xz-plane, J=6 (b) after three years of injection.

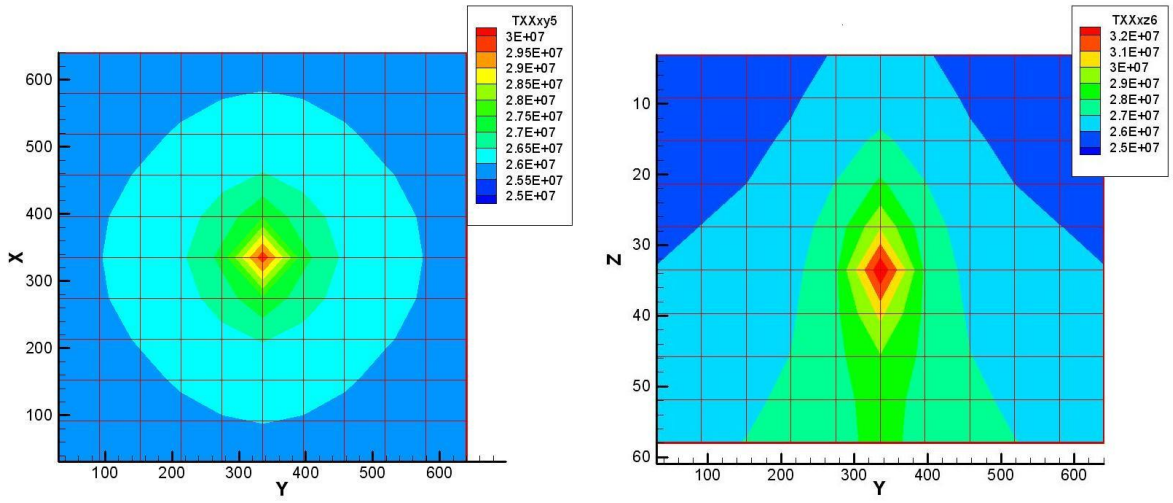

(a) (b)

Figure 6.11. Normal xx-stress cross sections for xy-plane, K=5 (a) and xz-plane, J=6 (b) after three years of injection.

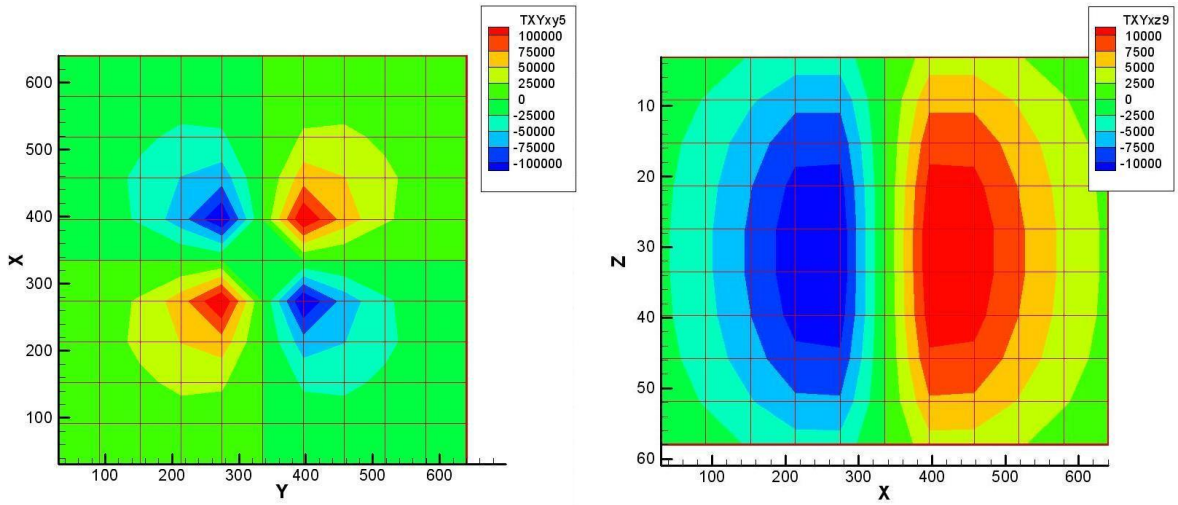

(a) (b)

Figure 6.12. Shear xy-stress cross sections for xy-plane, K=5 (a) and xz-plane, J=9 (b) after three years of injection.

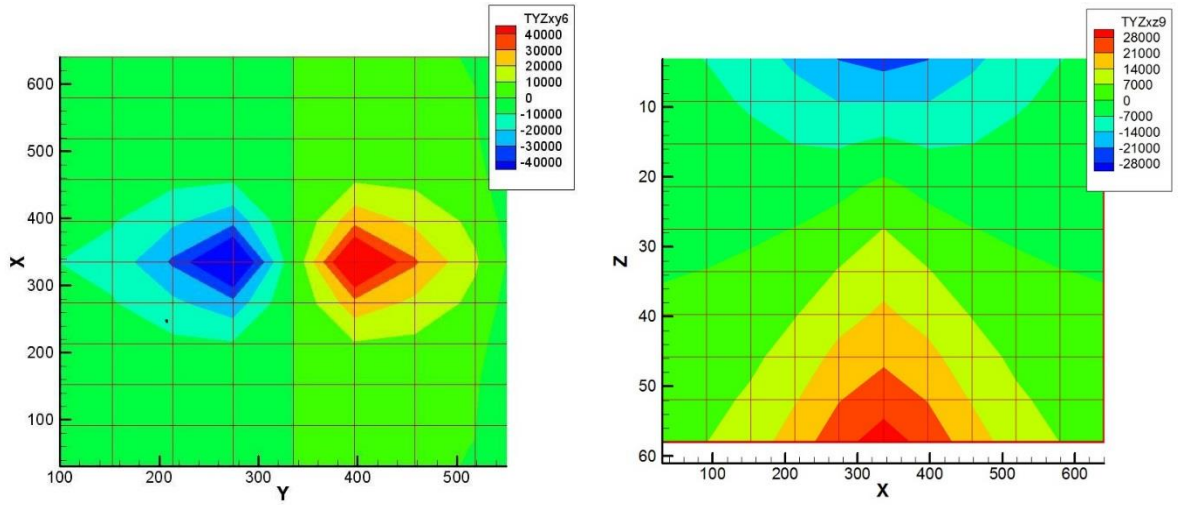

(a) (b)

Figure 6.13. Shear yz-stress cross sections for xy-plane, K=6 (a) and xz-plane, J=9 (b) after three years of injection.

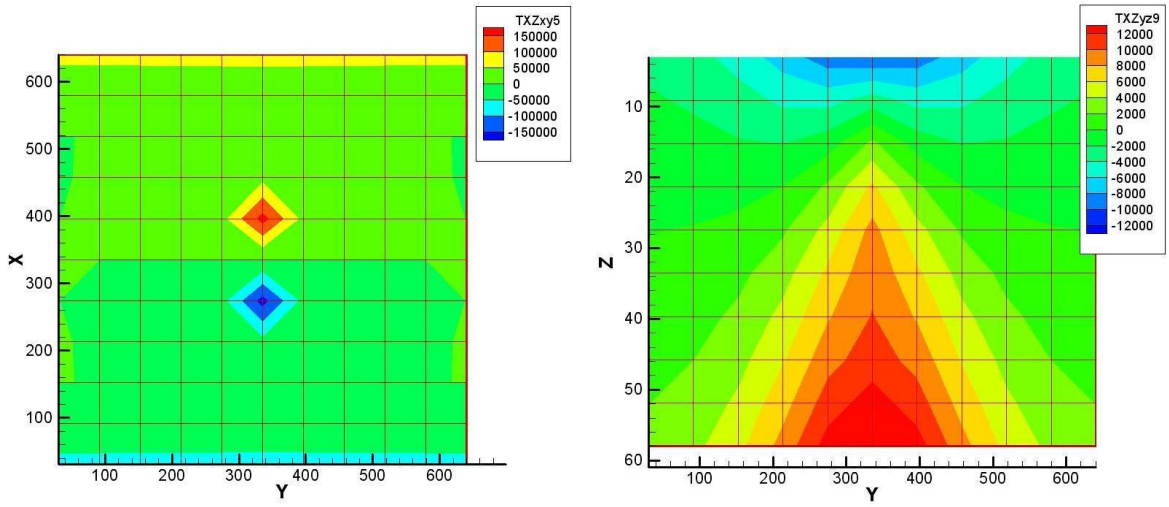

(a) (b)

Figure 6.14. Shear xz-stress cross sections for xy-plane, K=5 (a) and yz-plane, I=9 (b) after three years of injection.

Depletion of a single-phase reservoir

We simulated the depletion of a single-phase reservoir, adapted from Dean *et al.* (2006), as a comparison of our simulator to published results. A single phase (water) reservoir, 671 m^2 in area and 61 m thick, with a single vertical well at the center and completed along the entire thickness, was produced at a constant rate of 27.59 kg/sec for 500 days. Reservoir porosity was initially 0.20, horizontal permeability was $5 \cdot 10^{-14}$ m^2, vertical permeability was $5 \cdot 10^{-15}$ m^2, Young's modulus was $6.87 \cdot 10^7$ Pa, Poisson's ratio was 0.30, and the rock density was 2700 kg/m^3. The z-direction stress at the reservoir top was 41.4 MPa, and the constant horizontal stresses were 27.6 MPa. Pore pressure at the reservoir top was 20.7 MPa. Pore pressure was in hydrostatic equilibrium and z-direction stress was calculated using the technique developed in Task 4.

Our Cartesian grid was 11x11x10 with constant grid block dimensions, and our time step size was 50 days. We used the relations for porosity and grid block volume from Dean *et al.* (2006); grid block volume was constant and porosity varied with volumetric strain as:

$$\phi = \phi_i + \epsilon_{v,i} - \epsilon_v \tag{6.6}$$

where subscript "i" refers to initial conditions.

Figure 6.15 shows a comparison of average reservoir pressure and Figure 6.16 shows a comparison of subsidence around the well for our simulation and Dean *et al.* (2006). The average reservoir pressure match necessitated usage of the above grid block volume and porosity relations and would not have as good if other relations were used. Our subsidence is very similar to the published results and differs by about 5 percent at 500 days.

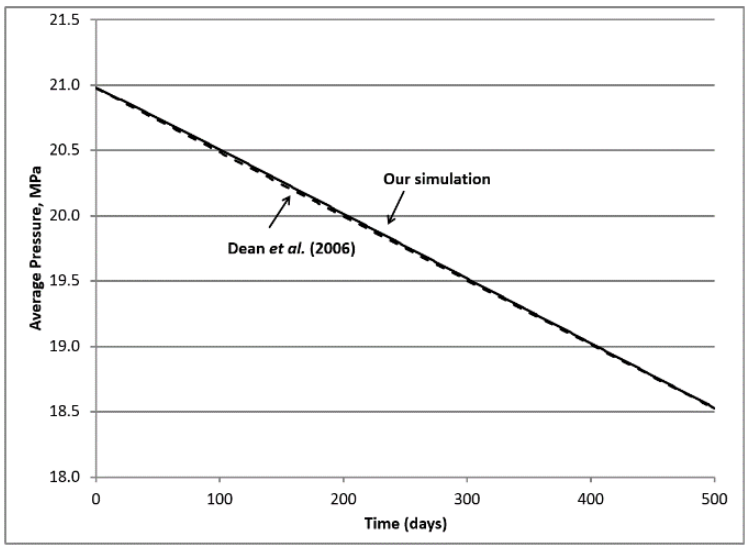

Figure 6.15. Average pore pressure from our simulation compared to Dean et al. (2006).

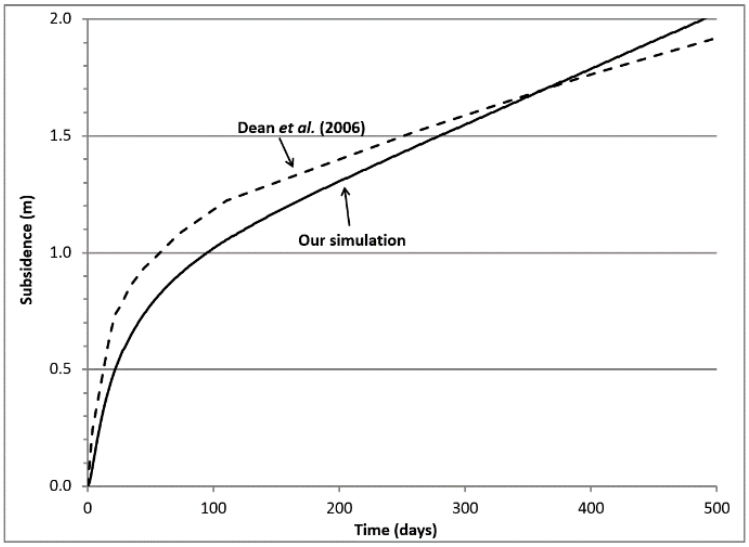

Figure 6.16. Subsidence from our simulation compared to Dean *et al*. (2006).

In Salah gas project surface uplift, I

The In Salah Gas Project, located in central Algeria, is a CO_2 storage project. Natural gas produced nearby is high in CO_2 and this CO_2 is injected back into the water leg of a depleting gas field for geological storage. Surface uplift from CO_2 injection has been measured by satellite-based interferometry and Rutqvist *et al*. (2010) did a reservoir-geomechanical analysis of In Salah CO_2 injection and surface uplift using the TOUGH2-FLAC numerical simulator (Rutqvist *et al*., 2002) in order to determine if the uplift can be explained by pressure changes and deformation in the injection zone only. We reran their analysis on our simulator in order to match their simulated results.

The domain was 10x10x4 km with one 1.5 km horizontal injection well at 1810 m depth and in the domain center. The domain consisted of four geological layers, Shallow Overburden, Caprock, Injection Zone, and Base, whose properties are shown in Table 6.1. The reservoir initially contained water at hydrostatic equilibrium. The initial temperature and pressure at the injection well were 90 °C and 18.5 MPa, respectively. The initial stress tensor was calculated as outlined in Task 4 with the normal stress ratios R_{xz} and R_{yz} being 1.2 and 0.8, respectively. The lateral reservoir boundaries were maintained at constant pressure, the reservoir boundaries were maintained at constant stress, and CO_2 was injected at 9.734 kg sec^{-1} for three years.

Our simulation was over a 5x5x4 km quarter symmetry element of the domain using a 50x50x60 grid. In all three directions, the grid was finer in the vicinity of the well and became coarser away from it. Figure 6.17 compares pressure change versus depth. We modified the Rutqvist et al. (2010) Injection Zone permeability somewhat in order to match the pressure change there after three years. Their simulation used a much coarser grid than ours (about 10,000 grid blocks for the entire domain) and is reflected by their piecewise-linear pressure profile. Figure 6.18 compares vertical displacement versus depth at the injection well center after three years. Both simulators give similar displacement profiles.

Table 6.1. Geological layer properties for InSalah CO_2 injection.

Property	Shallow Overburden (0–900 m)	Caprock (900–1800 m)	Injection Zone (1800–1820 m)	Base (> 1800 m)
Young's modulus, GPa	1.5	20.0	6.0	20.0
Poisson's ratio	0.2	0.15	0.2	0.15
Biot's Coefficient	1.0	1.0	1.0	1.0
Porosity	0.1	0.01	0.17	0.01
Permeability, m^2	$1.0 \cdot 10^{-17}$	$1.0 \cdot 10^{-19}$	$0.875 \cdot 10^{-14}$	$1.0 \cdot 10^{-21}$
Residual CO_2 saturation	0.05	0.05	0.05	0.05
Residual liquid saturation	0.3	0.3	0.3	0.3
Van Genuchten (1980) m	0.457	0.457	0.457	0.457
Van Genuchten, P_0, kPa	19.9	621.0	19.9	621.0

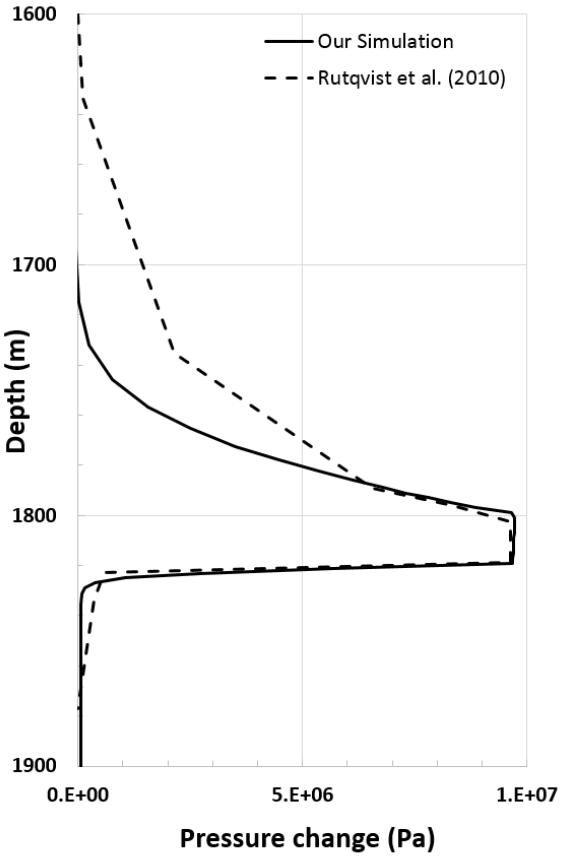

Figure 6.17. Pressure change at injection well center after three years of injection.

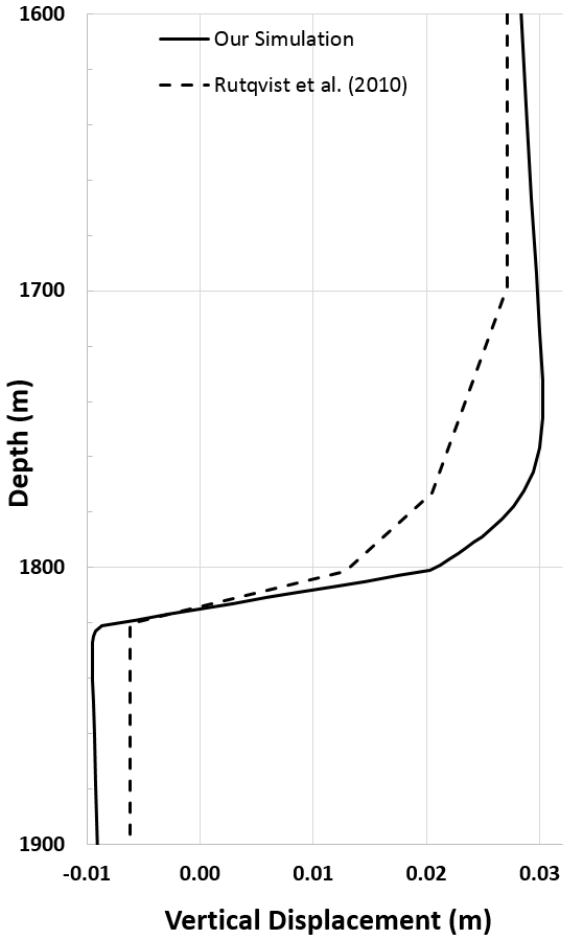

Figure 6.18. Vertical displacement at injection well center after three years of injection.

In Salah gas project surface uplift, II

Rinaldi and Rutqvist (2013) report on measurements of ground surface uplift at well KB-502 in the Krechba gas field at In Salah (Algeria). There, a double-lobe uplift pattern has been observed in the ground deformation data that is explained as resulting from the presence of a deep vertical fracture zone. They simulated CO_2 injection into this well using TOUGH-FLAC. The simulation domain was 20km×20km wide and 4 km in height and consisted of four layers: cretaceous sandstone and mudstone overburden (0–900 m), carboniferous mudstone (caprock, 900–1800 m), sandstone (CO_2 reservoir, 1800–1820 m), and mudstone basement (below 1820 m). Hydraulic and rock properties were given for each layer, and some layers were subdivided into sub-layers for specification of rock properties. The sandstone layer contained a 1.0 km horizontal injection well and CO_2 was injected at varying rates for about three years. The horizontal zone intersected a fault zone that extended into the caprock and was 80 m wide (along the horizontal well), 350 m in height, and 3500 m long (perpendicular to the horizontal well).

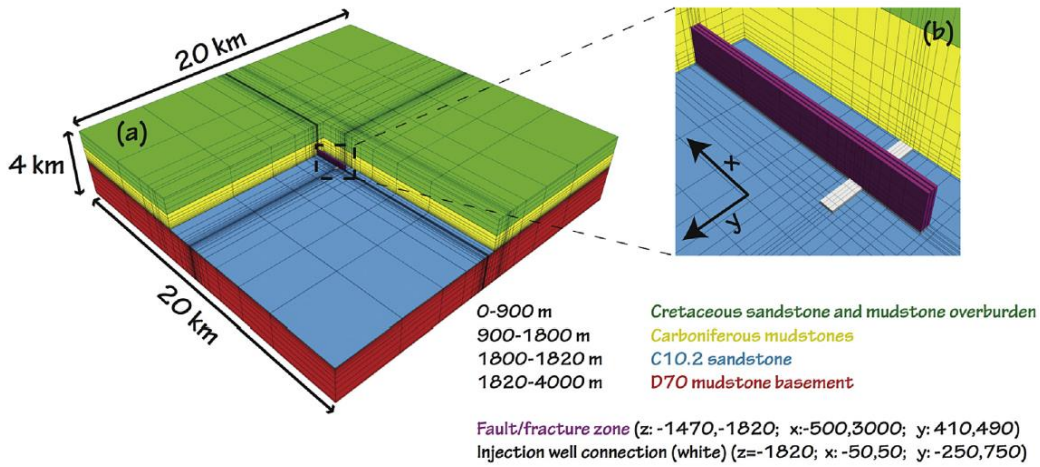

Figure 6.19. Simulation domain showing geological layers (a) and vertical fracture zone along with horizontal well in white (b) (Rinaldi and Rutqvist, 2013).

Figure 6.19 shows the geological formations and the horizontal well. Initially, the fault had the same properties as the rock in the same layers. When the fault activated, which was after a couple of months of injection, the fault permeability increased by a factor of 10^6 and the sandstone permeability increased by a factor of 2.5.

We reran this simulation using TOUGH2-CSM. In the reference, the fracture zone had anisotropic rock properties that we approximated as isotropic. Figure 6.20 shows a comparison of surface uplift at the end of injection (after about 2 3/4 years). Both show two lobes with uplifts around 2 cm, and there was a small zone with slightly higher uplift (2.5-3 cm) at one end of the injection well in our case.

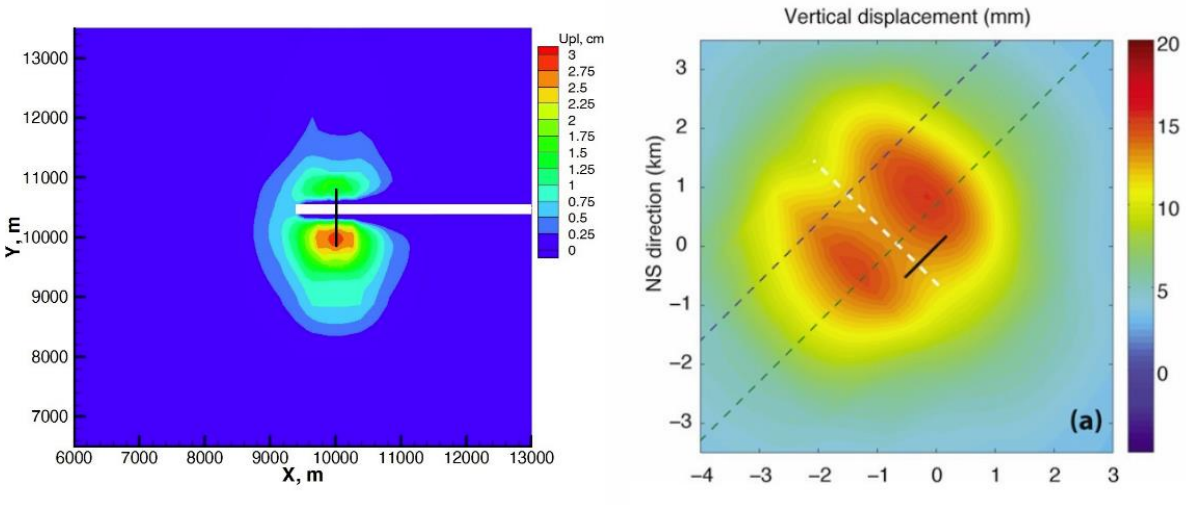

Figure 6.20. TOUGH2-CSM surface uplift, left, and that from Rinaldi and Rutqvist (2013), right. Black line indicates injection well and white one fault.

Induced thermal stress simulation

Vilarrasa and Laloui (2015) modeled a baserock–reservoir–caprock system in a normal faulting stress regime using an axisymmetric model into which cold CO_2 was injected in order to study the induced thermal stresses from this injection. Their model had an outer radius of 1000 m and a 20 m thick aquifer, with its top at 1500 m depth that was overlain by caprock and underlain by a 50 m thick baserock. Rock properties are shown in Table 6.2

Table 6.2. Rock properties of baserock–reservoir–caprock system, from Vilarrasa and Laloui (2015).

Property	**Aquifer**	**Caprock and Baserock**
Permeability, m^2	10^{-13}	10^{-18}
Porosity	0.15	0.01
Young's modulus, GPa	10.5	5.0
Poisson's ratio	0.3	0.3
Linear thermal expansion coefficient, $°C^{-1}$	10^{-5}	10^{-5}

CO_2 was injected uniformly into the aquifer center at a rate of 6.33762 kg/s (0.2 Mt/yr) for 180 days.

Our rz-coordinate grid dimensions were 100 x 211. Grid block radial thickness increased when traversing outward and axial thickness was 1 m in the vicinity of the aquifer and 10 m at some distance away from it from above and below. Figure 6.21 shows a comparison of liquid saturation

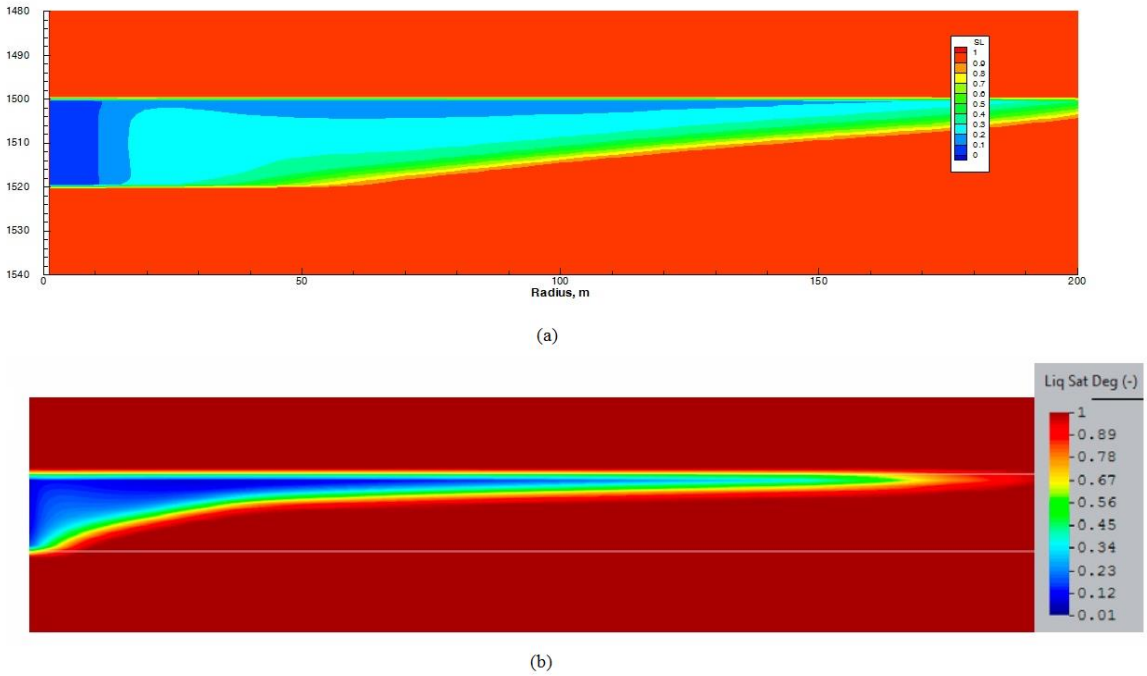

Figure 6.21. Liquid saturation for (a) TOUGH2-CSM simulation and (b) Vilarrasa and Laloui (2015) after 180 days.

for our TOUGH2-CSM simulation with the reference; they are similar, since the total CO_2 mass injected is the same in each case. Figure 6.22 shows a comparison of rz-shear stress for the TOUGH2-CSM simulation with the reference. Both shear stress profiles are similar in magnitude and extent, and it should be note that the colors in the two contour legends are inverted.

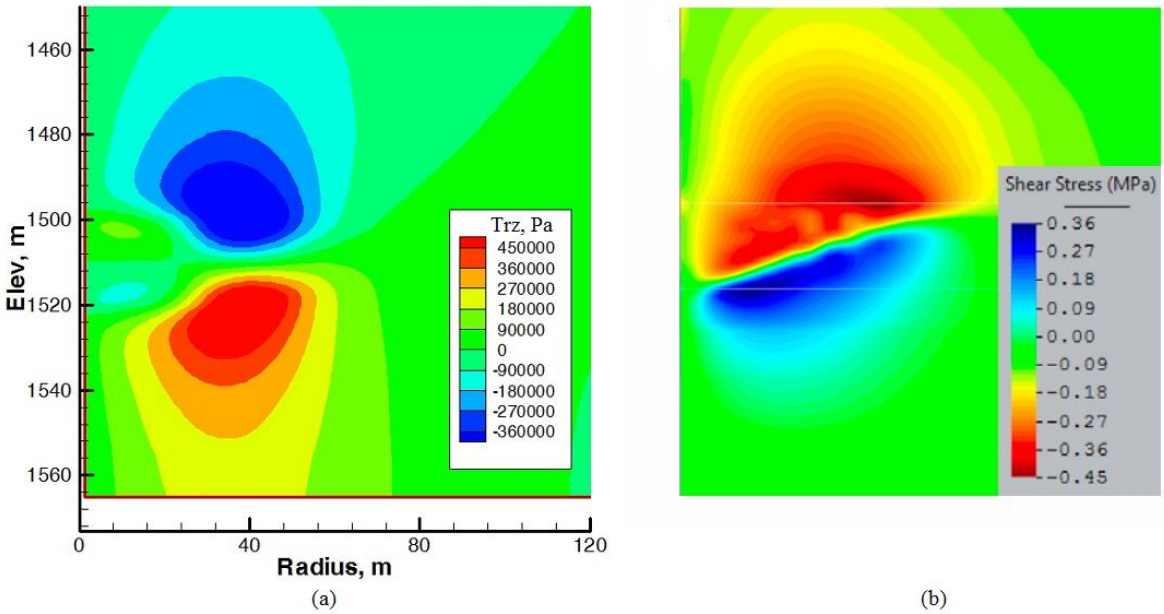

Figure 6.22. rz-shear stress for (a) TOUGH2-CSM simulation and (b) Vilarrasa and Laloui (2015) after 180 days.

CO_2 leakage through fault zones

Rinaldi at al. (2014) studied fault responses during underground carbon dioxide injection, and focused on the short-term integrity of the sealing caprock and the potential for leakage. They considered stress/strain-dependent permeability and studied leakage through a fault zone as its permeability changes during reactivation. We ran some of their simulations using our model. Their "Scenario 1" (Mazzoldi et al., 2012) was a two-dimensional system with a minor 1 km fault that intersected a 100 m thick injection aquifer bounded above and below by a 150 m thick low-permeability caprock, shown in Figure 6.23, with rock properties shown in Table 6.3. Permeability and porosity depend on effective stress, σ', and is given by (Rutqvist and Tsang, 2002; Davies and Davies, 2001):

$$\phi = \phi_1 + (\phi_0 - \phi_1)e^{-a\sigma'} \tag{6.7}$$

$$k = k_0 e^{c\left(\frac{\phi}{\phi_0}-1\right)} \tag{6.8}$$

where ϕ_0 is zero effective stress porosity, ϕ_1 is high effective stress porosity, exponent a is a parameter, constrant c is a parameter, and k_0 is zero effective stress permeability.

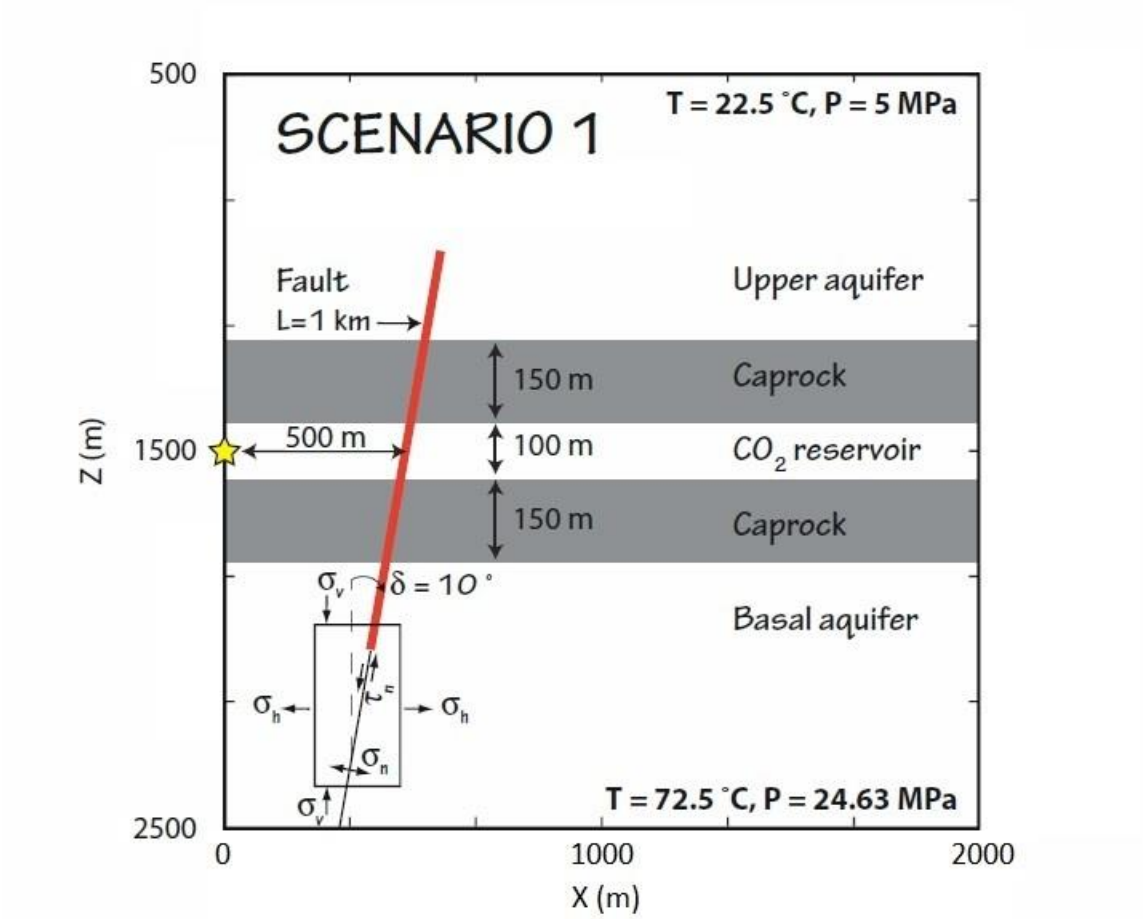

Figure 6.23. Schematic of "Scenario 1", adapted from Rinaldi et al. (2014), showing rock layers and fault. Injection site starred point at 1500 m depth.

Table 6.3. Rock properties used aquifer-caprock system, from Rinaldi at al. (2014).

Property\Layer	Upper	Caprock	CO_2 reservoir	Basal	Fault
Young's modulus, GPa	10.0	10.0	10.0	10.0	5.0
Poisson's ratio	0.25	0.25	0.25	0.25	0.25
Porosity	0.10	0.01	0.10	0.01	0.10
Permeability, m^2	10^{-14}	10^{-19}	10^{-13}	10^{-16}	10^{-14}-10^{-16}
Residual CO_2 saturation	0.05	0.05	0.05	0.05	0.05
Residual liquid saturation	0.3	0.3	0.3	0.3	0.3
Van Genuchten (1980) p0, kPa	19.9	621	19.9	621	19.9
Van Genuchten (1980) m	0.457	0.457	0.457	0.457	0.457

We simulated this system using a 190x145 grid. Grid block x-direction length was 20 m, except for the x-direction interval the fault was located in where it was 2 m. Grid block y-direction length was 20 m, except for the CO_2 reservoir and caprock layers where it was 10 m. The fault was represented by a series of connected grid blocks that approximately lie on the fault line shown in Figure 6.23. We ran two cases, the first with fault permeability 10^{-14} m^2 and CO_2 injection rate of 0.10 kg/sec-m, and the second with fault permeability 10^{-16} m^2 and CO_2 injection rate of 0.02 kg/sec-m, for five years. Figures 6.24 and 6.25 compare our fault permeability change at one and five years to those from the reference. There is good qualitative agreement between the two.

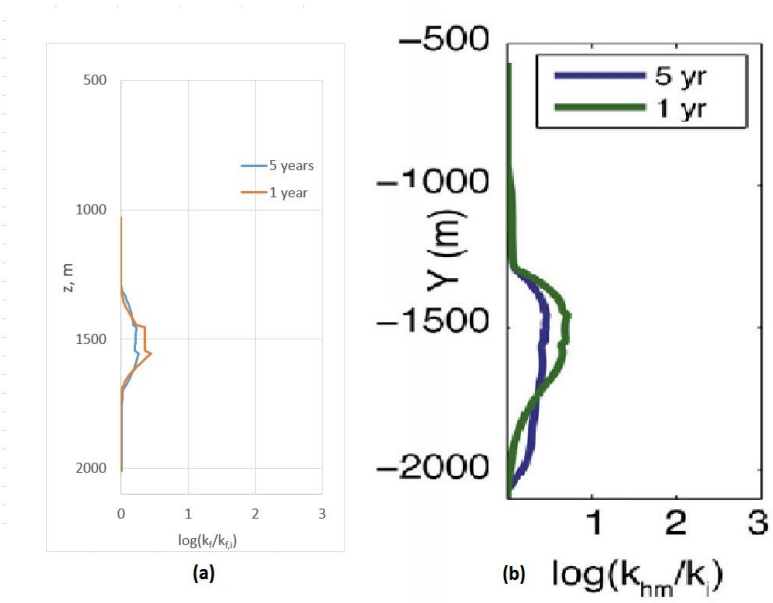

Figure 6.24. Fault permeability increase for our simulation (a) and reference (b) for fault permeability of 10^{-14} m^2 and CO_2 injection rate of 0.10 kg/sec-m.

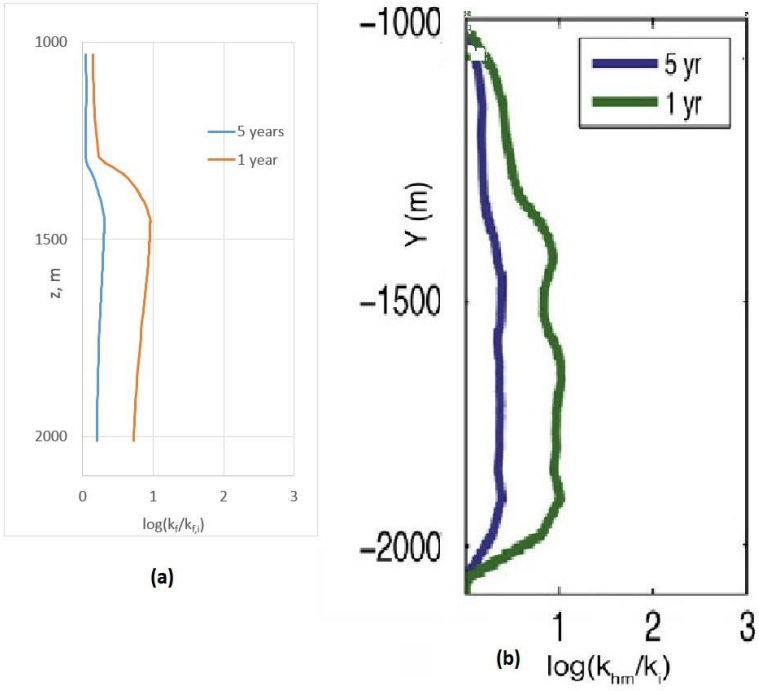

Figure 6.25. Fault permeability increase for our simulation (a) and reference (b) for fault permeability of 10^{-16} m^2 and CO_2 injection rate of 0.02 kg/sec-m.

We also ran this simulation with a Mohr-Coulomb failure envelope to demonstrate the capability of the simulator to predict where shear failure of the fault could occur. The cohesion was zero and the coefficient of internal friction was 0.6. Figure 6.26 shows the predicted failure regions at varying times. These regions only lie along the fault; those outside the fault are not subject to shear failure.

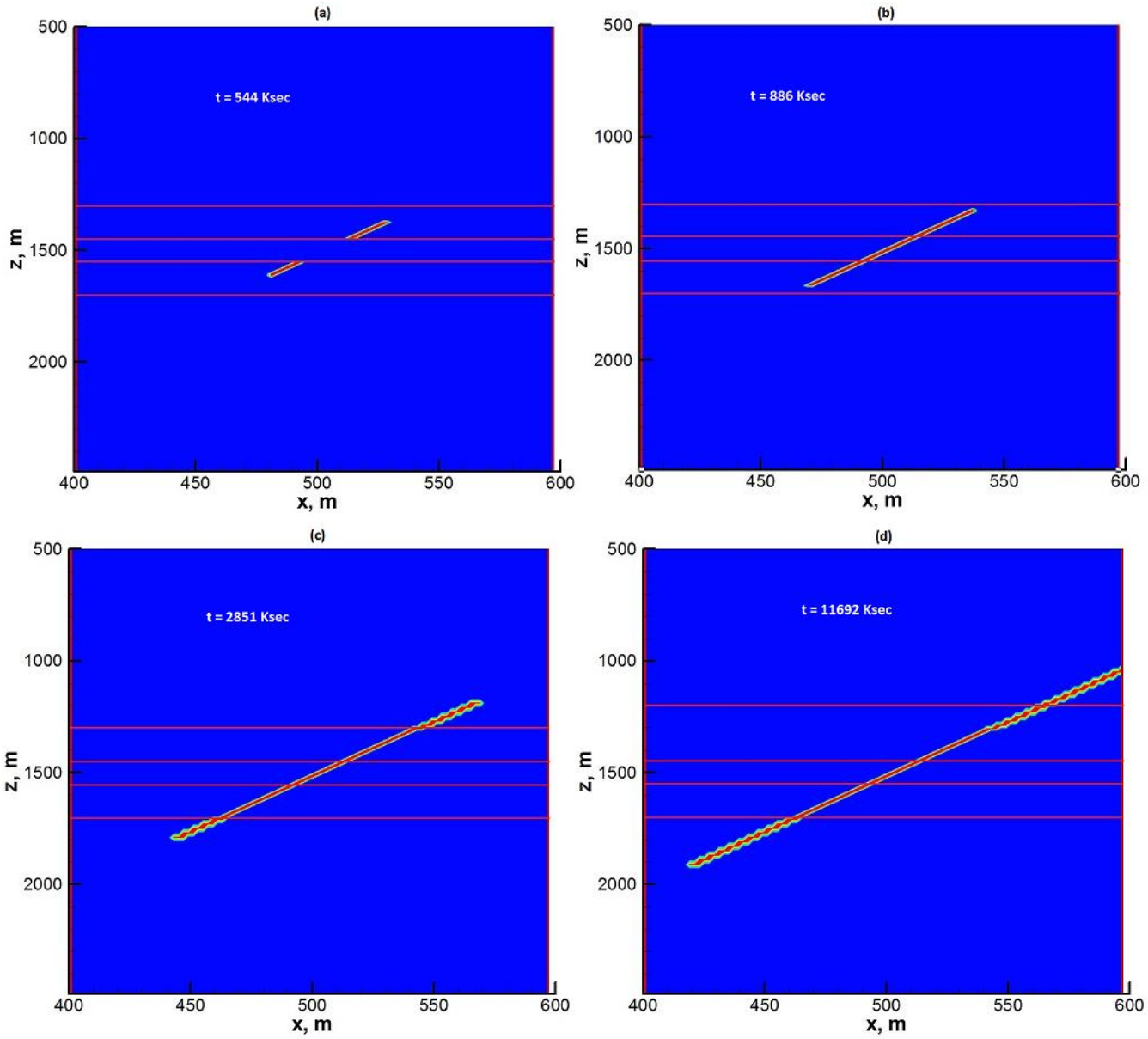

Figure 6.26. Mohr-Coulomb failure regions in fault shown at varying times: a) 544Ksec, b) 886 Ksec, c) 2851 Ksec, d) 11692 Ksec.

We then ran a variant of this problem to demonstrate the calculation of permeability and porosity as a function of normal stress for a fractured medium. Fracture aperture is correlated with normal effective stress according to:

$$b_i = b_{i,r} + b_{i,max} e^{-d_i \sigma_i'} \tag{6.9}$$

where b_i is fracture aperture in direction i, subscript r refers to a high effective stress residual aperture, subscript *max* refers to the maximum aperture increase at zero normal effective stress, and d_i is a parameter. Porosity is correlated to fracture aperture as:

$$\phi = \phi_0 \frac{\sum_i b_i}{\sum_i b_{i,0}} \tag{6.10}$$

where subscript *0* refers to a reference condition Permeability is correlated to fracture aperture as:

$$k_j = k_{j,0} \frac{\sum_{i \neq j} b_i^3}{\sum_{i \neq j} b_{i,0}^3} \tag{6.11}$$

The previous fault was changed to a vertical one, represented by a column of grid blocks, and located at x-direction 500 m and with z-direction range from 1000 to 2000 m. The fault permeability in the z-direction depends on normal stress and since the fault is vertical, it depends on the normal x-direction stress component. Fault permeability in the x-direction does not change. We reran the case with fault permeability 10^{-14} m^2 and CO_2 injection rate of 0.10 kg/sec-m for five years. Figure 6.27 shows the gas saturation at 1- and 5-years and Figure 6.28 shows the permeability ratio (permeability divided by initial value) at those times.

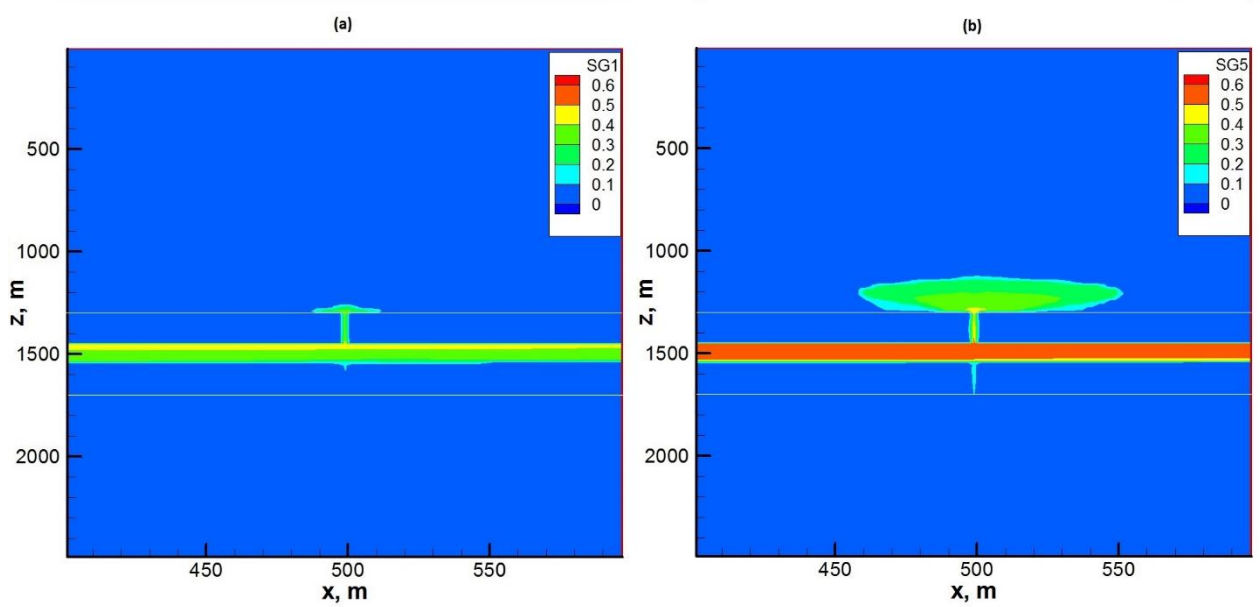

Figure 3.27. Gas saturation at one and five years. The white lines denote the boundaries between rock regions and the 1 km fracture, located at x=500m, is centered at z=1500m.

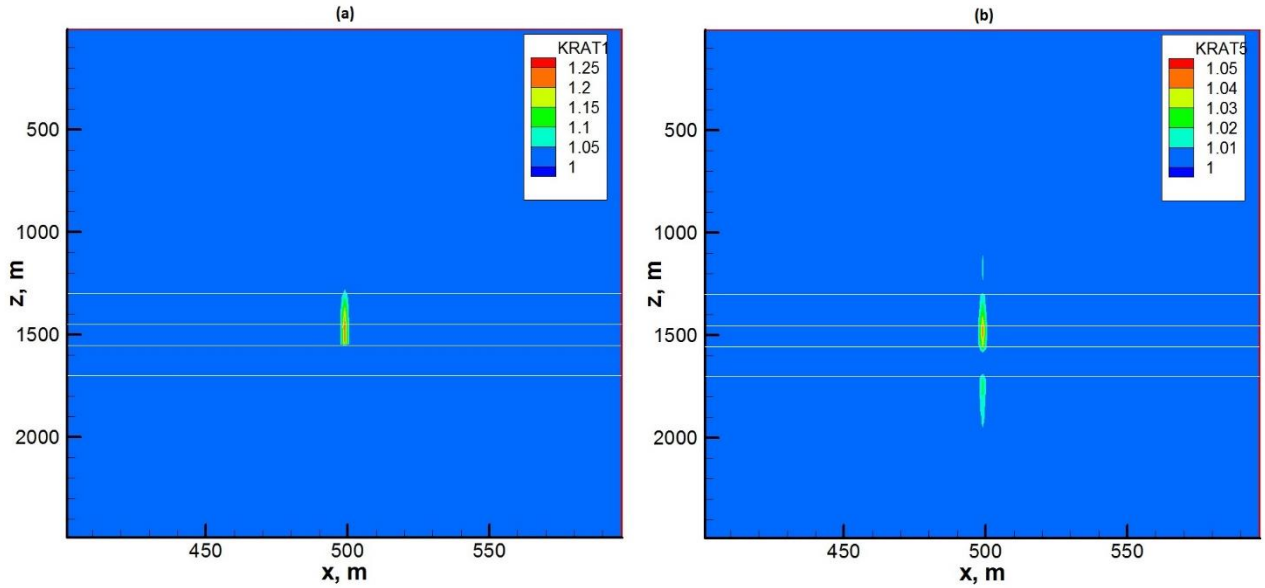

Figure 6.28. Permeability ratio at one and five years. The white lines denote the boundaries between rock regions and the 1 km fracture, located at x=500m, is centered at z=1500m.

Caprock failure in an aquifer-caprock system

We ran a simulation, based on Yamamoto et al. (2013), of caprock failure in an aquifer-caprock system. The simulation volume is axisymmetric, 1600 m thick, and 4100 m in radius. The aquifer extends from a depth of 1000 m to 1100 m and is overlain and underlain by caprock that extends to the surface above and an additional 500 m below. The injection well is located in the center of and along the entire aquifer, which is completed. Table 6.4 shows the aquifer and caprock properties.

Table 6.4. Aquifer and caprock properties from Yamamoto et al. (2013).

	Aquifer	Caprock
Young's modulus, GPa	0.23	3.1
Poisson's ratio	0.3	0.3
Porosity	0.35	0.30
Permeability, m^2	$1.0 \cdot 10^{-13}$	$1.0 \cdot 10^{-18}$
Biot's coefficient	1.0	1.0
Fraction angle, deg.	90	30
Cohesion, MPa	0.0	0.0

Relative permeability is calculated, for both aquifer and caprock, using the van Genuchten-Mualem model (Mualem, 1976; van Genuchten, 1980) with the following: λ=0.457, S_{lr}=0.30, S_{ls}=1.0, S_{gr}=0.5, and S_{gs}=1.0. Capillary pressure is calculated using the van Genuchten (1980) function with: λ=0.457, S_{lr}=0.0, and S_{ls}=0.999 for both caprock and aquifer, P_0=0.018 MPa for aquifer, and P_0=0.95 MPa for caprock. Permeability depends on porosity and uses the correlation from Davies and Davies (2001), Equation 6.8. Porosity depends on volumetric strain and is the following (Winterfeld and Wu, 2014):

$$\phi = 1 - (1 - \phi_0)\frac{(1-\epsilon_{v,0})}{(1-\epsilon_v)} \tag{6.12}$$

We first reran this simulation using a Cartesian grid of size 201x201x70 (2,828,070 grid blocks). Table 6.5 shows grid block dimensions.

Table 6.5. Grid block dimensions, (starting at top for z-direction)

z-direction		x,y-direction	
Number	Length, m	Number	Length, m
40	25	25	80
10	10	25	40
20	25	25	20
		51	10
		25	20
		25	40
		25	80

The reservoir initially contained water in hydrostatic equilibrium and at 40 ºC. The zz-direction normal stress is in mechanical equilibrium, the ratio of xx-direction stress to zz-direction stress is 0.8; the corresponding ratio for yy-direction stress is 1.2, and the reference pressure and stresses, evaluated at the surface, are atmospheric pressure. The lateral boundaries are maintained at the initial conditions. We injected 2 kg/sec CO_2 into the aquifer uniformly for 500 days.

Figure 6.29 shows the pressure, which is radially symmetric, after 500 days in a xy-cross section through the aquifer. The normal stresses show similar behavior. Figure 6.30 shows the xy-shear stresses there. They exhibit absolute maxima along the 45-degree lines. The magnitude of the shear stresses are quite low, however, being roughly 10^{-3} of the normal stress magnitude. Because the aquifer has relatively high permeability, the pressure gradients that would induce shear stresses there are small. Figure 6.31 shows the xz-shear stresses in an xz-cross section containing the well. These shear stresses are concentrated along the caprock-aquifer interface. Figure 6.32 shows the regions where caprock fails for an xz-cross section containing the well. The regions just above and below the aquifer (in caprock) near the well have exhibited failure. We have neglected aquifer failure here; such failure would only increase the aquifer permeability and not impact the sealing characteristics of the caprock. Figure 6.33 shows Mohr circles and the Mohr-Coulomb line for the grid block, in the caprock zone, located just above the completed interval. The initial Mohr circle (t=0) lies below the Mohr-Coulomb line so there is no rock failure there. At 500 days (t=500), the Mohr circle has shifted to the left due to pressurization from injected CO_2 and the Mohr circle has intersected the Mohr-Coulomb line, indicating that shear failure has occurred in that grid block.

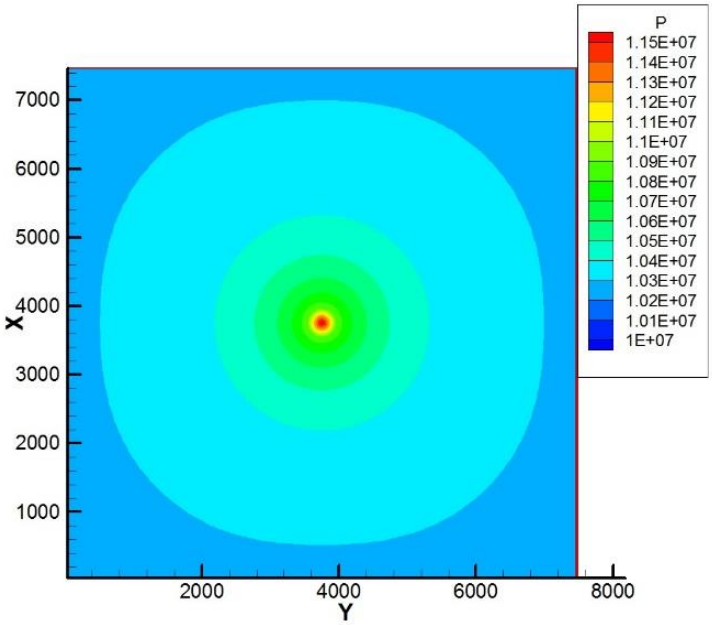

Figure 6.29. Pressure xy-cross section in aquifer, located at 1050 m depth.

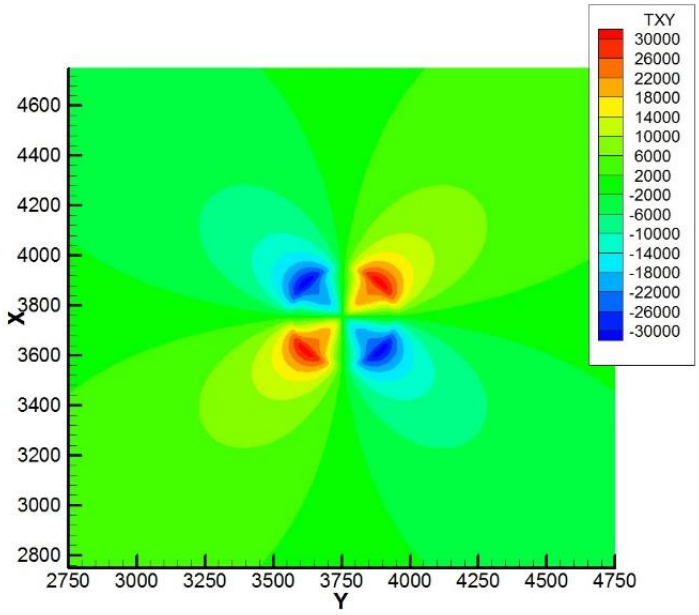

Figure 6.30. xy-shear stress xy-cross section in aquifer, located at 1050 m depth.

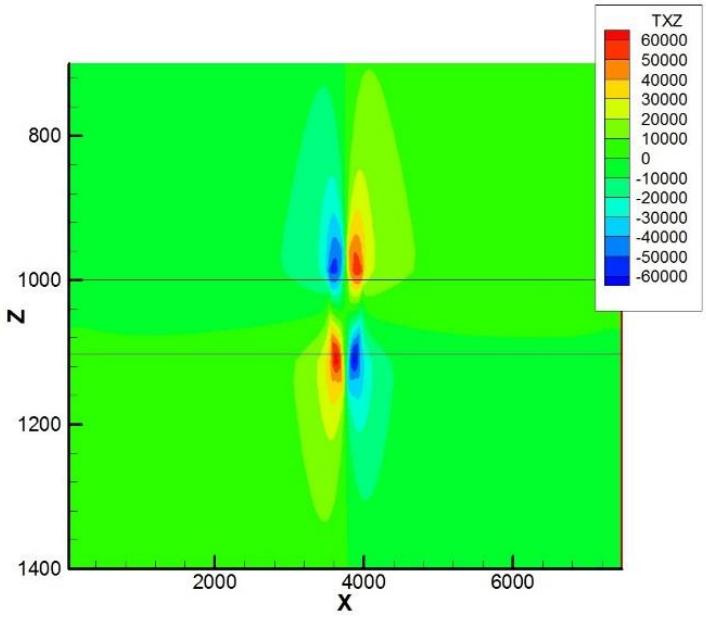

Figure 6.31. xz-shear stress xz-cross section, through center (3755 m in y-direction) and containing injection well (located at 3755 m in x-direction).

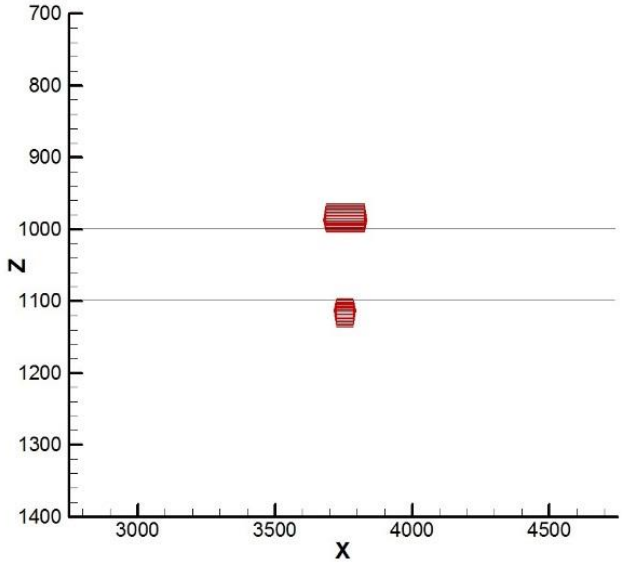

Figure 6.32. Regions of caprock failure (red) in xz-cross section through center (3755 m in y-direction) and containing injection well (located at 3755 m in x-direction).

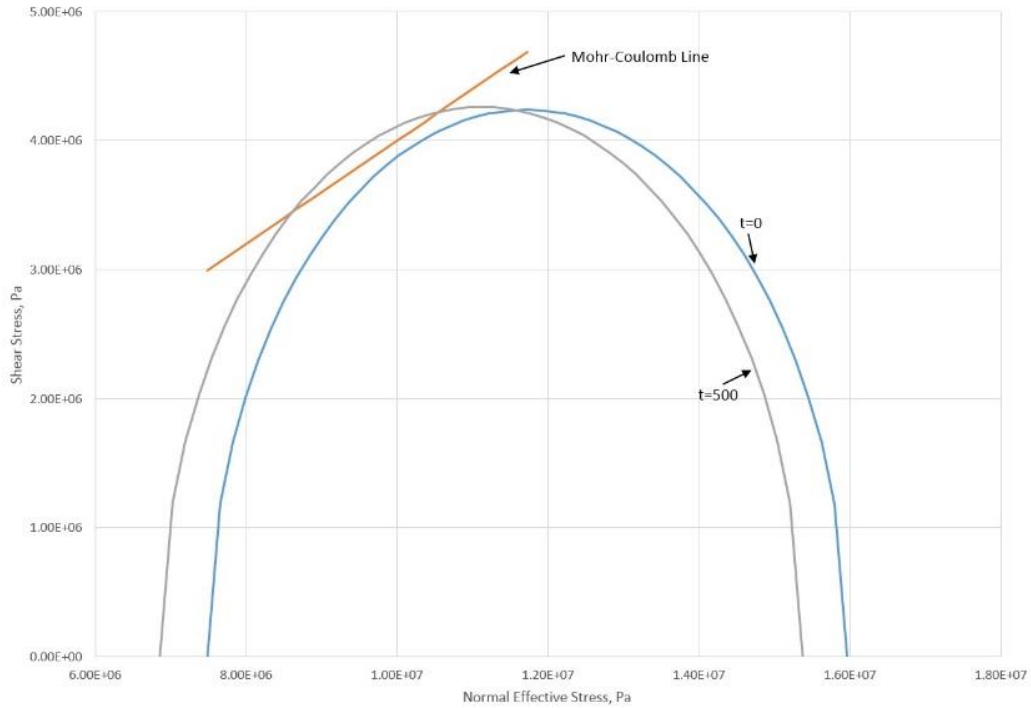

Figure 6.33. Mohr circles at simulation beginning and end, and Mohr-Colomb failure line, for grid block above injection well.

We later reran this problem in rz-coordinates. The outer radius was 4100 m, and the ratio of horizontal to vertical stress is 0.67. Figure 6.34 shows the gas saturation at 500 days. The gas extends to about 300 m radius. Figure 6.35 shows the rz-shear stress component. There are two lobes with opposite sign just around the aquifer top and bottom. This induced shear stress is in the vicinity of the axisymmetric center and reflects pressurization due to injection. Figure 6.36 shows the region of caprock failure. Caprock failure occurs around the region of maximum shear stress magnitude that is above the aquifer. As before, we did not allow caprock failure below the aquifer.

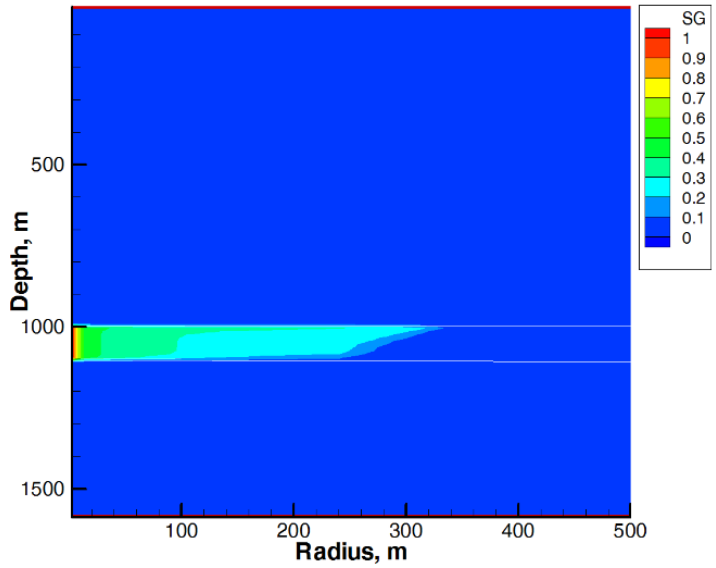

Figure 6.34. Gas saturation at 500 days injection.

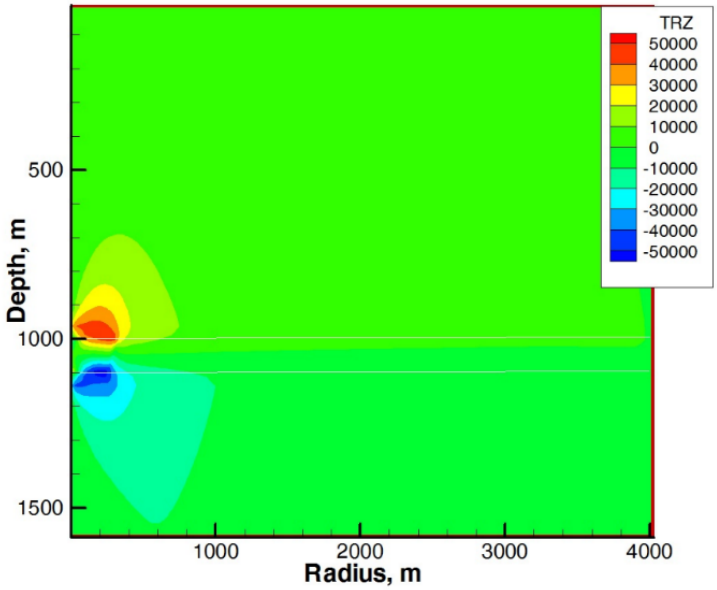

Figure 6.35. Shear stress rz-component after 500 days injection.

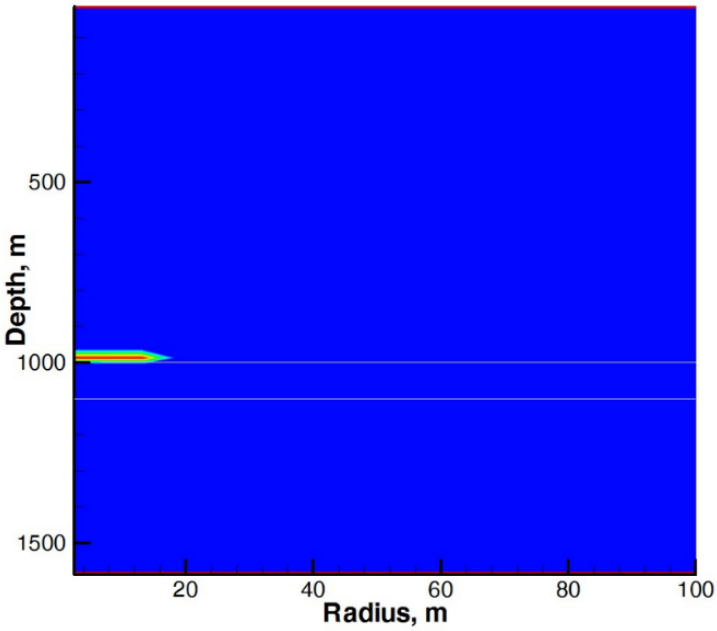

Figure 6.46. Region of caprock failure, just above the aquifer near the axisymmetric center.

Fracture of a Concrete Block

In order to develop a fundamental understanding of CO_2 injection pressure-induced fracturing, we are doing laboratory studies using concrete representations of caprock to determine the correlations between confining stress, fluid pressure and fracturing initialization during CO_2 injection. The equipment used for conducting these experiments includes a tri-axial loading system, an injection pump, and data acquisition devices and has been described in Task 2. Initially, we use injected brine to identify the critical stress needed to initiate fractures in these caprock representations, which are 8 inch cubes that are cored in the center to create a 6 inch bore hole. We simulate one of these experiments, called "Sample 39" in Task 2. The cube initially contains a gaseous phase and its properties are shown in Table 6.6. The bore hole is simulated as a porous medium with much higher permeability than the surrounding concrete.

Table 6.6. Properties for brine injection experiment.

	Concrete	Bore hole
Young's modulus, GPa	6.0	6.0
Poisson's ratio	0.2	0.2
Porosity	0.10	0.90
Permeability, m^2	$1.0 \cdot 10^{-15}$	$1.0 \cdot 10^{-14}$
Biot's coefficient	1.0	0.0
Tensile strength, MPa	2.0	—
Toughness, MPa	0.1	—
Fracture extension *A*, m/sec	10.0	—
Fracture extension *n*	1.0	—

The confining stresses are 1000 psi in x-direction, 1500 psi in y-direction, and 2000 psi in z-direction. The lateral boundaries are at constant pressure and brine is injected at 40 ml/min uniformly along the lower half of the bore hole. The 11x11x11 grid is uniform in size. Since the minimum confining stress is in the x-direction, the concrete block will fracture in the yz-plane that contains the bore hole. We allow fracturing to occur only in that plane, which has the x-direction index of 6 in the grid. Figure 6.37 shows the simulated fracture at a time of 531 seconds. The fracture is initiated along the bore hole and extends outward. After the experiment is completed, the concrete block is dyed and broken apart by nitrogen in order to reveal the fracture induced by fluid injection. Figure 6.38 shows the result of this. The fracture is shown by the darker zone that extends a distance from the bore hole. The simulated fracture is somewhat similar to the experiment in that the overall fracture extents are similar. The simulation is a highly idealized representation of this process and is not expected to match the experiment in detail. For example, the fracture obtained by the experiment is not symmetrical about the bore hole whereas the simulation must be due to the nature of the data input (constant rock properties, and symmetry about the bore hole).

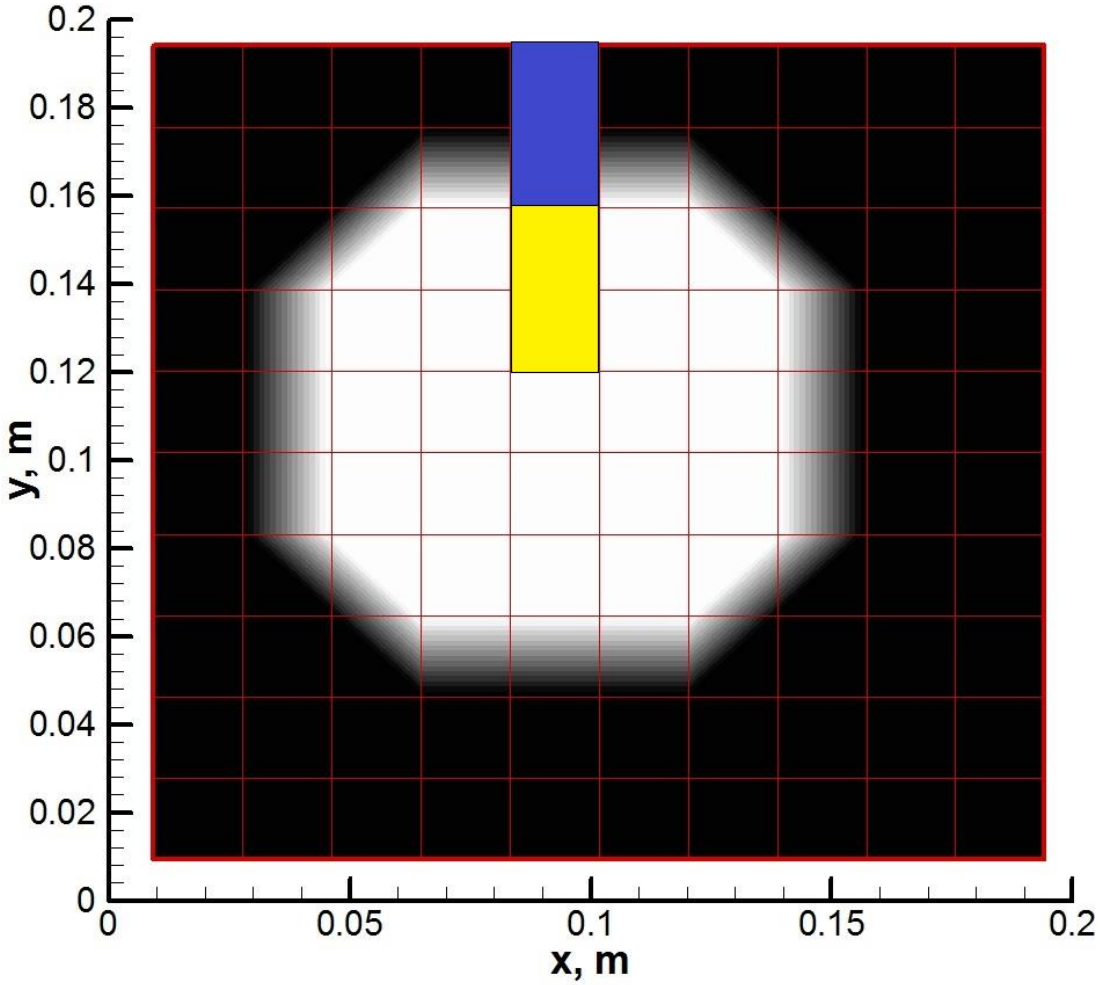

Figure 6.37. Simulated fracture of concrete block. White indicates fracture, bore hole is in yellow and blue, with yellow the perforated region and blue unperforated.

Figure 6.38. Internal fracture morphology of concrete sample after dyeing and gas breakdown.

TOUGH-FLAC Model

Simulation of fracture initiation and growth

A simple but effective approach for modeling fracture growth through the continuum mesh has been adopted. The key features in such an approach are a strain softening tensile behavior and softening of modulus considering a simple damage approach. With the strain softening approach, brittle to more ductile fracture behavior can be simulated by changing the strain softening characteristics.

The aperture changes when the fracture propagates through the continuum mesh is based on a concept of crack-opening-displacement and is related to the tensile strain normal to the fracture plane and the size of the element in a direction normal to the fracture plane. The permeability is governed by a cubic relation between fracture transmissivity and fracture aperture. The variation in fracture aperture along with fracture propagation results in a change in fracture porosity that plays a critical role in determining the fluid storage within the fracture elements along with fracture propagation. The TOUGH-FLAC model is based on sequential coupling between flow and mechanics, and fracture propagation is a problem that is associated with strong pore-volume coupling between flow and mechanics. This is a feature that can be verified against analytical solutions of fluid driven fracture growth.

To verify the model for fluid driven fracture growth we conducted as simulation test against solutions based on the KGD model. The numerical modeling mesh is shown in Figure 6.39. It is 400 by 800 m and with elements dedicated for fracture propagation calculations. We inject water from the left side at a constant rate. The first element of the fracture is made permeable from start so that fluid can penetrate and get the fracture propagation started. Note that the mesh in this case is rather coarse with element lengths of 2 m along the fractures.

The simulation results using TOUGH-FLAC fracture propagation model is in close agreement with the KGD closed form solution, shown in Figure 6.40. Two alternative KGD solutions are shown and the TOUGH-FLAC numerical results fall between the two KGD solutions. Figure 6.41 shows displacement vectors and strain at 40 seconds when the fracture has propagated about 110 m. From the displacements we may calculate aperture and then also the permeability to make sure reasonable values have been obtained in the numerical solution with TOUGH-FLAC.

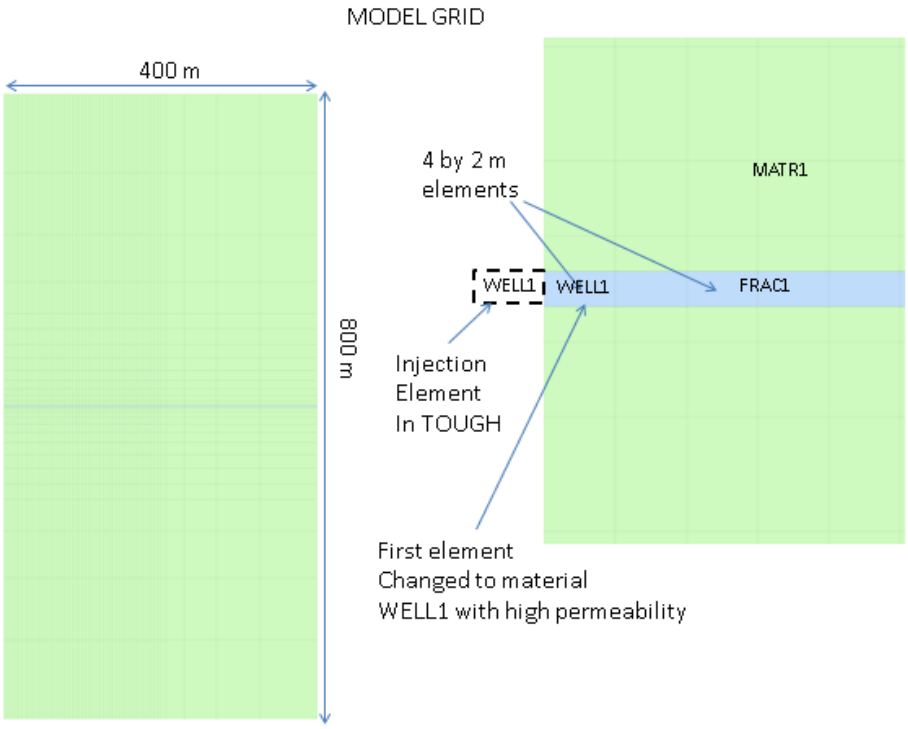

Figure 6.39. Model grid used for verification of TOUGH-FLAC fracture propagation model.

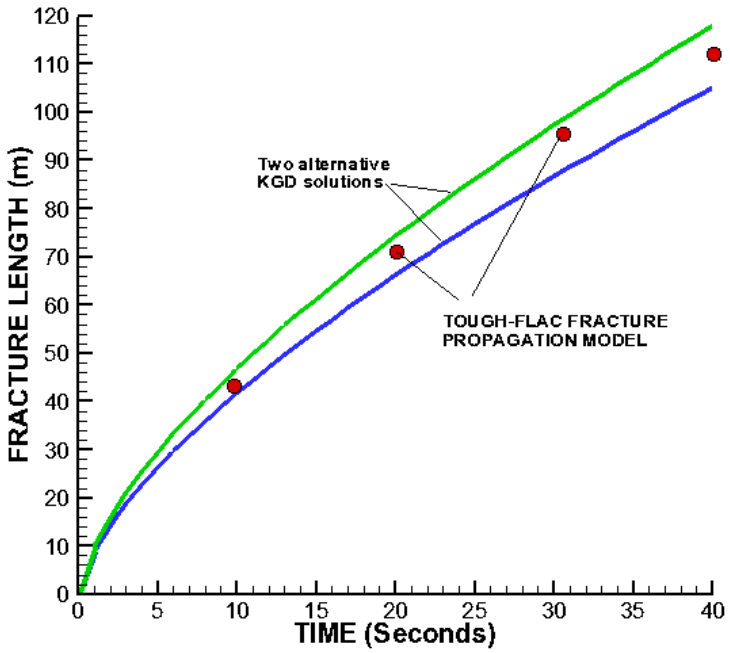

Figure 6.40. Comparison of TOUGH-FLAC fracture propagation results with that of the KGD model.

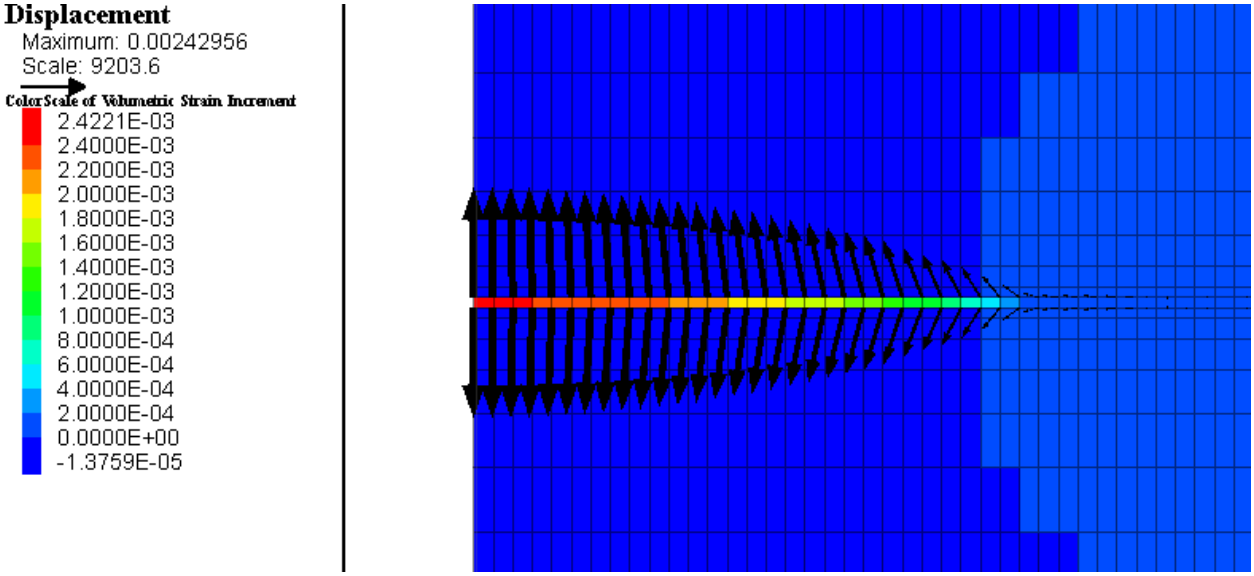

Figure 6.41. Facture displacement (opening) and strain normal to plane of fracture after 40 seconds when the fracture is about 110 m long.

Another way to check the TOUGH-FLAC fracture propagation was to consider a case with an inclined fracture and load it from the boundaries to achieve wing-crack propagation. The vertical compressive boundary stress S_v is 40 MPa, and the ratio *SR* between the horizontal boundary stress S_H and vertical boundary stress S_V was considered to be 0.10, 0.15, 0.20 and 0.25. Figure 6.42 shows simulations of wing-crack propagation for stress ratios of 0.10 and 0.15, and Figure 6.43 shows a comparison of the length *w* of the fracture extension (wing cracks), normalised by the length *f* of the fracture. Results show that the difference between the solution provided by analytical solutions and TOUGH-FLAC is larger for a *SR* equal to 0.10, but it is smaller than 15%.

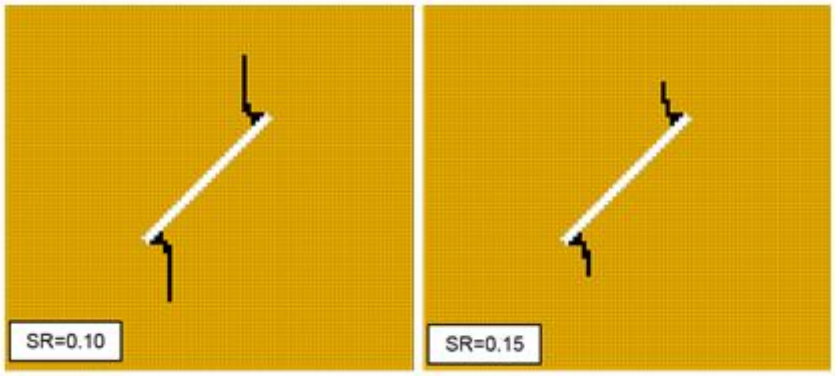

Figure 6.42 TOUGH-FLAC simulations of wing-crack propagation for different stress ratios.

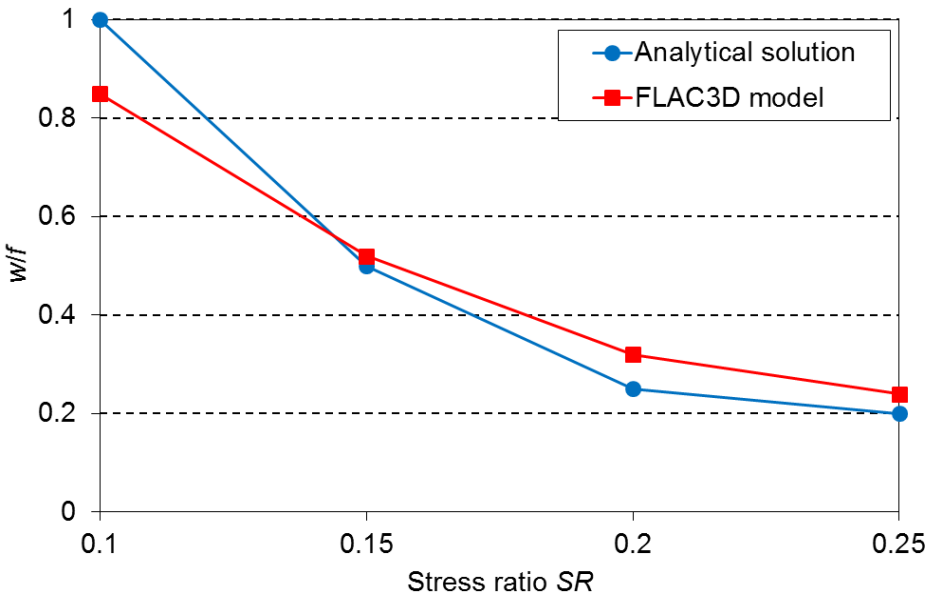

Figure 6.43. Results of fracture lengh versus stress ratio with comparison of numerical and analycal results.

LBNL has expanded to 3D for modeling injection induced fracture propagation around a vertical well, shown in Figure 6.44. The approach is the same as in 2D, including a strain softening tensile behavior and softening of modulus considering a simple damage approach. The simulation represents hydraulic fracturing stress measurement around a vertical well. It is done for verification and validation of the model with plans of comparison to field data.

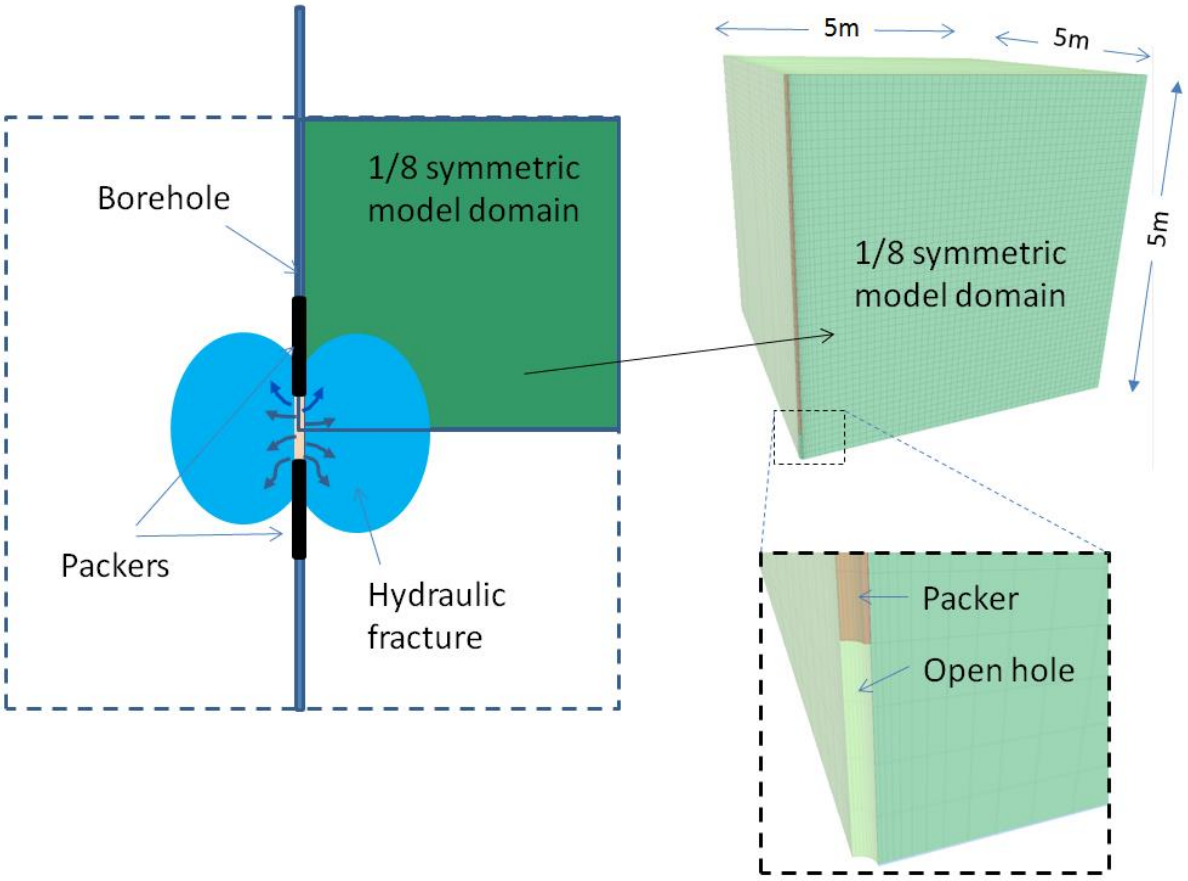

Figure 6.44. TOUGH-FLAC numerical grid for modeling of hydraulic fracturing stress measurement operation from a vertical well.

Figure 6.45 shows the borehole pressure evolution for simulation of a typical break-down cycle of the hydraulic fracturing operation. A constant injection rate of 1.2 liters/minute is simulated (with $1/8^{th}$ of this number in the $1/8^{th}$ symmetric model). The rock has a permeability of 1e-21 m^2 and Young's modulus is 77 MPa. The horizontal stress normal to the fracture was set to 20 MPa, and the stress parallel to the fracture was set to 40 MPa. It takes about 20 seconds to reach break-down, which is signified by the on-set of unstable fracture propagation. The injection then continues at a constant rate until 50 seconds, when the well is shut-in. The simulated shut-in pressure is close to the theoretical value of 20 MPa as this value should be close to the stress normal to the fracture. After 190 seconds, the pressure in the well is relived and the fracture is vented to prepare for re-opening cycle. Figure 6.46 shows the extent of the fracture at the end of the simulation. The fracture has propagated to radius of about 1.6 m. The next step will be to model subsequent re-opening cycles and to compare to analytical simulations on fracture extend for an assumed radial fracture.

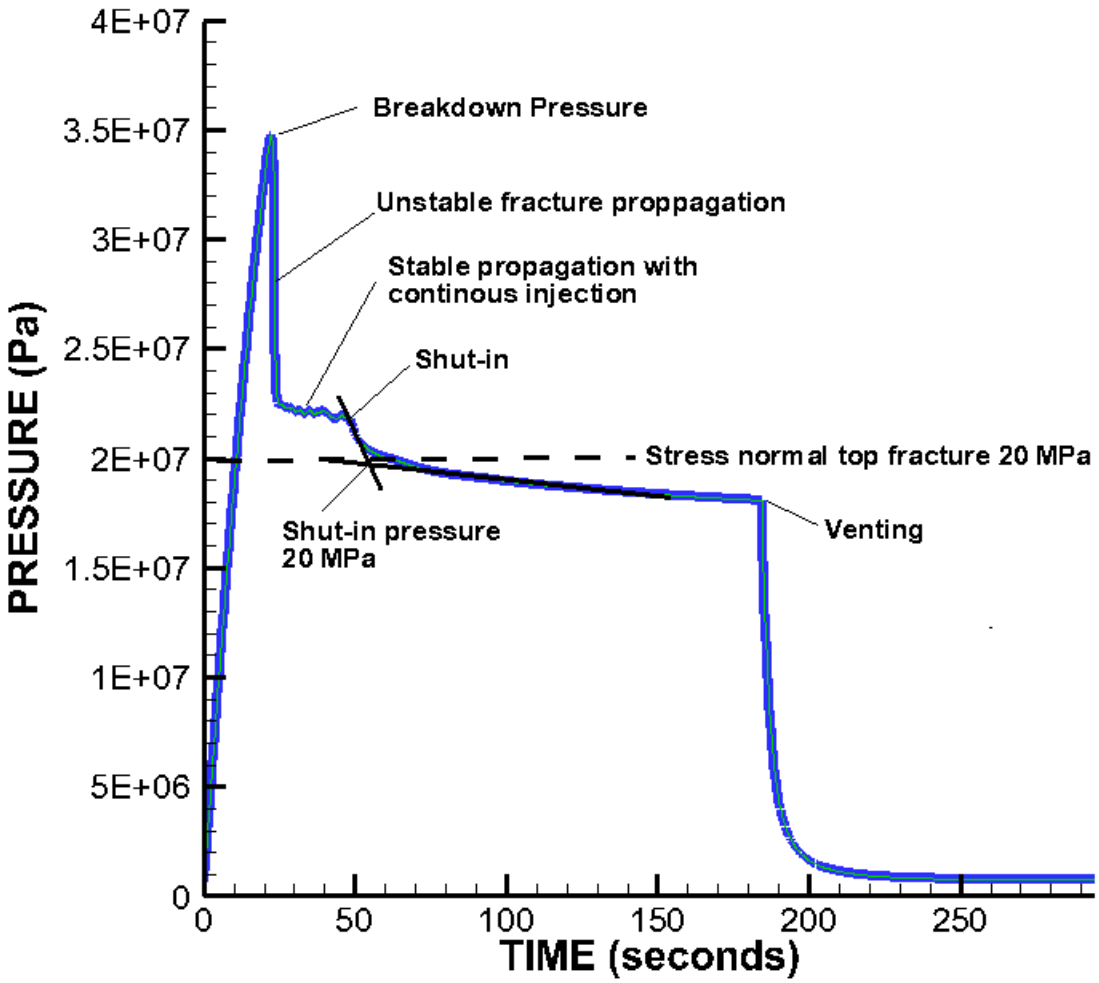

Figure 6.45. Borehole pressure evolution during simulated hydraulic fracturing stress measurement operation showing the first break-down cycle with shut-in and venting.

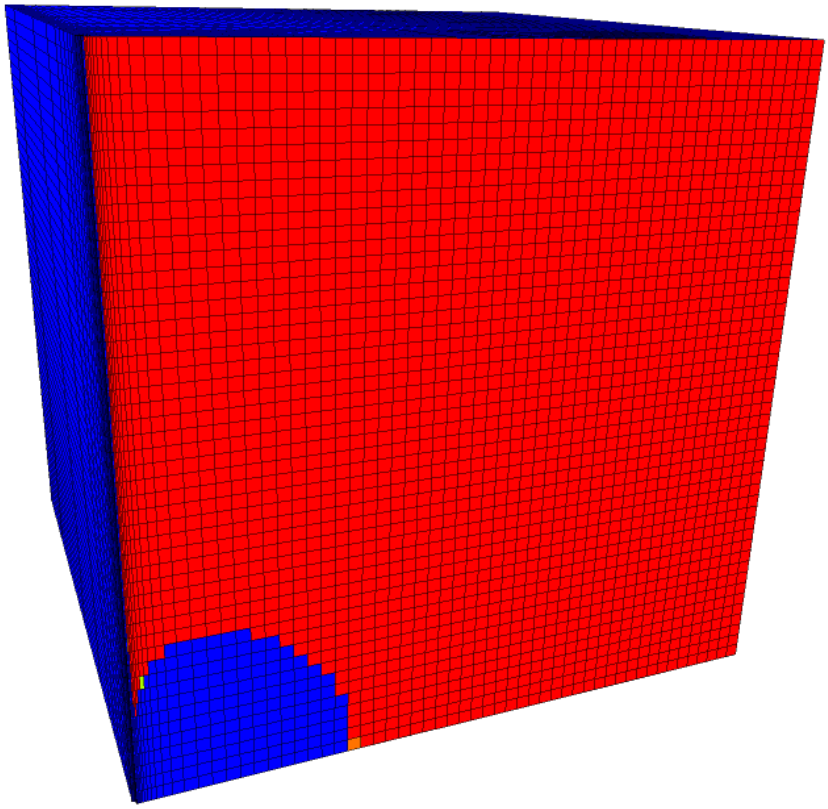

Figure 6.46. Extent of the hydraulic fracture at the end of the simulation.

Validation against deep fracture zone opening and surface uplift at In Salah

A deep fracture zone opening was inferred from field observations at the In Salah CO_2 storage project in Algeria. This feature was first inferred from satellite-based monitoring of ground uplift - one injection well (KB-502) included two parallel uplift lobes rather than one single lobe (Rutqvist et al., 2016). This double-lobe uplift pattern has been interpreted by a number of research groups to signify the opening of a linear feature within and around the injection zone. At the same time, the analysis of a 3D seismic survey indicated that such a fractured zone may indeed intersect the injection well KB-502, with a linear feature visible in the seismic signature up to a few hundred meters above the injection zone (Rutqvist et al., 2016). The linear feature was precisely parallel with the dominant fracturing orientation, exactly perpendicular to the minimum compressive principal stress, and it is well correlated with the double-lobe uplift on the ground surface (Rutqvist et al., 2016). This very precise linear alignment indicates the opening of fractures (which exist in the lower part of the caprock) or a fractured rock zone, or creation of new fractures, rather than opening or reactivation of a fault. A review of the modeling of this case, including TOUGH-FLAC is provided in Rutqvist et al. (2016). Here we present some of the field data and TOUGH-FLAC simulation results for model validation, which should later be used for comparison to TOUGH-CSM modeling results of the same case.

Figure 6.47 shows the TOUGH-FLAC model geometry that has been utilized in several studies of the KB-502 injection and surface deformation data. Figure 6.48 shows examples of comparison between simulation results and field data related to surface uplift. The uplift pattern and evolution

is reasonably well captured with modeling of a fracture zone opening 330 meters up into the overlying caprock. More details can be found in Rutqvist et al., (2016).

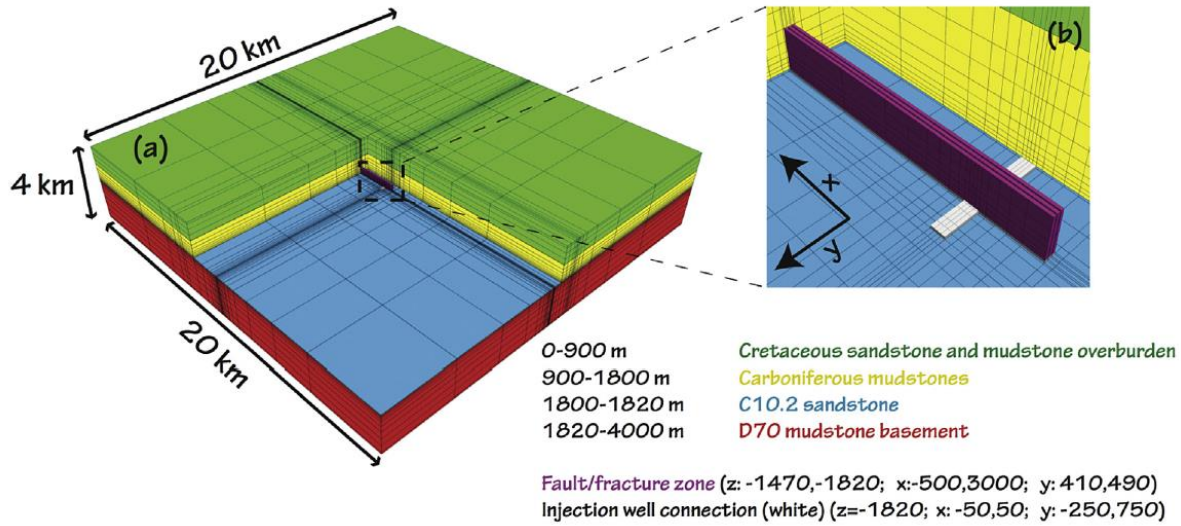

Figure 6.47. Computational domain. (a) 3D model with four hydrogeological formations. (b) Enlargement of the fracture zone, whose length along the x-direction depends on the simulation (Rutqvist et al., 2016).

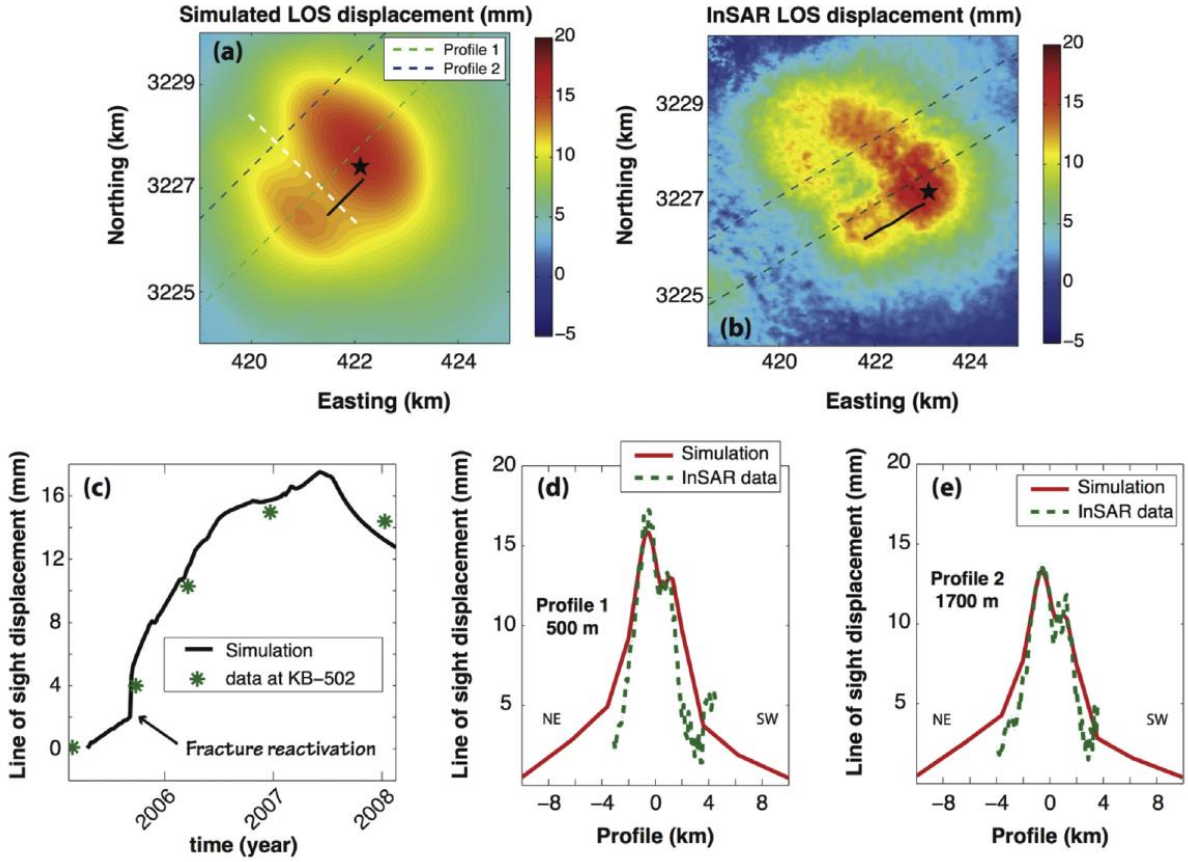

Figure 6.48. Comparison between TOUGH-FLAC simulated displacement and InSAR data (Rutqvist et al., 2016). (a) Resulting displacement in the satellite line of sight. Black segment represents the KB-502 injection well. White, dashed segment represents the simulated fracture zone direction. Green and blue, dashed lines represent the direction of two profiles for the comparison with InSAR data at 500 m and 1700 m from the injection well, respectively. (b) InSAR data after 618 days of injection (23 December 2006). (c) Comparison between simulated and observed ground surface uplifts. (d) Comparison between simulation (red line) and InSAR data (green dashed line) along the profile 1 (500 m from the injection well). (e) Comparison between simulation (red line) and InSAR data (green, dashed line) along the profile 2 (1700 m from the injection well).

We have now extended this analysis and performed an inverse analysis that improves the previous modeling approach by introducing an injection reservoir and a fracture zone, both responding to a Mohr-Coulomb failure criterion. In addition, we model a stress-dependent permeability and bulk modulus, according to a dual continuum model. Mechanical and hydraulic properties are determined through inverse modeling by matching the simulated spatial and temporal evolution of uplift to InSAR observations as well as by matching simulated and measured pressures. The inverse modeling was conducted using iTOUGH-PEST (Finsterle and Zhang, 2011) and TOUGH-FLAC (Rutqvist, 2011). A full description can be found in a paper that is now in press (Rinaldi et al., in press), whereas a brief summary of the results related to KB-502 well is presented here.

In the inverse modeling approach used here, the program iTOUGH2 is used as parameter estimation and optimization framework for the TOUGH-FLAC coupled fluid flow and geomechanics simulator. The coupling approach between the two codes is illustrated in Figure 6.49 (Rinaldi et al., in press). A parameter set estimation is performed in a series of iterations. For a single iteration, parameters to be calibrated (such as permeability, coupling parameters, and/or mechanical parameters) are given by iTOUGH2, which calls a PEST protocol to write input files needed for running TOUGH-FLAC. After completion of the forward run, a PEST protocol follows instructions to extract from the forward model output files. Finally the simulated values are analyzed in iTOUGH, which computes residuals with observation and calculates the parameters set for the next iteration. Some example of the results for the KB-502 well is shown in Figure 6.50, including comparison between simulated and observed data, and standard deviation reflecting data uncertainty. The figure shows that the numerical simulations are in agreement with both spatial and temporal observations.

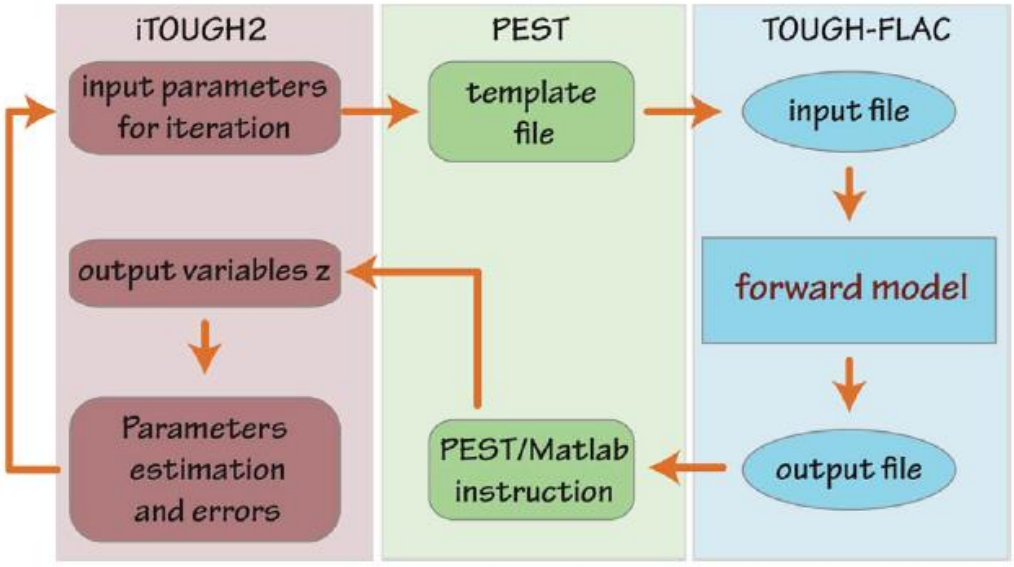

Figure 6.49. Scheme for inverse modeling iterations in iTOUGH2-PEST with TOUGH-FLAC (Rinaldi et al. in press)

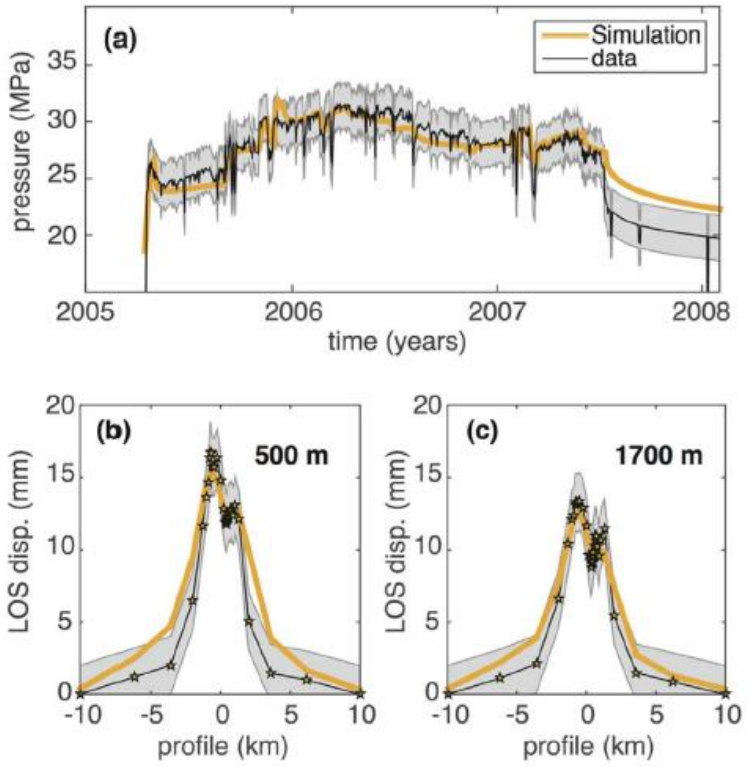

Figure 6.50. Comparison between simulated and observed data at KB-502: (a) temporal evolution of bottomhole pressure, (b) profile of ground uplift at 500 m after 618 days, (c) profile of ground uplift at 1700 m after 618 days. The gray area represents the 1 standard deviation (2 MPa and 2 mm for pressure and LOS displacement, respectively). (Rinaldi et al., in press).

Task 7: Development, implementation and application of advanced modeling and optimization schemes to maximize storage capacity and to identify leaking locations.

Optimization Algorithm

In this section, we develop a scheme that can be used to identify caprock leakage. Injection of fluid into a reservoir results in a time varying pressure profile that depends on the properties of the rock and the fluid. The presence of significant caprock leakage would effect this pressure profile, and we use inverse modeling to determine the leakage location from the pressure profile. Inverse modeling consists of estimating parameters, for example caprock leakage location, from measurements of the system response made at discrete points in space and time, for example pressure. This is formulated as an optimization problem, where the residual vector is the difference between "observed" and calculated quantities:

$$r_i = z_i^{obs} - z_i^{calc} \tag{7.1}$$

where *z* refers to that quantity. The measure of how the calculated and observed quantities match is the objective function, *S*, which is the sum of the residual squares over the observations:

$$S(\bar{p}) = \frac{1}{2}\sum_i r_i^2 \tag{7.2}$$

where $\bar{p}$ is the parameter vector.

We iterate on $\bar{p}$ where:

$$\bar{p}_{l+1} = \bar{p}_l + \Delta\bar{p}_l \tag{7.3}$$

An increment $\Delta\bar{p}_l$ must satisfy:

$$S(\bar{p}_{l+1}) < S(\bar{p}_l) \tag{7.4}$$

Expanding $S(\bar{p})$ in a Taylor series yields:

$$S(\bar{p}_{l+1}) = S(\bar{p}_l) + \bar{g}_l^t\Delta\bar{p}_l + \frac{1}{2}\Delta\bar{p}_l^t\bar{\bar{H}}_l\Delta\bar{p}_l \tag{7.5}$$

where $\bar{g}_l$ is the gradient vector and $\bar{\bar{H}}_l$ is the Hessian matrix. An element of the parameter vector is:

$$(\bar{p}_l)_k = p_{k,l} \tag{7.6}$$

An element of the gradient vector is:

$$(\bar{g}_l)_k = \sum_i r_i \frac{\partial r_i}{\partial p_{k,l}} \tag{7.7}$$

An element of the Hessian matrix is:

$$\left(\bar{\bar{H}}_l\right)_{jk} = \sum_i r_i \frac{\partial^2 r_i}{\partial p_{j,l} \partial p_{k,l}} + \frac{\partial r_i}{\partial p_{j,l}} \frac{\partial r_i}{\partial p_{k,l}} \tag{7.8}$$

The minimum for $S(\bar{p})$ is obtained when:

$$\bar{\bar{H}}_l \Delta \bar{p}_l = -\bar{g}_l \tag{7.9}$$

It is desirable to avoid calculating the exact Hessian matrix in Equation 7.8 because it has second derivative terms. In the Levenberg-Marquardt method (Levenberg, 1944; Marquardt, 1963), these second derivative terms are replaced by a diagonal matrix, the Levenberg parameter, λ, times the square of the residual derivative:

$$\left(\bar{\bar{H}}_l\right)_{jk} = \sum_i \delta_{jk} \lambda_k \frac{\partial r_i}{\partial p_{j,l}} \frac{\partial r_i}{\partial p_{k,l}} + \frac{\partial r_i}{\partial p_{j,l}} \frac{\partial r_i}{\partial p_{k,l}} \tag{7.10}$$

The Levenberg parameters are adjusted after each iteration. If the objective function increases, violating Equation 7.4, the Levenberg parameters are increased and the iteration is repeated; if the objective function decreases, the iteration is accepted and the Levenberg parameters are decreased. The derivatives of the residuals are approximated as:

$$\frac{\partial r_i}{\partial p_{k,l}} \approx \frac{r_i(p_{k,l}+\omega_k) - r_i(p_{k,l})}{\omega_k} \tag{7.11}$$

where ω_k is the increment for parameter $p_{k,l}$.

Two-Dimensional Example

We ran a problem based on simulations from Rutqvist and Tsang (2002) to identify caprock leakage location. They simulated CO_2 injection into a hypothetical two-dimensional aquifer-caprock system consisting of a 200 m thick aquifer bounded below by 1500 m thick base rock and above by 100 m caprock and a 1200 m upper zone that extends to the surface. Properties of these rock layers are shown in Table 7.1.

Table 7.1. Rock properties for aquifer-caprock system.

Property\Layer	Upper	Caprock	Aquifer	Base
Young's modulus, GPa	5.0	5.0	5.0	5.0
Poisson's ratio	0.25	0.25	0.25	0.25
Biot's coefficient	1.0	1.0	1.0	1.0
Porosity	0.094	0.0094	0.094	0.0094

Permeability, m^2	$4.0 \cdot 10^{-16}$	$4.0 \cdot 10^{-20}$	$4.0 \cdot 10^{-14}$	$4.0 \cdot 10^{-18}$

The caprock also had a vertical fault, simulated as a high permeability zone, located near the lateral center through which leakage could occur. The fault permeability was 10^{-12} m^2.

Our simulation domain was subdivided into a 201x100 grid with grid block dimensions shown in Tables 7.2 and 7.3. Thickness in the z-direction is smallest in the aquifer and its vicinity. Thickness in the x-direction is smallest at the lateral center. The first and last columns of grid blocks are maintained at constant pressure.

Table 7.2. Grid block thickness in the z-direction.

Thickness, m	Number of rows	Rock zone
60	10	Upper
40	10	Upper
20	10	Upper
10	10	Caprock
10	20	Aquifer
20	10	Base
40	10	Base
45	20	Base

Table 7.3. Grid block thickness in the x-direction.

Thickness, m	Number of columns
1600	10
800	10
400	10
200	10
100	10
50	101
100	10
200	10
400	10
800	10
1600	10

CO_2 was injected at a constant rate at the aquifer bottom and lateral center (column 101, layer 60) for ten years. The fault was located at column 103, layers 31-40, and it spaned the caprock height.

We first ran the simulation as described above and used the results as observed data. Then, we ran simulations where we assumed we had no knowledge of the fault location and tried to determine it from inverse modeling. Specifically, the observed data used for inverse modeling was average pressure over the duration of the simulation at three "observation" grid blocks (column index, row index): (50,40), (70,40), and (90,40). These grid blocks are all at the caprock bottom and are 2558,

1563, and 585 m from the injection well, respectively. The actual pressures versus time are shown in Figure 7.1.

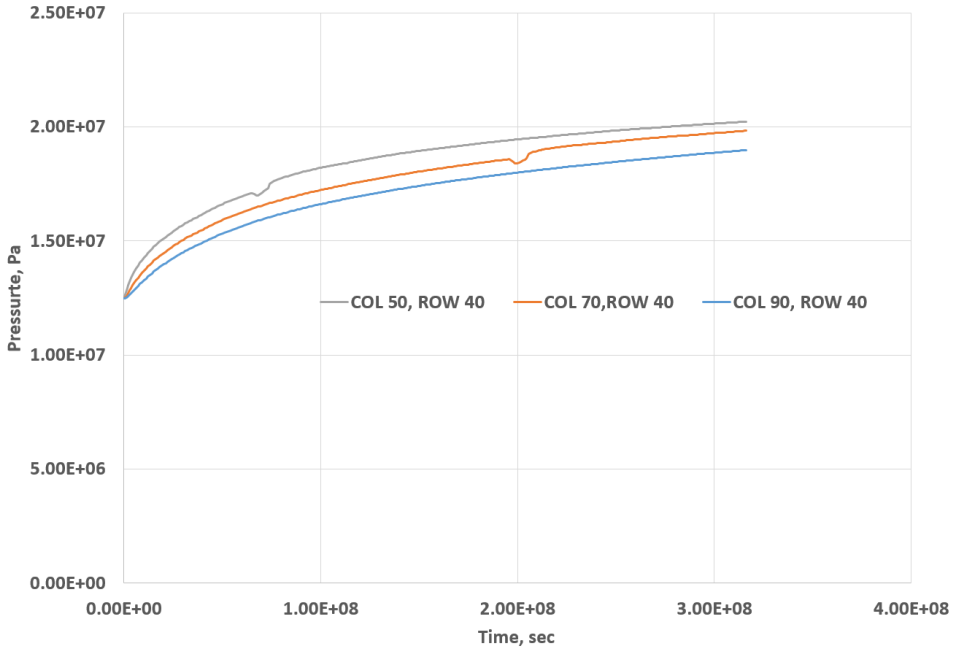

Figure 7.1. Pressure versus time for three "observation" grid blocks. Inverse modeling parameters are time averages of these pressures.

The parameter to be obtained from inverse modeling was the fault location, namely its column index. Our residual vector then was the difference between "observed" and simulated average pressure:

$$r_i = \bar{P}_i^{obs} - \bar{P}_i^{calc}(K) \tag{7.12}$$

where the parameter vector consists of index *K*, the fault column index.

Table 7.4 shows the application of the Levenberg-Marquardt method to this problem. In iteration 1, we arbitrarily choose column 60 as the starting point (iteration 1, K_1). The residual derivatives were approximated by incrementing the column index by -1. The objective functions are shown next, and then λ, which was arbitrarily chosen as 1.0 for the first iteration. The resulting increment for K is calculated using Equation 7.9, which determines K_1 for the second iteration. Since the objective function in the second iteration has decreased, λ is reduced by a factor of ten. Finally, the information for the third iteration is shown. One of the objective functions in that row is zero, so the problem is solved.

Table 7.4. Iterations for Levenberg-Marquardt method.

Iteration	K_1	$K_1+\Delta K$	$S(K_1)$	$S(K_1+\Delta K)$	λ

1	60	59	$6.92 \cdot 10^{10}$	$6.99 \cdot 10^{10}$	10^{0}
2	111	110	$4.46 \cdot 10^{9}$	$3.32 \cdot 10^{9}$	10^{-1}
3	104	103	$4.65 \cdot 10^{7}$	0	10^{-2}

Three-Dimensional Example

We also ran a three-dimensional case for identifying leakage location. The reservoir was based on that in Rutqvist et al. (2010). The simulation domain was 10 by 10 km in area and 4 km in depth with a 1.5 km injection well at a depth of 1810 m below the surface, oriented in the x-direction, and whose middle was at the areal center of the grid. There were four geological layers, Shallow Overburden (0–900 m), Caprock (900–1800 m), Injection Zone (1800–1820 m), and Base (below 1820 m). Properties of each geological layer are shown in Table 7.5

Table 7.5. Geological layer properties for InSalah CO_2 injection.

Property	Shallow Overburden	Caprock	Injection Zone	Base
Young's modulus, GPa	1.5	20.0	6.0	20.0
Poisson's ratio	0.2	0.15	0.2	0.15
Biot's Coefficient	1.0	1.0	1.0	1.0
Porosity	0.1	0.01	0.17	0.01
Permeability, m^2	$1.0 \cdot 10^{-14}$	$1.0 \cdot 10^{-19}$	$1.0 \cdot 10^{-14}$	$1.0 \cdot 10^{-21}$
Residual CO_2 saturation	0.05	0.05	0.05	0.05
Residual liquid saturation	0.3	0.3	0.3	0.3
Van Genuchten m	0.457	0.457	0.457	0.457
Van Genuchten, P_0, kPa	19.9	621.0	19.9	621.0

The simulation grid was 100x100x20 with uniform areal dimensions of 100 m. The Injection Zone was subdivided into five 4 m layers and layer thickness increased away from that zone. The injection rate of CO_2 was 2.433 kg/sec for three years.

We simulated fractures as high permeability (10^{-12} m^2) gridblocks with otherwise the same properties as the surroundings. We introduced a 1 km long fracture that spanned the Caprock depth, ran along the y-direction, and whose edge was 1200 m from the areal center in the x-direction and 700 m from it in the y-direction. In terms of grid block indices, the injection well was in layer 14, row 50, and columns 43 through 57. The fracture was in column 62, rows 57 through 66, and layers 4 through 11.

Figure 7.2 shows the pressure profile for the layer containing the injection well (layer 14). The horizontal line denotes the injection well and the vertical line denotes the projection of the fracture onto this layer.

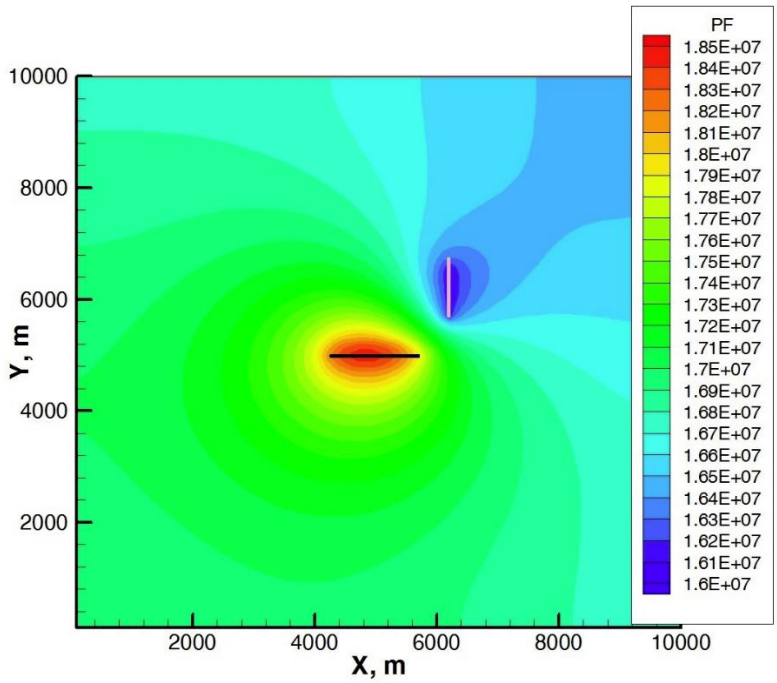

Figure 7.2. Pressure profile in the layer containing the injection well (layer 14) for the "field data" case after three years. The horizontal line denotes the injection well, the vertical one the projection of the fracture onto this layer.

This simulation supplies the "field data" that shows leakage through a fracture in the Caprock. We apply our inverse modeling algorithm to determine to location and length of the fracture. We "measure" pressure at five locations, all at the injection well depth (layer 14) and one at the areal center (row 50, column 50) plus the four points located 1500 m in the x-direction and 1500 m in the y direction from the areal center (row 35, column 35; row 35, column 65; row 65, column 35; row 65, column 65). In addition, we assumed the orientation of the fracture (along the y-direction) was given. The parameters we wanted to obtain from inverse modeling were the fracture x-direction position (column) and the fracture length (starting and ending rows).

Our residual vector is the difference between "observed" and simulated pressures at the end of the simulation:

$$r_i = P_i^{obs} - P_i^{calc}(\bar{K}) \tag{7.13}$$

where $\bar{K}$ is a vector containing the fracture column and starting and ending rows. As before, we use the Levenberg-Marquardt method to obtain this minimum. We approximate derivatives with respect to elements of $\bar{K}$ using Equation 7.11 with the increments being one.

In our first simulation, the fracture is arbitrarily located in column 50, rows 32 through 36. The pressure profile for that simulation after three years is shown in Figure 7.3.

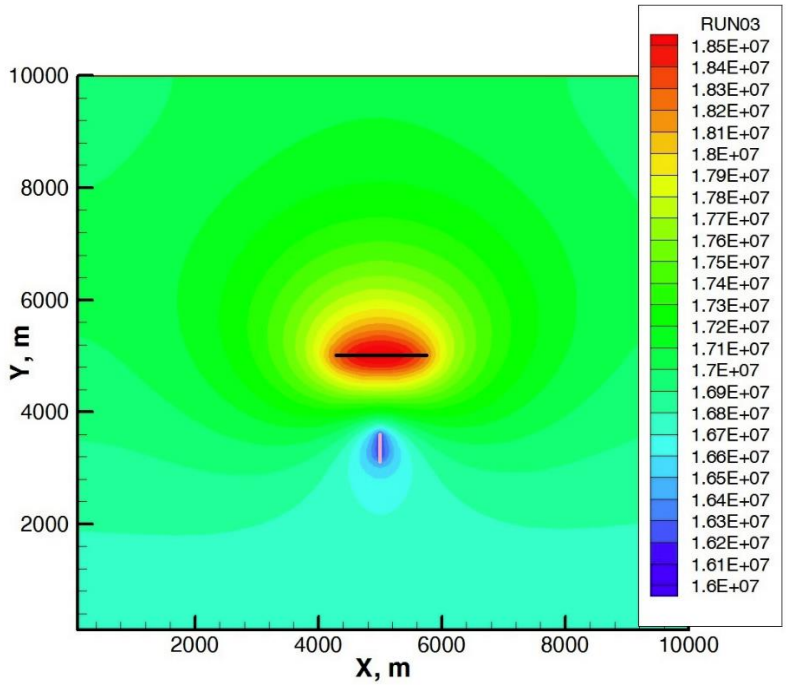

Figure 7.3. Pressure profile in the layer containing the injection well (layer 14) after three years for the fracture located in column 50 and rows 32 through 36.

Three such simulations were run along with the one above to obtain the needed derivatives. The gradient and Hessian were calculated, and the updated fracture location was column 55, rows 40 through 47. The pressure profile for that simulation after three years is shown in Figure 7.4.

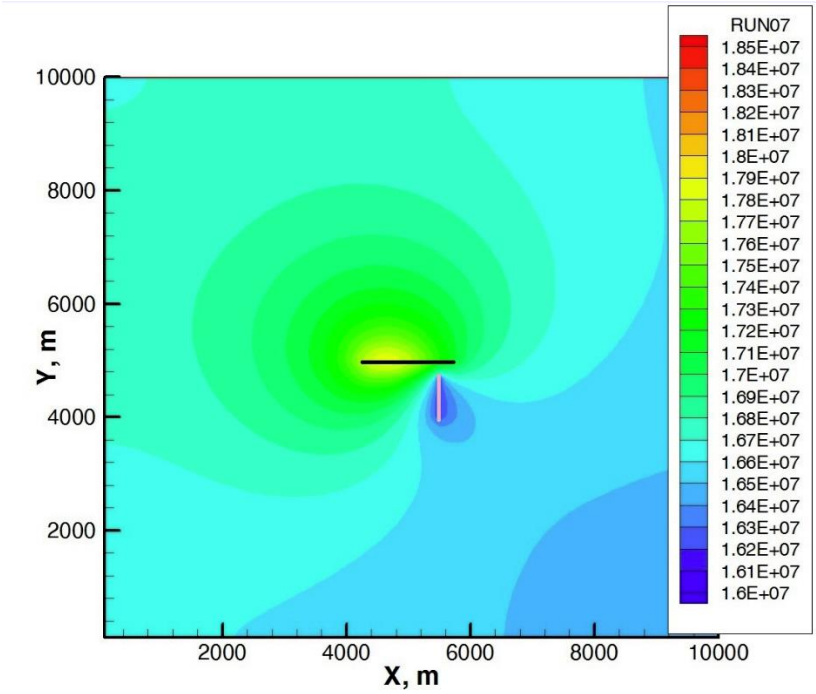

Figure 7.4. Pressure profile in the layer containing the injection well (layer 14) after three years for the fracture located at column 55 and rows 40 through 47.

This process was repeated until convergence to the "field data" after eight iterations. Table 7.6 shows the fracture location parameters for all of the simulations after three years and Figure 7.5 shows the corresponding pressure profiles.

Table 7.6. Fracture location parameters for each simulation.

Simulation	Column	Starting Row	Ending Row
1	50	32	36
2	55	40	47
3	61	37	44
4	60	38	45
5	58	45	53
6	63	53	66
7	61	55	66
8	62	57	66

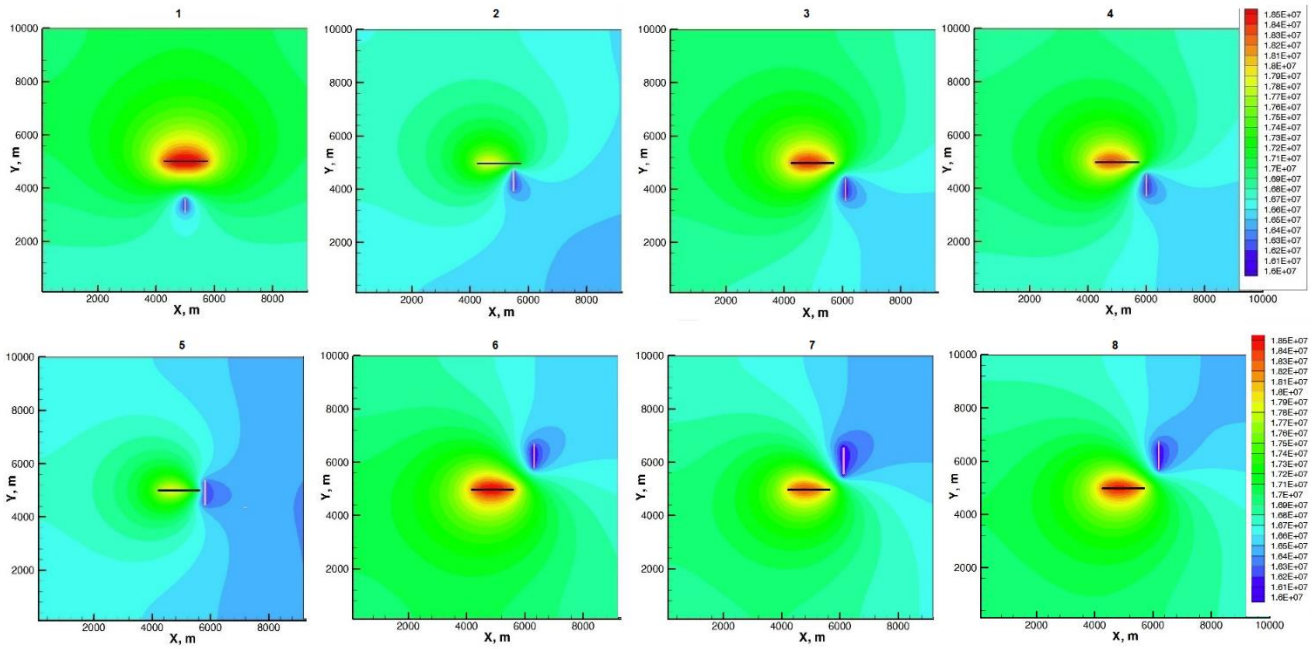

Figure 7.5. Pressure profiles for simulations in Table 7.6. Number 8 has converged to the "field data" case in Figure 7.3.

Conclusions

In Task 2, we did laboratory studies on the effects of geomechanics on CO_2 flow and transport properties in fractured rock by quantifying the correlation between mean effective stress and fracture effective permeability and porosity. We began by measuring rock properties (porosity, permeability, elastic constants, strength, and heat capacity) for three different rock types (concrete, sandstone and shale). Then, using the Brazilian technique to fracture samples, we measured their permeability under brine injection for varying effective stresses, followed by similar measurements of permeability under sc-CO_2 (super critical CO_2) injection. Permeability to brine and sc-CO_2 decreased as the effective stress increased. The apparent permeability to sc-CO_2 was an order of magnitude less than that for brine, a consequence of CO_2 being the non-wetting fluid.

In Task 3, we conducted laboratory studies of CO_2 and brine injection induced fracturing, obtaining the fracture initiation condition due to CO_2 injection as well as the dynamics of fracture propagation, for implementation in the thermo-hydrological-mechanical simulators. In our analysis of the failure of the concrete samples, we found that shear failure is the predominant failure mode, with a few of the samples undergoing tensile failure. Consequently, we incorporated both shear and tensile failure into our thermo-hydrological-mechanical simulators for modeling caprock failure.

Some concrete samples had pre-existing fractures that would be perpendicular to the CO_2 injection induced fractures. These pre-existing fractures had little to no effect on the fracture initiation pressure, but changed the fracture morphology significantly, causing the CO_2 induced fractures to deviate from their preferred plane and become tilted.

Some concrete samples were water saturated. The extent of CO_2 induced fractures in these samples are generally limited to a relative small area when compared to the other samples, which were dry. This limitation on the volume that injected CO_2 can reach is probably due the reduction in relative permeability from the presence of water and CO_2 phases, as opposed to a single CO_2-rich phase.

Some concrete samples were composite samples with a high permeability and low strength volume. The breakdown pressures of these samples were noticeably lower than the others. The high permeability volume acted as a pressure equalizer during fracturing.

The concrete samples were fractured with either CO_2 or brine. The breakdown pressure for CO_2 induced fracturing was generally around the minimum horizontal stress, i.e. tensile strength was not important. This might be due to the presence of cracks around wellbore that only allow CO_2 to enter due to its low viscosity and low interfacial tension. Once the CO_2 would enter those cracks, it would only need to overcome friction and minimum horizontal stress to propagate existing fractures instead of initiating new fractures. The breakdown pressure for brine induced fracturing was generally greater than that for CO_2. In addition, this result was specific to the imposed stresses of 1000 psi in the x-direction, 1500 psi in the y-direction, and 2000 psi in the z-direction.

Finally, fracture orientation is mostly dominated by confining stress. For most samples with large confining stress differential, the fracture planes were perpendicular to the minimum stress direction. When the stress differential, especially the difference between two smallest stresses, was small, the fracture orientation depended additionally on the magnitude of the confining stress, tensile strength of the rock, and break down pressure. In addition, when the stress differential was larger than the tensile strength of the rock and the maximum stress was much higher than the break down pressure, the fracture plane was perpendicular to the minimum stress direction; otherwise the fracture plane deviated from that direction.

In Tasks 4, 5, and 6, we developed and validated CO_2 flow and geomechanics-coupled models for modeling fracture growth by implementing approaches for modeling fracture propagation into the existing multiphase flow and geomechanics simulators, TOUGH2-CSM and TOUGH-FLAC. TOUGH2-CSM initially had a simplified geomechanical formulation that consisted of the Mean Stress equation and geomechanics was described only be the mean stress and volumetric strain. We extended this formulation to calculate the entire stress tensor efficiently and derived a finite difference approximation applicable to varying rock properties, i.e. Poisson's ratio. Approaches for modeling fracture propagation were then implemented in TOUGH2-CSM and TOUGH-FLAC and simulations were done to verify these approaches and apply them to field cases. This work represents a significant advance in modeling fracture propagation in the porous and fractured media.

In Task 7, we developed an inverse model to determine leakage location when an induced leakage occurs in a reservoir. Our model was successful in determining leakage location, which was based on changes in the pressure field resulting from this leakage. However, this was not the major emphasis of the project and much more work can be done in this area.

Goals versus Accomplishments

In Task 2, our goals were to do laboratory studies on the effects of geomechanics on CO_2 flow and transport properties in fractured rock by quantifying the correlation between mean effective stress and fracture effective permeability and porosity. We planned to accomplish this by obtaining reasonable representative rock cores, such as sandstone for reservoir cores and shale for caprock cores, and characterize them physically and mineralogically. Then, we would fracture the rock cores using the Brazilian method, reassemble with thin shims to create an aperture, and after installing the fractured rock cores in the appropriate apparatus, X-ray CT scan the cores to provide initial fracture aperture maps, and saturate with brine and measured single-phase permeability versus effective stress using brine as the flowing fluid. Later, following a similar procedure, the cores will be saturated with brine and effective permeability with be measured versus effective stress using sc-CO_2 as the flowing fluid. In addition, several loading and unloading tests will be done to examine possible wettability change effects.

All of these goals have been accomplished. We obtained core samples for three different rock types, concrete, sandstone and shale, and measured their rock properties (mechanical moduli, permeability, porosity, tensile strength, uniaxial compressive strength, heat capacity) using a variety of techniques (acoustic test, permeability and porosity measurement, Brazilian test, uniaxial compression test, and heat capacity measurement). Then, we used the Brazilian technique

to fracture the cores, placed spacers at the open corners, placed the core in a core holder, and measured permeability versus effective stress for flow of brine and sc-CO_2 under various loadings. In addition, we used X-ray CT scanning at each effective stress to observe the fracture aperture and fluid saturation in the fracture.

In Task 3, our goals were to conduct laboratory studies of CO_2 and brine injection induced fracturing, namely obtaining the fracture initiation condition due to CO_2 injection as well as the dynamics of fracture propagation, for implementation in the thermo-hydrological-mechanical simulators. We planned to accomplish this using brine and CO_2 under various stress and temperature conditions to identify the critical stress needed to initiate fractures in rocks that are representative of typical storage formations, and modify and employ dimensionless parameters or scaling laws to study quasi-static fracture propagation and investigate the effect of heterogeneities.

The laboratory studies of CO_2 and brine injection induced fracturing have been accomplished. We obtained the equipment to do this fracturing, including a tri-axial loading system, an injection pump, data acquisition devices, and acoustic measurement devices. We fractured concrete samples with brine under varying flowrates and tri-axial stresses and obtained breakdown pressure, acoustic data that would confirm the existence of fractures, and internal fracture morphology. Next, we used sc-CO_2 to fracture the concrete samples, with some having a composite structure intended to approximate caprock with a high permeability zone. Finally, we used sc-CO_2 to fracture the six shale samples under varying conditions. Analyses of the results from these experiments indicated most of the samples were fractured due to shear failure. Unfortunately, we were unsuccessful in the application of scaling laws to quasi-static fracture propagation.

In Tasks 4 and 5, our goals were to develop CO_2 flow and geomechanics-coupled models for modeling fracture growth by implementing approaches for modeling fracture propagation into the existing multiphase flow and geomechanics simulators, TOUGH-CSM and TOUGH-FLAC. We planned to accomplish this by conducting a thorough literature review of results from existing laboratory studies and theoretical development of criteria for fracture initiation, and growth and propagation, and based on the literature review results and theoretical analyses, modify the simulators to enable them to simulate fracture initiation, and fracture growth and propagation. Then, we would incorporate CO_2 injection-enhanced property and fracture correlations/models into the reservoir simulators by implementing approaches for mechanically induced changes in multiphase flow properties, e.g. how permeability changes with stress, and implement those into the existing multiphase flow and geomechanics simulators TOUGH-CSM and TOUGH-FLAC.

All of these goals have been accomplished. We extended the simplified TOUGH2-CSM geomechanical formulation to calculate the entire stress tensor, which would be needed when modeling fracture propagation and mechanically induced changes in multiphase flow properties. We did a literature survey to determine suitable correlations for fracture initiation, growth, and propagation and used the results to modify TOUGH2-CSM to simulate shear failure in faults and caprock, tensile failure, and fracture propagation. TOUGH-FLAC was modified to model stress-dependent fracture initiation, and growth and propagation based on the FLAC3D ubiquitous joint model, extended for the modeling of permeability changes induced by changes in effective normal stress across fracture as well permeability changes caused by shearing along fractures.

In Task 6, our goals were to validate our flow-mechanics coupled models using field data of stress and rock deformation measurement, as well as analytical solutions and problems from the literature.

All of these goals have been accomplished. Our TOUGH2-CSM modifications were validated using analytical solutions, including the displacement from a uniform load on semi-infinite elastic medium and the Mandel-Cryer effect, and problems from the literature, including the depletion of a single-phase reservoir, a reservoir with induced thermal stresses, caprock failure in an aquifer-caprock system, and validated against deep fracture zone opening and surface uplift at In Salah. Application of the model to a generic large-scale sequestration site was done for In Salah as well. In addition, the TOUGH-FLAC fracture growth modifications were verified against solutions based on the KGD model and it too was validated against deep fracture zone opening and surface uplift at In Salah.

In Task 7, our goals were to develop modeling tools for identification of potential leakage risks, considering reservoir heterogeneity and the complex CO_2 phase behavior at the reservoir scale in order to develop an inverse model to quickly and effectively maximize storage capacity, predict performance, and determine leakage location when an induced leakage occurs.

All of these goals have been accomplished. We used the Levenberg-Marquardt method to identify parameters through inverse modeling. We applied that method to determining leakage location for a two-dimensional example, and for a three-dimensional example, leakage location and leakage zone length.

References

Abousleiman Y., Cheng, A. H.-D., Cui L., Detournay, E., Roegiers, J.-C., 1996. Mandel's Problem Revisited. Géotechnique **46** (2), 187-195.

ASTM D3967-08 Standard Test Method for Splitting Tensile Strength of Intact Rock Core Specimens

Cappa, F. and Rutqvist, J., 2011. Modeling of coupled deformation and permeability evolution during fault reactivation induced by deep underground injection of CO_2, International Journal of Greenhouse Gas Control, 5, 336–346

Chen, Y., Nagaya, Y. and Ishida, T. 2015. Observations of Fractures Induced by Hydraulic Fracturing in Anisotropic Granite. Rock Mechanics and Rock Engineering, 48**,** 1455-1461.

Davies, J.P. and Davies, D.K., 2001. Stress-dependent permeability: characterization and modelling. SPE Journal 6:2, pp. 224-235.

Dean, R. H., Gai, X., Stone, C. M., and Minkoff, S. E. 2006. A Comparison of Techniques for Coupling Porous Flow and Geomechanics. SPE Journal, March, 132-140.

Finsterle, S., Zhang, Y., 2011. Solving iTOUGH2 simulation and optimization using PEST protocol. Environ. Modell. Softw. 26 (7), 959–968.

Garipov, T.T, Karimi-Fard, M., and Tchelepi, H.A., 2014. ARMA 14-7460: Fully coupled flow and geomechanics model for fractured porous media, presented at the 48th US Rock Mechanics / Geomechanics Symposium, Minneapolis, MN, June 1-4.

Goodzari, S., Settari, A., and Keith, D., 2012. Geomechanical modeling for CO_2 storage in Nisku aquifer in Wabamun Lake area in Canada, International Journal of Greenhouse Gas Control, 10, 113–122

Haimson, B. and Fairhurst, C. 1969. Hydraulic Fracturing in Porous-Permeable Materials. Journal of Petroleum Technology**,** 811-817.

Hubbert, M. K. and Willis, D. G. 1957. Mechanics Of Hydraulic Fracturing. Petroleum Transactions, AIME, 210**,** 16.

Karimnezhad, M., Jalalifar, H., and Kamari, M., 2014. Investigation of caprock integrity for CO_2 sequestration in an oil reservoir using a numerical method, Journal of Natural Gas Science and Engineering, 21, 1127-1137.

Karypis, G., Kumar, V., 1998. A parallel algorithm for multilevel graph partitioning and sparse matrix ordering. Journal of Parallel and Distributed Computing 48, 71-85.

Karypis, G., Kumar, V., 1999. A fast and high quality multilevel scheme for partitioning irregular graphs. Siam J. Sci. Comput. 20 (1), 359-392.

Kim S. and Hosseini S. A., 2014. Geological CO_2 storage: Incorporation of pore-pressure/stress coupling and thermal effects to determine maximum sustainable pressure limit, Energy Procedia, 63, 3339 – 3346.

Kim, Y., Wan, J., Kneafsey, T. K., and Tokunaga, T. K., 2012. Dewetting of Silica Surfaces upon Reactions with Supercritical CO_2 and Brine: Pore-Scale Studies in Micromodels, Environ. Sci. Technol. 46, 4228−4235.

Lei, H., Xu, T., and Jin G., 2015. TOUGH2Biot – A simulator for coupled thermal–hydrodynamic–mechanical processes in subsurface flow systems: Application to CO_2 geological storage and geothermal development, Computers & Geosciences, 77, 8–19.

Levenberg, K., 1944. A method for the solution of certain nonlinear problems in least squares, Quart. Appl. Math., 2, 164–168.

Mandel, J., 1953. Consolidation des sols (etude mathematique). Geotechnique 3287–3299.

Marquardt, D.W., 1963. An algorithm for least squares estimation of nonlinear parameters, SIAM J. Appl. Math., 11, 431–441.

Martinez, M. J., Newell, P., Bishop, J. E., Turner, D. Z., 2013. Coupled multiphase flow and geomechanics model for analysis of joint reactivation during CO_2 sequestration operations, International Journal of Greenhouse Gas Control, 17, 148–160.

Mastrojannis, E.N., Keer, L.M., and Mura, T., 1980. Growth of planar cracks induced by hydraulic fracturing, International Journal of Numerical Methods in Engineering, 15, 41–54.

Mualem, Y., 1976. A new model for predicting the hydraulic conductivity of unsaturated porous media. Water Resource Res. 12 (3), 513-522.

Narashimhan, T. N., Witherspoon, P. A., 1976. An integrated finite difference method for analysis of fluid flow in porous media. Water Resources Res. 12, 57–64.

Pan P.-Z., Rutqvist J., Feng X. –T., Yan, Y., 2013. Modeling of caprock discontinuous fracturing during CO2 injection into a deep brine aquifer, International Journal of Greenhouse Gas Control, 19, 559–575.

Pruess, K., Oldenburg, C., and Moridis G. 1999. TOUGH2 User's Guide, Version 2.0. Report LBNL-43134, Lawrence Berkeley National Laboratory, Berkeley, California.

Rinaldi, A.P. and Rutqvist J. 2013. Modeling of deep fracture zone opening and transient ground surface uplift at KB-502 CO_2 injection well, In Salah, Algeria. International Journal of Greenhouse Gas Control, 12, pp. 155-167.

Rinaldi, A. P, Rutqvist, J., and Cappa, F., 2014. Geomechanical effects on CO_2 leakage through fault zones during large-scale underground injection, International Journal of Greenhouse Gas Control, 20, 117–131.

Rinaldi A.P., Rutqvist J., Finsterle S., and Liu H.H, 2017. Inverse modeling of ground surface uplift and pressure with iTOUGH-PEST and TOUGH-FLAC: The case of CO_2 injection at In Salah, Algeria (in press).

Rutqvist J., 2011. Status of the TOUGH-FLAC simulator and recent applications related to coupled fluid flow and crustal deformations. Computers and Geosciences, 37, 739–750.

Rutqvist, J., Birkholzer, J., Cappa, F., and Tsang, C.-F., 2007. Estimating maximum sustainable injection pressure during geological sequestration of CO_2 using coupled fluid flow and geomechanical fault-slip analysis, Energy Conversion and Management, 48, 1798–1807.

Rutqvist J., Rinaldi A.P., Cappa F., Jeanne P., Mazzoldi A., Urpi L., Guglielmi Y., Vilarrasa V., 2016. Fault activation and induced seismicity in geologic carbon storage - Lessons learned from recent modeling studies. Journal of Rock Mechanics and Geotechnical Engineering, 8, 775-966.

Rutqvist, J. and Tsang, C.F., 2002. A study of caprock hydromechanical changes associated with CO_2-injection into a brine formation. Environ. Geol. 42, pp. 296–305.

Rutqvist, J., Vasco, D.W., Myer L., 2010. Coupled reservoir-geomechanical analysis of CO_2 injection and ground deformations at In Salah Algeria. Int. J. of Greenhouse Gas Control 4, 225–230.

Seyedi, D. M., Ducellier A., and Vu M.N., 2011. ARMA 11-257: A two-scale model for simulating the hydromechanical behavior of faults during CO_2 geological storage operation, presentated at the 45th US Rock Mechanics / Geomechanics Symposium held in San Francisco, CA, June 26–29.

Schneider, C. A.; Rasband, W. S., and Eliceiri, K. W. (2012a). NIH Image to ImageJ: 25 years of image analysis, Nature methods 9(7): 671-675.

Schindelin, J.; Arganda-Carreras, I. & Frise, E. et al. (2012b). Fiji: an open-source platform for biological-image analysis, Nature methods 9(7): 676-682.

Timoshenko, S. and Goodier, J. N. 1951. Theory of Elasticity. New York, NY: McGraw-Hill Book Company, Inc.

Tokunaga, T. K., Wan, J., Jung, J.-W., Kim, T. W., Kim, Y., and Dong, W., 2013. Capillary pressure and saturation relations for supercritical CO_2 and brine in sand: High-pressure Pc(Sw) controller/meter measurements and capillary scaling predictions, Water Resources Research 49, 4566–4579.

Tuminaro, R.S., Heroux, M., Hutchinson, S.A., Shadid, J.N., 1999. Official Aztec user's guide version 2.1. Massively Parallel Computing Research Laboratory, Sandia National Laboratories, Albuquerque, NM.

Van Genuchten, M.Th., 1980. A closed-form equation for predicting the hydraulic conductivity of unsaturated soils. Soil Sci. Soc. 44, 892-898.

Vilarrasa, V., Bolster, D., Olivella, S., Carrera, J., 2010. Coupled hydromechanical modeling of CO_2 sequestration in deep saline aquifers, International Journal of Greenhouse Gas Control, 4, 910–919.

Vilarrasa, V. and Laloui, L., 2015. Potential fracture propagation into the caprock induced by cold CO_2 injection in normal faulting stress regimes, Geomechanics for Energy and the Environment 2, 22–31.

Wan, J., Kim, Y., and Tokunaga, T. K., 2014. Contact angle measurement ambiguity in supercritical CO_2–water–mineral systems: Mica as an example, International Journal of Greenhouse Gas Control 31, 128-137.

Wang, Y., Fu, H., Liang, T., Wang, X., Liu, Y., Peng, Y., Yang, L. and Tian, Z. 2015. Large-Scale Physical Simulation Experiment Research for Hydraulic Fracturing in Shale. SPE Middle East Oil & Gas Show and Conference. Manama, Bahrain: Society of Petroleum Engineers.

Wang, S. and Tokunaga, T. K., 2015. Capillary Pressure−Saturation Relations for Supercritical CO_2 and Brine in Limestone/Dolomite Sands: Implications for Geologic Carbon Sequestration in Carbonate Reservoirs, Environ. Sci. Technol. 49, 7208−7217.

Winterfeld P. H., Wu Y.-S., 2014. Simulation of CO_2 sequestration in brine aquifers with geomechanical coupling. In Computational Models for CO_2 Sequestration and Compressed Air Energy Storage, edited by J. Bundschuh and R. Al-Khoury, Chapter 8, pp. 275-303, New York, NY: CRC Press.

Yamamoto, S., Miyoshi, S., Sato, S, and Suzuki, K., 2013. Study on geomechanical stability of the aquifer-caprock system during CO_2 sequestration by coupled hydromechanical modelling. Energy Procedia 37, 3989-3996.

Yew, C. H., 1997. Mechanics of hydraulic fracturing, Gulf Publishing Company, Houston, TX.

Zhang, X., Lu, Y., Tang, J., Zhou, Z. and Liao, Y. 2017. Experimental study on fracture initiation and propagation in shale using supercritical carbon dioxide fracturing. Fuel, 190**,** 370-378.

Zoback, M. D., Rummel, F., Jung, R. and Raleigh, C. B. 1977. Laboratory hydraulic fracturing experiments in intact and pre-fractured rock. International Journal of Rock Mechanics and Mining Sciences & Geomechanics Abstracts, 14**,** 49-58.

Research Personnel

Dr. Yu-Shu Wu, PI, Colorado School of Mines
Dr. Philip H. Winterfeld, Co-PI, Colorado School of Mines
Dr. Timothy Kneafsey, Co-PI, Lawrence Berkeley National Laboratory
Dr. Jonny Rutqvist, Co-PI, Lawrence Berkeley National Laboratory
Dr. Lei Wang, Postdoc Researcher, Colorado School of Mines
Bowen Yao, Ph. D. Student Researcher, Colorado School of Mines

Publications

Wang, L., Yao, B., Xie, H., Kneafsey, T. J., Winterfeld, P. H., Yin, X., and Wu, Y. S. (2017). Experimental investigation of injection-induced fracturing during supercritical CO_2 sequestration. International Journal of Greenhouse Gas Control, 63, 107-117.

Wang, L., Yao, B., Xie, H., Winterfeld, P. H., Kneafsey, T. J., Yin, X., and Wu, Y. S. (2017). CO_2 injection-induced fracturing in naturally fractured shale rocks. Energy, 139, 1094-1110.

Winterfeld, P. H. and Wu Y.-S., 2015. Simulation of Coupled Thermal-Hydrological-Mechanical Phenomena in Porous and Fractured Media, SPE 173210, presented at the SPE Reservoir Simulation Symposium, Houston, Texas, February 23-25, 2015.

Winterfeld, P. H. and Wu Y.-S., 2015. A Coupled Flow and Geomechanics Simulator for CO2 Storage in Fractured Reservoirs, presented at the TOUGH Symposium 2015, Lawrence Berkeley National Laboratory, Berkeley, CA, September 28-30, 2015.

Winterfeld, P. H. and Wu Y.-S., 2015. Simulation of Coupled Thermal-Hydrological-Mechanical Phenomena in Porous Media, SPE Journal, December 2016, p. 1041-1049.

P. H. Winterfeld and Yu-S. Wu, 2017. Coupled Reservoir-Geomechanical Simulation of Caprock Failure and Fault Reactivation during CO2 Sequestration in Deep Saline Aquifers, SPE 182605-MS, presented at SPE Reservoir Simulation Conference, 20-22 February, 2017 in Montgomery, TX.

P. H. Winterfeld and Yu-S. Wu, 2018. Development of a Coupled Reservoir-Geomechanical Simulator for the Prediction of Caprock Fracturing and Fault Reactivation during CO_2 Sequestration in Deep Saline Aquifers. In *Hydraulic Fracture Modelling,* edited by Y.-S. Wu, Chapter 11, Cambridge, MA: Elsevier.

Yao, B. and Wang, L., 2018. Modeling of Cryogenic Fracturing Processes. In *Hydraulic Fracture Modelling,* edited by Y.-S. Wu, Chapter 12, Cambridge, MA: Elsevier.

Winterfeld, P. H. and Wu Y.-S., 2018. Simulation of Coupled Thermal-Hydrological-Mechanical Phenomena in Heterogeneous and Radial Systems, to be presented at TOUGH Symposium 2018, Berkeley, CA, October 8-10, 2018.